

Ph.D. Thesis
Doctor of Philosophy

 DTU Physics
Department of Physics

Computational Studies of Two-Dimensional Materials and Heterostructures

Anders Christian Riis-Jensen

Kongens Lyngby 2020



DTU Physics
Department of Physics
Technical University of Denmark

Fysikvej
Building 309
2800 Kongens Lyngby, Denmark
Phone +45 4525 3344
info@fysik.dtu.dk
www.fysik.dtu.dk

Summary

Since the exfoliation of graphene in 2004, 2D materials have offered an intriguing playground for researchers to study new quantum mechanical effects at the quantum scale in materials. Due to the atomically thin nature of 2D materials these structures exhibit a very low dielectric screening which leads to strong light-matter interaction and pronounced many-body effects. It has in recent years become possible to not only isolate single monolayers of 2D sheets, but also to stack the monolayers into so-called van der Waals heterostructures (vdWHs) which, as the name suggests, are layered monolayers only weakly interacting through the van der Waals force. The possibility to seamlessly freely stack and rotate the individual monolayers in vdWHs relative to each other in the lab, makes accurate *ab-initio* calculations unable to describe such multilayer systems and effective models are needed to calculate the electronic and optical properties of vdWHs.

In this thesis, entitled *Computational Studies of Two-Dimensional Materials and Heterostructures*, computational methods and models have been applied, developed, and implemented into the electronic structure code GPAW to overcome the computational difficulties when performing *ab-initio* calculations of vdWHs. The Bethe-Salpeter Equation (BSE) has been implemented with the previously developed Quantum Electrostatic Heterostructure (QEH) model to efficiently calculate exciton binding energies and absorption spectra for multilayer vdWHs and is found to accurately calculate the redshift of intralayer exciton energies in vdWHs. A feature shown not to be accurately described by the already existing Mott-Wannier equation. An appealing feature of the BSE-QEH implementation is that the computational requirement scales linearly with the number of layers in the vdWH. The fact that excitonic states have previously been described accurately by the Mott-Wannier model shows the hydrogen-like nature of the exciton state. In this thesis it is shown that this picture is not complete in the presence of a dielectric substrate, where the system enters a substrate-dominated screening regime. This new dielectric screening regime of exciton physics is explored, where the exciton series becomes underbound rather than overbound as in the usual 2D excitonic hydrogen model. Furthermore, To help the scientific community in the calculation of electronic and optical properties of vdWHs, an efficient scheme has been developed to calculate the interlayer hybridisation and charge transfer in large vdWHs. The method corrects the (possibly) wrong description of the interlayer hybridisation offered by non-self-consistent state-of-the-art *ab-initio* methods such as the G0W0 approximation.

By combining the developed methods with *ab-initio* calculations we benchmark to

what accuracy exciton energies can be calculated in comparison to experimental measurements in vdWHs by explicitly calculating the effect of twist-angle and substrate effects on the exciton energies. Furthermore we show that the inherent non-locality of the dielectric screening in 2D can be used to accurately control quasi-particle energies in semiconductors by placing the 2D semiconductor on a gated graphene layer. A direct example of the potential in using vdWHs for applications such as photodetectors, pn-junctions, solar cells, or single-photon emission devices is shown by proving the existence of a vdWH with strong low-energy exciton states as a low-energy infrared photodetector.

In the final chapter is presented a thorough study of the properties of the new class of 2D Janus monolayers. This class of 2D monolayers exhibit an intrinsic out-of-plane dipole moment and it is shown how both the electronic and optical properties of vdWHs can be accurately manipulated and controlled by use of this class of structures. Finally, a new paradigm of materials science is introduced, by proving the existence of and examining self-intercalated bilayers: 2D bilayers with self-intercalated single-atoms. It is shown that the self-intercalation process in fact leads to stable self-intercalated structures, for a large set of host bilayers and that the self-intercalation significantly alters the electronic properties and magnetic phase of the bilayer.

Resume

Siden den første isolering af grafen i 2004, har 2D materialer været en ideel platform for at studere nye kvantemekaniske effekter på kvanteskalaen i materialer. På grund af deres atomer tynde karakter, har 2D materialer en meget lav dielektrisk afskærmning, hvilket giver en stærk lys-materiale interaktion og udtalte excitoniske effekter. Det har i de foregående år vist sig muligt, ikke bare at isolere enkelte 2D lag, men også at stakke lagene til såkaldte van der Waals heterostrukturer (vdWH), som er lagdelte monolag der kun interagerer svagt gennem van der Waals kraften. Da det er muligt tilsydenladende frit at stakke og rotere lagene relativt til hinanden, er det næsten umuligt korrekt at beskrive og beregne egenskaberne af disse strukturer med *ab-initio* metoder og effektive modeller som for eksempel den tidligere udviklede Quantum Electrostatic Heterostructure (QEH) model er nødvendige for at beregne de elektroniske og optiske egenskaber.

I denne afhandling, med titlen *Computational Studies of Two-Dimensional Materials and Heterostructures*, er beregningsmetoder og -modeller udviklet og implementeret i elektronstrukturkoden GPAW, til at overkomme de beregningsmæssige udfordringer når man udfører *ab-initio* beregninger for vdWH. I denne afhandling er Bethe-Salpeter Ligningen (BSE) blevet implementeret med den tidligere udviklede QEH model til effektivt at beregne exciton bindingsenergi, absorption spektra, og viser sig korrekt at beskrive rødforskydningen af excitonenergi i vdWH. En egenskab som ikke er præcist beskrevet af den allerede eksisterende Mott-Wannier ligning. En tiltrækkende egenskab af BSE-QEH implementering er at de beregningsmæssige krav skalerer lineært med antallet af monolag i vdWH. Siden excitoniske tilstande har vist sig at være velbeskrevet af Mott-Wannier modellen viser dette den hydrogen-lignende karakter af excitontilstanden. Vi viser her at det nuværende hydrogenbillede ikke er komplet i nærheden af et skjærmende dielektrisk substrat og undersøger dette nye substratdominerede regime af excitonfysik, hvor excitonserien bliver underbundet istedet for overbundet som i den sædvanlige excitoniske hydrogenmodel. For at hjælpe det videnskabelige miljø med at udføre præcise beregninger af de elektroniske og optiske egenskaber af vdWH, har vi udviklet en model til effektivt at beregne interlagshybridiseringen og -ladningsoverførslen i vdWH. Metoden korrigerer den (muligvis) forkerte beskrivelse af interlagshybridiseringen ved brug af ikke-selvkonsistente *ab-initio* metoder som for eksempel G0W0 approksimationen.

Ved at kombinere de udviklede metoder med *ab-initio* beregninger benchmarker vi præcisionen af beregnede excitonenergi der kan opnås når man sammenligner disse med eksperimentielt målte excitonenergi i vdWH. Vi viser desuden eksplicit afhængigheden af både rotationsvinklen mellem lagene samt tilstedeværelsen af et dielektrisk substrat på

excitonenergiene. Derudover viser vi hvordan kvasipartikelenergiene i halvledere kan kontrolleres og manipuleres ved at udnytte den ikke-lokale karakter af den dielektriske funktion. Dette bliver vist ved eksempel ved at placere en halvleder på et grafen lag. Et direkte eksempel af potentialet for anvendelse af vdWHs for eksempel fotodetektore, pn-overgange, solceller og/eller enkelt-foton-udsendere er vist ved at bevise eksistensen af en vdWH med stærke lavenergi excitontilstande som en lavenergi infrarød fotodetektor.

I det sidste kapitel præsenteres et grunddigt studie af egenskaberne af en ny klasse af 2D Janus monolag. Denne klasse af 2D monolag har et intrinsisk dipolmoment i retningen ud af planen og det påvises hvordan både de elektroniske og optiske egenskaber af vdWHs kan manipuleres og kontrolleres præcist ved anvendelse af denne klasse af strukturer. Endeligt introduceres et nyt paradigme af materialevidenskab, ved at påvise eksistensen af og undersøge selv-indskudte bilag: 2D bilag med selv-indskudte enkeltatomer. Det vises at selv-indskydelsesprocessen leder til stabile selv-indskudte strukturer, for et stort sæt af bilag og at selv-indskydelsesprocessen signifikant kan manipulere de elektroniske egenskaber og den magnetiske fase af bilagene.

Preface

This thesis is submitted in candidacy for the Ph.D degree in physics from the Technical University of Denmark (DTU). The work enclosed in this thesis has been carried out at the section for Computational Atomic-scale Materials Design at the Institute of Physics. The study was carried out in the period from July 2017 to July 2020 under the supervision of professor Kristian S. Thygesen and co-supervisor professor Karsten W. Jacobsen. The Ph.D project was funded by an internal scholarship from DTU.

"The agreement of this law with nature will be better seen by the repetition of experiments than by a long explanation."

- Hans Christian Ørsted

Kongens Lyngby, July 14, 2020

A handwritten signature in black ink, appearing to read 'AC Riis-Jensen', written in a cursive style.

Anders Christian Riis-Jensen

Acknowledgements

I would like to show my gratitude to Kristian for giving me the possibility to become part of a world-class scientific research group. You have guided me all the way through from my very first scientific publication to finalising my Ph.D thesis now and taught me a lot about the scientific world and for that I am very thankful. I will also give a special thanks to Karsten for always having your door open and taking your time to help me understand a broad range of physics. Your enthusiasm to always learn more and your broad deep knowledge about many aspects of physics have truly inspired me.

A special thanks also goes to Jens-Jørgen. The help you supply to all students and employees of CAMD cannot be underestimated. Without your knowledge I do not believe CAMD could produce research results at the very high level it does and you should know that we all appreciate your kindness, help, and knowledge about GPAW and ASE everyday. Just 10 min of your help can sometimes save us days of work! I would also like to thank Thomas for our valuable discussions about the physics of excitons and for helping me understanding the implementation flowchart of many aspects of GPAW. I do know I have come by your door and interrupted your lunch many times with questions, but it just shows your great knowledge about the practical part of using and implementing code in GPAW. And Jacob, for always bringing good mood into the daily life in the hallways and the group meetings, but especially also for your sharp and accurate comments about my projects at the group meetings. Your opinion and observations have helped me more than you think.

Ole, thank you very much for all your efforts in keeping Niflheim up and running and your help with all the technical aspects of my work. You always come with fast, accurate, and professional help and I can for sure say that many parts of my studies have been a lot more efficient because of your effort than they could have been. I will also give a big thanks to Marianne and Bettina for taking care of all the administrative work, something I must admit have not always been my strongest side, but you have really helped me when I was late on deadlines or did not understand the system.

To all the great colleagues I have had the last three years: Mohnish, Morten, Sten, Nicki, Thorsten, Per, Mikkel, Korina, Daniele, Line, Peter, Mark, Douglas, Henrik, Suranjan, Thorbjørn, Estefanía, Asbjørn, Luca, Fabian, Sami, Sajid, Nikolaj, Mads, Matthew, Simone, Hadeel, and Alireza. Thank you. You have all in each your own way brought a fantastic working environment into CAMD and every day I have been looking

forward to showing up at work and laugh and cry with you all. I can only hope that I in the future will get nearly as good colleagues and friends as you have been!

Til sidst vil jeg gerne give et kæmpe tak til min dejlige familie: min fantastise søster, mor og far og ikke mindst min vidunderlige kæreste. For al jeres støtte gennem svære tider, gennem frustrationer og for at lade fysik tage så meget af min tid. Jeg glæder mig enormt til at opleve en masse mange flere ting med jer de næste år og se hvor vores rejse går hen. Jeg elsker jer alle.

List of Papers

Paper I

Electrically Controlled Dielectric Band Gap Engineering in a Two-Dimensional Semiconductor

A. C. Riis-Jensen, J. Lu, and K. S. Thygesen

PRB Rapid Communication, **101**, 121110(R) (2020)

Editor's suggestion

Paper II

Anomalous Non-Hydrogenic Exciton Series in 2D Materials on High- κ Dielectric Substrates

A. C. Riis-Jensen, M. N. Gjerding, S. Russo, and K. S. Thygesen

Under review

Paper III

Functional Dielectric Screening for Potential Well Arrays of Excitons in 2D Materials

N. Peimyoo, H.-Y. Wu, J. Escolar, A. De Sanctis, G. Prando, F. Vollmer, F. Withers, K. S. Thygesen, A. C. Riis-Jensen, M. F. Craciun, and S. Russo

Under review

Paper IV

High Oscillator Strength Interlayer Excitons in 2D Heterostructures for Mid-IR Photodetection

S. Lukman, L. Ding, L. Xu, Y. Tao, A. C. Riis-Jensen, G. Zhang, Q. Steve Wu, M. Yang, S. Luo, C. Hsu, L. Yao, G. Liang, H. Lin, Y.-W. Zhang, K. S. Thygesen, Q. Jie Wang, Y. Feng, J. Teng

Nature Nanotechnology, <https://doi.org/10.1038/s41565-020-0717-2> (2020)

Paper V

Excitons and Band Alignment in 2D van der Waals Heterostructures: *Ab-Initio* Calculations versus Experiments

A. C. Riis-Jensen and K. S. Thygesen

Under preparation

Paper VI

The Computational 2D Materials Database: High-Throughput Modeling and Discovery of Atomically Thin Crystals

S. Hastrup, M. Strange, M. Pandey, T. Deilmann, P. S. Schmidt, N. F. Hinsche, M. N. Gjerding, D. Torelli, P. M. Larsen, [A. C. Riis-Jensen](#), J. Gath, K. W. Jacobsen, J. J. Mortensen, T. Olsen, and K. S. Thygesen
2D Mater., **5**, 042002 (2018)

Paper VII

Efficient Charge Separation in 2D Janus van der Waals Structures with Built-in Electric Fields and Intrinsic p–n Doping

[A. C. Riis-Jensen](#), M. Pandey, and K. S. Thygesen
J. Phys. Chem. C, **122**, 43 (2018)

Paper VIII

Classifying the Electronic and Optical Properties of Janus Monolayers

[A. C. Riis-Jensen](#), T. Deilmann, T. Olsen, and K. S. Thygesen
ACS Nano, **13**, 11, 13354-13364 (2019)

Paper IX

Engineering Atomically Sharp Potential Steps and Band Alignment at Solid Interfaces using 2D Janus Layers

[A. C. Riis-Jensen](#), S. Manti, and K. S. Thygesen
J. Phys. Chem. C, **124**, 17 (2020)

Paper X

Engineering Covalently Bonded 2D Layered Materials by Self-Intercalation

X. Zhao, P. Song, C. Wang, [A. C. Riis-Jensen](#), W. Fu, Y. Deng, D. Wan, L. Kang, S. Ning, J. Dan, T. Venkatesan, Z. Liu, W. Zhou, K. S. Thygesen, X. Luo, S. J. Pennycook, and K. P. Loh
Nature, **581**, 171–177 (2020)

Contents

Summary	i
Resume	iii
Preface	v
Acknowledgements	vii
List of Papers	ix
Contents	xi
1 Introduction	1
1.1 Outline	3
2 It is All About the Electrons	5
2.1 The Many-Body Problem	5
2.2 Density Functional Theory	7
2.3 The Projector Augmented Wave Function Method: Implementation in GPAW and Spin-Orbit Interaction	11
2.4 2D Materials, van der Waals Heterostructures, and van der Waals inter- actions	16
3 Electronic and Optical Properties of 2D Materials and van der Waals Heterostructures	21
3.1 Dielectric Response Theory and Dielectric Screening in 2D	23
3.2 Many-Body Perturbation Theory, the GW Approximation, and Vertex Correction	30
3.3 The Quantum Electrostatic Heterostructure Model	37
3.4 Interlayer Orbital Hybridisation	40
3.5 Tunable Dielectric Screening in a 2D Semiconductor	42
3.6 Excitons, The Mott-Wannier Equation, and the Bethe-Salpeter Equation	46
3.7 Implementation of the Bethe-Salpeter Equation with the Quantum Elec- trostatic Heterostructure Model	54
3.8 Screened Rydberg Series in 2D Materials	60
3.9 Interlayer Exciton in a 2D Heterostructure for IR Photodetection	67

4	Exciton Energies: Disentangling Dielectric Screening, Orbital Hybridisation, Twist-Angle, and Substrate Effects	73
4.1	Calculation of Interlayer Hybridisation Effects in van der Waals Heterostructures	74
4.2	Benchmarking <i>Ab-Initio</i> Calculated Exciton Energies in vdWHs against Experiments	82
5	The Computational 2D Materials Database	91
5.1	The C2DB	91
5.2	Photovoltaic Potential of Novel 2D Semiconductors	95
6	2D Janus Monolayers and Self-Intercalated Bilayers	99
6.1	Intrinsic Out-of-Plane Dipole Moment of 2D Janus Monolayers	100
6.2	Manipulation of Interface Band Line-Up and Schottky-Barriers	104
6.3	Electronic and Optical Properties of 2D Janus Monolayers	107
6.4	Self-Intercalation of Single Atoms in 2D Bilayers	113
7	Conclusion and Outlook	119
8	Papers	123
8.1	Paper I	123
8.2	Paper II	130
8.3	Paper III	136
8.4	Paper IV	149
8.5	Paper V	160
8.6	Paper VI	172
8.7	Paper VII	209
8.8	Paper VIII	217
8.9	Paper IX	234
8.10	Paper X	244
A	Abbreviations	255
B	Calculation of the Electronic Density in GPAW	257
C	Derivation of a State-Dependent Scissors-Operator within the Plane-Wave Description	259
D	Effect of the Tamm-Dancoff Approximation on the BSE Absorption Spectra of 2D TMD Monolayers	261
E	Quasi-Particle Ionisation Potentials and Electron Affinities from GLLB-SC and PBE	263
	Bibliography	265

CHAPTER 1

Introduction

Physics is the study of why things happen. It is the result of people staring into nothing observing a sycamore seed helicoptering its way down to Earth or a glass of beer falling to the ground in a bar, asking "why did that happen?" (the latter probably has a more straightforward answer than the first). While it is rather easy to develop a specific explanation as to the origin and nature of each observation we make, such a large set of specific explanations, let us call them theories, will in general contradict each other in the areas where the individual observations overlap. On the other hand, it is immensely difficult to develop a complete theory that describes all that has happened and all that will happen for a larger collection of observations. The fact that physics in many aspects has done this over hundreds of years is an astonishing achievement. Physics can to some extent be viewed as divided into several different "branches of physics" each exploring their own set of observations. However, it is intriguing that the theories and equations used in each branch of physics, let that be the study of fluid mechanics, general relativity, electrostatics, or quantum mechanics to mention a few, visually appear very similar. And not only do they look similar, the more one thinks about it, the more one realises that they indeed are very similar and merely differ by the length scale of the observations they are applied to and of the symmetries the mind of the physicists can find in a certain observation. To study one branch of physics in detail it can therefore be extremely beneficial to study other branches of physics to gain ideas and to understand specific observations. Because of the very high similarity between the theories and equations of different branches of physics, it is therefore fascinating how much of the "physics" is going on inside our head when we apply the equations to very different observations. Physics use mathematics to write down the physical theories and laws in the form of equations. Mathematics and physics differ in the way that while mathematics consists of generalised abstract theories, physics (the physicists) always know what it is (they are) talking about: the physical theories and laws are centered around objects and observations, which defines the above mentioned length scales.

In this thesis, the objects we will study are two-dimensional (2D) materials: atomically thin materials that were first discovered in 2004 by Geim and Novoselov [89]; a discovery that later granted them the Nobel prize in physics. The length scale of the objects and observations we will be concerned with will therefore be the atomic scale and the branch of physics we will apply will mainly be quantum mechanics. Quantum mechanics governs the peculiar effects pronounced at the atomic length scale such as the Heisenberg's uncertainty principle and discretisation of allowed energies. We will study the electronic and optical properties of 2D materials and stacks of 2D materials,

the so-called van der Waals Heterostructures (vdWHs) [98, 50, 27], which is the study of *what happens* when photons interact with matter. The peculiar optical properties of these structures have been studied extensively in the past years, where the properties have been shown to be very sensitive to the layer thickness [82, 114], which is one of the very reasons for the vast interest in vdWHs. Previous state-of-the-art research includes proving the existence of strongly bound states inside the band gap [101, 99, 127, 87, 81, 120, 18, 17], strong sensibility to the surrounding electrostatic environment [105, 60, 117, 10, 115], for instance electric fields [57] or mechanical strain [23, 14]. It is evident that 2D materials and vdWHs possess a large potential for (opto-)electronic devices, for which their application is currently being investigated. An outline of the content of the research and results obtained in this thesis can be found below. As we will already see in chapter 2, the quantum mechanical problem of 2D materials (and other fields of materials science) is an incredible difficult problem to solve both analytically and computationally. The complexity arises from the huge number of particles that are involved in single observations, the difficulties especially come from the electrons and we will see that the key to model the properties of materials is all about the electrons. As such efficient computational methods are necessary to even come close to a proper description of these materials. This thesis sets out to apply and develop such computational methods to investigate the electronic and optical properties of 2D materials and vdWHs.

Since the combined theory of physical laws necessary to understand and describe the whole world of quantum mechanics in the light of materials science, itself would take up several books, I have chosen to only go through the theory necessary to understand the presented methods and results in this thesis and this will be derived and/or discussed as it is needed. Furthermore the thesis contains several results, explanations, and ideas not presented in the included papers. The scientific study results in a considerable time spend in understanding problems and theory, that are not necessarily used in relation to any publications and thus not written down anywhere, but the back-head of the mind. However, the obtained knowledge still comes with a responsibility. These results, understandings, or ideas might be useful and save time for future students and some of them are therefore included in the main text when appropriate.

On a personal level I by far do not know nor understand everything in physics, however studying physics for many years now, allows me to understand, a little better, some of the phenomena we encounter in our everyday life and that is a gift I will bring with me for the rest of my life. I find myself privileged to do my doctorate degree in a field I find so incredibly interesting. While the thesis presents the results obtained by the author throughout the Ph.D study, the remaining part of the thesis is written in "we-form". This is because modern science is a highly collaborative field and the results obtained in this thesis, and in general in most scientific papers and reports in the literature nowadays, are a result of combining the skills and knowledge of several individuals.

1.1 Outline

The outline of the thesis is the following:

Chapter 2 starts out by examining the complexity of the quantum mechanical many-body problem to understand the need of effective methods for the study of the electronic and optical properties of materials. The theory of density functional theory is presented as an efficient formalism to overcome this complexity and its implementation flowchart in GPAW is outlined. Finally, the foundation of this thesis, namely the experimental realisation of 2D materials and vdWHs, is discussed where we will see that essentially any combination of 2D monolayers can be stacked together to form vdWHs.

Chapter 3 starts out with describing the theory of the dielectric response of a material to an external perturbation. We will study the fundamental difference between dielectric screening in 2D and 3D and the difficulties with accurately describing excited state properties of vdWHs are discussed. The many-body *ab-initio* formalism GW is introduced and derived as a mean of calculating quasi-particle states in materials. By combining the previously developed QEH model and the GW approximation we will compute quasi-particle energies in a vdWHs and show how the non-local nature of the dielectric screening, presented in the beginning of chapter 3, can be utilised to tune the electronic properties of a 2D semiconductor without changing the wave function nor hybridisation pattern of the semiconductor (paper I). Excitonic effects are then introduced and the Mott-Wannier equation and the Bethe-Salpeter equations (BSE) will be derived and presented as methods to calculate exciton energies. After this, the development and implementation of the BSE model with the QEH model is presented and shown to accurately calculate exciton binding energies in vdWHs and vdWH absorption spectra to be used in chapter 4. Finally, we will see that the current understanding of the 2D excitonic Rydberg series is not complete: we will study how the excitonic Rydberg series in 2D semiconductors can change qualitatively when placed on a strongly screening substrate (paper II and III). At the end of the chapter, we will show the existence of an excitonic type-II semiconducting vdWH as an efficient low-energy infrared photodetector (paper IV).

Chapter 4 will discuss the effect of interlayer orbital hybridisation on the quasi-particle and exciton energies in vdWHs, an effect that is in general not well described by most conventional *ab-initio* many-body methods. In this chapter we present and implement a method to correctly calculate the interlayer orbital hybridisation and interlayer charge transfer in vdWHs and apply it to calculate exciton energies in vdWHs. Furthermore, we will see that it is possible to accurately calculate (and isolate) the contribution from the interlayer hybridisation in the renormalisation of exciton energies in vdWHs, and finally show how this renormalisation in general can be disentangled into its three components: substrate dielectric screening, interlayer dielectric screening, and interlayer orbital hybridisation and charge transfer effects. This leads us to a benchmarking study

of how accurately exciton energies can be computed *ab-initio* relative to experimental observations (paper V).

Chapter 5 presents the Computational 2D Materials Database (C2DB) and the main components of the workflow that has been developed to carry out high-throughput materials discovery and large-scale calculation of materials properties (paper VI). A recipe of how the calculated properties in the database can be utilised to calculate the photovoltaic potential of 2D semiconductors is presented.

Chapter 6 studies the peculiar intrinsic properties of the new class of 2D Janus structures. We will classify the properties of this new class and show how these properties can be used to manipulate the electronic and optical properties of vdWHs (paper VII, VIII, and IX). In the last part of this chapter we will consider a new method for manipulating and achieving new and interesting properties of vdWHs, namely the process self-intercalation of single atoms in 2D bilayers which introduces a new paradigm of low-dimensional materials science. We will prove that the self-intercalation process leads to a new stable phase for a wide range of bilayers and the self-intercalation process can lead to the development of ferromagnetic order (paper X).

Chapter 7 discusses and puts the main results in the thesis in an overall perspective and concludes the thesis with an outlook.

Chapter 8 includes the papers of which the results are presented in the thesis.

CHAPTER 2

It is All About the Electrons

Given the many decades since the development of the theory of quantum mechanics and the fact that physicists spent years to understand this complex theory, it is intriguing that only few ideal problems can be solved analytically. The difficulty mainly arises from the enormous number of particles present in the minimal description of any realistic quantum system which makes only few many-body problems possible to be solved exact even numerically. In section 2.1 we will discuss the quantum mechanical many-body problem in greater detail and in section 2.2 present Density Functional Theory (DFT) which is a widely used formalism in quantum mechanical materials science to calculate ground-state properties of materials. It overcomes the complexity of the many-body problem by working with the electron density as the main parameter of interest instead of the position of all individual particles. This greatly simplifies the computational cost for solving many quantum mechanical problems, but also lacks accuracy in terms of some electronic properties in 2D materials and the need for more advanced methods is required. These will be presented in chapter 3, however as we will see, such many-body theories are based on the single-particle description provided by DFT and it is therefore advantageous to study the theory of DFT first. The implementation flowchart of the DFT formalism in GPAW [85] is outlined in section 2.3. Finally in the last section of chapter 2 we will discuss the experimental realisation of 2D materials and vdWHs.

2.1 The Many-Body Problem

To determine the allowed energies of any time-independent quantum mechanical problem, one starts out by writing down the time-independent Schrödinger's equation:

$$\hat{H}\Psi(\mathbf{r}) = E_n\Psi(\mathbf{r}) \quad (2.1)$$

where $\Psi(\mathbf{r})$ is the total wave function, E_n are the allowed energy levels, where n uniquely defines a quantum state, and \hat{H} is the Hamiltonian of the problem containing all possible interactions and energy contributions to E_n . We note already here that for the arguments in this chapter it suffices to consider the time-independent problem. Since Ψ is given by the particles in the system of consideration the allowed values of E_n are determined by the interactions included in the Hamiltonian. If one is interested in for instance the electronic or thermal properties of a material, let that be a bulk crystal, a 2D material, a nanorod or -tube, or a molecule, the governing interactions and terms in \hat{H} defining E_n are the Coulomb interactions between all charged particles and the kinetic energy of

all particles. Dividing the Coulomb interaction into electron-electron, electron-nucleus, and nucleus-nucleus interactions, \hat{H} reads:

$$\hat{H} = -\sum_i \frac{\nabla_i^2}{2} - \sum_i \frac{\nabla_i^2}{2M} + \frac{1}{2} \sum_{i \neq j} \frac{1}{|\mathbf{r}_i - \mathbf{r}_j|} + \frac{1}{2} \sum_{i \neq j} \frac{Z_i Z_j}{|\mathbf{R}_i - \mathbf{R}_j|} - \sum_{i,j} \frac{Z_j}{|\mathbf{r}_i - \mathbf{R}_j|} \quad (2.2)$$

where ∇_i is the real-space coordinate derivative in the electron and nuclei kinetic energy for particle i , M is the nuclei mass, \mathbf{r}_i (\mathbf{R}_i) is the real-space coordinate of electron (nuclei) i , Z_i is the charge of nuclei i , and the factor of a half on the Coulomb terms accounts for double counting. We note this is true for a non-radioactive material such that strong force interactions within the nuclei can be neglected.

Analytical solutions for eq. 2.1 with the Hamiltonian in eq. 2.2 exist for single electron systems (*i.e.* the hydrogen atoms and ionised heavier atoms) and numerical solutions can be found for only few configurations containing the very lightest atoms in the periodic system. However, since materials are not made up of a few single atoms, but bound collections of many atoms, further approximations are needed to obtain solutions for eq. 2.1 for realistic interesting systems. The problem comes from the fact that the Coulomb interaction has to be evaluated between any two charged particles, and that each particle has its own spatial coordinate dependence. We will already at this point apply a quite significant approximation known as the Born-Oppenheimer approximation [11], which is applied in all calculations in this study. The support for already employing the Born-Oppenheimer approximation at this point in our presentation of electronic structure theory calculations is that this approximation is widely used in most of computational materials and molecular science. The approach is to assume that the electronic properties is mainly governed by the shape and energy of the electronic orbitals and that the nuclei merely contribute with a constant background potential. To be precise, since the mass of the nuclei is much larger than the mass of the electrons we assume that the motion of the nuclei is confined to a much smaller region of space than the motion of the electrons and move significantly slower. First of all this means that the kinetic energy of the nuclei is much smaller than that of the electrons: $\sum_i \frac{\nabla_i^2}{2} \gg \sum_i \frac{\nabla_i^2}{2M}$. Second, if we let $\bar{\mathbf{r}}_k$ and $\bar{\mathbf{R}}_l$ be the mean position of electron k and nucleus l and let $\delta \mathbf{r}_k$ and $\delta \mathbf{R}_l$ be the standard deviation of their spatial positions the assumption above corresponds to $\delta \mathbf{r}_k \gg \delta \mathbf{R}_l$ for all k, l . Assuming the real-space coordinate system to be 1 dimensional for simplicity and writing the real space position as: $r_i = \bar{r}_i + \delta r_i$ the electron-electron Coulomb interaction can be Taylor expanded about $\frac{\delta r_i - \delta r_j}{|\bar{r}_i - \bar{r}_j|}$ to obtain:

$$\frac{1}{|r_i - r_j|} \approx \frac{1}{|\bar{r}_i - \bar{r}_j|} - \frac{\delta r_i - \delta r_j}{|\bar{r}_i - \bar{r}_j|^2}. \quad (2.3)$$

Similarly for the electron-nucleus and nucleus-nucleus interactions we get:

$$\frac{1}{|r_i - R_j|} \approx \frac{1}{|\bar{r}_i - \bar{R}_j|} - \frac{\delta r_i - \delta R_j}{|\bar{r}_i - \bar{R}_j|^2} \quad (2.4)$$

$$\frac{1}{|R_i - R_j|} \approx \frac{1}{|\bar{R}_i - \bar{R}_j|} - \frac{\delta R_i - \delta R_j}{|\bar{R}_i - \bar{R}_j|^2} \quad (2.5)$$

respectively. In all three expressions the first term on the right hand side is constant by definition. For a chemical bond the mean electron-electron, electron-nucleus, and nucleus-nucleus distances all attain similarly values (to within the same order of magnitude). However, under the assumption that $\delta r_i \gg \delta R_j$ we immediately get that: $|\delta R_i - \delta R_j| \ll |\delta r_i - \delta r_j| < |\delta r_i - \delta R_j|$, and the nucleus-nucleus Coulomb interaction can consequently be assumed to attain a constant value proportional to $\frac{1}{|R_i - R_j|}$ for each nucleus-nucleus pair. This approximation also means that the electronic and nuclei part of the total wave function can be decoupled and that the total wave function can instead be written as a product of the electronic wave function ($\psi^{\text{elec}}(\mathbf{r})$) and the nuclear wave function ($\Phi^{\text{nuc}}(\mathbf{R})$): $\Psi(\mathbf{r}) = \psi^{\text{elec}}(\mathbf{r})\Phi^{\text{nuc}}(\mathbf{R})$. Assuming the nucleus-nucleus interaction to be constant and neglecting the kinetic energy of the nuclei is the foundation of the Born-Oppenheimer approximation. In this approximation the Hamiltonian reads:

$$\hat{H} = -\sum_i \frac{\nabla_i^2}{2} + \frac{1}{2} \sum_{i \neq j} \frac{1}{|\mathbf{r}_i - \mathbf{r}_j|} - \sum_{i,j} \frac{Z_j}{|\mathbf{r}_i - \bar{\mathbf{R}}_j|} + \hat{V}^{\text{n-n}}. \quad (2.6)$$

In practice, the constant contribution from the nucleus-nucleus Coulomb interaction can be inserted as an effective field in the electron-nucleus Coulomb interaction or added as an extra constant term ($\hat{V}^{\text{n-n}}$). While this is a great simplification of the Hamiltonian in eq. 2.2 it is still computationally unsolvable for most realistic systems due to the double sums in the electron-electron and electron-nucleus Coulomb interactions. In the next section we will present the DFT formalism which effectively overcomes the double sums by taking the electronic density as the main parameter instead of the position of each single particle. The Born-Oppenheimer approximation breaks down when there is only a small energy difference between the total ground-state energy and the total energy of the second lowest solution to the Schrödinger equation. In this case, the wave function can undergo a rapid spatial change of shape for only small displacements of the nuclei, and as such the static picture of the nuclei positions is no longer a good approximation.

2.2 Density Functional Theory

Considering the eigenvalue problem of eq. 2.1 with the Hamiltonian in eq. 2.6, the expectation value of the total energy is given as:

$$E = \langle \Psi(\mathbf{r}) | \hat{H} | \Psi(\mathbf{r}) \rangle. \quad (2.7)$$

As mentioned above, evaluating this expression is difficult (in practice impossible for most systems) due to three main reasons: 1) the total wave function is a complex parameter to evaluate and store numerically, 2) evaluating the double sum in the electron-electron Coulomb interaction, and 3) evaluating the double sum in the electron-nucleus Coulomb interaction. We will in the following outline how each of these difficulties is overcome within the DFT approximation.

Even though we showed in the previous section that the total wave function can be decoupled into a product of an electronic and a nuclear wave function, and one therefore only has to evaluate the inner product with the Hamiltonian with the electronic wave function (including the nuclei contribution effectively through the electron-nucleus interaction), a further approximation is normally applied. We write the electronic wave function as a Slater determinant [113] of non-interacting single-particle electron wave functions:

$$\psi^{\text{elec}}(\mathbf{r}) = \frac{1}{\sqrt{N!}} \det\{\phi_1(\mathbf{r}_1), \phi_2(\mathbf{r}_2), \dots, \phi_N(\mathbf{r}_N)\} \quad (2.8)$$

for an N -electron wave function where $\phi_i(\mathbf{r}_i)$ is the non-interacting wave function for the single electron i . This expression for the electronic wave function is anti-symmetric by construction and fulfills the Pauli exclusion principle. The simplification of the total electronic wave function into a sum of products of single-particle electronic states already makes the evaluation of the kinetic energy term straightforward.

To simplify the electron-nucleus interaction term, instead of evaluating the Coulomb interaction between each nucleus and each electron, we model the nuclei contribution to the energy as an external effective background potential, $v_{\text{ext}}(\mathbf{r})$. This could in principle be applied to all individual single-particle electron states reducing the term to a single summation loop, however it turns out that it is convenient to introduce the definition of the electronic density $n(\mathbf{r})$ defined from the single-particle wave functions:

$$n(\mathbf{r}) = |\psi^{\text{elec}}(\mathbf{r})|^2 = \sum_i^N |\phi_i(\mathbf{r})|^2, \quad (2.9)$$

constructed to equal the true many-body electronic density. The usefulness of the electronic density comes from the existence of the *first Hohenberg-Kohn theorem* [53], which states that there exists a unique bijective mapping between the external potential and the ground-state electron density of the many-body interacting system. We denote the ground-state electronic density $n_0(\mathbf{r})$, and since the single-particle electronic density in eq. 2.9 is constructed to equal the true many-body electronic density, the Hohenberg-Kohn theorem applies. The main parameter of interest is thus the electronic ground-state density, calculated from the Slater determinant of the non-interacting single-particle ground-state wave functions. With the Hohenberg-Kohn theorem in our hands, to find the ground-state energy, we can rephrase the original ground-state energy problem:

$$E = \langle \Psi(\mathbf{r}) | \hat{H} | \Psi(\mathbf{r}) \rangle = \langle \Psi(\mathbf{r}) | \hat{T} + \hat{v}^{\text{e-e}} + \hat{v}^{\text{e-n}} | \Psi(\mathbf{r}) \rangle \quad (2.10)$$

where \hat{T} , and $\hat{v}^{\text{e-e}}$ and $\hat{v}^{\text{e-n}}$ are the kinetic energy, electron-electron, and electron-nucleus Coulomb interaction operators, into an effective problem defined by the non-interacting ground-state electronic density by letting the external potential act on the ground-state density:

$$E \rightarrow E[n_0] = F[n_0] + \int d\mathbf{r} n_0(\mathbf{r}) v_{\text{ext}}(\mathbf{r}) \quad (2.11)$$

where $F[n_0] = \langle \Psi[n_0] | T + v^{\text{e-e}} | \Psi[n_0] \rangle$ is a universal functional. By the *second Hohenberg-Kohn theorem* the energy $E[n_0]$ is known to be smaller than the energy obtained from

any other trial density, $n' \neq n_0$: $E[n_0] < E[n']$ and thus it is closer to the true ground-state energy of the many-body interacting system: $E^{\text{true}} < E[n_0] < E[n']$.

Before we approximate the electron-electron Coulomb interaction term we take a step back and discuss the physical characteristics any approximation must satisfy. Since any approximation to the electron-electron Coulomb interaction should be applied on the same length scale as the exact electron-electron Coulomb interaction, *i.e.* the potential must have a $1/r$ dependence on the interaction, the Coulomb interaction in the independent particle (single-particle) picture can readily be written in terms of the electronic density:

$$E_{\text{Hartree}} = \frac{1}{2} \sum_{i \neq j} \int \int d\mathbf{r}_1 d\mathbf{r}_2 \frac{n_i(\mathbf{r}_1)n_j(\mathbf{r}_2)}{|\mathbf{r}_1 - \mathbf{r}_2|} \quad (2.12)$$

which is known as the Hartree approximation. In principle we can plug this expression directly into the eigenvalue problem in the single-particle description to solve a wide set of problems, but this expression does not fulfill the energy contribution associated with the anti-symmetric nature of the electronic wave function. This effect is not physically intuitive, however it turns out there is in fact a finite contribution to the energy by what is commonly referred to as exchanging electrons of parallel spin. This point of concern can effectively be seen by the following argument (we note originally the exchange term comes out mathematically from derivation and does not have a physical origin apart from the fact that it is related to the anti-symmetric nature of the electronic wave function, but is interpreted as an exchange of electrons of parallel spin. We will still however here pursue an intuitive argument for its origin). Taking the inner product of E_{Hartree} with the electronic wave function and exchanging the coordinates of the electron single-particle wave function we also have to exchange the coordinates in the Coulomb interaction Hamiltonian: $n(\mathbf{r}_1)n(\mathbf{r}_2) = \sum_{i \neq j} \phi_i^*(\mathbf{r}_1)\phi_j^*(\mathbf{r}_2)\phi_i(\mathbf{r}_1)\phi_j(\mathbf{r}_2)$ and $n(\mathbf{r}_2)n(\mathbf{r}_1) = \sum_{i \neq j} \phi_i^*(\mathbf{r}_2)\phi_j^*(\mathbf{r}_1)\phi_i(\mathbf{r}_2)\phi_j(\mathbf{r}_1)$ which is not anti-symmetric upon exchange of the real-space coordinates and thus does not give an energy contribution from anti-symmetry considerations. This can be corrected by adding an exchange term, which accounts for the anti-symmetry of the electronic wave function and gives a finite contribution to the exchange of two electrons with the same spin in two quantum states:

$$E_x = - \sum_{i \neq j} \int \int d\mathbf{r}_1 d\mathbf{r}_2 \frac{\phi_i^*(\mathbf{r}_1)\phi_j^*(\mathbf{r}_2)\phi_i(\mathbf{r}_2)\phi_j(\mathbf{r}_1)}{|\mathbf{r}_1 - \mathbf{r}_2|}, \quad (2.13)$$

and is anti-symmetric upon exchange of \mathbf{r}_1 and \mathbf{r}_2 . Approximating the expectation value of the electron-electron Coulomb interaction by $E_{\text{hartree}} + E_x$ is known as the Hartree-Fock approximation [34]. This approximation slightly overestimates the energy of the electronic system. We note that the Hartree approximation for the Coulomb interaction is normally written in terms of the single-particle electron wave functions, since the Hartree(-Fock) approximation is a framework independent of the DFT framework. However, writing out the Hartree term as a function of the electronic density, makes more clear how DFT is combined with and build on Hartree-Fock theory.

In a simple picture the overestimation of the total energy within the Hartree-Fock approximation can be understood in the following way: when working within the single-particle picture, we lose information on the small-scale instantaneous Coulomb interaction between nearby electrons, affecting their relative distance and thus interaction potential. This effect, known as the electronic correlation, is to increase the average electron-electron interaction distance [92]. This in turn reduces the Coulomb interaction, which decreases the total energy of the system. The electronic correlation can be seen as the error associated with the total energy of the system, we make by approximating the true wave function by a Slater determinant. While no simple expression exists for this term, we define the expectation value of v_{xc} to be the exchange energy (E_x) plus the correlation energy (E_c) in the single-particle description. By defining the Hartree energy to be the expectation of v_{Ha} we can now write down the single-particle Kohn-Sham eigenvalue problem [65]:

$$\left(-\sum_j \frac{\nabla_j^2}{2} + v_{Ha}[n](\mathbf{r}) + v_{xc}[n](\mathbf{r}) + v_{ext}[n](\mathbf{r}) \right) \phi_i(\mathbf{r}) = \epsilon_i \phi_i(\mathbf{r}), \quad (2.14)$$

which can be solved self-consistently numerically for a wide range of systems and the problem is now reduced to apply an appropriate approximation for the exchange-correlation functional. The DFT description of the interacting many-body system gives an exact description of the ground-state energy, but as argued above one is usually also interested in the eigenvalues of the system, however this cannot formally directly be obtained from DFT. While E_i in the many-body picture are the true eigenvalues of states i , the eigenvalues, ϵ_i , in the Kohn-Sham equation have physically no exact meaning due to the single-particle nature of the equation. The only well-defined ϵ_i is that of the highest occupied molecular orbital (HOMO) which equals minus the ionisation energy of the system. It is important to stress that this is not given by Koopman's theorem [66] from Hartree-Fock theory, which cannot be applied to DFT due to the non-exact nature of the exchange-correlation term. Instead, to show the above statement, which is formally known in the literature as the "DFT Koopman's theorem", the argument can be carried out by realising that the non-interacting electronic density in DFT equals the interacting electronic density, and thus the removal energy of one electron must be the same for the two systems. Despite this, DFT has had some success in describing band gaps of materials, for instance by invoking the derivative discontinuity between the ionisation potential and the lowest unoccupied state, however, since the Hohenberg-Kohn theorem strictly governs the ground state of the system, DFT cannot be applied accurately to obtain excitation energies and more advanced many-body descriptions have to be applied, as we will see in the next chapter. On the other hand, what is well-defined is the total ground-state energy, which by the second Hohenberg-Kohn theorem is minimised using a variational approach with the ground-state electron density of the interacting system and can be written as:

$$E = T[n] + E_{xc}[n, \nabla n] + E_{Ha}[n] + E_{ext}[n] \quad (2.15)$$

where we have combined the exchange and correlation contributions in $E_{xc}[n, \nabla n]$ which possibly is also dependent on the gradient of the electronic density, depending on the

chosen approximation of the exchange-correlation interaction. We here write any generic density n since the expression is true for any electronic density and minimised by using the ground-state electronic density. We will not enter a deep discussion of the existing exchange-correlation functionals in the literature, but mention in passing the two most widely applied functionals. The Local Density Approximation (LDA) which estimates the exchange part of $v_{xc}[n](\mathbf{r})$ by the local homogeneous electron gas approximation: $E_x^{\text{LDA}}[n] \sim \int d\mathbf{r} n^{4/3}(\mathbf{r})$ and different schemes for estimating the correlation energy exist. Another widely applied approximation is the Generalised Gradient Approximation (GGA) (such as the Perdew-Burke-Ernzerhof (PBE) functional [95]), which also include the local gradient of the electron density in the description. In practice the GGA functionals are normally built by taking the LDA result for the local density description for the exchange part and adding a correction to this that is calculated from the local density gradient [59]: $E_x^{\text{GGA}} = E_x^{\text{LDA}}[n] + \Delta E[\nabla n(\mathbf{r})]$ and similarly for the correlation part. These are the two main exchange-correlation functionals applied in this thesis to solve the Kohn-Sham equations, and it is important to stress that none of the functionals includes the long range van der Waals interactions between atoms, which is important especially in the optimisation of the atomic structures of interest in this study. This effect has been included by applying for instance the BEEF-vdW [80] or D3 [45] functionals in the optimisation of the structures. Furthermore, both descriptions are inherently local and as we will see in the next chapter non-local effects play an important part in the description of the dielectric properties and many-body description of 2D materials. The application of exchange-functional is stated throughout this thesis and/or in the included papers when appropriate.

2.3 The Projector Augmented Wave Function Method: Implementation in GPAW and Spin-Orbit Interaction

To solve the DFT and many-body problems we are faced with in this thesis, the *ab-initio* electronic structure calculation software GPAW [31, 85] has been used. Since we will need to reference specific parts of the implementation of GPAW in chapter 4, we will here briefly go through the implementation flowchart of GPAW. GPAW supports three types of calculation modes for solving the DFT eigenvalue problem presented in the previous chapter: a finite difference (FD) mode, where the atomic orbitals are resolved on a real space grid, a mode where the wave functions are represented in a basis of a linear combinations of atomic orbitals (LCAO), and finally a plane-wave (PW) mode where the wave functions are expanded as a linear combination of plane-waves. All calculations throughout this thesis are performed in PW mode except in chapter 4 where we will encounter the LCAO mode.

As outlined in the previous chapter, when calculating the energy levels of single atoms, molecule, or periodic solid system we need to solve the generalised eigenvalue problem:

$$H\psi_n = E_n\psi_n \quad (2.16)$$

where n is a combined state index uniquely defining the quantum state (we will omit the "hat" notation on the Hamiltonian for simplicity in the following). While the DFT formalism greatly reduces the complexity and computational requirements of the general many-body problem, numerical problems arise in describing ψ_n close to the atomic cores. The core orbitals, subject to an immensely strong potential, must oscillate rapidly (this can intuitively be visualised from a simply quantum well picture), and is numerically difficult to represent in a feasible manner. To overcome this the general approach is simply to define a setup for each atomic orbitals, where a number of core states are calculated once and for all, and therefore assumed to be independent of the neighbourhood of the atoms. This approximation is in general valid when only properties related to the valence states are considered and is formally known as the frozen core approximation. However, since the set ψ_n have to be internally orthogonal to be the complete set of eigenfunctions for eq. 2.16, the valence states will also oscillate rapidly in the core regions, where they have a finite overlap with the core states. This means, that even within the frozen core approximation, it is numerically infeasible to describe the electronic properties of the valence states. In the following we will adapt the notation used in [31] and the discussion below will be focused on obtaining the expression for the Hamiltonian defining the eigenvalue problem in GPAW.

In PW mode the problem is overcome by assuming that the rapidly oscillating part of the valence wave function in the core region can be represented by a smooth wave function, to be denoted $\tilde{\psi}_n$, and that a transformation (\hat{T}) from the smooth wave function to the exact wave function exist:

$$\psi_n = \hat{T}\tilde{\psi}_n = (1 + \hat{T}^a)\tilde{\psi}_n. \quad (2.17)$$

The last equal sign stems for the fact that since the rapid oscillations are confined to a region of space close to the nuclei we define \hat{T} to be equal to unity outside and equal to \hat{T}^a inside confinement region, defined by a cutoff radius r_c^a . a is an atomic index since the value of r_c^a is atom-dependent. The eigenvalues in eq. 2.16 can be calculated from the expectation value of the Hamiltonian:

$$E_n = \langle \psi_n | H | \psi_n \rangle \quad (2.18)$$

which upon transformation to the smooth wave function reads:

$$E_n = \langle \tilde{\psi}_n | \hat{T}^\dagger H \hat{T} | \tilde{\psi}_n \rangle. \quad (2.19)$$

This introduces the need of defining the transformed Hamiltonian: $\tilde{H} = \hat{T}^\dagger H \hat{T}$ and defines the transformed eigenvalue problem in eq. 2.16 which can be obtained directly by inserting the smooth wave functions and applying \hat{T}^\dagger :

$$\tilde{H}\tilde{\psi}_n = E_n\tilde{\psi}_n, \quad (2.20)$$

where the overlap operator have been defined as: $\hat{S} = \hat{T}^\dagger \hat{T}$. Our aim is now to find an expression for the transformed Hamiltonian. To continue we state that the smooth wave function (and similarly the exact wave function) inside the augmentation sphere can be expanded as a linear combination of partial waves:

$$\tilde{\psi}_n^a = \sum_i \langle \tilde{p}_i^a | \tilde{\psi}_n \rangle \tilde{\phi}_i^a \quad (2.21)$$

where \tilde{p}_i^a are coefficients to be determined and we define the projection elements as projectors: $P_{i,n}^a = \langle \tilde{p}_i^a | \tilde{\psi}_n \rangle$. Furthermore, since $\tilde{\psi}_n$ is only defined within the augmentation sphere we must have $\tilde{p}_i^a = 0$ outside the augmentation sphere. From this we can define the atomic density matrix:

$$D_{i_1, i_2}^a = \sum_n f_n \langle \tilde{\psi}_n | \tilde{p}_{i_1}^a \rangle \langle \tilde{p}_{i_2}^a | \tilde{\psi}_n \rangle. \quad (2.22)$$

where f_n are occupation numbers. We are now finally in a position where we can directly determine the transformed Hamiltonian. As we saw in the previous section, the total energy (eq. 2.15) is composed of four terms: the kinetic energy, the electrostatic potential, the exchange-correlation potential, and the external perturbation potentials. The transformed Hamiltonian is determined by taking the functional derivative of the total energy with respect to the smooth wave function:

$$\frac{\delta E}{\delta \tilde{\psi}_n^*} = f_n E_n \hat{S} \tilde{\psi}_n = f_n \tilde{H} \tilde{\psi}_n. \quad (2.23)$$

The total energy to be inserted is the one defined from the smooth wave functions (and the derived smooth electronic densities). As a consequence of the transformed eigenvalue problem, the total energy has an extra non-physical atom-dependent contribution which is a function of the atomic density matrix: $\Delta E^a[D_{i_1, i_2}^a]$. Setting the external potential to zero for simplicity, the transformed operator form of the Coulomb and exchange-correlation potentials attains the following forms:

$$\tilde{v}_{\text{Ha}}[n] = \frac{\delta E_{\text{Ha}}[\tilde{n}]}{\delta \tilde{n}} \quad (2.24)$$

and

$$\tilde{v}_{\text{xc}} = \frac{\delta E_{\text{xc}}[\tilde{n}]}{\delta \tilde{n}} \quad (2.25)$$

where \tilde{n} is the electronic density determined from the smooth wave function. The first term is uniquely defined by the Poisson equation with the smooth electronic density and the latter term is defined by the choice of exchange-functional in the DFT Kohn-Sham description (LDA, GGA, etc.). We here see how this choice enters in the solution of the eigenvalue problem. The functional derivative of the non-local augmentation sphere correction is not straightforward since ΔE^a contains atomic corrections to both the kinetic, the Coulomb, the exchange-correlation, and an extra term not present in the physical expression for the total energy. For a full derivation of this term we refer to

[85], and here simply state that it can be written in a neat form as a projection of a tensor onto the projector expansion coefficients defined above. With these definitions the transformed Hamiltonian takes the form of:

$$\tilde{H} = -\frac{1}{2}\nabla^2 + \tilde{v}_{\text{Ha}} + \tilde{v}_{\text{xc}} + \sum_{i_1, i_2}^a |\tilde{p}_{i_1}^a\rangle \Delta H_{i_1 i_2}^a \langle \tilde{p}_{i_2}^a| \quad (2.26)$$

where the last term is the non-local atomic correction:

$$\Delta H_{i_1 i_2}^a = \frac{\partial \Delta E^a}{\partial D_{i_1 i_2}^a} + \int d\mathbf{r} \tilde{v}_{\text{Ha}} \frac{\partial \tilde{n}}{\partial D_{i_1 i_2}^a}. \quad (2.27)$$

Eq. 2.26 defines the Hamiltonian within the transformed eigenvalue problem. At this point it is important to comment on the orthogonality of the smooth wave functions. By construction, the exact wave functions are orthogonal: $\langle \psi_n | \psi_m \rangle = \delta_{nm}$. Upon transformation to the smooth wave functions we find that the orthogonality is only maintained in terms of the overlap operator: $\langle \tilde{\psi}_n | \hat{S} | \tilde{\psi}_m \rangle = \delta_{nm}$. In practice the completeness is controlled (and converged) by the number of plane-wave coefficients included in the expansion. This is important since $\tilde{\psi}_n$ is defined as a linear combination of plane-waves which consequently are not internally orthogonal.

While the full derivation of the implementation flowchart can be found elsewhere in greater detail [85, 31], including the electronic density, atomic forces, total energy etc. we will mainly be interested in referencing the PAW Hamiltonian, eq. 2.26, in chapter 4. We will therefore truncate our brief overview of the PW mode in GPAW, however the author could not refrain from giving a short introduction to the evaluation of the electronic density since this is the driving force in DFT. This discussion can be found in appendix B.

In chapter 4 we will encounter the use of GPAW in LCAO mode. As we will see, the main principle behind the LCAO mode is very similar to the PW mode, however it handles the numerical difficulty of representing the wave function close to the nuclei differently. Instead of expanding the smooth valence wave functions in eq. 2.17 as a linear combination of plane-waves, in the LCAO mode the valence states are represented as a linear combination of atomic orbitals (hence the name). Inspired by the solution of the standard hydrogen problem, the atomic orbitals, which we will denote by Ψ , are separated into a product of a radial component of the wave function (R) and spherical harmonical functions (Y): $\Psi(\mathbf{r}) = R(r)Y(\theta, \phi)$, where since R is only a function of the radial coordinate, R can be found by solving a usual 1D problem as encountered in a standard separation of variables problem. This means that in the LCAO mode the smooth wave function is represented as:

$$\langle \tilde{\psi}_n | = \sum_{\mu} c_{\mu n} \langle \Psi_{\mu} | = \sum_{\mu} c_{\mu n} \langle RY |, \quad (2.28)$$

where $c_{\mu n}$ are coefficients that gives the weight of each atomic-like orbital in the expansion and again n is a common state index uniquely defining the quantum state. For a detailed

discussion on how $c_{\mu n}$ and R_n are determined to define a basis setup for each atom we refer to [73] since this is not the main topic of this thesis.

Considering the definition of the projectors and the atomic density matrix in PW mode, their corresponding definitions in the LCAO mode now comes in naturally from eq. 2.28:

$$P_{i,\mu}^a = \langle \tilde{p}_i^a | \Psi_\mu \rangle \quad (2.29)$$

$$D_{i_1, i_2}^a = \sum_{\mu\nu} \sum_n f_n \langle \tilde{p}_{i_1}^a | c_{\mu n} | \Psi_\mu \rangle \langle \Psi_\nu | c_{\nu n}^* | \tilde{p}_{i_2}^a \rangle = \sum_{\mu\nu} \sum_n f_n P_{i_1, \mu}^a c_{\mu n} c_{\nu n}^* P_{i_2, \nu}^{a*}. \quad (2.30)$$

Since the smooth wave functions are defined by the expansion coefficients $c_{\mu n}$, the transformed eigenvalue problem in this formalism is defined in terms of these coefficients:

$$\sum_\nu \tilde{H}_{\mu\nu} c_{\nu n} = \sum_\nu \hat{S}_{\mu\nu} c_{\nu n} E_n \quad (2.31)$$

where the overlap operator defines the overlap between state ν and state μ of the atomic-like expansion orbitals: $\hat{S}_{\mu\nu} = \langle \Psi_\mu | \hat{S} | \Psi_\nu \rangle$ and the expansion orbitals are still only orthogonal with respect to the overlap operator: $\sum_{\mu\nu} c_{\mu n}^* \hat{S}_{\mu\nu} c_{\nu m} = \delta_{nm}$, meaning that the LCAO mode is subject to the same (lack of) completeness issue as the PW mode. Finally the transformed Hamiltonian in the LCAO mode takes the same form as the Hamiltonian in PW mode (eq. 2.26) where the LCAO projectors take the place of the PW projectors and the kinetic, Coulomb, and exchange-correlation terms are evaluated from the basis functions $\{\Psi\}$:

$$\hat{H}_{\mu\nu} = -\frac{1}{2} \langle \Psi_\mu | \nabla^2 | \Psi_\nu \rangle + \langle \Psi_\mu | \tilde{v}_{\text{Ha}} | \Psi_\nu \rangle + \langle \Psi_\mu | \tilde{v}_{\text{xc}} | \Psi_\nu \rangle + \sum_{i_1, i_2}^a P_{i_1, \mu}^a \Delta H_{i_1, i_2}^a P_{i_2, \nu}^{a*}. \quad (2.32)$$

In chapter 4 we will make use of the very neat discretised form of the LCAO eigenvalue problem in eqs. 2.31 and 2.32.

Finally, we will comment on the effect and calculation of spin-orbit coupling in GPAW. For heavier metals, such as the transition metals, which will have a special interest in this study, the spin-moment (\mathbf{s}) of the electron couples to the effective magnetic field (\mathbf{B}) present when moving with velocity \mathbf{v} relative to the positively charged nuclei setting up an electric field \mathbf{E} , in the reference point of the electron: $\mathbf{B} = -\frac{\mathbf{v} \times \mathbf{E}}{c^2}$. The coupling interaction is given by

$$H^{\text{SO}} = -\mathbf{s} \cdot \mathbf{B} \quad (2.33)$$

with $\mathbf{s} = \frac{e}{m_e} \mathbf{S}$ and $\mathbf{B} = \frac{1}{m_e e c^2 r} \frac{\partial v(r)}{\partial r} \mathbf{L}$. e is the electron charge, m_e the electron free space mass, c the speed of light, $v(r)$ the Kohn-Sham electrostatic potential, and \mathbf{S} and \mathbf{L} the spin and angular momentum vectors. We here changed to SI units to highlight the dependence on the electron mass and charge. Putting this together and accounting for the Thomas precession correction (a factor of $\frac{1}{2}$) results in:

$$H^{\text{SO}} = -\frac{1}{2m_e^2 c^2 r} \frac{\partial v(r)}{\partial r} \mathbf{S} \cdot \mathbf{L}. \quad (2.34)$$

To get the spin-orbit correction to the eigenvalues, one has to evaluate the inner product of the electron wave function (now a spinor state) with the spin-orbit Hamiltonian over all space. However, since the electrostatic potential oscillates most rapidly (*i.e.* $\frac{1}{r} \frac{\partial v(r)}{\partial r}$ is largest) near the core region, one approximates the inner product to only be evaluated within the augmentation sphere, *i.e.* the wave functions in the inner product in eq. 2.18 are taken to equal the (spinor) smooth wave functions in eq. 2.21 inside the augmentation sphere and equal 0 outside.

$$\delta E_n^{\text{SO}} = \sum_a \langle \tilde{\psi}_n^a | H^{\text{SO}} | \tilde{\psi}_n^a \rangle = \sum_a \sum_{ij} \langle \tilde{\psi}_n | \tilde{p}_i^a \rangle \langle \tilde{\phi}_i^a | H^{\text{SO}} | \tilde{\phi}_j^a \rangle \langle \tilde{p}_j^a | \tilde{\psi}_n \rangle \quad (2.35)$$

where state index i (and j) now also contains the spin state. For efficient computation, similarly to the LCAO flowchart, the wave function is split into a radial part ($R(r)$) and an angular part ($Y(\theta, \phi)$), such that the evaluation of the spin-orbit Hamiltonian can be split into a product of the expectation value of the radial part: $\langle R(r) | \frac{1}{r} \frac{\partial v(r)}{\partial r} | R(r) \rangle$ and angular part: $\langle Y(\theta, \phi) | \mathbf{S} \cdot \mathbf{L} | Y(\theta, \phi) \rangle$ evaluated separately. The spin-orbit effects have a considerable effect on the quasi-particle and exciton energies in 2D materials and vdWHs containing transition metals, and are fully included throughout this study, unless otherwise stated.

After this small note on the implementation flowchart of the DFT formalism in GPAW, we will in the next section discuss the very reason for this study, namely the experimental realisation of 2-dimensional monolayers, which will conclude the opening chapter on the basics of electronic structure theory and calculations.

2.4 2D Materials, van der Waals Heterostructures, and van der Waals interactions

The general density functional theory presented in the previous sections can readily be applied to a wide range of materials including bulk crystals, 2D materials, 1D nanotubes and -rods, and molecules to calculate for instance electronic band gaps, wave function patterns, and total energies, and also optical absorption spectra in combination with the Random Phase Approximation (RPA) [9, 96, 8]. The first exfoliation of monolayer graphene introduced a new paradigm to materials science with the introduction of 2D materials. While the 2D materials offer a wealth of interesting materials properties for application in electronic devices they also impose significant computational difficulties that are different from those found in 0D, 1D, and 3D materials. We will here discuss the class of 2D materials which will be of main interest in the following chapters and briefly discuss the specific computational problems that need to be overcome to accurately model the properties of 2D materials and how these differ from for instance 3D bulk crystals.

Since the first exfoliation of monolayer graphene in 2004, many more 2D materials have been experimentally synthesised. Some of the most well-known include monolayer hBN and the transition metal dichalcogenides (TMDs). The TMDs consist of a sheet of a transition metal encapsulated between two layers of chalcogenide atoms. MoS₂ was the first TMD monolayer to be exfoliated in 2010 [82] and introduced the world of 2D semiconductors for opto-electronic applications. The exfoliation of MoS₂ offered the opportunity to study how the optical properties in 2D materials differ from those of bulk crystals. Due to the atomically thin nature of 2D materials, the dielectric screening of the Coulomb interaction between charged particles in the monolayer is significantly reduced compared to bulk crystals. The reduced dielectric screening leads to more pronounced quasi-particle effects such as strongly bound excitonic states having optical transition energies below that of the electronic band gap. We will discuss the origin of these quasi-particle states in the next chapter. Consequently, advanced many-body methods, which are computationally significantly heavier than conventional DFT calculations, are needed to accurately describe the electronic band structure, quasi-particle states, and the absorption spectra of 2D materials. Furthermore, while the dielectric screening in semiconducting bulk crystals to a large degree can be considered to be a constant, a strong dependence on the reciprocal space lattice vector of the dielectric function is present in 2D materials. This is due to the atomically thin nature of 2D materials which have the consequence that the dielectric function have to approach one for arbitrarily small momentum vectors in reciprocal space. This imposes an additional challenge in the calculation of electronic and optical properties of 2D monolayer, especially when in close proximity to other materials.

In the years around 2011 it was experimentally demonstrated that 2D monolayers can be stacked together to form multilayer structures, van der Waals heterostructures, where the layers are bonded together by weak van der Waals forces [98, 50, 27]. The potential energy for the equilibrium distance between the layers is governed by the Lennard-Jones potential [61]:

$$U(r) \sim - \left(\frac{r_d}{r} \right)^6 + \left(\frac{r_p}{r} \right)^{12} \quad (2.36)$$

with r_d and r_p being constants and where the first term is an attractive dipole-dipole interaction (between two dipoles residing in neighbouring monolayers) and the last term is a Pauli repulsion interaction between the monolayers. We will here briefly comment in greater detail on the nature of these two interactions, since this discussion is significantly lacking in most descriptions of vdWHs. The first term is commonly known to be the dipole-dipole interaction between the two layers, however, what is usually not clarified is that this term in general have 3 contributions. The electronic charge distribution of a freestanding 2D monolayer will have a net zero dipole moment in the out-of-plane direction averaged over a long time interval for 2D monolayers with a mirror plane symmetry. However, at any instance of time, the charge distribution will be asymmetric, meaning that two neighbouring monolayers will be attracted by an instantaneous dipole-dipole interaction. The instantaneous dipole-dipole interaction is formally known as the London dispersion interaction and the potential energy associated with this interaction

is proportional to the product of the polarisabilities (α) and ionisation energies (I) of the two monolayers: $U^{\text{lon}}(r) \sim -\frac{\alpha_1\alpha_2 I_1 I_2}{I_1+I_2} \frac{1}{r^6}$. Secondly, if one of the monolayers lack a mirror plane symmetry resulting in a time-averaged finite out-of-plane dipole moment, this permanent dipole moment (p) interacts with the instantaneous dipole in the other layer known as the Debye interaction: $U^{\text{deb}}(r) \sim -p_1^2\alpha_2^2 \frac{1}{r^6}$. Finally, if both of the layers have a finite out-of-plane dipole moment, the attraction between the two layers have an additional contribution from the interaction between the two permanent dipoles. This interaction is known as the Keesom interaction and have the interesting feature that it is dependent on the temperature T : $U^{\text{kes}}(r) \sim -k_b T p_1^2 p_2^2 \frac{1}{r^6}$. The fact that all three terms are proportional to $\frac{1}{r^6}$, means that these are usually put together in the attractive term of the Lennard-Jones potential. The combined proportionality constant of the three terms determines r_d . For some of the most well-known vdWHs, consisting of TMDs, only the London dispersion interaction is present. However, for the class of 2D Janus structures, which we will study in chapter 6, both the Debye and Keesom interactions are present. In the future, it could be interesting to study the significance of these two interaction potentials on the distance dependent potential surface of vdWHs with Janus monolayers and its temperature dependency. The factor of the second term in the Lennard-Jones potential does not have a similar stringent physical explanation. While the term models the effect of the repulsive Pauli interaction between the electronic clouds of the neighbouring monolayers, its dependency on r is not known and the power of 12 is arbitrary with the only restriction to be higher than 6 to have a potential minimum. In practice, this means the factor r_d is determined from fit to experimental values to match the potential minimum and gradient near the minimum, in DFT functionals including van der Waals corrections.

While it is not too surprising that identical monolayers can be stacked to form a layered homostructure it is more surprising that different monolayers can be stacked to form so-called vdWHs irregardless of the lattice constant of the monolayers and with no significant strain effects on any of the monolayers. The latter is possible due to the weak interlayer coupling between the monolayers. The possibility to stack all 2D monolayers to vdWHs with an in principle arbitrary number of layers has been nicely depicted by the, by now, very well-known Lego-picture. Given the few hundred synthesisable 2D monolayer candidates this picture illustrates the close to infinite number of possible vdWHs that can be formed by forming vdWHs with 5, 10, or even more layers and offers a fantastic playground to manipulate and design materials with specific properties. The picture is further enlarged by the possibility to, to a large extend, freely rotate the individual layers relative to each other. Due to weak interlayer coupling and consequently rather long interlayer binding distance interlayer orbital hybridisation effects are limited. Nevertheless, it has recently been shown experimentally that by relative twisting of the layers it is possible to manipulate the interlayer hybridisation pattern to achieve a superconducting phase in bilayer graphene [12] and complicated intra- and interlayer exciton hybridisation effects in bilayer TMDs [3]. This gives yet another knot to turn in designing vdWHs.

When different 2D monolayers are stacked together they will in most cases have

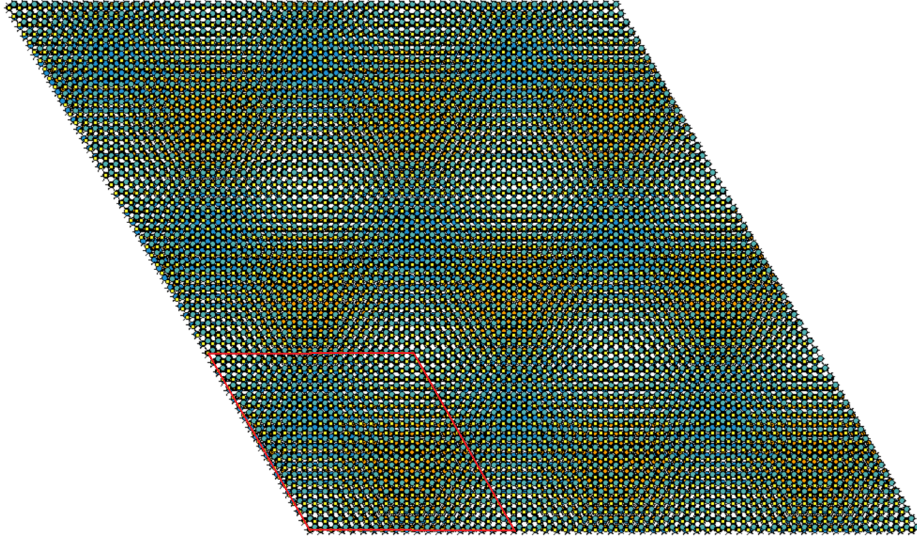


Figure 2.1: Supercell of rotated bilayer $\text{MoS}_2/\text{WSe}_2$ shown in red containing 2283 atoms. The supercell is repeated 3 times in both in-plane directions to illustrate the emerging Moiré pattern.

significantly different lattice constants. To apply computational methods such as DFT and many-body theories it is necessary to define a common unit cell for the full vdWH. When incommensurate layers are stacked or homo multilayer structures are rotated relative to each other it is consequently necessary to either significantly strain one or more layers (which is usually not desired) or define a supercell containing repeated unit cells for each layer. Such supercells are characterised by Moiré patterns that emerge as shown in fig. 2.1 where a supercell for incommensurate bilayer $\text{MoS}_2/\text{WSe}_2$ is shown. The supercell containing 2283 atoms is highlighted in red and is itself repeated 3x3 times to illustrate the Moiré pattern. The Moiré pattern leads to a small Moiré effect that have recently been shown to only alter the energy of optical states a few meV [83] and will not be studied further in this work. On one hand, the combination of the huge supercells needed to computationally model even few-layer vdWHs and the need to use advanced many-body methods to accurately describe electronic and excited states in these structures introduces an obvious obstacle. On the other hand, because of the tremendously large number of possible synthesisable vdWHs it is clear that experimentalists need guidance from computational predictions to point to which combinations of 2D monolayers potentially offer the most interesting materials properties for application or new physical phenomena to be studied. Vast efforts have been put and is currently put in the field of 2D monolayers and vdWHs to calculate, determine, and continuously develop methods and models for calculating the properties of vdWHs more efficiently. In the following chapters we will introduce the physical concepts, theory, and many-body formalisms necessary to accurately calculate the electronic and optical properties of 2D monolayers and vdWHs. The goal of the following chapters is to help

advance the theoretical understanding of vdWHs by applying such many-body methods and developing new theoretical and computational methods to more efficiently calculate excited state properties of vdWHs and aid the field of materials discovery.

CHAPTER 3

Electronic and Optical Properties of 2D Materials and van der Waals Heterostructures

Since for 2D materials the electronic density is confined to an atomically thin sheet, the movement of the electrons in the out-of-plane direction is significantly limited, an effect formally known as quantum confinement. In this regard, 2D materials have introduced a new paradigm of electronic structure calculations in materials science. Because of this, the electron density can only to a limited degree screen out external perturbations and consequently 2D materials are characterised by reduced dielectric screening compared to 3D bulk crystals. In the opening section we will review the theory of linear response and explain the peculiar form of the dielectric screening in 2D. The reduced dielectric screening offer an exciting playground to study the pronounced many-body effects in 2D materials, for example excitonic effects which we will be specially interested in, in the following chapters. In section 3.2 we will see that adopting a Green's function formalism and going beyond the single-particle description, leads to the introduction of so-called quasi-particle states: a many-body electronic state and we will derive the GW approximation which is the gold standard of calculating quasi-particle energies in materials. While advanced many-body methods such as the GW formalism are necessary to accurately describe electronic and optical properties of 2D materials and vdWHs, they come at a significant computational cost and it is consequently not possible to carry out such calculations for even few-layer vdWHs. However, the weak interlayer bonding between the layers in vdWHs opens up the possibility to combine many-body *ab-initio* calculations for the freestanding monolayers with analytical or feasible numerical algorithms to model the interlayer interaction. Such methods have previously been developed in the literature, and we will here consider the Quantum Electrostatic Heterostructure (QEH) model [4]. The QEH model has been shown to accurately capture the effect of interlayer dielectric screening on the quasi-particle energies [74, 75]. However, a major shortcoming of the QEH model is that it does not account for the effect of interlayer orbital hybridisation and interlayer charge transfer effects. We will return to this delicate subject in chapter 4 where we will implement these effects into the QEH model and apply it to

exciton energies in vdWHs. Meanwhile, in section 3.5 we will present the result of paper I, where we apply the G0W0 method in combination with the QEH model to calculate quasi-particle energies of 2D monolayer semiconductors on a gated graphene monolayer, and show how the non-local nature of the dielectric screening can be used to accurately control the quasi-particle band gap in 2D semiconductors, which concludes the first part of chapter 3 on quasi-particle energies.

In section 3.6 we will see that by including electron-hole interactions in the many-body description leads to bound electron-hole pair states, excitons, with an excitation energy lower than the electronic band gap. While such excitonic effects live on the meV scale in conventional 3D bulk semiconductors, they are significantly pronounced in 2D materials due to the low dielectric screening and are thus necessary to include in any accurate description of the optical properties of 2D materials and vdWHs. The Bethe-Salpeter Equation (BSE) has been shown to accurately describe excitonic states and we will derive and discuss this formalism. Due to the two-particle nature of the electron-hole pair it is maybe not too surprising that exciton energies can to some extent be modelled by hydrogen-like models, for instance the Mott-Wannier (MW) model, with much less computational effort than the BSE formalism. The QEH model has previously been implemented with the Mott-Wannier equation (the MW-QEH model) to calculate exciton binding energies [75] in vdWHs. This offers an efficient and fast algorithm to calculate the exciton binding energies in vdWHs including the dielectric screening of the electron-hole pair interaction. In chapter 3.7 we will expand upon this and implement the QEH model with the BSE method. This not only gives us the possibility of also calculating the absorption spectrum of many layers vdWHs including excitonic effects, but it also turns out to give a good description of the observed redshift of exciton energies in vdWHs. An effect that the MW-QEH does catch for few-layer vdWHs. Given that the excitonic spectrum can be accurately calculated by a hydrogen-like model, as the MW model suggests, the exciton shares a great resemblance with the hydrogen model. This is indeed true, and it has previously been shown that the exciton spectrum contains a full non-hydrogenic Rydberg series [21, 90]. In chapter 3.8 we will discuss the importance of the results of papers II and III, where we introduce a new dielectric screening regime of exciton physics, by studying the excitonic Rydberg series of intralayer excitons in 2D materials located on dielectric bulk substrates. In fact, we find that depending on the dielectric constant of the bulk substrate we show that an inherent *hydrogenic* 2D Rydberg series can be obtained in the 2D material and for high dielectric constants the 2D exciton enters a new unexplored dielectric screening regime in exciton physics. It is exciting that it is still possible to elaborate on and introduce new physical regimes to such fundamental models as hydrogen picture based models.

Finally this chapter will discuss how excitonic devices hold a great potential in terms of applications due to the strong light-matter interaction. This is illustrated by discussing the result in paper IV, where we study the WS₂/HfS₂ bilayer. In this system we locate a low-energy interlayer exciton in the absorption spectrum with a peak energy in the infrared (IR) spectrum. While such interlayer excitons usually have low oscillator

strengths, the detected interlayer exciton has a high oscillator strength making it ideal for application as an IR photodetector. Chapter 3.9 presents the main results of this work and discusses the peculiar nature of this excitonic state.

3.1 Dielectric Response Theory and Dielectric Screening in 2D

As we discussed in the introduction, physics is about observing an event and asking "why did that happen?". Since something new happened, this suggests that the system we are observing went from being in an equilibrium state to a non-equilibrium state upon some kind of external perturbation. In this section we will see that, if the external perturbation is small, the change (the non-equilibrium response) of the system can easily be obtained from its equilibrium properties. By pursuing this, we will see that this leads us to response theory and the response functions of our system quantified by the Kubo formulas [69].

If we assume that the system in equilibrium is governed by the Hamiltonian H_0 and the external perturbation is given by $H_{\text{ext}}(t)$, *i.e.* only the external perturbation depends on time, then the total Hamiltonian of the system is given by: $H(t) = H_0 + H_{\text{ext}}(t)$. Before we go into the world of quantum mechanics, it is instructive to first consider the classical case, since this discussion is lacking in most modern textbooks. Classically, if the system is described by a thermal distribution function, $\rho(t)$, then the time evolution of the system is governed by the Liouville equation of motion: $\frac{\partial \rho(t)}{\partial t} = L\rho(t)$, where L is the Liouville operator which contains the full Hamiltonian of the system. The trick is now to assume that the time-dependence of the thermal distribution function can be isolated, such that: $\rho(t) = \rho_0 + \Delta\rho(t)$. By inserting this in the Liouville equation of motion, we immediately capture the essence of (linear) response theory and the Kubo formulas: if one assumes the product of the external perturbation and the time-dependent thermal ensemble fluctuations to be small ($H_{\text{ext}}\Delta\rho \sim 0$), it is then possible to describe the response of the system to the external perturbation in a linear form, known as the Kubo formula. What is usually disregarded in the literature, is that the Kubo formalism comes in two different shapes, and we will present both in the following for completeness. If we let B be some physical observable of the system and δB the change of the observable upon the external perturbation H_{ext} , then Kubo showed that these three quantities are related by:

$$\delta B(t) = \int_{t_0}^t dt' \langle (B(t-t'); p, q), H_{\text{ext}}(t') \rangle_{\text{eq}} \quad (3.1)$$

where p and q are the canonical position and momentum variables respectively, the round parenthesis are the Poisson brackets, and the square brackets denote that the thermal average is taken in equilibrium. While it is astonishing that the change of the physical observable in non-equilibrium can be calculated from an equilibrium ensemble average, the Poisson parenthesis are in practice tedious to evaluate. Instead, one utilise

a mathematical trick, by factorising the external perturbation into a product of two conjugate variables: $H_{\text{ext}}(t) = K(t)A$, with only K being dependent on time. Mathematically, this eases the evaluation of the Liouville operator since the differentiation with respect to the canonical real-space coordinate and momentum only acts on A and in this form δB can now be found from:

$$\delta B(t) = \frac{1}{k_b T} \int_{t_0}^t dt' K(t') \langle B(t-t'; p, q) \dot{A} \rangle_{\text{eq}} \quad (3.2)$$

where the dot denotes the canonical Liouville derivative, k_b is the Boltzmann constant, and T is the temperature.

The Kubo formulas are general and widely used in most branches of physics. While we, in eqns. 3.1 and 3.2, considered the classical forms of the Kubo formulas, it is straightforward to derive the corresponding quantum mechanical counterparts starting from the Heisenberg equation of motion with a quantum mechanical ensemble description. In this study we will be interested in their applications to the calculation of materials properties. The form of the response functions shows that the change of the observable will be proportional to the external perturbation and to some proportionality constant, which we will here denote as the *response function*. It turns out, that the two main response functions of interest in materials science come about by asking what is the change of electronic density and the total potential upon some external perturbation to the potential. For the change in electronic density to an external perturbation this is given by:

$$\delta n(\mathbf{r}, t) = \int_{t_0}^t dt' \int d\mathbf{r}' \chi(\mathbf{r}t, \mathbf{r}'t') v_{\text{ext}}(\mathbf{r}'t') \quad (3.3)$$

and the total potential is given by:

$$v_{\text{tot}}(\mathbf{r}, t) = \int_{t_0}^t dt' \int d\mathbf{r}' \epsilon^{-1}(\mathbf{r}t, \mathbf{r}'t') v_{\text{ext}}(\mathbf{r}'t'). \quad (3.4)$$

The proportionality constant, from now to be denoted the response function, for the density response is known as the density response function, χ , and the response function for the total potential, ϵ , is known as the dielectric function. As we will see below, the electronic and optical properties of a material can be determined from these two functions. It is very interesting and it shows the strength of the Kubo formulas that the materials properties can be determined by simply asking what is the response of the material to an undefined external potential. It is useful to rewrite the expression for the perturbation of the electronic density to define the density response function as:

$$\chi(\mathbf{r}t, \mathbf{r}'t') = \frac{\delta n(\mathbf{r}t)}{\delta v_{\text{ext}}(\mathbf{r}'t')}. \quad (3.5)$$

We note here χ is also known as the reducible polarisability and is formally calculated from the correlation function of the electronic density operators:

$$\chi(\mathbf{r}t, \mathbf{r}'t') = -i\Theta(t-t') \langle [\hat{n}(\mathbf{r}t), \hat{n}(\mathbf{r}'t')] \rangle. \quad (3.6)$$

We will return to the actual calculation of χ below. The fact the χ is labelled the *reducible* polarisability heavily suggests the existence of an *irreducible* polarisability. The irreducible polarisability is defined as the functional derivative of the electronic density with respect to the total potential:

$$P(\mathbf{r}t, \mathbf{r}'t') = \frac{\delta n(\mathbf{r}t)}{\delta v_{\text{tot}}(\mathbf{r}'t')} \quad (3.7)$$

In the next section it will be obvious how this naming comes about. By simply expanding the reducible polarisability with the total potential and carrying out the functional derivative, it is easy to show that χ and P are related through a Dyson equation:

$$\chi(\mathbf{r}, \mathbf{r}', \omega) = P(\mathbf{r}, \mathbf{r}', \omega) + \int d\mathbf{r}_1 d\mathbf{r}_2 P(\mathbf{r}, \mathbf{r}_1, \omega) v(\mathbf{r}_1, \mathbf{r}_2) \chi(\mathbf{r}', \mathbf{r}_2, \omega) \quad (3.8)$$

where v is the bare Coulomb interaction. In this step we have also employed a Fourier transform from time- to frequency-space: in the following we assume the external potential to take the form of a plane-wave (in time) which makes the Fourier transform straightforward and simply transfers the time integral into a product in frequency-space. This approximation corresponds to assuming $(t, t') \rightarrow (t - t')$. Since the materials of consideration in this thesis are (in-plane) periodic, a similar trick can be done for the real-space coordinate, but we will refrain from doing for now. The introduction of the irreducible polarisability from the total potential offers a remarkable possibility as can be seen by examining eq. 3.4 again. Since ϵ , the dielectric function, similarly to P is defined in terms of the total potential it is in fact possible to relate all three response functions: the dielectric function and the irreducible polarisability can directly be related by a Dyson equation:

$$\epsilon(\mathbf{r}, \mathbf{r}', \omega) = \delta(\mathbf{r}, \mathbf{r}') - \int d\mathbf{r}_1 v(\mathbf{r}, \mathbf{r}_1) P(\mathbf{r}_1, \mathbf{r}', \omega) \quad (3.9)$$

which again can be related to the reducible polarisability through eq. 3.8. In other words, not only are the properties of a material defined by the response functions of the system to an undefined external potential perturbation, but the response functions are also internally related. The actual evaluation of the response function, starting from the definition of χ through the density correlation-correlation function is a difficult and complex exercise, since this involves and describes all interactions in the same manner as the eigenvalue problem in the many-body picture. To overcome this in practice, we employ a similar approach as in the previous chapter and define a non-interacting single-particle density response function:

$$\chi^0(\mathbf{r}, \mathbf{r}', \omega) = \sum_{\mathbf{k}, \mathbf{q}} \sum_{n, n'}^{\text{bz}} (f_{n\mathbf{k}} - f_{n'\mathbf{k}+\mathbf{q}}) \frac{\phi_{n\mathbf{k}}(\mathbf{r}) \phi_{n'\mathbf{k}+\mathbf{q}}(\mathbf{r}) \phi_{n\mathbf{k}}(\mathbf{r}') \phi_{n'\mathbf{k}+\mathbf{q}}(\mathbf{r}')}{(\epsilon_{n\mathbf{k}} - \epsilon_{n'\mathbf{k}+\mathbf{q}}) - \omega + i\eta} \quad (3.10)$$

where $\phi(\mathbf{r})$ is the single-particle Kohn-Sham wave function, similar to the definition of the single-particle electronic density in the DFT formalism in the previous chapter and ϵ_i are the Kohn-Sham eigenvalues. The non-interacting response function fulfills a

similar response relation as the irreducible polarisability (eq. 3.7), *i.e.* it relates the total potential to the fluctuation in the electronic density, however what makes χ^0 attractive to work with is that it can immediately be calculated within the single-particle picture. Consequently, the reducible polarisability and non-interacting density response function are also related by a Dyson equation:

$$\chi(\mathbf{r}, \mathbf{r}', \omega) = \chi^0(\mathbf{r}, \mathbf{r}', \omega) + \int d\mathbf{r}_1 d\mathbf{r}_2 \chi^0(\mathbf{r}, \mathbf{r}', \omega) v(\mathbf{r}_1, \mathbf{r}_2) \chi(\mathbf{r}_2, \mathbf{r}', \omega). \quad (3.11)$$

We note in passing that the Coulomb kernel also contains an exchange-correlation term, for which the adiabatic LDA is employed in GPAW, but we will not discuss this detail further. The similarity between χ^0 and P can be confusing. One of the most employed approximations in electronic structure theory calculations is to replace the irreducible polarisability in eq. 3.4 with χ^0 which is known as the Random Phase Approximation (RPA) and gives a direct flowchart to calculate the dielectric function, which we will see below is the main object of interest for the optical properties of materials. In the next sections we will more clearly see how this approximation comes about and the importance of many-body effects neglected in this approximation. In practice the dielectric function within the RPA is calculated in reciprocal lattice vectors \mathbf{G} (plane-wave components). In this formalism the expression for evaluating the dielectric function (eq. 3.9) within the RPA from the non-interacting density response function is in reciprocal space given as:

$$\epsilon_{\mathbf{G}\mathbf{G}'}(\mathbf{q}, \omega) = \delta_{\mathbf{G}\mathbf{G}'} - \frac{4\pi}{|\mathbf{q} + \mathbf{G}|} \chi_{\mathbf{G}\mathbf{G}'}^0(\mathbf{q}, \omega) \frac{1}{|\mathbf{q} + \mathbf{G}'|} \quad (3.12)$$

and $\chi_{\mathbf{G}\mathbf{G}'}^0$ is directly evaluated from the Kohn-Sham system. For a longer introduction to details of this evaluation the reader can consult [39].

We will comment on the relation between the theoretical framework for calculating the dielectric properties, quantified by the dielectric function, and the results obtained from performing an actual measurement. While the calculated dielectric function, contains detailed microscopic quantities and describes the physical variation down to the atomic length scale, actual experiments probing the optical properties of materials are working at wave lengths of several hundreds of nanometers. Consequently the result of optical measurements is an average over a large area of the material. To be able to compare computed optical properties to experimental measurements it is therefore necessary to define an averaged dielectric function, defining the macroscopic response of the system. To do this, one averages the external potential over all (in-plane in 2D) space, *i.e.* in a computation this corresponds to averaging over one unit cell. In the PW description picking out the macroscopic component of the dielectric function corresponds to evaluating the $\mathbf{G} = \mathbf{G}' = \mathbf{0}$ component of ϵ in eq. 3.12. However, since the microscopic details of the dielectric function are given by the off-diagonal elements of the dielectric matrix, the macroscopic dielectric function is defined by 1 over the inverse $\mathbf{G} = \mathbf{G}' = \mathbf{0}$ component of $\epsilon_{\mathbf{G}\mathbf{G}'}$:

$$\epsilon^{\text{M}}(\mathbf{q}, \omega) = \frac{1}{\epsilon_{\mathbf{0}\mathbf{0}}^{-1}(\mathbf{q}, \omega)}, \quad (3.13)$$

where ϵ^M is the macroscopic dielectric function which is the parameter that makes sense in relation to an experiment performed on a macroscopic scale. From this definition, where we effectively include the off-diagonal terms of $\epsilon_{\mathbf{G}\mathbf{G}'}$ in the definition of the macroscopic dielectric function is in the literature formally known as including the local-field effects. The introduction and definition of the macroscopic dielectric function further enables the theoretical definition of the absorbance. This is of particular interest since, the experimental optical measurement enables the extraction of the absorption spectrum of the material. In general, the dielectric function can be decomposed into a real and an imaginary part: $\epsilon = \epsilon_1 + \epsilon_2$, where ϵ_1 and ϵ_2 denote the real and imaginary part respectively. From classical electrostatics it is well known that the real part is related to the reflectance of the material, the imaginary part is related to the absorbance of the material, and furthermore that the imaginary part is proportional to the polarisability of the material [56], which in the optical limit in reciprocal space takes the form:

$$\text{Abs}(\mathbf{q} \rightarrow \mathbf{0}, \omega) = -4\pi \lim_{\mathbf{q} \rightarrow \mathbf{0}} \left[\frac{1}{q^2} \text{Im}P(\mathbf{q}, \omega) \right] \quad (3.14)$$

where Abs is the absorption coefficient at frequency ω . The problem of obtaining the absorption coefficient is thus reduced to finding an expression for the irreducible polarisability. The form of eq. 3.14 shows that the irreducible polarisability must be proportional to q^2 for the left hand side to be dimensionless. By taking the imaginary part of eq. 3.9 in reciprocal space directly gives: $\text{Im}\epsilon_{\mathbf{G}\mathbf{G}'}(\mathbf{q}, \omega) = v(\mathbf{q})\text{Im}P_{\mathbf{G}\mathbf{G}'}(\mathbf{q}, \omega)$ in a PW description. In 3D the Coulomb interaction scales as $1/q^2$, and thus by comparing to eq. 3.14 one can immediately define the optical absorbance in 3D from the imaginary part of the microscopic dielectric function:

$$\text{Abs}^{3D}(\mathbf{q} \rightarrow 0, \omega) = \lim_{\mathbf{q} \rightarrow \mathbf{0}} \left[\text{Im}\epsilon^M(\mathbf{q}, \omega) \right] = \lim_{\mathbf{q} \rightarrow \mathbf{0}} \left[\text{Im} \frac{1}{\epsilon_{\mathbf{0}\mathbf{0}}^{-1}(\mathbf{q}, \omega)} \right]. \quad (3.15)$$

In 2D where the Coulomb interaction scales as $1/q$ a similar definition cannot be carried out, in fact the macroscopic dielectric function equals unity as $\mathbf{q} \rightarrow \mathbf{0}$ as can be seen from examining eq. 3.12 in 2D and thus such a definition does not have any physical meaning. Instead we consider eq. 3.8 in reciprocal space. If we isolate the irreducible polarisability we get:

$$P(\mathbf{q}, \omega) = \chi(\mathbf{q}, \omega)(1 + v(\mathbf{q})\chi(\mathbf{q}, \omega))^{-1}. \quad (3.16)$$

In all dimensions the density response function scales as q^2 in the optical limit. This means that $v(\mathbf{q}_{\parallel})\chi(\mathbf{q}_{\parallel}, \omega) \sim \mathbf{q}_{\parallel}$ (in 2D we here explicitly state that we only consider in-plane q -vectors), which can be assumed to be much smaller than 1 in the $\mathbf{q}_{\parallel} \rightarrow 0$ limit. The 2D absorption coefficient can therefore instead be defined from the macroscopic density response function:

$$\text{Abs}^{2D}(\mathbf{q} \rightarrow 0, \omega) = -4\pi \lim_{\mathbf{q}_{\parallel} \rightarrow \mathbf{0}} \left[\text{Im} \frac{1}{q_{\parallel}^2} \chi_{\mathbf{0}\mathbf{0}}(\mathbf{q}_{\parallel}, \omega) \right]. \quad (3.17)$$

In principal the 3D absorption coefficient could similarly be defined from this expression. Due to q -dependence of the 3D Coulomb interaction, only the density response function in the denominator would carry a q -dependence on the right hand side, and the q -treatment would then in fact be exact in the 3D case.

At this point we still owe the reader a more intuitive explanation of the physical significance of the response functions in terms of the direct particle-particle interaction. From electrostatics, it is well known that the dielectric function of a material reduces the strength of electric field lines passing through the material. If we consider two charged particles in free space, both of charge c with a separation length \mathbf{r}_0 , the Coulomb interaction between the two particles is given by: $v(\mathbf{r}_0) = \frac{1}{4\pi\epsilon_0} \frac{c^2}{r_0}$, where we explicitly write the interaction potential out in SI units to highlight the presence of the vacuum permittivity. If the two charged particles instead were located inside a dielectric media, the interaction potential is reduced (physically due to the presence of all other free charged particles, which will reduce their interaction) by the dielectric function of the media. Since this physical dielectric screening is inherently non-local (the interaction strength at position \mathbf{r} depends on electronic density at all other positions), the screened Coulomb interaction is now given by integrating over all space:

$$W(\mathbf{r}, \mathbf{r}', \omega) = \int d\mathbf{r}_1 v(\mathbf{r}, \mathbf{r}_1) \epsilon^{-1}(\mathbf{r}_1, \mathbf{r}', \omega). \quad (3.18)$$

This definition can straightforwardly be carried out for the microscopic dielectric function (as shown here) and for the macroscopic dielectric function as well. We will refer to W as the screened Coulomb interaction and to v as the bare Coulomb interaction. If one considers the pair of interacting charged particles the electric field lines penetrate space in all 3 dimensions, and the strength of these can in a simple picture be seen to be reduced everywhere in space with the presence of other charge particles. In a 3D bulk crystal, the interacting charged particle pair are thus everywhere surrounded by other charged particles, which leads to a significant reduction of their interaction potential. However, in a 2D monolayer, where all charge is closely confined around the 2D plane, the majority of the electric field lines penetrate free space. As a consequence of this, the screened Coulomb interaction between charged particles is much stronger in 2D than in 3D. Another peculiar artefact of the dielectric function in 2D is its dependence on the reciprocal wave-vector \mathbf{q} . In most introductory text books, ϵ is taken to be a constant without elaborating on its intrinsic dependence on \mathbf{q} . As illustrated in fig 3.1, where we plot the macroscopic dielectric function, this is found to be a good approximation, since the macroscopic dielectric function in bulk 3D crystals (shown in black) is constant over a wide range of \mathbf{q} and can be taken to equal its values at $\mathbf{q} = \mathbf{0}$. The story is very different for 2D monolayers, where the macroscopic dielectric function changes rapidly even for small \mathbf{q} (shown in green). This can intuitively be understood from the following reasoning: at $\mathbf{q} = \mathbf{0}$, corresponding to an infinitely long separation between the charged interacting particles, varying the distance between the particles only have little effect in a bulk crystal, since one is effectively averaging over the full crystal. However, in a 2D monolayer, at an infinite separation distance, all electric field lines

are located in the vacuum surrounding the monolayer, and the macroscopic dielectric function must consequently attain the value one. As one reduces the distance in 2D ϵ takes a complicated form, since the electric field lines are partly located inside the 2D monolayer and in the vacuum. For large \mathbf{q} , the distance between the interacting charged particles becomes so close, that we are now in the limit where most electric field lines are located inside the 2D monolayer. Thus, in this limit the 2D macroscopic dielectric function will attain similar values to the 3D macroscopic dielectric function. Especially, when the interacting distance becomes smaller than the characteristic extension of the electronic density in the out-of-plane direction, it becomes impossible to differentiate between the 2D and the 3D case explaining the overlap between the two functions in this limit.

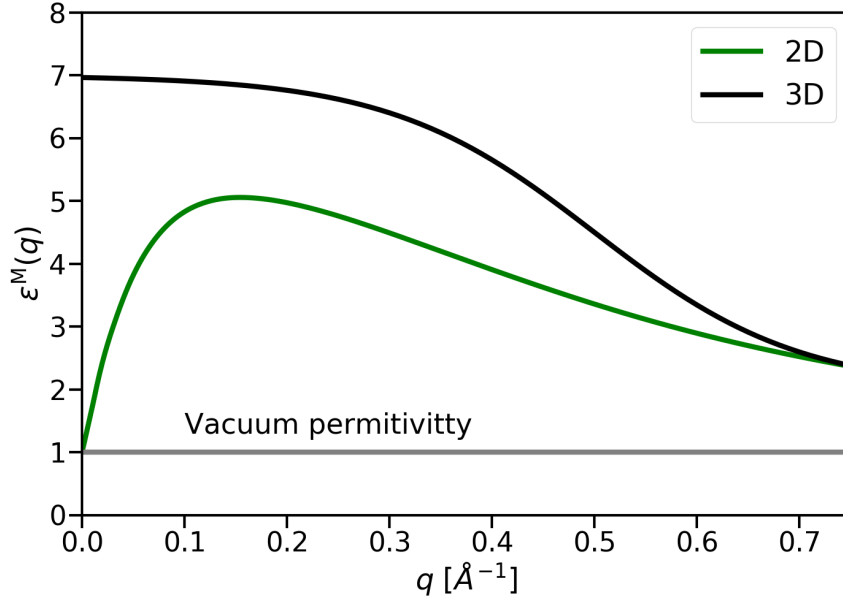


Figure 3.1: Illustration of the macroscopic dielectric function for a freestanding 2D monolayer (green) and a 3D bulk crystal (black) as a function of the reciprocal lattice vector. In grey is shown the vacuum dielectric permittivity.

If one further inspects the 2D macroscopic dielectric function in fig. 3.1 for small q , one finds that this takes a close to linear form around $\mathbf{q} = \mathbf{0}$. That the 2D dielectric function can be approximated to be linear in this limit, is now a well-known and widely used approximation in the 2D monolayer community [24, 117]. To verify the linear approximation for the dielectric function we consider the N -dimensional version of eq. 3.12 within the RPA:

$$\epsilon_{\mathbf{G}\mathbf{G}'}(\mathbf{q}, \omega) = \delta_{\mathbf{G}\mathbf{G}'} - v(\mathbf{q})\chi_{\mathbf{G}\mathbf{G}'}^0(\mathbf{q}, \omega) \quad (3.19)$$

where \mathbf{q}' is the Coulomb kernel which can take any value $\mathbf{q} + \mathbf{G}$. As mentioned above, in reciprocal space the non-interacting density response function, eq. 3.11, is known to

be proportional to q^2 for $q \rightarrow 0$ in all dimensions [24] (*i.e.* in the optical limit). Since in 2D the Coulomb kernel is proportional to $1/q$ while in 3D the Coulomb kernel is proportional to $1/q^2$, inserting this in eq. 3.19 one immediately gets for $\mathbf{G} = \mathbf{G}' = \mathbf{0}$:

$$\epsilon_{\mathbf{00}}^{2D}(\mathbf{q} \rightarrow 0) = \delta_{\mathbf{00}} + a^{2D} \mathbf{q}_{\parallel} \quad (3.20)$$

$$\epsilon_{\mathbf{00}}^{3D}(\mathbf{q} \rightarrow 0) = \delta_{\mathbf{00}} + a^{3D} \quad (3.21)$$

where a^{ND} is a combined (positive) constant of proportionality from the exact form of χ^0 . From this several aspects of fig. 3.1 can be explained. First it shows, that the dielectric function in 2D attains the value one for $\mathbf{q} = \mathbf{0}$, while it takes some finite value larger than one in 3D. Second, we see that the 3D bulk dielectric function is constant over a wide range of small \mathbf{q} while the 2D dielectric function increases linearly. In section 3.8 we will consider the 2D dielectric function in greater detail and show the origin of a new dielectric screening regime when the 2D monolayer is placed on a bulk dielectric substrate.

3.2 Many-Body Perturbation Theory, the GW Approximation, and Vertex Correction

In this section we will see how the single-particle description provided by DFT can be improved upon by introducing the concept of quasi-particle states, which allows us to more accurately calculate excited-state properties of materials. We will discuss this in the context of the widely adapted GW approximation, which in recent years has been used to accurately calculate quasi-particle energies for both solids [55, 29, 36, 97, 104, 88, 111] and molecular systems [13, 110, 68]. It is important to stress that the GW approximation has its success from predicting quasi-particle energies for transitions close to the Fermi level, but fails to accurately predict core-level excitations [43], which will not be a topic of this study. While the full derivation of the GW (and Hedin's equations [51]) is lengthy and well documented in many reviews [54, 43, 6], we will here restrict ourselves to go through the main steps and physical arguments leading to the GW approximation.

In section 2.1 we discussed the complexity of the many-body problem and in section 2.2 we discussed the Kohn-Sham formalism as a simplified approach to obtain single-particle wave functions, the ionisation potential, and the ground-state energy. We illustrated that the complexity of the many-body problem could be put together in a term describing the exchange and correlation effects. The most studied approximations for the exchange and correlation term include only considering the local density as in LDA or by including the gradient of the density to get a better description of the microscopic variation of the density such as in PBE. Within these approximations an adequate description of the ionisation potential and electron affinity can be obtained for some systems (even though the latter still does not owe any physical meaning within the DFT formalism but can accurately be predicted by invoking the derivative discontinuity) or

more generally the difference in energy between the occupied and unoccupied states, *i.e.* the single-particle transition energies. However, in systems with strongly interacting electrons the above approximations are not sufficient to obtain accurate single-particle transition energies (as compared to experimental values) for the full band structure. For such systems it is necessary to go beyond the homogeneous electron gas and properly describe the *screened* electron-electron interaction rather than the bare Coulomb interaction. As we saw in the previous section the screened electron-electron interaction is inherently non-local, suggesting that it is necessary to expand upon the Kohn-Sham equation and instead adapting a non-local quantity for the exchange correlation term:

$$\left[-\frac{1}{2}\nabla^2 + v_{\text{Ha}}[n](\mathbf{r}) + v_{\text{ext}}[n](\mathbf{r}) \right] \phi_i(\mathbf{r}) + \Pi(\mathbf{r}, \mathbf{r}')\phi_i(\mathbf{r}) = \epsilon_i\phi_i(\mathbf{r}) \quad (3.22)$$

where all terms in the Hamiltonian are the same as in the Kohn-Sham equation (2.14) and we have introduced a non-local parameter $\Pi(\mathbf{r}, \mathbf{r}')$, to be determined representing a non-local exchange-correlation functional. We will comment on the nature of the eigenstates below. To describe the excitations of strongly correlated systems, it turns out it is sufficient to introduce the idea of *quasi-particles*, *i.e.* the dressed electron-electron interaction. This is essentially the bare Coulomb interaction screened by a screening cloud of charged particles, which reduces the interaction strength compared to the bare Coulomb interaction as explained in the previous section in connection with the dielectric function. We start by defining the single-particle Green's function:

$$G(\mathbf{r}t, \mathbf{r}'t') \equiv -i\langle N | \hat{T} \{ \hat{\Psi}(\mathbf{r}t) \hat{\Psi}^\dagger(\mathbf{r}'t') \} | N \rangle \quad (3.23)$$

where $|N\rangle$ is the N -particle ground state, \hat{T} is the time-ordering operator, and $\hat{\Psi}(\mathbf{r}t)$ ($\hat{\Psi}^\dagger(\mathbf{r}'t')$) is the annihilation (creation) operator *i.e.* the field operators. Two approaches can now be employed to proceed. One approach is to write down the Heisenberg equation of motion for the field operators which can be rewritten into an equation of motion for the single-particle Green's function. The second approach is to directly insert a complete set, $\sum_i |\phi_i^{N\pm 1}\rangle \langle \phi_i^{N\pm 1}|$, of the $N \pm 1$ states of the N -particle many-body space and Fourier transform to frequency space. From both approaches we arrive at what is known as the Lehman representation of the single-particle Green's function:

$$G(\mathbf{r}t, \mathbf{r}'t', \omega) = \sum_i \frac{\langle N | \hat{\Psi} | \phi_i^{N+1} \rangle(\mathbf{r}t) \langle \phi_i^{N-1} | \hat{\Psi} | N \rangle(\mathbf{r}'t')}{\omega - \delta\xi_i}. \quad (3.24)$$

where $\delta\xi_i$ are the single-particle energies associated with the difference between the N and $N \pm 1$ states. We now directly define the quasi-particle wave functions and energies as the electron addition and removal energies, *i.e.* the cost of adding or removing an electron from the system:

$$\phi_i^{\text{QP}}(\mathbf{r}t) = \begin{cases} \langle N | \hat{\Psi} | \phi_i^{N+1} \rangle(\mathbf{r}t), \epsilon_i > E_F \\ \langle \phi_i^{N-1} | \hat{\Psi} | N \rangle(\mathbf{r}t), \epsilon_i < E_F \end{cases} \quad (3.25)$$

$$\epsilon_i^{\text{QP}} = \begin{cases} \xi_i^{N+1} - \xi_0, \epsilon_i > E_F \\ \xi_0 - \xi_i^{N-1}, \epsilon_i < E_F. \end{cases} \quad (3.26)$$

where E_F is the Fermi level. With these definitions eq. 3.24 can be rewritten into:

$$G(\mathbf{r}t, \mathbf{r}'t', \omega) = \sum_i \frac{\phi_i^{\text{QP}}(\mathbf{r})\phi_i^{\text{QP}*}(\mathbf{r}')}{\omega - \epsilon_i^{\text{QP}}}, \quad (3.27)$$

from which the quasi-particle energies can now be found as the poles of the denominator and where the quasi-particle wave functions can be determined from the solutions to the quasi-particle equation [51]:

$$\left[-\frac{1}{2}\nabla^2 + v_{\text{Ha}}(\mathbf{r}) + v_{\text{ext}}(\mathbf{r}) \right] \phi_i^{\text{QP}}(\mathbf{r}) + \int d\mathbf{r}' \Sigma_{\text{xc}}(\mathbf{r}, \mathbf{r}', \epsilon_i^{\text{QP}}) \phi_i^{\text{QP}}(\mathbf{r}') = \epsilon_i^{\text{QP}} \phi_i^{\text{QP}}(\mathbf{r}). \quad (3.28)$$

By comparing this to the form of our initial guess, eq. 3.22, we see that the to-be-determined non-local term takes the form of a non-local self-energy, $\Sigma_{\text{xc}}(\mathbf{r}, \mathbf{r}', \epsilon_i^{\text{QP}})$ and that the eigenstates are approximated as the quasi-particle wave functions defined above. Note that the quasi-particle wave functions are not the *true* eigenstates of the system. This means that the eigenenergies (the poles) of eq. 3.27 have an imaginary part which gives the lifetime of the quasi-particle states. To determine the quasi-particle energies, the problem is now reduced to determining the (interacting) Green's function and the self-energy, which, however is itself a function of the quasi-particle energy. The problem can be further simplified by relating the interacting Green's function and the self-energy by a Dyson equation:

$$G(\mathbf{r}, \mathbf{r}', \omega) = G_0(\mathbf{r}, \mathbf{r}', \omega) + \int \int d\mathbf{r}_1 d\mathbf{r}_2 G_0(\mathbf{r}, \mathbf{r}_1, \omega) \Sigma_{\text{xc}}(\mathbf{r}_1, \mathbf{r}_2, \omega) G_0(\mathbf{r}_2, \mathbf{r}', \omega). \quad (3.29)$$

Here G_0 is the non-interacting Green's function, and this now leaves the problem to only determine the self-energy. To ease the understanding we will for now change the notation to $(\mathbf{r}_i\omega) \rightarrow (i)$. In the previous section we introduced the irreducible polarisability as the functional derivative of the electron density with respect to the total potential (eq. 3.7) and the inverse dielectric function as the relation between the total potential and an externally applied potential (eq. 3.4). These are related through eq. 3.9, which can be inverted and inserted in eq. 3.18 to obtain:

$$W(1; 2) = v(1, 2) + \int d3d4 v(1; 3) P(3; 4) W(4; 2). \quad (3.30)$$

To close the set of equations and determine the self-energy we need to introduce the so-called *vertex*, which describes the change in the (inverse) interacting Green's function to the change in the total potential:

$$\Gamma(1, 2; 3) = -\frac{\delta G^{-1}(1; 2)}{\delta v_{\text{tot}}(3)}. \quad (3.31)$$

Comparing to eqs. 3.5 and 3.7 the vertex can to some extent be understood as a response function for the Green's function (with the little physical meaning this definition holds). It was shown by Hedin [51] that this quantity connects the interacting Green's function, the self-energy, the screened Coulomb interaction, and the irreducible polarisability. We

will here simply state the remaining three of Hedin's equations which together with eq. 3.29 and eq. 3.30 provide a closed set of equations to determine the self-energy, and refer to Hedin's original work for the derivation of the equations involving the vertex:

$$P(1; 2) = -i \int d3d4 G(1; 3)G(4; 1)\Gamma(3, 4; 2) \quad (3.32)$$

$$\Sigma_{xc}(1; 2) = i \int d3d4 G(1; 4)W(1, 3)\Gamma(4, 2; 3) \quad (3.33)$$

$$\Gamma(1, 2; 3) = \delta(1; 3)\delta(2; 3) + \int d4d5d6d7 \frac{\partial \Sigma_{xc}(1; 2)}{\partial G(4; 5)} G(4; 6)G(7; 5)\Gamma(6, 7; 3). \quad (3.34)$$

While this set of equations in principle can be solved self-consistently to obtain the self-energy and consequently the quasi-particle energies this is not computationally feasible. Instead, we will apply one of the physicists strongest methods: we will make an initial guess for the self-energy, iterate the set of equations once, and see what we obtain for the self-energy. The simplest guess for the self-energy is simply putting it equal to zero: $\Sigma_{xc} = 0$ which directly gives the vertex as:

$$\Gamma(1, 2; 3) = \delta(1; 3)\delta(2; 3). \quad (3.35)$$

Inserting this in eq. 3.32 we obtain for the irreducible polarisability:

$$P(1; 2) = -iG(1; 2)G(1; 2). \quad (3.36)$$

The screened Coulomb interaction becomes:

$$W(1; 2) = v(1, 2) - i \int d3d4 v(1; 3)G(1; 4)G(1; 4)W(4; 2)) \quad (3.37)$$

which can be inverted to give:

$$W(1; 2) = \frac{v(1)}{1 - v(1)\chi_0(1; 2)} \quad (3.38)$$

where we have inserted the definition of the non-interacting susceptibility: $\chi_0 = -iGG$. The interacting Green's function now simply becomes the non-interacting Green's function:

$$G(1; 2) = G_0(1; 2). \quad (3.39)$$

Note that this is the closest we get to a formal definition of the difference between the interacting and non-interacting Green's function within this framework, namely that the non-interacting Green's function satisfies the Green's function equation of motion when the self-energy is put to zero. Finally for the self-energy we obtain:

$$\Sigma_{xc}(1; 2) = iG(1; 2)W(1; 2) = \frac{iG(1; 2)v(1)}{1 - v(1)\chi_0(1; 2)} \quad (3.40)$$

This approximation for the self-energy is formally known as the GW approximation. The expression obtained for the irreducible polarisability in eq. 3.36 is the formal definition

of the RPA as we also encountered in the previous section (when putting $P = \chi^0$) and shows that the screened Coulomb interaction in the G0W0 is calculated within the RPA.

It is now tempting to iterate Hedin's equations again with the new expression for the self-energy, however it turns out that doing this will lead us to the Bethe-Salpeter equation as we will see later, which includes electron-hole interactions in the description of the excitations. Instead we will take inspiration from the fact that in the GW approximation the self-energy can be viewed as a modified bare Coulomb interaction with an inherent non-locality. Thus we will now iterate Hedin's equations with a more general guess for the self-energy: $\Sigma(1; 2) = \delta(1, 2)v_{\text{xc}}(1)$, where $v_{\text{xc}}(1)$ is the exchange-correlation functional from the Kohn-Sham formalism, for instance the LDA or a GGA functional. Inserting this into the Dyson equation for the vertex yields:

$$\Gamma(1, 2; 3) = \delta(1; 3)\delta(2; 3) + i\delta(1; 2) \int d5d6d7 \frac{\partial v_{\text{xc}}(1)}{\partial G(5)} G(5; 6)G(7; 5)\Gamma(6, 7; 3). \quad (3.41)$$

We note here that $G(i)$ by the definition of the single-particle Green's function (eq. 3.23) is simply the expectation value of the electronic density: $-i\rho(i)$, and the derivative of the Kohn-Sham exchange correlation function therefore can be regarded as an *effective* potential which we will denote by: $v_{\text{xc}}^{\text{eff}}(1, 2) = \frac{\partial v_{\text{xc}}(1)}{\partial G(2)}$. To proceed we have to insert this in eq. 3.32 and follow the flowchart of the derivation of the GW method. We will spare the reader these merely mathematical steps, and instead state that despite how unpleasant the procedure looks, it turns out that the final expression for the screened interaction, and therefore the self-energy, take a form very close to that of eq. 3.40:

$$\Sigma_{\text{xc}}(1; 2) = iG(1; 2)W(1; 2) = \frac{iG(1; 2)v(1)}{1 - (v(1) + v_{\text{xc}}^{\text{eff}}(1))\chi_0(1; 2)} \quad (3.42)$$

which can to some extent simply be viewed as a modified screened interaction, with a correction to the bare Coulomb interaction from the Kohn-Sham exchange correlation functional, and the GW approximation is restored simply by putting the vertex correction equal to unity, *i.e.* putting $v_{\text{xc}}^{\text{eff}} = 0$. Using this expression for the self-energy is formally known as the G Γ approximation. The interest for this approximation is that it has proven to give better descriptions of ionisation potentials and electron affinities [46] of solid state materials.

With an expression for the self-energy in hand it is now possible to directly solve the quasi-particle equation self-consistently to obtain the quasi-particle energies. This is however not computationally feasible in practice and further approximations are needed. The problem arises from the fact that the G in the self-energy has to be calculated from the quasi-particle energies. If the Kohn-Sham description already offers an adequate description of the system, the difference between the self-energy and the Kohn-Sham exchange-correlation contribution can be expected to be small. The trick is to add and subtract the Kohn-Sham exchange-correlation functional to the quasi-particle equation, so we get a term in the quasi-particle equation that involves: $\Sigma_{\text{xc}}(\mathbf{r}, \mathbf{r}', \epsilon_i^{\text{QP}}) - v_{\text{xc}}^{\text{KS}}(\mathbf{r})$,

where $v_{\text{xc}}^{\text{KS}}(\mathbf{r})$ is the Kohn-Sham exchange correlation function. By assumption this term is small and can thus be expanded around the quasi-particle energies to first order:

$$\Sigma_{\text{xc}}(\mathbf{r}, \mathbf{r}', \epsilon_i^{\text{QP}}) = \Sigma_{\text{xc}}(\mathbf{r}, \mathbf{r}', \epsilon_i^{\text{KS}}) + (\epsilon_i^{\text{QP}} - \epsilon_i^{\text{KS}}) \frac{\partial \Sigma_{\text{xc}}(\omega)}{\partial \omega} \Big|_{\omega=\epsilon_i^{\text{QP}}}. \quad (3.43)$$

The main advantage of this simplification is that the self-energy is now evaluated from Kohn-Sham eigenvalues rather than the quasi-particle energies. This reduces the accuracy of the GW method, but also reduces the computational requirements significantly since the quasi-particle energies now can be evaluated from a one-shot GW calculation, known as a G0W0 calculation, by taking the expectation value of the quasi-particle equation (with Kohn-Sham wave functions) in the linearised expression for the self-energy:

$$\epsilon_i^{\text{QP}} = \epsilon_i^{\text{KS}} + Z_i \langle \psi_i^{\text{KS}} | \Sigma_{\text{xc}}(\epsilon_i^{\text{KS}}) - v_{\text{xc}}^{\text{KS}}(\mathbf{r}) | \psi_i^{\text{KS}} \rangle, \quad (3.44)$$

which can be directly evaluated once the Kohn-Sham wave functions and eigenvalues are obtained from DFT. The renormalisation factor, $Z_i = \langle \psi_i^{\text{KS}} | 1 - \frac{\partial \Sigma_{\text{xc}}(\omega)}{\partial \omega} \Big|_{\omega=\epsilon_i^{\text{QP}}} | \psi_i^{\text{KS}} \rangle^{-1}$, expresses to which degree the Kohn-Sham wave function resembles the quasi-particle state, *i.e.* if $\frac{\partial \Sigma_{\text{xc}}(\omega)}{\partial \omega} \Big|_{\omega=\epsilon_i^{\text{QP}}}$ is very large the linearisation of $\Sigma_{\text{xc}} - v_{\text{xc}}^{\text{KS}}$ is not a good approximation and the ansatz that the Kohn-Sham formalism offer an adequate description of the quasi-particle picture breaks down. The renormalisation factor therefore attains values close to 1, in practice around 0.8-0.9 for well-described systems. The approximation is known as the non-self-consistent GW approximation or simply the G0W0 approximation, and is the method from which we will calculate quasi-particle energies in this thesis based on either the GW or GWT expressions for the self-energy.

All calculations in this study are performed at 0 K, without including the effect of zero-point-motion phonon contributions. Finite temperature effects enter through a coupling between the electronic and the phononic states, which is not present in the standard GW (and BSE) approximations presented and applied in this thesis. The electron-phonon coupling has two effects: first, it shifts the excitation energy of the quasi-particle and exciton states, and second, it introduces an imaginary part to the eigenvalues corresponding to the lifetime of the quasi-particle states. This is visually seen as a broadening of the excitation peaks in absorption and photoluminescence spectra. One way to computationally account for the electron-phonon coupling is to add corrections arising from the electron-phonon interaction to the self-energy in eq. 3.44 in a perturbative manner. In this approach the first two order terms, corresponding to a first order scattering event: $\langle n\mathbf{k} | \rightarrow \langle n\mathbf{k} - \mathbf{q}_1 | + \langle \lambda\mathbf{q}_1 |$ for phonon state λ with amplitude $g_{n\mathbf{n}'\mathbf{k}}^{\lambda\mathbf{q}_1}$ and a second order scattering event: $\langle n\mathbf{k} | \rightarrow \langle n\mathbf{k} - \mathbf{q}_1 - \mathbf{q}_2 | + \langle \lambda\mathbf{q}_1 | + \langle \lambda'\mathbf{q}_2 |$ with amplitude $b_{n\mathbf{n}'\mathbf{k}}^{\lambda\mathbf{q}_1, \lambda'\mathbf{q}_2}$, give rise to the Fan [32] (Σ^{F}) and Debye-Waller [41] (Σ^{DW}) self-energy corrections respectively:

$$\Sigma_{n\mathbf{k}}^{\text{F}}(\epsilon, T) = \sum_{n'\lambda\mathbf{q}_1} \frac{|g_{n\mathbf{n}'\mathbf{k}}^{\lambda\mathbf{q}_1}|^2}{N_{\mathbf{q}}} \left(\frac{N_{\mathbf{q}}(T) + 1 - f_{n'\mathbf{k}-\mathbf{q}_1}}{\epsilon - \epsilon_{n'\mathbf{k}-\mathbf{q}_1} - \omega_{\lambda\mathbf{q}_1}} \right) \left(\frac{N_{\mathbf{q}}(T) + f_{n'\mathbf{k}-\mathbf{q}_1}}{\epsilon - \epsilon_{n'\mathbf{k}-\mathbf{q}_1} + \omega_{\lambda\mathbf{q}_1}} \right) \quad (3.45)$$

$$\Sigma_{\mathbf{nk}}^{\text{DW}}(\epsilon, T) = \sum_{\mathbf{n}'\lambda\mathbf{q}_1\lambda'\mathbf{q}_2} \frac{|b_{\mathbf{nn}'\mathbf{k}}^{\lambda\mathbf{q}_1,\lambda'\mathbf{q}_2}|^2}{N_{\mathbf{q}}} (2N_{\mathbf{q}}(T) + 1) \quad (3.46)$$

where T is the temperature, $N_{\mathbf{q}}$ is the phonon Bose distribution, $f_{\mathbf{n}'\mathbf{k}}$ is the electron Fermi distribution, $\omega_{\lambda\mathbf{q}}$ is the phonon energy, and $\epsilon_{\mathbf{n}'\mathbf{k}-\mathbf{q}_1}$ the electron eigenvalue energy. Finite temperature effects enter through the phonon population, however even at $T = 0$ K, a non-neglecting contribution comes from the phonon population due to the zero-point-energy. Furthermore, note that only the Fan self-energy carries a contribution to the imaginary part of the quasi-particle energies, and thus the quasi-particle lifetime. The Fan and Debye-Waller self-energies are in practice added to the pure GW self-energy in eq. 3.44, such that: $\Sigma_{\text{xc}}(\epsilon_i^{\text{KS}}) \rightarrow \Sigma_{\text{xc}}(\epsilon_i^{\text{KS}}) + \Sigma_{\mathbf{nk}}^{\text{F}}(\epsilon_i^{\text{KS}}, T) + \Sigma_{\mathbf{nk}}^{\text{DW}}(\epsilon_i^{\text{KS}}, T)$. In chapter 4 we will consult the literature for how these effects affect quasi-particle energies in few-layers vdWHs, since these contributions are not implemented in GPAW.

Finally, we will briefly comment on the implementation flowchart in GPAW since this will be necessary for reference in the next section. The GW formalism is implemented in the PW formalism, where the self-energy is directly calculated by summing over all occupied and unoccupied states (index m) and averaging over the Brillouin zone with area Ω :

$$\begin{aligned} \Sigma_{\mathbf{nk}}(\epsilon_{\mathbf{nk}}^{\text{KS}}) &= \langle \mathbf{nk} | \Sigma(\omega) | \mathbf{nk} \rangle \\ &= \frac{1}{\Omega} \sum_{\mathbf{G}\mathbf{G}'} \sum_{\mathbf{q}} \sum_{m}^{\text{all}} \frac{i}{2\pi} \int_{-\infty}^{\infty} d\omega' W_{\mathbf{G}\mathbf{G}'}(\mathbf{q}, \omega') \times \frac{\rho_{\mathbf{mq}-\mathbf{k}}^{\mathbf{nk}}(\mathbf{G}) \rho_{\mathbf{mq}-\mathbf{k}}^{\mathbf{nk}*}(\mathbf{G}')}{\epsilon_{\mathbf{nk}}^{\text{KS}} - \epsilon_{\mathbf{nk}-\mathbf{q}}^{\text{KS}} - \omega' + i\eta \text{sgn}(\epsilon_{\mathbf{mk}-\mathbf{q}} - E_{\text{F}})}, \end{aligned} \quad (3.47)$$

where $|\mathbf{nk}\rangle$ is the Kohn-Sham wave function and ρ is the pair-density: $\rho_{\mathbf{mq}-\mathbf{k}}^{\mathbf{nk}}(\mathbf{G}) = \langle \mathbf{nk} | e^{i(\mathbf{q}+\mathbf{G})\mathbf{r}} | \mathbf{nk} \rangle$. It is well known that, in the averaging over the Brillouin zone, the screened interaction diverges for $\mathbf{q} \rightarrow \mathbf{0}$. This limit is excluded from the summation in the self-energy and is instead calculated analytically as explained in [102]. As we saw above, the irreducible polarisability takes its form within the RPA, and consequently the screened interaction has to be evaluated from the dielectric function calculated from the RPA:

$$W_{\mathbf{G}\mathbf{G}'}(\mathbf{q}, \omega) = \frac{4\pi}{|\mathbf{q} + \mathbf{G}|} \left((\epsilon_{\mathbf{G}\mathbf{G}'}^{\text{RPA}}(\mathbf{q}, \omega))^{-1} - \delta_{\mathbf{G}\mathbf{G}'} \right) \frac{1}{|\mathbf{q} + \mathbf{G}'|}. \quad (3.48)$$

We note that in all G0W0(Γ) calculations in this thesis, the quasi-particle band gap (and thus the ionisation potential and electron affinity levels) are determined by a $1/E_{\text{cut}}^{3/2}$ extrapolation of the band gap to infinite PW cut-off energy, where E_{cut} is the PW cut-off energy of the PW expansion.

3.3 The Quantum Electrostatic Heterostructure Model

The QEH model presented in this section is originally derived in [4], which can be consulted for further details than presented in this section. The corner stones of the QEH model will be discussed here, since the QEH model in its original version has been used to obtain the results for dielectric screening of quasi-particle energies in section 3.5 in this chapter. Later in chapter 3 and in chapter 4 we will then expand the QEH model to include interlayer hybridisation effects and allow for accurate excited states properties, such as exciton energies and absorption spectra in vdWHs to be calculated. While the GW-formalism has been proven to yield accurate quasi-particle energies for both 2D monolayers and 3D bulk systems, difficulties arise when *ab-initio* many-body formalisms, such as GW, are applied to vdWHs. As outlined in section 2.4, when 2D monolayers are stacked into vdWHs, large supercells are required to represent the atomic structure of the (many layers) vdWH if the monolayers are either incommensurate or rotated relative to each other. This means that G0W0 calculations are only computationally feasible for specific vdWH such as lattice matched few-layer vdWHs or by straining one or more layers significantly. While conventional DFT codes can be applied to vdWH of up to a few thousand atoms, apart from the band gap problem of such methods, DFT does not capture the long-range dielectric screening in vdWH. A proper description of the long-range dielectric screening in vdWH is important as can be seen from eq. 3.47, since the screened electron-electron interaction in layer i ($W(\mathbf{q}, \omega)$) is affected by the $N - i$ other layers in the vdWH and consequently have a direct impact on the quasi-particle energies. This suggests that an alternative method is needed to accurately calculate quasi-particle energies in vdWHs. This section will present the QEH model, which allows quasi-particle energies of a general vdWH to be calculated at the G0W0(Γ) level without straining any of the layers. This is done calculating the in-plane dielectric properties of each (freestanding) monolayer fully *ab-initio* and modelling the interlayer interaction purely electrostatically. The success of this model lies in the weak van der Waals interaction between neighbouring layers and it is important to stress that this only provides a proper description of the quasi-particle states, which are only little affected by interlayer hybridisation affects, since this is not included in the original QEH model - we will return to this point in section 3.4 and chapter 4.

Encouraged by the weak interlayer interaction in vdWHs it is convenient to split the full Coulomb interaction into an intra- and interlayer component:

$$v = v^{\text{intra}} + v^{\text{inter}}. \quad (3.49)$$

In this, v^{intra} contains the electron-electron interaction present within each monolayer and v^{inter} defines the weak electrostatic interlayer interaction. Already at this point we again stress interlayer hybridisation effects are not included in v^{inter} . In a simple picture, the electrostatic interaction between two charge distributions can effectively be modelled

with an image charge model, *i.e.* that an additional charge is induced in each layers due to the presence of one and another. In this picture, the electrostatic interaction between layers i and k in a vdWH is given by:

$$v_{i,k}^{\text{inter}}(\mathbf{q}_{\parallel}) = \int dz \rho_i(z, \mathbf{q}_{\parallel}) \Phi_k(z, \mathbf{q}_{\parallel}) \quad (3.50)$$

where ρ_i is the *induced* charge distribution in layer i (from the presence of layer k) and Φ_k is the total potential in layer k generated by the induced charge distribution. Once the induced charge distributions are found the potentials can be determined by solving the Poisson equation for each layer. This shows that, to effectively model the interlayer interaction we need to obtain the induced charge distributions in each layer. To do this, we consider the density response function within the RPA for the full vdWH, *i.e.* including both intra- and interlayer components:

$$\chi(\mathbf{r}_1, \mathbf{r}_2, \omega) = \chi^0(\mathbf{r}_1, \mathbf{r}_2, \omega) + \int d\mathbf{r}_3 d\mathbf{r}_4 \chi^0(\mathbf{r}_1, \mathbf{r}_3, \omega) v(\mathbf{r}_3, \mathbf{r}_4) \chi(\mathbf{r}_3, \mathbf{r}_2, \omega) \quad (3.51)$$

where χ is the interacting density response function, χ^0 is the non-interacting density response function, and $v(\mathbf{r}_3, \mathbf{r}_4)$ is the full Coulomb interaction. Keeping in mind we seek an expression for the induced density in each layer, it is natural to define a density response function of each layer. We do this by assuming the external electrostatic potential in one layer, from the other layers in the vdWH, can be expressed as a multipole expansion, in the out-of-plane direction. We therefore define the intralayer density response, $\tilde{\chi}$, for layer i to pole α of the multipole expansion as:

$$\tilde{\chi}_{i\alpha}(\mathbf{q}_{\parallel}, \omega) = \int dz dz_1 z^\alpha \chi_i(z, z_1, \mathbf{q}_{\parallel}, \omega) z_1^\alpha. \quad (3.52)$$

where χ_i is calculated for each freestanding monolayer *ab-initio* and thus only contains in-plane interactions and z is the position coordinate in the out-of-plane direction. In practice it is only necessary to consider the monopole and dipole components of $\tilde{\chi}$. From this, it is straightforward to calculate the (normalised) induced densities in each layer:

$$\rho_{i\alpha}(z, \mathbf{q}_{\parallel}, \omega) = \frac{1}{\tilde{\chi}_{i\alpha}(\mathbf{q}_{\parallel}, \omega)} \int dz_1 \tilde{\chi}_i(z, z_1, \mathbf{q}_{\parallel}, \omega) z_1^\alpha. \quad (3.53)$$

To obtain macroscopic properties of the vdWH we need to couple eqs. 3.52 and 3.53 to the full density response function, eq. 3.51 for the vdWH. To do this, we insert the intra- and interlayer components for v , eq. 3.49 into eq. 3.51. It is easy to show that this defines two Dyson equations: one for the intralayer Coulomb interaction and one for the interlayer Coulomb. The Dyson equation for the interaction between layer i and k takes the form:

$$\chi_{i\alpha, j\beta}(\mathbf{q}_{\parallel}, \omega) = \tilde{\chi}_{i\alpha} \delta_{i\alpha, j\beta} + \tilde{\chi}_{i\alpha}(\mathbf{q}_{\parallel}, \omega) \sum_{ik, \gamma} v_{i\alpha, k\gamma}^{\text{inter}}(\mathbf{q}_{\parallel}) \chi_{k\gamma, j\beta}(\mathbf{q}_{\parallel}, \omega), \quad (3.54)$$

where k is a layer index, and α , β , and γ are index for the multipole expansion. This relates the full density response function to the freestanding monolayer density response

function. Since eq. 3.51 can be solved fully *ab-initio* for each *freestanding* monolayer, eqns. 3.52 and 3.53 define the dielectric building block of layer i in a vdWH. A large set of dielectric building blocks have been calculated previously and are freely available [4]. We now find that the interlayer Coulomb interaction, defined in eq. 3.50, takes the form:

$$v_{i\alpha,k\gamma}^{\text{inter}}(\mathbf{q}_{\parallel}) = \int dz \rho_{i\alpha}(z, \mathbf{q}_{\parallel}) \Phi_{k\gamma}(z, \mathbf{q}_{\parallel}). \quad (3.55)$$

Finally following the definition in section 3.1 it is straightforward to obtain the macroscopic dielectric function of the vdWH:

$$\epsilon_{i\alpha,j\beta}^{-1}(\mathbf{q}_{\parallel}, \omega) = \delta_{i\alpha,j\beta} + \sum_{k,\gamma} v_{i\alpha,k\gamma}(\mathbf{q}_{\parallel}) \chi_{k\gamma,j\beta}(\mathbf{q}_{\parallel}, \omega). \quad (3.56)$$

This shows that, given a vdWH, by calculating the density response function of each freestanding monolayer calculated fully *ab-initio* (at the level of the RPA) and by applying an electrostatic interlayer coupling, it is possible to obtain the macroscopic dielectric properties of the vdWH.

In the last part of this section we will see how the QEH model can be used to calculate corrections to the quasi-particle energies, of each layer in vdWHs, from the interlayer dielectric screening. We start by generally defining the effective screened electron-electron interaction for a specific layer in terms of the macroscopic dielectric function:

$$W_i^{\text{vdWH}}(\mathbf{q}_{\parallel}, \omega) = \rho_i^e(\mathbf{q}_{\parallel}, \omega) (\epsilon^{\text{M}}(\mathbf{q}_{\parallel}, \omega))^{-1} \phi_i^e(\mathbf{q}_{\parallel}, \omega), \quad (3.57)$$

where ρ_i^e and ϕ_i^e are the induced electronic density and induced potential for the layer in question. By calculating the screened interaction for the freestanding monolayer, it is possible to obtain the correction to the screened interaction in layer i originating from the neighbouring layers as the difference between these two:

$$\Delta W_i(\mathbf{q}_{\parallel}, \omega) = W_i^{\text{vdWH}}(\mathbf{q}_{\parallel}, \omega) - W_i(\mathbf{q}_{\parallel}, \omega), \quad (3.58)$$

where $W_i(\mathbf{q}_{\parallel}, \omega)$ is the screened electron-electron interaction for the freestanding monolayer calculated fully *ab-initio*. The correction to the quasi-particle energies in layer i , due to the additional dielectric screening from the surrounding layers, is then obtained by calculating the correction to the GW self-energy in eq. 3.47 from ΔW_i :

$$\Delta \Sigma_{n\mathbf{k},i} = \frac{1}{\Omega} \frac{i}{2\pi} \int_{\text{BZ}} d\mathbf{q} \int_{-\infty}^{\infty} d\omega' \Delta W_i(\mathbf{q}, \omega) \sum_m^{\text{all}} \frac{\rho_{m\mathbf{q}-\mathbf{k}}^{\text{nk}}(\mathbf{G} = \mathbf{0}) \rho_{m\mathbf{q}-\mathbf{k}}^{\text{nk}} * (\mathbf{G}' = \mathbf{0})}{\epsilon_{n\mathbf{k}}^{\text{KS}} - \epsilon_{n\mathbf{k}-\mathbf{q}}^{\text{KS}} - \omega' + i\eta \text{sgn}(\epsilon_{m\mathbf{k}-\mathbf{q}} - E_{\text{F}})}. \quad (3.59)$$

In the PW basis only the macroscopic part of the pair-density matrices are included ($\mathbf{G} = \mathbf{G}' = \mathbf{0}$). The corresponding change to the quasi-particle energies for layer i is then immediately obtained through the real part of the correction to the GW self-energy:

$$\Delta \epsilon_i^{\text{QP}} = Z_i \text{Re}(\Delta \Sigma_{n\mathbf{k},i}) \quad (3.60)$$

This defines what for the remaining part of this chapter will be denoted as the G0W0(Γ)-QEH method for obtaining quasi-particle energies in vdWH, and can readily be evaluated

for each layer in a vdWH. In practice, to obtain the quasi-particle energies for layer i in a vdWH a G0W0(Γ) calculation for the freestanding monolayer is performed, and subsequently the correction to the quasi-particle energies are then calculated by first calculating the macroscopic dielectric function of the vdWH, then calculating the change in the self-energy from the interlayer dielectric screening, and finally evaluating the actual quasi-particle energy corrections. By utilising the library of previously calculated dielectric building blocks the correction to the quasi-particle energies can be calculated with little computational power compared to a standard monolayer G0W0 calculation.

3.4 Interlayer Orbital Hybridisation

In this section we will take a step back for a brief comment of the effect of interlayer orbital overlap in vdWHs on the quasi-particle state energies. In general, the (bare) Coulomb interaction between two electrons will, at a fixed time, be proportional to the integral of the two electron densities, n_1 and n_2 divided by the distance between their charge distributions: $v \sim \int d\mathbf{r}_1 d\mathbf{r}_2 \frac{n_1(\mathbf{r}_1)n_2(\mathbf{r}_2)}{|\mathbf{r}_1 - \mathbf{r}_2|}$. Similarly, if the two electrons are put in two bound states in close proximity their energies will be affected if there is a finite overlap between their wave functions: $u \sim \int d\mathbf{r} n_1(\mathbf{r})n_2(\mathbf{r})$, with an unknown distance dependence. While the Coulomb interaction, v , remains finite if the charge densities have a zero overlap, the overlap interaction, u , disappears as the overlap goes to zero. We will regard the latter effect as an orbital hybridisation effect. This effect is fundamentally different to the dielectric screening effect studied in the previous chapters, which describes how the mutual interaction between the two electrons is affected by the presence of *other* electrons which electronic densities do not necessarily overlap with electron density of the two electrons considered here. In the previous three sections we have studied how the nature of the dielectric environment affects the ground-state energies and especially that the effect of dielectric screening is non-local. This effect can be accurately calculated in the QEH model and in fact this renormalisation of the quasi-particle energies is almost constant for all bands and throughout the Brillouin zone. The success of the QEH model to accurately predict the renormalisation of the quasi-particle energies for vdWHs relies mainly on the rather big interlayer distances between the neighbouring layers in the vdWHs. This means that there is a very small overlap between the electronic orbitals located on the neighbouring layers and following the argument above, it is therefore expected that the effect on the quasi-particle energies due to interlayer orbital overlap is small. Opposite to the dielectric screening the orbital hybridisation effect is highly band and k -point dependent. While the effect on the quasi-particle energies is in general small for most multilayer structures, it can give rise to a considerable quasi-particle energy renormalisation in localised parts of the Brillouin zone. To show this, in fig. 3.2 we show the band structure of bilayer MoS₂/WS₂ calculated with the G0W0 approximation (left) and the G0W0-QEH approximation (right). While both methods describe the effect of dielectric screening, only the full G0W0 includes the effect of interlayer orbital hybridisation at the level of self-consistent GGA. The

color indicates the projected weight of each state onto the MoS₂ (red) and WS₂ (blue) monolayer respectively. Overall, the effect of interlayer orbital hybridisation does not alter the qualitative features significantly and both unoccupied and occupied states around the K-point are unaffected by the orbital hybridisation (but slightly altered due to interlayer charge transfer effects). Still it is evident that the degenerate valence states around the Γ -point split due to the interlayer orbital hybridisation introducing an indirect band gap and the conduction states between K- Γ are significantly lowered in energy. A purely dielectric screening description of the interlayer interaction in vdWHs is however still sufficient to describe many properties, for instance the K-K electronic band gap in multilayer TMDs.

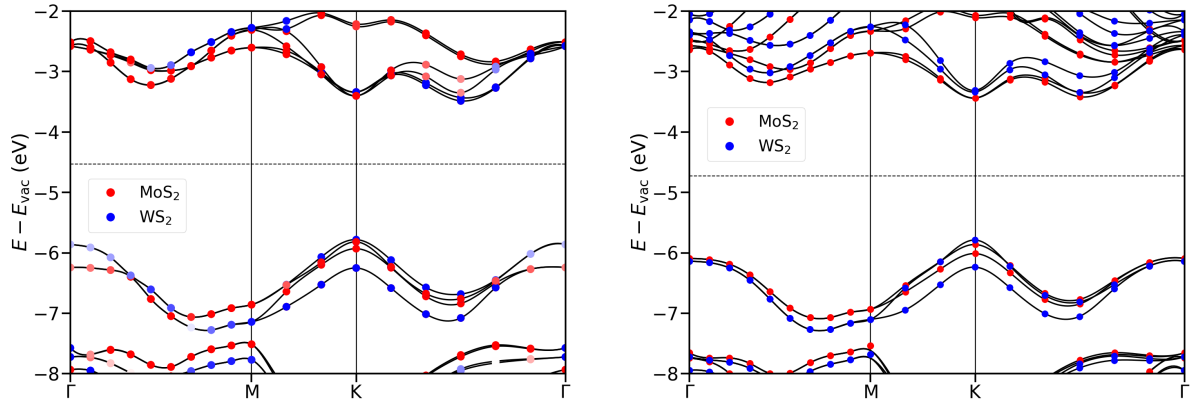


Figure 3.2: Quasi-particle energies calculated with the G0W0 approximation (left) and the G0W0-QEH model (right) for bilayer MoS₂/WS₂. The red (blue) indicates the orbital weight of the state projected onto the MoS₂ (WS₂) monolayer. Faint red or blue color shows interlayer hybridised states. The black lines are the interpolated quasi-particle energies. The Fermi levels are shown by the horizontal dashed lines. Note the full G0W0 calculations contains less conduction bands than the G0W0-QEH calculation.

As explained above, the need for the QEH model is due to the large number of atoms necessary to represent multilayer vdWHs or even incommensurate twisted bilayer structures. Since the interlayer orbital hybridisation is highly dependent on the relative twist-angle between neighbouring layers [3, 42, 72] and possible Moiré pattern effects [83] large supercells are needed to calculate the interlayer orbital hybridisation. It is therefore only possible to calculate the interlayer orbital hybridisation for small lattice matched structures as the one in fig. 3.2 - and even in this case the hybridisation pattern is not necessarily well described. We will return to this delicate subject later and in chapter 4 we will show how such interlayer orbital hybridisation effects can accurately be accounted for when calculating quasi-particle energies for vdWHs.

3.5 Tunable Dielectric Screening in a 2D Semiconductor

In this section we will see the first example of how the non-locality of the dielectric screening gives rise to, and can effectively be utilised in a predictable manner, to manipulate electronic states and electronic structure design of vdWHs. We will restrict ourselves to a setup where the lowest energy transitions and features are not significantly affected by interlayer orbital hybridisation effects such that the electronic properties can be accurately calculated by only considering the interlayer dielectric screening. To this end, we therefore choose to study a system consisting of a monolayer TMD semiconductor placed on top of a gated graphene layer as sketched in fig. 3.3 (left). In addition to this, below we will study the effect of a variable number of intercalated hBN monolayers on the electronic properties of the 2D semiconductor. As we saw in the previous section, the direct quasi-particle band gap in monolayer TMDs is not affected by the interlayer orbital hybridisation of bilayer TMD systems and similarly we expect this to be true at hBN and graphene monolayers interfaces, since the orbital state at the K-point is strongly localised around the central metal atom in the TMD monolayer. Thus, the direct band gap in the monolayer semiconductor should give a good description of the effect of the non-local dielectric screening in such systems. The results presented in this section are a part of the results that can also be found in paper I, however in this section we will discuss it in a different light than in the paper.

In section 3.1 and 3.3 we showed that in general, the strength of the screened electron-electron and electron-hole interaction depends on the dielectric properties of the surrounding dielectric media, making it an inherently non-local interaction. In the system sketched in fig. 3.3, this means that the strength of the electron-electron interaction in the monolayer semiconductor is altered by the carrier density in the graphene layer (and if present, also the dielectric function of the hBN layers). We will here quantify the carrier concentration in the graphene layer by the position of the Fermi level in the graphene layer. The change in the quasi-particle energies are calculated by adding the change in the self-energy, $\Delta\Sigma = G\Delta W$ induced by the graphene (and hBN) monolayer(s) evaluated by the QEH model as described in section 3.3, to the linearised quasi-particle equation via eq. 3.59. In fig. 3.3 (right) we show the G0W0 direct quasi-particle band gap for four freestanding TMD monolayers (MoS₂, WS₂, MoSe₂, and WSe₂) with horizontal dashed lines, and when placed on monolayer graphene (dots). This is shown as a function of the position of the Fermi level in the graphene monolayer (*i.e.* the carrier concentration in the graphene monolayer).

We find that the direct quasi-particle band gap is heavily reduced when placed on intrinsic graphene and further reduced when the carrier concentration in the graphene monolayer is increased (within experimentally realisable carrier concentrations in the graphene monolayer [100]). This shows that the non-local contribution to the dielectric function significantly influences the quasi-particle energies. We find a reduction of the

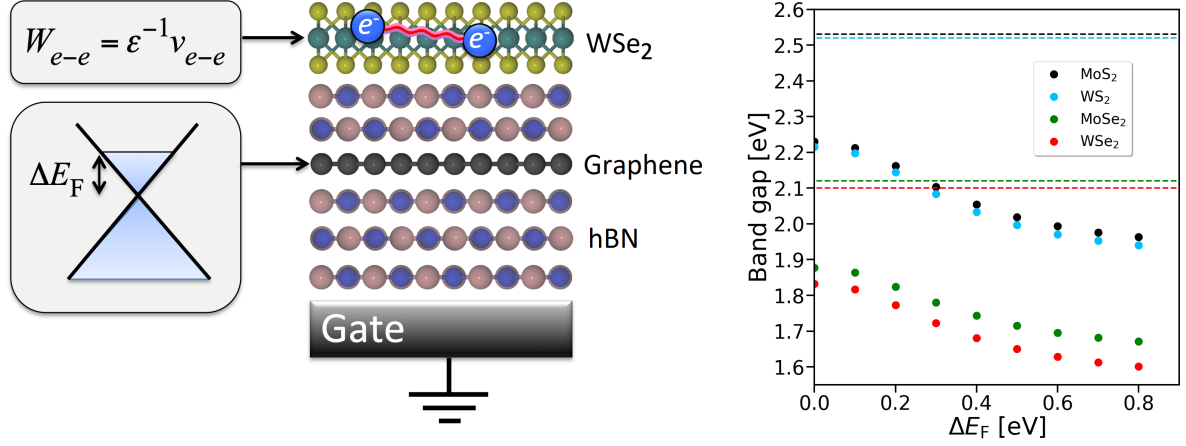


Figure 3.3: Left: setup consisting of a 2D monolayer semiconductor (here depicted by WSe₂) on top of gated graphene with a variable number of hBN monolayers between the semiconductor and graphene monolayers. Right: direct quasi-particle band gap for four 2D semiconductors placed in the setup to the left as a function of the carrier concentration in the graphene monolayer, quantified by the position of the Fermi level in the graphene monolayer. The horizontal dashed lines show the G0W0 quasi-particle band gaps of the freestanding semiconductors. The figure is modified from the included paper I.

direct quasi-particle band gaps of around 0.3 eV when placed on intrinsic graphene and a further reduction of about 0.25 eV, when the carrier concentration is further enhanced in the graphene monolayer. It is interesting that these two effects are of similar size and introduces the possibility to significantly manipulate the quasi-particle energies by gating the graphene monolayer. Another interesting and fascinating aspect is that the significant manipulation of the quasi-particle energies is achieved purely from the dielectric screening, *i.e.* without affecting the orbital shapes nor the hybridisation patterns of the 2D semiconductor. The effect of the increased carrier density in the graphene monolayer on the dielectric properties in the 2D semiconductor can be visualised by defining the effective dielectric function as the bare Coulomb interaction (V) over the screened Coulomb interaction (W) projected onto the 2D semiconductor:

$$\epsilon(q_{\parallel}, \omega) = \frac{V(q_{\parallel}, \omega)}{W(q_{\parallel}, \omega)}, \quad (3.61)$$

where q_{\parallel} is the in-plane wave vector and ω the frequency. This is plotted for three different carrier concentrations in fig. 3.4 in the contour plots for monolayer MoS₂ on a graphene monolayer. The bottom right plot shows the effective dielectric function as a function of frequency evaluated along $q_{\parallel} = 0.05 \text{ \AA}^{-1}$ (black, green, and blue, also indicated by the vertical line the contour plots). The effective dielectric function of

freestanding intrinsic monolayer MoS₂ is shown in gray in the bottom right corner. From this, the effect on the screened electron-electron interaction from the presence of the graphene layer is obvious, by comparing the gray and black line in the bottom right corner. As the carrier concentration in the graphene layer is increased the graphene plasmon mode is enhanced, however it is not obvious how this affects the dielectric screening in the 2D semiconductor. Conversely the higher dielectric screening seem to stem from an increase in the size of the dielectric function at low frequencies (before the onset of the plasmon). A similar plot of the effective dielectric function of freestanding intrinsic monolayer MoS₂ would show a close to non-existing dependence on ω for the frequency range in fig. 3.4 (*i.e.* below the gap of the semiconductor), while a significant ω -dependence is found in the presence of a graphene monolayer. This is in general true comparing 2D semiconductors and (semi-)metals. We will discuss the frequency-dependence of the dielectric function in further detail and its relation to excitonic states which will be the topic of the following sections.

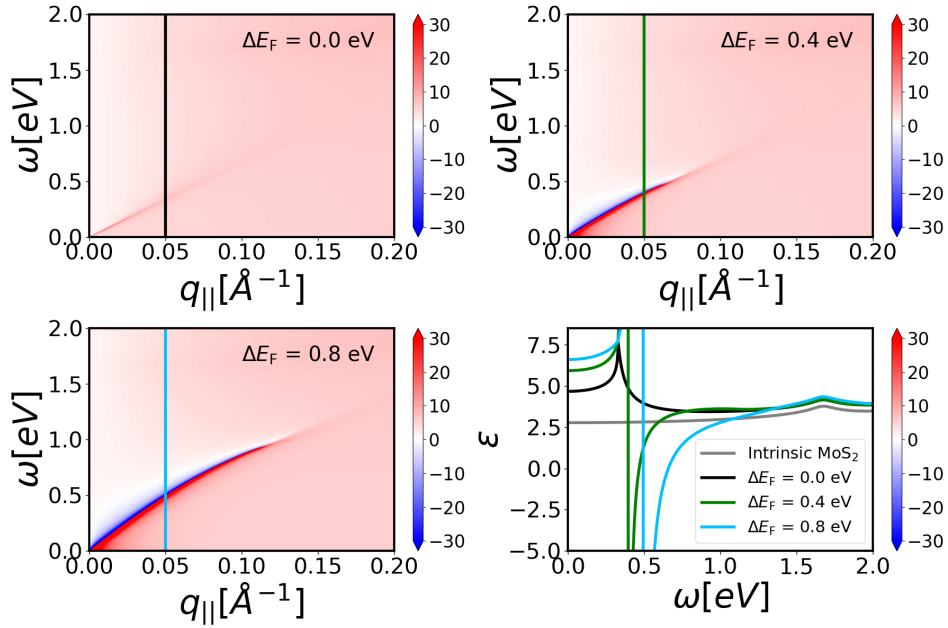


Figure 3.4: The contour plots shows the real part of the dielectric function of monolayer MoS₂ placed on graphene with different carrier concentrations. The dielectric function is evaluated in the MoS₂ monolayer. The bottom right plots shows the frequency dependence of the real part of the dielectric function (evaluated along $q_{||} = 0.05 \text{ \AA}^{-1}$) for intrinsic monolayer MoS₂ (gray) and for monolayer MoS₂ on graphene with the three carrier concentrations shown in the contour plots (black, green, and blue). The figure is taken from the included paper I.

Because of the distance dependence to the surrounding dielectric media in the non-local screened Coulomb interaction, the manipulation of the quasi-particle energies can

further be controlled by intercalating hBN monolayers between the semiconductor and the gated graphene monolayer. We demonstrate this by intercalating up to 6 hBN layers between monolayer MoS₂ and graphene, and calculate the direct quasi-particle band gap for different carrier concentrations in the graphene monolayer. This is illustrated in fig. 3.5 (left). Here the three different carrier concentrations are shown by black, green, and blue, while the horizontal gray dashed line shows the direct quasi-particle band gap for monolayer MoS₂ on bulk hBN. Since the dielectric screening of the electron-electron interactions is lower for hBN than for graphene, the effective dielectric screening in the 2D semiconductor is reduced as more hBN monolayers are intercalated between the semiconductor and the graphene monolayer, since the high carrier concentration is moved away from the 2D semiconductor (in the image charge picture, the strength of the image charge self-interaction is reduced). To elaborate on this effect, we show that the effect is approximately inversely proportional to the distance between the 2D semiconductor and the graphene monolayer by fitting a function of the form: $a(E_F)/(N + b) + E_{\text{gap}}^\infty$, where N is the number of hBN layers, $a(E_F)$ is a free parameter that depends on the carrier concentration and is a measure of the screening strength, b is a measure of the distance from the interacting charges in the semiconductor to the image charges in the graphene monolayer, and E_{gap}^∞ is the direct quasi-particle band gap for monolayer MoS₂ on bulk hBN, which is determined by direct calculation. By fitting this function to the *ab-initio* calculations we find b to be about two times the MoS₂/graphene interlayer and because of the overall good 1/distance fit, we can conclude that the manipulation of the quasi-particle energies can be well interpreted in terms of an image charge model. Encouraged by this we now further explore the image charge picture and calculate the direct quasi-particle band gap reduction for a wide range of 2D semiconductors when placed on intrinsic (black) and gated graphene (green) (for the latter corresponding to $\Delta E_F = 0.4$ eV). This is plotted in fig. 3.5 (right) against the static in-plane polarisability of the 2D semiconductor. The orange data point is taken from an experimental realisation of monolayer ReS₂ on gated graphene [100]. It is clear that higher reductions of the quasi-particle band gaps are found for 2D semiconductors with lower static in-plane polarisability. To understand this we take a step back to take a closer look at the image charge model. In the case of the bare Coulomb interaction between two particles the total charge of the interacting particle is simply the sum of the charge of the two particles. If one considers the screened Coulomb interaction, the reduction of the strength of the interaction can simply be understood from the presence of a screening cloud around the two particles reducing the strength of the interaction. The total charge of the quasi-particle is now given by the combined system of the two particles and the screening cloud. As the dielectric screening of the environment (*i.e.* the intrinsic polarisability of the 2D semiconductors) is increased, so is the effect of the screening cloud. This leads to a smaller image charge self-interaction and thus a smaller effect on the quasi-particle energies from external effects such as the presence of the graphene monolayer. This concludes that the quasi-particle energies, of the 2D semiconductor in the setup in fig. 3.3 (left), can effectively and predicatively be manipulated by tuning the strength of the image charge self-interaction by means of three different methods: first, through the carrier concentration in the graphene monolayer (controlled via a gate-voltage), second,

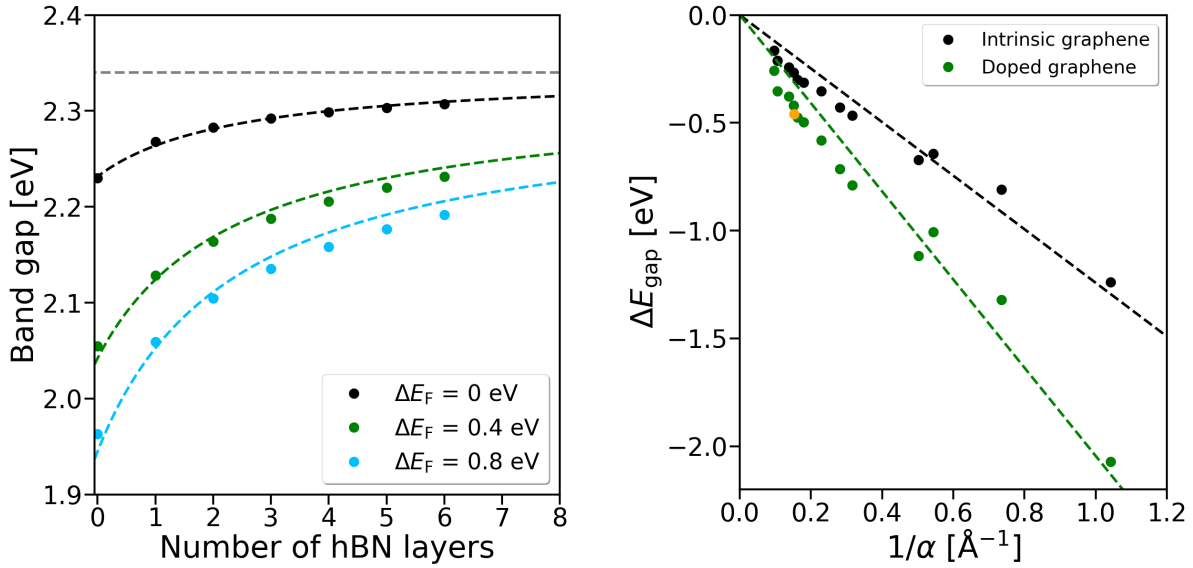


Figure 3.5: Left: quasi-particle band gap of mono MoS₂ in the setup of fig. 3.3 as a function of the number of hBN layers between the MoS₂ monolayer and the graphene monolayer. The horizontal dashed line shows the quasi-particle band gap of monolayer MoS₂ on bulk hBN and the dashed fitted lines are fits of the form: $a(E_F)/(N + b) + E_{\text{gap}}^{\infty}$ as discussed in the main text. Right: reduction of the quasi-particle band gap of different semiconductors when placed on intrinsic graphene (black) and doped graphene (green) as a function of the in-plane static polarisability of the semiconductor. The orange data point show values from previous experimental work [100]. The figure is taken from the included paper I.

by the inverse distance dependence on the strength image charge self-interaction, and/or third, by the intrinsic dielectric properties of the 2D semiconductor.

3.6 Excitons, The Mott-Wannier Equation, and the Bethe-Salpeter Equation

In the previous sections we defined the quasi-particle valence band maximum as the electron removal energy and the quasi-particle conduction band minimum as the electron addition energy. From these the quasi-particle band gap is defined as the difference between these two. In the forthcoming sections we will move on and study the optical properties of vdWHs. It is important to note that we consider excitonic states confined localised in-plane excited by light polarised in the in-plane direction. Out-of-plane excitons, the movement and oscillation of which is strongly confined and consequently has a fundamentally different behaviour, have in recent years received only little attention in

2D monolayers [47]. What we referred to as simply the *band gap* in the previous sections will now be redefined to be labelled the *electronic band gap* and we will introduce the *optical band gap* as the energy difference associated with exciting an electron from the valence states to the lowest bound state. The necessity of distinguishing between these two arises from the low dielectric screening in 2D materials and few-layer vdWHs. As illustrated in fig. 3.6, when an electron is excited from a valence band state to a conduction band state, this conversely moves a hole state from the conduction band state to the valence band state. In a simple picture the negatively charge excited electron located in the conduction band, interacts with the positively charged hole located in the valence band through the screened Coulomb interaction. The effect of this is that the electron does not jump to the lowest quasi-particle conduction band state, but instead resides in a bound state energetically located inside the electronic band gap. The bound state constitutes a full Rydberg series as shown in fig 3.6 in purple and outlined in the caption. The bound electron-hole state is formally known as an exciton and the band gap associated with the exciton state (*i.e.* the position of the emission peak in a photoluminescence (PL) spectrum) is known as the optical band gap. The difference between the electronic band gap and the optical band gap defines the exciton binding energy (E_B). The exciton binding energy is usually found to be a few meV in bulk crystals and so the electronic and optical band gap essentially coincide in such structures. However, in 2D materials and few-layer vdWHs, the low dielectric screening means that exciton binding energies attain values up to several hundreds meV for monolayer TMDs [82, 76] and a few eV for hBN. The excitonic states show up as narrow peaks below the electronic band gap in PL measurements and are for many materials easily identified due to their high oscillator strength. One of the best known examples of this is the A and the B exciton peak in monolayer MoS₂ [82]. Both excitons have their origin of the excitation from the spin-orbit split states at the VBM to the spin-orbit split states at the CBM. Since time-reversal-symmetry shifts the ordering of the spin-channels at the VBM at the K- and the K'-point in the Brillouin zone of the hexagonal unit cell, this gives rise to two distinct exciton peaks with different energies. It is evident that it is necessary to accurately calculate the exciton binding energy of excited states to accurately model the optical properties of 2D materials. Inspired by the hydrogen-like picture of the bound electron-hole state it is not surprising that this can effectively be done by applying a hydrogen model as we will outline in the following.

Solving the Schrödinger equation for the hydrogen atom, one typically utilises the spherical symmetry of the problem and split the electron wave function into its angular and radial components: $\psi(r, \theta, \psi) = R(\mathbf{r})Y(\theta, \psi)$, where R and Y denote the radial and angular components respectively. Since the potential energy in the Hamiltonian of the hydrogen problem only has a dependence on r , it is enough to solve, what we will call "the radial equation", namely the eigenvalue problem with only the radial part of the wave function. For the system consisting of two charged particles with the charge of one

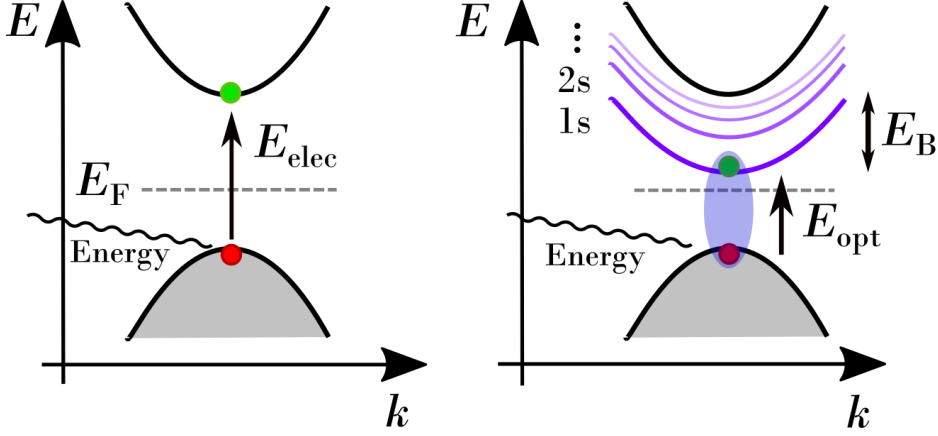


Figure 3.6: Illustration of the excitation of an electron from the occupied bands to the unoccupied bands not including (including) the interaction between the excited electron (green) and the created hole in the valence state (red) to the left (right). The bound electron-hole (purple) pair (exciton) state is shown to the right with the Rydberg series of the exciton states shown in purple bands residing inside the electronic band gap (E_{elec}). The excitation energy to the 1s exciton state is defined as the optical band gap (E_{opt}), and the exciton binding energy is then defined as: $E_{\text{B}} = E_{\text{elec}} - E_{\text{opt}}$. The Fermi level is shown in dashed grey.

electron charge and $l = 0$ in SI units this reads:

$$\left[-\frac{\hbar^2}{2m_e} \frac{\partial^2}{\partial r^2} + \frac{e^2}{4\pi\epsilon_0 r} \right] R(r) = E_n R(r), \quad (3.62)$$

where m_e is the electron mass, ϵ_0 is the vacuum permittivity, and E_n is the spectrum of allowed energies. It is well known that the solutions to this eigenvalue problem (for the bound states) are given by [44]:

$$E_n = -\frac{m_e}{2\hbar^2} \left(\frac{e^2}{4\pi\epsilon_0} \right)^2 \frac{1}{n^2}. \quad (3.63)$$

This series is known as the Rydberg series. We will now study how this can be applied to an exciton located in a 2D monolayer. First of all, the problem now consists of a particle with mass $\mu = \frac{m_e m_h}{m_e + m_h}$, which we will denote the exciton mass and is the effective mass of the bound electron-hole particle. Secondly, while the potential that enters the Hamiltonian in the hydrogen problem in eq. 3.62 is the bare Coulomb potential, the exciton is located inside a 2D monolayer, and therefore the electron-hole interaction is screened by the intrinsic (q -dependent) dielectric screening of the 2D monolayer. This means that the Hamiltonian of the exciton in a 2D monolayer takes the form (in SI units): $H_{\text{ex}} = -\frac{\hbar^2}{2m_e} \frac{\partial^2}{\partial r^2} + \frac{e^2}{4\pi\epsilon_0\epsilon(r_{\parallel})r_{\parallel}}$, where the coordinate r is now the in-plane radial

vector describing the distance between the electron and the hole, r_{\parallel} , and $\epsilon(r_{\parallel})$ is the intrinsic dielectric screening of the 2D monolayer. Denoting the screened 2D Coulomb interaction W^{2D} this Hamiltonian gives the exciton eigenvalue problem

$$\left[-\frac{\nabla^2}{2\mu} + W^{2D}(\mathbf{r}_{\parallel}) \right] F(\mathbf{r}_{\parallel}) = E_n F(\mathbf{r}_{\parallel}), \quad (3.64)$$

where $|F(\mathbf{r}_{\parallel})|^2$ describes the probability distribution of the in-plane distance between the electron and the hole and E_n is the Rydberg series of the exciton binding energies. eq. 3.64 is known as the Mott-Wannier model and can be solved numerically to yield quantitatively accurate exciton binding energies. We note that we in eq. 3.64 (and throughout this study) neglect an exchange term given by the dipole moment of the exciton projected onto the exciton wave vector, and thus is present for indirect momentum excitons. This term is known to be small and similarly neglected in previous studies of 2D excitons [90, 21].

The Mott-Wannier equation can easily be integrated with the QEH model to computationally cheaply calculate exciton binding energies in vdWHs. This has been done previously [75] by simply generalising eq. 3.57 to include the induced hole potential ($\phi_i^h(\mathbf{q}_{\parallel}, \omega)$) instead of the induced electron potential:

$$W_i(\mathbf{q}_{\parallel}, \omega) = \rho_i^e(\mathbf{q}_{\parallel}, \omega) (\epsilon^M(\mathbf{q}_{\parallel}, \omega))^{-1} \phi_i^h(\mathbf{q}_{\parallel}, \omega), \quad (3.65)$$

This gives the screened electron-hole interaction and can readily be calculated and plugged into eq. 3.64 and it has previously been shown to yield accurate exciton binding energies [75]. This, as we will label the MW-QEH model, offers an efficient cheap method for obtaining exciton binding energies, however it has two main shortcomings: first, it only supplies the distinct exciton binding energies and it is therefore in general not possible to obtain the full absorption spectrum of a 2D monolayer or vdWH including excitonic effects. Second, when the MW-QEH model is used in combination with the G0W0-QEH model to calculate the shift of the exciton peaks (in energy) upon insertion in vdWHs the two models combined predict a blueshift of the A exciton peaks for few-layer TMD vdWHs (relative to the freestanding monolayer) while in general a redshift is found experimentally [82, 76]. In the following we will go through the Bethe-Salpeter Equation [107] (BSE) which is a methodology to obtain the full absorption spectrum of a 2D monolayer or vdWH including the effect of excitonic states. Furthermore, we will show by in this thesis directly implementing the BSE formalism with the QEH model that the absorption spectrum of a multilayer vdWH can be obtained including interlayer dielectric screening and that the experimentally observed redshift can be restored by combining the herein developed BSE-QEH model with the G0W0-QEH model.

To develop a compact many-body formalism for describing the electron-hole interaction it is from an initial point not straightforward nor obvious how to start. It is tempting to follow a Green's function approach similar to the derivation of the of G0W0

approximation, however matters are complicated by the form of the irreducible polarisation in the G0W0 approximation, eq. 3.36. From a physical point of view this is merely an electron and a hole propagator, propagating simultaneously without interacting. This form of the irreducible polarisation is known as the RPA as we saw previously and shows that, although the G0W0 approximation is a many-body formalism, by definition, it does not account for electron-hole interactions, and consequently excitonic states are not included in the G0W0 formalism. Instead we are searching for a formalism where the irreducible polarisability takes a form similar to: $P \sim GvG$, where v couples the electron and hole propagators, *i.e.* a propagating interacting electron and hole pair.

It turns out, as shown by Bethe and Salpeter [107], that it is possible to derive a Dyson equation that includes a form of the irreducible polarisation suggested above, by iterating Hedin's equations again starting from the G0W0 result for the self-energy. In other words we plug eq. 3.40 into the expression for the vertex, eq. 3.34 and assume that the screened Coulomb interaction does not depend on the Green's function propagator. This gives us an expression for the vertex that in comparison to the first iteration of Hedin's equations in contains a term including the screened Coulomb interaction, suggesting that we are moving in the right direction:

$$\Gamma(1, 2; 3) = \delta(1; 3)\delta(2; 3) + i \int d6d7W(1; 2)G(1; 6)G(7; 2)\Gamma(6, 7; 3). \quad (3.66)$$

At this point, since the technical steps are very similar to the derivation of the G0W0 approximation (the next step is to insert this expression for the vertex in the Hedin's equation expression for the irreducible polarisation), we will focus on the physical arguments instead of the mathematical steps, and give a more intuitive argumentation. Due to the nature of the electron-hole interaction and the fact that the irreducible polarisability has to take a form similar to: $P \sim GvG$, it is necessary to introduce a four-point kernel. To this end we introduce the four-point form of the (non-interacting) irreducible polarisability:

$$L^0(1, 2; 3, 4) = -iG(1; 3)G(4; 2). \quad (3.67)$$

By carrying out the second iteration of Hedin's equations we started above and similarly generalising eq. 3.32, these few steps are left as an exercise to the reader, Bethe and Salpeter showed that the (interacting) four-point reducible polarisability satisfies a Dyson equation:

$$L(1, 2; 3, 4) = L^0(1, 2; 3, 4) + \int d5d6d7d8L^0(1, 2; 3, 4)K(5, 6, 7, 8)L(1, 2; 3, 4), \quad (3.68)$$

where the kernel, K , contains all electrostatic electron-hole interactions and is given by:

$$K(1, 2, 3, 4) = v(1, 3)\delta(1, 2)\delta(3, 4) - W(1, 2)\delta(1, 3)\delta(2, 4). \quad (3.69)$$

We immediately see that W exactly gives the screened coupling between the two "propagators" as expected and supplies the electron-hole interaction we were aiming for. The first term on the right hand side can be understood as an exchange interaction. We note here that we have employed the G0W0 approximation for the exchange-correlation

self-energy, as is typically done in *ab-initio* calculations, already in the expression for the vertex (from the assumption of the independence of W on G above), however it is straightforward to not employ the G0W0 approximation in which case the kernel takes the form: $K(1, 2, 3, 4) = v(1, 3)\delta(1, 2)\delta(3, 4) + i\frac{\delta\Sigma_{xc}(1;2)}{\delta G(3;4)}$.

To solve eq. 3.68 to proceed and obtain the excitation energies we have to utilise several tricks. We start out by introducing a two-particle state, defined by the product of the electron and hole wave functions of the electron-hole pair state:

$$\psi_{n_1, n_2, \mathbf{k}, \mathbf{k}+\mathbf{q}}(\mathbf{r}_e, \mathbf{r}_h) = \psi_{n_1, \mathbf{k}}(\mathbf{r}_e)\psi_{n_2, \mathbf{k}+\mathbf{q}}(\mathbf{r}_h), \quad (3.70)$$

which is the exciton state defined by the product of the electron and hole in the Kohn-Sham orbital states n_1 and n_2 with momentum \mathbf{k} and $\mathbf{k} + \mathbf{q}$, and defines a basis for a two-particle space. From now we will use the contracted notation $S = n_1, n_2, \mathbf{k}, \mathbf{k} + \mathbf{q}$ (and S' for (n_3, n_4) etc.) common in the literature. While the frequency dependence of eq. 3.68 is given but not written explicitly (since there is only one frequency variable), we will from now write it out since we will have to take special care of the frequency dependence. If one assumes that the Kohn-Sham orbitals form a complete basis it is possible to rewrite the BSE equation into another Dyson-like problem for the reducible polarisation in the two-particle space [123]:

$$L_{SS'}(\omega) = L_{SS'}^0(\omega) \left[\delta_{n_1 n_3} \delta_{n_2 n_4} + \sum_{S''} K_{SS''}(\omega) L_{SS''}(\omega) \right]. \quad (3.71)$$

The assumption of completeness of the single-particle basis has the consequence that a significant number of unoccupied bands are needed to converge BSE calculations. In practice, typically 4-6 times as many unoccupied bands as occupied bands are needed to be included. In the two-particle basis the kernel is given by:

$$K_{SS'}(\mathbf{q}) = V_{SS'}(\mathbf{q}) - \frac{1}{2}W_{SS'}(\mathbf{q}). \quad (3.72)$$

The factor of $\frac{1}{2}$ is a direct consequence of the optical selection rules *i.e.* that only singlet excitations are allowed. In the next section we will write out the PW expression of the screened interaction when we need it. To continue we must adopt an expression for the non-interacting reducible polarisability. This is easy in the two-particle space, by realising that by definition L^0 does contain mixing of different states. This means that the non-interacting reducible polarisability must be diagonal in the two-particle space and furthermore have the single-particle transition energies, ϵ_S , as roots:

$$L_{SS'}^0(\omega) = \frac{f_S}{\epsilon_S - \omega + i\eta} \delta_{SS'}, \quad (3.73)$$

where η is a small parameter to avoid numerical singularities and f_S is the occupation density of state S . With this expression for $L_{SS'}^0(\omega)$ and by rewriting eq. 3.71 into an eigenvalue problem for the excitation energies we get:

$$[(\epsilon_S - \omega + i\eta)\delta_{SS'} - K_{SS'}(\omega)f_S] L_{SS'}(\omega) = f_{S'}. \quad (3.74)$$

Solving this equation is not straightforward due to the omega dependence of the Kernel, and can simply not be carried out computationally for any 2D material in question. To continue it is therefore necessary to employ an approximation to the Kernel and simply *fix* the frequency to some value. Usually one puts $\omega = 0$. It is important to stress that this approximation is not justified. For semiconducting systems, where the dielectric matrix only weakly depends on the frequency the resulting exciton energies are close to independent the choice of ω (for ω chosen close to or below the quasi-particle band gap). However for (semi-)metallic systems it is not scientifically sound to use the static approximation and consequently BSE calculations are not being carried out for such systems. This is the exact reason we did not study excitonic states in the study of semiconducting 2D monolayers on a gated graphene monolayer in section 3.5, as is obvious by examining fig. 3.4 again. Within the static approximation the eigenvalue problem can be re-written into:

$$[\mathcal{H} - (\omega + i\eta)I]_{SS'}^{-1} f_{S'} = L_{SS'}(\omega) \quad (3.75)$$

where the two-particle BSE Hamiltonian is defined as:

$$\mathcal{H}_{SS'} = \epsilon_S \delta_{SS'} - f_S K_{SS'} \quad (3.76)$$

and the kernel is now evaluated at a fixed frequency. From the expression of the BSE Hamiltonian we see (as we would expect intuitively and also stated above when stating the expression for the non-interacting reducible polarisation in the two-particle basis) that only the diagonal contains the single-particle transition energies and the off-diagonal contains the coupled electron-hole pair states, which are also present in the diagonal. The Hamiltonian is non-hermitian, however if one only consider positive excitation energies, *i.e.* restricting the excitation space to electron-hole excitations such that we only consider one entry in the two-particle basis, the Hamiltonian becomes hermitian. This is known as the Tamm-Dancoff approximation. In appendix D we show that the Tamm-Dancoff approximation has a negligible effect on the excitation energies and oscillator strengths on the BSE absorption spectrum for 2D TMD monolayers to validate this approximation. The reason to write the inverse form of the eigenvalue equation is that the term in the parenthesis can be transformed into its spectral representation, from which we can define the BSE eigenvectors A_λ^S and eigenvalues E_λ^S :

$$\mathcal{H}_{SS'} A_\lambda^S = E_\lambda^S A_\lambda^S \quad (3.77)$$

and from which the transition energies can readily be found. The practical step of writing out the inverse Hamiltonian in eq. 3.75 in its spectral representation is well-defined, at least under the Tamm-Dancoff approximation where the BSE Hamiltonian is a normal operator (since it is Hermitian) defined on a Hilbert space. Without the Tamm-Dancoff approximation the BSE Hamiltonian is non-hermitian and unbounded (the BSE Hamiltonian is also not bounded within the Tamm-Dancoff approximation), since it is not possible to find a value k such that the eigenvalue of ωI is smaller than or equal to k , when applied to an arbitrary function within the functional space the BSE Hamiltonian

is defined on. Thus, strictly mathematically, the definition of the BSE hamiltonian on its spectral representation form without the Tamm-Dancoff approximation is not well-defined, but makes sense and gives sensible excitation values since the two-particle BSE eigenvectors A_λ^S are bounded. The computational advantage of this step is, because of the separation of the two-particle BSE Hamiltonian the ω in eq. 3.75, can simply be diagonalised once for all frequencies.

While the BSE Hamiltonian is usually build from Kohn-Sham orbitals and Kohn-Sham eigenvalues (since self-consistent G0W0 calculations are very rarely carried out for these systems) it is customary to apply a scissors-operator to the Kohn-Sham eigenvalues and shift the valence and conduction band extrema to the G0W0 electron ionisation and electron affinity energies. From this the spectrum of exciton binding energies is defined as the difference between the quasi-particle energy spectrum and the spectrum of E_λ values. These eigenvalues corresponds to the optical excitation values one would obtain by directly calculating the imaginary part of the two-particle polarisability (*i.e.* the definition of the absorption spectrum in eq. 3.17) and thus defines the absorption coefficients within the BSE formalism. The physical interpretation of the eigenvectors, A_λ^S , can be seen as a measure of the oscillator strength of the exciton state.

Finally we comment on the form of the reducible polarisability in the BSE@G0W0 formalism and directly show the effect of excitonic effects on the absorption spectrum of 2D materials. If one considers eq. 3.68 and put the Kernel equal to zero we recover the non-interacting electron-hole picture, *i.e.* the RPA. It is now instructive to directly illustrate the effect of excitonic states on the absorption spectrum. In fig. 3.7 we plot the absorbance of MoS₂ within the RPA (red) and the BSE (blue) approximations. The PBE single-particle band gap is shown in dashed red, the G0W0 quasi-particle in dashed blue, and the lowest exciton energy in dashed black. The definition of the exciton binding energy (E_B) is shown and the RPA (BSE) spectra are calculated with respect to the PBE (G0W0) band gaps. As expected, the RPA absorbance spectrum has its onset at the single-particle band gap (the oscillator strength in both approximations are discrete peaks, therefore the small weight below the band gap is due to finite Fermi smearing effects) while in the BSE approximation significant excitonic states below the quasi-particle band gap is found with large oscillator strengths signifying the low dielectric screening in 2D materials. The two exciton peaks below the quasi-particle band gap are labelled as the A and B excitons and have their origin from the spin-orbit split transitions involving the K- and K'-points in the Brillouin zone as we discussed previously.

It is here also fit to discuss the sketch of the excitonic states in fig. 3.6. While this illustration is pedagogical and informative it is to some extent incorrect since it mixes the energy of single-particle and two-particle excited states. It is important to stress that it is only the difference between the electronic band gap and the exciton energy that is well-defined and that the exciton is defined as the difference between these as illustrated in fig. 3.7. In other words, the "position" of the exciton states in fig. 3.6 is arbitrary relative to the quasi-particle band structure edges. This is equivalent to the statement that only the relative (or change of) potential energy has a physical meaning and the absolute value of the potential energy cannot be a driving force itself.

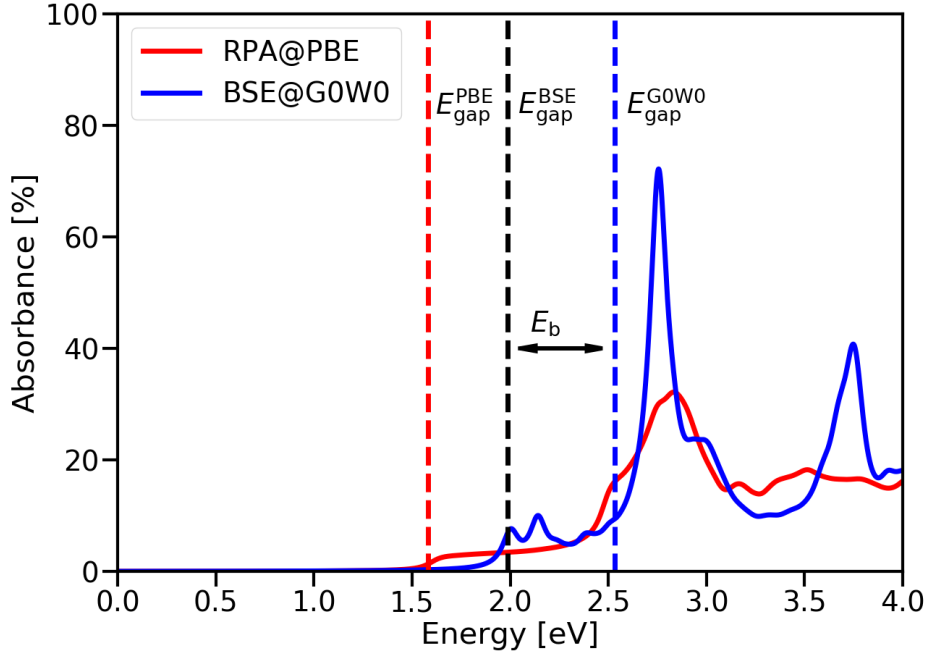


Figure 3.7: Absorption spectrum of freestanding 2D monolayer MoS₂ calculated within the RPA (red) and the BSE (blue) approximations. The single-particle band gap is shown in dashed red calculated with the PBE functional, the G0W0 quasi-particle band gap is shown in dashed blue, and the lowest exciton energy is shown in dashed black.

Even with the G0W0 self-energy and static approximations the BSE eigenvalue problem is a computationally heavy problem to solve and can as such only be solved accurately for small systems and cannot directly be applied to rotated or even few-layer vdWHs. In the next section we will however make this possible for vdWHs by implementing the QEH model with the BSE to calculate the absorbance spectrum for multilayer vdWHs.

3.7 Implementation of the Bethe-Salpeter Equation with the Quantum Electrostatic Heterostructure Model

Similarly to the effect of dielectric screening on the quasi-particle band gap we studied in section 3.5, the exciton binding energy is reduced when a 2D monolayer is embedded in a vdWH, due to the dielectric screening of the electron-hole interaction. We will in this section present the implementation workflow developed and implemented in this

thesis of what will be denoted the BSE-QEH method for calculating intralayer exciton binding energies in vdWHs and show that it gives a better description of the experimentally found energy redshift of exciton energies in vdWHs as opposed to the blueshift predicted by the MW-QEH (in combination with the G0W0-QEH model). In chapter 4 we will directly apply the developed BSE-QEH model and the results of this can be found in paper V.

As we saw in the previous section the two-particle BSE Hamiltonian takes the form of eq. 3.75 and the BSE Kernel as eq. 3.72. The screened Coulomb interaction in the BSE kernel can be expanded in plane-waves as [123]:

$$W_{SS'}(\mathbf{q}) = \frac{4\pi}{\omega} \sum_{\mathbf{G}\mathbf{G}'} n_{\mathbf{n}\mathbf{k},\mathbf{n}'\mathbf{k}'}^*(\mathbf{G}) W_{\mathbf{G}\mathbf{G}'}(\mathbf{k}' - \mathbf{k}) n_{\mathbf{m}\mathbf{k}+\mathbf{q},\mathbf{m}'\mathbf{k}'+\mathbf{q}}(\mathbf{G}'), \quad (3.78)$$

where $n_{\mathbf{n}\mathbf{k},\mathbf{n}'\mathbf{k}'}^*(\mathbf{G})$ and $n_{\mathbf{m}\mathbf{k}+\mathbf{q},\mathbf{m}'\mathbf{k}'+\mathbf{q}}(\mathbf{G}')$ are charge density matrices and $W_{\mathbf{G}\mathbf{G}'}(\mathbf{k}' - \mathbf{k})$ is the screened electron-hole interaction for all \mathbf{G} vectors in the plane-wave description. The dielectric screening from the neighbouring layers in the vdWHs as calculated by the QEH model is formally given by:

$$W_i^{\text{vdWH}}(\mathbf{r}, \mathbf{r}', \omega) = W_i(\mathbf{r}, \mathbf{r}', \omega) + \Delta W_i(\mathbf{r}, \mathbf{r}', \omega), \quad (3.79)$$

where $W_i^{\text{vdWH}}(\mathbf{r}, \mathbf{r}', \omega)$ is the total screened potential for layer i in the vdWH, $W_i(\mathbf{r}, \mathbf{r}', \omega)$ is the screened potential calculated for the freestanding 2D monolayer, and $\Delta W_i(\mathbf{r}, \mathbf{r}', \omega)$ is the change in the screened potential for layer i due to dielectric screening from the neighbouring layers. $\Delta W_i(\mathbf{r}, \mathbf{r}', \omega)$ is calculated by the QEH model as explained by eq. 3.58. The optical response of a material is mainly given by the $\mathbf{G} = \mathbf{0}$ component of the screened Coulomb interaction, with the contribution for higher reciprocal lattice vectors falling off exponentially. In the BSE-QEH implementation we therefore add the change in the screened potential ($\Delta W_i(\mathbf{r}, \mathbf{r}', \omega)$ in eq. 3.79) to the $\mathbf{G} = \mathbf{G}' = \mathbf{0}$ component of eq. 3.78. By doing this, in the BSE formalism we obtain the screened electron-hole interaction including the environmental screening from the neighbouring layers in the vdWH and consequently one would expect the exciton binding energies to be reduced (compared to the freestanding 2D monolayer) due to the stronger dielectric screening. This implementation also allows us to obtain the absorption spectrum of each layer in a vdWH including the effect of the screened electron-hole interaction, and as we will see below then to obtain the absorption spectrum of the vdWH by the sum of the absorption spectrum of each layer. The shortcoming of this model is that it is not possible to calculate interlayer exciton binding energies, since this requires a full treatment of the orbital coupling between electrons and holes on neighbouring layers. As such the resulting absorption spectrum accounts for all (screened) intralayer transitions in each layer of the vdWH of consideration.

It has previously been shown that the MW-QEH method already gives a good description of the intralayer exciton binding energies. In general for vdWHs consisting of monolayer TMDs we find exciton binding energies with the BSE-QEH model that are

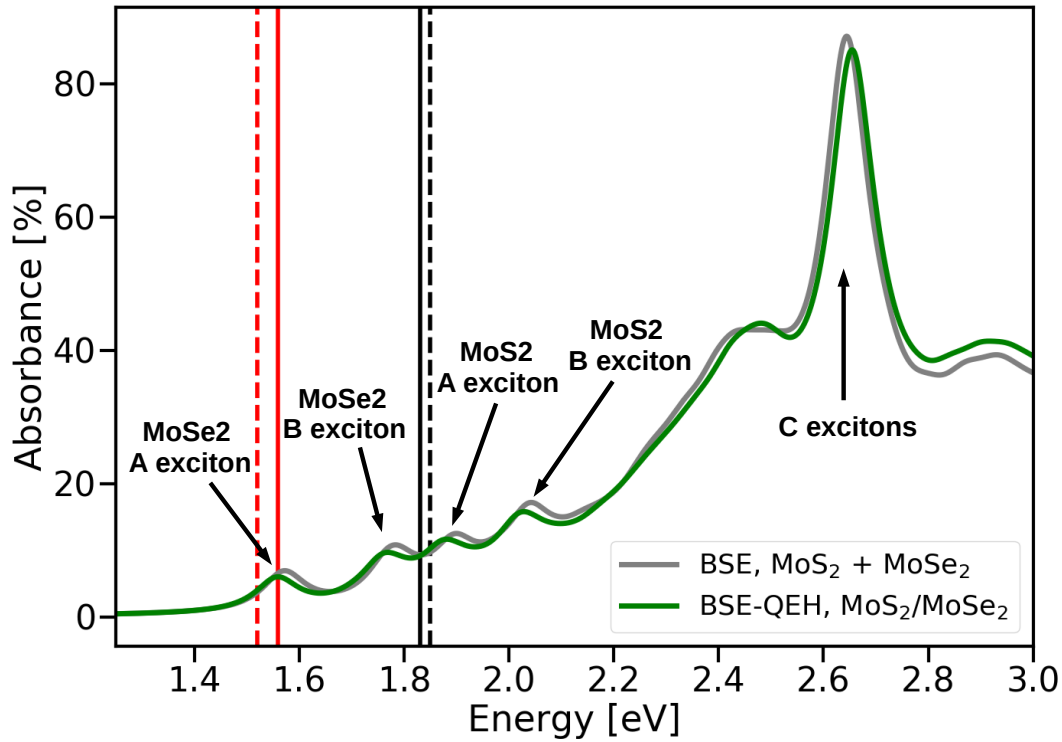


Figure 3.8: Absorption spectrum and excitation energies for bilayer $\text{MoS}_2/\text{MoSe}_2$ with respect to the G0W0 quasi-particle band gap. The absorption spectrum is calculated as the sum of the absorption spectra of the non-interacting freestanding monolayers (grey) and with the BSE-QEH method (green) for the bilayer. In the BSE-QEH method the quasi-particle band gap is corrected with the G0W0-QEH method. The vertical dashed lines show the MW-QEH values for the lowest lying exciton and the full lines are the average of the experimentally measured A exciton energies (see paper V). Red is for MoSe_2 and black is for MoS_2 . This figure is taken from the included paper V.

very close to those predicted by the MW-QEH model, and in general on the order of 20-40 meV lower. This is encouraging since the MW-QEH is expected to slightly overestimate the exciton binding energy due to the assumption that the electron and hole wave functions are smeared out over the 2D monolayer in the MW model. In chapter 4 we will present and compare exciton binding energies for a number of vdWHs and discuss this.

Instead we will in this section focus on the energy shift of the intralayer exciton peaks (here focusing on the A peaks on monolayer TMDs) when comparing the exciton energy in the freestanding monolayer and when embedded in a vdWH. As we saw in section 3.2

and 3.3 the quasi-particle band gap of a monolayer is reduced when embedded in a vdWH due to the increased dielectric screening. Similarly, the Coulomb interaction between the bound electron-hole pair is reduced due to the increased dielectric screening in the vdWH and consequently the exciton binding energy decreases. The energy shift of the exciton peak upon embedding in a vdWH is therefore a trade-off between the dielectric screening of the quasi-particle band gap and the exciton binding energy. The interlayer hybridisation can of course also influence this, however in this section we will consider the A exciton peak in TMD monolayers for which it is well known that interlayer orbital hybridisation and charge transfer have little-to-no effect on the intralayer exciton energy and the resulting shift is purely an effect of dielectric screening. Experimentally it is found that the A exciton is redshifted upon embedding a monolayer in a vdWH, best illustrated by the redshift of the A exciton in MoS₂ going from freestanding monolayer to bilayer [82] and that the magnitude of the redshift increases with the number of layers added. The big shortcoming of the MW-QEH model is that this predicts a blueshift of the A exciton in TMD monolayer for few-layer vdWHs when combined with the G0W0-QEH model and below we will show the BSE-QEH correctly predicts a redshift. We will now first see how the increased dielectric screening affects the monolayer absorption spectrum in the BSE-QEH model and that the effect on the intralayer exciton binding energy can be determined from this. Then we will do a thorough study on the exciton energy shift comparing the BSE-QEH and the MW-QEH model for multilayer vdWHs and compare this to available experimental data.

To see the effect of environmental dielectric screening on the absorption spectrum, we calculate the absorption of bilayer MoS₂/MoSe₂ by two different methods. We note that the unit cells of the two monolayers are incommensurate and that this system requires hundreds of atoms to apply less than 1% to the layers. Such *ab-initio* calculations are consequently not possible with a full conventional BSE calculation. In the first step we simply calculate the BSE absorption spectrum of each freestanding monolayer and add the two absorption spectra. This is plotted in gray in fig. 3.8, where the spectrum is calculated with respect to their G0W0 quasi-particle band gaps. In the second method we calculate the BSE-QEH absorption spectrum of each monolayer including the dielectric screening from the other monolayer, as described above, and add them together. For this cases we also calculate the change of quasi-particle band gap of each layer with the G0W0-QEH method. The result is plotted in green in fig. 3.8. Considering the A and B exciton peaks of both layers we find a small redshift of the excitation energy compared to the freestanding monolayers as expected. Combining the screening of the exciton binding energy with the screening of the quasi-particle band gap from the G0W0-QEH method, we find a redshift of the energy of about 5 meV. Overall, the two spectra have a very high resemblance which suggests that the dielectric screening is close to constant for all states, in agreement with previous findings [122].

To this end we now compare the shift of the A exciton energy predicted by the MW-QEH and the BSE-QEH model. In fig. 3.9 we plot the change of the A exciton peak energy of the multilayer homostructure compared to freestanding monolayer for MoS₂ (black), MoSe₂ (blue), WS₂ (red), and WSe₂ (green), where the exciton binding energy is

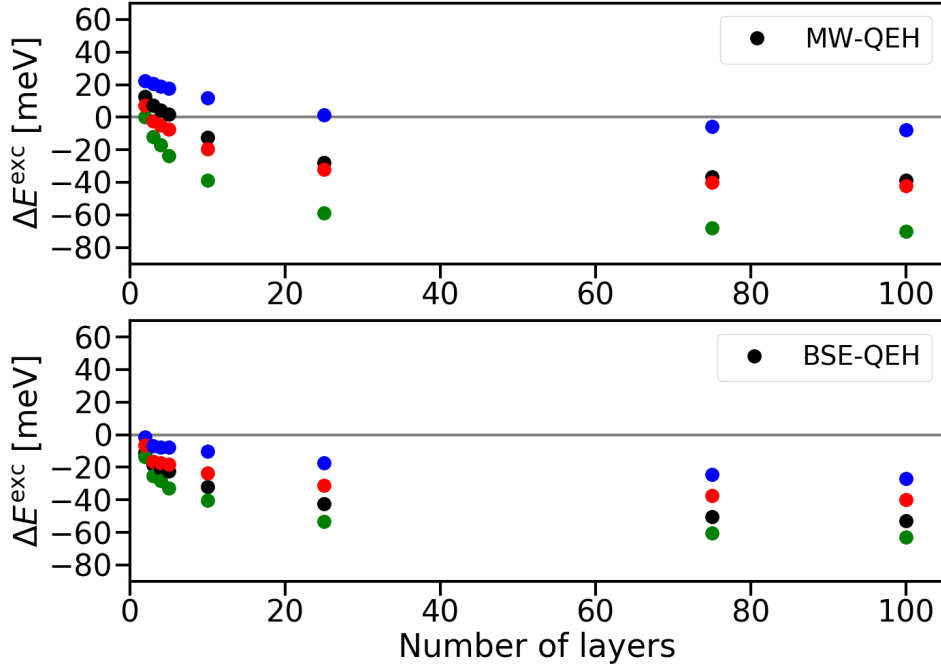


Figure 3.9: Shift of the exciton energy (ΔE^{exc}) of the A exciton for multilayer TMD van der Waals homostructures (2, 3, 4, 5, 10, 25, 75, 100 layers) relative to the exciton energy in the freestanding monolayer for MoS₂ (black), MoSe₂ (blue), WS₂ (red), and WSe₂ (green). This is shown where the screening of exciton binding energy is calculated with the MW-QEH model (top) and the BSE-QEH model (bottom). For all cases the screening of the quasi-particle energies is calculated with the G0W0-QEH model.

evaluated with the MW-QEH model (top) and with the BSE-QEH model (bottom). In both cases the quasi-particle states are calculated with the G0W0-QEH method. With the MW-QEH model we generally find a blueshift of the A exciton energy for up to around 5 layers transitioning into a redshift thereafter and for MoSe₂ a blueshift up to many more layers. We stress this blueshift predicted by the MW-QEH model, for any number of layers, is in direct contrast to experimental data. The BSE-QEH model predicts a redshift of the exciton energy for multilayer TMD stacks for all number of layer that increases with the number of layers in agreement with experiments. The asymptotic bulk values for the redshift is close to the value shown at 100 layers.

While accurate experimental data on exciton redshifts in vdWHs is limited, two experimental studies on bilayer systems are of specific interest. From experimental data the exciton energy is known to redshift already comparing monolayer and bilayer TMD structures which is accurately predicted by the BSE-QEH method. In fact for bilayer MoS₂ a redshift of the A exciton of around 15 meV is found [82] (± 5 meV adjusting for the broadness of the peaks). We find a redshift of 11 meV and a blueshift of 12 meV with

the BSE-QEH and MW-QEH methods respectively. Similarly, for bilayer MoS₂/WSe₂ a redshift A exciton in MoS₂ (WSe₂) of 25 meV (20 meV) is found [72] with an estimated error on both values around of around 10 meV. In comparison we calculated a redshift of 16 meV (19 meV) with the BSE-QEH method and a blueshift of 9 meV (4 meV) with the MW-QEH model. While a definite benchmarking of the BSE-QEH method is difficult it is clear that it accurately calculates exciton binding energies similar to the MW-QEH method and that it significantly improves upon the description of exciton energy shifts in vdWHs compared to the MW-QEH. It is also tempting to compare the asymptotic value of the redshift in fig. 3.9 *i.e.* comparing the energy of the A exciton in the freestanding monolayer and in the bulk crystal. For MoS₂ we find this to be close to 60 meV with the BSE-QEH model and a slightly smaller redshift with the MW-QEH model. However such an analysis is difficult due to the discrepancy of available experimental data. Two independent studies report a monolayer to bulk redshift of the A exciton in multilayer MoS₂ of around 25 meV [15] and 70 meV [76]. While this offers only little possibility for accurate benchmarking we can conclude that the BSE-QEH (with the G0W0-QEH) model predicts a redshift within this range of values. While both models seem to predict monolayer to bulk exciton energy redshift in good agreement with available data, the main advantage in the BSE-QEH for calculation exciton redshift are for few-layer vdWHs where the MW-QEH model fails to predict the correct redshift.

We here include a brief comment on the apparent blueshift of the C excitons with BSE-QEH method (fig. 3.8) and the redshift of the C (or D) excitons found experimentally [76]. The C exciton in the TMDs is an excitation around the Γ -point in the Brillouin zone. As we saw in fig. 3.2, multilayer vdWHs involving the TMDs exhibit very strong interlayer hybridisation effects on the quasi-particle energies close to and around the Γ -point. This means that to properly describe the redshift of the C exciton it is necessary to include a description of the interlayer hybridisation affecting the energies around the Γ -point.

As shown in fig. 3.8 it is possible to obtain intralayer absorption spectra with the BSE-QEH method. This enables an additional benchmarking test. Due to the enhanced dielectric screening in multilayer systems the oscillator strength of the exciton states is reduced *per layer* in vdWHs, compared to the freestanding monolayer. This is shown in fig. 3.10 where the relative intensity (defined as the averaged integral over the peak relative to the freestanding monolayer) for multilayer MoS₂ is shown with experimental data in green triangles [15] and values obtained from the BSE-QEH spectra in black circles. The fit is better than what can be expected for most *ab-initio* calculations, however it does show that the BSE-QEH model well captures the reduction in the oscillator strength for each monolayer in a vdWH. The oscillator strength of the A exciton is reduced to around 70% of the value of the freestanding monolayer already for 5 layers and from fig. 3.9 it is expected that this value only saturates after a few hundreds layers.

Overall the BSE-QEH model present a strong tool for calculating exciton binding energies, but especially intralayer absorption spectra and redshifted exciton energies for vdWHs with an arbitrary number of layers. Because of the implementation flowchart

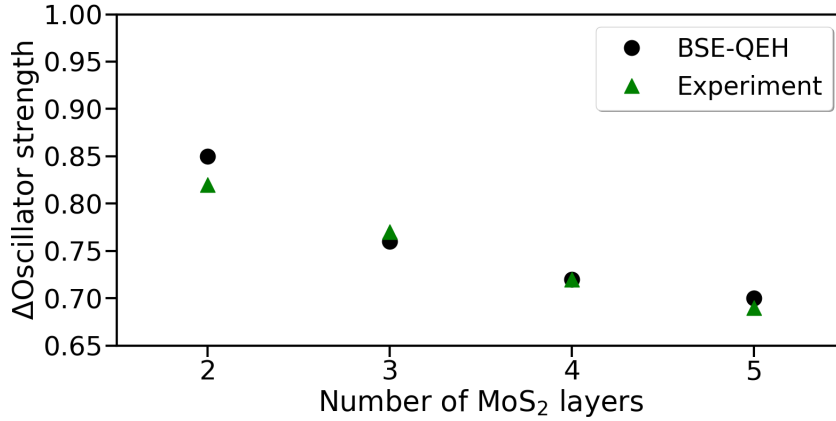


Figure 3.10: The oscillator strength of the A exciton per layer for multilayer MoS₂ normalised to the oscillator strength of the A exciton in freestanding monolayer MoS₂. The green triangles show the experimentally measured values [15] and the black dots are the BSE-QEH calculated values.

of the BSE-QEH model, calculating the intralayer part of the absorption spectrum of a N layer vdWH stack requires N BSE calculations for the freestanding monolayers. This is because the interlayer coupling algorithm takes up an insignificant amount of computational power. This means that the computational limitations of using the BSE-QEH model for vdWHs do not lie in the number of layers, but in the number of atoms in the unit cell of each freestanding monolayer. This enables accurate *ab-initio* calculation of the absorption spectra at level of BSE for vdWH systems which have not been possible to carry out before with conventional many-body codes.

3.8 Screened Rydberg Series in 2D Materials

Up to now we have studied how the dielectric environment affects the quasi-particle energies and the A, B, and C excitons in 2D monolayers. The fact that the exciton energies can be well described by a numerical solution of hydrogen-like models suggest that the excitonic states share a greater resemblance with the hydrogen atom. This is indeed the case, considering the A exciton of monolayer MoS₂ this exciton has a Rydberg state of excitonic state, where the state with the lowest energy (*i.e.* highest exciton binding energy), corresponds to the $n = 1$ state of the Rydberg state. In the previous chapters we have mainly considered the $n = 1$ state of the A, B, and C excitons since these have the highest oscillator strengths and therefore are most easily accessible to experimental measurements. In this chapter we will study the Rydberg series of the A exciton of the TMD monolayers and how this series is affected by its dielectric environment, *i.e.* in a vdWH and on a dielectric bulk medium. At the end we will prove that, when the dielectric constant of the bulk substrate becomes very high and dominates the intrinsic dielectric screening of the 2D monolayer, the system enters a new dielectric screening

regime, where the exciton is overscreened in great contrast to the underscreened case known so far in 2D exciton physics (paper II and III).

In sections 3.6 and 3.7 we discussed how the exciton state can be modelled using a hydrogen-picture. This lead us to the Mott-Wannier model for computational feasible calculation of exciton energies by numerically solving an eigenvalue problem (eq. 3.64). However, given the great resemblance with the hydrogen atom it is worthwhile to study the analytic solutions to eq. 3.64. To arrive at an analytical expression for the allowed exciton energies in 2D, we follow the method similar to the derivation leading to eq. 3.63 for the hydrogen atom. Due to the 2D nature of the problem it has been shown, that the allowed states are half-integer values of n in eq. 3.63 [124], *i.e.* in 2D we have $n \rightarrow n - \frac{1}{2}$. The form of the screened electron-hole interaction in the exciton Hamiltonian is discussed in section 3.6. The effective exciton dielectric function to enter this Hamiltonian is the integrated intrinsic 2D dielectric function over the extension of the exciton. In reciprocal space this is calculated as [90]:

$$\epsilon_{\text{eff}} = \frac{a_{\text{R}}^2}{\pi} \int_0^{2\pi} d\theta \int_0^{1/a_{\text{R}}} dq q \epsilon(q) \quad (3.80)$$

for an exciton confined to a 2D plane, where a_{R} is the exciton real space radius. Since a_{R} is itself a function of the effective exciton dielectric constant [124]

$$a_{\text{R}} = \frac{3n(n-1) + 1}{2\mu} \epsilon_{\text{eff}}, \quad (3.81)$$

(here given for quantum number $l = 0$) eq. 3.80 has to be solved self-consistently. In general the higher states in the Rydberg series have a larger spatial extension in real space (*i.e.* smaller extension in reciprocal space). Also, as shown earlier in contrast to the close-to-constant dielectric function in 3D the dielectric constant in 2D is a varying function of q . This means that the exciton effective dielectric constant to enter the screened Coulomb interaction in the exciton Hamiltonian itself becomes a function of state index n . Putting all this together it is evident that the 2D exciton version of the hydrogen Rydberg series (eq. 3.63) becomes:

$$E_n = -\frac{\mu}{2} \frac{1}{\epsilon_n^2 (n - \frac{1}{2})^2} \quad (3.82)$$

where ϵ_n is the exciton effective dielectric constant evaluated by eq. 3.80 for state n . For the typical extension of excitons in q -space, which for the TMDs is typically up to around 0.15 \AA^{-1} , the 2D dielectric function felt by the exciton can be approximated as a linear function: $\epsilon_{2\text{D}}(q_{\parallel}) \approx 1 + 2\pi\alpha_{\parallel}q_{\parallel}$, where α_{\parallel} is the in-plane static polarisability of the 2D monolayer. Inserting this in eq. 3.80 the exciton effective dielectric constant for exciton state n takes the form [90]:

$$\epsilon_n = \frac{1}{2} \left(1 + \sqrt{1 + \frac{32\pi\mu\alpha}{9n(n-1) + 3}} \right). \quad (3.83)$$

With the state dependent exciton effective dielectric constant in eq. 3.83, eq. 3.82 gives the exciton binding energy for state n . This has been shown to give results close to numerical solutions of the Mott-Wannier equation [90]. One consequence of the state dependent exciton effective dielectric function, that has been extensively studied in the previous literature, is that for a freestanding 2D monolayer, the relative decrease of the energy of the higher Rydberg states (compared to the 1s state), is lower than that of the bulk hydrogen Rydberg series [90, 21]. This is explained by the smaller extension in q -space of the higher Rydberg states leads to a lower exciton effective screening due to the positive slope of the dielectric function around $q = 0$ over the extension of the exciton wave function in reciprocal space. This is therefore a direct consequence of the linearly increasing screening in 2D (for small q) compared to the constant dielectric constant in the hydrogen model and in 3D bulk systems.

We will now in this thesis show that it is possible to generalise eq. 3.83 to include the effect of environmental dielectric screening, *i.e.* for instance the case of a 2D monolayer located on (or encapsulated between) a dielectric media. We will then show that this introduces a new dielectric screening regime of exciton physics in 2D where the slope of the exciton effective dielectric function changes sign at $q = 0$, and that this leads to underbound exciton states rather than overbound exciton states in the Rydberg series. To this end we consider a 2D monolayer located on a dielectric screening media with dielectric constant κ *i.e.* $\epsilon_{\text{sub}}(q = 0) = \kappa$, where $\epsilon_{\text{sub}}(q)$ is the full q -dependent dielectric function of the substrate. In this setup, the dielectric screening felt by the exciton is the intrinsic screening from the 2D monolayer plus an exponentially decreasing contribution from the substrate screening. The exponentially decreasing contribution from the substrate follows directly from the fact, that the charge distribution is strictly confined to the 2D monolayer and can be well described with an oscillating shape in-plane dependence: $\rho(\mathbf{r}, z) = e^{i\mathbf{q}\cdot\mathbf{r}}\delta(z)$, in polar coordinates with origin in the center of the 2D monolayer. It is easy to show that the electrostatic potential from this charge distribution decreases exponentially with q in the out-of-plane direction. To continue, we first calculate the effective dielectric function defined as $\epsilon(q) = V(q)/W(q)$, projected onto the exciton wave function, where $V(q)$ is the bare Coulomb interaction between the electron and the hole and $W(q)$ is the screened Coulomb interaction between the electron and the hole. We calculate $W(q)$ using the QEH model. The calculation of $W(q)$ follows the method described in section 3.3 for vdWHs, *i.e.* by the method of image charges and contains the full q -dependent (bulk) contribution to the 2D monolayer dielectric function from the substrate. We do not include any frequency dependence in the dielectric matrix from the substrate. In fig. 3.11 we plot $V(q)/W(q)$ projected onto the exciton wave function for three cases: freestanding WSe₂ (black), WSe₂ located on a substrate with $\kappa = 4$ (blue, S1), and WSe₂ located on a substrate with $\kappa = 26$ (red, S2). The effective κ , as plotted by the dashed lines, are then defined as: $\kappa_{\text{eff}} = (1 + \kappa_{\text{sub}})/2$. We will from now reference S1 and S2 as the weakly and strongly screening substrates respectively. For the freestanding 2D monolayer we find the well-known shape of the 2D dielectric function as discussed previously. When the monolayer is located on the weakly screening substrate we find that the dielectric function is still dominated by the

intrinsic 2D screening, however we now have that the $\epsilon(q=0)$ limit differs from 1 as a consequence of the contribution from the substrate. When the monolayer is located on the strongly screening substrate the shape of the dielectric function differs significantly, most pronounced with the sign of the slope of $\epsilon(q)$ reversed around $q=0$ and the exponential decrease of $\epsilon(q)$. In addition to the well-known 2D screening regime and bulk screening regime this substrate dominated regime introduces a new dielectric screening regime of exciton physics, and is a unique artefact of the 2D monolayer on a bulk dielectric. Below we will study the implications this screening regime has on the exciton physics. The grey lines in fig. 3.11 show the transition from the 2D screening regime to the substrate dominated screening regime. We stress that values chosen for κ in fig. 3.11 are experimentally realisable values [26, 94].

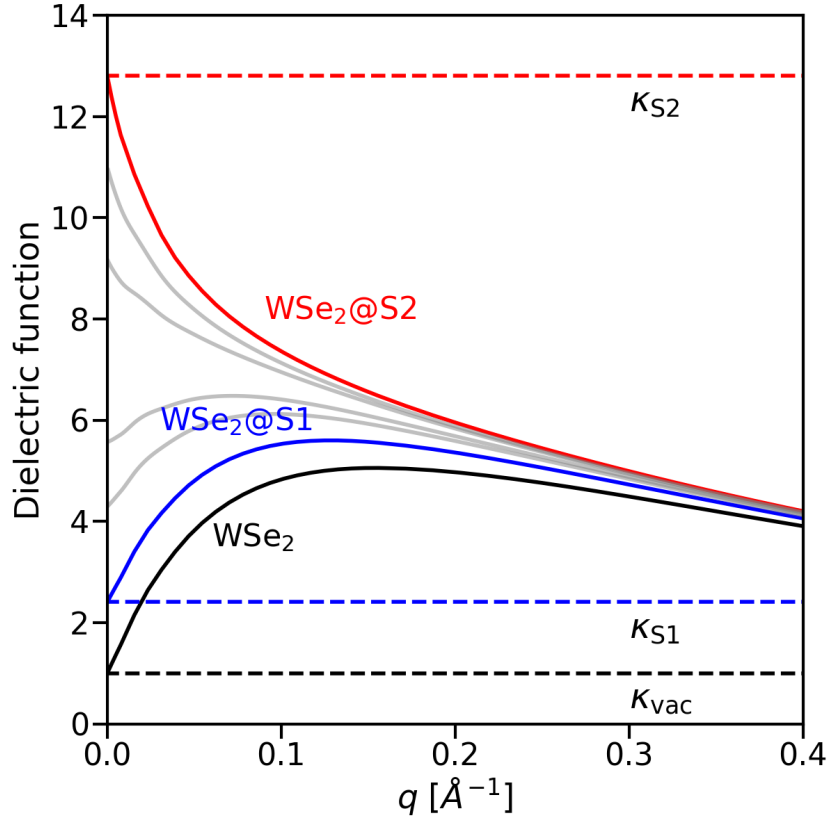


Figure 3.11: q -dependent dielectric function projected onto the exciton wave function for freestanding WSe_2 (black), WSe_2 on a weakly screening substrate (blue), and WSe_2 on a strongly screening substrate (red). The gray lines indicate the transition from one screening regime to the other and the horizontal dashed lines show the effective κ as defined in the main text. This figure is taken from included paper II.

We now return to deriving an analytical model to calculate the exciton effective dielectric constant and exciton binding energies for the systems in fig. 3.11, to analytically

calculate the excitonic properties in the substrate dominated screening regime. Since the intrinsic substrate screening can be taken to be close to constant over the extension of the exciton wave function, we approximate the intrinsic contribution from the substrate as constant, κ . This means that the dielectric function in the 2D monolayer, over the extension of the exciton wave function, can be well approximated as:

$$\epsilon(q) = 1 + 2\pi\alpha q + \kappa e^{-qd} \quad (3.84)$$

where d is the distance from the center of the 2D monolayer to its image charge in the substrate. To proceed we insert eq. 3.84 in eq. 3.80 to calculate the exciton effective dielectric function. It is straightforward to evaluate the integral to obtain: $\epsilon_{\text{eff}} = 1 + \frac{4}{3}\pi\alpha\frac{1}{a_{\text{R}}} - 2\frac{\kappa a_{\text{R}}^2}{d^2} \left(\frac{d}{a_{\text{R}}} + 1\right) e^{-d/a_{\text{R}}} + \frac{\kappa}{d^2}$. To find a closed analytical solution we realise that a_{R} is at least twice as big as d (and for most states in the Rydberg much bigger). We therefore expand the exponential function to second order in d/a_{R} . This leaves us with a polynomial function we can readily solve to obtain:

$$\epsilon_{\text{n}} = \frac{1}{2}(1 + \kappa) \left(1 + \sqrt{1 + \frac{8\mu(\frac{4}{3}\pi\alpha - \kappa d)}{(3n(n-1) + 1)(1 + \kappa)^2}} \right). \quad (3.85)$$

This expression is plotted in fig. 3.12 with full lines. In circles are plotted a numerical average of the dielectric functions in fig. 3.11 up to $1/a_{\text{R}}$ obtained by self-consistently solving eq. 3.81 until convergence is achieved. For both models, the results is shown for the three screening regimes shown in fig. 3.11. As expected and explained above, we find a decrease of the exciton effective dielectric constant due to the negative slope of the dielectric function for a freestanding 2D monolayer (black) and for a 2D monolayer on a weakly screening substrate (blue). We find excellent agreement between the numerical solution and eq. 3.85. For the substrate dominated screening regime we find a qualitative and fundamentally different behaviour, where a higher exciton effective dielectric constant is found for the higher states in the Rydberg series. As the exciton wave function expands in real-space for the higher Rydberg states, the exciton wave function becomes more localised around $q = 0$, and consequently the exciton effective dielectric constant increases due to the negative slope of the dielectric function for the substrate dominated regime in fig. 3.11.

The result in fig. 3.12 introduces a new screening regime of exciton physics, where the relation between the dielectric screening of the exciton and the exciton extension is reversed compared the 2D screening regime and where the excitons become underbound opposite to overbound in the already known 2D screening regime. We are now ready to calculate the exciton binding energies for 2D materials on strongly screening substrates. We do this by numerically solving the 2D Mott-Wannier equation for the exciton binding energies, eq. 3.64, with the screened electron-hole interaction used to calculate the exciton effective dielectric function in fig. 3.11 *i.e.* including the substrate dielectric screening. This is done for the three systems discussed above and shown in fig. 3.13, where we plot the exciton binding energy for the Rydberg series normalised

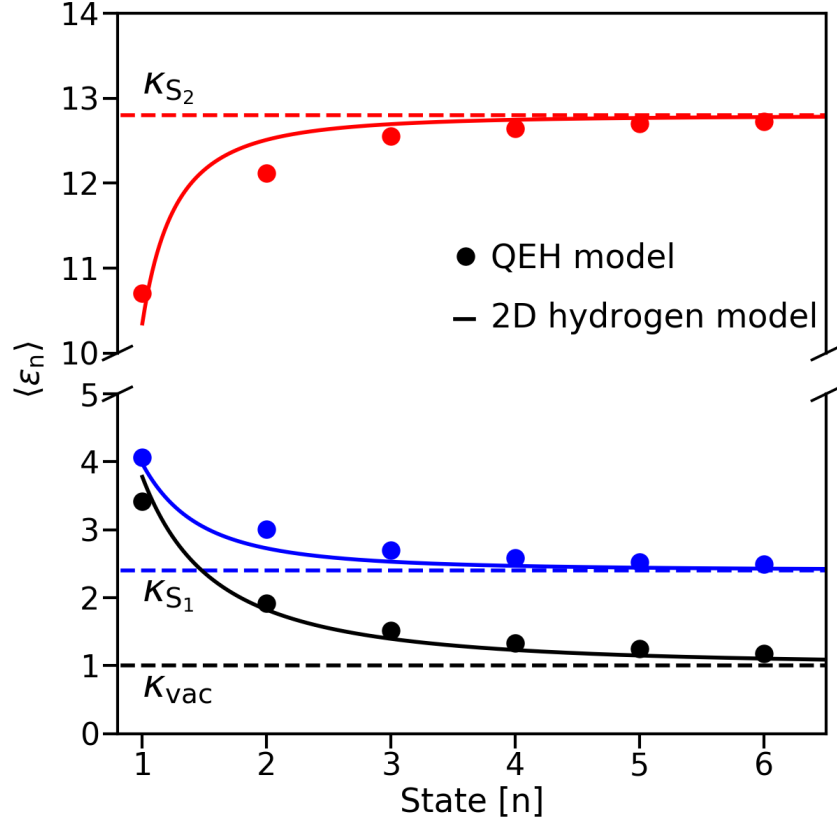


Figure 3.12: Exciton effective dielectric constant for state n in the Rydberg series of the three systems shown in fig. 3.11, calculated numerically with the QEH model (circles) and from the analytical solution (full lines) to the exciton effective dielectric constant, eq. 3.85. The dashed lines show the κ defined in the main text and also shown in fig. 3.11. This figure is taken from included paper II.

to the 1s exciton binding energy. The color coding follows that of figs. 3.11 and 3.12. In grey is shown the 2D hydrogen Rydberg series. For the freestanding 2D monolayer (black) we find the well-known non-hydrogenic Rydberg series [90, 21], where the excitons are overbound compared to the hydrogenic series. As a consequence of the increased exciton screening in the substrate dominated screening regime (red), the higher states in the Rydberg series become underbound. In the inset is shown the actual exciton binding energies on a logarithmic scale for the numerical solution to the Mott-Wannier equation (triangles) and from the analytical model, *i.e.* calculating the exciton binding energies from eq. 3.82 with the exciton effective dielectric constant from eq. 3.85 (empty circles). Similar to the exciton effective dielectric constants we find an excellent agreement between the numerical and analytical results. For the 1s states we find the largest discrepancy, as high as about 0.1 eV for the freestanding 2D monolayer (black) which was also found in the original work for freestanding 2D monolayers [90]. This can most

likely be subscribed to the linear approximation of the dielectric function being least accurate for the 1s state, since this has the largest extension in q -space. Furthermore, an additional error for the 1s state for systems including substrate screening could be expected since the expansion of d/a_R in the derivation of eq. 3.85 is least accurate for this state, however we find the inaccuracy of the exciton binding energy of the 1s states to be dominated by the inherent inaccuracy of the linear approximation of $\epsilon(q)$.

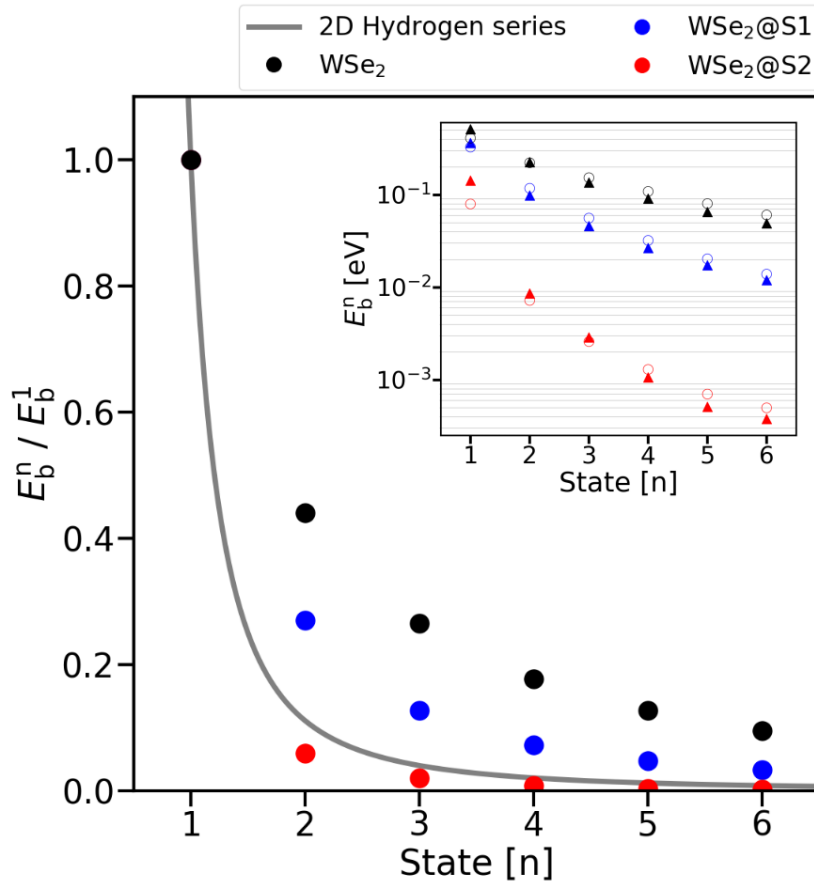


Figure 3.13: Exciton binding energies, normalised to the 1s state, for the Rydberg series for the systems shown in fig. 3.11, calculated by numerically solving the Mott-Wannier equation with the screened electron-hole interaction calculated by the QEH model. The gray line shows the 2D exciton hydrogen series from which the non-hydrogenic behaviour of the 2D and quasi-2D systems is obvious. The inset shows the exciton binding energies on a logarithmic scale. Full triangles are values from the numerical solution of the Mott-Wannier equation (corresponding to the data in the main plot) and the empty circles are the binding energies obtained from the analytical model, eqns. 3.82 and 3.85. The color coding follows that of figs. 3.11 and 3.12. This figure is taken from included paper II.

We finally show that the new exciton screening regime is experimentally realisable and show that the transition from the non-hydrogenic to hydrogenic regime and onto the new screening regime, is well described by combining experimental and calculated exciton energies. To study this, in a joint experimental study monolayer WSe₂ has been grown on different substrates, ranging over quartz, HfO_x, hBN, encapsulated HfO_z, and In₂Se₃, with a wide spectrum of different κ -values. The 1s and 2s exciton energies were then determined from photoluminescence measurements. The experimentally determined 1s (black) and 2s (red) exciton energies are shown in fig. 3.14 (left). From the 2D and 3D hydrogen models it can easily be deduced that the exciton binding energy of the 1s state in the hydrogenic and non-hydrogenic series are then simply related to the difference in 1s and 2s exciton energy by: $E_b = 9/8\Delta E_{12}$ (hydrogenic regime) and $E_b = 2\Delta E_{12}$ (non-hydrogenic regime). In fig 3.14 (right) the exciton energies in the two screening regimes (determined from the experimentally determined 1s and 2s exciton energies) are plotted in orange and red. It is clear that the non-hydrogenic exciton binding energies are higher than the hydrogenic exciton binding energies due to the reduced screening in this regime. We now calculate the exciton binding energies by numerically solving a Mott-Wannier equation with the induced dielectric screening from the substrate, as outlined above. We do this for the systems studied experimentally and plot the calculated exciton binding energies in green in fig. 3.14. For small κ -systems we find that the calculated exciton energies lies close to the non-hydrogenic series and in between the two non-hydrogen and hydrogenic exciton series, resembling the 2D character of the exciton screening. For κ -values around 4-10 we achieve the hydrogenic series (*i.e.* the bulk screening regime) and for very high κ -values the calculated exciton energies are found below both the non-hydrogenic and hydrogenic screening regime and enters the new over-screened regime. The fact that the new over-screened exciton regime can be achieved experimentally opens new pathways for exciton physics and introduces a new world of manipulating excited states at the atomic level.

3.9 Interlayer Exciton in a 2D Heterostructure for IR Photodetection

We will now discuss the connection between the oscillator strength of an optical excitation and the peak of the excitation in the absorption spectrum. The oscillator strength is a measure of the transition probability for an electron between the initial state and the final state and it is calculated by taking the matrix element with the transition dipole moment operator. In a simple picture, multiplying the oscillator strength with the joint density of states essentially gives the peak height in the absorption spectrum for this transition. This means that the amplitude of an excitation peak can be altered by changing the joint density of states or the coupling parameter between the two states as stated by Fermi's golden rule. While the former is determined from the electronic band structure the latter is known to have a strong dependence on a variety of factors.

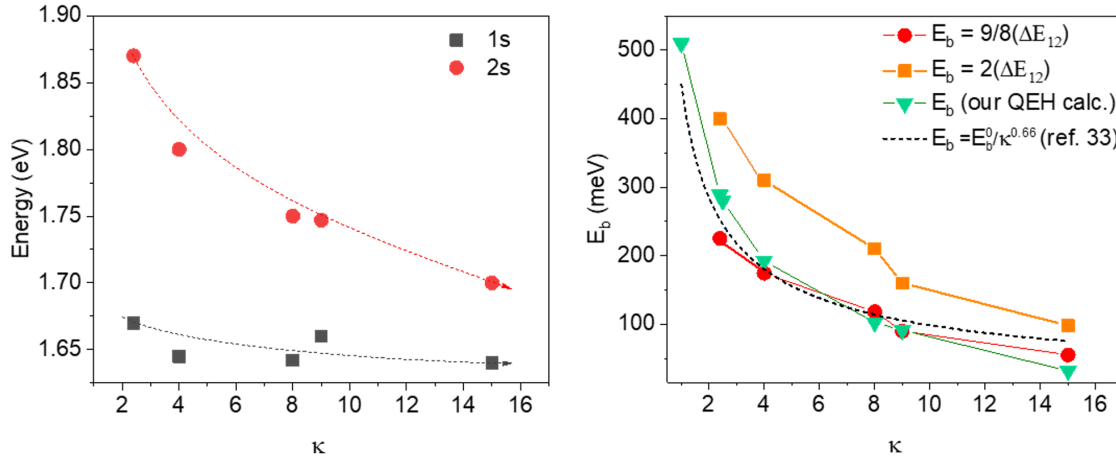


Figure 3.14: Left: Experimentally determined 1s (black) and 2s (red) exciton energies obtained from photoluminescence spectra for WSe₂ on different dielectric substrates (see main text). Right: Exciton binding energies assuming a non-hydrogenic screening regime (orange) and hydrogenic screening regime (red) deduced from the experimentally determined 1s and 2s exciton energies. In green is shown numerically calculated exciton energies. This figure is taken from included paper III.

This includes the dielectric screening (as shown above) and the nature of the transition (momentum indirect transitions in general have lower oscillator strengths since it requires the simultaneous absorption of a photon and a phonon to account for the momentum conservation). Also, a larger spatial distance between the final and initial states in general lowers the coupling strength. This has huge implications for interlayer excitons which have much lower oscillator strengths and can be difficult to detect in many absorption measurements. Since the lowest bright energy transition in few-layer vdWHs is given by the energy of the lowest lying interlayer exciton makes only few vdWH interfaces possible candidates for IR photodetectors due to two reasons: 1) only few vdWH interfaces have a interlayer exciton energy in the IR region and 2) such an exciton state needs to have an exciton binding energy much higher than the room temperature *and* a high oscillator strength. Previous developed IR photodetectors either have an excitonic absorption peak in the mid-high IR spectrum or are not environmentally stable [125, 126, 48, 19, 103], and as such the need for a stable low-energy IR photodetector is of special interest.

We have shown that such a low IR photodetector with stable exciton states can be achieved at the heterointerface between WS₂ and few-layer HfS₂. This result is shown in paper IV, and here we will explain in greater details the peculiar mixed intra- and interlayer character of this exciton state and its relation to its oscillator strength. In fig 3.15 is shown the experimentally measured absorbance as a function of transition energy for various setups including monolayer WS₂ (blue filled), few-layer HfS₂ (open

red dots), the heterointerface between monolayer WS_2 and few-layer HfS_2 (open dark red) and bulk HfS_2 (dark red filled). The intralayer exciton peaks for both WS_2 and HfS_2 (irregardless of the specific system) is located around 2 eV. This is in agreement with our findings in the previous chapters, where we showed intralayer exciton energies are redshifted of the order of a few hundreds meV in vdWHs. For the heterointerface systems we in addition find a low lying exciton state located close to 0.2 eV. As we will discuss below this exciton has been determined to have a mixed intra- and interlayer exciton character and we calculate its exciton binding energy to be orders of magnitude larger than the room temperature energy as generally found in few-layer vdWHs.

By calculating the electronic band structure from DFT we find that the bilayer WS_2/HfS_2 has its CBM at the M-point (of the hexagonal Brillouin zone) purely localised on the HfS_2 monolayer. We find two close to degenerate VBMs: one located at the K-point localised on the WS_2 monolayer and one at the Γ -point with joint weight on both monolayers. This gives two almost degenerate momentum indirect transitions: K-M and Γ -M and at a first hand it is not obvious if the peak around 0.2 eV in fig 3.15 is the result of a mix of both transition or only one of the transitions has a high enough oscillator strength to be observed in an absorption spectra measurement. An interesting aspect of the exciton peak at around 0.2 eV is that a reversed dependence on the dielectric environment is found compared to fig. 3.10: the amplitude of the absorbance peaks increases with the strength of the dielectric environment quantified by the number of HfS_2 layers.

To investigate this phenomenon we calculate the orbital character of the CBM state the M-point and the two (almost degenerate) VBM states at the K- and Γ -points. The

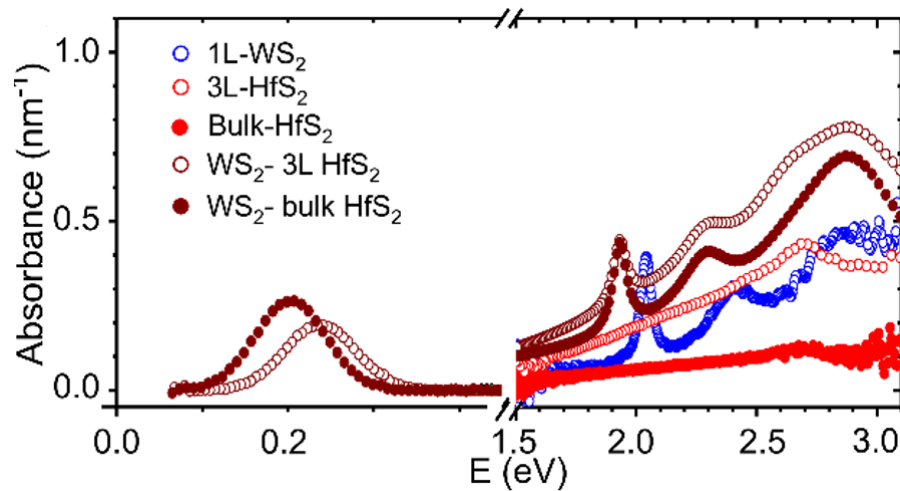


Figure 3.15: Experimentally measured absorbance spectrum for monolayer WS_2 (open blue), 3 layers HfS_2 (open red), buk HfS_2 (full red), heterointerface of WS_2 with 3 layers HfS_2 (open dark red) and with bulk HfS_2 (full dark red). This figure is taken from included paper IV.

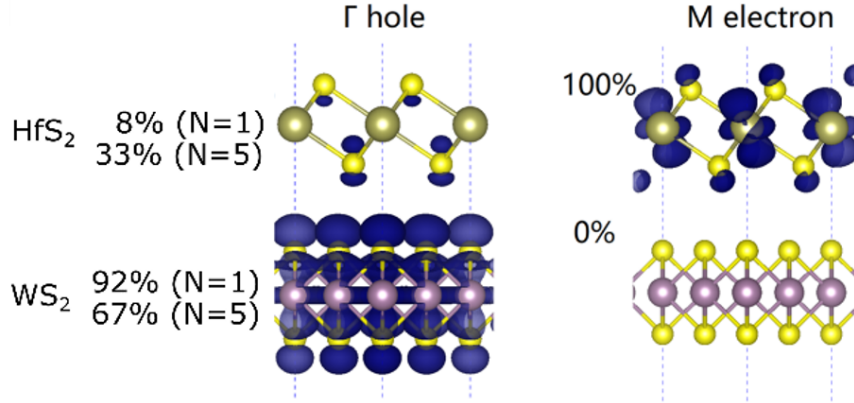


Figure 3.16: The calculated weight of the HfS₂ and WS₂ layers for the WS₂/HfS₂ heterointerface with 1 and 5 layers of HfS₂ respectively. This is shown for the hole state at the Γ -point and for the electron at the M-point. This figure is taken from included paper IV.

state at the M-point in the conduction band is solely located on the HfS₂ layer, however with mixed orbital presence of both Hf *d*- and S *p*-orbitals. For the K-point we find that this state is on the other hand solely located on the *d*-orbital of W which is not surprising from our previous knowledge about the TMD monolayers. A clue to our investigation now arises by considering the Γ -point. From our studies of multilayer TMD structures (in the previous sections and in following chapter 4) we know that a significant interlayer orbital hybridisation is affecting the energies around the Γ -point with joint orbital character of the *d*-orbitals of the transition metals and *p*-orbitals of the chalcogenides atoms in both layers resulting in an interlayer hybridised state at the Γ -point. We find that the weight on the S (*p*) on the HfS₂ layer increases with the number of HfS₂ layers. The Γ -M exciton can evidently be regarded as a hybridised exciton with both inter- and intralayer character and that the degree to which it resembles an intralayer exciton depends on the number of HfS₂ layers. We stress that the orbital character of the K-point remains purely of W (*d*) character independently of the number of HfS₂ layers. This together with the fact that the M-point also has a S (*p*) orbital character can explain why this transition can have an oscillator strength comparable to that of intralayer excitons and explains why the peak amplitude increases with the number of HfS₂ layers in the measured absorbance spectrum. We stress that this does not rule out that the peak around 0.2 eV does not have a contribution from the K-M transition.

To the extent of the author's knowledge the study of vdWHs built with TMD monolayer based on transition metals with few electrons in the *d*-orbitals (Hf, Zr, Ti, Sc etc.) have received only scant attention in the recent years. The above study suggests that it is possible to utilise the presence of orbitals localised on the halogen/chalcogenide atoms in the valence band edge states to achieve interesting interlayer hybridised states with a stronger interlayer coupling strength, than the well-explored TMD monolayers based on V, W, Mo, Pt, Pd, Cr and etc. This could possibly lead to the development of more

devices in the IR and optical spectrum not only limited to photodetectors. The suggested IR photodetector has a tunable peak position of the IR exciton peak which can be predictably manipulated with the number of HfS₂ layers of about 150 meV as shown by both calculations and experiments with a strong oscillator strength over the full range of few layers to bulk form. It can be hypothesised that the strong oscillator strength, even with bulk HfS₂ is only related to the first 5-10 HfS₂ over which the electron wave function is distributed. If this is true, it means that one could potentially replace the remaining HfS₂ with monolayers with a higher dielectric screening potential to achieve a further tuning of the exciton energy and reach even lower excitation energies.

CHAPTER 4

Exciton Energies: Disentangling Dielectric Screening, Orbital Hybridisation, Twist-Angle, and Substrate Effects

As we saw in chapter 3, extensive studies of the quasi-particle and excitonic states of many vdWHs can be carried out, without including a detailed and correct description of the interlayer orbital hybridisation. However, even though vdWHs are indeed characterised by a weak interlayer interaction, and thus a weak interlayer orbital hybridisation, it is becoming increasingly important to understand and calculate this effect accurately. This is especially highlighted by the recent discovery of the onset of superconductivity in bilayer graphene [12] and interlayer hybridised exciton states in vdWHs [3]. In section 4.1, we will discuss the difficulties of correctly calculating interlayer orbital hybridisation effects in vdWHs, and why such effects are not even accurately described by the state-of-the-art G0W0 formalism presented in chapter 3. This is mainly due to the fact that the G0W0 formalism adopts the (possibly wrong) band line-up description provided by conventional DFT methods. In this chapter we will show how this effect can be properly calculated and implemented into GPAW, by an efficient computationally cheaper scheme. We will denote this developed method the 'LCAO Scissors-operator (LCAOS) method' and it is in this thesis implemented into the QEH model. This redefines the QEH model to both include interlayer dielectric screening *and* interlayer orbital hybridisation and charge transfer effects, such that excited state properties can now efficiently be calculated for multilayer vdWHs including interlayer hybridisation effects. In section 4.2 the new, redefined QEH model, is then, in combination with the G0W0(Γ) and BSE-QEH methods, applied to calculate exciton energies in vdWHs. With the use of the redefined QEH model, it is now possible to split the exciton energies in vdWHs into its components *i.e.* the renormalisation of the exciton energies due to dielectric screening, interlayer hybridisation, charge transfer, bulk substrate effects etc., to better understand the nature of the lowest excitonic states in vdWHs. By comparing our calculated exciton

energies for a set of vdWHs to a large library of intra- and interlayer exciton energies obtained from the literature, we benchmark to what accuracy *ab-initio* calculations can be expected to fit with experimental values. These results are mainly presented in paper V, and section 4.2 outlines some of the main results of this work and shows an example of the calculated twist-angle dependency of exciton energies on interlayer hybridisation effects.

4.1 Calculation of Interlayer Hybridisation Effects in van der Waals Heterostructures

In chapter 3 we studied how the quasi-particle energies and exciton energies are influenced by the dielectric screening from the environment due to the non-locality of the dielectric function. However, even though the interlayer interaction between the 2D monolayers in a vdWH is of van der Waals character, it is well-known that in some systems there can be a substantial interlayer hybridisation of the wave functions which leads to a significant renormalisation of the quasi-particle and exciton energies in parts of the Brillouin zone. Examples of this include the strong interlayer hybridisation around the Γ -point for MoS₂ transitioning from monolayer to bulk [122] shifting the direct band gap at the K-point to an indirect band gap from the Γ -point to the K-point. Other examples include the twist-angle dependent exciton hybridisation for bilayer TMDs [3] and the magic-angle superconductivity for bilayer graphene at a twist-angle close to 1.1 degrees [12]. Before we discuss how the interlayer hybridisation can be accurately modelled we must first understand what is meant by *accurately*. In experiments measuring the electronic band structure and exciton energies, it is not possible to disentangle the different contributions from environmental screening, interlayer wave function hybridisation, interlayer charge transfer, and other effects, but merely to measure single excitation energies. We therefore do not have any reliable experimental values to benchmark the disentangled effects against and we are left to benchmark against numerical methods. In the literature it is common to rely on the G0W0 (or self-consistent GW) approximation to give the best possible description of the electronic band structure. However, a full G0W0 or self-consistent GW description for most vdWHs is not possible (which is the very reason for the need of the QEH model) and such methods are therefore not an obvious choice for benchmarking. The G0W0 approximation also fails to properly describe the interlayer hybridisation, as we will return to below, eliminating this method for benchmarking. The obvious choice is therefore to use numerical methods with less computational cost and less numerical accuracy, that calculates the interlayer interaction self-consistently. We settle on benchmarking the model we develop below against self-consistent HSE calculations.

We can understand the idea of the LCAOS method by realising that GGA calculations include the effect of interlayer hybridisation self-consistently, and since the GGA is an inherent single-particle description it does not contain the many-body dielectric

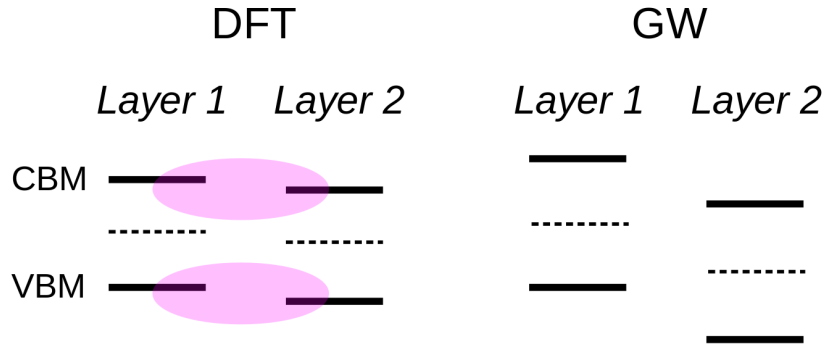


Figure 4.1: Illustration of an example band line-up of the valence band maximum (VBM) and conduction band minimum (CBM) for two 2D monolayers, predicted by DFT (left) and by the GW approximation (right). As discussed in the main text, the poor description provided by most DFT functionals of the electronic band gap leads to a poor description of the predicted band line-up, and therefore a wrong description of interlayer orbital hybridisation. In the given example the DFT description predicts a strong interlayer orbital hybridisation while the self-consistent GW description predicts little to no interlayer orbital hybridisation. The dashed lines indicate the Fermi levels.

screening outlined in the first sections of chapter 3. Therefore it is possible to isolate the interlayer charge transfer and hybridisation effects from such calculations by comparing the electronic band structure of the vdWH to GGA calculated electronic band structures of the freestanding monolayers. However, as simple as this idea is, it will in general not give a proper description of the interlayer orbital hybridisation as illustrated in fig. 4.1. It is well-known that GGA heavily underestimates the electronic band gap and consequently the exact position of the VBM and CBM relative to vacuum. As illustrated, the band line-up will in some cases lead to the GGA calculation overestimating (this is the example shown in fig. 4.1) or underestimating the interlayer hybridisation compared to a self-consistent many-body description. We therefore seek a method, where we do a self-consistent GGA calculation for the vdWH, with a set of scissors-operators in the self-consistent loop, to start from the many-body quasi-particle band line-up (relative to vacuum). In this way, it is possible to self-consistently calculate the interlayer orbital hybridisation for the vdWH starting from the correct many-body band line-up. As outlined in section 2.3, GPAW supports three different modes for electronic structure calculations: a plane-wave based description (PW), a basis set based description (LCAO), and a finite-difference (FD) method. While all three modes are suitable for the desired implementation, the supercells describing multilayer vdWHs and even twisted bilayers contain hundreds (or thousands) of atoms and, of the three modes, LCAO is able to carry out converged calculations for the largest supercells within GPAW. We therefore pursue the implementation of the method within the LCAO mode.

In the meantime, a derivation of the implementation scheme for a state-dependent (k -point, band) scissors-operator in PW mode is presented in appendix C. Here an analytical expression for the correction matrix to the DFT Hamiltonian is derived, to achieve the desired eigenvalue corrections for all states, only based on freestanding monolayer eigenvalues. We will not follow this approach further, but the method is presented in appendix C in case it will be found useful for future studies.

Within the framework of LCAO we consider the LCAO eigenvalue problem in eq. 2.31. Our aim is to apply a constant scissors-operator to both the occupied and unoccupied states, where the constant scissors-operator can be different for the occupied and unoccupied states, to match the G0W0(Γ) quasi-particle band edges. In addition, we want to do this for all monolayers in the vdWH of consideration, where the scissors-operator for occupied and unoccupied states can also differ from layer to layer. If we add a correction to $\tilde{H}_{\mu\nu}$ in eq. 2.31: $\tilde{H}_{\mu\nu} \rightarrow \tilde{H}_{\mu\nu} + \tilde{H}_{\mu\nu}^S$ (where 'S' is short for 'scissors-operator'), this gives a correction to the eigenvalues of: $\Delta E_n^S = \sum_{\mu\nu} S_{\mu\nu} c_{\mu n} \tilde{H}_{\mu\nu}^S c_{\nu n}$. In other words, it is possible to find a correction to the LCAO Hamiltonian, $\tilde{H}_{\mu\nu}^S$, defined from the desired corrections to the eigenvalues of states n . In practice, we define a constant eigenvalue shift for both the occupied and unoccupied states for each layer in the vdWH of consideration (*i.e.* the number of corrections equal two times the number of layers in the vdWH). For a single monolayer, the eigenvalue corrections to the occupied and unoccupied states are defined as the difference between the eigenvalue of a specific state obtained from a LCAO calculation for the freestanding monolayer and the desired eigenvalue for the same state (this could for instance be defined as the difference between the LCAO and G0W0 eigenvalue at the VBM (CBM) at the K-point in the Brillouin zone for the occupied (unoccupied) states). The desired eigenvalues will in this study in practice be given by G0W0(Γ) quasi-particle energies for the freestanding monolayers. When all energy corrections (ΔE_n^S) have been defined, the corresponding Hamiltonian corrections are determined from the above definition of the correction Hamiltonian, and an LCAOS calculation is performed for the full vdWH, where the determined Hamiltonian corrections are added and projected onto the wave functions of the layer it should be applied to. This is in practice done from the available wave functions from the freestanding monolayer calculations. This defines what we will label as the LCAOS method in the remaining. The proposed method enables us to carry out calculations for up to more than 1000 atoms and to correctly assess the effect of interlayer hybridisation and charge transfer, by studying the interface self-consistently from the G0W0(Γ) band line-up, and by applying a minimal strain to the monolayers. Such calculations cannot be performed with conventional many-body *ab-initio* methods and thus, this approach offers a unique tool with the already existing QEH model for calculating interlayer dielectric screening and the BSE-QEH model developed in the chapter 3 to calculate exciton binding energies in vdWHs irregardless of the number of layers and/or twist-angles. Furthermore the method can effectively be utilised in combination with the big library of G0W0 quasi-particle energies available in C2DB.

We stress that we find little-to-no difference between the eigenvalues near the Fermi level of interest for the usual class of TMD structures between the LCAO, FD, and PW modes in GPAW. Below we will present a benchmarking study of the proposed method and then apply it to multilayer- and twisted vdWHs in combination with the already existing QEH model and the MW-QEH and BSE-QEH models for calculating exciton energies in these structures.

We benchmark the LCAOS method against self-consistent calculations with the hybrid functional HSE and consider bilayer MoS₂ (in the AB-stacking configuration) as a first test system to avoid an initial erroneous description of the band line-up, since PW HSE is the highest level of self-consistent computational theory we can apply reliably to few-atoms vdWHs. In practice, this is done by first performing a self-consistent HSE calculation and LCAO calculation for freestanding monolayer MoS₂. The LCAO and LCAOS calculations are performed with the PBE functional. The difference between the valence- and conduction band edges for the two calculations at a chosen point in the Brillouin zone (here the K-point), defines the scissors-operator for the valence- and conduction states respectively. Next, we perform a LCAOS calculation with this defined scissors-operator for bilayer MoS₂ and compare to the self-consistent HSE calculation for the same system. The result is shown in fig. 4.2 (left) where the HSE band structure for bilayer (monolayer) MoS₂ is shown in black (grey) and similarly the LCAOS (LCAO) band structure for bilayer (monolayer) MoS₂ is shown in red (blue). Overall we find an excellent agreement between the HSE and LCAOS band structures for bilayer MoS₂. We first notice the lack of interlayer hybridisation effects at the K-point for both the valence and conduction band in both methods where the bilayer states coincide with the monolayer states for the HSE calculation and the LCAOS calculation agrees with the self-consistent HSE calculation. Furthermore, the well-known effect and size of interlayer hybridisation on the valence state energies around the Γ -point is also well-described by the LCAOS method and so is the downshift of the conduction band between the K- and Γ -point. The LCAOS method accurately describes the magnitude of the hybridisation around the Γ -point leading to the direct to indirect band gap transition well-known for the transition from monolayer to bilayer MoS₂ [82]. A few features are not well captured, for instance are the energies of some of the lower valence states between the K- and Γ -point overestimated by the LCAOS method. This effect is found even for freestanding TMD monolayers by comparing GGA band structures (in both PW and LCAO mode) and G0W0 quasi-particle energies, suggesting that this is an inherent self-energy effect not related to the interlayer interaction. Despite this, the overall resemblance between the HSE and LCAOS band structures shows the high accuracy and proficiency of the proposed LCAOS method.

At the interface between any two 2D materials (and throughout a vdWH independent of the number of layers) the states in all layers will line up with respect to a common Fermi level. Since the position of the Fermi level of the freestanding monolayers in general will be different relative to the vacuum energy, a finite interlayer charge transfer from one layer to the other(s) is therefore required to restore a common Fermi level for the combined system. The interlayer charge transfer will set up small interface dipoles

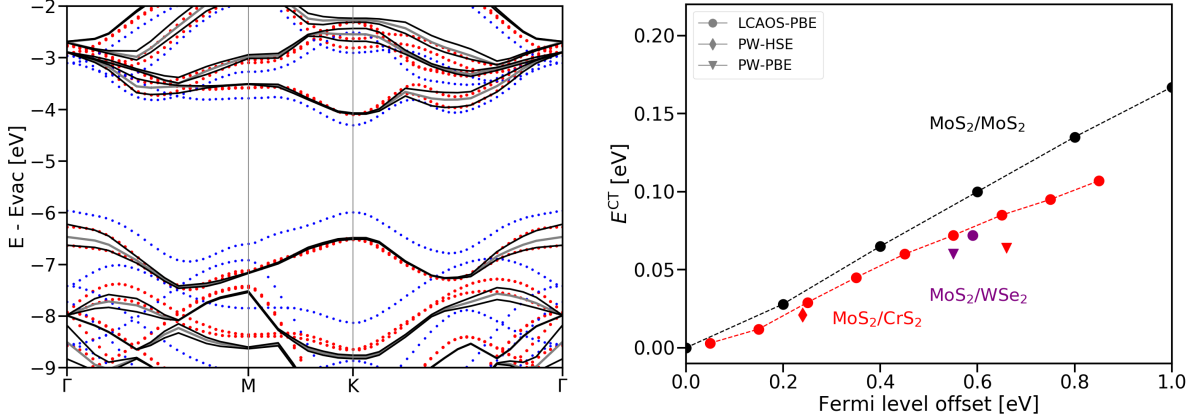


Figure 4.2: Left: band structure of bilayer MoS₂ calculated with two different methods: PW HSE (full black) and LCAOS PBE (dotted red). In dotted blue is shown a LCAO PBE calculation for monolayer MoS₂ and in full grey the monolayer MoS₂ PW HSE calculation. All calculations are performed fully self-consistently. Right: energy shift of band edge states located on Mo at the K-point (E^{CT}) for 3 different bilayer systems: MoS₂/CrS₂ (black), MoS₂/WSe₂ (purple), and bilayer MoS₂ (red) plotted against the difference in the position of the Fermi level for the two freestanding monolayers. This is shown in black for bilayer MoS₂ with the LCAOS PBE method and in red circles (triangle) ((diamond)) for MoS₂/CrS₂ with the LCAOS PBE (PW PBE) ((PW HSE)) method. Finally for MoS₂/WSe₂ the calculated value in Ref. [75] (purple triangle) is compared to a LCAOS PBE calculation (purple circle).

which give a shift of the states located on the different layers relative to each other. This effect is obviously not found at homointerfaces such as bilayer MoS₂, and thus not present in fig. 4.2 (left), but will in general be present at any heterointerface. To study how well the LCAOS method describes the interlayer charge transfer we set out to study a set of bilayer systems: bilayer MoS₂, MoS₂/CrS₂, and MoS₂/WSe₂. The last system has previously been studied in Ref. [75]. We note in passing that the two latter systems are not lattice matched and a small strain is applied to the two monolayers to match them in a minimal unit cell, however this does not influence the validity of the test as long as both the bilayer and freestanding monolayer systems are considered with the same lattice constant and bond lengths. For the 3 systems we calculate the offset of the band edges at the K-point (relative to the freestanding monolayer band edges) due to the interlayer charge transfer (E^{CT}) which is plotted against the Fermi level difference of the freestanding monolayers in fig. 4.2. We utilise the flexibility of the LCAOS method and determine E^{CT} over a range of different Fermi level line-ups, *i.e.* different scissor operators are applied to achieve a set of *artificial* Fermi level differences, and we then evaluate E^{CT} for each configuration by direct calculation. The result for bilayer MoS₂ is shown in black and defines a reference for comparison for the

heterointerfaces. For bilayer MoS_2 we find a linear relation between the Fermi level difference and the shift of the band edge at the K-point. In red we show the calculated values for bilayer $\text{MoS}_2/\text{CrS}_2$. The interesting aspect of this system is that the PW PBE method (red triangle) and PW HSE calculation (red diamond) predict a significantly different Fermi level difference (offset) for the freestanding monolayers and as can be seen consequently also a significantly different interlayer charge transfer. We note here that the Fermi level of MoS_2 in both cases reside above that of CrS_2 such that a charge transfer from the MoS_2 layer to the CrS_2 layer is expected. We now *artificially* vary the band line-up of this system with the LCAOS method and calculate the band offset (red circles). While the LCAOS method overestimates the interlayer charge transfer, it gives an overall good description of the two cases and follows a similar trend to bilayer MoS_2 . The magnitude of transferred charge at a given Fermi level difference is influenced by a set of different parameters such as the interlayer distance, the difference in electronegativity between the atoms of the two layers, etc. Comparing bilayer MoS_2 and bilayer $\text{MoS}_2/\text{CrS}_2$ we find an insignificant difference in the interlayer distance, however since Mo has a considerably higher electronegativity than Cr it seems reasonable that we find a smaller charge transfer in $\text{MoS}_2/\text{CrS}_2$ compared to bilayer MoS_2 . Finally we consider $\text{MoS}_2/\text{WSe}_2$ where the interlayer charge transfer has previously been studied [75], and it was in fact shown that the band offset only weakly depends on the applied strains. The result of Ref. [75] is shown with a purple triangle (performed with the PW PBE functional) and the LCAOS result is shown with a purple circle; also here an excellent agreement is found. In summary, with the available calculated and obtained data, we find the LCAOS method gives a very good description of the band offset due to the interlayer charge transfer by comparing to PW PBE and PW HSE calculations. This method can readily be combined with the dielectric screening effects already contained in the QEH model and the BSE-QEH developed in chapter 3 to accurately calculate quasi-particle and exciton energies in vdWHs, to enable accurate calculation of states strongly affected by interlayer hybridisation effects.

We now change gears and study a heterointerface in greater detail and to directly extract the effect of interlayer orbital hybridisation and charge transfer effects on the quasi-particle energies. To do this we consider bilayer MoS_2/WS_2 . We calculate the LCAOS band structure with the scissors-operator defined in terms of the LCAO and $G0W0\Gamma$ band edges at the K-point for the freestanding monolayers. We note in passing the $G0W0\Gamma$ calculation have been carried out based on PBE eigenvalues and norm-conserving PAW setups. The results can be found in fig. 4.4 (left) where the LCAOS band structure is shown in red for the bilayer and the sum of the freestanding monolayer LCAO band structures are shown in blue. The freestanding monolayer LCAO band structures have been artificially shifted to match the $G0W0\Gamma$ band edges *after* calculation. We now define the effect of interlayer orbital hybridisation and charge transfer on the band structure energies as the difference in energy of each state in the bilayer configuration compared to the state of the freestanding monolayer. This definition is well-defined for states with little-to-no interlayer orbital hybridisation, where the state in the bilayer can be projected onto one of the monolayers. However for mixed states, for

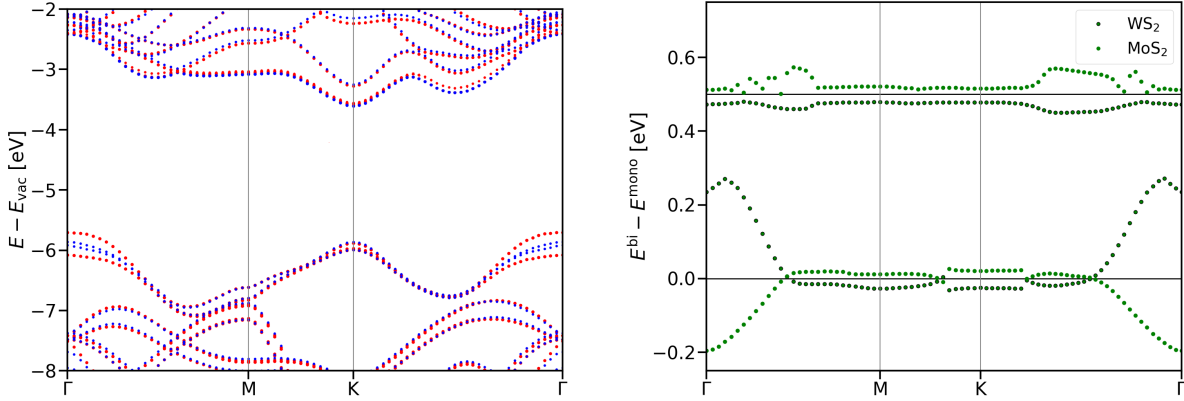


Figure 4.3: Left: band structure of MoS₂/WS₂ calculated with the LCAOS PBE method (red). In blue is shown the sum of the band structures of the freestanding monolayers calculated with LCAO PBE, which is shifted with the same scissors-operators as the LCAOS calculation *after* the monolayer calculations have been performed. The scissor-operator is defined from the G0W0 Γ band edges at the K-point. Right: the derived interlayer hybridisation and charge transfer effect on the two valence (bottom) and two conduction (top) bands defined as the difference in the monolayer (E^{mono}) and bilayer (E^{bi}) eigenvalues. The conduction bands are shifted +0.5 eV for clarity. See main text for the definition of the projection of each state onto one of the two monolayers. The numerical disturbances are due to band crossings.

instance for the valence states around the Γ -point, this definition bears little meaning and we simply assign each state to one of the monolayers. In the further analysis in the rest of the chapter we however keep in mind that both layers are subject to the splitting due to hybridisation for these states. The result of this analysis is shown in fig. 4.3 (right), where the effect is shown for the two valence- (bottom) and conduction (top) bands. The small disturbances close the K- and Γ -point arise from band crossing effects. This enables us, for the first time, to quantify and extract the effect of interlayer orbital hybridisation and charge transfer explicitly. As expected we find a large splitting of the valence bands around the Γ -point where the effect on the quasi-particle energies is close to three times the effect of the (almost constant) interlayer dielectric screening effect. We also find a significant effect of orbital hybridisation between the K- and Γ -point for the conduction bands. The interlayer charge transfer gives a small constant shift of about 0.02 eV down (up) for the WS₂ (MoS₂) monolayer consistent with the Fermi level for freestanding monolayer MoS₂ is found to be located below the Fermi level of freestanding WS₂ in the G0W0 Γ description. It is here evident that the interlayer charge transfer does not affect the intralayer exciton energies, but increases the interlayer exciton energy. On the other hand, the effect of orbital hybridisation significantly reduces the momentum indirect exciton energies involving the valence Γ -point.

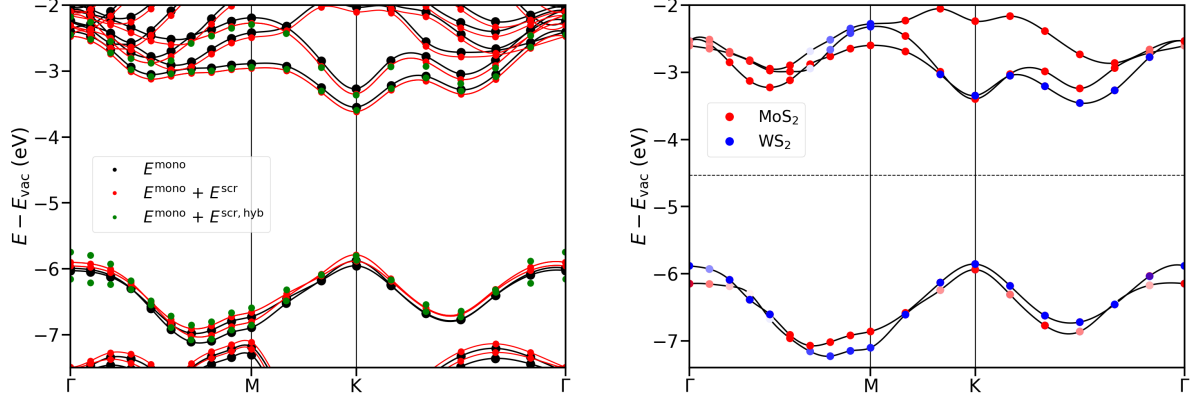


Figure 4.4: Left: quasi-particle energies for MoS₂/WS₂ obtained with the G0W0 Γ -QE model showing the sum of the quasi-particle energies of the freestanding monolayers (E^{mono} , black), including the interlayer screening from the QE model (E^{scr} , red), and including both dielectric screening and the interlayer orbital hybridisation effects (E^{hyb} , green). Right: full G0W0 calculation for the same structure based on PW PBE eigenvalues. Note both calculations are shown without the effect of spin-orbit interaction for clarity. A similar full G0W0 calculation can be found in fig. 3.2 including spin-orbit interaction. The comparison between the left and right figures and to fig. 3.2 also allows us to see the effect of the vertex correction. The same color coding as fig. 3.2 is used in this plot. Note that less conduction bands are included in the full G0W0 calculation than in the G0W0 Γ -QE calculation. The left figure is taken from the included paper V.

We remind ourselves that the G0W0(Γ)-QE model introduced and used in chapter 3 only includes the effect of interlayer dielectric screening. We are now in a position where we can expand upon the G0W0(Γ)-QE model by including the effect of interlayer hybridisation and charge transfer in vdWHs, through the quantification of this effect in fig. 4.3 (right). To take this into effect, in fig. 4.4 (left) we show the sum of the G0W0 Γ quasi-particle energies of the freestanding monolayers: MoS₂ and WS₂ in black. In red we have added the, almost constant, effect of the interlayer dielectric screening to the quasi-particle energies, and finally in green we have also added the effect of interlayer orbital hybridisation and charge transfer for the 2 top (bottom) valence (conduction) bands from fig. 4.3, as calculated by the redefined QE model.

This disentangling of the dielectric screening, interlayer hybridisation, and charge transfer effects redefines the QE model. It enables us to accurately describe quasi-particle states in vdWHs subject to a significant interlayer orbital hybridisation and in detail examine which effect(s) the renormalisation of quasi-particle energies can be subscribed to in vdWHs in different parts of the Brillouin zone. This tool can serve as a valuable method to understand and learn from complex vdWH interfaces and not only

answers the question: "what happens" upon interface line-up, but also "why it happens". The calculated $G_0W_0\Gamma$ -QEH band structure is shown together with a full G_0W_0 calculation for bilayer MoS_2/WS_2 to the right in fig. 4.4. We note this comparison also allows to see the effect of the vertex correction and norm-conserving PAW setups by also comparing to fig. 3.2. The effect is especially notable for the broken degeneracy of the CBM by performing the calculation with norm-conserving PAW setups and applying the vertex correction. While the resemblance between the two quasi-particle band structures is rather large, we stress that it is to this point not possible to define what is the *correct* quasi-particle band structure for bilayer MoS_2/WS_2 . This is because while the $G_0W_0\Gamma$ -QEH model gives a better description of the interlayer orbital hybridisation and charge transfer it lacks a proper description of how the GW self-energy correction is influenced by a better description of the band line-up. On the other hand, the description of the interlayer hybridisation in the full G_0W_0 is inherited from the (possibly) wrong band line-up provided by the PBE calculation. In future studies it will be interesting to see how the LCAOS method can be used in combination with full $G_0W_0(\Gamma)$ calculations to give a better guess at the initial band line-up and act as a pre-self-consistent loop to correct the main flaw of the $G_0W_0(\Gamma)$ formalism.

4.2 Benchmarking *Ab-Initio* Calculated Exciton Energies in vdWHs against Experiments

In recent years vast efforts have been put into determining exciton energies in mono- and few-layer vdWHs as accurately as possible. This has been done theoretically using computationally heavy methods such as the G_0W_0 and the BSE approximations and experimentally with for instance absorbance and photoluminescence experiments. Experimentally the field has moved into studying the effect of relative twist-angles between neighbouring monolayers on the electronic and optical states [3, 72, 12] and very accurate experiments, down to the meV range, have been carried out to determine the small redshift of exciton energies in vdWHs discussed in relation to the BSE-QEH model in chapter 3. It is indeed important to keep pursuing to fine tune both experimental and theoretical methods, however a direct comparison between the exciton energies obtained within the two fields is not straightforward. This is because while computationally heavy *ab-initio* methods are usually performed for idealised structures, for instance a freestanding bilayer, possibly with applied strain to the monolayers and without temperature effects, experiments are usually carried out with the presence of a supporting substrate, at a finite temperature, and possibly a finite relative twist-angle between the two monolayers, which cannot be modelled by computationally heavy *ab-initio* many-body methods. Furthermore, when applying *ab-initio* methods the researchers always know which quasi-particle states they are talking about, while in experimental studies

it is often difficult to obtain other information than only the transition energies. The situation is further complicated by the fact that the optical transitions that can be optically measured in an experiment heavily rely on the quality of the interface(s) and can as such be difficult to reproduce. It is evident that a systematic study on how the mentioned effects affects the *ab-initio* calculated exciton energies is needed.

To shine light on this issue we have calculated the lowest lying exciton energies for a set of bilayer TMD structures. We do this by utilising the BSE-QEH model (and the MW-QEH model for interlayer and finite momentum intralayer exciton binding energies) and the G0W0-QEH, including the developed method for obtaining the correct interlayer hybridisation and charge transfer from section 4.1. We are now able to not only accurately calculate exciton energies, but also disentangling and quantifying the contribution of interlayer dielectric screening, interlayer hybridisation, charge transfer, substrate, and twist-angle effects on each of the lowest lying exciton states, in the spirit of fig. 4.4 (left). This is a strong tool to understand the nature of the lowest optical transitions in few-layer vdWHs and to understand the discrepancy found between state-of-the-art *ab-initio* calculations and experimental measurements. To carry out a proper comparison to experiments the calculated exciton energies are compared to a large library of experimentally measured exciton energies from literature (which can be found in paper V). The discrepancy between different measurements (in different experimental studies) of the same exciton state for the same system quantifies the deviation that can be expected within experimental setups and evidently gives the lowest accuracy that can be expected for *ab-initio* methods. This is here modelled by the standard deviation of all experimental measurements (in the library of experimental studies) of the same exciton state.

The study not only addresses to which accuracy *ab-initio* calculations and experimental measurements can be expected to agree, it also supplies a valuable "hand-book" for both experimentalists and theoreticians to see how large specific physical effects can be expected to be when calculating, measuring, and comparing exciton energies between different studies. Here we will comment on some of the key details to understand the complex nature of exciton energies at heterointerfaces. The detailed results can be found in paper V.

We start out by considering how the relative twist-angle between two monolayers in bilayer TMDs affects the exciton energies. When the monolayers are rotated relative to each other the dielectric screening remains close to unchanged while the interlayer orbital hybridisation can be significantly affected since only the latter involves the spatial orbital overlap of the orbitals confined to each monolayer. For few-layer vdWHs with degenerate intra- and interlayer exciton energies, it has recently been shown experimentally that the exciton energies are twist-angle dependent [3], as shown in purple in fig. 4.5, where the experimentally measured lowest energy K-K exciton is plotted for MoSe₂/WS₂. To assess this feature computationally we calculate the quasi-particle band structure of MoS₂/WS₂, where we find both the K-K and Γ -K lowest energy quasi-particle transitions to host close to degenerate intra- and interlayer exciton states. We

calculate this for a range of relative twist-angles using the G0W0-QEH model (with the interlayer hybridisation derived from the LCAOS method) and plot the (electronic) quasi-particle band gap (full circles) in fig. 4.5. The empty circles are LCAO-PBE calculations *i.e.* within the single-particle picture without applying a scissors-operator to correct the band line-up. We stress the experimentally measured exciton energy is for a different system than the one we calculate here, but it is shown to illustrate the twist-angle dependent effect found experimentally for bilayers with degenerate intra- and interlayer exciton energies (at this point it was not possible to obtain calculated twist-angle dependent quasi-particle energies for MoSe₂/WS₂, but we note this is work in progress). We note again that all reference to the G0W0-QEH model from now includes the description of the interlayer hybridisation and charge transfer presented in section 4.1. In fig. 4.5 we show the calculated smallest quasi-particle (QP) gap in MoS₂/WS₂ for the two transitions hosting degenerate transitions: the direct band gap from K-K (black) and the indirect band gap from Γ -K (green). We start by considering the calculated (with the G0W0-QEH method) quasi-particle energies and find the Γ -K quasi-particle band gap to be the lowest quasi-particle band gap independent of the twist-angle, however the figure excellently illustrates the care that must be taken when assigning exciton energies to specific transitions in the band structure. As an example, consider a PL measurement performed on MoS₂/WS₂ finding an exciton energy of 2.2 eV (minus the exciton binding energy). Given the uncertainty in most experimental setups the measured energy can be ascribed to all three transitions in the Brillouin zone shown in fig. 4.5. If the layers are rotated by about 10 degrees the conclusion would incorrectly state that the lowest lying interlayer exciton has an energy almost 150 meV higher than the *ab-initio* calculated value at a 0 degrees twist-angle. This underlines the important care that must be taken when comparing exciton energies between different studies. We now rest a second with the peculiar dependence on the twist-angle for the direct band gap and the Γ -K gap. When the two unit cells are rotated relative to each other, both band gaps shifts up about 100 meV relative to the aligned bilayer. This shift is close to constant over the full range of rotation. As mentioned, previous experimental work have reported a similar observation for exciton energies in TMD bilayer systems having close to degenerate intra- and interlayer excitonic states, which has been explained by an inter-exciton hybridisation effect. It is therefore interesting that we find this effect for MoS₂/WS₂ where we indeed predict both the K-K and Γ -K quasi-particle transitions to host close to degenerate intra- and interlayer exciton states. On the other hand, when the interlayer hybridisation is derived from a LCAO PBE calculation (empty black circles), the lowest energy transition shows an opposite dependence on the twist-angle. In this case, where no scissors-operator is applied, the intra- and interlayer band gaps are not nearly degenerate. Consequently, within a standard LCAO description we find a weaker interlayer hybridisation around the Γ -point (open circles) compared to the LCAOS method (full circles). The result in fig. 4.5 suggests that the experimentally observed effect can to some extent be understood already from the hybridisation effect on the quasi-particle band structure. If we examine the LCAO and LCAOS results in greater detail we find that in the LCAOS calculations the opening of both the K-K and Γ -K quasi-particle gaps results from a downshift of about 60 meV of both the valence K-

and Γ -point states and an upshift of about 40 meV of the conduction K-point states (relative to 0 degrees relative rotation). With the LCAO method we find a downshift of the states at the valence Γ -point of only about half of that found within the LCAOS method. The valence K-point states are close to unaltered and the conduction K-point states have a downshift of about 40 meV, which leads to the small closing of the quasi-particle band gap. The K-point states are purely located on the d -orbitals of the transition metal while the Γ -point have mixed contribution from the d -orbitals of the transition metals and the p -orbitals from the chalcogenide atoms (which is the very reason of the strong interlayer hybridisation at this point in the Brillouin zone). We now hypothesise the origin of the observed artefact. Due to the lattice match of MoS₂ and WS₂ it is possible to describe the bilayer in a 1x1 unit cell without applying strains (at a 0 degrees relative rotation) and where the minimal energy stacking configuration is AB. This stacking configuration has the maximum average interlayer distance between the chalcogenide atoms on the two layers possible. As the two layers are rotated relative to each other the average distance between the chalcogenide atoms on the two layers decreases and consequently a stronger interlayer hybridisation around the Γ -point is expected. This (small) effect is also observed in our twisted bilayer calculations for this system. An increased interlayer orbital interaction would shift a greater part of the electron density located on the chalcogenide atoms into the van der Waals (free space) gap between the two monolayers to take part in the interlayer orbital interaction. In a very simple picture the chalcogenide atoms can be regarded as a quantum well, and as electronic density is shifted into the van der Waals gap the width of the atomic quantum well is increased shifting down the quantum energy levels. While this is a very simple picture it qualitatively describes the observed larger downshift of the Γ -point states with the LCAOS method than with the LCAO. (We mention again that we find a stronger interlayer hybridisation between the chalcogenide atoms within the LCAOS method than in the LCAO method). The fact that the K-point valence states shift down within the LCAOS method and not within the LCAO method could potentially be described by an inter-quasi-particle hybridisation between the K-K and Γ -K transition states for the degenerate case (in the LCAOS calculation) forcing the valence K-point states to shift down with the same magnitude as the Γ -point to keep the two quasi-particle transitions degenerate or "locked". The opposite behaviour of the K-point conduction states is harder to explain in a simple picture. If electronic density from the chalcogenide atoms is shifted into the van der Waals gap between the layers, this leaves more space for the d -orbitals on the transition metals. Intuitively this would result in a downshift of the K-point conduction band state as observed in the LCAO calculation, while the opposite effect is found in the LCAOS calculation. In conclusion, the complex behaviour found in fig. 4.5 can to some extent be understood qualitatively, however more work will have to go into this topic to determine the reasoning of the observed effect. It is however pleasing to see that a better description of the interlayer hybridisation leads to a quantitatively better description of the twist-angle dependent excitation energies.

The next matter we will elaborate on is the effect of the presence of a supporting dielectric substrate in close proximity to the vdWHs. In most experimental setups the

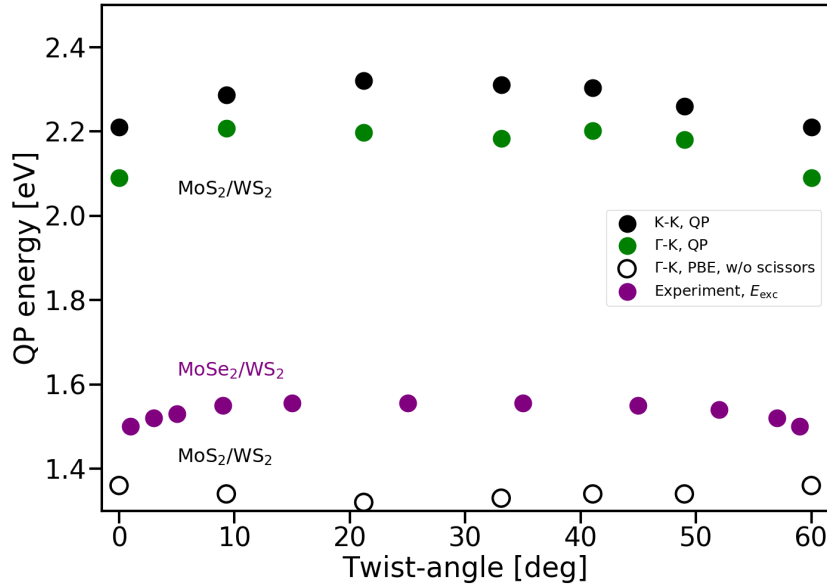


Figure 4.5: Calculated quasi-particle (QP) gap for the two lowest energy transitions in MoS_2/WS_2 hosting degenerate transitions (see main text for description) as a function of the relative twist-angle between the unit cell vectors of the two monolayers in black and green. With full circles are shown G Γ W Γ QEH calculations (including the scissors-operator described in section 4.1 to correctly describe the band line-up). With empty circles are shown the Γ -K transition calculated with LCAO-PBE (*i.e.* without applying the scissors-operator). In purple is shown the twist-angle dependence of the interlayer exciton energy (E_{exc}) for $\text{MoSe}_2/\text{WS}_2$ from experimental measurement [3]. It is stressed the experimentally measured exciton energy is for a different system than the computed values, but is shown to illustrate the qualitative effect found experimentally. This figure is modified from the included paper V.

vdWH is either directly grown on or transferred to a weakly screening supporting substrate such as a hBN or SiO crystal. Conversely, in most *ab-initio* calculations the calculation is performed for the freestanding vdWH due to computational limitations. Most supporting crystals, as the two mentioned above, are wide band gap crystals to avoid interlayer hybridisation effects, affecting the states involved in the lowest energy transitions. This suggests that the influence of the substrate can be modelled by only including the dielectric screening effect of the substrate. As we learned from fig. 3.5 the effect of the dielectric screening on the quasi-particle band gap depends on the (static) polarisability of the monolayers in question and from fig. 3.9 we know that the exciton energies are redshifted when the dielectric environment is enhanced. We can therefore predict that the direct effect on the exciton energies will be a redshift of the exciton energies, the size of which depends on: 1) the nature of the monolayers, 2) the dielectric constant of the substrate, and 3) the thickness of the substrate. Evidently the effect

is system dependent, however to determine the approximate size of these effects we calculate the renormalisation of the two intralayer A excitons in MoS₂/MoSe₂ together with the lowest interlayer exciton as a function of the thickness of a supporting hBN substrate. This is shown in fig. 4.6. For the intralayer exciton binding energies we apply the BSE-QEH method and for the interlayer exciton binding energy we apply the MW-QEH method for calculating the exciton binding energies. In both cases the screening of the quasi-particle band gap is calculated from the G0W0-QEH model. As expected we find a redshift of the intralayer excitons in correspondence with the result in fig. 3.9 having an asymptotic value around 40-50 meV on bulk hBN. The effect is generally smaller than the redshifts in fig. 3.9 due to the lower static polarizability of hBN than of the TMD monolayers. The difference in exciton energy between the freestanding (suspended) vdWH and the vdWH on a substrate approaches the accuracy claimed by many theoretical and experimental groups showing dielectric screening effects from bulk substrates indeed is an important factor to take into account comparing experimental measurements and *ab-initio* calculations. The effect for a given system can be estimated by combining the knowledge from figs. 3.5 and 4.6.

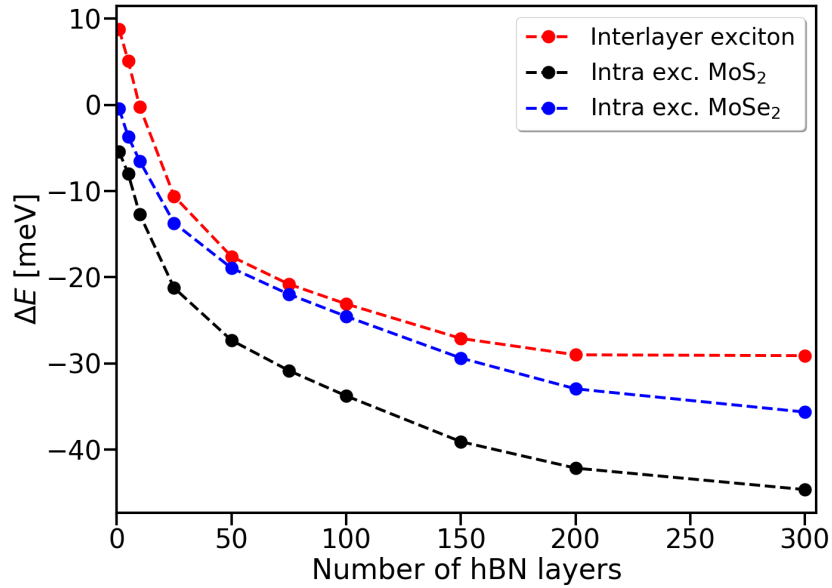


Figure 4.6: Shift of intra- and interlayer exciton energies in bilayer MoS₂/MoSe₂ as a function of the number of supporting hBN layers. The intralayer exciton energies in MoS₂ (black) and MoSe₂ (blue) are calculated with the BSE-QEH model. The shift of the interlayer exciton energy (red) is calculated with the MW-QEH model. The dielectric screening of the quasi-particle energies is calculated with the G0W0-QEH method in all cases. This figure is taken from the included paper V.

We conclude this chapter by commenting on the accuracy of *ab-initio* calculated intra- and interlayer exciton energies in multilayer vdWHs. Specifically we have calculated the

lowest K-K and Γ -K intra- and interlayer exciton energies for all six heterobilayer combinations that can be made from: MoS₂, MoSe₂, WS₂, and WSe₂ and we compare this to a large library of experimental exciton energies from the literature. The detailed comparison and exact exciton energies are presented in paper V and here we will comment more specifically on some details and on the general tendencies. The band line-up and the possible degeneracy of the band edges at the K- and Γ -point are controlled by the nature of the chalcogenide atom. The states at the K-point (for both the valence and conduction bands) are purely located on the *d*-orbital of the metal atom and the states at the valence Γ -point and the conduction K- Γ path is mixed metal *d*- and chalcogenide *p*-orbital. We find that the chalcogenide atom fully determines the lattice constant of all the monolayer structures meaning that MoS₂/WS₂ and MoSe₂/WSe₂ are lattice matched and that the ionisation potential and electron affinity energies are determined by the lattice constant, with little effect of the metal atom. This directly transfers into the valence and conduction states at both the K- and Γ -points are close to degenerate for the lattice matched bilayers and the governing parameters to determine the band line-up can thus be understood from an "indirect straining" effect by the chalcogenide atoms. While the monolayers with sulfur atoms have close to the same ionisation potential for the valence K- and Γ -point states the monolayers with selenide have an ionisation potential for the Γ -point around 300 meV lower than that of the K-point. However, since we find a larger effect of hybridisation at the Γ -point for systems with selenide and a slightly larger (both intra- and interlayer) exciton binding energy for the Γ -K transition for these systems, we find that several bilayers have close to degenerate intra- and interlayer exciton energies, and thus are subject to the effect illustrated in fig. 4.5. In addition to this, the mixed state at the Γ -point complicates the definition of the Γ -K exciton for some bilayers, since what in experiments could possibly be classified as an interlayer exciton has significant intralayer character and thus a larger exciton binding energy. In paper V we thus compare both intra- and interlayer calculated Γ -K excitons to the measured interlayer exciton energy for these systems (the difference in the calculations lies in the calculation of the exciton binding energy). This rationale is supported by the fact that we for systems with degenerate intra- and interlayer Γ -K excitons find a larger interlayer exciton energy than the reported value. The intralayer character of the measured interlayer excitons cannot, however, fully explain the lower measured interlayer exciton energy. For the six TMD bilayers we find similar values for the dielectric screening of the quasi-particle energies, the size of the interlayer hybridisation effects, and a smaller effect of the charge transfer shift of the bands. The dielectric screening of the quasi-particle energies takes values between 60 meV and 110 meV and we find it close to independent of *k*-point index, with slightly larger effect on the conduction bands than the valence bands. For the highest valence- and lowest conduction bands, the interlayer hybridisation effect is closely confined to the valence bands around the Γ -point and the conduction states between the K- Γ point, similar to the findings in the previous section, with an effect up to 190 meV around the Γ -point. This effect is only found for bilayers with close to degenerate states at the Γ -point. Interlayer charge transfer is found to shift the states of the two layers relative to each other up around 70 meV.

Without including the calculated effect of substrate and finite temperature effects, we find 6 out of the 12 calculated intralayer exciton energies to agree within the experimental uncertainty, with the discrepancy for the remaining intralayer excitons ranging between -20 meV to +120 meV. We stress here that only 1/12 of the intralayer exciton energies are calculated to have a lower energy than that of the average of the experimentally measured exciton energies. For the interlayer exciton energies we calculate 2/6 exciton energies within the experimental measurements with the discrepancy for the remaining exciton states ranging between -50 to +250 meV. As discussed in chapter 3, all calculations in this study are carried out at 0 K without electron-phonon coupling effects, since this is not currently implemented in the GPAW code for many-body perturbation theory methods. However, it has previously been shown that by including the Fan and Debye-Waller self-energy corrections accounting for electron-phonon interactions, 0 K phonons and finite temperature effects shifts down the A exciton energy of monolayer MoS₂ of about 90 meV [84] (from 0 K to 300 K). This is encouraging since it shows that including calculated substrate and finite temperature effects, can redshift the exciton energies up to 140 meV. The library of experimentally measured exciton energies, contains measurements carried out in different environments (*i.e.* substrate, temperature, etc). Thus, including substrate and finite temperature effects is not straightforward to benchmark against the big ensemble of experimental data. We include substrate and temperature effects effectively in our calculated energies by renormalising the calculated exciton energies, by a combined factor, $\delta = 140$ meV, that accounts for both substrate and finite temperature effects corresponding to bulk hBN and a temperature of 300 K. In detail, denoting a calculated exciton energy E_{exc} we renormalise this energy to: $(E_{\text{exc}} - \delta/2) \pm \delta/2$. In words, we redshift all calculated exciton energies by half of the total effect of bulk substrate and room temperature effects and apply an uncertainty of $\delta/2$. From this, we find that 11/12 intralayer excitons and 3/6 interlayer excitons agree with experimental observations, with a discrepancy of 20 meV for the remaining intralayer exciton and discrepancies ranging from -50 to +180 meV for the remaining interlayer excitons. This is a significant improvement of the agreement between calculated and experimentally measured energies and we stress only a small improvement of the agreement is found by simply applying an uncertainty of $\delta/2$ without redshifting the calculated energies. We still find a significant overestimation of the calculated interlayer exciton energy for the two lattice matched systems. The above calculations have been performed for the (super)cells corresponding to a 5 degrees and 0 degrees relative twist-angle for the lattice mismatched and lattice matched bilayers respectively. We therefore expect to, on average, calculate a slightly smaller exciton energy for the lattice matched systems, where the effect of degenerate intra- and interlayer exciton shown in fig. 4.5 is present. However, conversely we overestimate the interlayer exciton energy for the two lattice matched systems and the discrepancy thus cannot be explained by the effect of twist-angle. We also note here that previous many-body *ab-initio* calculations for the exciton energies in lattice matched MoS₂/WS₂ results in even greater discrepancies for the interlayer exciton energy of +330 meV [116] and +450 meV [28] respectively. Both calculations are based on G0W0 quasi-particle energies and highlight the importance of correctly calculating the interlayer orbital hybridisation in these structures. In

conclusion, we have shown that even by properly calculating the interlayer orbital hybridisation in vdWHs and including the effect of finite temperature, twist-angle, and substrate effects on the exciton energies, it is not possible to calculate interlayer exciton energies in lattice matched few-layer vdWHs to within the experimental uncertainty.

The fact that the prediction of the interlayer exciton is less accurate is not surprising since this has a strong dependence on the vacuum level band line-up, which the intralayer exciton energies does not depend on. The lower accuracy of the interlayer exciton can thus most likely be described to an inaccuracy of the $G_0W_0(\Gamma)$ description of the electron affinity and ionisation potentials. The two lattice matched bilayers, in which the *ab-initio* many-body calculations significantly overestimates the interlayer exciton energy, are the only two of the considered bilayers that host both degenerate intra- and interlayer exciton energies for two different transitions in the Brillouin zone, which are themselves close to degenerate. One can hypothesise that this can lead to a hybridised bi-exciton state, a 4-particle state, splitting the two interlayer excitons up and down in energy similar to the hybridisation effect found around the valence Γ -point in the lattice matched bilayers. This effect would shift down the interlayer exciton energy and could potentially explain the discrepancy. It is, however, questionable if such a state would have a strong enough oscillator strength to be measured by multiple independent experiments. We note in passing that we find a better description of the interlayer exciton energies based on $G_0W_0\Gamma$ quasi-particle energies than on G_0W_0 quasi-particle energies. Similar to the previous section all $G_0W_0\Gamma$ calculations have been carried out based on PBE eigenvalues and norm-conserving PAW setups.

Finally, it is important to underline the care that must be taken when comparing exciton state energies between computational and experimental results, by commenting on the specific case of $\text{MoS}_2/\text{WSe}_2$. For many years, the lowest lying interlayer exciton energy was from experimental measurements reported to be around 1.55-1.60 eV [33, 22] for an unknown transition in the Brillouin zone, while computational results, including the results in this study, reported values almost 0.5 eV lower for the Γ -K transition. Recently, an experimental study relieved this discrepancy by conducting a thorough study on the nature of the different interlayer excitons in Mo_2/WSe_2 [63]. In this it was shown, that there is in fact an interlayer exciton with an energy around 1.55 eV, however this exciton arise from the K-K transition. The study also proved the existence of an interlayer exciton with an energy around 1.05 eV, for the Γ -K transition. This example excellently illustrates the care that must be taken when comparing computational results to experimental data.

CHAPTER 5

The Computational 2D Materials Database

In the remaining two chapters of this thesis we will change gears and look more into materials discovery and applications. In this chapter the computational 2D materials database (C2DB) will be presented which is the result of a big joint development in the research group and which has been a significant part of this thesis (presented in paper VI). Chapter 5.1 will briefly explain the overall ideas and governing workflow of the developed database and in chapter 5.2 we will see an example of how the C2DB can be used to aid the discovery of new materials design and applications by considering photovoltaic applications of 2D materials, which have received vast interest in recent years [67, 16, 70]. Chapter 6 will look more into two new classes of materials studied in this thesis and their (possible) applications. All materials and calculated properties are freely accessible at: <https://cmr.fysik.dtu.dk/c2db/c2db.html>.

5.1 The C2DB

Currently there exist a range of open materials databases. This non-exhaustive list includes the Open Quantum Materials Databases (OQDM) [106], the Automatic Flow for Materials Discovery [25] (AFLOW), Novel Materials Discovery [1] (NOMAD), and the Inorganic Crystal Structure Database [2] (ICSD). While these databases contain millions of materials in 0, 1, 2, and 3 dimensions they are characterised by presenting basic materials properties determined experimentally and/or materials properties calculated mostly within the DFT formalism. This makes such databases ideal for comparison of calculated properties between codes, it gives a range of commonly known benchmark systems, and allows statistical and machine learning algorithms to be applied to determine correlations between materials properties [52, 109, 40, 30, 91]. To supplement these databases the C2DB is based on consistency and accuracy. The goal is to supply a database of materials properties calculated with a consistent use of convergence parameters and with many-body methods such as the G0W0 and BSE methods for obtaining the most accurate materials properties possible computationally. This is done by developing a well-defined workflow which is applied to all materials in the database. At the time of publication the database contained close to 1500 2D materials, which shows that a significant amount of computational power has been devoted to this project. At the time of writing the number has grown to around 2500. In this context it is important

to mention a relatively recent study by Mounet et al. [86], which also presents calculated materials properties for 2D materials. A main difference between the C2DB and the work by Mounet et al. is that while the materials in the C2DB are constructed by substituting elements of known synthesised 2D materials, the materials in Mounet et al. are found by determining possible exfoliable monolayers of layered bulk materials (known as the top-down approach). In the following we will present the main parts of the C2DB and in the next section we will see a direct application of the data in the C2DB to predict new 2D materials as efficient light absorbers for photovoltaic devices.

The main result of the C2DB is the development of a robust workflow to calculate the thermodynamic and dynamic stability together with electronic, magnetic, optical properties, and other materials properties of 2D materials. The workflow is presented in fig. 5.1. In general, the workflow takes an atomic structure (in this case a 2D material) as input and generates a set of atomic properties as output. While the computational details and full list of results can be found in the paper we will here go through some of the main characteristics of the C2DB, give a brief overview of the initialisation of the workflow, and give an example of its use related to the results obtained in chapters 3 and 4 about electronic and optical properties.

To generate the database of computationally calculated properties of 2D materials, three ingredients are needed: a set of atomic structures, a robust workflow, and a set of parameters to be applied in each step in the workflow (*i.e.* stability assessment, convergence parameters etc.). The atomic structures are constructed by starting from the atomic structures of experimentally synthesised materials. The symmetry groups and stoichiometry of a structure defines what we denote as prototypes. At the time of publication, from a set of 55 experimentally known synthesised 2D materials, this generated 32 different prototypes. Within each prototype new candidate materials are then generated by combinatorial lattice decoration *i.e.* substituting each element in the structure with other elements with similar electronic configuration and/or properties. This initially generated a set of over 1900 materials that was run through the workflow in the first version of the database. As mentioned above, one of the main strengths of the C2DB is the accuracy and reliability of the presented data. The first step of the workflow is therefore to assess the stability of the 2D materials. This is done based on two measures: the thermodynamic and dynamic stability. The thermodynamic stability is determined by calculating the energy above convex hull of the material where the convex hull is constructed from all materials in the OQMD database [106]. This ensures that not only the heat of formation favours a crystal lattice, but also that no other competing phase is energetically more favourable. Secondly the dynamic stability, *i.e.* the materials urge to distort into a different structure with another space group, is calculated by calculating the phonon eigenvalues at the Γ -point. The parameters to assess the stability are determined by benchmarking the calculated stability measures for the experimentally known synthesised 2D materials. At the time of publication this generated close to 200 *new* candidate 2D materials that were determined to be highly stable and therefore possibly synthesisable. The full workflow has been applied for these materials including the majority of all considered materials, which are predicted to be

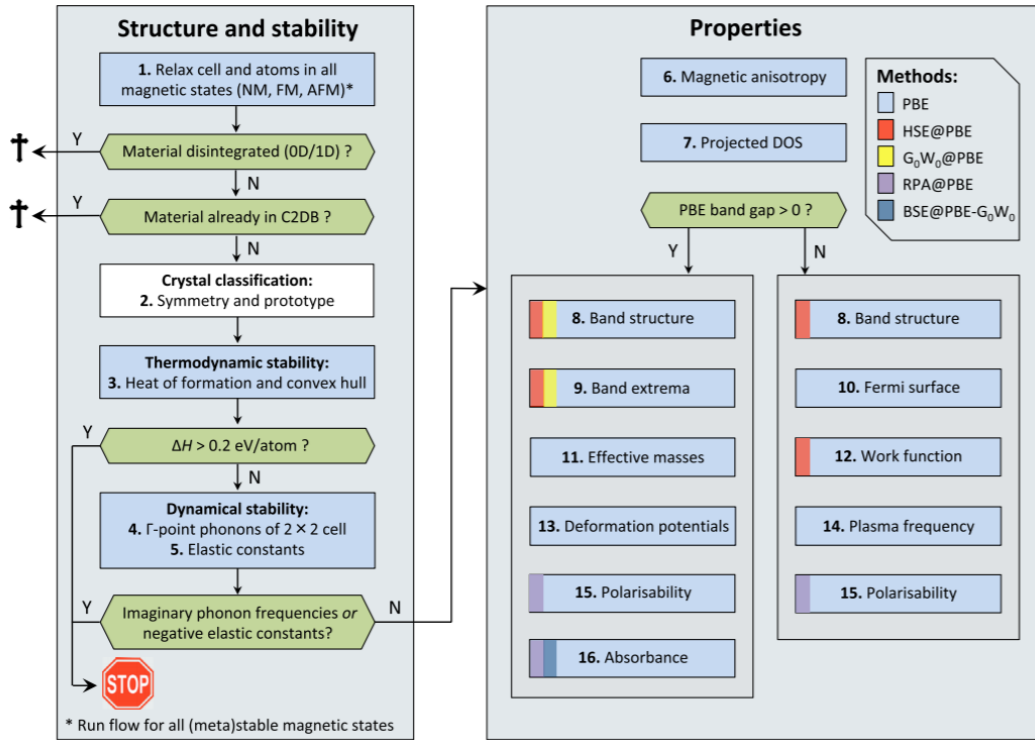


Figure 5.1: Workflow for the Computational 2D Materials Database. This figure is taken from the included paper VI.

possibly stable. If a material is determined to be unstable the workflow is terminated after the stability assessment.

The remaining part of the workflow calculates a variety of properties (as can be deduced from fig. 5.1 and the online webpage) including PBE and G0W0 band structures and BSE absorption spectra which were discussed in the previous chapters. To give an example of the application of the C2DB we will here briefly discuss one of the main results of the C2DB which relates to the methods and results from chapter 3 and chapter 4. In fig. 5.2 (left) is shown the G0W0 quasi-particle band gap plotted against the electronic band gap calculated at the level of DFT with a set of exchange-correlation functionals: The PBE, the HSE, and the GLLBSC [71] functional. This is shown for all materials in the C2DB that are semiconducting, predicted to be stable, and contain less than 7 atoms in the unit cell. Here we see illustrated what we have continuously stated throughout chapters 3 and 4, and was argued as the main reason for applying many-body methods such as G0W0 and BSE: the DFT and hybrid methods in general underestimates the electronic band gap. This is especially pronounced for the PBE functional, which on average almost underestimates the electronic band gap by a factor of 2. The hybrid functional, HSE, significantly improves upon this, but still underestimates the band gap by almost 30% on average. Band gaps calculated with GLLBSC on aver-

age get values very close to the G0W0 quasi-particle band gap, however it is important to specify that there is still a considerable standard deviation involved with this description. The GLLBSC method invokes the derivative discontinuity to correct the size of the electronic band gap as discussed in chapter 2 and it is therefore not surprising that this on average provides a good description of the electronic band gap. In fig. 5.2 (right) we see that the center of the electronic band gap (with respect to the vacuum energy) is poorly described with especially the GLLBSC functional. This means that While the GLLBSC functional gives a good description of the electronic band gap it is not reliable to use this method in combination with for instance the QEH model or simply applying the Anderson model for calculating band line-ups and electronic properties of vdWHs. On the other hand, the PBE functional gives a good description of the band gap center. Interestingly, this means that an adequate, and computationally feasible, description of the band line-up of a vdWH can be obtained by applying the PBE band gap center (and band edges) symmetrically opened to the GLLBSC electronic band gap. This idea is explored in appendix E, where it is shown to significantly improve upon the description of the position of the band edges relative to the vacuum energy compared to G0W0 ionisation potentials and electron affinity energies. This can potentially be used in combination with the QEH screening and hybridisation flowchart presented in chapter 4, to achieve accurate band structure energies for vdWHs.

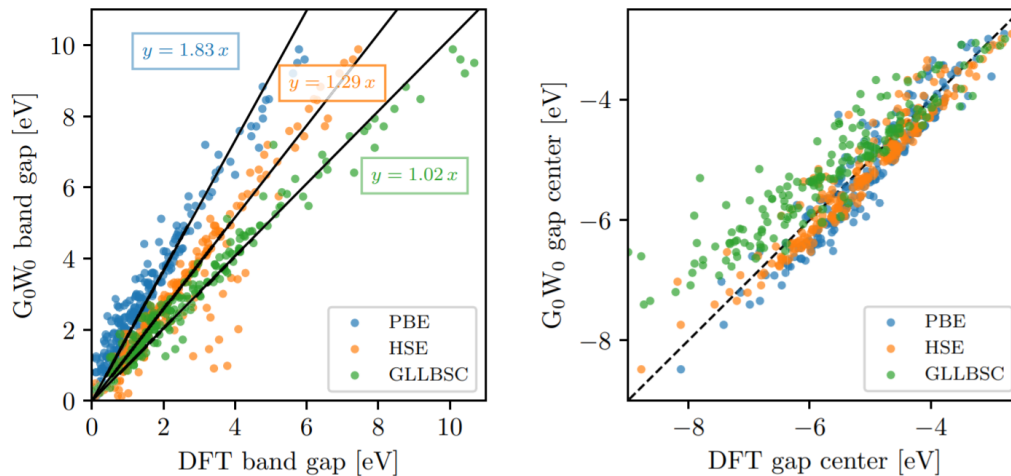


Figure 5.2: Left: electronic band gap calculated with the G0W0 approximation and at the DFT level with three different exchange-correlation functionals: PBE, HSE, and GLLBSC. Right: comparison of the band gap center relative to the vacuum energy between the same methods as the plot to the right. This figure is taken from the included paper VI.

5.2 Photovoltaic Potential of Novel 2D Semiconductors

In this section we will show an example of how the data in the C2DB can effectively be used to predict new materials properties and present a scheme to predict the photovoltaic potential of the 2D materials in the C2DB. It is important to stress that while the work on this has taken up a significant amount of time during the study, the results and manuscript are not ready for manuscript submission and have therefore not been included in this thesis. We will therefore not discuss the results of this study in this section, but merely go through the main ideas and the governing theory and principles for the photovoltaic potential of a 2D material.

Because of the strong-light matter interaction in 2D materials it is rather obvious, and not new, to explore the optical properties of 2D materials in terms of solar cell applications. However, previous studies have been hindered by the significant computational costs of accurately calculating the absorbance *ab-intio* of 2D materials due to the importance of including many-body effects. Consequently previous large-scale studies have relied on a simple picture, where the absorbance is assumed to be a step function above the electronic band gap as seen in for instance [77]. It is needless to say that this poor approximation leads to non-trustworthy and suspicious results. With the large number of BSE and RPA absorption spectra calculated and accessible in the C2DB it is now possible to carry out an accurate large-scale study of the photovoltaic potential of a large number of 2D materials and utilise the stability prediction in C2DB to estimate the likelihood that the most interesting 2D materials can be experimentally synthesised. This study can pinpoint experimentalists to a short list of potential superior atomically thin solar cells.

We will here outline the method to assess the photovoltaic potential of an atomically thin material as presented by Bernardi et al. [7] and see that this is quantified by the Power Conversion Efficiency (PCE). To generate power, a solar cell relies on the photo-excitation of electrons, and subsequently extracting the excited electrons (and left behind holes) at different potentials. This generates a power given by the product of the current generated by the electrons and holes and the potential difference between the electron and hole states. The generated electron-hole current is directly related to the convolution of the absorbance of the 2D material ($Abs(\omega)$) with the photon-flux of the incident light ($J_{ph}(\omega)$):

$$J_{abs} = e \int_0^{\infty} Abs(\omega) J_{ph}(\omega) d\omega. \quad (5.1)$$

After excitation, the electrons and holes have to be extracted from the 2D material in a transport process that is generally faster than the characteristic electron-hole recombination time. The loss of electron-hole current due to recombination effects is known as the Internal Quantum Efficiency (IQE) and evidently the short-circuit voltage is given

by:

$$J_{\text{sc}} = J_{\text{abs}} \times IQE. \quad (5.2)$$

While the IQE can differ significantly from system to system it usually takes values between 0.60-0.80. The open-circuit voltage, *i.e.* the difference in potential between the electron and hole states, is in equilibrium given by the lowest excitation energy. For a 2D material this is given by the quasi-particle band gap minus the exciton binding energy: $eV_{\text{oc}} = E_{\text{gap}}^{\text{elec}} - E_{\text{B}}$, see for instance fig. 5.3 (left) where the separation of a photo-generated exciton to an ideal electron- and hole-acceptor is shown. This is true in equilibrium, however the excited state is inherently a non-equilibrium state. Since the electron and hole distribution under illumination differs from the Fermi-Dirac distribution, the valence and conduction bands are no longer in thermal equilibrium with each other and they no longer share the same Fermi level. This results in a reduction of the open-circuit voltage (formally known as the difference between the quasi-Fermi-levels) and has been shown to be of the order of 0.2-0.3 eV. We will label the reduction in open-circuit voltage ΔV_{QFL} , due to the difference in quasi-Fermi-levels between the conduction and valence bands. Finally there are losses in connection with especially the contact at the interface between the 2D material and the electron/hole-acceptors, but also general Ohmic losses related to the finite conductance of the 2D material and the acceptor material. Such Ohmic resistances are very system specific and it is common to model this by a constant "fill factor" (FF). Given the large number of absorption spectra in the C2DB (both at the level of the RPA and the BSE), we now have all quantities that go into the calculation of the generated power from the photon absorption. To relate the calculated powers to literature it is standard to normalise the calculated power to the total integrated incident power (P_{tot}):

$$P_{\text{tot}} = \int_0^{\infty} \hbar\omega J_{\text{ph}}(\omega) d\omega, \quad (5.3)$$

and from this define the Power Conversion Efficiency of the solar cell as:

$$\text{PCE} = \frac{FF \times IQE \times (V_{\text{oc}} - \Delta V_{\text{QFL}}) \times J_{\text{abs}}}{P_{\text{tot}}}. \quad (5.4)$$

Some of the most well-known solar cells such as GaAs and Si reach PCE values close to 30% and 20 % respectively, while lower values around 1 % are found in previous accurate calculations of the PCE of 2D materials [7]. However, it is important to bear in mind that while the 2D materials are atomically thin the above stated PCE values for GaAs and Si are for μm thick bulk crystals and that the PCE *per* unit thickness is orders of magnitude larger for 2D materials than for GaAs and Si. This makes 2D materials interesting for thin-film solar cell applications where they outperform state-of-the-art bulk solar cells.

The highest possible achievable PCE is limited by the Shockley-Queisser limit (SQL) which is an open-circuit voltage dependent theoretical upper limit for the maximum possible PCE taking all losses into account [112]. The maximum possible PCE

is close to 33 % for a single p-n junction at around 1.1 eV, *i.e.* close to the PCE of GaAs. This underlines the larger potential for 2D materials for atomically thin solar cell application than for conventional bulk solar cells. It is possible to even overcome the SQL with 2D heterointerfaces, so-called tandem devices. The idea is sketched in fig. 5.3 (right) where two 2D materials are combined into a vdWH. The advantage of this setup is that, if the two 2D materials have different optical band gaps it is possible to efficiently absorb light at a broader frequency range by combining a small band gap semiconductor with a large band gap semiconductor. On the other hand the open-circuit voltage for such systems will in general be lower due to the type-II band line-up of this system. Since the C2DB also includes G0W0 electron ionisation and electron affinity values for most materials where the BSE absorption spectrum is calculated, it is possible to simply obtain a good guess at the band line-up using the Anderson rule [5]. A more accurate guess could also be obtained by making a qualified guess of the dielectric screening of the band edges from the knowledge of the RPA static polarisability of the two layers, which however still does not account for interlayer hybridisation effects.

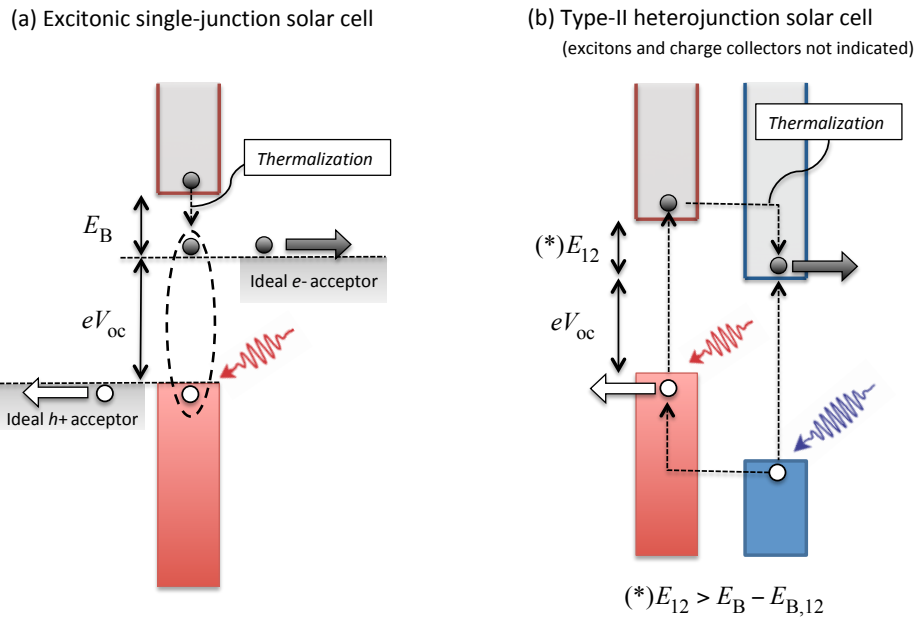


Figure 5.3: Left: illustration of an excitonic photon absorber with ideal electron- and hole acceptors. The open-circuit voltage (V_{oc}) is defined as the electronic band gap minus the exciton binding energy. Right: illustration of bilayer tandem photon-absorber setup with a type-II band line-up in which the open-circuit voltage is defined as the interlayer band gap. * the energy requirement for the sketched tandem solar cell to work efficiently.

While the discussion has been based on excitonic solar cells, it is also possible to utilise the vast number of RPA absorption spectra for materials where the BSE absorption spectra have not been calculated. Since the RPA absorption spectra has been

calculated based on the PBE Kohn-Sham electronic band gap, and since the GLLBSC electronic band gap is calculated for all semiconductors, with the knowledge from fig. 5.2 it would be straightforward to shift the RPA absorption spectra to the GLLBSC band gap and estimate the exciton binding energy from the 2D exciton hydrogen model including environmental screening explained in section 3.8, by estimating κ through the static polarisability of the monolayers.

Finally it is worth commenting on the dissociation of the electron-hole pair for generating the electron-hole current. In principle the electron and hole dissociability and therefore the charge separability can be estimated from the electron and hole effective masses calculated in the C2DB. However, while the effective electron masses for a 2D material is only defined in-plane, the separation of the electron-hole pair is taking place in the out-of-plane direction. It is therefore immediately not obvious how to obtain a valid estimate of the electron-hole dissociation to the electron and hole acceptors. Furthermore, the efficiency of the solar cell will also be affected by second order recombination effects, such as Auger recombinations[64]. These effects will slightly lower the generated efficiency and will have to be included in a more detailed description for the most promising solar cell candidates.

CHAPTER 6

2D Janus Monolayers and Self-Intercalated Bilayers

Until now we have mainly studied the the electronic and optical properties of 2D materials and vdWHs, with particular interest in investigating the physical mechanisms of manipulation of excited states via dielectric screening and interlayer orbital hybridisation effects. In this chapter we will take a step back and study how the electronic and optical properties can be tuned in a more general perspective with a broader range of applications in mind. The first part of the chapter will be devoted to a detailed study that has been carried out of a new class of 2D monolayers, 2D *Janus structures*, which to a large degree resemble the well-known class of 2D TMDs monolayers, however as we will see, the lack of out-of-plane mirror symmetry in the Janus class monolayers, leads to interesting intrinsic properties, that can be used to manipulate electronic and optical properties of vdWHs and 2D/bulk interfaces. In the second part of the chapter we will turn our attention to a new class of materials, the self-intercalated 2D bilayers, which opens up new pathways in low-dimensional materials science and offers new methods for manipulation of the materials properties of vdWHs. We will show that the self-intercalation process for a range of bilayer hosts is thermodynamically stable and leads to the possibility of on/off-switching of a ferromagnetic phase and will discuss the prospects of this new paradigm of vdWHs. In this chapter we will mainly discuss how this affects the potential for the future of engineering the properties of vdWHs, and the main experimental and computational details of this study can be found in paper X.

The results of this chapter on 2D Janus structures can be found in papers VII, VIII, and IX. The first two sections will introduce the intrinsic out-of-plane dipole moment in 2D Janus monolayers and outline the results of paper VII and IX which cover the physics of 2D Janus monolayers at semiconductor-semiconductor and semiconductor-metal interfaces. We will discuss some of the interesting features in a different light than in the publications, especially the nature of the intrinsic dipole and the effect of the environment on the magnitude of the intrinsic dipole moment. Section 6.3 outlines the systematic screening study presented in paper VIII, where we will discuss in greater detail the origin of the intrinsic dipole and the Rashba splitting in 2D Janus monolayers.

6.1 Intrinsic Out-of-Plane Dipole Moment of 2D Janus Monolayers

The name *Janus* structure has its origin from the Roman god Janus, who has a two-faced head: one face looking to the past and one face looking to the future. While the two faces look very much alike, small details differ making them inherently different. This is also very true for the structures we are about to study. A 2D Janus monolayer is in general terms a 2D monolayer that lacks mirror symmetry in the out-of-plane direction. Examples of such structures are already known and well-studied, one example is phosphorene, however here we will study a new class the Janus monolayers, namely that of TMD and pnictogen based Janus structures (simply to be denoted 2D Janus monolayers from now). As illustrated in fig. 6.1 where MoSSe is shown as example, 2D Janus monolayers are the well-known 2D TMD monolayers where all chalcogenide (and in practice also halogen) atoms on one side of the monolayer are substituted by a different chalcogenide (or halogen) atom. Similar to the TMD class monolayers are denoted MX_2 structures we will denote Janus class 2D materials by MXY . We stress that this includes combinations of halogen atoms on one side and chalcogenide atoms on the other side and transition metals or pnictogens as the metal atom. For the 2D monolayer shown in fig. 6.1, the monolayer consists of molybdenum atoms in the center sandwiched between sulfur atoms on one side and selenium atoms on the other side. One remarkable aspect about these 2D Janus monolayers are that both MoSSe [79, 128] (H-phase) and BiTeI [38] (T-phase) have been experimentally synthesised and therefore shown to exist as a stable monolayer. This fact encourages us to study this new class of 2D Janus monolayers in greater detail.

As we will see, just like MoS_2 and MoSe_2 share a great resemblance in terms of both electronic and optical properties, so do MoSSe with both of these monolayers, but yet the lack of out-of-plane mirror symmetry leads to some fascinating properties. One is illustrated in fig. 6.2 (left) where the in-plane averaged electrostatic potential is shown for MoSSe in the out-of-plane direction. A unique definition of the vacuum level energy reference is theoretically possible in 2D, in contrary to bulk structures,

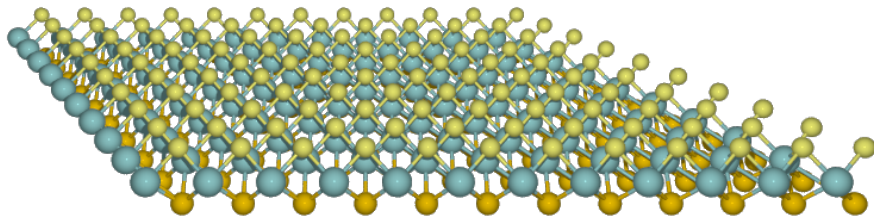


Figure 6.1: Atomic plot of one of the first experimentally synthesised 2D monolayer Janus structures: monolayer MoSSe .

due to the non-periodicity in the out-of-plane direction in 2D, and a finite change in electrostatic potential across the layer is therefore well-defined. Because of the difference in electronegativity between the sulfur and selenium atoms, there is a charge transfer across the monolayer (compared to the neutral charge of the free atoms), which sets up an intrinsic dipole moment of the 2D monolayer in the out-of-plane direction. This leads to the difference in electrostatic potential across the monolayer shown in fig. 6.2 of about $\Delta\Phi = 0.75$ eV. At this point we hypothesise that the difference in reference potential energy on either side could potentially be used to control and/or manipulate the electronic properties of other structures on either side of the Janus monolayer with respect to each other. An example of how this could look is hypothesised in fig. 6.2 (right) where an example of how the band line-up of a stack of 4 layers of the same Janus 2D monolayer is illustrated. Because of the shift of electrostatic potential energy across each Janus monolayer the band extrema could possibly have a staggered band line-up with a spontaneous dissociation of excitons. In the following we will show that this is indeed the case.

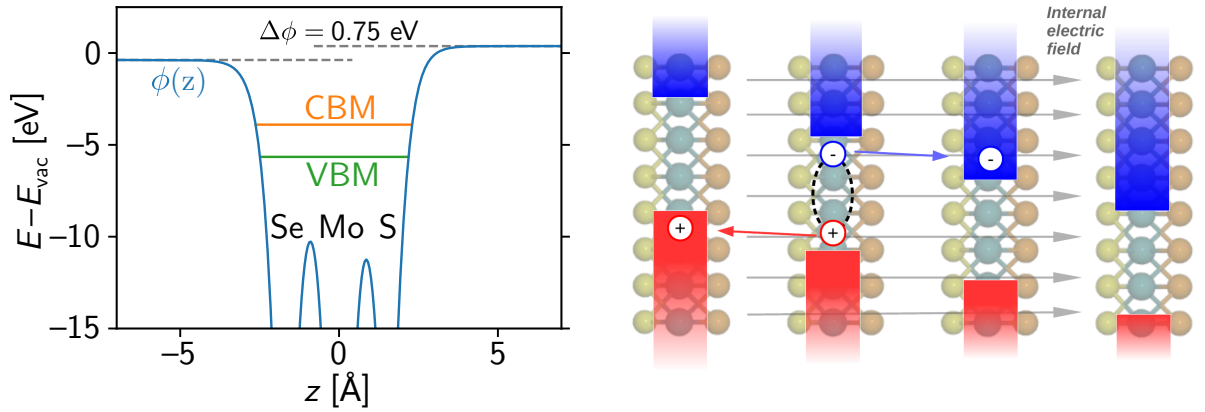


Figure 6.2: Left: in-plane averaged electrostatic potential of 2D H-phase monolayer MoSSe shown in the out-of-plane direction (variable z). The position of the conduction band minimum (CBM) and valence band maximum (VBM) relative to the vacuum potential energy is shown. Right: sketch of band alignment of a multilayer Janus structure. The energetically favourable exciton dissociation is shown as discussed in relation to fig. 6.3. The figures are taken from included papers VII and IX.

To study this hypothesis we calculate the electronic band structure for monolayer MoSSe and stacks of MoSSe of up to 6 layers of MoSSe. We do this at the level of DFT (with the PBE functional) since it is well-known that the qualitative features are well described by DFT for the TMD structures. By calculation we find, as shown in the band structure plot in paper VII by studying the effect on the K-point (where we know the states have little-to-no influence of the interlayer orbital hybridisation), that the otherwise degenerate states at the K-point, are shifted apart with an energy close to $\Delta\Phi$. This is true up to 3 layers after which the band extrema are pinned to the Fermi surface and the vdWH enters a metallic state. This result confirms that the intrinsic out-

of-plane dipole moment remains rather unaltered in (at least semiconducting) vdWHs and indeed can be used to manipulate the electronic properties on either side of the Janus structures relative to each other as depicted in fig. 6.2.

When the MoSSe multilayer structure has a thickness of more than 3 layers it transits from a semiconducting to metallic regime. This transition depends on the vacuum level shift across one monolayer, $\Delta\Phi$, and the band gap, E_G , of one freestanding monolayer. The splitting of the bands in neighbouring layers corresponds to $\Delta\Phi$ as long as the stack remains in the semiconducting state, with only a minor cancellation of the dipole moment. We will return to this small cancellation of the intrinsic dipole upon stacking later. Therefore, for any Janus structure, the number of layers for the semiconductor to metal transition can be estimated as:

$$N_{\text{IM}} = \frac{E_G}{\Delta\Phi} + 1. \quad (6.1)$$

With the PBE band gap of 1.54 eV this gives $N = 3$ layers and with the calculated G0W0 band gap of 2.33 eV this yields $N = 4$ layers. For any van der Waals homostructure this onset can be estimated from eq. 6.1. We now turn our attention to the metallic regime, *i.e.* for the case of multilayer MoSSe for $N \geq 4$ layers. After the onset of the metallic state, the additional dipole moment added when more layers are stacked, will be counteracted by a second oppositely directed dipole moment setup by a charge transfer from the bottom to the top layer (or vice versa). This oppositely directed dipole have the effect that the change in electrostatic potential across the multilayer structure remains constant independent of the number of layers. The metallic multilayer structure with build-up charge densities at the bottom and top layer can be modelled as a capacitor system with the internal MoSSe layers giving an effective dielectric environment. Requiring that the build-up charge densities has to counteract the intrinsic dipole moment from the MoSSe layers (after the onset of the metallic state), this can from standard electrostatics easily be shown to be given by:

$$\sigma(N) = \frac{\epsilon_{\perp} \Delta\Phi}{d} \left(1 - \frac{N_{\text{IM}}}{N} \right), \quad (6.2)$$

where σ is the charge density at the top and bottom layers, ϵ_{\perp} is approximated as the bulk dielectric constant of bulk MoSSe (in the out-of-plane direction) which we calculated within the RPA, d is the MoSSe interlayer distance, and N is the number of layers after the onset of the metallic state. The highest charge density is achieved for $N \rightarrow \infty$ for which we estimate: $\sigma(N \rightarrow \infty) = 2.3 \times 10^{13}$ e/cm². The lowest value is found for $N = 5$ for which we get $\sigma(N = 5) = 5 \times 10^{12}$ e/cm². This makes metallic multilayer Janus structures intrinsic pn-junctions, where the charge densities can effectively be controlled solely by the number of layers without any external bias voltage, applied strain etc.

After having studied the basic electronic properties relating to the intrinsic dipole moment of Janus structures, we now return to study the exciton dissociation hypothesised in fig. 6.2. For this to happen, two aspects have to be fulfilled: first, it has to

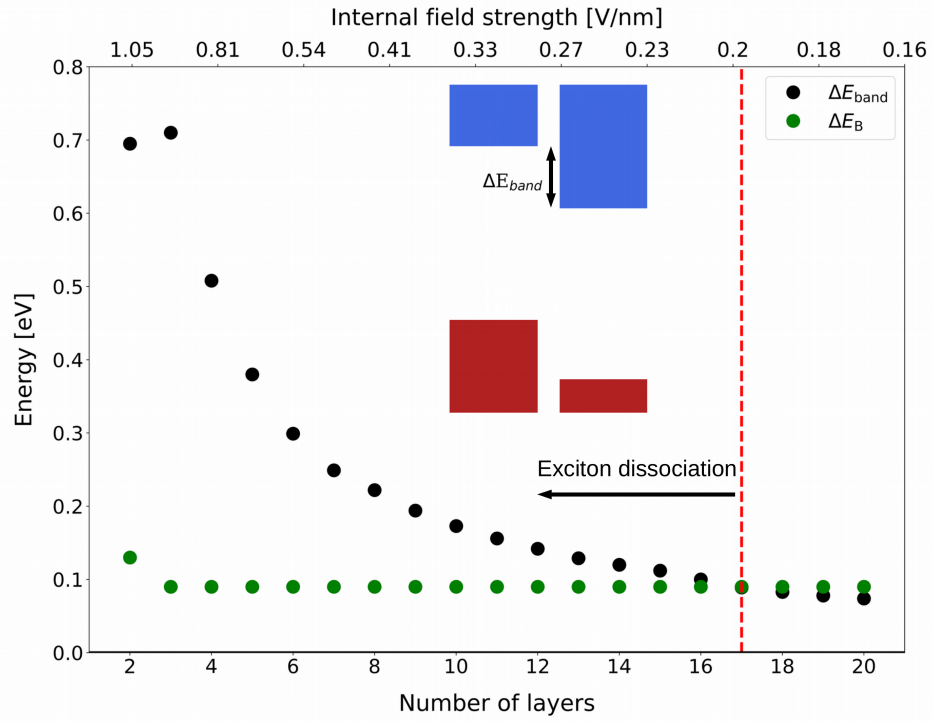


Figure 6.3: Band offset between the two middle layers of multilayer MoSSe (black, ΔE_{band}) and difference in intra- and interlayer exciton binding energy (green, ΔE_{B}) as a function of the number of layers. On the top x -axis is shown the calculated intrinsic electric field strength. The inset shows the definition of ΔE_{band} and the red dashed line shows that exciton dissociation is possible for less than around 17 layers for multilayer MoSSe. This figure is taken from included paper VII.

be energetically favourable for the electrons and holes to dissociate to the edge-layers of the multilayer structures. Second, the dissociation rate of excitons in the multilayer structure should be higher than the electron-hole recombination rate. As we have seen in our study of exciton binding energies in chapter 3 and 4, intralayer excitons generally have a higher exciton binding energy than interlayer excitons, due to the spatially larger distance between the electron and hole for the latter. This means, if the VBM and CBM are degenerate for neighbouring layers, such an exciton dissociation is not energetically favourable. However, as illustrated in fig. 6.2 (right), a staggered band line-up is achieved in multilayer Janus homostructures. Since $\Delta\Phi$ is much larger than the difference between the intra- and interlayer binding energies (this difference typically being around 0.1 eV for TMDs), exciton dissociation is energetically favourable even for bilayer MoSSe. As more layers are added to the MoSSe multilayer structure the band offset (ΔE_{band}) between the CBMs (and VBMs) for neighbouring layers becomes smaller, which is evident by calculating the band structure of the multilayer system. To evaluate up to how many layers in multilayer MoSSe exciton dissociation is energetically

favourable, we calculate the band offset and the intra- and interlayer exciton binding energies for multilayer MoSSe. The band offset can be evaluated directly from the DFT band structure calculations. The intra- and interlayer exciton binding energies are calculated by solving a Mott-Wannier equation where the screened electron-hole interaction is calculated by the QEH method (eq. 3.64). The results are shown in fig. 6.3 where we show the band offset (black) and the difference in intra- and interlayer exciton binding energy (green, ΔE_B) for the middle layer for multilayer MoSSe. While ΔE_B stays close to constant independent of the number of layers ΔE_{band} decreases rapidly. From this we can conclude that for multilayer MoSSe exciton dissociation is energetically favourable up to around 17 layers. In general, exciton recombination rates for excitons in TMD like structures are well below values around 10^{12} s^{-1} . In fig. 6.3 we show the calculated electric field strength in the multilayer structures (top x -label) in the out-of-plane direction, which is directly related to the electron and hole dissociation rate. We find that in the exciton dissociation regime the internal electric field strength exceeds 0.2 V/nm . According to previous work for bulk MoS_2 and MoSe_2 , the out-of-plane dissociation rate in these structures exceeds 10^{13} s^{-1} already at an internal field strength of 0.1 V/nm [93]. These two arguments combined show that exciton dissociation is energetically favourable and takes place at time scales much faster than exciton recombination time scales.

6.2 Manipulation of Interface Band Line-Up and Schottky-Barriers

After an introduction of the intrinsic dipole moment of mono- and multilayer MoSSe, we will now extend the scope and consider possible applications of 2D Janus monolayers by studying the effect at semiconductor-metal heterointerfaces. At a semiconductor-metal interface, the Fermi level of the metal and the semiconductor will have to align to reach an equilibrium state. This will force the valence and conduction bands of the semiconductor to bend in the interface region, creating an extra tunneling barrier for electron transport across the interface known as the Schottky barrier height (SBH). The SBH is a well-known and well-studied problem in relation to many applications such as tunneling diodes and transistors, since it provides an additional electrical resistance in the internal electrical circuits. Several methods for reducing the effect of band bending are used, for instance, applying a bias voltage or insertion of single atoms to reduce the overall SBH. While the line-up of the VBM and CBM with respect to the common Fermi level at the interface, is a complicated process involving charge transfer and interface dipoles, the intrinsic properties of the Janus monolayers open new possibilities to alter the relative energy between the band edges of the semiconductor and the position of the Fermi level in the metal. We will show it is possible to change the reference vacuum energy of the semiconductor and the metal relative to each other at the interface, by insertion of 2D Janus monolayers, and thus to manipulate the SBH at semiconductor-metal interfaces.

It is important to note that the SBH is not uniquely defined [58]. Here we will define the SBH as the energy difference between the position of the Fermi level and the energy of the CBM of the semiconducting monolayer within a DFT description. We stress, as discussed below, that the SBH does not define the actual tunneling barrier for electron (and hole) transport, but gives the energy gain *after* electron (or hole) transport in equilibrium and thus affects the tunneling rate.

The 2D Janus monolayers are possible candidates to achieve this due to their atomically thin nature and natural shift of the electrostatic potential energy over sub-nm distances. The desired reduction of the distance between the CBM of the semiconductor and the Fermi level at the interface can be achieved by inserting a 2D Janus monolayer between the semiconductor and the metal. To prove this, we set out to study the SBH at two interfaces: at the interface between 2D bilayer H-MoS₂/T-MoS₂ (in the H- and T-phase respectively) and at the interface between 2D monolayer H-MoS₂ and a bulk gold (111) surface. All calculations are performed with the PBE functional due to the large number of atoms required to represent the interfaces. If we first consider 2D bilayer H-MoS₂/T-MoS₂ we calculate the band structure of bilayer H-MoS₂/T-MoS₂ with and without MoSSe inserted between the two layers. In both calculations, H-MoS₂ and T-MoS₂ are strained to match the lattice constant of H-MoSSe. In fig. 6.4 (left) the calculated band structure of bilayer H-MoS₂/T-MoS₂ is illustrated with the orbital weight of each state projected on to the H-MoS₂ (T-MoS₂) layer is shown in blue (red). We find that the CBM located on H-MoS₂ is located about 0.7 eV above the common Fermi level. To compare, in figure 6.4 (right) the calculated band structure with H-MoSSe sandwiched between the two layers is shown, where the orbital weight of each state projected onto H-MoSSe is shown in black. As shown above, the shift in electrostatic potential energy across freestanding monolayer H-MoSSe is about 0.76 eV. This is therefore the maximum reduction of the SBH we can expect. After insertion of the Janus monolayer the CBM on H-MoS₂ is pinned at the Fermi surface showing that little to no cancellation of the intrinsic dipole moment of H-MoSSe takes place. We conclude it is therefore possible to use 2D Janus structures as a reliable accurate tuning of SBH at 2D semiconductor-metal interfaces.

The fact that the intrinsic out-of-plane dipole moment of 2D Janus monolayers remains close to unchanged upon insertion in (metallic) vdWHs is promising, however due to the interlayer distances being characterised by van der Waals bonds, questions can be asked on how this fact transfers to interfaces between 2D semiconductors and bulk metallic systems such as Au or Pd, where interface interactions are characterised by covalent bonds [35]. As shown in greater detail in paper IX we show that the intrinsic out-of-plane dipole is indeed to a large extent unaltered at such bulk metal heterointerfaces by studying a 5x5 supercell of H-MoS₂ at an Au (111) surface, where the Au (111) surface is modelled by 5 layers of Au atoms. Without a Janus monolayer the SBH is found to be 0.65 eV. The insertion of H-MoSSe results in a reduction of the SBH of around 0.6 eV and the intrinsic out-of-plane dipole moment of H-MoSSe is reduced about 20 % upon insertion at the interface. Due to the well-known short range and complex nature of the interface between H-MoS₂ and bulk Au we take this reduction as an approximate

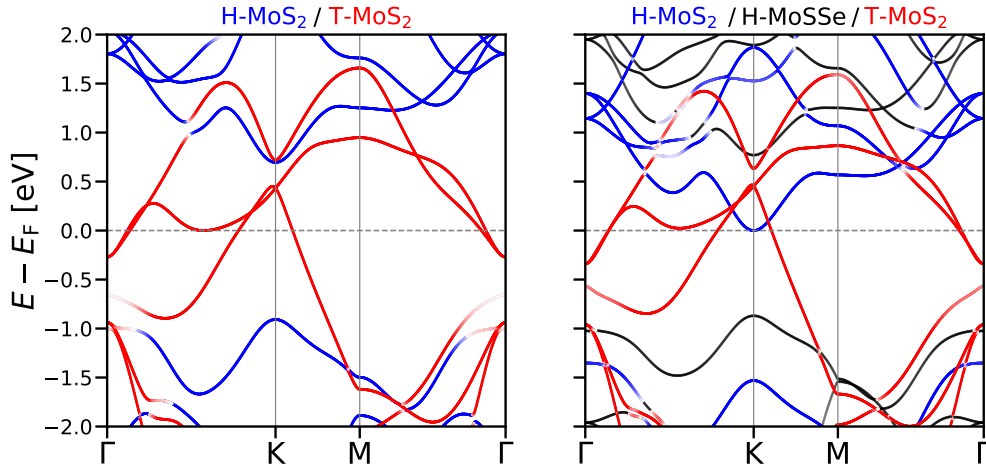


Figure 6.4: Left: band structure of bilayer H-MoS₂/T-MoS₂. The orbital weight projected on to the H-MoS₂ (T-MoS₂) monolayer for each state is indicated by blue (red). Faded color shows interlayer hybridized states. Right: Same as left figure with H-MoSSe inserted between the two monolayers. The orbital weight projected on to the H-MoSSe monolayer for each state is shown in black. This figure is taken from included paper VIII.

upper bound of the reduction of the intrinsic dipole moment of 2D Janus structures at complex semiconductor/metal interfaces. This fact is rather intriguing and the physical understanding might not be straightforward. It can be beneficial to take a step back and think about what this result tells us. The intrinsic dipole moment of the 2D is inherently set up by a non-symmetric charge distribution across the monolayer. The separation of positive and negative charge centers for the Janus monolayer arise from a difference in electronegativity of the encapsulating atoms (*i.e.* S and Se in the case of MoSSe), however, as we will see in the next section the nature of the intrinsic dipole cannot be fully understood simply from the difference in electronegativity of the encapsulating atoms. When the 2D Janus monolayer is put in proximity of a dielectric screening media (2D or bulk) we know from the previous chapters that the 2D monolayer is affected by both interlayer dielectric screening, hybridisation, and charge transfer effects. To change the intrinsic dipole moment of the Janus monolayer an external effect has to alter the asymmetric charge distribution. The additional electron (and hole) charge residing on either side of the central axis of the Janus monolayer can to some degree be regarded as located at the S/Se atoms (in the case of MoSSe) in a Bader charge analysis and therefore residing on orbitals confined to those atoms. To affect the intrinsic dipole moment of the Janus monolayer, any external perturbation would have to affect the local potential of those states, and change the relative potential between the orbitals on either side of the Janus monolayer, to change the equilibrium asymmetric charge distribution. It is maybe not too surprising that the dielectric screening itself does not alter the asymmetric charge distribution since we know that the effect of dielectric screening on the band

structure is close to constant for all bands and k-points. But it is not clear that the orbital hybridisation between the halogen/chalcogenides atoms and the bulk interface atoms does not affect this local potential and asymmetric distribution. Thus, the result above indicates that the orbitals involved in the interlayer (orbital) bonding, *i.e.* the orbitals around especially the Γ -point which have mixed contribution from *d*-orbitals and *s*-orbitals of the transition metal and halogen/chalcogenide atoms respectively, do not play a significant part in setting up the intrinsic out-of-plane dipole moment.

After showing that the intrinsic dipole moment of 2D Janus monolayers remains close to unaltered, even at bulk metal interfaces, we now show that 2D Janus monolayers can be used to not only manipulate the SBH at semiconductor-metal interfaces but also control the excited states properties of semiconductor-semiconductor systems. We do this by a similar approach to the one above in relation to SBHs. As we showed in chapter 3 and 4, for 2D TMD homobilayers the CBM at the K-point is subject to no interlayer hybridisation effects. We will now again utilise this fact to study the effect on the optical properties of 2D TMD homobilayers after insertion of 2D Janus monolayers between two monolayer semiconductors. To do this, we choose to study 2D bilayer H-MoS₂ and 2D bilayer H-MoS₂/H-WS₂, combined with a set of 2D Janus monolayers with a broad range of intrinsic out-of-plane dipole moments. We then calculate the energy splitting between the CBM of the two semiconductors after insertion of the 2D Janus monolayers and plot this as a function of the shift in electrostatic potential energy across each *freestanding* 2D Janus monolayer in fig. 6.5. The definition of the energy splitting is depicted in the inset. We find that the splitting of the two states is linearly proportional to the intrinsic dipole moment of the freestanding 2D Janus monolayer independent of the size of the dipole moment. This result shows that 2D Janus monolayers can be used to control detailed electronic and optical properties of semiconducting vdWHs, for instance the possibility to tune interlayer exciton energies independently at semiconductor-semiconductor interfaces. This could expand the scope of the use of vdWHs in the use in for instance (IR-)photodetectors discussed in the last section of chapter 3, where it could potentially be used to tune the energy range of the photodetector or for tandem solar cell devices discussed in section 5.2.

6.3 Electronic and Optical Properties of 2D Janus Monolayers

In the previous two sections we studied monolayer MoSSe and multilayer stacks of MoSSe in detail and showed the effect of the intrinsic out-of-plane dipole at semiconducting and metallic interfaces. Since the properties studied in the previous chapter have been specifically related to a few 2D Janus monolayers this section will be devoted to and present a larger study of a wide range of Janus 2D monolayers to broaden the spectrum of predicted stable 2D Janus structures and therefore enlarge the spectrum of possible

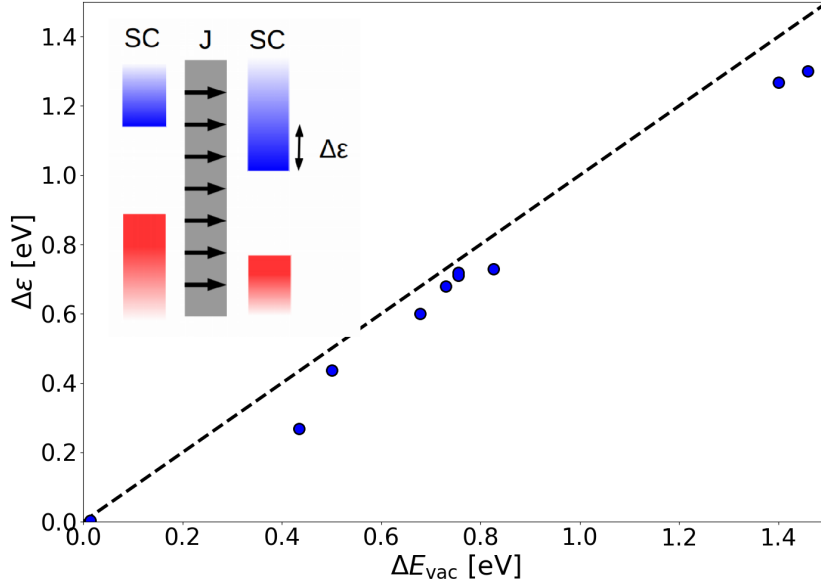


Figure 6.5: Energy split of degenerate band edge states ($\Delta\epsilon$) of semiconductor-semiconductor homobilayers upon insertion of a 2D Janus monolayer between the two semiconductors plotted against the shift in electrostatic potential energy across the freestanding 2D Janus monolayer (ΔE_{vac}). Different semiconductor bilayers and Janus materials are combined as explained in the main text. The dashed line has slope one. This figure is modified from included paper VIII.

applications.

Inspired by the experimental synthesis of MoSSe [79, 128] (H-phase) and BiTeI [38] (T-phase) we set out to study structures in the H- and T-phase containing a mix of a selection of transition metals, the pnictogens, the halogens, and the chalcogenides. Specifically we study structures with transition metals as the central atom in combination with either pnictogens as the side atoms or a mix of halogens and chalcogenides as the side atoms. Furthermore we study structures with pnictogens as the central metal atom and a mix of halogens and chalcogenides as the side atoms. The full set of 216 structures can be depicted from the details and figures in paper VIII. To quantify the thermodynamic stability we calculate the energy above convex hull which, as discussed previously, is a measure of the thermodynamic stability of the structure. From the C2DB we know that a 2D monolayer can be expected to be thermodynamically stable if the energy above convex hull is smaller than around 0.1 eV/atom [49]. Dynamical stability is determined from analysing the imaginary eigenvalues of the phonon spectrum. We will not go through the details of the screening studies since a comprehensive study can be found in paper VIII, but briefly summarise the results and instead here focus on the peculiar nature of the intrinsic out-of-plane dipole moment and the Rashba effect.

For the computational screening study we first note that the experimentally syn-

thesised monolayers, MoSSe and BiTeI, are lying at or just below the convex hull and thus predicted to be stable. In general we find group VI and VII transition metals in combination with chalcogenides (H-phase), group IV transition metals in combination with halogens (H-phase), group IV transition metals in combinations with chalcogens (T-phase), and all combinations with a pnictogen atom as the central metal atom in the T-phase are predicted thermodynamically stable. This includes the two experimentally synthesised monolayers. In addition to this, with few exceptions, all thermodynamically stable monolayers are found dynamically stable. In total we find 93 stable materials, of which 70 are semiconducting. Among the 23 metallic structure 7 are predicted to be in a ferromagnetic phase. This shows great promise for more 2D Janus monolayer to be experimentally synthesised and encourage further study and classification of the properties of 2D Janus monolayer structures.

For all stable monolayers we have calculated a broad range of electronic and optical properties including, PBE, HSE, and GW band structures and band gaps, effective masses, out-of-plane dipole moments, RPA and BSE absorption spectra, exciton binding energies, Rashba splitting parameters, etc. The calculated properties follows the workflow outlined in chapter 5. A large part of this data is presented in the data tables of paper VIII and is also available at the C2DB. The electronic and optical properties of the Janus class 2D materials qualitatively resemble that of the well-known TMD class of 2D monolayers, with both direct (at the K-point for most H-phase monolayers) and indirect electronic and optical band gaps, (G0W0) electronic band gaps in the range of 0.7-2.9 eV, exciton binding energies between around 0.4-1.1 eV, and for most monolayers a significant redshift of some of the features in the absorption spectrum comparing the absorption spectra calculated at the RPA and BSE level. In addition to this, the 2D Janus class monolayers possess out-of-plane shifts of the vacuum level potential up to about 1.7 eV and for many structures significant Rashba-split states at the Γ -point. We will return to the nature of the Rashba splitting at the end of this section. A very interesting aspect of our study of the 2D Janus class materials is that it turns out that the electronic properties of the Janus class 2D materials can be classified as presented in paper VIII from the symmetry and chemical composition. The qualitative classification can with very few exceptions predict if the monolayer is metallic or semiconducting and for the latter case the location of the band extrema in the Brillouin zone only from the chemical composition and phase of the monolayer. On one hand it is fascinating that these properties can be found simply by knowing the M, X, and Y atoms. On the other hand, at a very fundamental level all that make the properties of one material different from another is the atomic composition and the symmetry group, which is exactly the information contained in this classification.

As discussed above, the finite out-of-plane dipole moments of the Janus class 2D materials can intuitively be understood from the difference in electronegativity between the two side atoms (X and Y atoms). Here we look at this statement in greater detail by plotting the change in electrostatic potential energy across the freestanding 2D Janus monolayers against the difference in electronegativity between the X and Y atoms. This

is shown in fig. 6.6. While a weak correlation can be seen significant deviations from this trend are found. This is best illustrated by the H-phase structures MoSSe and WSSe. The difference in electronegativity of sulfur and selenium is very small, but still these monolayers possess a large out-of-plane dipole moment. Another example is H-phase ZrSTe having a very small out-of-plane dipole moment even though the electronegativity of sulfur and tellurium is very different. This does not rule out that the out-of-plane dipole moment depends on the difference in electronegativity between the X and Y atom (conversely this difference is most likely the main driving force of this feature), however it strongly suggests that the out-of-plane dipole moment is a property that cannot be modelled by electrostatic models, but depends on more elaborate features such as inter-atomic wave function overlaps.

One fascinating aspect of the 2D Janus monolayers is the strong Rashba splitting of band edge states found for many of the monolayers studied above. It can be seen in the electronic band structure as a symmetric splitting of the spin-up and spin-down channels at either the VBM or CBM. We will here elaborate on the Rashba discussion in paper VIII and discuss how the textbook picture of the Rashba splitting on one hand gives an intuitive explanation for this effect, however that it is fundamentally lacking as a quantitative correct description. Considering a 2D Janus monolayer as depicted in fig. 6.1 the electrostatic potential changes rapidly close to the nuclei. This means that the intrinsic electric field has small-range microscopic oscillations within the 2D monolayer. Considering this problem from an electrostatic point of view, we know that the electrostatic potential at either side of the 2D Janus monolayer differs by a size proportional to the macroscopic out-of-plane dipole moment. This means, despite the fact that the electric field varies at a microscopic length scale, the integral of the in-plane averaged electric field over the full width of the 2D monolayer in the out-of-plane direction has to equal the change in electrostatic potential across the layer, and therefore has to be finite. We now (greatly) simplify the problem and approximate the electric field in the out-of-plane direction as a constant, E_z . In this case, from the reference point of an electron moving around inside the 2D monolayer, the electron will be subject to a magnetic field of the size: $\mathbf{B} = \frac{1}{c^2} \mathbf{E} \times \mathbf{v} = \frac{1}{mc^2} \mathbf{E} \times \mathbf{p}$, where \mathbf{v} and \mathbf{p} are the velocity and (classical) momentum of the electron in the reference frame of the stationary 2D monolayer. Similarly to the discussion of spin-orbit coupling effects in chapter 2, we will use SI units to illustrate the dependence on the electron mass. Similar to the effect of spin-orbit coupling, the spin of the electron will interact with the magnetic field, which is given by projecting the effective magnetic field onto the Pauli spin matrices. If we simply consider all other contributions to the potential energy to be contained in V , we can write the Hamiltonian of the system, including the Rashba term, as:

$$\mathbf{H} = -\frac{\hbar^2 \nabla^2}{2m} + \hat{V} + \frac{g_s \mu_B}{2mc^2} \hat{\sigma} \cdot (\mathbf{E} \times \mathbf{p}) \quad (6.3)$$

where the first term is the kinetic energy, g_s is the g-factor, μ_B is the Bohr magneton, and $\hat{\sigma}$ are the Pauli spin matrices. Assuming that the electric field only has a z component,

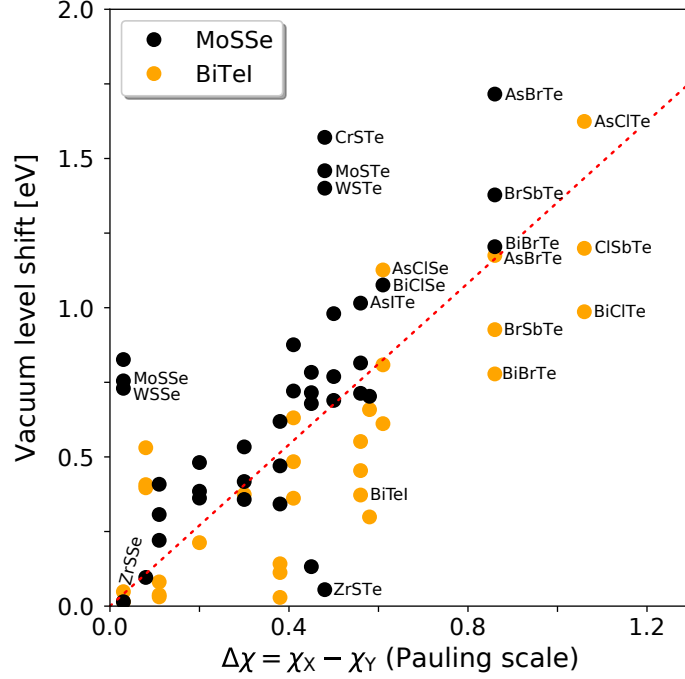


Figure 6.6: Shift in vacuum level energy across the monolayer for the semiconducting 2D Janus monolayers found to be stable in paper IX for the H-phase (MoSSe, black) and T-phase (BiTeI, orange) plotted against the difference in electronegativity between the side atoms (X and Y). This figure is taken from included paper IX.

eq. 6.3 can be written in matrix form as:

$$\mathbf{H} = \begin{bmatrix} -\frac{\hbar^2 \nabla^2}{2m} + V & \frac{g_s \mu_B E_z}{2mc^2} (\partial_x - i\partial_y) \\ \frac{g_s \mu_B E_z}{2mc^2} (\partial_x + i\partial_y) & -\frac{\hbar^2 \nabla^2}{2m} + V \end{bmatrix}. \quad (6.4)$$

Assuming that the eigenstates are plane waves confined to the 2D monolayer and assuming that the contribution from \hat{V} to the eigenenergies is V_0 , for an isotropic system, the eigenvalues near the band edges can readily be found to yield:

$$\epsilon_k = \frac{\hbar^2 k^2}{2m} + V_0 \pm \frac{g_s \mu_B E_z}{2mc^2} k = \frac{\hbar^2 k^2}{2m} + V_0 \pm \alpha_R k. \quad (6.5)$$

What we find is, that the spin of the electron coupling to the (constant) electric field in the out-of-plane direction gives rise to a k -dependent term that splits the band edge state in the two spin channels, giving two symmetrically split band edge states. $\alpha_R = \frac{g_s \mu_B E_z}{2mc^2}$ is known as the Rashba coupling parameter, which is linearly proportional to the electric field strength and therefore controls the degree of splitting. It is useful to bring in an alternative definition of the Rashba coupling parameter, which makes it easier to numerically and experimentally quantify the coupling parameter. Defining k_R as the distance

in momentum space between the band edge extrema and the symmetry axis and E_R as the Rashba energy, namely the energy difference between the band edge extrema and the point where the energy dispersion crosses the symmetry line, the coupling parameter can be defined as $\alpha_R = 2E_R/k_R$. Computed values for E_R and k_R are given in the data tables in the paper for all systems where Rashba-split states were observed. The calculated values for E_R and k_R are in good agreement with previous experimentally verified and numerically calculated values [20, 38] for similar TMD Janus structures. Since α_R is linear in the electric field, the Rashba energy should be proportional to the change in electrostatic potential energy across the 2D Janus monolayer. This is plotted in fig. 6.7 (left). At the same time, since the argument leading to the Hamiltonian (eq. 6.3) is similar to the derivation of the spin-orbit corrections to the eigenvalues, it is expected that the Rashba splitting will also correlate with the strength of the spin-orbit coupling, which we here quantify as the difference between the electronic band gap calculated with and without spin-orbit interaction included. This is plotted in fig. 6.7 (right). Following similar arguments to the derivation above, the textbook reasoning and explanation mostly found in the literature behind the Rashba-split states are, that the lack of out-of-plane mirror symmetry and strong spin-orbit coupling are the driving parameters for strongly Rashba-split states [38]. However, as it is evident from fig. 6.7 we find no correlation between the Rashba energy and neither the shift in electrostatic potential nor the strength of the spin-orbit coupling. This is a very important point, and shows that the generally assumed picture of the physics of Rashba splitting, outlined by the derivation above, does not give a satisfactory description of the physical mechanism. This is most likely due to the microscopic details of the electrostatic field which are ignored in the simplified model. In other words, it can be speculated, that the microscopic features of the electric field in the region of space where the Rashba-split states are confined to, are highly important, which are difficult to describe properly even with numerical methods. Nevertheless, the high Rashba coupling parameters found here are of great interest, since systems possessing Rashba-split states have caught the interest in the spintronics community because these states allow for easy control of the spin-up and spin-down channels separately.

To summarise we have studied the detailed properties of the new class of 2D Janus monolayers including a classification of the stability and their electronic and optical properties, the Rashba splitting, and the intrinsic out-of-plane dipole moment, and shown that the latter can be used to accurately manipulate SBHs at semiconductor-metal interfaces, electronic and optical properties of vdWHs, and to form intrinsic pn-junction in multilayer Janus structures. While only two 2D Janus monolayers have been synthesised to this date, the large number of stable 2D Janus monolayers predicted in this study opens a broad range of possible applications for this class of materials such as intrinsic pn-junctions or tuning of the interlayer exciton energy in semiconducting type-II vdWHs for photodetection. While the electronic properties of 2D monolayers and vdWHs to a large degree right now can only be manipulated by "external" parameters such as straining the monolayers, applying a gate voltage, or by changing the atomic composition by doping, such measures can in general introduce undesired side effects

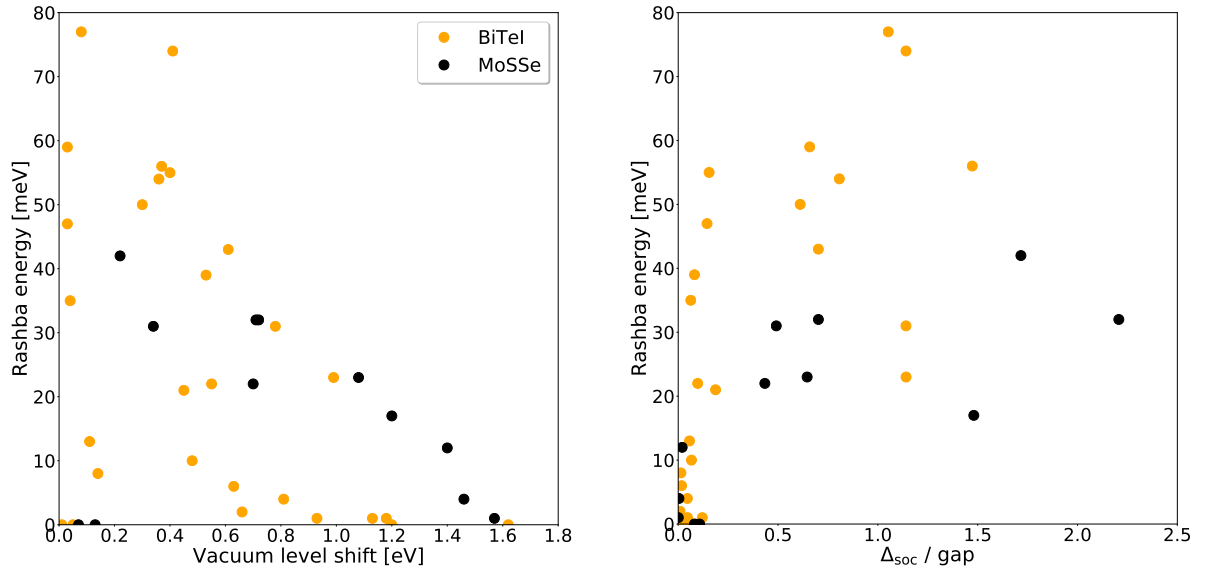


Figure 6.7: Left: Rashba energy against the shift in electrostatic potential energy across the 2D monolayer for all stable structures possessing Rashba-split band edges states for the H-phase (black) and T-phase (orange). Right: Rashba energy against the difference in electronic band gap calculated with and without spin-orbit coupling included in the ground state calculation (normalized by band gap including spin-orbit coupling) for the same data set as the left figure. The figures are taken from included paper IX.

that can be difficult to predict and control. In this aspect the class of atomically thin Janus structures offers a clean method for electronic manipulation. It will be interesting to what extent this will be utilised in applications in the upcoming years.

6.4 Self-Intercalation of Single Atoms in 2D Bilayers

In the previous chapters we have studied how the electronic and optical properties of vdWHs can be manipulated by the means of different techniques including; the nature of the monolayers (the atomic species), the dielectric environment including substrate screening or applied gate-voltage(s), the relative twist-angle between neighbouring monolayers, strains, doping, and as shown in the previous section, insertion of 2D Janus monolayers at interfaces to alter the electrostatic potential. In this final section of the final chapter we introduce a new paradigm of vdWH engineering, namely that of atomic self-intercalation in vdWHs. In this section we will present a few of the main results of the study in paper X and discuss the future prospects of this new class of quasi-2D materials. The remaining technical details can be found in the publication.

Due to the van der Waals nature of the interlayer interaction in vdWHs it is no surprise that the interlayer gaps could potentially offer a platform for further engineering of the vdWHs by insertion of single atoms, 1D chains, or molecules. However, it is by no means obvious if this can be achieved experimentally or if such structures will be stable or immediately disintegrate into other compounds. It is therefore rather surprising that not only can such self-intercalated bilayers be synthesised by two of the most standard growth methods, molecular beam epitaxy (MBE) and chemical vapor deposition (CVD), but that self-intercalated bilayers are also found to be stable for a wide range of combinations of atoms, as shown in this thesis. Furthermore, the concentration of self-intercalated atoms can be accurately controlled. The fact that these structures can be grown by both MBE and CVD enlarge the potential of the applications of these structures since it opens the possibility for many labs to potentially grow self-intercalated vdWHs in the future. In fig. 6.8 we show an example of self-intercalated bilayer Ta_7S_{12} by a STEM image where the Ta atoms are shown by purple and the S atoms are vaguely found in the background in dark purple (it should be stressed the STEM image is obtained from experimental collaborators of the author). The self-intercalated Ta atoms are highlighted by yellow rings. The hexagonal lattice by the Ta in the pristine bilayer layers can be easily spotted and the self-intercalated Ta atoms occupies the octahedral vacancies.

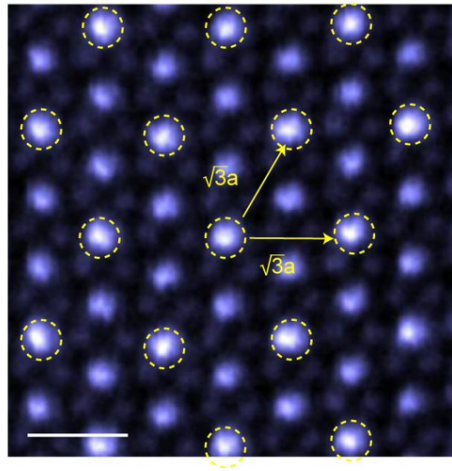


Figure 6.8: STEM image of self-intercalated bilayer Ta_7S_{12} . The self-intercalated Ta atoms, occupying the octahedral sites are highlighted by yellow rings. The shown example corresponds to an intercalation concentration of 33.3% (see main text for definition). The scale bar has a length of 5 Å. This figure is taken from included paper X.

The structure shown in fig 6.8 is an example of a self-intercalated bilayer with a 33.3% self-intercalation concentration. The concentration degree is defined as the number of occupied octahedral vacancies over the number of octahedral vacancies in the pristine bilayer system. As mentioned, the self-intercalation concentration can be accurately controlled in the growth process, for instance using MBE, which can be done by carefully

controlling the ratio of Ta to S atoms. From this it is found that the concentration of self-intercalated Ta atoms can be tuned over a range of: 0%, 25%, 33.3%, 50%, 66.6%, and 100%. This gives a new spectrum of possibilities to explore the materials property of the vdWH by not only inserting single atoms, but also precisely control the distance between the self-intercalated atoms through the self-intercalation concentration.

By exploring this spectrum, both experimentally and through DFT calculations we find an intriguing dependence of the magnetic phase of the vdWH on the self-intercalation concentration for TaS₂. While intrinsic bilayer TaS₂ is non-magnetic and remains non-magnetic for various self-intercalation concentrations it is found that the most stable phase is a ferromagnetic phase at a self-intercalation concentration of 33.3% as illustrated in fig 6.9. It therefore turns out that it is possible to control the magnetic phase of the bilayer directly by controlling the self-intercalation concentration in the growth process. We have performed DFT calculations to analyse this phase transition and found that the ferromagnetic phase arises due to a significant charge transfer from the self-intercalated Ta atoms to the native bilayer layers. This leaves an unpaired electron at the self-intercalated atom in a *d*-orbital crossing the Fermi surface. We speculate that the exact self-intercalation concentration at which the phase transition takes place is closely related to the orbital overlap between the self-intercalated atoms, which determines the onset of when the charge transfer to the native bilayers is energetically favourable together with the amount of the transferred charged.

To test the generality of the observed self-intercalation of bilayer TaS₂ we have conducted a substantial screening study calculating and analysing various self-intercalated bilayers. We calculate the ground state of bilayer combinations of 16 different transition metals with both S, Se, and Te. This is done for both the intrinsic bilayer and at 33.3% and 66.6% self-intercalation concentrations (see paper X for all bilayer combinations). For each system we calculate the energy above convex hull (in the same manner as in the C2DB workflow). We stress here that the pristine bilayer has been included in the convex hull for this analysis. From this analysis we find 14 different configurations that develop ferromagnetism upon self-intercalation (*i.e.* we exclude systems which are already magnetic in the pristine bilayer structure). As illustrated in fig. 6.10 we predict 12 of these self-intercalated bilayers to be thermodynamically stable. We also stress that 33.3% self-intercalated Ta₇S₁₂ is found as one of these 12 systems. Of the 14 systems all structures containing Ta, Nb, and Mo have been attempted to be grown. A successful growth was achieved for the self-intercalated bilayer containing Ta and Nb, while self-intercalated bilayers containing Mo disintegrated into other compounds immediately. We therefore satisfactory found a one-to-one correspondence between the computationally predicted stable self-intercalated bilayers and the successfully grown self-intercalated bilayers.

The fact that the self-intercalation process and development of ferromagnetism is not limited to bilayer TaS₂, but turns out to be a more general feature, opens new possible pathways for more general manipulation of the properties of vdWHs using self-intercalated single atoms. This window, and extend, of additional tuning of the properties are now to be explored. Future studies should now be carried out to reveal

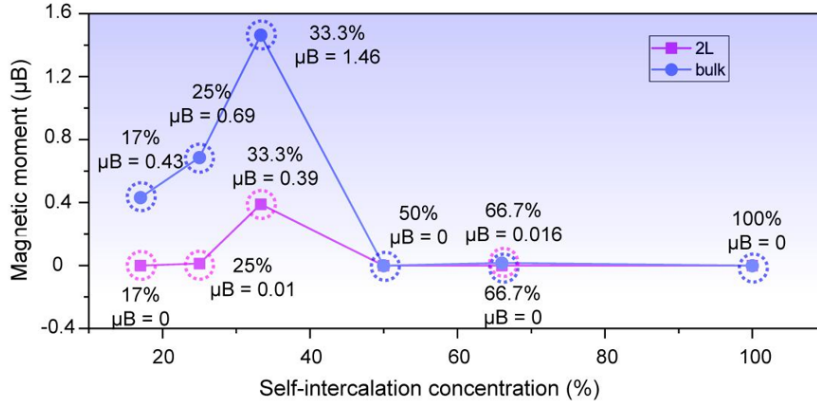


Figure 6.9: Magnetic moment as a function of concentration of self-intercalated Ta atoms for bilayer (purple) and bulk (blue) TaS₂. The onset of the ferromagnetic phase of self-intercalated bilayer TaS₂ is found at an self-intercalation concentration of 33.3%. This figure is taken from included paper X.

if other materials properties than the on/off-switching of a ferromagnetic phase can be manipulated by this method. While the intercalation of foreign atoms have already been achieved in bulk crystals there exist only few examples of this process in few-layer layered materials [62, 121, 37, 118, 119]. It will be interesting to see the result of a systematic study to test if the intercalation process in few-layer vdWHs is only limited to atoms already present in the intrinsic bilayer and few others or how general the intercalation process can be made. In either case, the (self-)intercalation of atoms in between the layers in vdWHs offers yet another knot to turn to assemble vdWHs with unique new materials properties and can be used in combination with the above mentioned methods such as twist-angles, dielectric screening and gate-voltage, strain effects, Janus monolayers etc. to expand the already almost infinite possible combinations of vdWHs.

At this point we are free to hypothesise what other possibilities the intercalated bilayer structures opens up. The intercalated bilayer systems can to some extent be considered as a quasi-2D system. On one hand, the system is still characterised by the familiar 2D nature *i.e.* low dielectric screening, strongly bound exciton states, and strong light-matter interaction. On the other hand, a recent study has shown that intercalation of Cu atoms into the van der Waals gap of bilayer NbS₂ changes the transport properties in the out-of-plane direction of the bilayer [78]. We note in passing that this intercalation process was performed at a very high Cu chemical potential from a Cu surface and the general stability of this intercalated system is questionable. Otherwise Cu contamination of vdWHs would most likely present a huge problem. However, it very well illustrates the hint of 3D character few-layer intercalated vdWHs possesses. From another perspective the intercalated bilayers can also be viewed as a quasi-0D/2D material: a host material (the intrinsic 2D bilayer) hosting single atoms. With very low intercalation concentrations the orbitals of the intercalated atoms would have close to

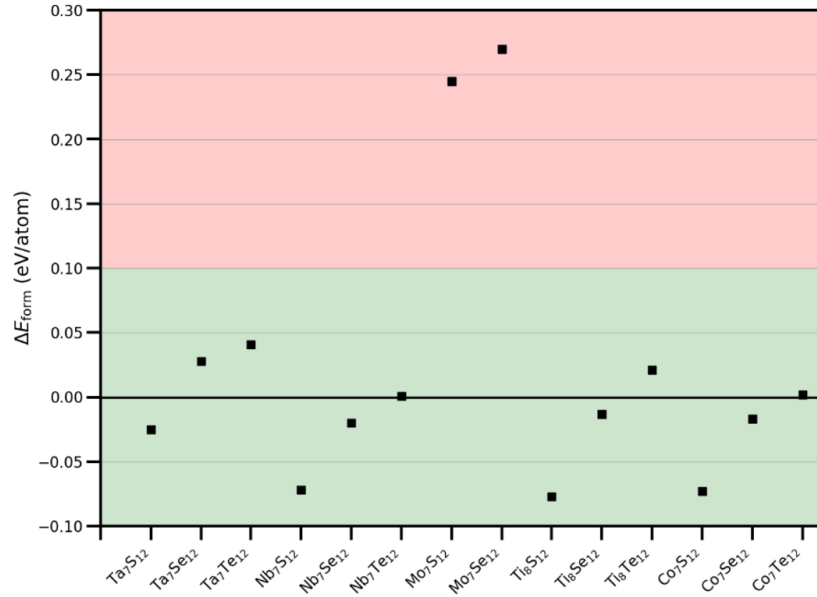


Figure 6.10: Energy above convex hull for the 14 self-intercalated bilayers found to develop a ferromagnetic phase upon self-intercalation. The definition of thermodynamic stability is chosen to be at 0.1 eV/atom over the convex hull according to the stability analysis performed in the C2DB [49]. This figure is taken from included paper X.

no overlap and would essentially be non-interacting. While the intercalated atoms will still be covalently bonded to the bilayers it could potentially be possible to utilise some of the properties of free atoms. This could for instance be single frequency emission peaks from the intercalated atoms, which would have sharp atomic optical transitions when intercalated in a wide band gap intrinsic bilayers. It will be exciting to follow how the (self-)intercalated atoms will contribute to research in vdWHs in the following years.

CHAPTER 7

Conclusion and Outlook

In this thesis we have applied analytical models and state-of-the-art *ab-initio* computational methods to calculate and explore the electronic and optical properties of 2D materials and vdWHs. We have reviewed the state-of-the-art computational *ab-initio* many-body methods, the GW, and BSE formalisms, and seen the importance of including many-body effects in the description of 2D materials and vdWHs to capture the strong quasi-particle and excitonic effects in these systems. In general, *ab-initio* computational methods can only be applied to a very limited number of vdWHs, due to the computational requirements of such calculations and the large number of atoms necessary to represent even few-layers vdWHs. This thesis has addressed these computational requirements by having developed efficient algorithms for such calculations.

To summarise the results in this thesis, we have in section 3.5 shown how the non-locality of the dielectric function can be used to manipulate and control the quasi-particle band gap of 2D monolayer semiconductors on a graphene layer (and other dielectric screening media), by applying a gate-voltage to the graphene monolayer. We also showed how the magnitude of this effect depends on the static polarisability of the 2D semiconductor and that the effect can be further manipulated in a predictive manner by intercalating monolayer hBN layers.

In section 3.7 we implemented the BSE method with the QEH model to be able to accurately calculate exciton energies in multilayer vdWHs. This makes possible the calculation of the absorption spectrum including excitonic effects of multilayer vdWHs and furthermore we saw that this accurately captures the redshift of exciton energies in vdWHs - an artefact not captured correctly by the Mott-Wannier model for few-layers vdWHs previously developed. We showed in section 3.9 that a strong interlayer exciton state exists at the heterointerface of WS_2/HfS_2 with a peculiar thickness dependent interlayer to intralayer character transition. The exciton state exhibits an energy in the infrared spectrum and resolves a long standing issue of finding optically strong and active photodetectors in the infrared spectrum. Finally in chapter 3 we introduced a new dielectric screening regime of 2D exciton physics that exists when a semiconducting 2D monolayer is placed on a strongly dielectric screening bulk media. Consequently the exciton Rydberg series becomes overscreened - in contrast to the underscreened screening regime previously known for freestanding 2D monolayers. Furthermore we showed how the nature of the Rydberg series can be varied by changing the dielectric constant of the bulk dielectric media and that an inherent hydrogenic Rydberg series can in fact be obtained in a semiconducting 2D monolayer. The new exciton screening regime is

yet to be fully explored and can potentially open up new pathways for designing new exciton states in vdWHs.

In chapter 4 we discussed and showed that it is necessary to go beyond the non-self-consistent state-of-the-art *ab-initio* methods (such as G0W0) to obtain a correct description of the interlayer orbital hybridisation and charge transfer effects in vdWHs. We developed a computational method to accurately describe this interlayer interaction and implemented this with the QEH model. We then combined the developed model with *ab-initio* G0W0, BSE, and Mott-Wannier calculations to benchmark the accuracy that can be expected of calculated intra- and interlayer exciton energies in vdWHs against experimental observations. Interestingly we found that it is important to treat the interlayer interaction self-consistently from the quasi-particle band line-up to accurately describe the twist-angle dependence of exciton energies for systems with degenerate intra- and interlayer exciton state. In this, we also benchmarked the discrepancy that can be expected from the dielectric screening from supporting substrates in experiments, from interlayer orbital hybridisation effects, and studied finite temperature effects on optical transition energies. From this, we benchmarked the discrepancy that can be expected between experimental measurements and *ab-initio* calculated exciton energies in vdWHs. The developed methods for computationally feasible calculating excitonic absorption spectra and interlayer orbital hybridisation effects in vdWHs offers an important tool to accurately calculate quasi-particle energies and excitonic states in multilayer vdWHs which have not been possible up to this date.

After studying electronic and optical states in vdWHs we turned our attention to materials discovery and manipulation of materials properties of vdWHs. First we presented and outlined the developed workflow of the Computational 2D Materials Database. The database offers a comprehensive study of the stability, single-particle, and many-body electronic and optical properties of close to 3000 monolayers. The hope is that this database will help guiding both theoreticians and experimentalists in future studies. Our work included a significant study of the new Janus class of 2D monolayers where we conducted a thorough classification study of their electronic and optical properties. We found that the 2D Janus monolayers can be used to manipulate the Schottky barrier at semiconductor-metal heterointerfaces, tune the band line-up and interlayer exciton energies at semiconductor-semiconductor interfaces, and that in fact multilayer Janus structures are natural inherent pn-junctions. While only two 2D Janus monolayers have been experimentally synthesised to this date, the results in this study suggests that Janus monolayers have a huge potential to influence the future of vdWH design and applications, due to their wide range of out-of-plane dipole moments and their inherent strong Rashba split states. Finally we introduced a new paradigm of materials science by showing it is possible to self-intercalate single atoms in 2D bilayers and that such self-intercalated structures in fact are stable for a large set of bilayers. We found that the self-intercalation process influences the electronic properties and for several bilayer systems can change the magnetic phase dependent on the concentration of self-intercalated atoms. It will be interesting to follow the future of these cross-dimensional structures,

where it is possible to both combine the characteristic 2D properties with out-of-plane 3D-like properties and possibly utilise single-atom properties in low-concentration self-intercalated bilayers.

CHAPTER 8

Papers

8.1 Paper I

Electrically Controlled Dielectric Band Gap Engineering in a Two-Dimensional Semiconductor

A. C. Riis-Jensen, J. Lu, and K. S. Thygesen

PRB Rapid Communication, **101**, 121110(R) (2020)

Editor's suggestion

© Copyright 2020 American Physical Society All Rights Reserved

<https://journals.aps.org/prb/abstract/10.1103/PhysRevB.101.121110>

Electrically controlled dielectric band gap engineering in a two-dimensional semiconductor

Anders C. Riis-Jensen,¹ Jiong Lu,² and Kristian S. Thygesen^{1,3,*}

¹*CAMD, Department of Physics, Technical University of Denmark, DK-2800 Kongens Lyngby, Denmark*

²*Department of Chemistry, National University of Singapore, 3 Science Drive 3, 117543 Singapore*

³*Center for Nanostructured Graphene (CNG), Department of Physics, Technical University of Denmark, DK-2800 Kongens Lyngby, Denmark*



(Received 15 January 2020; accepted 28 February 2020; published 16 March 2020)

The emergent class of atomically thin two-dimensional (2D) materials has opened up completely new opportunities for manipulating electronic quantum states at the nanoscale. Here we explore the concept of dielectric band gap engineering, i.e., the controlled manipulation of the band gap of a semiconductor via its dielectric environment. Using first-principles calculations based on the *GW* self-energy approximation we show that the band gap of a two-dimensional (2D) semiconductor, such as the transition metal dichalcogenides, can be tuned over several hundreds of meV by varying the doping concentration in a nearby graphene sheet. Importantly, these significant band gap renormalizations are achieved via nonlocal Coulomb interactions and do not affect the structural or electronic integrity of the 2D semiconductor. We investigate various heterostructure designs, and show that, depending on the size of the intrinsic dielectric function of the 2D semiconductor, the band gap can be tuned by up to 1 eV for graphene carrier concentrations reachable by electrostatic doping. Our work provides opportunities for electrically controllable band gap engineering in 2D semiconductors.

DOI: [10.1103/PhysRevB.101.121110](https://doi.org/10.1103/PhysRevB.101.121110)

I. INTRODUCTION

Two-dimensional (2D) materials such as graphene, hexagonal boron nitride (hBN), and the semiconducting transition metal dichalcogenides (TMDCs), represent an emergent class of materials with unique electronic and optical properties making them interesting candidates for applications in a number of areas including (opto)electronics, photonics, energy, and quantum technology [1–5]. A unique merit of these materials is that their properties can be tuned much more easily than is possible with conventional bulk materials. This feature stems from the extreme thinness of 2D materials, which makes the electronic states living inside them highly susceptible to their environment [6]. In particular, 2D semiconductors encapsulated in van der Waals heterostructures constitute an ideal platform for practicing and exploiting the art of band gap engineering.

In addition to the conventional band gap engineering schemes based on doping and alloying, the band gap of 2D semiconductors can be controlled via mechanical strain [7,8], layer stacking [9,10], and external electric fields [11,12]. In all these cases, the fundamental physical mechanism underlying the band gap modification can be explained within a single-particle picture. A fundamentally different type of band gap engineering can be achieved in 2D materials by exploiting the dependence of the electronic quasiparticle (QP) energies on the dielectric environment outside the 2D layer. This dependence stems from the electron's self-energy, which describes the interaction between the electron (or hole) and its self-induced screening cloud. Because the shape and size of the screening cloud depends on the dielectric environment,

this effect can be exploited to change the QP energies without changing the spatial shape or hybridization pattern of the 2D semiconductor wave functions. Because of its nonlocal and dynamical nature, dielectric screening effects on QP energies are not captured by traditional mean-field approximations, but require more rigorous QP theories such as the many-body *GW* method [13,14].

Quasiparticle screening effects manifest themselves most clearly in molecules deposited on metallic or dielectric substrates. In such systems, the dielectric screening from the substrate can shift the molecule's orbital energies by several eV relative to the gas-phase energies. These effects, which have been demonstrated both experimentally [15–17] and theoretically [18–20], are essential to take into account for a proper description of electron transport in molecular junctions. Here the dielectric screening from the metallic electrodes can strongly influence the position of the frontier molecular orbitals relative to the electrode Fermi level and thereby affect the tunneling rate [21,22]. The shift in molecular energy levels can often be explained semiquantitatively by a classical image charge model [18,19], although dynamical corrections and wave function modifications may also play a role [23,24]. Compared to molecules, 2D semiconductors have better intrinsic screening ability making them less susceptible to their dielectric environment. Still, the internal screening is weak enough that the QP band gap can be reduced by up to 1 eV by substrate screening, as first shown by first-principles *GW* calculations for hBN on graphene [13]. Experimentally, it was demonstrated using nonlinear optical spectroscopy that the QP band gap of monolayer WS₂ can be varied by 0.3 eV depending on the choice of substrate [25], and by *GW* calculation that the QP band gap is reduced by about 0.5 eV for MoS₂ on a gold substrate [26]. Subsequently, the concept of dielectric band gap engineering in

*thygesen@fysik.dtu.dk

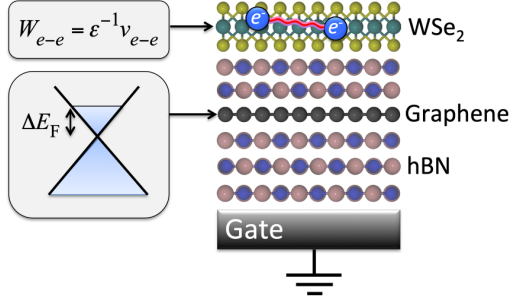


FIG. 1. The setup considered for electrically controlled band gap engineering. A semiconducting 2D material is placed on top of a graphene sheet separated by N layers of hBN. The concentration of charge carriers in the graphene sheet can be adjusted via a bottom gate. An increased doping level enhances the dielectric function of the graphene sheet, which in turn weakens the screened electron-electron interaction inside the 2D semiconductor leading to a reduction of its QP band gap.

2D materials has been explored for both lateral [27,28] and vertical [29–31] heterostructure designs. In a recent work, Qiu *et al.* [32] investigated the effect of dielectric screening on the quasiparticle band gap of a single layer of ReS₂ placed on top of a back-gated graphene sheet. They found that the band gap can be tuned between 2.15 and 1.93 eV when the gate voltage was varied between -63 and 45 V.

In this work we present a theoretical analysis of a similar setup providing both fundamental insight into the physical mechanisms governing the idea of *electrically controllable* dielectric band gap engineering in a 2D semiconductor and numerical relations between key system parameters that can be used to guide the future design of van der Waals (vdW) structures with tailored band gaps. To this end we consider a van der Waals heterostructure consisting of the 2D semiconductor placed on a graphene sheet (see Fig. 1). For various types of 2D semiconductors, we explore how the QP band gap depends on the doping concentration in the graphene sheet. In practice, the latter can be controlled by an electrostatic bottom gate. This setup allows the strength of the screened Coulomb interaction inside the 2D semiconductor and thus the electron self-energy, to be controlled externally via the concentration of free charge carriers in the graphene sheet. The calculations are made possible by the recently developed $G\Delta W$ method [29], which calculates the change in the GW self-energy due to the additional screening provided by the heterostructure environment, which in turn is obtained using the quantum electrostatic heterostructure (QEH) model [33].

II. RESULTS AND DISCUSSION

The QP energies are obtained from the linearized QP equation

$$\varepsilon_n^{\text{QP}} = \varepsilon_n + Z_n \langle \psi_n | \Sigma(\varepsilon_n) - v_{xc} | \psi_n \rangle, \quad (1)$$

where ψ_n and ε_n represent approximate single-particle wave functions and energies that are typically obtained from a density functional theory calculation. In this work, we use the Perdew-Burke-Ernzerhof (PBE) exchange-correlation (xc)

functional to determine ψ_n and ε_n . In the QP equation, the self-energy operator, Σ , which describes the interaction of the electron/hole with its self-induced screening cloud, replaces the local mean-field exchange-correlation potential, v_{xc} . The renormalization factor Z_n accounts for the energy variation of $\Sigma(\varepsilon)$ around the energy ε_n .

Within the so-called G_0W_0 method, the electron self-energy is approximated by the product of the Green's function (G) and dynamically screened electron-electron interaction (W). The 0 subscript indicates that G and W are evaluated from the noninteracting ψ_n and ε_n , i.e., the non-self-consistent GW approximation. The screened interaction, which is the main object of interest in the present work, is defined as

$$W(\mathbf{r}, \mathbf{r}', \omega) = \int \varepsilon^{-1}(\mathbf{r}, \mathbf{r}'', \omega) \frac{1}{|\mathbf{r}'' - \mathbf{r}'|} d\mathbf{r}'', \quad (2)$$

where $\varepsilon(\mathbf{r}, \mathbf{r}', \omega)$ is the microscopic dielectric function of the material. We shall not go deeper into the theory of the GW method here but refer the interested reader to one of the many excellent reviews on the topic [34,35]. For the purpose of the present work it suffices to note that due to the strong nonlocality of the Coulomb kernel and dielectric function, it is possible to affect the screened interaction W between electrons in one region of space (here the 2D semiconductor) by modifying the dielectric response in another region (here the graphene sheet).

Conventional implementations of the GW method do not readily allow for the study of systems like the one shown in Fig. 1. This is due to the sheer size of the supercells needed to describe vdW heterostructures comprising 2D materials with different in-plane lattice constants. For example, the smallest supercells required to model a WS₂/graphene bilayer when the strain on each layer is not allowed to exceed 1%, contains more than 300 atoms, which exceeds the system sizes that can be treated by conventional GW codes. Furthermore, a proper treatment of the dielectric function of doped graphene requires extremely dense k -point sampling around the Dirac cones making standard calculations intractable. In this work we rely on the $G\Delta W$ method [29] in combination with the QEH model [33]. The QEH model is used to compute the dielectric function of the entire vdW heterostructure from the dielectric functions of the individual layers. The method circumvents the problem of large supercells due to lattice mismatched 2D layers and allows for very fine k -point meshes for the individual layers. We use the QEH model to calculate the change in the screened interaction of the 2D semiconductor, ΔW , due to the presence of the other layers of the heterostructure (hBN and doped graphene). In a next step, we calculate the change in the self-energy as $\Delta\Sigma = G\Delta W$ (integral over frequency not shown), which in turn yields the change in the QP gap of the semiconductor. For more details on the $G\Delta W$ methods we refer to Ref. [29]. We note in passing that other approximation schemes for dealing with dielectric screening in GW calculations for large systems have been proposed [36,37].

In the following we consider the setup shown in Fig. 1 consisting of a monolayer transition metal dichalcogenide (TMD) placed on top of a graphene sheet, possibly with a number of hBN layers inserted in between. In Fig. 2 we plot the QP band gap of four different TMDs as a function of

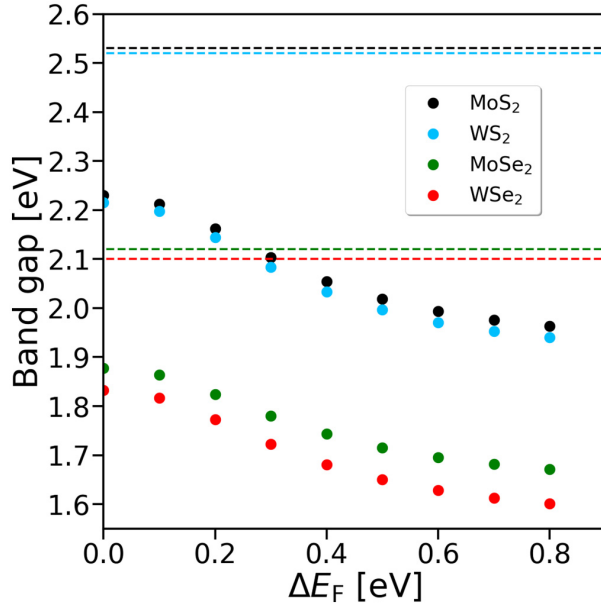


FIG. 2. The quasiparticle band gap of four different TMD monolayers placed on top of a graphene sheet as a function of the position of the Fermi level (i.e., carrier concentration) in graphene. The configuration corresponds to Fig. 1 without any hBN layers between the TMD and graphene sheet. The band gap of the freestanding TMDs is indicated by dashed lines.

the Fermi level in the graphene sheet for the case where the TMD is placed directly on top of the graphene layer. As the Fermi energy is raised, the concentration of free carriers in the graphene sheet increases leading to an enhanced dielectric screening. This effect is visible in Fig. 5, which shows the real part of the dielectric function of the TMD monolayer for different values of the Fermi energy. The dielectric function of the TMD is defined as the ratio between the screened and bare Coulomb interaction in the TMD sheet,

$$W(q_{\parallel}, \omega) = \frac{1}{q_{\parallel} \epsilon(q_{\parallel}, \omega)}, \quad (3)$$

where $1/q_{\parallel}$ is the bare 2D Coulomb interaction and $W(q_{\parallel}, \omega)$ is the screened interaction between charges in the TMD obtained from the QEH model, and q_{\parallel} is the in-plane 2D wave vector. The graphene plasmon is clearly visible at finite doping concentrations. The intensity of the graphene plasmon increases with the doping level leading to an enhanced dielectric screening in the TMD layer. The lower right panel of Fig. 5 shows the real part of the dielectric function for fixed wave vector $q_{\parallel} = 0.05 \text{ \AA}^{-1}$.

In the quasiparticle picture, where an electron is surrounded by a positive screening cloud (together making up the quasiparticle), the enhanced dielectric screening corresponds to a larger/more effective screening cloud. The attractive interaction between the bare particle and its screening cloud, i.e., the self-energy of the electron, then increases resulting in a stabilization of the quasiparticle and thus a reduction of the band gap.

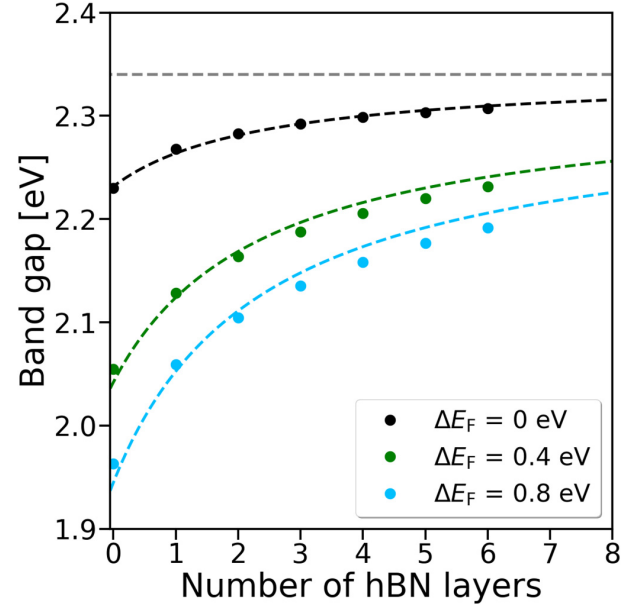


FIG. 3. Quasiparticle band gap of MoS₂ in the geometry depicted in Fig. 1 as a function of the number of hBN layers between MoS₂ and graphene. Results are shown for three different doping concentrations in the graphene layer. The dashed black, green, and blue lines are fits of the form $a(E_F)/(N+b) + E_{\text{gap}}^{\infty}$ where the asymptotic value E_{gap}^{∞} is the calculated QP band gap of MoS₂ on bulk hBN.

In the configuration considered in Fig. 1 (no hBN layers between the TMD and graphene), the screening from undoped graphene reduces the TMD band gap by around 0.30 eV, as compared to the freestanding TMD. The band gaps are then further reduced by 0.25 eV as the graphene Fermi level is increased from 0 to 0.8 eV. We stress that these very substantial band gap reductions are achieved without modifying the atomic structure, the shape of the wave functions, or their hybridization patterns, and highlights the unique opportunities offered by atomically thin materials for tuning electronic properties.

In Fig. 3 we show the variation of the TMD band gap (here exemplified by MoS₂) as a function of the number of hBN layers separating the TMD and the graphene sheet. Results are shown for the case of intrinsic graphene and for doping concentrations corresponding to Fermi level shifts of 0.4 and 0.8 eV, respectively. The band gap shows an approximate $1/N$ dependence on the number of hBN layers. The dashed lines indicate best fits to the functional form $a(E_F)/(N+b) + E_{\text{gap}}^{\infty}$, where the asymptotic value E_{gap}^{∞} is the band gap of MoS₂ on bulk hBN (which we calculate explicitly), b is an image plane position, and a is the strength of the image charge. In these fits only a was taken to depend on the doping concentration in the graphene layer. The good quality of the fit confirms the interpretation of the band gap reduction as an “image charge” effect, i.e., the band gap reduction is due to the interaction between the electron/hole in the TMD and its self-induced screening cloud in the graphene layer. Furthermore we find b to be very close to two times the MoS₂/graphene interlayer

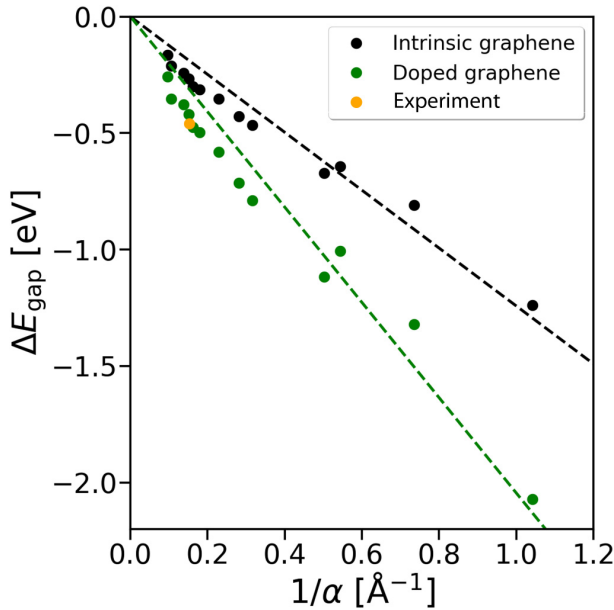


FIG. 4. The reduction of the QP band gap of the semiconductor monolayers listed in Table I when placed on intrinsic and doped graphene (corresponding to $\Delta E_F = 0.4$), respectively. The band gap reduction is plotted versus $1/\alpha$, where α is the static in-plane polarizability of the freestanding 2D semiconductor. It is clear that the band gap reduction is stronger for 2D materials with weaker intrinsic screening suggesting that the band gap renormalization is determined by the *relative* change in screening provided by the graphene layer. The dashed lines are added as guides to the eye and the orange dot corresponds to previous experimental work [32] (see main text).

distance, and we therefore believe this accurately reproduces the distance to the image charge plane.

In the simplest image charge model, the band gap reduction is given by the electrostatic interaction between a point charge in the TMD and its image charge in the graphene layer. Indeed, this picture has been found to hold to a very good approximation for molecules on metallic or insulating surfaces [18,19]. In Fig. 4 we show the calculated band gap renormalization for a number of different 2D semiconductors when placed on top of the graphene layer. The considered 2D semiconductors are listed in Table I together with their QP band gaps and static in-plane polarizability taken from the Computational 2D Materials Database (C2DB) [38]. The band gap reductions are plotted against the size of the static in-plane polarizability of the 2D semiconductor. It is clear that, independent of the doping concentration in the graphene sheet, the band gap reduction is larger for 2D materials with lower polarizability. This behavior can be understood by realizing that the magnitude of the screening cloud in the graphene layer, i.e., the image charge, depends on the total charge of the quasiparticle in the 2D semiconductor, i.e., the bare electron/hole *plus* its screening cloud in the 2D semiconductor. The latter is obviously larger in 2D semiconductors with a high intrinsic polarizability. This shows that the amount by which the band gap can be tuned via the dielectric

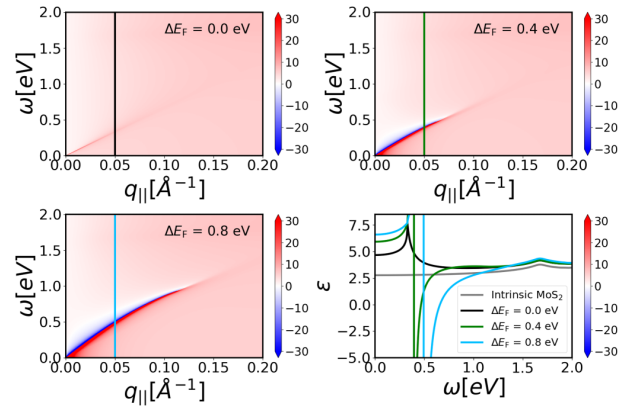


FIG. 5. Contour plots: real part of the dielectric function of MoS₂/graphene evaluated in the MoS₂ layer for different doping concentrations along the in-plane wave vector. Bottom right plot: The real part of the dielectric function evaluated along $q_{||} = 0.05 \text{ \AA}^{-1}$ for intrinsic MoS₂ (gray) and for three different doping concentrations for MoS₂/graphene (black, green, and blue).

environment depends on the degree of internal screening in the 2D semiconductor itself. We note the band gap reduction found by Jiong *et al.* [32], where a reduction of about 0.6 eV of the band gap was found when monolayer ReSe₂ was placed on doped graphene. We have calculated the averaged in-plane static polarizability of ReSe₂ to be 6.58 \AA , corresponding to the orange dot in Fig. 4 and we find an excellent agreement with the calculated values for the band gap reduction of other 2D monolayers.

In this work we have focused on the effect of dielectric screening on the QP band gap. In general, optical excitations, in particular bound excitons, are less affected by dielectric screening because of the neutral nature of such excitations. On the other hand, more loosely bound excitons or excitons with charge transfer character [39,40], present larger electron-hole separations and consequently experience stronger renormalization by the dielectric environment. While the effect of dielectric screening on optical excitations, in particular the

TABLE I. Band gap and static in-plane polarizability for the 13 monolayers shown in Fig. 4.

Monolayer	Band gap (eV)	Static polarizability (\AA^{-1})
BN	7.17	0.96
HfO ₂	4.70	1.36
SnO ₂	1.84	1.84
TiO ₂	3.95	1.99
HfS ₂	2.94	3.16
SnS ₂	2.29	3.56
HfSe ₂	2.12	4.38
WS ₂	2.52	5.58
MoS ₂	2.53	6.19
WSe ₂	2.10	6.59
MoSe ₂	2.12	7.28
MoTe ₂	1.56	9.47
CrSe ₂	1.17	10.31

lowest bound excitons in 2D materials, are easier to probe experimentally as compared to the QP gap, the theoretical treatment is limited by the assumption of static screening. This assumption is valid when the dielectric function shows weak variation with frequency up to a characteristic frequency given by the exciton binding energy. This condition is usually satisfied in intrinsic semiconductors and insulators. However, when the dielectric function used to screen the electron-hole interaction has a metallic component (like the intraband screening in doped graphene; cf. Fig. 5) the assumption of static screening cannot be justified and more elaborate methods are required in order to deal with the frequency dependent electron-hole interaction [41].

In conclusion, our *ab initio* GW calculations show that it is possible to control the quasiparticle band gap of an atomically thin 2D semiconductor by varying the doping concentration in a nearby graphene sheet. The physical mechanism underlying the band gap renormalization is that the size of the screening cloud dressing an electron/hole of the 2D semiconductor, which determines its self-energy, is controlled by the screening ability of the graphene. The effect was shown to be well described by a simple image charge model with the caveat that the magnitude of the image charge depends on the intrinsic screening of the 2D semiconductor. Thus, in general, the effectiveness of dielectric band gap engineering is determined by the intrinsic screening properties of the 2D material itself. Our work highlights the unique opportunities for shaping electron energy landscapes in 2D materials by dielectric engineering without altering the atomic or electronic integrity of the 2D material itself.

III. METHOD

All calculations have been performed with the electronic structure software code GPAW [42]. The atomic structures

were relaxed using PBE with a plane-wave cut-off energy of 800 eV, on a k -point grid with a density of 6.0 \AA^{-3} , and with a Fermi smearing of 0.05 eV. All structures were relaxed until the maximum force on any atoms was 0.01 eV/\AA and the maximum stress on the unit cell was 0.002 eV/\AA^3 . The ground state was calculated using the same parameters as for the relaxation, but with a k -point grid of 12.0 \AA^{-3} . The GW calculations were performed starting from the PBE wave functions. Three GW calculations were done with a cut-off energy for the self-energy of 170, 185, and 200 eV from which the band gap was determined by extrapolating to an infinite plane-wave cut-off. The electronic band gaps for the van der Waals heterostructures were determined by calculating the screening correction to the valence and conduction bands for the freestanding monolayer semiconductor in the QEH model [33] which have previously been shown to yield accurate results for heterostructures with a low degree of hybridization at the band edges. The static polarizabilities are calculated within the random phase approximation (RPA), which were based on a PBE ground state calculation with a 20 \AA^{-3} k -point density grid and a cut-off energy of 50 eV was used for the RPA calculation. In both the GW and the RPA calculations a truncated Coulomb interaction was used. All band structure calculations are calculated including spin-orbit interaction.

ACKNOWLEDGMENTS

This project has received funding from the European Research Council (ERC) under the European Union's Horizon 2020 Research and Innovation Programme (Grant Agreement No. 773122, LIMA). The Center for Nanostructured Graphene is sponsored by the Danish National Research Foundation, Project No. DNR103.

-
- [1] A. C. Ferrari, F. Bonaccorso, V. Fal'Ko, K. S. Novoselov, S. Roche, P. Bøggild, S. Borini, F. H. Koppens, V. Palermo, N. Pugno *et al.*, *Nanoscale* **7**, 4598 (2015).
 - [2] K. Novoselov, A. Mishchenko, A. Carvalho, and A. C. Neto, *Science* **353**, aac9439 (2016).
 - [3] A. Gupta, T. Sakthivel, and S. Seal, *Prog. Mater. Sci.* **73**, 44 (2015).
 - [4] F. Withers, O. Del Pozo-Zamudio, A. Mishchenko, A. Rooney, A. Gholinia, K. Watanabe, T. Taniguchi, S. Haigh, A. Geim, A. Tartakovskii *et al.*, *Nat. Mater.* **14**, 301 (2015).
 - [5] J. S. Ross, P. Klement, A. M. Jones, N. J. Ghimire, J. Yan, D. Mandrus, T. Taniguchi, K. Watanabe, K. Kitamura, W. Yao *et al.*, *Nat. Nanotechnol.* **9**, 268 (2014).
 - [6] K. S. Thygesen, *2D Mater.* **4**, 022004 (2017).
 - [7] H. J. Conley, B. Wang, J. I. Ziegler, R. F. Haglund, Jr., S. T. Pantelides, and K. I. Bolotin, *Nano Lett.* **13**, 3626 (2013).
 - [8] A. Castellanos-Gomez, R. Roldán, E. Cappelluti, M. Buscema, F. Guinea, H. S. van der Zant, and G. A. Steele, *Nano Lett.* **13**, 5361 (2013).
 - [9] K. F. Mak, C. Lee, J. Hone, J. Shan, and T. F. Heinz, *Phys. Rev. Lett.* **105**, 136805 (2010).
 - [10] A. Splendiani, L. Sun, Y. Zhang, T. Li, J. Kim, C.-Y. Chim, G. Galli, and F. Wang, *Nano Lett.* **10**, 1271 (2010).
 - [11] L. A. Jauregui, A. Y. Joe, K. Pistunova, D. S. Wild, A. A. High, Y. Zhou, G. Scuri, K. De Greve, A. Sushko, C.-H. Yu *et al.*, *Science* **366**, 870 (2019).
 - [12] A. C. Riis-Jensen, M. Pandey, and K. S. Thygesen, *J. Phys. Chem. C* **122**, 24520 (2018).
 - [13] F. Hüser, T. Olsen, and K. S. Thygesen, *Phys. Rev. B* **87**, 235132 (2013).
 - [14] M. S. Hybertsen and S. G. Louie, *Phys. Rev. B* **34**, 5390 (1986).
 - [15] S. Kubatkin, A. Danilov, M. Hjort, J. Cornil, J.-L. Brédas, N. Stühr-Hansen, P. Hedegård, and T. Bjørnholm, *Nature (London)* **425**, 698 (2003).
 - [16] J. Repp, G. Meyer, S. M. Stojković, A. Gourdon, and C. Joachim, *Phys. Rev. Lett.* **94**, 026803 (2005).
 - [17] M. L. Perrin, C. J. Verzijl, C. A. Martin, A. J. Shaikh, R. Eelkema, J. H. Van Esch, J. M. Van Ruitenbeek, J. M. Thijssen, H. S. Van Der Zant, and D. Dulić, *Nat. Nanotechnol.* **8**, 282 (2013).
 - [18] J. B. Neaton, M. S. Hybertsen, and S. G. Louie, *Phys. Rev. Lett.* **97**, 216405 (2006).

- [19] J. M. Garcia-Lastra, C. Rostgaard, A. Rubio, and K. S. Thygesen, *Phys. Rev. B* **80**, 245427 (2009).
- [20] C. Freysoldt, P. Rinke, and M. Scheffler, *Phys. Rev. Lett.* **103**, 056803 (2009).
- [21] S. Y. Quek, L. Venkataraman, H. J. Choi, S. G. Louie, M. S. Hybertsen, and J. Neaton, *Nano Lett.* **7**, 3477 (2007).
- [22] M. Strange, C. Rostgaard, H. Häkkinen, and K. S. Thygesen, *Phys. Rev. B* **83**, 115108 (2011).
- [23] M. Strange and K. S. Thygesen, *Phys. Rev. B* **86**, 195121 (2012).
- [24] C. Jin and K. S. Thygesen, *Phys. Rev. B* **89**, 041102(R) (2014).
- [25] M. M. Ugeda, A. J. Bradley, S.-F. Shi, H. Felipe, Y. Zhang, D. Y. Qiu, W. Ruan, S.-K. Mo, Z. Hussain, Z.-X. Shen *et al.*, *Nat. Mater.* **13**, 1091 (2014).
- [26] J. Ryou, Y.-S. Kim, K. Santosh, and K. Cho, *Sci. Rep.* **6**, 29184 (2016).
- [27] M. Rosner, C. Steinke, M. Lorke, C. Gies, F. Jahnke, and T. O. Wehling, *Nano Lett.* **16**, 2322 (2016).
- [28] A. Raja, A. Chaves, J. Yu, G. Arefe, H. M. Hill, A. F. Rigosi, T. C. Berkelbach, P. Nagler, C. Schüller, T. Korn *et al.*, *Nat. Commun.* **8**, 15251 (2017).
- [29] K. T. Winther and K. S. Thygesen, *2D Mater.* **4**, 025059 (2017).
- [30] Y. J. Zheng, Y. L. Huang, Y. Chen, W. Zhao, G. Eda, C. D. Spataru, W. Zhang, Y.-H. Chang, L.-J. Li, D. Chi *et al.*, *ACS Nano* **10**, 2476 (2016).
- [31] D. Y. Qiu, F. H. da Jornada, and S. G. Louie, *Nano Lett.* **17**, 4706 (2017).
- [32] Z. Qiu, M. Trushin, H. Fang, I. Verzhbitskiy, S. Gao, E. Laksono, M. Yang, P. Lyu, J. Li, J. Su *et al.*, *Sci. Adv.* **5**, eaaw2347 (2019).
- [33] K. Andersen, S. Latini, and K. S. Thygesen, *Nano Lett.* **15**, 4616 (2015).
- [34] F. Aryasetiawan and O. Gunnarsson, *Rep. Prog. Phys.* **61**, 237 (1998).
- [35] D. Golze, M. Dvorak, and P. Rinke, *Front. Chem.* **7**, 377 (2019).
- [36] M. Rohlfing, *Phys. Rev. B* **82**, 205127 (2010).
- [37] K. Noori, N. L. Q. Cheng, F. Xuan, and S. Y. Quek, *2D Mater.* **6**, 035036 (2019).
- [38] S. Hastrup, M. Strange, M. Pandey, T. Deilmann, P. S. Schmidt, N. F. Hinsche, M. N. Gjerding, D. Torelli, P. M. Larsen, A. C. Riis-Jensen *et al.*, *2D Mater.* **5**, 042002 (2018).
- [39] J. M. Garcia-Lastra and K. S. Thygesen, *Phys. Rev. Lett.* **106**, 187402 (2011).
- [40] A. Raja, L. Waldecker, J. Zipfel, Y. Cho, S. Brem, J. D. Ziegler, M. Kulig, T. Taniguchi, K. Watanabe, E. Malic *et al.*, *Nat. Nanotechnol.* **14**, 832 (2019).
- [41] S. Gao, Y. Liang, C. D. Spataru, and L. Yang, *Nano Lett.* **16**, 5568 (2016).
- [42] J. Enkovaara, C. Rostgaard, J. J. Mortensen, J. Chen, M. Dułak, L. Ferrighi, J. Gavnholt, C. Glinsvad, V. Haikola, H. A. Hansen, H. H. Kristoffersen, M. Kuisma, A. H. Larsen, L. Lehtovaara, M. Ljungberg, O. Lopez-Acevedo, P. G. Moses, J. Ojanen, T. Olsen, V. Petzold *et al.*, *J. Phys.: Condens. Matter* **22**, 253202 (2010).

8.2 Paper II

Anomalous Non-Hydrogenic Exciton Series in 2D Materials on High- κ Dielectric Substrates

A. C. Riis-Jensen, M. N. Gjerding, S. Russo, and K. S. Thygesen

Under review

Anomalous Non-Hydrogenic Exciton Series in 2D Materials on High- κ Dielectric Substrates

Anders C. Riis-Jensen,¹ Morten N. Gjerding,¹ Saverio Russo,² and Kristian S. Thygesen¹

¹*Center for Atomic-scale Materials Design, Department of Physics, Technical University of Denmark, DK - 2800 Kongens Lyngby, Denmark*

²*Centre for Graphene Science, College of Engineering, Mathematics and Physical Sciences, University of Exeter, Exeter EX4 4QL, UK*

(Dated: June 25, 2020)

Engineering of the dielectric environment represents a powerful strategy to control the electronic and optical properties of two-dimensional (2D) materials without compromising their structural integrity. Here we show that the recent development of high- κ 2D materials present new opportunities for dielectric engineering. By solving a 2D Mott-Wannier exciton model for WSe₂ on different substrates using a screened electron-hole interaction obtained from first principles, we demonstrate that the exciton Rydberg series changes qualitatively when the dielectric screening within the 2D semiconductor becomes dominated by the substrate. In this regime, the distance dependence of the screening is reversed and the effective screening increases with exciton radius, which is opposite to the conventional 2D screening regime. Consequently, higher excitonic states become underbound rather than overbound as compared to the Hydrogenic Rydberg series. Finally, we derive a general analytical expression for the exciton binding energy of the entire 2D Rydberg series.

Intense research during the past decade has established the unique optical properties of two-dimensional (2D) semiconductors such as single layers of transition metal dichalcogenides (MX₂ and MX₂Y with M=Mo,W and X=S,Se,Te)¹⁻⁵. Most fundamentally, these ultrathin materials host strongly bound excitons with binding energies reaching up to 25% of the band gap⁶⁻⁸ making them candidates for excitonic devices that can be operated at room temperature. Another unique feature is the extreme degree to which these excitons can be manipulated and controlled externally, e.g. via the dielectric environment⁹⁻¹⁶. Higher-lying excitonic states also exhibit unusual properties. In particular, the Rydberg series does not follow the $1/n^2$ Hydrogenic series known from 3D materials, but show a distinct non-Hydrogenic behavior as a direct consequence of the non-local nature of the 2D dielectric function^{17,18}. For a translation invariant system the q -dependent dielectric function obeys

$$\epsilon(\mathbf{q}) = \int d(\mathbf{r} - \mathbf{r}') \epsilon(\mathbf{r} - \mathbf{r}') e^{i\mathbf{q} \cdot (\mathbf{r} - \mathbf{r}')} \quad (1)$$

From this it follows that non-locality in real space translates into q -dependence in reciprocal space. In bulk semiconductors it is typically a good approximation to set $\epsilon(\mathbf{r} - \mathbf{r}') = \epsilon\delta(\mathbf{r} - \mathbf{r}')$, which yields a q -independent dielectric function. In contrast, for a freestanding 2D semiconductor $\epsilon(q) = 1 + \alpha q$ (for small q), from which it follows that screening in 2D is notoriously non-local. Furthermore, it has been shown that the dielectric function of a 2D material is sensitive to its dielectric environment, e.g. a substrate. However, with a few notable exceptions^{19,20}, all experiments on excitons in 2D semiconductors reported to date employed substrates with weak dielectric screening, e.g. hBN, SiO₂ or sapphire²¹⁻²⁴. As a consequence, the developed theory of excitons in atomically thin materials have also exclusively focused on this sce-

nario.

In this work, we explore what happens to the excitonic states of a 2D semiconductor, here exemplified by WSe₂, when the dielectric screening inside the 2D material becomes dominated by the environment. For WSe₂ on low-screening substrates we obtain the well known non-hydrogenic exciton series^{17,25} where higher exciton states are screened less than the $n = 1$ ground state. Here we show that this trend is reversed when the dielectric screening from the substrate exceeds the intrinsic screening in the 2D layer. At the end we generalize the 2D hydrogen-like model previously developed²⁵ for the exciton effective dielectric constant in a 2D semiconductor to include the effect of neighbouring substrate screening and obtain excellent agreement with numerical solutions.

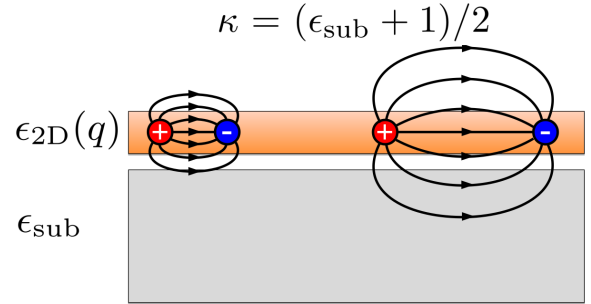


FIG. 1. A 2D layer with non-local, i.e. q -dependent, dielectric function located on a dielectric media with constant permittivity. The extension of the electric field lines from two 2D excitons with different spatial radius is depicted. The larger the exciton radius, the more the screening is determined by the environment outside the 2D material.

The excitonic states of the WSe₂ monolayer are obtained by solving the Mott-Wannier equation for the ex-

citon envelope wave function

$$\left[-\frac{\hbar^2}{2\mu} \left(\frac{\partial^2}{\partial x^2} + \frac{\partial^2}{\partial y^2} \right) + W(\mathbf{r}) \right] F(\mathbf{r}) = E_n F(\mathbf{r}) \quad (2)$$

where μ is the exciton effective mass, $W(\mathbf{r})$ is the screened electron-hole interaction, E_n the binding energy of state n , and $F(\mathbf{r})$ is the probability amplitude for finding the electron and hole at separation \mathbf{r} . We use an exciton mass for WSe₂ of $\mu = 0.187$ adopted from the Computational 2D Materials Database²⁶ To calculate the screened interaction between the electron and hole in the 2D layer we use the Quantum Electrostatic Heterostructure (QEH) model²⁷, which has previously been shown to yield accurate energies for excitons in van der Waals heterostructures^{28,29}. The QEH model takes the *ab-initio* response functions of the 2D layer as input and thus accounts fully for the non-local screening in the monolayer. Screening from the environment is taken into account by the method of image charges. We define the effective permittivity of the environment as $\kappa = (\epsilon_{\text{sub}} + 1)/2$, where ϵ_{sub} and 1 are the permittivities of the half spaces above and below the 2D material, see Fig. 1. We here restrict our calculations to merely consider a 2D monolayer on a dielectric substrate. We do this since by the virtue of the definition of κ , the results obtained for a 2D monolayer on a dielectric substrate with dielectric constant ϵ_a , will be quantitatively very close to the same 2D monolayer encapsulated between two substrates, both with dielectric constants $\epsilon_a/2$, and therefore this method is straightforward to generalize to the case of an encapsulated 2D monolayer. All future calculations and references for substrates therefore addresses the setup in Fig. 1 with a substrate on one side and vacuum on the other side.

Before turning to the results of the exciton calculations, we discuss how the dielectric function of the WSe₂ monolayer is influenced by the dielectric environment. We define the dielectric function of the 2D monolayer by

$$\epsilon(q) \equiv \frac{V(q)}{W(q)} \quad (3)$$

where $V(q) = 1/q$ is the 2D Fourier transform of $1/r$ and $W(q)$ is the screened Coulomb interaction between two point charges in the 2D layer as obtained from the QEH model. In Fig. 2 we show the dielectric function of freestanding WSe₂ (black), WSe₂ on a weakly screening substrate (blue, denoted S1), and a strongly screening substrate (red, denoted S2). The horizontal dashed lines (κ_{2D} , κ_{S1} , and κ_{S2}) mark the $q = 0$ limits of the dielectric functions, which equal the effective permittivity of the environment (see below). We note that, $\kappa_{S2} = 13$, could easily be realized upon encapsulation of WSe₂ in the high-layered materials HfOx^{30,31}, while the $\kappa_{S1} = 2.5$ corresponds to WSe₂ on a hBN substrate.

We can rationalize the small- q behaviour of the dielectric functions in Fig. 2, by combining two basic facts about screening in 2D. Firstly, in the small q -limit, the

density response function of a semiconductor takes the form, $\chi^0(q) = -\alpha q^2$ (independent of dimensionality). Secondly, the electrostatic potential from a 2D charge distribution of the form $\rho(\mathbf{r}, z) = e^{i\mathbf{q}\cdot\mathbf{r}}\delta(z)$, equals

$$V(\mathbf{r}, z) = \frac{1}{q} e^{i\mathbf{q}\cdot\mathbf{r}} e^{-q|z|}. \quad (4)$$

Focusing first on the case of an isolated 2D layer, i.e. ignoring the z -dependence, the dielectric function becomes $\epsilon_{2D}(q) = 1 - V(q)\chi^0(q) = 1 + \alpha q$. In particular, there is no intrinsic screening from the 2D layer in the $q \rightarrow 0$ limit. Next, consider the effect of a substrate. It should be clear from Eq. (4), that in the $q = 0$ limit all screening is due to the environment and thus $\epsilon(0) = \kappa$ (potentials do not decay away from the layer and there is no intrinsic screening from the layer itself). Moreover, the contribution to the dielectric function from the environment will be exponentially suppressed for larger q . These considerations are evidently in agreement with the results in Fig. 2. Interestingly, when κ becomes comparable to the maximum permittivity of the 2D layer, $\epsilon(q)$ changes qualitatively; in particular, the slope at $q = 0$ changes from positive to negative.

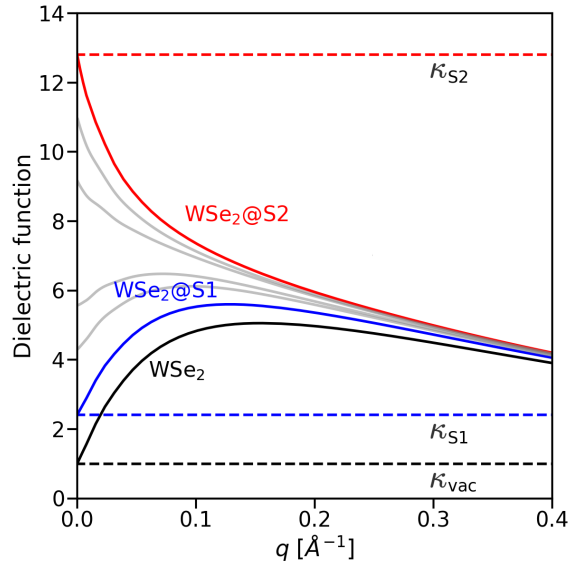


FIG. 2. The \mathbf{q} -dependent dielectric function of monolayer WSe₂ in isolation (black), in a weakly screening environment (blue), and in a strongly screening environment (red). In the limit $q \rightarrow 0$, the dielectric function becomes equal to the constant permittivity of the environment, κ . When the screening from the environment exceeds the intrinsic screening in WSe₂, the slope of $\epsilon(q)$ at $q = 0$ changes from positive to negative. The light gray lines show intermediate systems illustrating the transition from one screening regime to the other.

At this point we return to the Mott-Wannier exciton model Eq. (2). It is well known that the exciton Ryd-

berg series in a 2D semiconductor is distinctly different from the usual Hydrogenic series observed in 3D bulk materials¹⁷. This can be understood as a direct consequence of $\epsilon(q)$ being an increasing function of q in the relevant wavevector range from 0 to around $1/a$ where a is a characteristic exciton size ($a > 10 \text{ \AA}$) for the TMDs. This form of $\epsilon(q)$ results in excitons with higher n being less screened due to their more delocalized nature²⁵ (more delocalized in real space corresponds to more localized in reciprocal space). This trend is reflected by the black symbols in Fig. 3, which shows the binding energies obtained from Eq. (2) for the lowest ($l = 0$) exciton states of freestanding WSe₂ normalized to the $n = 1$ state. As a reference, the grey curve shows the result for a 2D Hydrogen model

$$E_n^{\text{Hydrogen}} = -\frac{\mu}{2(n - \frac{1}{2})^2 \kappa^2}. \quad (5)$$

Note that the constant permittivity, κ , and exciton mass, μ , do not enter the scaled binding energy, $E_n^{\text{Hydrogen}}/E_1^{\text{Hydrogen}}$, which can thus be taken as a universal curve corresponding to the situation of local screening.

When WSe₂ is placed in a weakly screening environment, e.g. on an hBN substrate corresponding to the blue curve in Fig. 2, the scaled exciton binding energies move closer to the Hydrogenic series but still display the same trend of higher excitonic states being underscreened relative to the $n = 1$ ground state. In contrast, when WSe₂ is placed in a strongly screening environment, e.g. encapsulated in HfO_x corresponding to the red curve in Fig. 2, the exciton binding energies move below the Hydrogenic series. This marks a new screening regime in which the excitons become more efficiently screened the larger n .

To understand the transition to the new exciton screening regime, we calculate the exciton wave function for the three cases studied in Figs. 2 and 3 and from this extract the exciton radius for the first six states in the Rydberg series. We find an increasing exciton radius for higher states in the Rydberg series as well known from the hydrogen atom model. For the $n = 1$ state of the freestanding monolayer, we obtain an exciton radius around 16 \AA in good agreement with previous results³². We can define an effective dielectric constant for the n th exciton state by averaging the q -dependent dielectric function over a disc with radius $1/a_n$

$$\langle \epsilon_n \rangle = 2a_n^2 \int_0^{1/a_n} dq q \epsilon(q). \quad (6)$$

The result is shown in Fig. 4 represented by the circular dots. As the exciton radius increases monotonically with n the size of the averaging disc shrinks and the effective dielectric constant $\langle \epsilon_n \rangle$ increases or decreases with n depending on the sign of $d\epsilon/dq$ at $q = 0$.

It is instructive to supplement the reciprocal-space analysis by a real space picture. As shown in Fig. 1, an increasingly larger fraction of the field lines between

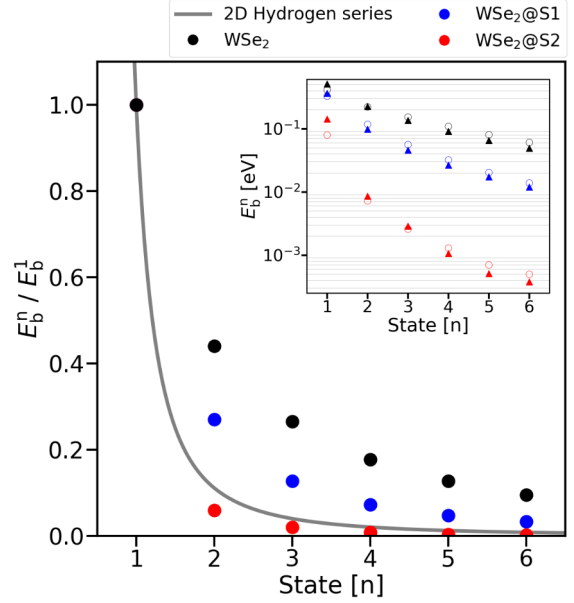


FIG. 3. Exciton Rydberg series of WSe₂ plotted relative to the $n = 1$ state. The different colors represent the exciton binding energies obtained from the Mott-Wannier model with environmental screening corresponding to the three dielectric functions in Fig. 2. The universal Hydrogenic series is shown by the grey curve. The inset shows the actual exciton binding energies for the Mott-Wannier model (triangles) and from Eq. 5, with the analytical expression for the effective screening, Eq. 7 (empty circles)

the electron and hole will pass through the environment as the exciton radius increases. Therefore, as n increases the effective screening will change from being dominated by the 2D layer to being dominated by the environment. Consequently, whether screening of the exciton will increase or decrease with n is determined by the permittivity of the environment relative to the intrinsic permittivity of the 2D layer.

We now derive an analytical expression for the effective dielectric constant determining the screening of the exciton. We do this by generalizing the previously developed screened Hydrogen model developed in Ref.²⁵ for freestanding 2D layers, to include the dielectric screening from a substrate. First we note that the exciton wave functions in reciprocal space, i.e. $F(q)$, are typically confined to small q -values where the intrinsic dielectric function of the 2D layer is linear. We therefore take $\epsilon(q) \approx 1 + 2\pi\alpha q + \kappa e^{-2dq}$, where α is the 2D static polarizability and d is the distance between the center of the 2D layer and the surface of the substrate (the factor 2 accounts for the distance to the image charge). The linear term describes the intrinsic screening from the 2D semiconductor while the last term is the substrate screening which decays exponentially away from the sub-

strate as discussed previously. Since the exciton radius (a_n) is itself a function of the effective exciton dielectric constant²⁵, Eq. (6) has to be solved self-consistently with the proposed form of $\epsilon(q)$. The integration can be readily carried out analytically, however to obtain a closed analytical form we Taylor expand the exponential term around d/a_n after integration, which is in general a good approximation for the the integration limits in eq. 6. Given the large spatial extension of the exciton wave function for the higher Rydberg states the accuracy of this approximation increases with n . To relate $\langle\epsilon_n\rangle$ and a_n we use the relation from the ideal 2D hydrogen model with angular momentum quantum number $l = 0$ (see for instance Ref.²⁵). Combining this we arrive at an expression for the effective exciton dielectric constant:

$$\langle\epsilon_n\rangle = \frac{1}{2}(1 + \kappa) \left(1 + \sqrt{1 + \frac{8\mu \left(\frac{4}{3}\pi\alpha - \kappa d\right)}{(3n(n-1) + 1)(1 + \kappa)^2}} \right). \quad (7)$$

The result plotted in Fig. 4 (full lines) shows good agreement with the QE model for both low- and high- κ substrates and demonstrating that the analytical expression captures the combined effect of intrinsic 2D and the substrate screening. We stress that the analytical Eq. (7) contains no free parameters, but is completely defined by α , κ , and d . The exciton binding energy can be obtained from the 2D Hydrogen model, Eq. 5, by replacing the κ by the effective exciton dielectric constant. Except for underestimating the exciton binding energy of the 1s state for the 2D and 2D@S2 systems of about 100 meV and 50 meV respectively, we find excellent agreement for all other Rydberg states, generally within about 15 % compared to the QE results, as shown in the inset of Fig. 3. The underestimated value of the exciton binding energy for the 1s state was also found in the original work on freestanding 2D monolayers²⁵ and can be ascribed to the larger extent of $F(q)$ for the 1s state which reduces the accuracy of the linear approximation to the intrinsic 2D screening, $\epsilon_{2D}(q) \approx 1 + 2\pi\alpha q$. In fact this approximation overestimates the intrinsic screening for larger q leading to an underestimation of the binding energy for the spatially localized 1s exciton.

Finally, we comment on the absolute size of the exciton binding energies. While the first few states of the Rydberg series of WSe₂ on the weakly screening substrate ($\kappa = 2.5$) are at least 100 meV, the 1s state in the strongly screening environment ($\kappa = 13$) has a binding energy around 140 meV which is reduced by more than a factor 10 for the 2s state, making it unstable at room temperature. By inserting 3 (or more) layers of hBN ($\epsilon_{\text{hBN}} = 4$) between WSe₂ and the substrate, the binding energy of the 2s state increases to 40 meV, making it stable at room temperature. While the exciton binding energies are significantly increased, the system remains in the anomalous screening regime.

In conclusion, we have identified a new screening regime for 2D semiconductors, which arises when the 2D material is placed in a dielectric environment with

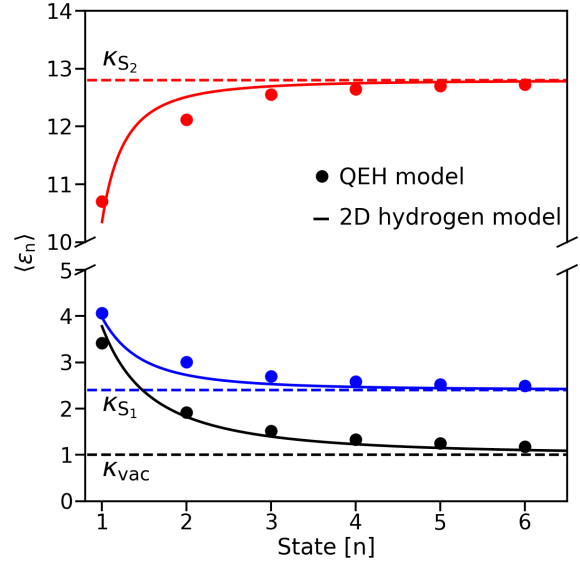


FIG. 4. Effective state-dependent dielectric constant for the excitons in the Rydberg series of WSe₂ (circular dots), see definition in Eq. 6, and from the analytical solution (full lines), see definition in Eq. 7. The different colors correspond to WSe₂ in different screening environments and the colour coding follows the previous figures. For $n \rightarrow \infty$, the effective dielectric constants converge towards the permittivity of the environment, κ .

a permittivity exceeding that of the 2D layer itself. This anomalous screening regime is characterized by a non-local 2D dielectric function, $\epsilon(q)$, which decreases monotonically with q . As a consequence, whereas the usual non-Hydrogenic 2D exciton Rydberg series is characterized by states of higher n being less screened and therefore stronger bound as compared to the Hydrogen series, the opposite trend is observed in the anomalous 2D screening regime. The new screening regime presents new opportunities for advancing our understanding and ability to control exciton physics in 2D semiconductors.

ACKNOWLEDGMENTS

The Center for Nanostructured Graphene (CNG) is sponsored by the Danish Research Foundation, Project DNRF103. The project has received funding from the European Research Council (ERC) under the European Union's Horizon 2020 research and innovation programme (Grant No. 773122, LIMA). SR acknowledges financial support by RC-UK EPSRC (EP/K010050/1 and EP/L015331/1) and the Leverhulme Trust (Research grant: Quantum revolution).

-
- ¹ K. F. Mak, C. Lee, J. Hone, J. Shan, and T. F. Heinz, *Physical review letters* **105**, 136805 (2010).
- ² T. Cheiwchanhangij and W. R. Lambrecht, *Physical Review B* **85**, 205302 (2012).
- ³ W. Zhao, Z. Ghorannevis, L. Chu, M. Toh, C. Kloc, P.-H. Tan, and G. Eda, *ACS nano* **7**, 791 (2013).
- ⁴ A. Molina-Sánchez, M. Palummo, A. Marini, and L. Wirtz, *Physical Review B* **93**, 155435 (2016).
- ⁵ A. C. Riis-Jensen, T. Deilmann, T. Olsen, and K. S. Thygesen, *ACS nano* **13**, 13354 (2019).
- ⁶ A. Ramasubramaniam, *Physical Review B* **86**, 115409 (2012).
- ⁷ D. Y. Qiu, H. Felipe, and S. G. Louie, *Physical review letters* **111**, 216805 (2013).
- ⁸ C. Zhang, H. Wang, W. Chan, C. Manolatou, and F. Rana, *Physical Review B* **89**, 205436 (2014).
- ⁹ D. A. Ruiz-Tijerina and V. I. Fal'ko, *Physical Review B* **99**, 125424 (2019).
- ¹⁰ C. Jin, E. C. Regan, A. Yan, M. I. B. Utama, D. Wang, S. Zhao, Y. Qin, S. Yang, Z. Zheng, S. Shi, *et al.*, *Nature* **567**, 76 (2019).
- ¹¹ M. L. Trolle, T. G. Pedersen, and V. Véniard, *Scientific reports* **7**, 39844 (2017).
- ¹² S. Borghardt, J.-S. Tu, F. Winkler, J. Schubert, W. Zander, K. Leosson, and B. E. Kardynał, *Physical Review Materials* **1**, 054001 (2017).
- ¹³ S. Park, N. Mutz, T. Schultz, S. Blumstengel, A. Han, A. Aljarb, L.-J. Li, E. J. List-Kratochvil, P. Amsalem, and N. Koch, *2D Materials* **5**, 025003 (2018).
- ¹⁴ A. Raja, A. Chaves, J. Yu, G. Arefe, H. M. Hill, A. F. Rigosi, T. C. Berkelbach, P. Nagler, C. Schüller, T. Korn, *et al.*, *Nature communications* **8**, 1 (2017).
- ¹⁵ A. Steinhoff, T. Wehling, and M. Rösner, *Physical Review B* **98**, 045304 (2018).
- ¹⁶ Y. Lin, X. Ling, L. Yu, S. Huang, A. L. Hsu, Y.-H. Lee, J. Kong, M. S. Dresselhaus, and T. Palacios, *Nano letters* **14**, 5569 (2014).
- ¹⁷ A. Chernikov, T. C. Berkelbach, H. M. Hill, A. Rigosi, Y. Li, O. B. Aslan, D. R. Reichman, M. S. Hybertsen, and T. F. Heinz, *Physical review letters* **113**, 076802 (2014).
- ¹⁸ E. Liu, J. van Baren, T. Taniguchi, K. Watanabe, Y.-C. Chang, and C. H. Lui, *Physical Review B* **99**, 205420 (2019).
- ¹⁹ M. M. Ugeda, A. J. Bradley, S.-F. Shi, H. Felipe, Y. Zhang, D. Y. Qiu, W. Ruan, S.-K. Mo, Z. Hussain, Z.-X. Shen, *et al.*, *Nature materials* **13**, 1091 (2014).
- ²⁰ Z. Qiu, M. Trushin, H. Fang, I. Verzhbitskiy, S. Gao, E. Laksono, M. Yang, P. Lyu, J. Li, J. Su, *et al.*, *Science advances* **5**, eaaw2347 (2019).
- ²¹ H.-P. Komsa and A. V. Krasheninnikov, *Physical Review B* **86**, 241201 (2012).
- ²² W.-T. Hsu, J. Quan, C.-Y. Wang, L.-S. Lu, M. Campbell, W.-H. Chang, L.-J. Li, X. Li, and C.-K. Shih, *2D Materials* **6**, 025028 (2019).
- ²³ J. Yan, S.-Y. Chen, T. Goldstein, T. Taniguchi, K. Watanabe, and J. Tong, *Bulletin of the American Physical Society* **63** (2018).
- ²⁴ D. Y. Qiu, F. H. da Jornada, and S. G. Louie, *Nano letters* **17**, 4706 (2017).
- ²⁵ T. Olsen, S. Latini, F. Rasmussen, and K. S. Thygesen, *Physical review letters* **116**, 056401 (2016).
- ²⁶ S. Hastrup, M. Strange, M. Pandey, T. Deilmann, P. S. Schmidt, N. F. Hinsche, M. N. Gjerding, D. Torelli, P. M. Larsen, A. C. Riis-Jensen, *et al.*, *2D Materials* **5**, 042002 (2018).
- ²⁷ K. Andersen, S. Latini, and K. S. Thygesen, *Nano letters* **15**, 4616 (2015).
- ²⁸ A. C. Riis-Jensen, M. Pandey, and K. S. Thygesen, *The Journal of Physical Chemistry C* **122**, 24520 (2018).
- ²⁹ S. Latini, K. T. Winther, T. Olsen, and K. S. Thygesen, *Nano letters* **17**, 938 (2017).
- ³⁰ A. De Sanctis, I. Amit, S. P. Hepplestone, M. F. Craciun, and S. Russo, *Nature communications* **9**, 1 (2018).
- ³¹ N. Peimyoo, M. Barnes, J. Mehew, A. De Sanctis, I. Amit, J. Escolar, K. Anastasiou, A. Rooney, S. Haigh, S. Russo, *et al.*, *Science advances* **5**, eaau0906 (2019).
- ³² S. Latini, T. Olsen, and K. S. Thygesen, *Physical Review B* **92**, 245123 (2015).

8.3 Paper III

Functional Dielectric Screening for Potential Well Arrays of Excitons in 2D Materials

N. Peimyoo, H.-Y. Wu, J. Escolar, A. De Sanctis, G. Prando, F. Vollmer, F. Withers, K. S. Thygesen, A. C. Riis-Jensen, M. F. Craciun, and S. Russo

Under review

Functional dielectric screening for potential well arrays of excitons in 2D materials

N. Peimyoo¹, H.-Y. Wu², J. Escolar¹, A. De Sanctis¹, G. Prando¹, F. Vollmer², F. Withers¹, K. S. Thygesen^{3,4}, A.C. Riis-Jensen^{3,4}, M. F. Craciun¹, S. Russo^{1*}

¹Centre for Graphene Science, College of Engineering, Mathematics and Physical Sciences, University of Exeter, Exeter EX4 4QL, UK.

²Living Systems Institute, Department of Physics and Astronomy, University of Exeter, Exeter EX4 4QD, UK.

³CAMD, Department of Physics Technical University of Denmark, DK-2800 Kongens Lyngby, Denmark, DK-2800 Kongens Lyngby, Denmark

⁴Center for Nanostructured Graphene (CNG), Department of Physics, Technical University of Denmark, DK-2800 Kongens Lyngby, Denmark

*Corresponding author. Email: S.Russo@exeter.ac.uk

Abstract

Tailoring of the band gap in semiconductors is essential to the development of novel devices. In standard semiconductors this modulation is generally achieved through highly energetic ion implantation. In two-dimensional (2D) materials the photo-physical properties are strongly sensitive to the surrounding dielectric environment presenting novel opportunities through van der Waal heterostructures encompassing atomically thin high- κ dielectrics. Here we demonstrate a giant tuning of the exciton binding energy of monolayer WSe₂ as a function of the dielectric environment. Upon increasing the average dielectric constant from 2.4 to 15, the exciton binding energy is reduced by as much as 300 meV in ambient conditions. The experimentally determined exciton binding energies are in excellent agreement with the theoretical values predicted from a Mott-Wannier exciton model with parameters derived from first principles calculations. Finally we show how texturing of the dielectric environment can be used to realize potential well arrays for excitons in 2D materials, that is a first step towards exciton metamaterials.

Introduction

The reduced dimensionality characterizing atomically thin materials, such as the semiconducting two-dimensional transition metal dichalcogenides (2D-TMDs), leads to strongly reduced screening of the Coulomb interaction. This results in a large binding energy of neutral excitons of up to 1 eV (1-4), which is dependent on the dielectric constant of the surrounding environment (5-8). Therefore, at room temperature the optical properties of 2D materials are largely dominated by the physics of excitons. Understanding the underpinning physics of 2D excitons is essential to enable novel integrated photonics based on these quasiparticles. For example, the electric field manipulation of the oscillator strength of one exciton species in a field-effect gated 2D-TMD transistor embedded in an optical microcavity was recently shown to alter the nature of multiple hybridizations of exciton-polariton states (9). Such a modulation enabled the observation of room temperature exciton energy exchange between spatially separated TMDs in a microcavity (10), which is a first step towards the wireless exchange of information embedded in the valley degree of freedom of charges.

The exciton binding energy of monolayer TMDs can be experimentally determined by optical spectroscopy measurements displaying features associated to the excitons excited states known as Rydberg states. These states are directly measurable by means of optical reflectivity (11, 12), linear absorption (12, 13), one- and two-photon photoluminescence excitation (13-15) and second-harmonic spectroscopy (16). Very recently, the Rydberg series has been observed in the photoluminescence spectra of ultra clean monolayer WSe₂ encapsulated in hBN (17). In the linear optical spectra, the s-like Rydberg states of the A exciton in monolayer TMDs have been found to exhibit many interesting properties including non-hydrogenic behaviour (11) driven by due the non-local nature of 2D dielectric screening (18), superior valley polarization and coherence (19), and Zeeman splitting under magnetic field (17, 20) generating a wide interest in the scientific community.

Earlier experimental work explored the modification of the exciton binding energy (E_b) and quasiparticle gap of 2D-TMDs in contact with low- κ dielectrics (e.g. hBN, sapphire, semimetal and PDMS substrates (17-19)) with a relative dielectric constant smaller than or equal to that of the TMDs [The complexity of the problem grows upon reducing the thickness of the TMDs down to the monolayer for which the dielectric permittivity is a linear function of the wave-vector in the small wavelength limit.] The experimental results have been explained by solution of a Mott-Wannier type exciton model which depicts the exciton as a 2D Hydrogenic atom with a Coulomb interaction screened by the substrate and the monolayer itself (21-24). However, this scenario can now be enriched by the recent discovery of 2D high- k dielectrics such as photo-oxidised HfO_x and ferroelectrics leading to an average dielectric constant of the environment larger than that of the 2D semiconductors. Such novel dielectrics could enable a breakthrough in the giant modulation of the exciton binding energy in 2D materials, with textured high- k dielectrics possibly used for creating potential profiles able to guide or confine excitons. At the same time, this innovation can mark the birth of exciton metamaterials whereby the collective response of an array of

exciton potential wells depends on the geometrical characteristics of the array and differs profoundly from the response of an isolated individual potential well.

In this work, we explore, both experimentally and theoretically, the effect on the exciton binding energy and quasiparticle band gap of monolayer WSe_2 when placed in a dielectric environment with dielectric screening lower than, comparable to, and larger than the intrinsic screening in WSe_2 , respectively. A systematic study of the optical transmission for WSe_2 in various dielectric environments (quartz, hBN, photo-oxidised HfO_x and ferroelectric In_2Se_3) reveals a monotonous scaling of the exciton binding energy with increasing dielectric constant. We observe a relative change as large as 300 meV between exciton binding energies measured in WSe_2 on quartz and encapsulated in the high-k dielectric HfO_x . We show that the dependence of the WSe_2 exciton binding energy on the dielectric constant of the environment is accurately captured by a 2D Mott-Wannier model with parameters obtained from first principles. Finally, we demonstrate the lateral modulation of the exciton binding energy by texturing the dielectric environment paving the way towards exciton metamaterials in 2D systems.

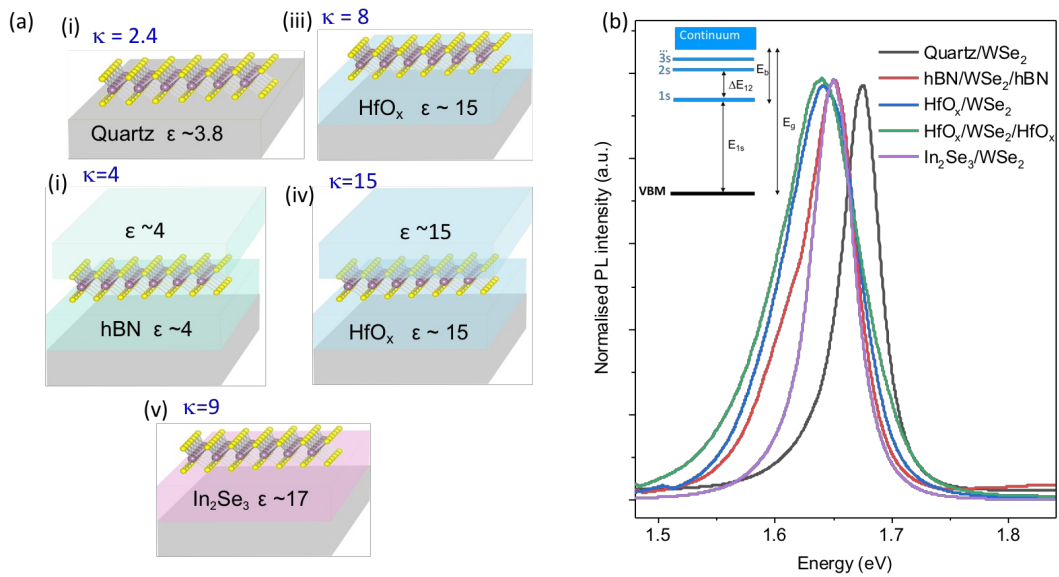


Figure 1 Material combination and heterostructures for different dielectric environments (a) Schematic illustration of different heterostructures used in this work. Different dielectric materials including quartz ($\epsilon = 3.8$), h-BN ($\epsilon = 4$), HfO_x ($\epsilon = 15$), and In_2Se_3 ($\epsilon = 17$). The average dielectric constants for each configuration are marked on the top left corner. (b) Photoluminescence spectra of WSe_2 in configurations acquired at room temperature showing the shift of the exciton ground state (1s). Inset: schematic illustration of the excitonic spectrum consisting of the 1s excitonic groundstate and the excited states (2s, 3s...). The diagram shows the relationship between the quasiparticle band gap (E_g), exciton binding energy (E_b), and the energy of the excited states (E_{2s}).

E_b , the lowest excitonic transition (E_{1s}) and the energy difference between the 1s and 2s states (ΔE_{12}).

van der Waals heterostructures of mechanically exfoliated monolayer WSe_2 with a range of dielectrics were prepared on optically transparent quartz substrates and on reflective SiO_2/p -Si using a dry-transfer technique based on a PDMS stamp (25). The thickness of monolayer WSe_2 was confirmed by photoluminescence (PL) spectroscopy, which exhibits intense PL and the emission is strongly quenched in bilayer and its bulk counterpart. This is due to crossover from a direct optical transition to an indirect optical transition (26). The dielectrics used in our work are quartz ($\epsilon = 3.8$), h-BN ($\epsilon = 4$), HfO_x ($\epsilon = 15$), and α - In_2Se_3 ($\epsilon = 17$) which is a ferroelectric (27). The HfO_x is obtained through a recently discovered controlled photo-oxidation process of HfS_2 (28) which can be successfully carried out even after the assembly of HfS_2 in a van der Waals heterostructures without any degradation of the adjacent WSe_2 (29). In these structures, we define the average dielectric constant of the top and bottom adjacent dielectric mediums to the WSe_2 as

$$\kappa = (\epsilon_{top} + \epsilon_{bottom}) / 2$$

parameter range from $\kappa = 2.4$ for WSe_2 /quartz (i.e. $\kappa < \kappa_{WSe_2}$) up to $\kappa = 15$ for $HfO_x/WSe_2/HfO_x$ (i.e. $\kappa > \kappa_{WSe_2}$), see Figure 1a.

Figure 1b shows the photoluminescence spectra for the structures of Figure 1a. For bare monolayer WSe_2 on quartz the emerging measured peak is at $1.67 eV$, which corresponds to the A exciton from the direct optical transition at the K and K' points. The A exciton peak position is found to be heavily dependent on the dielectric environment, displaying a redshift of $30 meV$ for $\kappa = 15$ compared to $\kappa = 2.4$.

Whilst PL probes the emission of the excitons, this is also heavily dependent on the doping and strain of the TMDs which *a priori* can be sample and materials dependent (30, 31). Furthermore, the states of the Rydberg series are usually not distinguishable in the PL spectra, making it impossible to characterize the exciton binding energy.

To probe the excitons Rydberg series, we employ optical transmission spectroscopy, which is a well-established technique for this purpose. Figure 2a-e show the first and second derivatives of the measured optical transmission spectra through the WSe_2 (T) normalized to that of the substrate (T_0). The peak energies of the 1s and 2s exciton states in the transmission spectra T/T_0 correspond to the inflection points in the first derivative and peaks in the second derivative. For WSe_2 monolayer on quartz substrate the 1s state of the neutral A exciton appears at $1.67 eV$ and its 2s

excited state is at $1.87 eV$, resulting in an energy difference ΔE_{12} of $200 meV$

(Figure 2a). The corresponding energy difference for the dielectric environments shown in Figure 1a are found to be $155 meV$ (hBN/ WSe_2 /hBN, see Figure 2b),

$105 meV$ (HfO_x/WSe_2 , see Figure 2c), $80 meV$ (In_2Se_3/WSe_2 , see Figure 2e) and $49 meV$ ($HfO_x/WSe_2/HfO_x$, see Figure 2d).

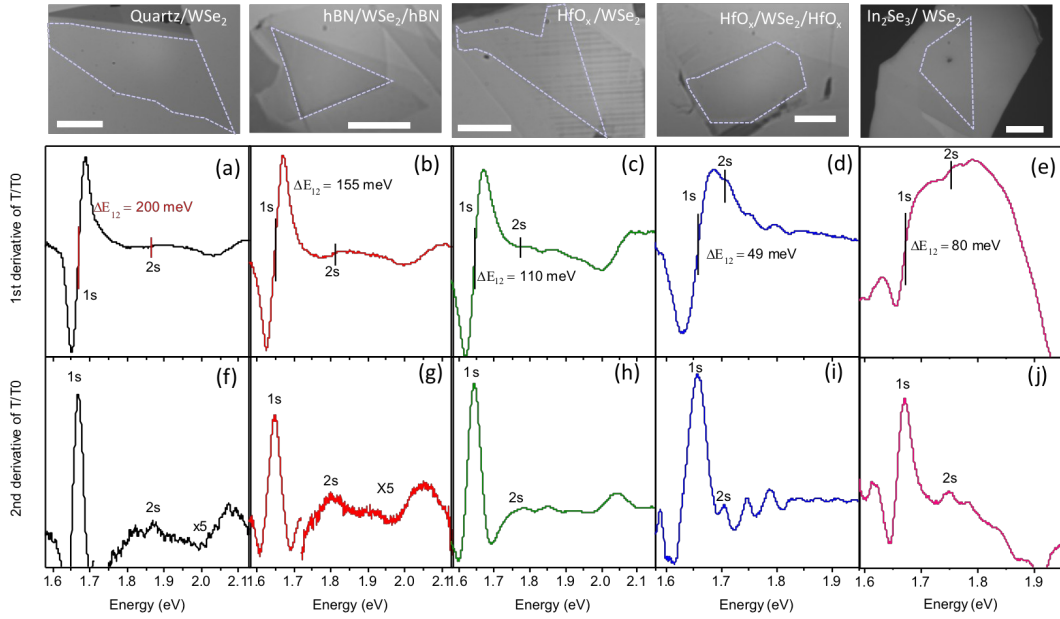


Figure 2 Transmission spectroscopy results (a-e) The first derivative of transmission spectra T/T_0 of WS_2 on quartz substrate, WSe_2 encapsulated between hBN, WSe_2 supported by HfO_x flake, WSe_2 sandwiched between HfO_x flakes and WSe_2 supported by In_2Se_3 flake, respectively. Optical micrographs of the corresponding heterostructures are presented in the first row. The outlines in optical images indicate the WSe_2 monolayer active area. Scale bars: $15 \mu m$ (f-j) The second derivative of transmission spectra T/T_0 . The energy differences between the exciton ground state and the first excited exciton state are marked as ΔE_{12} which decrease when the WSe_2 are adjacent to dielectric layers compared with that of WSe_2 on quartz substrate.

The energies of the 1s and 2s exciton states as a function of the average dielectric constants of the environment (κ) are shown in Figure 3a. We observe that both the 2s and 1s states redshift with increasing κ , though the relative shift of the 1s peak is much weaker than that of the 2s consistently with theoretical predictions for $2.4 < \kappa < 15$ (32). Indeed, the weak dependence of the 1s state on the dielectric environment has not been previously observed owing to the limited range of κ ($1.5 - 3.8$) presented in previous experimental studies (7). A plot of ΔE_{12} as a function of κ reveals that ΔE_{12} has a monotonous dependence on the average dielectric constant, see Figure 3b.

To elucidate the effects of dielectric screening on the excitonic states, we analyse theoretically ΔE_{12} and the exciton binding energy E_b of monolayer WSe_2 in different dielectric environments by numerical solution of a 2D Mott-Wannier exciton model. In atomic units the 2D Mott-Wannier Hamiltonian takes the form

$$H = \frac{1}{2\mu} \left(\frac{\partial^2}{\partial x^2} + \frac{\partial^2}{\partial y^2} \right) + W(r)$$

where μ is the exciton effective mass and W is the screened electron-hole interaction. We use the value $\mu = 0.19m_0$ from the *ab-initio* C2DB database (Ref. 37). Following Ref. 5, the screened interaction is calculated with the quantum electrostatic heterostructure (QEH) model (Ref. 24), which takes as input the q -dependent dielectric function of the **WSe₂** monolayer (obtained from density functional theory, see Methods), the static bulk dielectric constants of the substrate and capping materials (here represented by κ), and the distance from the monolayer to the substrate/capping. For all substrates the distance to the W atom in WSe₂ was set to $d=5.3$ Å. This value was fixed for the case of an hBN substrate and corresponds to the weighted average of interlayer distance in bulk WSe₂ and hBN. However, the precise value of d has very little effect on the exciton energies. The results for ΔE_{12} obtained from the Mott-Wannier model are shown in Figure 3b along with the experimental values. The agreement is truly remarkable given the parameter-free nature of the theoretical model.

Since ΔE_{12} is expected to be proportional to the exciton binding energy (E_b), a measurement of ΔE_{12} can reveal information on the quasiparticle gap in the TMD.

The simple 2D-hydrogen model with a Coulombic $1/\epsilon r$ electron-hole interaction, predicts $E_b = 9/8(\Delta E_{12})$. However, Chernikov *et al.* reported that Rydberg states in

a monolayer TMD (on a low- κ substrate) follow a non-hydrogenic model with $E_b = 2\Delta E_{12}$ (11). The exciton binding energies estimated from the experimental

ΔE_{12} using both the 2D hydrogen and non-hydrogenic models are plotted in Figure 3c. In addition, we show E_b obtained from the numerical solution of the Mott-Wannier model with electron-hole interaction obtained from the more elaborate QEH model. It is clear that the non-hydrogenic model by Chernikov *et al.* deviates significantly from the Mott-Wannier-QEH result, which in turn agrees fairly well with the hydrogen model, in particular for larger κ -values. This shows that while the non-hydrogenic behaviour of the Rydberg series prevails for 2D materials in low- κ environments, the 2D hydrogen model is more appropriate for medium- to high- κ environments.

Previous theoretical studies based on the screened Keldysh models have shown that the binding energy of the A exciton in TMDs has a power law dependence on κ such that $E_b = E_b^0/\kappa^\alpha$, with $\alpha=0.7$ (33) and E_b^0 the exciton binding energy of the TMD in vacuum ($\kappa=1$). We find that our Mott-Wannier-QEH results agree well with this model for $\alpha=0.66$. The dashed black line shows the exciton binding energy obtained from this model (33) using the calculated exciton binding energy of monolayer WSe₂ in vacuum of 450 meV (22, 33).

Figure 3d shows the quasiparticle gap of monolayer WSe₂ determined from $E_g = E_{1s} + E_b$ as a function of κ . In this expression E_{1s} is the experimental transition energy (cf. Figure 1b) while E_b is obtained from each of the three different models discussed above. Using E_b from the Mott-Wannier-QEH model, the value of E_g for WSe₂ on quartz is found to be 2.07 eV , whereas this value is reduced by 330 meV upon encapsulation of the TMD in the high- κ dielectric HfO_x. To date, this is the largest reported reduction of the quasiparticle gap in monolayer TMD induced by an oxide dielectric environment.

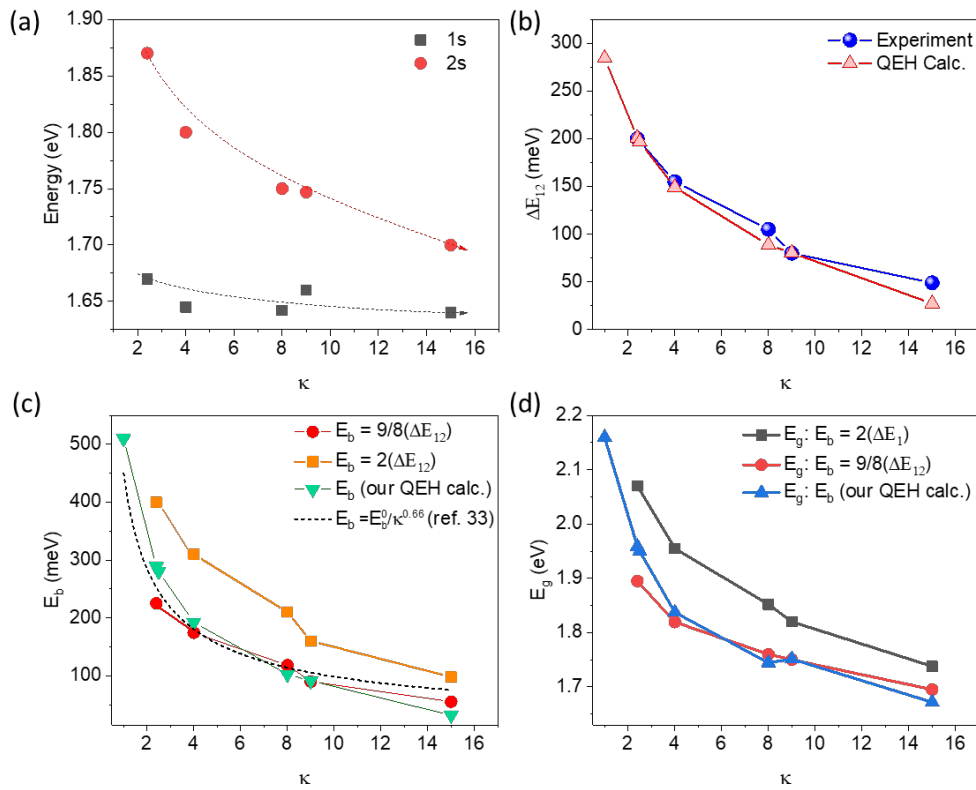


Figure 3 Modulation of excitons and the band gap via dielectric engineering (a)

Peak energies for 1s and 2s exciton states as function of average dielectric constants κ ranging from 2.4 to 15, extracted from the second derivative spectra of T/T0 in Figure 3. The dashed arrows are guide to the eye (b) The experimentally obtained ΔE_{12} values of monolayer WS₂ as a function of κ are compared with theoretical results. (c) The κ dependence of the exciton binding energies experimentally determined from the measured ΔE_{12} using the 2D hydrogen model ($E_b = 9/8(\Delta E_{12})$) and non-hydrogen model ($E_b = 2\Delta E_{12}$). The exciton binding energies obtained from the numerical solution of the Mott-Wannier model with

screened electron-hole interaction obtained from the QEH model are also shown. (d) The variation of the band gap as function of κ , estimated from

$$E_g = E_{1s} + E_b$$

Understanding the role of the dielectric environment on the exciton binding energy and quasiparticle gap of a TMD is a first step to the development of specific exciton potential profiles which can guide or trap excitons. To this end, we first study the spatial change of the exciton binding energy of a monolayer WSe₂ across the dielectric boundary with $\kappa=2.4$ (quartz/WSe₂) to $\kappa=8$ (quartz/WSe₂/HfO_x), see

Figure 4a. Figure 4b and c show the second derivative of the normalized optical transmission spectra (T/T_0) acquired at different points along the green line (see Figure 4a) cutting across the aforementioned dielectric boundary. The peaks corresponding to the 1s and 2s excitonic states of WSe₂ taken from different spatial positions shift according to the value of κ . More specifically, we find that ΔE_{12} for WSe₂ on quartz is $\approx 196 \text{ meV}$ and it reduces to $\approx 107 \text{ meV}$ in the region of WSe₂ on HfO_x. These values are consistent with data shown in Figure 2. The spatial dependence of the exciton binding energy is summarised in the plot of Figure 4d, where $E_b = 2\Delta E_{12}$.

To further demonstrate the ability to tune the exciton binding energy of 2D crystals through the texturing of the dielectric environment we have considered SiO₂/WSe₂/PMMA stacks. Hence, we define a dielectric array corresponding to a triangular lattice of holes using standard electron-beam lithography, see Figure 4e. Spatially-resolved PL mapping reveals a shift in the WSe₂ peak in correspondence of the holes ($\epsilon_{air}=1, \kappa=2.45$) with respect to the regions covered by PMMA ($\epsilon_{pmma}=3, \kappa=3.45$), see Figure 4f. This shift is consistent with the change in the relative dielectric constant induced by the PMMA.

In first approximation, that the PL peak energy is given by

$$E_g = E_{1s} + E_b$$

Experimentally we observe that E_{1s} is weakly dependent on κ , and it can be

considered constant in the range of κ of our sample, see Figure 3a. Hence, the exciton binding energy shift is equal to the change of the quasiparticle energy gap:

$$\Delta E_b(\kappa) = \Delta E_g(\kappa), \text{ where } \Delta E_g(\kappa) = E_g(\kappa_0) - E_g(\kappa) \text{ and for the case of the}$$

experiment $\kappa_0 = 2.45$. Furthermore, using the relationship we can

$$E_b = \frac{E_b(\kappa_0)}{\kappa^{0.66}}$$

estimate the value of κ using $\kappa = \left(\frac{E_b(\kappa_0)}{\Delta E_b} \right)^{-0.66} + \kappa_0$ and $E_b(\kappa_0) = 225 \text{ meV}$. The computed values of ΔE_b and κ are shown in Figure 4g,h and they agree very well with what is expected for our choice of dielectrics. The change of the exciton binding energy shows that texturing of the dielectric environment can be used to create potential wells for excitons in 2D materials, whilst maintaining their atomic integrity

(see Figure 4h). Finally, we note that in our experiment we have chosen the diameter of the holes to be sufficiently large to probe the photophysics of textured dielectrics using PL mapping with a sub-diffraction limited laser beam (34). However, with the use of recently demonstrated tip enhanced direct laser writing techniques in 2D materials (35), it should be possible to reduce the size of the disks in a regime where quantum confinement becomes prominent.

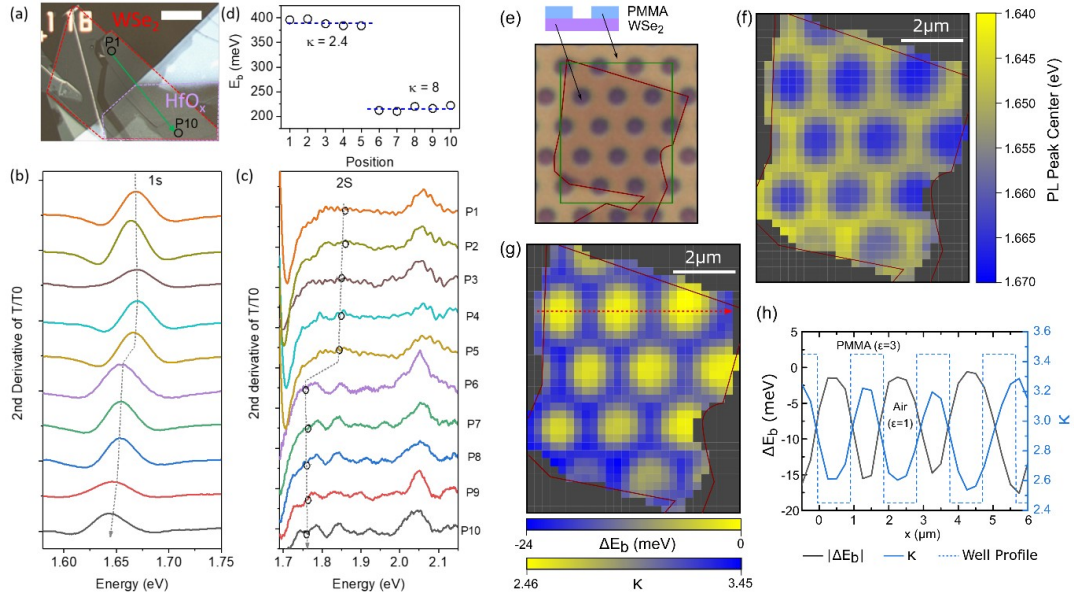


Figure 4 Spatial modulation of exciton binding energy in monolayer WSe₂. (a) An optical **micrograph** of monolayer WSe₂ spreading across different dielectric environments on quartz and photo-oxidised HfO_x (red, monolayer WSe₂; purple, HfO_x). Scale bar: 15 μm. The second derivative of T/T₀ of monolayer WSe₂ taken from different locations along the green line from position 1-5 (on quartz) to position 6-10 (on HfO_x) showing the variation of the exciton ground stage 1s state (b) and the first excited excitonic state 2s (c). (d) Lateral modulation of the exciton binding energy of WSe₂ along the green dashed line determined from $E_b = 2\Delta E_{12}$. (e)

Optical micrograph of SiO₂/WSe₂/PMMA stack with a triangular lattice arrangement of holes defined by electron-beam lithography. (f) Spatially-resolved PL map of the SiO₂/WSe₂/PMMA stacks showing the shift in peak position across the scanned area (green box in panel (e)). Red lines outline the edges of the monolayer WSe₂. (g) Exciton binding energy shift ΔE_B and κ extrapolated from the PL map data in panel (f). (h) Line-cut across the red dashed line in panel (g) showing the change in binding energy and κ according to the PMMA profile (blue dashed line).

Conclusion

In conclusion, we have demonstrated a giant tuning of the exciton binding energy in monolayer WSe₂ as a function of the dielectric environment. For the first time, we employ an atomically thin high-k dielectric such as HfO_x to attain an average

dielectric constant much larger than that of the TMD, i.e. $k=15$, leading to a suppression close to 30meV of the exciton binding energy in ambient conditions.

The quantitative changes of the exciton binding energies of monolayer WSe_2 for a range of dielectrics are in good agreement with our numerical solution of a 2D Mott-Wannier model which accounts for both the intrinsic nonlocal screening in the monolayer and the screening from the dielectric environment. Finally, we study the spatial modulation of the exciton binding energy across boundaries of different dielectrics. Hence, we show experimentally that a textured dielectric environment can be used to create potential wells for excitons in 2D materials without hampering the structural integrity of these atomically thin semiconductors. These results pave the way towards the development of exciton metamaterials in the form of arrays of textured dielectrics exhibiting a collective optical response which differs profoundly from that of an individual potential well.

References

1. T. Cheiwchanchamnangij, W. R. L. Lambrecht, Quasiparticle band structure calculation of monolayer, bilayer, and bulk MoS_2 . *Phys Rev B* **85**, (2012).
2. A. Ramasubramaniam, Large excitonic effects in monolayers of molybdenum and tungsten dichalcogenides. *Phys Rev B* **86**, (2012).
3. D. Y. Qiu, F. H. da Jornada, S. G. Louie, Optical Spectrum of MoS_2 : Many-Body Effects and Diversity of Exciton States. *Phys Rev Lett* **111**, (2013).
4. H. P. Komsa, A. V. Krasheninnikov, Effects of confinement and environment on the electronic structure and exciton binding energy of MoS_2 from first principles. *Phys Rev B* **86**, (2012).
5. S. Latini, T. Olsen, K. S. Thygesen, Excitons in van der Waals heterostructures: The important role of dielectric screening. *Phys Rev B* **92**, (2015).
6. S. Borghardt *et al.*, Engineering of optical and electronic band gaps in transition metal dichalcogenide monolayers through external dielectric screening. *Phys Rev Mater* **1**, (2017).
7. W. T. Hsu *et al.*, Dielectric impact on exciton binding energy and quasiparticle bandgap in monolayer WS_2 and WSe_2 . *2d Mater* **6**, (2019).
8. S. Park *et al.*, Direct determination of monolayer MoS_2 and WSe_2 exciton binding energies on insulating and metallic substrates. *2d Mater* **5**, (2018).
9. F. W. Henry A. Fernandez, Saverio Russo, and William L. Barnes, Electrically Tuneable Exciton-Polaritons through Free Electron Doping in Monolayer WS_2 Microcavities. *Adv Opt Mater* **7**, (2019).
10. H. A. Fernandez, F. Withers, S. Russo, W. L. Barnes, Electrically tuneable exciton energy exchange between spatially separated 2-dimensional semiconductors in a microcavity. *Appl Phys Lett* **115**, (2019).
11. A. Chernikov *et al.*, Exciton Binding Energy and Nonhydrogenic Rydberg Series in Monolayer WS_2 . *Phys Rev Lett* **113**, (2014).
12. A. T. Hanbicki, M. Currie, G. Kioseoglou, A. L. Friedman, B. T. Jonker, Measurement of high exciton binding energy in the monolayer transition-metal dichalcogenides WS_2 and WSe_2 . *Solid State Commun* **203**, 16-20 (2015).
13. K. L. He *et al.*, Tightly Bound Excitons in Monolayer WSe_2 . *Phys Rev Lett* **113**, (2014).
14. B. R. Zhu, X. Chen, X. D. Cui, Exciton Binding Energy of Monolayer WS_2 . *Sci Rep-Uk* **5**, (2015).
15. H. M. Hill *et al.*, Observation of Excitonic Rydberg States in Monolayer MoS_2 and WS_2 by Photoluminescence Excitation Spectroscopy. *Nano Lett* **15**, 2992-2997 (2015).
16. G. Wang *et al.*, Giant Enhancement of the Optical Second-Harmonic Emission of WSe_2 Monolayers by Laser Excitation at Exciton Resonances. *Phys Rev Lett* **114**, (2015).

17. E. F. Liu *et al.*, Magnetophotoluminescence of exciton Rydberg states in monolayer WSe₂. *Phys Rev B* **99**, (2019).
18. T. Olsen, S. Latini, F. Rasmussen, K. S. Thygesen, Simple Screened Hydrogen Model of Excitons in Two-Dimensional Materials. *Physical review letters* **116**, (2016).
19. S. Y. Chen *et al.*, Superior Valley Polarization and Coherence of 2s Excitons in Monolayer WSe₂. *Phys Rev Lett* **120**, (2018).
20. A. V. Stier *et al.*, Magneto-optics of Exciton Rydberg States in a Monolayer Semiconductor. *Phys Rev Lett* **120**, (2018).
21. G. Gupta, S. Kallatt, K. Majumdar, Direct observation of giant binding energy modulation of exciton complexes in monolayer MoSe₂. *Phys Rev B* **96**, (2017).
22. A. V. Stier, N. P. Wilson, G. Clark, X. D. Xu, S. A. Crooker, Probing the Influence of Dielectric Environment on Excitons in Monolayer WSe₂: Insight from High Magnetic Fields. *Nano Lett* **16**, 7054-7060 (2016).
23. M. L. Trolle, T. G. Pedersen, V. Veniard, Model dielectric function for 2D semiconductors including substrate screening. *Sci Rep-Uk* **7**, (2017).
24. K. Andersen, S. Latini, K. S. Thygesen, Dielectric Genome of van der Waals Heterostructures. *Nano Lett* **15**, 4616-4621 (2015).
25. A. Castellanos-Gomez *et al.*, Deterministic transfer of two-dimensional materials by all-dry viscoelastic stamping. *2d Mater* **1**, 011002 (2014).
26. K. F. Mak, C. Lee, J. Hone, J. Shan, T. F. Heinz, Atomically Thin MoS₂: A New Direct-Gap Semiconductor. *Phys Rev Lett* **105**, (2010).
27. D. Wu *et al.*, Thickness-Dependent Dielectric Constant of Few-Layer In₂Se₃ Nanoflakes. *Nano Lett* **15**, 8136-8140 (2015).
28. A. De Sanctis, I. Amit, S. P. Hepplestone, M. F. Craciun, S. Russo, Strain-engineered inverse charge-funnelling in layered semiconductors. *Nat Commun* **9**, (2018).
29. N. Peimyoo *et al.*, Laser-writable high-k dielectric for van der Waals nanoelectronics. *Sci Adv* **5**, (2019).
30. N. Peimyoo *et al.*, Chemically Driven Tunable Light Emission of Charged and Neutral Excitons in Mono layer WS₂. *Acs Nano* **8**, 11320-11329 (2014).
31. O. B. Aslan, M. D. Deng, T. F. Heinz, Strain tuning of excitons in monolayer WSe₂. *Phys Rev B* **98**, (2018).
32. A. R. Lutz Waldecker, Malte Rosner, Christina Steinke,, R. J. K. Aaron Bostwick, Chris Jozwiak, Takashi Taniguchi, Kenji, E. R. Watanabe, Tim O. Wehling, and Tony F. Heinz, Rigid band shifts in two-dimensional semiconductors through environmental screening. *Arxiv*, (2019).
33. I. Kylanpaa, H. P. Komsa, Binding energies of exciton complexes in transition metal dichalcogenide monolayers and effect of dielectric environment. *Phys Rev B* **92**, (2015).
34. A. D. Sanctis, G. F. Jones, N. J. Townsend, M. F. Craciun, S. Russo, An integrated and multi-purpose microscope for the characterization of atomically thin optoelectronic devices. *Review of Scientific Instruments* **88**, 055102 (2017).
35. A. De Sanctis *et al.*, Extraordinary linear dynamic range in laser-defined functionalized graphene photodetectors. *Science Advances* **3**, e1602617 (2017).
36. J. Enkovaara *et al.*, Electronic structure calculations with GPAW: a real-space implementation of the projector augmented-wave method. *J Phys-Condens Mat* **22**, (2010).
37. S. Hastrup *et al.*, The Computational 2D Materials Database: high-throughput modeling and discovery of atomically thin crystals. *2d Mater* **5**, (2018).

Methods

Material preparation

Monolayer WSe_2 , hBN, HfS_2 and In_2Se_3 were prepared by mechanical exfoliation of their bulk crystals. A variety of heterostructures were produced using a dry-transfer technique. For HfO_x -supported WSe_2 and HfO_x -encapsulated WSe_2 , the HfS_2 layers are first used for stacking. Once the heterostructures are complete. The laser oxidation is then scanned onto the desired region to transform HfS_2 into high-k oxide following our previous report. The 473 nm laser wavelength with the energy density of $53 \text{ mJ}/\mu\text{m}^2$ is used. The laser exposure time of 10 s and the step size of $0.5 \mu\text{m}$ are used. The WSe_2 , HfS_2 were purchased from 2Dsemiconductors and hBN was provided by Manchester Nanomaterials.

PMMA/ WSe_2 samples were prepared by spinning 300nm of PMMA (MicroChem 950K) on top of the mechanically-exfoliated crystals and curing at 180°C for 60sec. Electron-beam lithography (NanoBeam NB4) was used to define the patterns and developed in a 3:1 IPA:MIBK solution (Sigma Aldrich).

Transmission and PL measurements

The transmission measurement was performed at room temperature using a x white-light source. The light was passed through the structures and transmitted light was collected by an objective lens. The transmitted light was then dispersed in a 300 g/mm grating spectrometer and detected by a CCD.

Spatially-resolved photoluminescence spectra were acquired in a custom-built setup using a 514 nm laser for excitation (34). Light was collected by a x50 objective (Olympus MPLAN-FL) and dispersed by a 300 g/mm grating and collected by a CCD camera.

Theoretical Methods

All *ab initio* calculations have been performed using the GPAW code(36). The 1s and 2s exciton binding energies are obtained by numerical solution of a 2D Mott-Wannier equation. The quantum electrostatic heterostructure (QEH) model is used to obtain the screened electron-hole interaction taking the full q-dependent dielectric screening from the WSe_2 layer itself and the substrate/capping layers into account (24).

The atomic structure of the WSe_2 monolayer and the electron and hole effective masses, which defines the exciton effective mass, were adopted from the Computational 2D Materials Database (C2DB)(37). The q-dependent dielectric function of the WSe_2 monolayer, used as input for the QEH model, is calculated in the random phase approximation (RPA) with local field effects included up to 50 eV cut-off on the reciprocal lattice vectors and a similar energy cut-off on the sum over empty states. In these calculations the monolayers were separated by 15 \AA of vacuum and a truncated Coulomb interaction is used in the out-of-plane direction to avoid unphysical screening arising from the periodic boundary conditions on the supercell.

8.4 Paper IV

High Oscillator Strength Interlayer Excitons in 2D Heterostructures for Mid-IR Photodetection

S. Lukman, L. Ding, L. Xu, Y. Tao, A. C. Riis-Jensen, G. Zhang, Q. Steve Wu, M. Yang, S. Luo, C. Hsu, L. Yao, G. Liang, H. Lin, Y.-W. Zhang, K. S. Thygesen, Q. Jie Wang, Y. Feng, J. Teng

Nature Nanotechnology, DOI: <https://doi.org/10.1038/s41565-020-0717-2> (2020)

© 2020 Nature Nanotechnology All Rights Reserved

<https://www.nature.com/articles/s41565-020-0717-2>



High oscillator strength interlayer excitons in two-dimensional heterostructures for mid-infrared photodetection

Steven Lukman¹, Lu Ding¹, Lei Xu², Ye Tao³, Anders C. Riis-Jensen⁴, Gang Zhang⁵, Qing Yang Steve Wu¹, Ming Yang^{1,2}, Sheng Luo⁶, Chuanghan Hsu⁶, Liangzi Yao⁷, Gengchiao Liang⁶, Hsin Lin⁷, Yong-Wei Zhang⁵, Kristian S. Thygesen⁴, Qi Jie Wang³, Yuanping Feng² and Jinghua Teng¹✉

The development of infrared photodetectors is mainly limited by the choice of available materials and the intricate crystal growth process. Moreover, thermally activated carriers in traditional III-V and II-VI semiconductors enforce low operating temperatures in the infrared photodetectors. Here we demonstrate infrared photodetection enabled by interlayer excitons (ILEs) generated between tungsten and hafnium disulfide, WS₂/HfS₂. The photodetector operates at room temperature and shows an even higher performance at higher temperatures owing to the large exciton binding energy and phonon-assisted optical transition. The unique band alignment in the WS₂/HfS₂ heterostructure allows interlayer bandgap tuning from the mid- to long-wave infrared spectrum. We postulate that the sizeable charge delocalization and ILE accumulation at the interface result in a greatly enhanced oscillator strength of the ILEs and a high responsivity of the photodetector. The sensitivity of ILEs to the thickness of two-dimensional materials and the external field provides an excellent platform to realize robust tunable room temperature infrared photodetectors.

Mid- and long-wavelength infrared (MW-LWIR) photodetectors are useful for many important applications, such as in medical, security, surveillance and material evaluation. A photodetector consists of light-sensitive material that can absorb electromagnetic radiation, and the photons are subsequently converted into a measurable current. In the MW-LWIR regime (3–15 μm), which corresponds to photon energy of around 83–413 meV, there are only a handful of narrow bandgap semiconductors that are suitable for this purpose. The widely available infrared photodetectors are made of III-V and II-VI compound semiconductors, such as Hg_{1-x}Cd_xTe, In_{1-x}Ga_xAs and InSb (ref. ¹). However, delicate and expensive processes are required to grow these compounds and the lattice matching between the materials and substrate further limits their availability.

The performance of infrared photodetectors is largely determined by the charge-generation efficiency from absorbing impinging photons on the active region, the lifetime and mobility of the charge carriers and the dark current from thermally activated carriers. The small binding energy ($E_b < 25$ meV) (refs. ^{2,3}) of electron-hole pairs (excitons) in conventional narrow bandgap infrared photodetectors means the thermal energy at room temperature (25 meV) is sufficient to overcome it, and thus excitons spontaneously dissociate into free carriers once formed. Similarly, the thermal-carrier generation and lattice phonon is evident at room temperature. Therefore, the infrared-generated carriers can easily decay to the ground state

in the absence of cooling^{4,5}. These processes shorten the carrier lifetime and prevent charge extraction that eventually lowers the efficiency of the photodetectors, especially at higher temperatures. The necessity to operate at substantially reduced temperatures to suppress these processes complicates the detector architecture and limits their sensitivity at room temperature.

For the past few years, two-dimensional (2D) materials and their heterostructures have emerged as a promising platform for electronic and optoelectronic applications, with a particular interest in transition metal dichalcogenides (TMDs) semiconductors^{6–10}. The out-of-plane van der Waals bond in 2D materials is advantageous as it allows the 2D materials to be fabricated on any substrate without a lattice-matching constraint. Subsequently, the absence of dangling bonds on the surface would eliminate dark current from surface-recombination, which is ideal for photodetectors. 2D semiconductors have strongly bound excitons due to a strong quantum confinement and reduced dielectric screening^{11,12}. The recombination of electron and hole, that is, the decay of the exciton, is limited by resonance stabilization due to the overlap of electron and hole wavefunctions, which results in an extended lifetime for the exciton^{5,13}. The indirect bandgap character of many 2D semiconductors benefits from phonons at a higher temperature, which aids in momentum conservation on photoabsorption. Therefore, the thermal effect could potentially have a positive effect for infrared photodetectors based on 2D semiconductors. Furthermore, 2D

¹Institute of Materials Research and Engineering, Agency for Science, Technology and Research (A*STAR), Singapore, Singapore. ²Department of Physics, National University of Singapore, Singapore, Singapore. ³School of Electrical and Electronic Engineering, Nanyang Technological University, Singapore, Singapore. ⁴CAMD and Center for Nanostructured Graphene (CNG), Department of Physics, Technical University of Denmark, Kongens Lyngby, Denmark. ⁵Institute of High Performance Computing, Agency for Science, Technology and Research (A*STAR), Singapore, Singapore. ⁶Department of Electrical and Computer Engineering, Faculty of Engineering, National University of Singapore, Singapore, Singapore. ⁷Institute of Physics, Academia Sinica, Taipei, Taiwan. ✉e-mail: jh-teng@imre.a-star.edu.sg

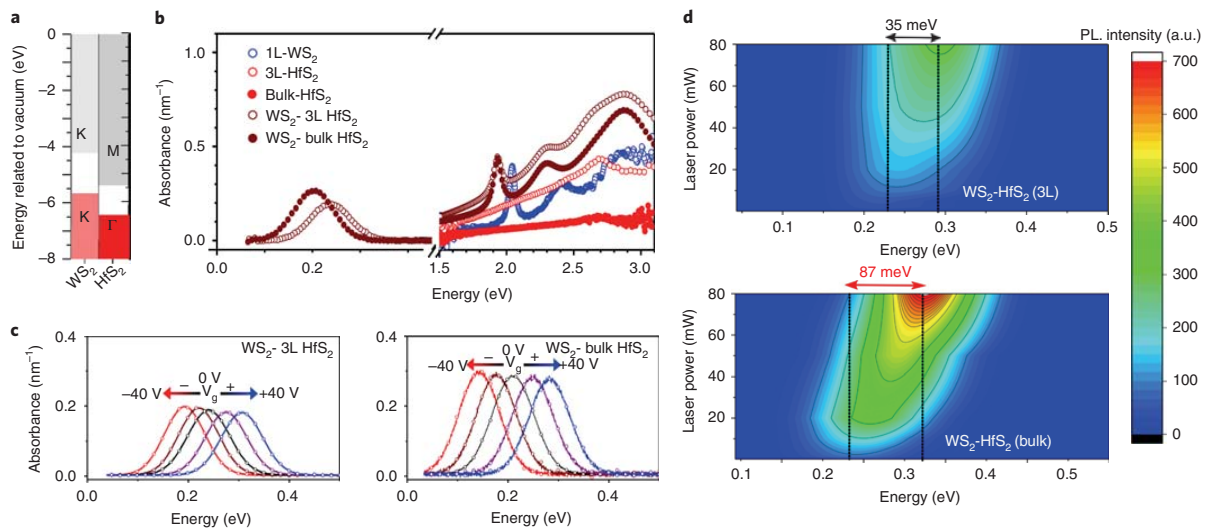


Fig. 1 | Optical characteristics of ILEs in WS_2/HfS_2 heterostructures. **a**, Energy band diagram illustrating the VBM and CBM of monolayers of WS_2 and HfS_2 . **b**, Absorption spectra of the parent materials (WS_2 and HfS_2) in the visible range, and the stacked heterostructures in the infrared and visible ranges normalized to the thickness. $\lambda_{exc} = 532$ nm. 1L, one layer; 3L, three layers; bulk, ~30 layers. **c**, The effect of an externally applied V_g that ranges from -40 V to $+40$ V on the absorption spectra of monolayer WS_2 with 3L HfS_2 (left) and bulk HfS_2 (right). **d**, The evolution of ILE PL spectra observed in monolayer WS_2 with 3L HfS_2 (top) and bulk HfS_2 (bottom) as a function of laser power. The ILE PL spectra blueshift with increasing power (excitation density). The shifts are more prominent in bulk HfS_2 than in 3L HfS_2 . The ILE energy in WS_2 /bulk HfS_2 is lower than that in WS_2 /3L HfS_2 . The PL spectra are bi-Gaussian for 3L HfS_2 and mono-Gaussian for bulk HfS_2 . a.u., arbitrary units.

semiconductors have been shown to integrate easily with metals¹⁴ or graphene¹⁵, which makes them suitable for optoelectronic applications as facile carrier extraction or injection sites.

Graphene has attracted numerous interests in MW-LWIR detection due to its broadband absorption and high carrier mobility. However, the low-absorption coefficient, high dark current and short-carrier lifetime hamper the performance¹⁶. An intrinsically narrow-bandgap black phosphorus^{17,18} shows a thickness and electrostatic-gating bandgap dependence adjustable from 0.2 to 2.0 eV (0.62–6.2 μ m). The bandgap can be further extended down to 0.15 eV (8.3 μ m) by alloying with arsenic (black AsP)^{19,20}. However, this material is not thermodynamically stable. Alternatively, a handful of narrow-bandgap TMD semiconductors with $E_{gap} < 1$ eV have also emerged recently as promising candidates for infrared detectors, such as (Zr, Ni, Pd, Pt, Bi)Se₂/Te₂ (ref. 21). Nonetheless, the difficulties in fabrication and controlling the bandgap impose greater challenges on their practical applications^{22–24}.

When two dissimilar TMD semiconductors are stacked together to form a type II heterostructure, a space-indirect interlayer exciton (ILE) will form through charge hopping between materials. These ILEs have a large E_b (refs. 25–27), which is comparable to that of the intralayer excitons generated within parent materials^{11,12}. The photoactive range of ILEs is determined by the band-energy alignment of the constituent material, which offers the potential to utilize ILEs for a tunable infrared photodetector. Nevertheless, the space-indirect character of the ILE renders it with a weak optical absorption^{25,26,28}. Here we explore the unique properties of ILEs in a 2D TMD heterostructure formed between WS_2 and HfS_2 and demonstrate a highly responsive room-temperature-operated MW-LWIR photodetector with a tunable detection range. Based on the study of the thickness dependence, response to electric field and excitation density and ab initio calculations, we postulate that the observed ILEs have the same order of oscillator strength as intralayer excitons. An enhanced spatial orbital overlap and

phonon-assisted momentum conservation favour the optical transition of ILEs. The findings here provide insights to tailor ILEs for optoelectronic applications that offer a promising way to make a compact and efficient room-temperature photodetector that can be extended down to the far infrared.

Formation and characteristics of ILEs. The conduction band minimum (CBM) and valence band maximum (VBM), relative to vacuum²⁴, of monolayer WS_2 and HfS_2 are illustrated in Fig. 1a. HfS_2 (d^0 semiconductor) was chosen for this study because it has a deep CBM and high electron mobility, in which it is favourable for ILE electrons to reside when paired with d^2 semiconductors (that is, WS_2) (ref. 29). Different thicknesses of HfS_2 were laid on top of monolayer WS_2 to maintain a direct bandgap for optical excitation. For subsequent discussion, ‘thinner’ and ‘thicker’ HfS_2 refer to ~3 and 30 layers (bulk), respectively, unless otherwise specified.

The optical responses of individual TMDs and the heterostructures are plotted in Fig. 1b. The reported absorbance was calculated from the differential reflectance contrast of the flakes and normalized to the thickness (details in Supplementary Information). The A exciton peak, which is associated with the band-edge transitions in monolayer WS_2 , centres around 2.04 eV (Fig. 1b). This value is close to the previously reported value³⁰. However, HfS_2 is an indirect-bandgap material, so the bandgap is inferred from extrapolation to the abscissa. We notice the main excitonic peaks of the heterostructures are slightly broadened and redshifted (1.94 eV) compared with those of the parent materials. The observed broadening, $\Delta\Gamma$, is associated with a shortened lifetime of the photo-generated excitons as $\tau = \hbar/\Delta\Gamma$ (ref. 31) (where \hbar is the Planck constant/ 2π) due to charge hopping at the interface.

Interestingly, the heterostructure has an additional strong absorption peak in the lower energy region as shown in Fig. 1b, which is not present in the constituent materials. The heterostructure peaks are centred at 0.24 eV for WS_2 /3L HfS_2 and at 0.21 eV for WS_2 /

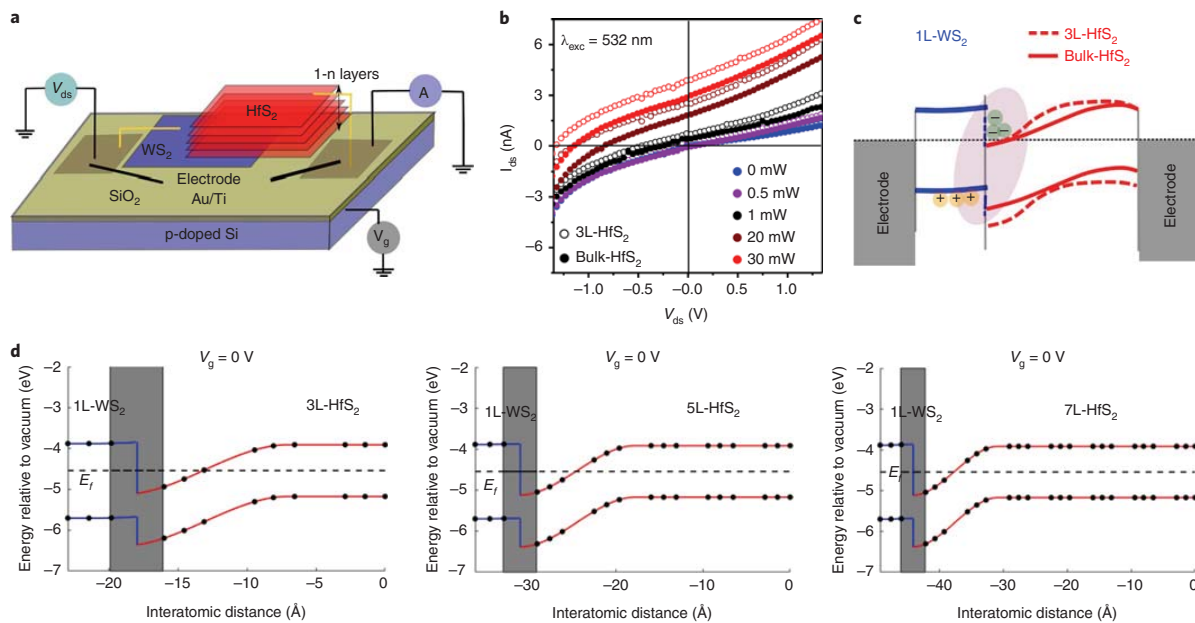


Fig. 2 | Electrical characterization of WS₂/HfS₂ ILEs. **a**, Schematic diagram of the device structure used in this study, which consists of an exfoliated WS₂ flake with a different number of layers of HfS₂ on a doped silicon substrate. A V_g was applied to control the band alignment and interlayer bandgap. Similarly, a V_{ds} was used for charge extraction when the device was used as a photodetector. **b**, I - V curves of the heterostructure in WS₂/3L HfS₂ and WS₂/bulk HfS₂ at different excitation powers. The curves shift to the second quadrant with increasing power, which indicates charge carrier accumulation at the interface. **c**, Schematic diagram illustrating the band bending at the interface. Details of the band bending are given in the text. We assumed that only the VBM of HfS₂ shifts relative to the VBM of WS₂ as the number of layers increases, because the calculation shows the shift in CBM is relatively small. All of the measurements were conducted at room temperature and photoexcitation was achieved by laser with the photon energy centred at 2.33 eV. **d**, Band profiles of 1L-WS₂/3L-, 5L- and 7L-HfS₂ heterojunctions without an external bias ($V_g = 0$). The energy reference was set to be the vacuum level ($E_{vac} = 0$ eV). The areas highlighted in grey area are the spaces between WS₂ and HfS₂. E_f is plotted as a black dashed line. The black dots denote the location of atoms in the out-of-plane direction. WS₂ is slightly n doped, with an E_f of 0.15 eV above the intrinsic E_f ($E_{gap} = 1.82$ eV).

bulk HfS₂. The absorption becomes stronger and redshifts with increasing layers of HfS₂ (Extended Data Fig. 1). These low-energy absorptions show no obvious sample angular dependence (Extended Data Fig. 2). Furthermore, the peak energy is responsive to an external electric field (Fig. 1c). The gate dependence suggests these peaks are associated with ILEs with the dipole moment pointing from HfS₂ to WS₂, which substantiates the charge transfer at the interface. Strong intralayer exciton quenching of WS₂ (Supplementary Fig. 4) also suggests electron transfer to HfS₂ (refs. 32,33). We can rule out the possibility of energy transfer as the photoluminescence (PL) of HfS₂ decreases compared to that of bare HfS₂.

Exciton accumulation and band structure at the interface. The ILE PL ($\lambda_{exc} = 532$ nm) is prominent even at room temperature, which demonstrates a robust radiative recombination. The PL spectral shape changes with the thickness of HfS₂—a thinner HfS₂ consists of a broader emission peak made of two Gaussian peaks (Fig. 1d). The energy difference between the two peaks (Δ_{ILE}) decreases with an increasing number of HfS₂ layers and finally merges into one broad peak in bulk HfS₂ (Fig. 1d and Extended Data Fig. 3). Increasing excitation density results in blue-shifts of overall PL peak (Fig. 1d). The more substantial blueshift in WS₂-bulk HfS₂ indicates a stronger excitonic dipole-dipole repulsion³⁴.

We also found that the PL intensity in WS₂/bulk HfS₂ saturates at a lower fluence than the thinner counterpart (8×10^4 for bulk versus 5×10^5 W μm^{-2} for 3L HfS₂; Extended Data Fig. 4), which confirms a more prominent exciton-exciton annihilation in thicker samples. The higher density of ILEs in the WS₂/bulk

HfS₂ interface is responsible for the stronger excitonic repulsion and annihilation observed. We fitted the integrated PL intensity (I) with the exponential function $I \approx CP^\alpha$, with C a constant and P the excitation power, and we obtained $\alpha \approx 0.8$ – 0.9 (Extended Data Fig. 4). Although the dependence is sublinear, α is higher than in typical p–n junctions (~ 0.5) (refs. 14,34–36), in which ILEs favourably separate into charge carriers. The fact that we encountered an unusually high sublinear power dependence suggests ILEs probably remain as excitons.

The accumulation of ILEs at the interface is also supported by a simple estimation of ILE density via the plate capacitor formula³⁷. The maximum ILE density based on the blueshift yields a lower boundary value of $n_{ILE} = 4.7 \times 10^{11}$ cm⁻² and 1.3×10^{12} cm⁻² for WS₂ with 3L and bulk HfS₂, respectively (details in Supplementary Information). These values are comparable with the intralayer WS₂ exciton density generated from the same excitation density, which is in the order of 10^{11} – 10^{12} cm⁻². We postulate that the observed high exciton density at the interface is due to band bending, which favours electron and hole accumulation in HfS₂ and WS₂, respectively.

To verify the interfacial band bending, we studied the photoreponse of the heterostructure under the illumination of a 532 nm laser. A schematic diagram of the device used in this study is given in Fig. 2a. The current–voltage (I - V) curves under different excitation powers are shown in Fig. 2b. As the metal–TMD junction forms an ohmic contact at near-zero voltage (Supplementary Fig. 8), the sign of the photovoltage and photocurrent correlates with the band structure at the interface. The photocurrent shifts the I - V

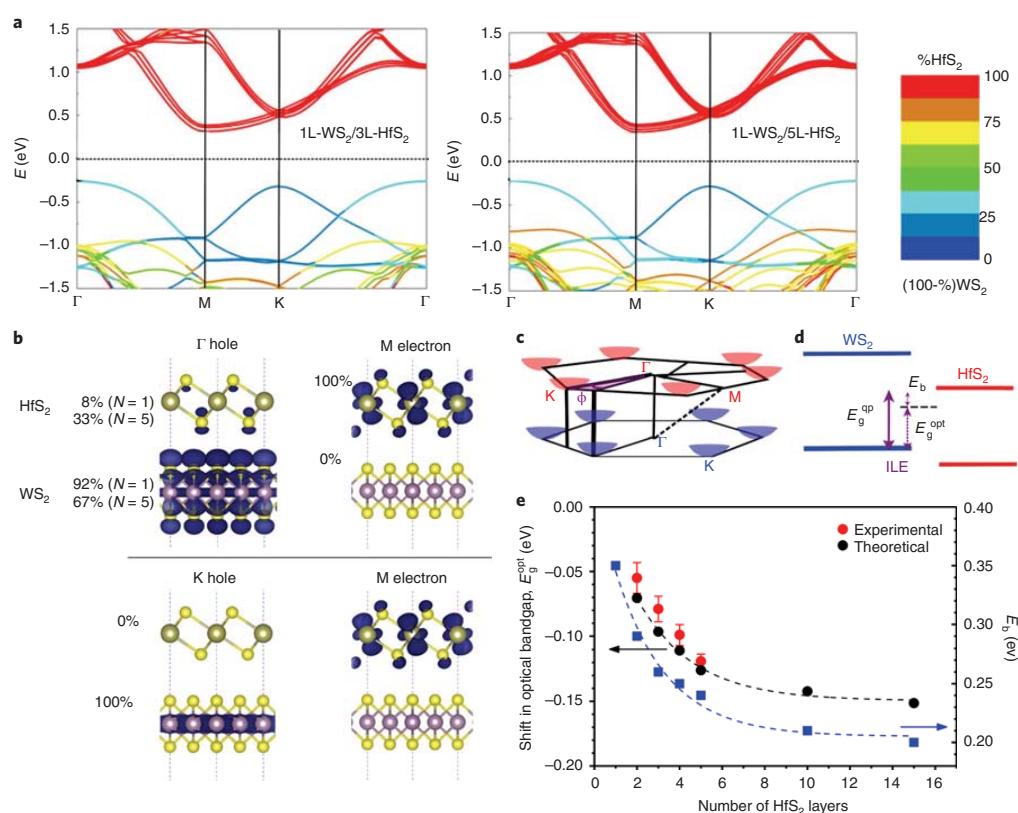


Fig. 3 | The nature of an indirect ILE with a large amplitude optical transition. **a**, Band structures of the 1L- WSe_2 / N L- HfS_2 heterostructures for $N=3$ (left) and 5 (right) layers of HfS_2 , respectively. The colour scale denotes the relative contribution of each material to the band states (VBM and CBM) of the ILE. **b**, The hole and electron states of the ILE for the Γ -M and K-M transitions. Although the electron state is localized only in the HfS_2 layer, the hybrid Γ hole state is delocalized over both layers, and the degree of delocalization increases with the number of HfS_2 layers, whereas the hole and electron states of the K-M transition are localized in the individual layers. **c**, A schematic illustration showing the momentum indirect Γ -M transition of the ILE, and the angle stacking mismatch (ϕ) between the two 2D materials. **d**, Energy diagram showing the correlation between the ILE binding energy to the electronic quasiparticle bandgap and optical bandgap, derived from the WSe_2 and HfS_2 valence and conduction bands. The large difference in the ILE and intralayer energy prohibits hybridization and thus explains the angular independence between the two materials (detail in the text). **e**, Ab initio calculated interface exciton E_b as a function of number of HfS_2 layers (blue squares) on the right axis. Black and red filled circles are the theoretical and experimental redshifts, respectively, of the ILE optical band gap ($E_{\text{gap}}^{\text{opt}}$) plotted as a function of the number of HfS_2 layers. Dashed lines are fitted exponential functions. The mean \pm s.d. of the experimental values result from the averaging of multiple measurements.

curve into the second quadrant, which suggests that carriers accumulate near the junction, instead of being depleted as occurs in a typical p-n diode.

Band bending at the heterostructure junction of 2D materials is possible and has been verified experimentally^{38–40}. The band bending at the heterostructure junction is dependent on the relative Fermi energy level (E_F) and carrier concentration at the junctions. If we assume a similar E_F for 3L and bulk HfS_2 , the magnitude of band bending in both cases is expected to be similar, yet with a narrower depletion width in 3L HfS_2 , as space is more constrained than in bulk HfS_2 (Fig. 2c). We performed a theoretical calculation to estimate the band-bending diagram through a self-consistent calculation for charge density and potential in real space; the results are plotted in Fig. 2d (for WSe_2 /3L, 5L and 7L- HfS_2). The change in band bending when an external bias is applied is shown in Extended Data Fig. 5. The reduction of the bandgap in bulk HfS_2 is mainly reflected as the upward shift of the VBM of HfS_2 , as the CBM hardly changes with thickness (Supplementary Fig. 17). In this model, we assume that the band bending in monolayer WSe_2 is small or non-existent as it

is physically not practical. The model clearly shows an increasing depletion width with the number of HfS_2 layers.

The aforementioned junction at the heterostructure interface acts as a trap for ILEs, as illustrated in Fig. 2c, and results in their accumulation at the interface. These trapped ILEs work as antennas that borrow their oscillator strength, f , from the surroundings^{41,42}. From a classical viewpoint, when an electron is bound to the nuclear framework and has an oscillating dipole, the oscillator strength f is directly proportional to the integral over the absorption band. The ILE absorption in this study has the same magnitude as those of intralayer A excitons (Fig. 1b), and thus direct ILE generation via photoexcitation is highly favourable. Also, the accumulation of ILEs could have enhanced the electron-hole overlap at the interface, which overcomes the spatially indirect nature of the transition and contributes to the large f , as proposed by Lau et al.⁴³. This is an experimentally observed large interband oscillator strength of ILEs in 2D materials^{27,44,45}, which is generally two orders of magnitude smaller than the intralayer exciton f due to the spatially separated wavefunction. To better understand the nature of the optical transition in the

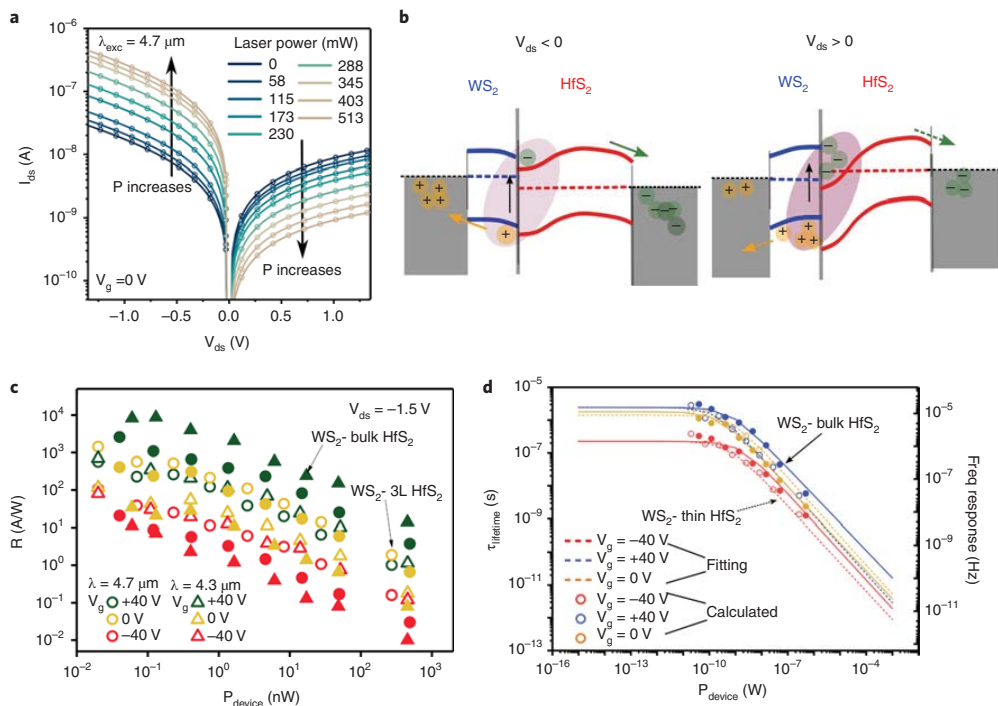


Fig. 4 | Infrared photodetectors based on interface excitons. **a**, I - V curve of the heterostructure in a device made of WS_2 and 3L HfS_2 under different laser excitation powers (P) ($\lambda = 4.7 \mu\text{m}$, $V_g = 0$). **b**, Schematic diagram illustrating the band alignment of WS_2 and HfS_2 under positive and negative V_{ds} biases and the charge extraction process. Under a positive V_{ds} , the charge carrier needs to overcome a higher energy barrier to move to the electrode. The darker shading of the ellipses at the interface indicates a stronger recombination. **c**, The calculated R of $\text{WS}_2/3\text{L HfS}_2$ and $\text{WS}_2/\text{bulk HfS}_2$ under two different excitation wavelengths ($\lambda = 4.3$ and $4.7 \mu\text{m}$) and different gating voltages, with $V_{ds} = -1.5 \text{ V}$. P_{device} is defined as the incident power on the active device, $P_{\text{device}} = P_{\text{in}} \times (L \times W / A_{\text{laser}})$, where L and W are the length and width, respectively, of the photoactive area rounded to the nearest number. The filled triangles and circles refer to a device made of WS_2 -bulk HfS_2 , the empty shapes represent a device made of WS_2 -3L HfS_2 . **d**, The calculated lifetimes of the charge carriers in the device, which correspond directly to the device response time or frequency, one of the parameters that defines the performance of a photodetector. Dashed lines and solid lines are fits to the data from $\text{WS}_2/3\text{L HfS}_2$ and $\text{WS}_2/\text{bulk HfS}_2$ devices, respectively. Only the data from $\text{WS}_2/3\text{L HfS}_2$ (device 1) and $\text{WS}_2/\text{bulk HfS}_2$ are plotted. The filled and empty circles refer to a device made of WS_2 -bulk HfS_2 and WS_2 -thin HfS_2 , respectively. The data for the remaining devices and details of the calculations can be found in the Supplementary Information.

ILEs, we conducted an ab initio calculation of the band structure at the heterostructure interface.

Calculated band structure at the heterointerface. In type II heterostructures formed between WS_2 and HfS_2 , the VBM of WS_2 shifts from the K point to the Γ point. The states in the K point are mainly built by d orbitals of the W atom and are hardly affected by HfS_2 due to a large separation between the layers. However, the S_p state, which contributes to the occupied states in the Γ point, can directly interact with neighbouring layers and shifts the VBM to the Γ point. Also, the maximum energy differences at the K and Γ points in WS_2 are very small (Fig. 3a), and thus when spin-orbit coupling is introduced, it raises the energy at the K point and moves the VBM back to the K point (details in the Supplementary Information). In contrast, the CBM of HfS_2 is unaffected by the hybridization and remains at the M point.

From the ab initio calculation, we found the hole states at the Γ point extend over both the WS_2 and HfS_2 layers (Fig. 3b). Hence, the interlayer coupling strength is substantial at the Γ point due to interlayer hybridization, and dependent on the thickness of HfS_2 . It is worth noting that the HfS_2 orbital contribution to the VBM increases with the number of layers (colour scale in Fig. 3a), which means the optical transition from the Γ to the M point becomes less

interlayer (more intralayer) in character and the matrix elements for this transition are more favourable. In contrast, the wavefunction overlap at the K point is negligible. Therefore, we conclude that the observed ILE absorption originates from the Γ -M instead of the K-M transition even though the VBM could be located at the K point after hybridization (Fig. 3c). It is worth mentioning that the observed ILEs share certain similarities with interface excitons in lateral heterostructures, partly due to the charge delocalization and wavefunction overlap.

The large energy difference of the CBM and VBM in WS_2 and HfS_2 in our heterosystem results in a non-degenerate and non-interacting ILE and intralayer exciton, which explains the small or negligible angular dependence on the ILE oscillator strength and energy. This outcome is in agreement with previous work by Falko and co-workers.^{46,47} In their study, they observed a prominent angular dependence (Φ) of the ILEs close to 0 and 60° rotation angles due to the strong hybridization of an ILE with an intralayer exciton via interlayer conduction-band tunnelling.

We further investigated the decrease in the optical bandgap of ILEs with increasing thickness of HfS_2 by calculating the quasiparticle bandgap at the GW level and the ILE binding energy from first-principles calculations for the heterostructure (Supplementary Section 11). The optical band gap can be determined as

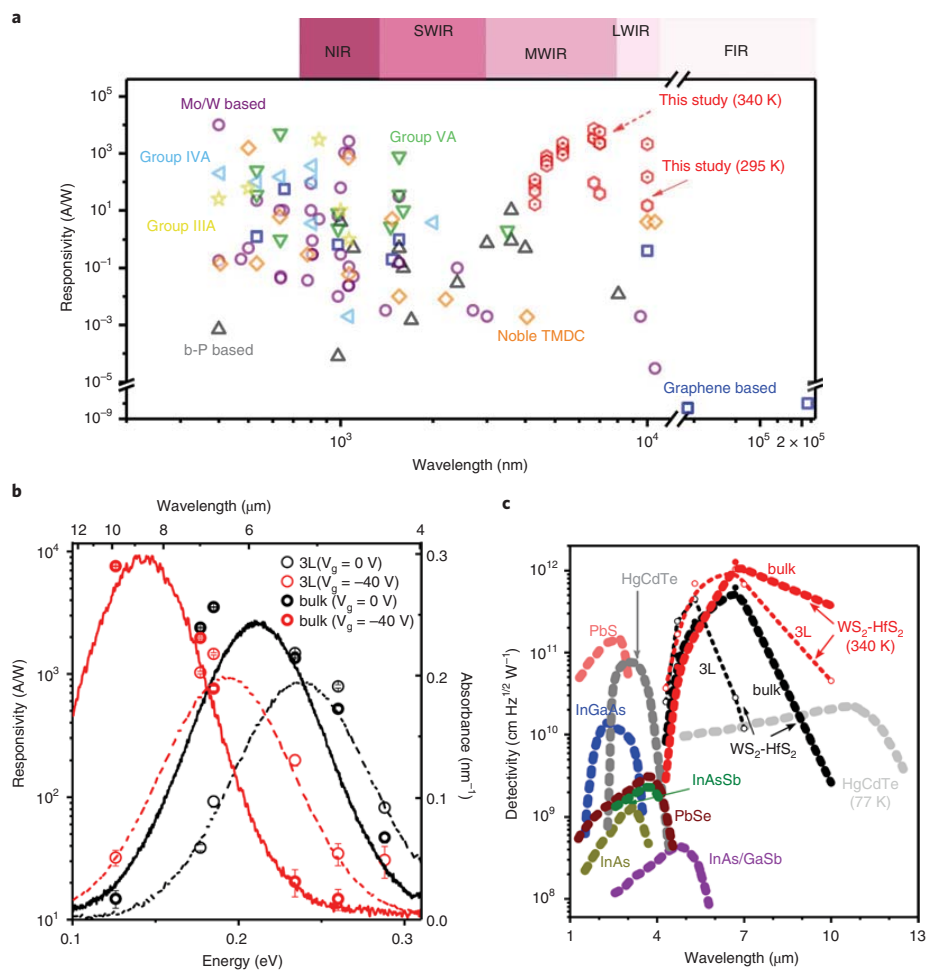


Fig. 5 | Responsivity and detectivity of infrared photodetectors. **a**, Comparison of the peak responsivity of WS_2/HfS_2 devices ($V_g = 0\text{ V}$, $V_{ds} = -1.5\text{ V}$ and $I_{\text{device}} = 0.5\text{ nW}$) to other recently reported top-performing 2D-based photodetectors in the visible and infrared range. References to the selected studies can be found in the Supplementary Information. The fixed large bandgap of most 2D materials limits their application to the visible–NIR region, whereas the large dark current and small absorption limit graphene application. **b**, The responsivity of WS_2/HfS_2 devices ($V_{ds} = -1.5\text{ V}$ and $P_{\text{device}} = 0.5\text{ nW}$) at $V_g = 0$ and -40 V . By tuning the interlayer band alignment and the bandgap, the responsivity of the device changes according to the shift of the ILE absorption peak. The s.d. is calculated from multiple devices of particular heterostructures. **c**, Specific detectivity as a function of wavelength for WS_2/HfS_2 devices and the commercially available photodetectors at room temperature, unless otherwise specified. At higher temperatures, the exciton spectral broadening increases the spectral detectivity range, whereas the increase in photon absorption via phonon-assisted transition increases the detectivity. The small open circles are the raw data, whereas the dashed-line is a spline-interpolation of the raw data points. FIR, far infrared; LWIR, long-wave infrared; MWIR, medium-wave infrared; SWIR, short-wave infrared; TMDC, transition metal dichalcogenide.

$E_{\text{gap}}^{\text{opt}} = E_{\text{gap}}^{\text{qp}} - E_{\text{b,IE}}$, where $E_{\text{gap}}^{\text{qp}}$ is the quasiparticle bandgap and $E_{\text{b,IE}}$ is the ILE binding energy (Fig. 3d). As a consequence of the higher dielectric screening with increasing HfS_2 layers, we found that both $E_{\text{gap}}^{\text{qp}}$ and $E_{\text{b,IE}}$ decrease, which results in an overall small redshift of $E_{\text{gap}}^{\text{opt}}$ (Fig. 3e). Hence, the change in $E_{\text{gap}}^{\text{opt}}$ is a result of a complex interplay of both factors, which can be manipulated to tune the ILE energy.

Highly sensitive and responsive infrared photodetector. The enhanced optical properties of the ILEs of WS_2/HfS_2 heterostructures renders them suitable for infrared photodetection. The device structure is shown in Fig. 2a. The device was operated in a photoconductive mode, with the voltage applied between the drain and

source (V_{ds}) to dissociate the ILE and extract free carriers. The photocurrent is defined as $I_{\text{ph}} = |I_{\text{ds,illum}}| - |I_{\text{ds,dark}}|$, where $I_{\text{ds,illum}}$ and $I_{\text{ds,dark}}$ are the current under illumination and the dark current, respectively. Figure 4a shows the I – V curve of $\text{WS}_2/3\text{L HfS}_2$ when photoexcited with an infrared laser ($\lambda_{\text{exc}} = 4.7\ \mu\text{m}$). When a negative voltage is applied to the drain relative to the source, I_{ph} increases because the charge extraction is favourable under this condition, which we called a positive feedback (Fig. 4b, left). However, a positive V_{ds} confines the ILE to the interface, which results in more recombination (relative to zero V_{ds}) and fewer extractable carriers (negative feedback; Fig. 4b, right). A thicker HfS_2 has a larger $I_{\text{ds,dark}}$ which stems mainly from a stronger confinement and recombination of the electrons and holes at the interface. We also found that the change in

interlayer bandgap energy did not noticeably affect the dark current (Extended Data Fig. 6). From the current generated, we calculated the responsivity, which is defined as ($R = I_{\text{ph}}/P_{\text{device}}$), where P_{device} is the effective laser power on the sample area, $P_{\text{device}} = P_{\text{in}}A_{\text{device}}/A_{\text{laser}}$, P_{in} is the incident laser power, A_{device} is the effective sample area and A_{laser} is the laser spot area. Peak responsivities of 8.2×10^2 and $9.5 \times 10^2 \text{ A W}^{-1}$ were observed for $\text{WS}_2/3\text{L HfS}_2$ on laser illuminations of $\lambda = 4.7$ and $4.3 \mu\text{m}$, respectively, at a gate voltage (V_g) of $+40 \text{ V}$ (Fig. 4c). With increasing exciton concentration (as P_{device} increases), the I_{ph} and R decrease primarily due to a higher exciton scattering and recombination. We note that the thickness of the HfS_2 and the bias V_g determine the value of R , which is expected as both variables determine the ILE absorption edge.

We analysed the fundamental operating speeds of the WS_2/HfS_2 -heterostructure photodetectors by calculating the average lifetime of the photocarriers in the channel. Using the transit time (τ_{transit}) calculated from the charge carrier mobility (details in Supplementary Information), we can estimate the carrier lifetime (τ_{lifetime}) from the photoconductive gain G by using $\tau_{\text{lifetime}} = G \times \tau_{\text{transit}}$ (ref. 48). Figure 4d shows the calculated carrier lifetime of the ILEs under different V_g and excitation power along with the respective fitted values by using the Hornbeck–Haynes model (details in Supplementary Information). The calculated response time is $\sim 1 \text{ ns}$ at $V_g = 0 \text{ V}$ with $V_{\text{ds}} = -1.5 \text{ V}$ and $P_{\text{device}} \approx 400 \text{ nW}$. We can also extrapolate the carrier lifetime of the photodetector to an excitation power that is not achievable in our set-up. Based on the model, a fundamental response time of $\sim 1 \text{ ps}$ is possible at $P_{\text{device}} = 1 \text{ mW}$ at $V_{\text{ds}} = -1.5 \text{ V}$. The fast intrinsic response time is anticipated because HfS_2 and WS_2 have high mobilities for electron and hole transport, respectively^{49,50}. Nonetheless, the operating speed of our device is in the millisecond range (Extended Data Figs. 7 and 8). It is not the fastest infrared photodetector reported, but we believe there is room for improvement.

Discussion and future directions. Figure 5a compares the responsivity of the heterostructures in our study to other 2D-based photodetectors (hybrid 2D-systems are excluded), regardless of their bias voltage and excitation power. The high responsivity of the Mo/W 2D photodetector in visible and near infrared (NIR) range results from the direct bandgap nature of the band-edge excitation. The enhanced absorption of the ILEs in this study boosted the responsivity by two orders of magnitudes in the MW–LWIR range, which makes it comparable to those of Mo/W-based photodiodes in the visible and near infrared range (Fig. 5a). Furthermore, the intrinsic dipole of an ILE, which is responsive to the externally applied field, can be exploited to dynamically tune the detection range and sensitivity (Fig. 5b).

The calculated detectivities, D^* , of our WS_2/HfS_2 -heterostructure photodiodes is higher than those of other commercially available infrared photodetectors, especially for room and elevated temperature operations (Fig. 5c). The spectral broadening and increase in phonon-assisted transition at high temperatures enhance the detection range and detectivity, respectively. We also demonstrated that absorption is tunable and extendable up to $20 \mu\text{m}$ (0.06 eV) by electrostatic doping, as shown in Extended Data Fig. 9. Theoretically, the absorption bandwidth can be further extended to the far-infrared range, either by applying a higher V_g or choosing a suitable combination of materials with the right band alignment. The versatility of ILEs in 2D heterostructures is not limited to two materials (AB stacking). Further stacking with similar or dissimilar materials on top of the second material would create either ABA or ABC structures (Extended Data Fig. 10). ABA stacking potentially produces a ‘quantum well’ structure that increases the efficiency further from AB stacking, whereas ABC stacking allows the simultaneous formation of two different ILEs, which could be tailored to either dual photodetection or photoemission systems.

Conclusions. In summary, a tunable, highly responsive and room-temperature MW–LWIR photodetector based on a WS_2/HfS_2 heterostructure has been demonstrated. The absorption band can be tuned and extended to $20 \mu\text{m}$ under a modest electric field, far beyond the cutoff wavelength of black phosphorus/black AsP. A strongly enhanced ILE absorption due to the unique band alignment and orbital hybridization contributed to the strong photoresponse. Our study provides a glimpse of the physics of ILEs in the unique heterostructures and offers a promising technology for infrared photodetection and, potentially, a photoemitter.

Online content

Any methods, additional references, Nature Research reporting summaries, source data, extended data, supplementary information, acknowledgements, peer review information; details of author contributions and competing interests; and statements of data and code availability are available at <https://doi.org/10.1038/s41565-020-0717-2>.

Received: 8 August 2019; Accepted: 19 May 2020;

Published online: 29 June 2020

References

- Rogalski, A., Adamiec, K. & Rutkowski, J. *Narrow-gap Semiconductor Photodiodes* Vol. 77 (SPIE Press, 2000).
- Iotti, R. C. & Andreani, L. C. A model for exciton binding energies in III–V and II–VI quantum wells. *Semicond. Sci. Technol.* **10**, 1561–1567 (1995).
- Zrenner, A. et al. Indirect excitons in coupled quantum well structures. *Surf. Sci.* **263**, 496–450 (1992).
- Hu, W. et al. Analysis of temperature dependence of dark current mechanisms for long-wavelength HgCdTe photovoltaic infrared detectors. *J. Appl. Phys.* **105**, 104502 (2009).
- Piotrowski, J. Uncooled operation of IR photodetectors. *Opto-Electron. Rev.* **12**, 111–122 (2004).
- Mak, K. F. & Shan, J. Photonics and optoelectronics of 2D semiconductor transition metal dichalcogenides. *Nat. Photon.* **10**, 216–226 (2016).
- Wang, Q. H., Kalantar-Zadeh, K., Kis, A., Coleman, J. N. & Strano, M. S. Electronics and optoelectronics of two-dimensional transition metal dichalcogenides. *Nat. Nanotechnol.* **7**, 699–712 (2012).
- Manzeli, S., Ovchinnikov, D., Pasquier, D., Yazyev, O. V. & Kis, A. 2D transition metal dichalcogenides. *Nat. Rev. Mater.* **2**, 17033 (2017).
- Novoselov, K., Mishchenko, A., Carvalho, A. & Neto, A. C. 2D materials and van der Waals heterostructures. *Science* **353**, aac9439 (2016).
- Koppens, F. et al. Photodetectors based on graphene, other two-dimensional materials and hybrid systems. *Nat. Nanotechnol.* **9**, 780–793 (2014).
- Cheiwchanamangij, T. & Lambrecht, W. R. Quasiparticle band structure calculation of monolayer, bilayer, and bulk MoS_2 . *Phys. Rev. B* **85**, 205302 (2012).
- He, K. et al. Tightly bound excitons in monolayer WSe_2 . *Phys. Rev. Lett.* **113**, 026803 (2014).
- Kaviraj, B. & Sahoo, D. Physics of excitons and their transport in two dimensional transition metal dichalcogenide semiconductors. *RSC Adv.* **9**, 25439–25461 (2019).
- Rivera, P. et al. Observation of long-lived interlayer excitons in monolayer MoSe_2 - WSe_2 heterostructures. *Nat. Commun.* **6**, 6242 (2015).
- Wang, L. et al. One-dimensional electrical contact to a two-dimensional material. *Science* **342**, 614–617 (2013).
- Nair, R. R. et al. Fine structure constant defines visual transparency of graphene. *Science* **320**, 1308–1308 (2008).
- Chen, X. et al. Widely tunable black phosphorus mid-infrared photodetector. *Nat. Commun.* **8**, 1672 (2017).
- Guo, Q. et al. Black phosphorus mid-infrared photodetectors with high gain. *Nano Lett.* **16**, 4648–4655 (2016).
- Liu, Y. et al. Gate-tunable giant Stark effect in few-layer black phosphorus. *Nano Lett.* **17**, 1970–1977 (2017).
- Long, M. et al. Room temperature high-detectivity mid-infrared photodetectors based on black arsenic phosphorus. *Sci. Adv.* **3**, e1700589 (2017).
- Long, M., Wang, P., Fang, H. & Hu, W. Progress, challenges, and opportunities for 2D material based photodetectors. *Adv. Funct. Mater.* **29**, 1803807 (2018).
- Yu, X. et al. Atomically thin noble metal dichalcogenide: a broadband mid-infrared semiconductor. *Nat. Commun.* **9**, 1545 (2018).
- Qin, D. et al. Monolayer PdSe_2 : a promising two-dimensional thermoelectric material. *Sci. Rep.* **8**, 2764 (2018).

24. Haastrup, S. et al. The computational 2D materials database: high-throughput modeling and discovery of atomically thin crystals. *2D Mater.* **5**, 042002 (2018).
25. Latini, S., Winther, K. T., Olsen, T. & Thygesen, K. S. Interlayer excitons and band alignment in MoS₂/hBN/WSe₂ van der Waals heterostructures. *Nano Lett.* **17**, 938–945 (2017).
26. Kunstmann, J. et al. Momentum-space indirect interlayer excitons in transition metal dichalcogenide van der Waals heterostructures. *Nat. Phys.* **14**, 801–805 (2018).
27. Merkl, P. et al. Ultrafast transition between exciton phases in van der Waals heterostructures. *Nat. Mater.* **18**, 691–696 (2019).
28. Fogler, M., Butov, L. & Novoselov, K. High-temperature superfluidity with indirect excitons in van der Waals heterostructures. *Nat. Commun.* **5**, 4555 (2014).
29. Gong, C. et al. Band alignment of two-dimensional transition metal dichalcogenides: application in tunnel field effect transistors. *Appl. Phys. Lett.* **103**, 053513 (2013).
30. Frisenda, R. et al. Micro-reflectance and transmittance spectroscopy: a versatile and powerful tool to characterize 2D materials. *J. Phys. D* **50**, 074002 (2017).
31. Rigosi, A. F., Hill, H. M., Li, Y., Chernikov, A. & Heinz, T. F. Probing interlayer interactions in transition metal dichalcogenide heterostructures by optical spectroscopy: MoS₂/WS₂ and MoSe₂/WSe₂. *Nano Lett.* **15**, 5033–5038 (2015).
32. Hong, X. et al. Ultrafast charge transfer in atomically thin MoS₂/WS₂ heterostructures. *Nat. Nanotechnol.* **9**, 682 (2014).
33. Kozawa, D. et al. Evidence for fast interlayer energy transfer in MoSe₂/WS₂ heterostructures. *Nano Lett.* **16**, 4087–4093 (2016).
34. Nagler, P. et al. Interlayer exciton dynamics in a dichalcogenide monolayer heterostructure. *2D Mater.* **4**, 025112 (2017).
35. Rivera, P. et al. Valley-polarized exciton dynamics in a 2D semiconductor heterostructure. *Science* **351**, 688–691 (2016).
36. Baranowski, M. et al. Probing the interlayer exciton physics in a MoS₂/MoSe₂/MoS₂ van der Waals heterostructure. *Nano Lett.* **17**, 6360–6365 (2017).
37. Butov, L. V., Shashkin, A. A., Dolgoplov, V. T., Campman, K. L. & Gossard, A. C. Magneto-optics of the spatially separated electron and hole layers in GaAs/Al_xGa_{1-x}As coupled quantum wells. *Phys. Rev. B* **60**, 8753–8758 (1999).
38. Zhang, C., Johnson, A., Hsu, C.-L., Li, L.-J. & Shih, C.-K. Direct imaging of band profile in single layer MoS₂ on graphite: quasiparticle energy gap, metallic edge states, and edge band bending. *Nano Lett.* **14**, 2443–2447 (2014).
39. Liu, X. et al. Rotationally commensurate growth of MoS₂ on epitaxial graphene. *ACS Nano* **10**, 1067–1075 (2016).
40. Liu, H. et al. Molecular-beam epitaxy of monolayer and bilayer WSe₂: a scanning tunneling microscopy/spectroscopy study and deduction of exciton binding energy. *2D Mater.* **2**, 034004 (2015).
41. Rashba, E. & Gugenishvili, G. To the theory of the edge absorption in semiconductors. *Sov. Phys. Solid State* **4**, 759–760 (1962).
42. Rashba, E. A theory of impurity absorption of light in molecular crystals. *Opt. Spektrosk.* **2**, 568–577 (1957).
43. Lau, K. W., Calvin, Gong, Z., Yu, H. & Yao, W. Interface excitons at lateral heterojunctions in monolayer semiconductors. *Phys. Rev. B* **98**, 115427 (2018).
44. Meckbach, L., Huttner, U., Bannow, L., Stroucken, T. & Koch, S. Interlayer excitons in transition-metal dichalcogenide heterostructures with type-II band alignment. *J. Phys. Condens. Matter* **30**, 374002 (2018).
45. Ross, J. S. et al. Interlayer exciton optoelectronics in a 2D heterostructure p–n junction. *Nano Lett.* **17**, 638–643 (2017).
46. Alexeev, E. M. et al. Resonantly hybridized excitons in moiré superlattices in van der Waals heterostructures. *Nature* **567**, 81–86 (2019).
47. Ruiz-Tijerina, D. A. & Fal'ko, V. I. Interlayer hybridization and moiré superlattice minibands for electrons and excitons in heterobilayers of transition-metal dichalcogenides. *Phys. Rev. B* **99**, 125424 (2019).
48. Saleh, B. E., Teich, M. C. & Saleh, B. E. *Fundamentals of Photonics* (Wiley, 1991).
49. Kanazawa, T. et al. Few-layer HfS₂ transistors. *Sci. Rep.* **6**, 22277 (2016).
50. Jin, Z., Li, X., Mullen, J. T. & Kim, K. W. Intrinsic transport properties of electrons and holes in monolayer transition-metal dichalcogenides. *Phys. Rev. B* **90**, 045422 (2014).

Publisher's note Springer Nature remains neutral with regard to jurisdictional claims in published maps and institutional affiliations.

© The Author(s), under exclusive licence to Springer Nature Limited 2020

Methods

Sample fabrication. Multilayer samples were fabricated by means of a mechanical exfoliation transfer process. For this, we initially exfoliated WS₂ and HfS₂ flakes from bulk crystals (bought from 2D semiconductors) onto polydimethylsiloxane substrates. Monolayer regions of these flakes were identified via optical microscopy, atomic force microscopy and Raman spectroscopy. Then, we first transferred the WS₂ flake onto the target substrate, a silicon wafer covered with a SiO₂ layer and predefined metal markers. Subsequently, the HfS₂ flake was transferred on top of the WS₂ flake. After the transfer, the samples were annealed under Ar gas at 150 °C for a few hours.

Optical spectroscopy. The absorption spectra were obtained by reflectance measurements of the samples at room temperature. The reflectance measurements were performed using the broadband emission from a tungsten halogen lamp. The spot size on sample was about 2–3 μm. The reflected light was collected by the same objective and deflected by a beam-splitter to a spectrometer equipped with a CCD (charge-coupled device) camera cooled to liquid-nitrogen temperature. For λ > 1,700 nm, we utilized a Fourier transform infrared set-up (Bruker FTIR spectroscopy, Vertex 80v) with a HgCdTe detector and Hyperion 2000 microscope to measure the sample reflectance. A commercial Au mirror was used as the reference. The reflectance spectra of the samples were determined by normalizing them to the reflection spectra of the substrate, which is highly transparent in the wavelength range of interest. Quartz and silicon substrates were used for the measurements in the visible to NIR, and mid-to-far infrared, respectively. Here, $\Delta r/r = (r_t - r_s)/r_s$, where r_t denotes the reflectance from the sample on the substrate and r_s is the reflectance of the substrate. For a thin film, the differential reflectance spectra $\Delta r/r$ is related to the absorption coefficient of the material $\alpha(\lambda)$ as^{51,52}:

$$\frac{\Delta r}{r} = \frac{4n}{n_0^2 - 1} \alpha(\lambda) \quad (1)$$

where n is the refractive index of the flakes under investigation and n_0 is the refractive index of the substrate. For the heterointerface, the average value of n is used to calculate the absorption coefficient. The values reported in this study are the absorption coefficient of the material normalized to its thickness for an impartial comparison.

The PL of the heterostructures in the infrared range was measured in the same set-up by exciting the samples with a 532 nm laser. Raman and PL (<900 nm) measurements were performed in a photon scanning tunnelling microscope set-up (Alpha 300S, WITec GmbH). A continuous-wave laser at 532 nm was coupled to a ×50 microscope objective and focused on a submicrometre spot on the sample surface. PL and scattered light were collected with the same objective, passed through long-pass filters, coupled into a grating spectrometer and detected with a Peltier-cooled CCD. Information was extracted from the spectra by using a fitting routine undertaken manually, which yields the integrated intensity, spectral position and full-width at half-maximum for each spectral feature extracted using a Gaussian fit. All of the experiments were performed under a low excitation density to obtain a reasonable signal-to-noise ratio and to minimize the generation of trions.

Device structure and characterization. The metal contact patterns were written using electron beam lithography (Elionx ELS7000) and an electron beam evaporator (Denton Vacuum Explorer). The devices were initially coated with polymethyl methacrylate by spin coating at 5,000 r.p.m. for 90 s. The post bake was performed at 180 °C for 2 min. The design of the electrodes was done with AutoCAD software. The patterns (designed with AutoCAD) were then written with a 100 pA current and a registration dose of 960 μC cm⁻² (0.06 μJ dot⁻¹). The written patterns were developed by using methyl isobutyl ketone and isopropyl alcohol with a developing time of 70 s. The electrode pads consisted of Ti and Au, in which Ti was used to improve the adhesion, with thicknesses of 5 and 50 nm and deposition rates of 0.1 and 1 Å s⁻¹, respectively. The samples were then soaked with acetone for 24 h for the metal contact liftoff. The heterostructures were exfoliated on SiO₂, which provides insulation from the heavily doped silicon back gate. Electrostatic doping was performed by grounding the gold contact and applying a voltage to the back gate. Furthermore, the silicon chip was glued on a ceramic chip carrier using conductive silver paste. The metal contacts of the source and drain as well as the back gate were wire bonded to the selected pins using metal wires. In a typical measurement, the source and back gate were biased by two independent Keithley (2450 and 2420) sourcemeters and the drain is the common ground. The sourcemeters were controlled by a computer to measure the I - V relation of the device. The responsivity measurement in the infrared range was measured with mid-infrared lasers (tunable continuous wave/pulsed external cavity quantum cascade laser). The lasers were focused by an infrared lens to a final spot size of approximately 100 μm.

Experimental data analysis. For each 2D layer and heterostructure, the absorption and PL were measured at room temperature, unless specified. To take into account the spatial inhomogeneity of the ILE absorption/emission, spatial averaging was employed. For this, the average absorption/emission energy of the ILE, and its s.d.,

were calculated from the values extracted from a routine procedure for normal curve fitting applied to the spectra collected from the heterostructure regions. On average, 5–10 spectra were evaluated for each individual heterostructure. Multiple devices were made by stacking the 2D materials together, without any control on the alignment.

Computational methods. The first-principle calculations for the band structure as a function of the number of HfS₂ layers were performed by using the Vienna ab initio simulation package⁵³ with a generalized gradient approximation of the Perdew–Burke–Ernzerhof (PBE) functional⁵⁴ without spin–orbit corrections included. The ion–electron interaction was treated by the projector-augmented wave method⁵⁵, and the van der Waals interaction was taken into consideration using the DFT-D3 method⁵⁶. The electron wavefunction was expanded on a plane-wave basis set with a cutoff energy of 450 eV. A 6 × 6 × 1 Γ -centred Monkhorst–Pack grid was adopted for the Brillouin-zone integration. A vacuum slab of more than 15 Å was applied along the z direction (normal to the interface) to avoid spurious interactions between repeated slabs. To construct the quasiparticle bandgap at the GW level, a GW calculation was done using GPAW^{57,58} for the WS₂ and HfS₂ monolayers with a plane-wave cutoff energy of 800 eV for the ground state and 300 eV for the GW calculation on a 18 × 18 × 1 k -point grid, which included spin–orbit corrections. The quasiparticle bandgap was then constructed by correcting the GW monolayer band structures with the N -dependent screening correction calculated from the quantum electrostatic heterostructure model⁵⁹ and an N -dependent hybridization correction from the PBE band-structure calculations for each k point in each band. This method has previously been shown accurate for calculating the band structure of multilayer van der Waals heterostructures⁶⁰. The ILE binding energies were calculated by solving the Mott–Wannier equation with the screened electron–hole interaction calculated within the quantum electrostatic heterostructure model. The effective electron and hole masses were calculated from the PBE band structures. Structural relaxation was carried out using the conjugate-gradient algorithm until the total energy converged to 10⁻⁴ eV and the Hellmann–Feynman force on each atom was less than 0.01 eV Å⁻¹, respectively.

The calculation of the band diagram of WS₂/HfS₂ was conducted through a self-consistent calculation for the charge density and electric potential in real space. The tight-binding Hamiltonian of 1L-WS₂/3L-HfS₂ was interpolated by a Wannier basis via the Wannier90 package⁶¹, for which the input was provided from the first-principles results. In the tight-binding Hamiltonian, we considered $W d$, $Hf d$ and $S p$ orbitals for the Wannier bases and the Hamiltonian can reproduce bands around the highest valance band and the lowest conduction band obtained from the first-principles calculations. The spatial electric potential was obtained by solving self-consistently the Poisson equation, with the charge density obtained from the wavefunction of the Wannier tight-binding Hamiltonian. In the self-consistent calculation, we applied the real-space finite element method⁶² to numerically solve the Poisson equation, and the relative permittivities for HfS₂ and WS₂ were 2 (ref. 63) and 4.13 (ref. 64), respectively. To approximate the experimental bulk-HfS₂ device, the 3L-HfS₂ Hamiltonian was further extended to various numbers of layers of HfS₂. The extension was achieved by inserting n layers of the HfS₂ Hamiltonian with interlayer coupling extracted from the 3L-HfS₂ layers. 1L-WS₂ was lightly n doped with a doping concentration $\sim 1 \times 10^6$ cm⁻² and the HfS₂ was intrinsic. The band profiles were plotted according to the band-edge shifting information given by the calculated electric potential profile.

Data availability

The data within this paper are available in a public data repository at <https://doi.org/10.6084/m9.figshare.12220454> (ref. 65). Source data are provided with this paper.

References

- Dhakal, K. P. et al. Confocal absorption spectral imaging of MoS₂: optical transitions depending on the atomic thickness of intrinsic and chemically doped MoS₂. *Nanoscale* **6**, 13028–13035 (2014).
- McIntyre, J. & Aspnes, D. E. Differential reflection spectroscopy of very thin surface films. *Surf. Sci.* **24**, 417–434 (1971).
- Kresse, G. & Furthmüller, J. Efficient iterative schemes for ab initio total-energy calculations using a plane-wave basis set. *Phys. Rev. B* **54**, 11169–11186 (1996).
- Perdew, J. P., Burke, K. & Ernzerhof, M. Generalized gradient approximation made simple. *Phys. Rev. Lett.* **77**, 3865–3868 (1996).
- Blöchl, P. E. Projector augmented-wave method. *Phys. Rev. B* **50**, 17953–17979 (1994).
- Grimme, S., Antony, J., Ehrlich, S. & Krieg, H. A consistent and accurate ab initio parametrization of density functional dispersion correction (DFT-D) for the 94 elements H–Pu. *J. Chem. Phys.* **132**, 154104 (2010).
- Mortensen, J. J., Hansen, L. B. & Jacobsen, K. W. Real-space grid implementation of the projector augmented wave method. *Phys. Rev. B* **71**, 035109 (2005).

ARTICLES

NATURE NANOTECHNOLOGY

58. Enkovaara, J. et al. Electronic structure calculations with GPAW: a real-space implementation of the projector augmented-wave method. *J. Phys. Cond. Matter* **22**, 253202 (2010).
59. Andersen, K., Latini, S. & Thygesen, K. S. Dielectric genome of van der Waals heterostructures. *Nano Lett.* **15**, 4616–4621 (2015).
60. Winther, K. T. & Thygesen, K. S. Band structure engineering in van der Waals heterostructures via dielectric screening: the G Δ W method. *2D Mater.* **4**, 025059 (2017).
61. Mostofi, A. A. et al. An updated version of Wannier90: a tool for obtaining maximally-localised Wannier functions. *Comp. Phys. Comm.* **185**, 2309–2310 (2014).
62. *LiveLink for MATLAB User's Guide* (COMSOL, Inc., 2018).
63. Chen, Q. Y., Liu, M. Y., Cao, C. & He, Y. Engineering the electronic structure and optical properties of monolayer 1T-HfX₂ using strain and electric field: a first principles study. *Physica E* **112**, 49–58 (2019).
64. Ghosh, R. K. & Mahapatra, S. Monolayer transition metal dichalcogenide channel-based tunnel transistor. *IEEE J. Electron Devices Soc.* **1**, 175–180 (2013).
65. Lukman, S. & Teng, J. High oscillator strength interlayer excitons in 2D heterostructures for mid-IR photodetection. *Figshare* <https://doi.org/10.6084/m9.figshare.12220454.v1> (2020).

Acknowledgements

The work is supported by the Agency for Science, Technology and Research (A*STAR) under the 2D Materials Pharos Program (grant no. 152 700014 and grant no. 152 700017). Q.J.W. acknowledges funding from the National Research Foundation Competitive Research Program (NRF-CRP18-2017-02 and NRF-CRP19-2017-01). K.S.T. acknowledges support from the Center for Nanostructured Graphene (CNG) under the Danish National Research Foundation (project DNRF103) and from the

European Research Council (ERC) under the European Union's Horizon 2020 research and innovation programme (grant no. 773122, LIMA). G.L. acknowledges the supported under the grant MOE2017-T2-1-114. H.L. acknowledges the support by the Ministry of Science and Technology (MOST) in Taiwan under grant no. MOST 109-2112-M-001-014-MY3. J.T. and S. Lukman thank C. W. Lee, A. Ngo and M. Zhao for their valuable inputs and K Hippalgaonkar for sharing tools in the device fabrication.

Author contributions

S. Lukman and J.T. conceived the idea and designed the experiments; S. Lukman, L.D., Q.S.W. and Y.T. performed the experiments; S. Lukman, L.D., Q.J.W. and J.T. analysed the data; L.X., A.C.R.-J., G.Z., M.Y., S. Luo, C.H., L.Y., G.L., H.L., Y.-W.Z., K.S.T. and Y.F. contributed to the theoretical calculations. S. Lukman, J.T. and Q.J.W. co-wrote the paper. All the authors discussed the results and commented on the manuscript.

Competing interests

The authors declare no competing interests.

Additional information

Extended data is available for this paper at <https://doi.org/10.1038/s41565-020-0717-2>.

Supplementary information is available for this paper at <https://doi.org/10.1038/s41565-020-0717-2>.

Correspondence and requests for materials should be addressed to J.T.

Peer review information *Nature Nanotechnology* thanks Yanqing Wu and the other, anonymous, reviewer(s) for their contribution to the peer review of this work

Reprints and permissions information is available at www.nature.com/reprints.

8.5 Paper V

Excitons and Band Alignment in 2D van der Waals Heterostructures: *Ab-Initio* Calculations versus Experiments

A. C. Riis-Jensen and K. S. Thygesen

Under preparation

List of points to be addressed:

- General revision.
- Obtain calculated quasi-particle energies for twisted MoSe₂/WS₂.
- Implement Mott-Wannier-QEH model for calculating screened exciton binding energies for excitons with electron and/or hole states located on both layers in bilayer structures.

Excitons and Band Alignment in 2D van der Waals Heterostructures: *Ab-Initio* Calculations versus Experiments

Anders C. Riis-Jensen¹ and Kristian S. Thygesen,¹

¹*Center for Atomic-scale Materials Design, Department of Physics,
Technical University of Denmark, DK - 2800 Kongens Lyngby, Denmark*

(Dated: July 12, 2020)

In this study we resolve a long-standing issue in exciton physics of van der Waals heterostructures (vdWHs); we address the matter of to which accuracy *ab-initio* calculated intra- and interlayer exciton energies can be expected to agree with experimentally measured exciton energies. We do this by computationally quantifying substrate-, finite temperature-, and twist-angle effects on calculated exciton energies within *ab-initio* many-body perturbation theory methods. Such effects affects exciton energies in experimental measurements, but are not present in conventional *ab-initio* many-body calculations. We combine *ab-initio* many-body GW and BSE calculations with electrostatic and computational effective models, to perform accurate many-body calculations for vdWHs containing up to more than a thousand atoms. Specifically we employ a self-consistent numerical scheme to correct the wrong interlayer hybridization predicted by non-self-consistent *ab-initio* many-body calculations, such as the G0W0 approximation. From this we directly calculate the effect of substrate and twist-angle effects on the exciton energies, which are shown to redshift the exciton energies up to about 30-50 meV and 60-120 meV respectively. By including these effects, we calculate exciton energies for several commensurate and incommensurate few-layer vdWHs and compare the calculated exciton energies to a large library of experimentally measured energies obtained from the literature. By including computed substrate-, temperature, and twist-angle-effects on the calculated exciton energies we benchmark intralayer excitons can be calculated to within 20 meV of the experimentally measured values and significantly improves upon the accuracy compared to experimental measurements. We also find that interlayer excitons can be calculated to within the experimental uncertainty for incommensurate bilayers, while the calculated interlayer exciton energies in commensurate MoS₂/WS₂ and MoSe₂/WSe₂ are overestimated and outside the experimental range of uncertainty. The commensurate bilayers are furthermore subject to degenerate intra- and interlayer excitons resulting in a further blueshift of the exciton energies upon rotation, and we show it is necessary to treat the interlayer hybridization self-consistently from the quasi-particle band line-up to correctly quantify this energy shift.

I. INTRODUCTION

The exfoliation of monolayer graphene in 2004¹ opened a new paradigm of materials science by introducing the class of 2-dimensional (2D) materials. The class of 2D materials are unique in the field of materials science and are characterized by their atomically thin extension in the out-of-plane direction. Since then, the discovery of monolayer MoS₂², the first 2D semiconducting material showing extraordinary strong excitonic effects^{3,4} and the discovery that any set of 2D monolayers can be stacked into so-called van der Waals heterostructures⁵⁻⁷ (vdWHs) opened up new pathways and potentials for the world of 2D materials. In recent years special attention have been paid to experimentally investigate and map out intra- and interlayer exciton energies in few layer semiconducting vdWHs (see table I). Furthermore, detailed experiments have been carried out to prove the existence of a superconducting phase in bilayer graphene⁸, intralayer to interlayer exciton dissociation times⁹, Moiré effects on exciton energies⁹, twist-angle dependence of exciton energies¹⁰, and fascinating intra- and interlayer exciton hybridization effects¹¹. While the vdWHs are characterized by weak interlayer van der Waals bonds and only little interlayer orbital hybridization, the above experiments prove that it becomes increasingly important

to accurately incorporate interlayer hybridization effects into *ab-initio* calculations. Non-self-consistent state of the art *ab-initio* methods, such as the G0W0 approximation, are challenged by the fact that such calculations cannot be carried out for large vdWHs and that the description of the interlayer hybridization is inherited from the DFT band line-up and thus fundamentally wrong.^{12,13} Furthermore, experiments are carried out on a supporting substrate and for vdWHs at different relative twist-angles between the layers. This have an effect on the measured exciton energies, however these effects are not contained in conventional *ab-initio* calculations. This makes a one-to-one comparison between experimental observations and *ab-initio* calculations cumbersome, and a study quantifying these effects in the literature is needed to benchmark the effect on exciton energies to be able to properly compare experimental observations with *ab-initio* calculations.

In this work we resolve this issue and benchmark to what accuracy intra- and interlayer energies can be calculated *ab-initio* compared to experimentally measured exciton energies for large vdWHs. We calculate the intra- and interlayer exciton energies for 6 different TMD heterobilayers by combining state of the art *ab-initio* computational many-body methods with effective electrostatic and computational models. Specifically we

treat the interlayer dielectric screening with the previously developed QEH model¹⁴ and apply a herein developed computational model for correctly treating the interlayer hybridization and interlayer charge transfer self-consistently from the G0W0 Γ quasi-particle band line-up. This corrects the wrong interlayer description of the interlayer hybridization pattern predicted by non-self-consistent many-body *ab-initio* methods (such as full G0W0 calculations) widely applied in the computational society. This enables us of accurately calculating exciton energies for vdWHs containing thousands of atoms not possible with conventional codes and to directly disentangle the effect of interlayer dielectric screening, interlayer orbital hybridization, and interlayer charge transfers effects. This let us directly calculate the effect of twist-angle rotations and dielectric substrate screening on the exciton energies - effects also not possible to calculate by conventional many-body *ab-initio* methods and let us quantify the uncertainty related to these effects for computational methods. We benchmark the accuracy of the calculated intra- and interlayer exciton energies against a large library of experimentally measured exciton energies obtained from the literature and discuss the uncertainty within the experimental measurements, which gives a lower bound on the accuracy that can be expected from computational methods. By including the uncertainty from calculated substrate-, twist-angle-, and temperature effects, we show that intralayer exciton energies can be calculated to within 20 meV of the experimental uncertainty, while interlayer exciton energies can be calculated to within the experimental uncertainty for all considered incommensurate bilayers. For the two commensurate bilayers our calculated exciton energies overestimate the interlayer exciton energy. We discuss this issue in relation to the hybridised intra- and interlayer exciton energies found in the two commensurate bilayer systems.

II. METHODS

To calculate vdWH quasi-particle energies we split the calculation into an *ab-initio* calculation for the freestanding monolayers and effective models for the interlayer interaction. We calculate the quasi-particle energies for the freestanding monolayers by the G0W0 Γ approximation. This approximation is obtained by iterating Hedin's equations¹⁵ starting from the initial guess of the self-energy: $\Sigma^0(1,2) = \delta(1,2)v_{xc}(1)$ which after 1 iteration leads to a self-energy of the form:

$$\Sigma = iGv[1 - \chi^0(v + f_{xc})]^{-1}. \quad (1)$$

Here χ^0 is the non-interacting density response function, v is the bare Coulomb interaction, and $f_{xc} = \delta v_{xc}/\delta n$ is the vertex xc-kernel. We note that all calculations are performed with norm-conserving (NC) atomic PAW setups. The effect of the vertex kernel is to shift the band alignment up relative to vacuum (compared to a G0W0

calculations), and the overall effect of doing a G0W0 Γ calculation with NC atomic setups compared to a G0W0 calculation with non-NC atomic setups, is only a minor change of the quasi-particle band gap, but a better description of the band line-up relative to the vacuum energy¹⁶.

The interlayer interaction is split into three components: interlayer dielectric screening, interlayer orbital hybridization effects, and interlayer charge transfer effects. The interlayer dielectric screening is calculated by the previously developed QEH¹⁴ model. We stress that the handling of the dielectric screening in 2D needs special care due to the fundamentally different behaviour of the dielectric function in the $\mathbf{q} \rightarrow \mathbf{0}$ limit: in 2D $\epsilon(\mathbf{q} = \mathbf{0}) = 1$, while in 3D $\epsilon(\mathbf{q} = \mathbf{0}) > 1$. For a mathematically strict isotropic 2D system, the static dielectric function takes the form¹⁷:

$$\epsilon_{2D}(\mathbf{q}) = 1 + 2\pi\alpha|\mathbf{q}| \quad (2)$$

for small \mathbf{q} . Here α is the static 2D in-plane polarizability of the material and the $\mathbf{q} \rightarrow \mathbf{0}$ limit is easily recovered. From the 2D dielectric function the screened Coulomb interaction takes the well known form:

$$W_{2D}(\mathbf{q}) = -\frac{2\pi}{\mathbf{q}}\epsilon_{2D}^{-1}(\mathbf{q}). \quad (3)$$

In the QEH model the interlayer dielectric screening is modelled by coupling the individual monolayers in the vdWH using a classical electrostatics model. First the interacting density response function of each monolayer in the vdWH (index i) are calculated *ab-initio* in their freestanding form within the Random Phase Approximation (RPA) by solving the Dyson equation

$$\begin{aligned} \chi_i(\mathbf{r}, \mathbf{r}', \omega) &= \chi_i^0(\mathbf{r}, \mathbf{r}', \omega) \\ &+ \int \int d\mathbf{r}_1 d\mathbf{r}_2 \chi_i^0(\mathbf{r}, \mathbf{r}_1, \omega) \frac{1}{|\mathbf{r}_1 - \mathbf{r}_2|} \chi_i(\mathbf{r}_1, \mathbf{r}_2, \omega) \end{aligned} \quad (4)$$

where $\chi_i^0(\mathbf{r}, \mathbf{r}', \omega)$ is the non-local non-interacting density response function for layer i . From this the induced density in each freestanding monolayer, from an external multipole electrostatic potential, is determined to model the electrostatic part of the interlayer interaction. After this, the response functions for all monolayers are coupled through a Dyson equation for the full density response function of the vdWH, from which the difference in the screened Coulomb interaction between the vdWH and the individual freestanding monolayers can be obtained. Finally the screened Coulomb interaction for the vdWH is defined as:

$$\bar{W}_i^{\text{vdWHs}}(\mathbf{r}, \mathbf{r}', \omega) = \bar{W}_i(\mathbf{r}, \mathbf{r}', \omega) + \Delta\bar{W}_i(\mathbf{r}, \mathbf{r}', \omega). \quad (6)$$

Here $\bar{W}_i(\mathbf{r}, \mathbf{r}', \omega)$ is the screened interaction for a freestanding monolayer, $\Delta\bar{W}_i(\mathbf{r}, \mathbf{r}', \omega)$ is the change in the screened interaction in layer i due to the presence of all the other layers in the vdWH evaluated by the

QEH model, and $\bar{W}_i^{\text{vdWHs}}(\mathbf{r}, \mathbf{r}', \omega)$ is the resulting total screened potential for layer i in the vdWH. From this the effect on the quasi-particle energies can directly be obtained from the change in the GW self-energy due to the change in W .

To accurately calculate the effect of interlayer orbital hybridization we apply a herein developed method, in which we perform a LCAO calculation for the full vdWH, applying (possibly different) scissors operators to the valence- and conduction band states for each individual monolayer in the vdWH to match the G0W0 Γ quasi-particle band edges for the freestanding monolayers. In practice we consider the LCAO eigenvalue problem

$$\sum_{\nu} \tilde{H}_{\mu\nu} c_{\nu n} = \sum_{\nu} \hat{S}_{\mu\nu} c_{\nu n} E_n \quad (7)$$

where the smooth wave functions within the PAW formalism are expanded in a linear combination of atomic orbitals: $\langle \psi_n | = \sum_{\mu} c_{\mu n} \langle \Psi_{\mu} |$ with weight $c_{\mu n}$. $\hat{S}_{\mu\nu}$ is the overlap operator between states $|\mu\rangle$ and $|\nu\rangle$: $\hat{S}_{\mu\nu} = \langle \Psi_{\mu} | \hat{S} | \Psi_{\nu} \rangle$. $\tilde{H}_{\mu\nu}$ is the LCAO Hamiltonian, E_n the allowed quantum level energies, and we refer to the original work for the implementation of the LCAO mode in the GPAW code^{18–20}. By adding a correction to the LCAO Hamiltonian, $\tilde{H}_{\mu\nu}^S$, this gives rise to a correction to the eigenvalues: $\Delta E_n^S = \sum_{\mu\nu} S_{\mu\nu} c_{\mu n} \tilde{H}_{\mu\nu}^S c_{\nu n}$. By defining the desired eigenvalue corrections, it is thus possible to determine $\tilde{H}_{\mu\nu}^S$ and correct the initial band line-up. In this way, we can self-consistently evaluate the interlayer orbital hybridization and charge transfer starting from the many-body G0W0 Γ band line-up. This corrects the possibly wrong description of the interlayer hybridization offered by non-self-consistent *ab-initio* many-body calculations, which inherits the description of the interlayer band line-up and hybridization pattern from a single-particle description. We denote this method the LCAOS method and the calculations will be performed with the PBE functional. The LCAOS calculation for the vdWH allows the direct extraction of the effect of interlayer hybridization and charge transfer on the band structure energies by comparing to the band structure of the freestanding monolayers. We will label the calculation of screened quasi-particle energies in vdWHs by combining G0W0 Γ calculations for the freestanding monolayers with the presented models for the interlayer interactions as the G0W0 Γ -QEH model.

In fig. 1 is shown an example where we have calculated the quasi-particle band structure of MoS₂/WS₂ with the method outlined above. The sum of the G0W0 Γ quasi-particle energies for the freestanding non-interacting monolayers is shown in black. We then explicitly divide the interlayer interaction into its component of the interlayer interaction to highlight the state dependence of the different components. The interlayer hybridization is only shown for the two top (bottom) valence (conduction) bands for simplicity. In red the effect of the interlayer dielectric screening is added to the

quasi-particle energies which we find to be close to constant throughout the Brillouin zone in agreement with previous findings²¹. In green we have also added the effect of interlayer hybridization and charge transfer. A constant shift up (down) throughout the Brillouin zone of the states localised on MoS₂ (WS₂) of about 20 meV is found due to the interlayer charge transfer. We find no effect on the quasi-particle energies around the K-point due to interlayer hybridization while we find a symmetric splitting of the valence states around the Γ -point of about 190 meV. This shows that the effect of orbital hybridization in parts of the Brillouin zone have a larger effect on the quasi-particle energies than the interlayer dielectric screening, which is found to be a constant shift of the quasi-particle energies of about 70-90 meV. We note that the calculation in fig. 1 is carried out without including spin-orbit effects for simplicity, but that the calculation of the exciton energies in the remaining part of this study fully includes spin-orbit interaction effects.

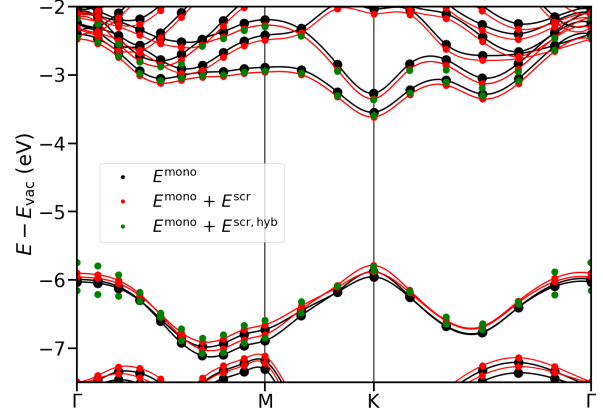


FIG. 1. Quasi-particle band structure of MoS₂/WS₂ calculated with the G0W0 Γ -QEH model. In black is shown the sum of the quasi-particle energies calculated for the freestanding non-interacting monolayers (E^{mono}). In red is added the effect of interlayer dielectric screening (E^{scr}) and in green is on top of this added the effect of interlayer orbital hybridization and charge transfer ($E^{\text{scr,hyb}}$). The interlayer coupling is calculated with the QEH model as outlined in the main text.

To obtain excitation energies we calculate the zero momentum intralayer exciton binding energies by solving the Bethe-Salpeter Equation (BSE) for the freestanding monolayers including the interlayer dielectric screening from the QEH model. This is done by considering the two-particle BSE Hamiltonian:

$$\mathcal{H}_{SS'}(\mathbf{q}) = (\epsilon_{m\mathbf{k}+\mathbf{q}}^{\text{QP}} - \epsilon_{n\mathbf{k}}^{\text{QP}}) \delta_{SS'} - (f_{m\mathbf{k}+\mathbf{q}} - f_{n\mathbf{k}}) K_{SS'}(\mathbf{q}), \quad (8)$$

with the two-particle kernel $K_{SS'}$:

$$K_{SS'}(\mathbf{q}) = V_{SS'}(\mathbf{q}) - \frac{1}{2} W_{SS'}(\mathbf{q}). \quad (9)$$

The first term on the right hand side is the electron-hole

exchange interaction and the second term is the direct screened electron-hole interaction. In a plane-wave expansion the static screened electron-hole interaction is given by²²:

$$W_{SS'}(\mathbf{q}) = \frac{4\pi}{\omega} \sum_{\mathbf{G}\mathbf{G}'} n_{n\mathbf{k},n'\mathbf{k}'}^*(\mathbf{G}) W_{\mathbf{G}\mathbf{G}'}(\mathbf{k}' - \mathbf{k}) n_{m\mathbf{k}+\mathbf{q},m'\mathbf{k}'+\mathbf{q}}(\mathbf{G}) \quad (10)$$

where $n_{n\mathbf{k},n'\mathbf{k}'}^*(\mathbf{G})$ and $n_{m\mathbf{k}+\mathbf{q},m'\mathbf{k}'+\mathbf{q}}(\mathbf{G}')$ are charge density matrices and $W_{\mathbf{G}\mathbf{G}'}(\mathbf{k}' - \mathbf{k})$ is the screened electron-hole interaction for all \mathbf{G} vectors in the plane-wave description. To correct the screened interaction for the presence of all other layers in the vdWH, we calculate $\Delta\bar{W}_i(\mathbf{r}, \mathbf{r}', \omega)$ for layer i using the QE model and add this correction to the $\mathbf{G} = \mathbf{G}' = \mathbf{0}$ component in equation 10. This method is labelled as the BSE-QEH model. We find an overall small redshift of the exciton energies in vdWHs by combining the G0W0 Γ -QE model and the BSE-QEH model to calculate screened quasi-particle and exciton binding energies in agreement with experimental observations² upon stacking of the monolayers.

Finite momentum intralayer and interlayer exciton binding energies are calculated by solving a Mott-Wannier model including the interlayer dielectric screening of the electron-hole interaction and calculating the effective mass of the exciton state in question. In the Mott-Wannier model it is assumed that the exciton state is governed by the hydrogen-like form:

$$\left[-\frac{\nabla^2}{2\mu_{\text{ex}}} + W_{2D}(\mathbf{r}_{||}) \right] F(\mathbf{r}_{||}) = E_b F(\mathbf{r}_{||}), \quad (11)$$

where W_{2D} is the screened electron-hole interaction calculated by the QE model, $F(\mathbf{r}_{||})$ gives the probability amplitude for the distance between the electron and the hole, μ_{ex} is the effective in-plane exciton mass, ∇ is the kinetic energy, and E_b is the exciton binding energy. The exciton effective mass is given by: $\frac{1}{\mu_{\text{ex}}} = \frac{1}{\mu_e} + \frac{1}{m_h}$, where the electron is located in the conduction band and the hole in the valence band. The electron and hole effective masses are calculated from the second derivative of the DFT band structures of the freestanding monolayers. Once the effective masses has been computed from the band structure, the exciton binding energies can be calculated. This will be referred to as the MW-QEH model.

In fig. 2 we show an example of the absorption spectrum of MoS₂/MoSe₂ calculated with the BSE-QEH model (green) and for the sum of the absorption spectra of the freestanding non-interacting monolayers (grey). The interlayer dielectric screening of the quasi-particle energies are calculated with the G0W0 Γ -QE model. We find a small downshift of the lowest lying excitation energies as expected due to the environmental dielectric screening. The average of the experimentally measured exciton energies for MoS₂/MoSe₂ from table I is shown with vertical full lines and the excitation energies calculated with the MW-QEH is shown with vertical dashed lines. We note that due to the large lattice mismatch

between MoS₂ and MoSe₂ such an excitonic absorption spectrum would not be possible to calculate *ab-initio* at the level of the BSE with conventional codes, without applying significant strains to one or both of the layers. We also stress that we do not apply strains to any layers within the BSE-QEH and MW-QEH models applied in this study and under 0.1% of strain to any of the monolayers in the G0W0 Γ -QE model.

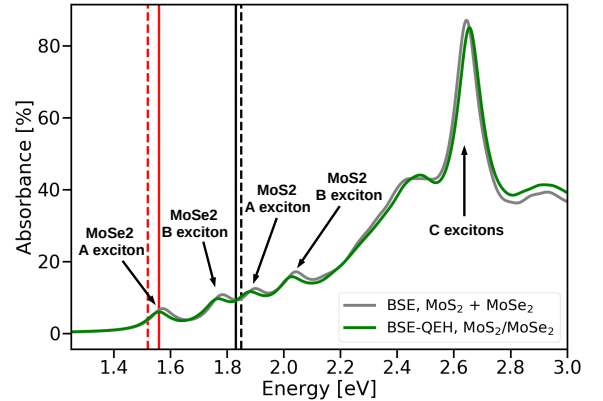


FIG. 2. Absorption spectrum for bilayer MoS₂/MoSe₂ with the BSE-QEH model in green. For reference is shown the sum of the absorption spectrum of the freestanding monolayers, i.e. without any interlayer interaction in grey. The A and B exciton peaks of the two layers are labelled and experimental data is shown in vertical full lines, see tables I and II. With vertical dashed lines are shown the peak position predicted by the MW-QEH model.

III. RESULTS AND DISCUSSION

To determine the possible accuracy of computational methods for calculating exciton energies in vdWHs it is necessary to first assess the experimental accuracy of experimentally measured intra- and interlayer exciton energies. A library of experimentally measured intra- and interlayer exciton energies obtained from the literature, for the 6 bilayer systems considered in this study, can be found in table I. In the same table we also list the substrate and temperature for the given experiment where known. For experimentally measured intralayer exciton energies we find a variation of about 120 meV within the experiments and up to about 130 meV for the interlayer exciton energies. One exception of these values is the interlayer exciton state in MoS₂/WSe₂ which we will return to later. The lower bound of the expected accuracy that can be achieved by *ab-initio* calculations will in the following be defined by the standard deviation of the exciton energies listed in table I for each exciton state in each system. Thus we will compare our calculated exciton energies to the uncertainty (standard deviation) of the experimentally

measured exciton energies centered around the average of the experimentally measured exciton energy. The reported energies in table I are all taken from photoluminescence measurements.

While conventional many-body *ab-initio* calculations are performed at 0 K without the presence of a dielectric screening substrate, from the data in table I it is evident that temperature, substrate, and possibly other effects alters the experimentally measured exciton energies. Previous studies have quantified finite temperature effects in *ab-initio* many-body calculations for the A exciton in MoS₂ where a redshift of about 90 meV from 0 to 300 K was found⁴⁴, however a systematic computational study on the effect of substrate screening and twist-angle of the exciton energies lacks in the literature. Since the dielectric substrates in experimental setups usually are wide band gap insulators such as hBN and SiO₂, the substrate only very weakly hybridize with the valence and conduction bands of the TMD vdWHs and as such the effect of the substrate on the exciton energies can be limited to only considering the effect of dielectric screening. We here utilize the G0W0Γ-QEH, BSE-QEH, and MW-QEH models to computationally benchmark the effect of substrate screening on the exciton energy of the K-K intra- and interlayer exciton energies of MoS₂/MoSe₂ by calculating the exciton energies on a varying number of supporting hBN layers. This is shown in fig. 3 and we note that the K-K transition should be representative for the lowest energy exciton states since we find the dielectric screening to be close to constant throughout the Brillouin zone. We stress again that such calculations cannot be carried out with conventional *ab-initio* codes due to the lattice mismatch of MoS₂, MoSe₂, and hBN, without applying significant strains to one or more of the layers, and that we here do not apply strains to any of the layers. As mentioned above, the screening of the quasi-particle energies is calculated from the G0W0Γ-QEH model, the screening of the intralayer exciton binding energies is calculated with the BSE-QEH model, and the interlayer exciton binding energy is calculated with the MW-QEH model. For the intralayer exciton energies we find a redshift of about 50 meV for the intralayer exciton in MoS₂ (black) and about 40 meV for the intralayer exciton in MoSe₂ (blue) comparing the freestanding bilayer with the asymptotic value of the bilayer on an infinitely thick hBN substrate. We note 300 layers of supporting hBN corresponds to a thickness of about 100 nm. The calculated redshift of the intralayer exciton is expected and of the same magnitude as experimentally measured exciton redshifts in multilayer vdWHs². While the effect is small it is of the same size as the standard deviation (i.e. the uncertainty) of most experimental values for exciton energies as listed in table II and so is an important parameter to take into account. We find an overall redshift of the interlayer exciton of about 40 meV, with a small blueshift for few layers of hBN. The blueshift is a wrong artefact of the MW-QEH which also predicts a

blueshift of the intralayer exciton energy for few layer vdWHs. We therefore expect a slightly larger redshift of the interlayer exciton energy in a complete BSE description. The result presented here can be used to assess the effect of hBN, however a recent study⁴⁵ have quantified the dependence of the dielectric screening on the static polarizability of both the 2D semiconductor monolayer and substrate and showed this have a predictable dependence on these parameters. This, together with the result in fig. 3 allows both experimentalists and theoreticians to estimate the effect of substrate screening when comparing *ab-initio* calculations with experimental observations for different substrates and thicknesses for any semiconductor/dielectric-support system.

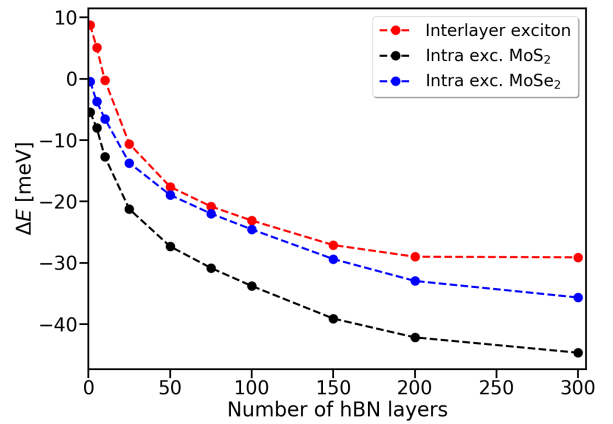


FIG. 3. Change in exciton energy (ΔE) of the intra- (black and blue) and interlayer (red) K-K excitons in MoS₂/MoSe₂ when placed on N number of hBN layers. The change in the exciton binding energy is calculated with the BSE-QEH model for the intralayer exciton binding energies and with the MW-QEH model for the interlayer exciton energy. The screening of the quasi-particle energies is calculated from the G0W0Γ-QEH model for all states.

It has recently been show that in vdWHs with nearly degenerate intra- and interlayer exciton states, the two excitons hybridize and the exciton energies attains a peculiar twist-angle dependence. This have been found experimentally for MoSe₂/WS₂¹¹ where the conduction band minima of the two monolayers are nearly degenerate, and the two degenerate exciton states are the K-K intra- and interlayer exciton states. The lowest exciton energy remains constant over a wide range of twist-angles and shift down about 100 eV close to 0 degrees of relative twist-angle. This effect is explained by a hybridised intra- and interlayer excitonic state. By studying MoS₂/WS₂ where we similarly find close to degenerate intra- and interlayer exciton states (see fig. 1), we demonstrate this effect can be captured and well described by the theoretical framework in this study. In fig. 4 we show the calculated K-K (black) and Γ-K (green) smallest quasi-particle (QP) energy gaps for bilayer MoS₂/WS₂ as a function of the twist-angle between

the two monolayers calculated with the G0W0 Γ -QE method. Upon rotation, we find an upshift of both the Γ -K and K-K quasi-particle band gaps of about 110 meV and 100 meV respectively that remains close to constant over the full range of rotation. This is in agreement with the experimental observation for the exciton energy in MoSe₂/WS₂³³, which is plotted in purple for reference on the qualitative effect. We note the experimentally measured exciton energy change is observed for the K-K exciton, while we find both the K-K and Γ -K transitions to host degenerate intra- and interlayer exciton states for MoS₂/WS₂. The observed effect is a result of a non-symmetric opening of the quasi-particle band gaps where the valence bands shift down about the double amount as the upshift of the conduction states. We also perform a calculation with the PBE functional⁴⁶, i.e. within a non-interacting single-particle description without applying the scissors operator to correct the band line-up (open circles). In this description the intra- and interlayer electronic band gaps are not nearly degenerate and we find the opposite effect: the Γ -K band gap shifts down about 25 meV on average upon rotation and as such the effect would not be captured by non-self-consistent *ab-initio* methods such as G0W0 where the interlayer hybridization is inherited from the single-particle band line-up. The results in fig. 4 shows that the experimentally observed effect can be understood already from the quasi-particle energies and underlines the importance of a correct self-consistent description of the band line-up to properly describe the interlayer hybridization.

Finally we are in a position where we can assess the computational accuracy that can be obtained for intra- and interlayer exciton energies in few layers vdWHs by including the effects of substrate, twist-angle, and temperature effects in *ab-initio* many-body calculations. Furthermore we apply the proper accurate description of the interlayer orbital hybridisation outlined above. We have calculated the lowest lying intra- and interlayer exciton energies for the K-K and Γ -K transitions in each of the 6 freestanding bilayer systems considered in this study, with the method outlined above. In general we find that the position of the ionization potential and electron affinity levels relative to the vacuum energy, to a large degree is determined by the nature of the chalcogenide atoms. The lattice constant of each monolayer is similarly determined by the nature of the chalcogenide atoms. This means that monolayer MoS₂ (MoSe₂) and WS₂ (WSe₂) are found to be lattice matched and consequently MoS₂/WS₂ and MoSe₂/WSe₂ have close to degenerate ionization potentials and/or electron affinity levels. At the same time monolayers with selenide have the ionization potential of the valence Γ -point states significantly lower than that of the K-point states, while monolayers with sulfur have the K- and Γ -point ionization potentials close to degenerate. This combined with the fact that the exciton binding energy, for some sys-

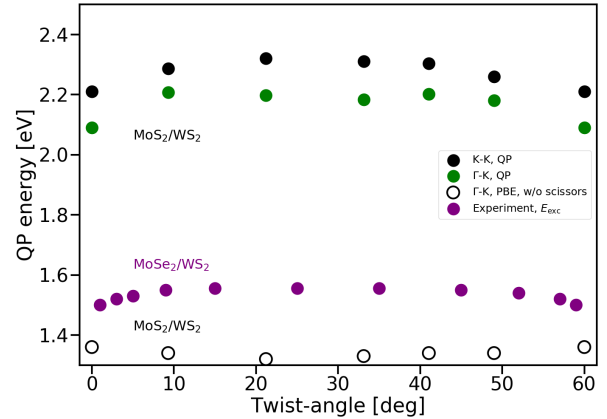


FIG. 4. Calculated Quasi-particle band gaps as a function of twist-angle for MoS₂/WS₂. The full circles show the G0W0 Γ -QE quasi-particle (QP) energies for the K-K (black) and Γ -K (green) lowest energy transitions. In empty circles is shown the Γ -K quasi-particle energy calculated in a single-particle picture with the PBE functional, i.e. without applying a scissors-operator to correct the band line-up and achieve a correct description of the interlayer hybridization. In purple is shown experimental exciton energies³³ for bilayer MoSe₂/WS₂ for a reference on the qualitative effect.

tems, is slightly higher when the hole is located at the Γ -point makes the overall exciton energy map complex and no overall picture can easily be deduced for which points in the Brillouin zone host the lowest lying exciton states. The picture is further blurred by the fact that the definition of interlayer excitons is not well-defined for systems with degenerate Γ -point states. In these bilayers the hole state at the Γ -point resides in both layers, however the exciton state could potentially still be experimentally determined to be an interlayer exciton state. Thus, for these systems we calculate the theoretical lower and upper limit of the "interlayer" exciton energy corresponding to the hole fully located in the same and opposite layer as the electron state respectively.

The calculated exciton energies (without accounting for substrate, finite temperature, and twist-angle effects) are shown in tab. II (left 4 columns). The average of the experimental data from the literature are shown in the right 2 columns. Without taking substrate, twist-angle, and temperature effects on the calculated exciton energies into account we find that the lowest intralayer exciton energies can be predicted to within the experimental uncertainties for 6/12 of the lowest intralayer exciton states. For the remaining intralayer excitons we find discrepancies between the calculated exciton energy and the experimentally measured energy (including the experimental uncertainty) between -20 meV to +120 meV, with only one intralayer exciton energy underestimated by our calculations. For the interlayer exciton energies we find 2/6 exciton energies within the experimental uncertainty, with a discrepancy between -50 meV to +250

meV for the remaining interlayer exciton energies (assuming intralayer character of mixed exciton states which are all overestimated in energy). For the interlayer excitons we similarly only find one exciton energy to be computationally underestimated. The experimental measurements in table I are carried out at a wide range of substrate and temperatures. To include substrate and temperature effects in the benchmarking of the calculated energies, we define δ to be the combined calculated energy redshift of substrate and finite temperature effects (from 0 K to room temperature) to be: $\delta = 140$ meV, following the discussion above and fig. 3. Since the substrate and temperature effects redshifts the exciton energies, we introduce these effects by redefining the calculated exciton energies in table II (denoted E_{exc}) to be: $(E_{\text{exc}} - \delta/2) \pm \delta/2$ i.e. we redshift the calculated exciton energy by $\delta/2$ and define a calculated uncertainty from substrate and temperature effects to be $\delta/2$. The introduction of this definition allows us to make an overall comparison to all experimentally measured exciton energies regardless of the substrate and temperature. We will not include the effect of twist-angle energy dependence, since this effect is only present for a few bilayers, but will discuss its effect on systems with degenerate intra- and interlayer excitons below. Including the calculated substrate and temperature effects 11/12 calculated and experimentally measured exciton energies are found to agree (including their uncertainties), except the lowest energy intralayer exciton in bilayer MoS₂/MoSe₂, which is underestimated by 20 meV. For interlayer excitons we now find 3/6 exciton energies to agree with a discrepancy for the remaining energies ranging from -50 meV to +180 meV (assuming an intralayer character of the mixed excitons states). We note again in passing that these effects are not present in conventional *ab-initio* many-body calculations and that simply applying an uncertainty of $\pm\delta/2$ without redshifting the exciton energies by $\delta/2$ only slightly improves the results. We thus find including substrate and finite temperature effects improves upon to the comparison to experimentally measured exciton energies. Including substrate and finite temperature effects still leaves the interlayer exciton energy in MoS₂/WS₂ MoSe₂/WSe₂ significantly overestimated and MoS₂/MoSe₂ slightly underestimated. It is interesting the significantly overestimated exciton energies are found for the two lattice matched bilayers, where we find hybridized intra- and interlayer exciton energies. As discussed above this introduces an extra uncertainty in relation to the twist-angle dependence of the calculated and experimentally measured exciton energies.

Focusing on lattice matched MoS₂/WS₂ the calculated overestimated interlayer exciton energy in this study is also found by previous studies applying full BSE@G0W0 calculations finding an interlayer exciton energy of 1.83 eV¹² and 1.95 eV¹³ respectively. The lower limit in this study is closer to the experimental value, suggests the importance of correctly calculating the interlayer hybridization self-consistently, however a significant discrepancy is

still found. As shown above, substrate and temperature effects can reduce this discrepancy by about 150 meV (fig. 3) bringing the energy closer to the experimental value, however since the computations for the lattice matched bilayers are carried out at a 0 degree relative twist-angle, a further upshift of the calculated exciton energy can be expected at other twist-angles (fig. 4). This suggests a more fundamental lack of accuracy of the quasi-particle ionisation potential or electron affinity levels offered by the G0W0(Γ) approximation and shows *ab-initio* many-body methods cannot calculate interlayer exciton energies in vdWHs to within the experimental accuracy.

Another point worth a comment is the significantly different experimentally measured interlayer exciton energies for bilayer MoS₂/WSe₂ listed in table I. While the two experimental references reporting values between 1.55-1.59 eV were the governing values for the interlayer exciton energy for several years, these two studies reported a lowest lying interlayer exciton energy about 0.5 eV higher than computational studies. Recently, a new study³² resolved the issue by showing the existence of an interlayer exciton with an energy around 1.60 eV for the K-K transition and a significantly lower energy interlayer exciton for the Γ -K transition around 1.05 eV. We find that lowest lying measured energy for the Γ -K to correspond well with our calculated value. This study underlines the great care that must be taken when comparing experimentally measured exciton energies with computationally calculated exciton energies, when the exact nature of the former is not known.

IV. CONCLUSION

In this work we have performed *ab-initio* many-body perturbation theory calculations, for predicting intra- and interlayer exciton energies in 6 different TMD bilayer van der Waals heterostructures. We have presented an efficient numerical scheme for accurately calculating interlayer hybridisation effects on exciton energies in van der Waals heterostructures, by self-consistently calculating the interlayer hybridisation from the G0W0 Γ band lineup. This corrects the substantially lacking description of the interlayer charge transfer and interlayer hybridisation offered by widely used non-self-consistent *ab-initio* many-body perturbation theory models. By combining this with the BSE approximation and the quantum electrostatic heterostructure model, allowed us to perform *ab-initio* many-body perturbation theory calculations, for predicting intra- and interlayer exciton energies in 6 different TMD bilayers. By the use of the developed models, accurate *ab-initio* calculations have been performed for systems with up to more than 1000 atoms. Furthermore, by directly calculating the effect of twist-angle and substrate effects and considering finite temperature effects, we benchmarked the calculated intra- and interlayer exciton energies against a large library of experimentally measured exciton energies. Substrate and temperature

effects computationally accounts for a redshift of up to about 50 meV and 90 meV respectively. Including the computed uncertainties in relation to these effects, we can conclude that many-body *ab-initio* calculations can predict and reproduce experimentally measured lowest energy intralayer exciton energies to within the experimental uncertainty for 11/12 of the considered excitons in the 6 TMD bilayers, with the remaining intralayer exciton state underestimated by 20 meV. Including substrate and temperature effects 3/6 of the interlayer exciton energies can be calculated to within the experimental uncertainty. The inclusion of substrate and finite temperature effects significantly improves upon the comparison between *ab-initio* calculated and experimentally measured exciton energies. We find the computed energy for the interlayer exciton in the two lattice matched systems: MoS₂/WS₂ and MoSe₂/WSe₂ to both be significantly overestimated and outside the range of the experimental uncertainty. These two systems furthermore have degenerate intra- and interlayer exciton states, resulting in a twist-angle dependent blueshift of the exciton energies of 50-100 meV upon rotation. This effect cannot account

for the discrepancy suggesting a fundamental error in the GW quasi-particle band edge energy description for lattice matched systems. One can hypothesise the effect can be explained by realising that the two lattice matched bilayers, in which the *ab-initio* many-body calculations significantly overestimates the interlayer exciton energy, are the only two of the considered bilayers that host both degenerate intra- and interlayer exciton energies for two different transitions in the Brillouin zone. This can lead to a hybridised bi-exciton state, a 4-particle state, splitting the two interlayer excitons up and down in energy similar to the hybridisation effect found around the valence Γ -point in the lattice matched bilayers and thus reduce the interlayer exciton energy.

ACKNOWLEDGMENTS

The Center for Nanostructured Graphene (CNG) is sponsored by the Danish Research Foundation, Project DNRF103.

-
- ¹ K. S. Novoselov, A. K. Geim, S. V. Morozov, D. Jiang, Y. Zhang, S. V. Dubonos, I. V. Grigorieva, and A. A. Firsov, *science* **306**, 666 (2004).
 - ² K. F. Mak, C. Lee, J. Hone, J. Shan, and T. F. Heinz, *Physical review letters* **105**, 136805 (2010).
 - ³ A. Ramasubramaniam, *Physical Review B* **86**, 115409 (2012).
 - ⁴ D. Y. Qiu, H. Felipe, and S. G. Louie, *Physical review letters* **111**, 216805 (2013).
 - ⁵ L. Ponomarenko, A. Geim, A. Zhukov, R. Jalil, S. Morozov, K. Novoselov, I. Grigorieva, E. Hill, V. Cheianov, V. Fal'Ko, *et al.*, *Nature Physics* **7**, 958 (2011).
 - ⁶ S. Haigh, A. Gholinia, R. Jalil, S. Romani, L. Britnell, D. Elias, K. Novoselov, L. Ponomarenko, A. Geim, and R. Gorbachev, *Nature materials* **11**, 764 (2012).
 - ⁷ C. R. Dean, A. F. Young, I. Meric, C. Lee, L. Wang, S. Sorgenfrei, K. Watanabe, T. Taniguchi, P. Kim, K. L. Shepard, *et al.*, *Nature nanotechnology* **5**, 722 (2010).
 - ⁸ Y. Cao, V. Fatemi, S. Fang, K. Watanabe, T. Taniguchi, E. Kaxiras, and P. Jarillo-Herrero, *Nature* **556**, 43 (2018).
 - ⁹ P. Merkl, F. Mooshammer, P. Steinleitner, A. Girnghuber, K.-Q. Lin, P. Nagler, J. Holler, C. Schüller, J. Lupton, T. Korn, *et al.*, *Nature materials* , 1 (2019).
 - ¹⁰ J. Kunstmann, F. Mooshammer, P. Nagler, A. Chaves, F. Stein, N. Paradiso, G. Plechinger, C. Strunk, C. Schüller, G. Seifert, *et al.*, *Nature Physics* **14**, 801 (2018).
 - ¹¹ E. M. Alexeev, D. A. Ruiz-Tijerina, M. Danovich, M. J. Hamer, D. J. Terry, P. K. Nayak, S. Ahn, S. Pak, J. Lee, J. I. Sohn, *et al.*, *Nature* **567**, 81 (2019).
 - ¹² E. Torun, H. P. Miranda, A. Molina-Sánchez, and L. Wirtz, *Physical Review B* **97**, 245427 (2018).
 - ¹³ T. Deilmann and K. S. Thygesen, *Nano letters* **18**, 1460 (2018).
 - ¹⁴ K. Andersen, S. Latini, and K. S. Thygesen, *Nanoletters* **15**, 4616 (2015).
 - ¹⁵ L. Hedin, *Physical Review* **139**, A796 (1965).
 - ¹⁶ P. S. Schmidt, C. E. Patrick, and K. S. Thygesen, *Phys. Rev. B* **96**, 205206 (2017).
 - ¹⁷ S. Latini, T. Olsen, and K. S. Thygesen, *Physical Review B* **92**, 245123 (2015).
 - ¹⁸ J. Enkovaara, C. Rostgaard, J. J. Mortensen, J. Chen, M. Duřak, L. Ferrighi, J. Gavnholt, C. Glinsvad, V. Haikola, H. Hansen, *et al.*, *Journal of physics: Condensed matter* **22**, 253202 (2010).
 - ¹⁹ J. J. Mortensen, L. B. Hansen, and K. W. Jacobsen, *Physical Review B* **71**, 035109 (2005).
 - ²⁰ A. H. Larsen, M. Vanin, J. J. Mortensen, K. S. Thygesen, and K. W. Jacobsen, *Physical Review B* **80**, 195112 (2009).
 - ²¹ K. T. Winther and K. S. Thygesen, *2D Materials* **4**, 025059 (2017).
 - ²² J. Yan, K. W. Jacobsen, and K. S. Thygesen, *Physical Review B* **86**, 045208 (2012).
 - ²³ S. Mouri, W. Zhang, D. Kozawa, Y. Miyauchi, G. Eda, and K. Matsuda, *Nanoscale* **9**, 6674 (2017).
 - ²⁴ D. H. Luong, H. S. Lee, G. P. Neupane, S. Roy, G. Ghimire, J. H. Lee, Q. A. Vu, and Y. H. Lee, *Advanced Materials* **29**, 1701512 (2017).
 - ²⁵ H. Heo, J. H. Sung, G. Jin, J.-H. Ahn, K. Kim, M.-J. Lee, S. Cha, H. Choi, and M.-H. Jo, *Advanced Materials* **27**, 3803 (2015).
 - ²⁶ Y. Gong, J. Lin, X. Wang, G. Shi, S. Lei, Z. Lin, X. Zou, G. Ye, R. Vajtai, B. I. Yakobson, *et al.*, *Nature materials* **13**, 1135 (2014).
 - ²⁷ H. Heo, J. H. Sung, S. Cha, B.-G. Jang, J.-Y. Kim, G. Jin, D. Lee, J.-H. Ahn, M.-J. Lee, J. H. Shim, *et al.*, *Nature communications* **6**, 7372 (2015).
 - ²⁸ S. Tongay, W. Fan, J. Kang, J. Park, U. Koldemir, J. Suh, D. S. Narang, K. Liu, J. Ji, J. Li, *et al.*, *Nano letters* **14**,

- 3185 (2014).
- ²⁹ H. Chen, X. Wen, J. Zhang, T. Wu, Y. Gong, X. Zhang, J. Yuan, C. Yi, J. Lou, P. M. Ajayan, *et al.*, *Nature communications* **7**, 12512 (2016).
- ³⁰ H. Fang, C. Battaglia, C. Carraro, S. Nemsak, B. Ozdol, J. S. Kang, H. A. Bechtel, S. B. Desai, F. Kronast, A. A. Unal, *et al.*, *Proceedings of the National Academy of Sciences* **111**, 6198 (2014).
- ³¹ M.-H. Chiu, M.-Y. Li, W. Zhang, W.-T. Hsu, W.-H. Chang, M. Terrones, H. Terrones, and L.-J. Li, *ACS nano* **8**, 9649 (2014).
- ³² O. Karni, E. Barré, S. C. Lau, R. Gillen, E. Y. Ma, B. Kim, K. Watanabe, T. Taniguchi, J. Maultzsch, K. Barmak, *et al.*, *Physical Review Letters* **123**, 247402 (2019).
- ³³ E. M. Alexeev, A. Catanzaro, O. V. Skrypka, P. K. Nayak, S. Ahn, S. Pak, J. Lee, J. I. Sohn, K. S. Novoselov, H. S. Shin, *et al.*, *Nano letters* **17**, 5342 (2017).
- ³⁴ M. Z. Bellus, F. Ceballos, H.-Y. Chiu, and H. Zhao, *ACS nano* **9**, 6459 (2015).
- ³⁵ F. Ceballos, M. Z. Bellus, H.-Y. Chiu, and H. Zhao, *Nanoscale* **7**, 17523 (2015).
- ³⁶ P. Rivera, K. L. Seyler, H. Yu, J. R. Schaibley, J. Yan, D. G. Mandrus, W. Yao, and X. Xu, *Science* **351**, 688 (2016).
- ³⁷ N. R. Wilson, P. V. Nguyen, K. Seyler, P. Rivera, A. J. Marsden, Z. P. Laker, G. C. Constantinescu, V. Kandyba, A. Barinov, N. D. Hine, *et al.*, *Science advances* **3**, e1601832 (2017).
- ³⁸ B. Miller, A. Steinhoff, B. Pano, J. Klein, F. Jahnke, A. Holleitner, and U. Wurstbauer, *Nano letters* **17**, 5229 (2017).
- ³⁹ C. Jiang, W. Xu, A. Rasmita, Z. Huang, K. Li, Q. Xiong, and W.-b. Gao, *Nature communications* **9**, 753 (2018).
- ⁴⁰ P. K. Nayak, Y. Horbatenko, S. Ahn, G. Kim, J.-U. Lee, K. Y. Ma, A.-R. Jang, H. Lim, D. Kim, S. Ryu, *et al.*, *ACS nano* **11**, 4041 (2017).
- ⁴¹ P. Nagler, M. V. Ballottin, A. A. Mitioglu, F. Mooshammer, N. Paradiso, C. Strunk, R. Huber, A. Chernikov, P. C. Christianen, C. Schüller, *et al.*, *Nature Communications* **8**, 1551 (2017).
- ⁴² J. S. Ross, P. Rivera, J. Schaibley, E. Lee-Wong, H. Yu, T. Taniguchi, K. Watanabe, J. Yan, D. Mandrus, D. Cobden, *et al.*, *Nano letters* **17**, 638 (2017).
- ⁴³ K. Wang, B. Huang, M. Tian, F. Ceballos, M.-W. Lin, M. Mahjouri-Samani, A. Boulesbaa, A. A. Puzos, C. M. Rouleau, M. Yoon, *et al.*, *ACS nano* **10**, 6612 (2016).
- ⁴⁴ A. Molina-Sánchez, M. Palummo, A. Marini, and L. Wirtz, *Physical Review B* **93**, 155435 (2016).
- ⁴⁵ A. C. Riis-Jensen, J. Lu, and K. S. Thygesen, *Physical Review B* **101**, 121110 (2020).
- ⁴⁶ J. P. Perdew, K. Burke, and M. Ernzerhof, *Physical review letters* **77**, 3865 (1996).

System	E^{intra}	E^{intra}	E^{inter}	Substrate	Temperature
MoS ₂ /MoSe ₂ ²³	1.83	1.53		SiO ₂	Room temp.
MoS ₂ /MoSe ₂ ²³	1.82	1.60	1.47	SiO ₂	5 K
MoS ₂ /MoSe ₂ ²⁴	1.83	1.55	1.34	SiO ₂	Room temp.
MoS ₂ /WS ₂ ²⁵	1.83	1.96	1.50	SiO ₂	
MoS ₂ /WS ₂ ²⁶	1.82	1.97	1.42	SiO ₂	Room temp.
MoS ₂ /WS ₂ ²⁷	1.83	1.94	1.5		
MoS ₂ /WS ₂ ²⁸	1.85	2.01	1.5	SiO ₂	
MoS ₂ /WS ₂ ²⁹	1.86	1.96	1.55	CaF ₂	
MoS ₂ /WSe ₂ ³⁰	1.87	1.64	1.55	SiO ₂	Room temp.
MoS ₂ /WSe ₂ ³¹	1.85	1.65	1.59	Al ₂ O ₃	
MoS ₂ /WSe ₂ ³²			1.05	hBN	20 K
MoSe ₂ /WS ₂ ³³	1.57	1.97	1.55	SiO ₂	Room temp.
MoSe ₂ /WS ₂ ³⁴	1.58	2.01	1.53	SiO ₂	Room temp.
MoSe ₂ /WS ₂ ³⁵	1.58	2.02	1.53	SiO ₂	Room temp.
MoSe ₂ /WSe ₂ ³⁵	1.57	1.65	1.35	SiO ₂	Room temp.
MoSe ₂ /WSe ₂ ³⁶			1.32	SiO ₂	30 K
MoSe ₂ /WSe ₂ ³⁷	1.57	1.66	1.38	Graphite	Room temp.
MoSe ₂ /WSe ₂ ³⁸	1.65	1.74	1.33	Schott borofloat®33	3 K
MoSe ₂ /WSe ₂ ³⁹	1.67	1.74	1.34	SiO ₂	2.3 K
MoSe ₂ /WSe ₂ ⁴⁰	1.57	1.66	1.35	SiO ₂	Room temp.
MoSe ₂ /WSe ₂ ⁴¹	1.68	1.71	1.39	SiO ₂	4 K
MoSe ₂ /WSe ₂ ⁴²	1.56	1.74	1.35	BN	5 K
WS ₂ /WSe ₂ ⁴³	1.99	1.66		SiO ₂	Room temp.
WS ₂ /WSe ₂	1.95		1.45	SiO ₂	78 K

TABLE I. Overview of experimentally measured intra- (E^{intra}) and interlayer (E^{inter}) exciton energies together with the substrate on which the bilayer was placed and temperature under which the measurement was conducted. For the intralayer exciton energies the left column is the exciton energy for the layer labelled to the left in the system statement (and vice versa for the right column). All energies are obtained from photoluminescence measurements. All energies are in eV and temperatures are in kelvin. The data is taken from the literature.

System	Calculated		Calculated		Experimental	
	K-K ^{intra}	Γ -K ^{intra}	K-K ^{inter}	Γ -K ^{inter}	Intralayer	Interlayer
MoS ₂	1.88	1.80	1.27	1.58	1.83 ± 0.01	1.41 ± 0.09
MoSe ₂	1.55	1.85			1.56 ± 0.04	
MoS ₂	1.90	1.80	1.94	1.80-1.86	1.83 ± 0.01	1.50 ± 0.05
WS ₂	2.11	1.94			1.97 ± 0.04	
MoS ₂	1.90	1.95	1.25	1.06	1.86 ± 0.01	1.57 ± 0.03
WSe ₂	1.73	2.06			1.65 ± 0.01	
MoSe ₂	1.57	1.86	1.57	1.89	1.58 ± 0.01	1.54 ± 0.03
WS ₂	2.09	2.16			2.00 ± 0.01	
MoSe ₂	1.57	1.62	1.65	1.62-1.71	1.61 ± 0.05	1.35 ± 0.02
WSe ₂	1.73	1.88			1.70 ± 0.04	
WS ₂	2.11	2.18	1.55	1.93	1.97	1.45
WSe ₂	1.74	2.07			1.66	

TABLE II. Calculated intra- and interlayer exciton energies for the six bilayers listed in the left column, without accounting for substrate, temperature, and twist-angle effects. For both intra- and interlayer excitons we show the intra- and interlayer K-K and Γ -K transition energies. Experimental values are the average exciton energies taken from table I for each exciton for each system and the uncertainty is taken as the standard deviation within the experimental data. For MoS₂/WSe₂ we explicitly list the significantly lower interlayer exciton energy³² and for mixed interlayer exciton states we list bound the intra- and interlayer character energies (see main text for a discussion). Including substrate and finite temperature effects redefines the calculated exciton energies to: $(E_{exc} - \delta/2) \pm \delta/2$ (see main text for discussion) which is shown to significantly improve the agreement between calculations and experiments. All values are in eV.

8.6 Paper VI

The Computational 2D Materials Database: High-Throughput Modeling and Discovery of Atomically Thin Crystals

S. Hastrup, M. Strange, M. Pandey, T. Deilmann, P. S. Schmidt, N. F. Hinsche, M. N. Gjerding, D. Torelli, P. M. Larsen, A. C. Riis-Jensen, J. Gath, K. W. Jacobsen, J. J. Mortensen, T. Olsen, and K. S. Thygesen
2D Mater., **5**, 042002 (2018)

© Copyright 2018 IOP Science All Rights Reserved

<https://iopscience.iop.org/article/10.1088/2053-1583/aacfc1/meta>

2D Materials

OPEN ACCESS

TOPICAL REVIEW

RECEIVED
28 March 2018REVISED
8 June 2018ACCEPTED FOR PUBLICATION
28 June 2018PUBLISHED
7 September 2018Original content from
this work may be used
under the terms of the
[Creative Commons
Attribution 3.0 licence](#).Any further distribution
of this work must
maintain attribution
to the author(s) and the
title of the work, journal
citation and DOI.

The Computational 2D Materials Database: high-throughput modeling and discovery of atomically thin crystals

Sten Haastrup¹, Mikkel Strange¹, Mohnish Pandey¹, Thorsten Deilmann¹, Per S Schmidt¹, Nicki F Hinsche¹, Morten N Gjerding^{1,2}, Daniele Torelli¹, Peter M Larsen¹, Anders C Riis-Jensen¹, Jakob Gath¹, Karsten W Jacobsen¹, Jens Jørgen Mortensen¹, Thomas Olsen¹ and Kristian S Thygesen^{1,2}¹ CAMD, Department of Physics, Technical University of Denmark, 2800 Kgs. Lyngby, Denmark² Center for Nanostructured Graphene (CNG), Technical University of Denmark, 2800 Kgs. Lyngby, DenmarkE-mail: thygesen@fysik.dtu.dk**Keywords:** ab initio calculations, opto-electronic properties, database, materials discovery, materials design, 2D materials, many-body perturbation theory**Abstract**

We introduce the Computational 2D Materials Database (C2DB), which organises a variety of structural, thermodynamic, elastic, electronic, magnetic, and optical properties of around 1500 two-dimensional materials distributed over more than 30 different crystal structures. Material properties are systematically calculated by state-of-the-art density functional theory and many-body perturbation theory (G_0W_0 and the Bethe–Salpeter equation for ~ 250 materials) following a semi-automated workflow for maximal consistency and transparency. The C2DB is fully open and can be browsed online (<http://c2db.fysik.dtu.dk>) or downloaded in its entirety. In this paper, we describe the workflow behind the database, present an overview of the properties and materials currently available, and explore trends and correlations in the data. Moreover, we identify a large number of new potentially synthesisable 2D materials with interesting properties targeting applications within spintronics, (opto-)electronics, and plasmonics. The C2DB offers a comprehensive and easily accessible overview of the rapidly expanding family of 2D materials and forms an ideal platform for computational modeling and design of new 2D materials and van der Waals heterostructures.

1. Introduction

Over the past decade, atomically thin two-dimensional (2D) materials have made their way to the forefront of several research areas including batteries, (electro-) catalysis, electronics, and photonics [1, 2]. This development was prompted by the intriguing and easily tunable properties of atomically thin crystals and has been fueled by the constant discovery of new 2D materials and the emergent concepts of lateral [3] and vertical [4] 2D heterostructures, which opens completely new possibilities for designing materials with tailored and superior properties.

So far more than fifty compounds have been synthesised or exfoliated as single layers (see figure 7). These include the well known monoelemental crystals (Xenes, e.g. graphene, phosphorene) [5] and their ligand functionalised derivatives (Xanes, e.g. CF, GeH) [6], transition metal dichalcogenides (TMDCs, e.g. MoS_2 , TaSe_2) [7], transition metal carbides and -nitrides (MXenes, e.g. Ti_2CO_2) [8], group III–V

semiconductors and insulators (e.g. GaN, BN) [9, 10], transition metal halides (e.g. CrI_3) [11, 12], post-transition metal chalcogenides (e.g. GaS and GaSe) [13, 14] and organic-inorganic hybrid perovskites (e.g. $\text{Pb}(\text{C}_4\text{H}_9\text{NH}_3)_2\text{I}_4$) [15]. However, the already known monolayers are only the tip of a much larger iceberg. Indeed, recent data mining studies indicate that several hundred 2D materials could be exfoliated from known layered bulk crystals [16–19]. In the present work we take a complementary approach to 2D materials discovery based on combinatorial lattice decoration and identify another few hundred previously unknown and potentially synthesisable monolayers.

In the search for new materials with tailored properties or novel functionalities, first-principles calculations are playing an increasingly important role. The continuous increase in computing power and significant advancements of theoretical methods and numerical algorithms have pushed the field to a point where first-principles calculations are comparable to experiments in terms of accuracy and greatly

surpass them in terms of speed and cost. For more than a century, experimental databases on e.g. structural, thermal, and electronic properties, have been a cornerstone of materials science, and in the past decade, the experimental data have been augmented by an explosion of computational data obtained from first-principles calculations. Strong efforts are currently being focused on storing and organising the computational data in open repositories [20, 21]. Some of the larger repositories, together containing millions of material entries, are the Materials Project [22], the Automatic Flow for Materials Discovery (AFLOW-LIB) [23], the Open Quantum Materials Database (OQMD) [24, 25], and the Novel Materials Discovery (NOMAD) Repository [26].

The advantages of computational materials databases are many. Most obviously, they facilitate open sharing and comparison of research data whilst reducing duplication of efforts. In addition, they underpin the development and benchmarking of new methods by providing easy access to common reference systems [27]. Finally, the databases enable the application of machine learning techniques to identify deep and complex correlations in the materials space and to use them for designing materials with tailored properties and for accelerating the discovery of new materials [28–30]. Among the challenges facing the computational databases is the quality of the stored data, which depends both on the numerical precision (e.g. the employed k -point grid and basis set size) and the accuracy of the employed physical models (e.g. the exchange-correlation functional). Most of the existing computational databases store results of standard density functional theory (DFT) calculations. While such methods, when properly conducted, are quite reliable for ground state properties such as structural and thermodynamic properties, they are generally not quantitatively accurate for excited state properties such as electronic band structures and optical absorption spectra.

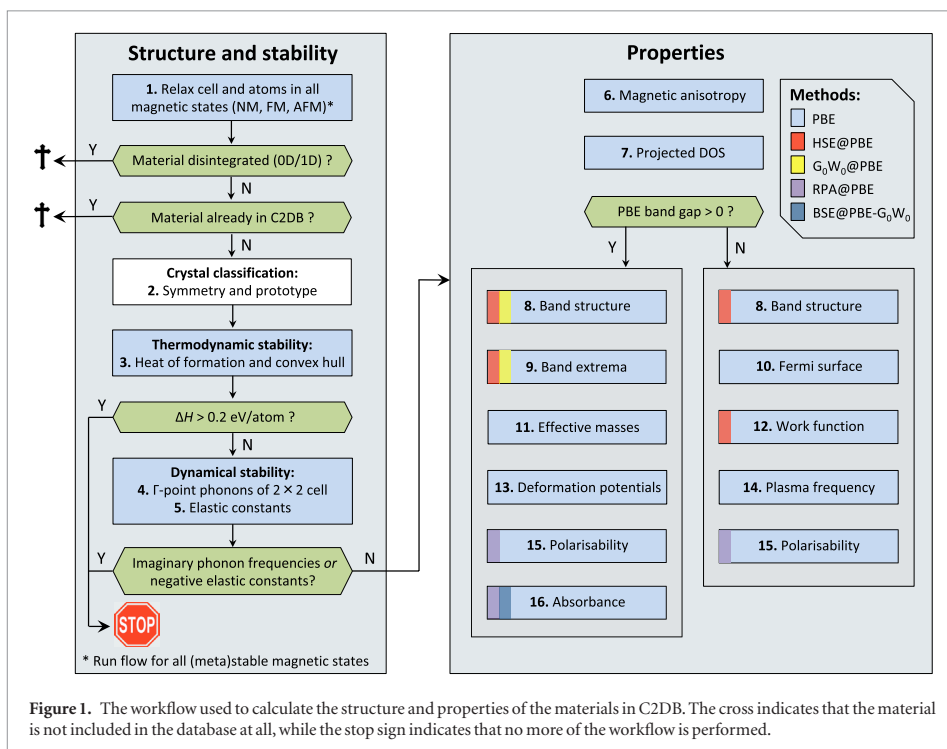
Compared to databases of bulk materials, databases of 2D materials are still few and less developed. Early work used DFT to explore the stability and electronic structures of monolayers of group III–V honeycomb lattices [31, 32] and the class of MX_2 transition metal dichalcogenides and oxides [33]. Later, by data-filtering the inorganic crystal structure database (ICSD), 92 experimentally known layered crystals were identified and their electronic band structures calculated at the DFT level [34]. Another DFT study, also focused on stability and band structures, explored around one hundred 2D materials selected from different structure classes [35]. To overcome the known limitations of DFT, a database with many-body G_0W_0 band structures for 50 semiconducting TMDCs was established [36]. Very recently, data mining of the Materials Project and experimental crystal structure databases in the spirit of [34], led to the identification of close to one thousand experimentally known layered crystals from which single layers could potentially be exfoliated

[16–19]. These works also computed basic energetic, structural and electronic properties of the monolayers (or at least selected subsets) at the DFT level.

In this paper, we introduce the open Computational 2D Materials Database (C2DB) which organises a variety of *ab initio* calculated properties for more than 1500 different 2D materials. The key characteristics of the C2DB are:

- **Materials:** the database focuses entirely on 2D materials, i.e. isolated monolayers, obtained by combinatorial lattice decoration of known crystal structure prototypes.
- **Consistency:** all properties of all materials are calculated using the same code and parameter settings following the same workflow for maximum transparency, reproducibility, and consistency of the data.
- **Properties:** the database contains a large and diverse set of properties covering structural, thermodynamic, magnetic, elastic, electronic, dielectric and optical properties.
- **Accuracy:** Hybrid functionals (HSE06) as well as beyond-DFT many-body perturbation theory (G_0W_0) are employed to obtain quantitatively accurate band structures, and optical properties are obtained from the random phase approximation (RPA) and Bethe–Salpeter equation (BSE).
- **Openness:** the database is freely accessible and can be directly downloaded and browsed online using simple and advanced queries.

The systematic combinatorial approach used to generate the structures in the database inevitably produces many materials that are unstable and thus unrealistic and impossible to synthesise in reality. Such ‘hypothetical’ structures may, however, still be useful in a number of contexts, e.g. for method development and benchmarking, testing and training of machine learning algorithms, identification of trends and structure-property relationships, etc. For this reason we map out the properties of all but the most unstable (and thus chemically unreasonable) compounds. Nevertheless, the reliable assessment of stability and synthesisability of the candidate structures is an essential issue. Using the 55 materials in the C2DB, which have been experimentally synthesised in monolayer form, as a guideline, we set down the criteria that a hypothesised 2D material should fulfill in order for it to be ‘likely synthesisable’. On the basis of these criteria, we introduce a simple *stability scale* to quantify a candidate material’s dynamic and thermodynamic stability. Out of an initial set of around 1900 monolayers distributed over 32 different crystal structures, we find 350 in the most stable category. In addition to the 55 experimentally synthesised monolayers, this set also includes around 80 monolayers from experimentally known vdW layered bulk materials, and thus around 200 completely new and potentially synthesisable 2D materials.



In section 2, we describe the computational workflow behind the database. The structure and properties of the materials are calculated using well established state-of-the-art methodology. Technical descriptions of the different steps in the workflow are accompanied by illustrative examples and comparisons with literature data. Since *documentation and validation* is the main purpose of the section, we deliberately focus on well known 2D materials like the Xenex and transition metal dichalcogenides where plenty of both computational and experimental reference data is available. It should be clear that the novelty of the present work does not lie in the employed methodology nor in the type of materials properties that we calculate (we note, however, that to the best of our knowledge the present compilation of GW and BSE calculations represents the largest of its kind reported so far). The significance of our work is rather reflected by the fact that when large and consistently produced data sets are organised and made easily accessible, new scientific opportunities arise. As outlined below, this paper presents several examples of this effect.

In section 3 we give an overview of the materials and the data contained in the C2DB and provide some specific examples to illustrate its use. Using an extensive set of many-body G_0W_0 calculations as a reference, we establish the performance of various DFT xc-functionals for predicting band gaps, band edge positions, and band alignment at hetero-interfaces, and we propose an optimal strategy for obtaining accurate band energies at low computational cost. Similarly,

the 250 BSE calculations allow us to explore trends in exciton binding energies and perform a statistically significant and unbiased assessment of the accuracy and limitations of the widely used Mott–Wannier model for 2D excitons. From the data on more than 600 semiconductor monolayers, we present strong empirical evidence against an often employed relation between effective masses and band gaps derived from $\mathbf{k} \cdot \mathbf{p}$ perturbation theory. Inspired by the potential of using 2D materials as building blocks for plasmonics and photonics, we propose a model to predict the plasmon dispersion relations in 2D metals from the (intraband) plasma frequency and the onset of interband transitions and use it to identify 2D metals with plasmons in the optical frequency regime. We propose several new magnetic 2D materials (including both metals and semiconductors) with ferromagnetic or anti-ferromagnetic ordering and significant out-of-plane magnetic anisotropy. Finally, we point to new high-mobility 2D semiconductors including some with band gaps in the range of interest for (opto)electronic applications.

In section 4 we provide our conclusions together with an outlook discussing some opportunities and possible future directions for the C2DB.

2. Workflow

The workflow used to generate the data in the C2DB is illustrated in figure 1. It consists of two parts: In the first part (left panel) the unit cell and atom positions

are optimised for different magnetic configurations: non-magnetic (NM), ferro-magnetic (FM) and antiferro-magnetic (AFM). Materials satisfying certain stability and geometry criteria (indicated by green boxes) are subject to the second part (right panel) where the different properties are computed using DFT and many-body methods. The G_0W_0 band structure and BSE absorbance calculations have been performed only for semiconducting materials with up to four atoms in the unit cell. Per default, properties shown in the online database include spin-orbit coupling (SOC); however, to aid comparison with other calculations, most properties are also calculated and stored without SOC.

All DFT and many-body calculations are performed with the projector augmented wave code GPAW [37] using plane wave basis sets and PAW potentials version 0.9.2. The workflow is managed using the Python based atomic simulation environment (ASE) [38]. We have developed a library of robust and numerically accurate (convergence verified) ASE-GPAW scripts to perform the various tasks of the workflow, and to create the database afterwards. The library is freely available, under a GPL license.

Below we describe all steps of the workflow in detail. As the main purpose is to document the workflow, the focus is on technical aspects, including numerical convergence and benchmarking. An overview of the most important parameters used for the different calculations is provided in table 1.

2.1. Structure relaxation

The workflow is initiated with a crystal structure defined by its unit cell (Bravais lattice and atomic basis). The crystal lattice is typically that of an experimentally known prototype (the ‘seed structure’) decorated with atoms picked from a subset of the periodic table, see figure 2. We refer to materials by the chemical formula of their unit cell followed by the crystal structure. The latter is indicated by a representative material of that prototype, as described in section 3.1. For example, monolayer MoS_2 in the hexagonal H and T phases are denoted $\text{MoS}_2\text{-MoS}_2$ and $\text{MoS}_2\text{-CdI}_2$, respectively. Now, MoS_2 is in fact not stable in the T phase, but undergoes a 2×1 distortion to the so-called T’ phase. Because the T’ phase is the thermodynamically stable phase of WTe_2 , we denote MoS_2 in the distorted T phase by $\text{Mo}_2\text{S}_4\text{-WTe}_2$. In the following, we shall refer to the unit cell with which the workflow is initiated, i.e. the unit cell of the seed structure, as the primitive cell or the 1×1 cell, even if this cell is not dynamically stable for the considered material (see section 2.4).

The unit cell and internal coordinates of the atoms are relaxed in both a spin-paired (NM), ferromagnetic (FM), and anti-ferromagnetic (AFM) configuration. Calculations for the AFM configuration are performed only for unit cells containing at least two metal atoms.

The symmetries of the initial seed structure are kept during relaxation. All relevant computational details are provided in table 1.

After relaxation, we check that the structure has remained a covalently connected 2D material and not disintegrated into 1D or 0D clusters. This is done by defining clusters of atoms using the covalent radius [39] + 30% as a measure for covalent bonds between atoms. The dimensionality of a cluster is obtained from the scaling of the number of atoms in a cluster upon repetition of the unit cell following the method described by Ashton *et al* [16]. Only materials containing exactly one cluster of dimensionality 2 are given further consideration (an exception is made for the metal-organic perovskites (prototype PbA_2I_4) for which the metal atom inside the octahedron represents a 0D cluster embedded in a 2D cluster). To illustrate the effect of the covalent radius + 30% threshold, figure 3 shows the distribution of the candidate structures in the database as a function of the covalent factor needed to fully connect the structure. Most materials have a critical covalent factor below 1.3 and fall in the green shaded region. There is, however, a tail of around 100 disconnected materials (red region); these materials are not included in the database (see first green box in figure 1).

We also check that the material is not already contained in the database (second green box in figure 1). This is done by measuring the root mean square distance (RMSD) [40] relative to all other materials in the C2DB with the same reduced chemical formula. A threshold of 0.01 Å is used for this test.

In case of multiple metastable magnetic configurations (in practice, if both a FM and AFM ground state are found), these are regarded as different phases of the same material and will be treated separately throughout the rest of the workflow. To indicate the magnetic phase we add the extensions ‘FM’ or ‘AFM’ to the material name. The total energy of the spin-paired ground state is always stored, even when it is not the lowest. If the energy of the non-magnetic state is higher than the most stable magnetic state by less than 10 meV/atom, the workflow is also performed for the non-magnetic state. This is done in recognition of the finite accuracy of DFT for predicting the correct energetic ordering of different magnetic states.

We have compared the lattice constants of 29 monolayers with those reported in [41], which were obtained with the VASP code using PBE and very similar numerical settings and find a mean absolute deviation of 0.024 Å corresponding to 0.4%. The small yet finite deviations are ascribed to differences in the employed PAW potentials.

2.2. Crystal structure classification

2.2.1. Symmetry

To classify the symmetries of the crystal structure the 3D space group is determined using the crystal

Table 1. Overview of the methods and parameters used for the different steps of the workflow. If a parameter is not specified at a given step, its value equals that of the last step where it was specified.

Workflow step(s)	Parameters
Structure and energetics (1–4) ^a	vacuum = 15 Å; k -point density = $6.0/\text{Å}^{-1}$; Fermi smearing = 0.05 eV; PW cutoff = 800 eV; xc functional = PBE; maximum force = 0.01 eV/Å; maximum stress = 0.002 eV/Å ³ ; phonon displacement = 0.01 Å
Elastic constants (5)	k -point density = $12.0/\text{Å}^{-1}$; strain = $\pm 1\%$
Magnetic anisotropy (6)	k -point density = $20.0/\text{Å}^{-1}$; spin-orbit coupling = True
PBE electronic properties (7–10 and 12)	k -point density = $12.0/\text{Å}^{-1}$ ($36.0/\text{Å}^{-1}$ for step 7)
Effective masses (11)	k -point density = $45.0/\text{Å}^{-1}$; finite difference
Deformation potential (13)	k -point density = $12.0/\text{Å}^{-1}$; strain = $\pm 1\%$
Plasma frequency (14)	k -point density = $20.0/\text{Å}^{-1}$; tetrahedral interpolation
HSE band structure (8–12)	HSE06@PBE; k -point density = $12.0/\text{Å}^{-1}$
G ₀ W ₀ band structure (8, 9)	G ₀ W ₀ @PBE; k -point density = $5.0/\text{Å}^{-1}$; PW cutoff = ∞ (extrapolated from 170, 185 and 200 eV); full frequency integration; analytical treatment of $W(q)$ for small q ; truncated Coulomb interaction
RPA polarisability (15)	RPA@PBE; k -point density = $20.0/\text{Å}^{-1}$; PW cutoff = 50 eV; truncated Coulomb interaction; tetrahedral interpolation
BSE absorbance (16)	BSE@PBE with G ₀ W ₀ scissor operator; k -point density = $20.0/\text{Å}^{-1}$; PW cutoff = 50 eV; truncated Coulomb interaction; at least 4 occupied and 4 empty bands

^a For the cases with convergence issues, we set a k -point density of 9.0 and a smearing of 0.02 eV.

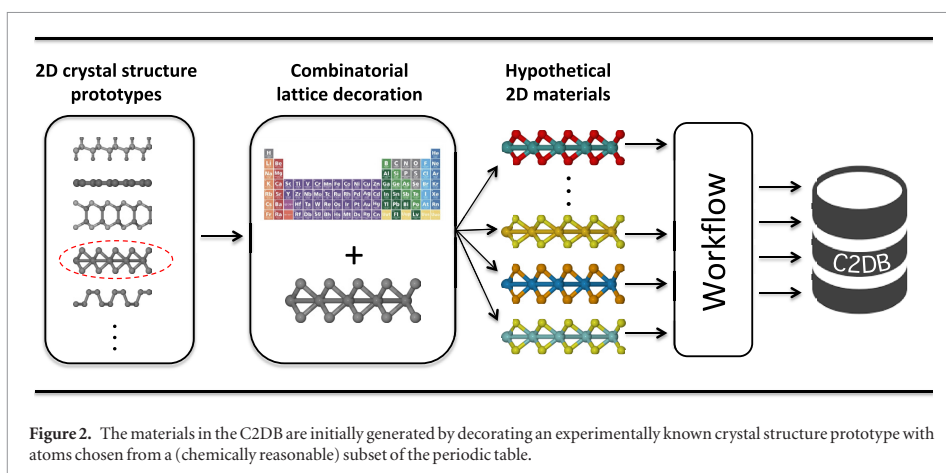


Figure 2. The materials in the C2DB are initially generated by decorating an experimentally known crystal structure prototype with atoms chosen from a (chemically reasonable) subset of the periodic table.

symmetry library Spglib [42] on the 3D supercell with a tolerance of 10^{-4} Å.

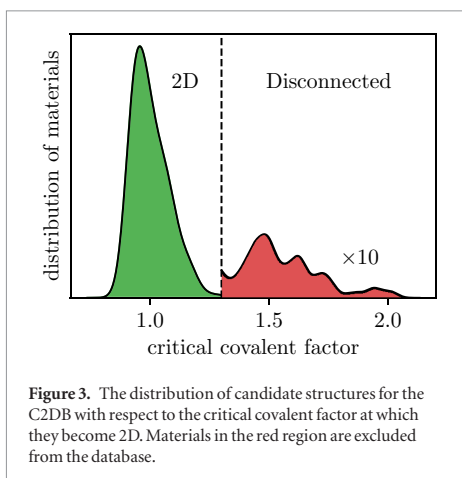
2.2.2. Prototypes

The materials are classified into crystal structure prototypes based on the symmetry of the crystals. For two materials to belong to the same prototype, we require that they have the same space group, the same stoichiometry, and comparable thicknesses. The last requirement is included to distinguish between materials with the same symmetry and stoichiometry but with different number of atomic layers, see for example monolayer BN and GaS in figure 4. Each prototype is labelled by a specific representative material. For prototypes which have been previously

investigated, we comply with the established conventions. However, since the field of 2D materials is still young and because C2DB contains a large number of never-synthesised materials, some of the considered crystal structures fall outside the known prototypes. In these cases we have chosen the representative material to be the one with the lowest energy with respect to the convex hull. Some of the crystal structure prototypes presently contained in the C2DB are shown in figure 4.

2.3. Thermodynamic stability

The heat of formation, ΔH , is defined as the energy of the material with respect to the standard states of its constituent elements. For example, the heat of formation per atom of a binary compound, A_xB_y , is



$$\Delta H = (E(A_xB_y) - xE(A) - yE(B))/(x + y), \quad (1)$$

where $E(A_xB_y)$ is the total energy of the material A_xB_y , and $E(A)$ and $E(B)$ are the total energies of the elements A and B in their standard state. When assessing the stability of a material in the C2DB, it should be kept in mind that the accuracy of the PBE functional for the heat of formation is only around 0.2 eV/atom on average [43]. Other materials databases, e.g. OQMD, Materials Project, and AFLOW, employ fitted elementary reference energies (FERE) [44] and apply a Hubbard U term [45] for the rare earth and transition metal atoms (or a selected subset of them). While such correction schemes in general improve ΔH they also introduce some ambiguity, e.g. the dataset from which the FERE are determined or the exact form of the orbitals on which the U term is applied. Thus in order not to compromise the transparency and reproducibility of the data we use the pure PBE energies.

For a material to be thermodynamically stable it is necessary but not sufficient that $\Delta H < 0$. Indeed, thermodynamic stability requires that ΔH be negative not only relative to its pure elemental phases but relative to all other competing phases, i.e. its energy must be below the *convex hull* [46]. We stress, however, that in general, but for 2D materials in particular, this definition cannot be directly applied as a criterion for stability and synthesizability. The most important reasons for this are (i) the intrinsic uncertainty on the DFT energies stemming from the approximate xc-functional (ii) substrate interactions or other external effects that can stabilise the monolayer (iii) kinetic barriers that separate the monolayer from other lower energy phases rendering the monolayer (meta)stable for all practical purposes.

We calculate the energy of the 2D material relative to the convex hull of competing bulk phases, ΔH_{hull} . The convex hull is currently constructed from the 2836 most stable binary bulk compounds which were obtained from the OQMD [24]. The energies of the

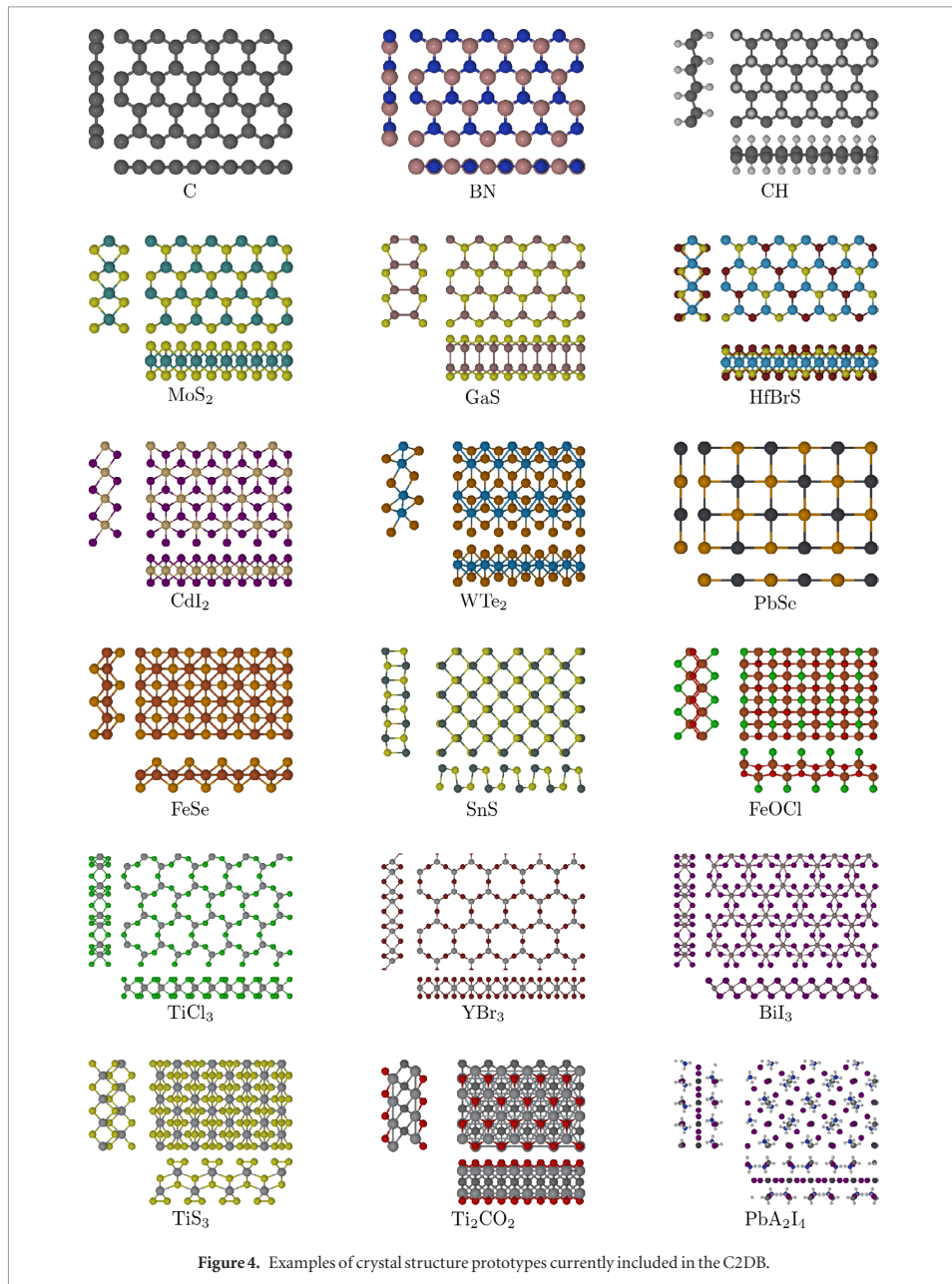
bulk phases were recalculated with GPAW using the PBE xc-functional and the same numerical settings as applied for the 2D materials (but the structure was not re-optimised). Because the bulk reference structures from OQMD were optimised with the VASP code and with Hubbard U corrections for materials containing $3d$ elements, and because the PBE misses attractive vdW interaction, the bulk energies could be slightly overestimated relative to the monolayers. As a consequence, monolayers that also exist in a layered bulk phase could have $\Delta H_{\text{hull}} < 0$, even if the layered bulk phase is part of the convex hull and thus should be energetically more stable than the monolayer. Comparing our ΔH_{hull} values for 35 compounds with the exfoliation energies calculated in [18] employing vdW compliant xc-functionals for both bulk and monolayer, we estimate the errors in the convex hull energies to be below 0.1 eV/atom.

As an example, the convex hull for $\text{Fe}_x\text{Se}_{1-x}$ is shown in figure 5. The convex hull as defined by the bulk binaries is indicated by the blue lines. The labels for the 2D materials refer to the crystal prototype and magnetic order. Clearly, most 2D materials lie above the convex hull and are thus predicted to be thermodynamically unstable in freestanding form under standard conditions. However, as mentioned above, depending on the material, errors on the PBE formation energies can be sizable and thus the hull diagram should only be taken as guideline. Nevertheless, in the present example we find that FeSe (which is itself a prototype) with anti-ferromagnetic ordering lies slightly below the convex hull and is thus predicted to be thermodynamically stable. This prediction is consistent with the recent experimental observation that monolayer FeSe deposited on SrTiO_3 exhibits AFM order [47].

2.4. Phonons and dynamic stability

Due to the applied symmetry constraints and/or the limited size of the unit cell, there is a risk that the structure obtained after relaxation does not represent a local minimum of the potential energy surface, but only a saddle point. We test for dynamical stability by calculating the Γ -point phonons of a 2×2 repeated cell (without re-optimising the structure) as well as the elastic constants (see section 2.5). These quantities represent second-order derivatives of the total energy with respect to atom displacements and unit cell lengths, respectively, and negative values for either quantity indicate a structural instability.

The Γ -point phonons of the 2×2 supercell are obtained using the finite displacement method [48]. We displace each atom in the primitive cell by $\pm 0.01 \text{ \AA}$, and calculate the forces induced on all the atoms in the supercell. From the forces we construct the dynamical matrix, which is diagonalised to obtain the Γ -point phonons of the 2×2 cell (or equivalently the Γ -point and zone boundary phonons of the primitive cell). The eigenvalues of the dynamical matrix correspond to the



square of the mass-renormalised phonon frequencies, $\tilde{\omega}$. Negative eigenvalues are equivalent to imaginary frequencies and signal a saddle point.

Our procedure explicitly tests for stability against local distortions of periodicities up to 2×2 and thus provides a necessary, but not sufficient condition for dynamic stability. We stress, however, that even in cases where a material would spontaneously relax into a structure with periodicity larger than 2×2 , the Γ -point dynamical matrix of the 2×2 cell could

exhibit negative eigenvalues. Our test is thus more stringent than it might seem at first glance. In principle, a rigorous test for dynamic stability would require the calculation of the full phonon band structure. Mathematically, the instabilities missed by our approach are those that result in imaginary phonons in the interior of the BZ but *not* at the zone boundary. Physically, such modes could be out of plane buckling or charge density wave-driven reconstructions with periodicities of several unit cells. In general, however, these types of

instabilities are typically rather weak (as measured by the magnitude of the imaginary frequency) as compared to more local distortions such as the T to T' distortion considered below. Moreover, they could well be a special property of the isolated monolayer and become stabilised by the ubiquitous interactions of the 2D material with its environment, e.g. substrates. This is in fact supported by the full phonon calculations by Mounet *et al* for ~ 250 isolated monolayers predicted to be easily exfoliable from experimentally known layered bulk phases [18]. Indeed, most of the instabilities revealed by their calculations are of the type described above and would thus be missed by our test. However, these instabilities cannot be too critical as the monolayers are known to be stable in the vdW bonded layered bulk structure.

As an example, figure 6 compares the dynamical stability of a subset of transition metal dichalcogenides and -oxides in the T and T' phases (CdI₂ and WTe₂ prototypes). The two upper panels show the smallest eigenvalue of the Γ -point dynamical matrix of the 2×2 cell. Only materials above the dashed line are considered dynamically stable (for this example we do not consider the sign of the elastic constants which could further reduce the set of dynamically stable materials). Since the unit cell of the T' phase contains that of the T phase it is likely that a material initially set up in the T' phase relaxes back to the T phase. To identify these cases, and thereby avoid the presence of duplicates in the database, the third panel shows the root mean square distance (RMSD) between the structures obtained after relaxations starting in the T- and T' phase, respectively. Structures below the dashed line are considered identical. The color of each symbol refers to the four different potential energy surfaces illustrated at the bottom of the figure.

2.4.1. Stability criteria

To assess the stability of the materials in the C2DB, we turn to the set of experimentally synthesised/exfoliated monolayers. For these materials, the calculated energy above the convex hull and minimum eigenvalue of the dynamical matrix are shown on figure 7. It is clear that all but five known monolayers have a hull energy below 0.2 eV/atom, and three of these have only been synthesised on a metal substrate. Turning to the dynamical stability, all but one of the experimentally known monolayers have a minimum eigenvalue of the dynamical matrix above -2 eV \AA^{-2} , and 70% have a minimum eigenvalue above $-1 \times 10^{-5} \text{ eV \AA}^{-2}$.

Guided by these considerations, we assign each material in the C2DB a stability level (low, medium or high) for both dynamical and thermodynamic stability, as illustrated in table 2. For ease of reference, we also define the overall stability level of a given material as the lower of the dynamical and thermodynamic stability levels. If a material has 'low' overall stability (marked by bold in the table), we consider it unstable and do not carry out the rest of the workflow. Materials

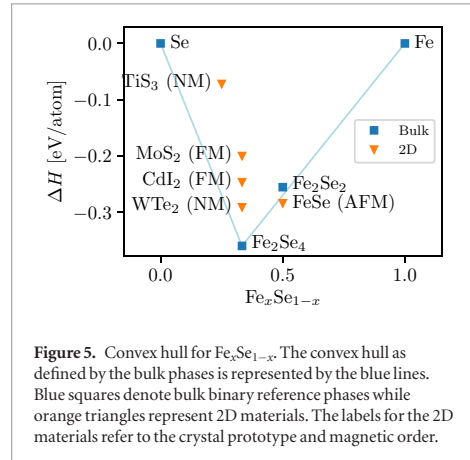


Figure 5. Convex hull for Fe_xSe_{1-x}. The convex hull as defined by the bulk phases is represented by the blue lines. Blue squares denote bulk binary reference phases while orange triangles represent 2D materials. The labels for the 2D materials refer to the crystal prototype and magnetic order.

with 'high' overall stability are considered likely to be stable and thus potentially synthesisable. Materials in the 'medium' stability category, while unlikely to be stable as freestanding monolayers, cannot be discarded and might be metastable and possible to synthesise under the right conditions. For example, freestanding silicene has a heat of formation of 0.66 eV/atom, but can be grown on a silver substrate. Likewise, the T' phase of MoS₂ (WTe₂ prototype) has an energy of 0.27 eV/atom higher than the thermodynamically stable H phase, but can be stabilised by electron doping.

2.5. Elastic constants

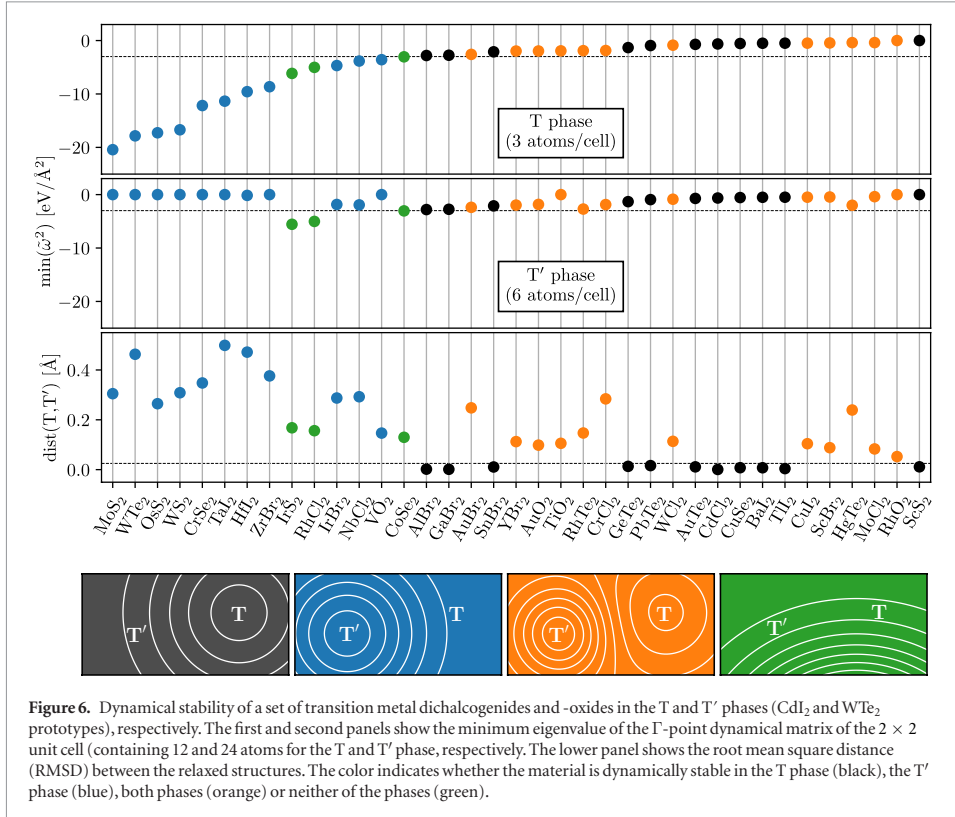
The elastic constants of a material are defined by the generalised Hooke's law,

$$\sigma_{ij} = C_{ijkl} \varepsilon_{kl} \quad (2)$$

where σ_{ij} , C_{ijkl} and ε_{kl} are the stress, stiffness and strain tensors, respectively, and where we have used the Einstein summation convention. In two dimensions, the stress and strain tensors have three independent components, namely planar stress/strain in the x and y directions, as well as shear stress/strain. The stiffness tensor is a symmetric linear map between these two tensors, and therefore has up to six independent components. Disregarding shear deformations, the relationship between planar strain and stress is

$$\begin{bmatrix} \sigma_{xx} \\ \sigma_{yy} \end{bmatrix} = \begin{bmatrix} C_{11} & C_{12} \\ C_{12} & C_{22} \end{bmatrix} \begin{bmatrix} \varepsilon_{xx} \\ \varepsilon_{yy} \end{bmatrix}. \quad (3)$$

For all materials in the C2DB, we calculate the planar elastic stiffness coefficients C_{11} , C_{22} , and C_{12} . These are calculated using a central difference approximation to the derivative of the stress tensor: the material is strained along one of the coordinate axes, x or y , and the stress tensor is calculated after the ions have relaxed. We use strains of $\pm 1\%$ which we have found to be sufficiently large to eliminate effects of numerical



noise and sufficiently small to stay within the linear response regime.

Table 3 shows the calculated planar stiffness coefficients of a set of 2D materials. As can be seen the values from the C2DB are in very good agreement with previously published PBE results. For the isotropic materials MoS₂, WSe₂ and WS₂, C_{11} and C_{22} should be identical, and we see a variation of up to 0.6%. This provides a test of how well converged the values are with respect to numerical settings.

2.6. Magnetic anisotropy

The energy dependence on the direction of magnetisation, or magnetic anisotropy (MA), arises from spin-orbit coupling (SOC). According to the magnetic force theorem [96] this can be evaluated from the eigenvalue differences such that the correction to the energy becomes

$$\Delta E(\hat{\mathbf{n}}) = \sum_{\mathbf{kn}} f(\varepsilon_{\mathbf{kn}}^{\hat{\mathbf{n}}}) \varepsilon_{\mathbf{kn}}^{\hat{\mathbf{n}}} - \sum_{\mathbf{kn}} f(\varepsilon_{\mathbf{kn}}^0) \varepsilon_{\mathbf{kn}}^0, \quad (4)$$

where $\varepsilon_{\mathbf{kn}}^{\hat{\mathbf{n}}}$ and $f(\varepsilon_{\mathbf{kn}}^{\hat{\mathbf{n}}})$ are the eigenenergies and occupation numbers, respectively, obtained by diagonalising the Kohn-Sham Hamiltonian including SOC in a basis of collinear spinors aligned along the direction $\hat{\mathbf{n}}$, while $\varepsilon_{\mathbf{kn}}^0$ and $f(\varepsilon_{\mathbf{kn}}^0)$ are the bare Kohn-Sham eigenenergies and occupation numbers without SOC.

For all magnetic materials we have calculated the energy difference between out-of-plane and in-plane magnetisation $E_{\text{MA}}(i) = \Delta E(\hat{\mathbf{z}}) - \Delta E(i)$, ($i = \hat{\mathbf{x}}, \hat{\mathbf{y}}$). Negative values of $E_{\text{MA}}(i)$ thus indicate that there is an out-of-plane easy axis of magnetisation.

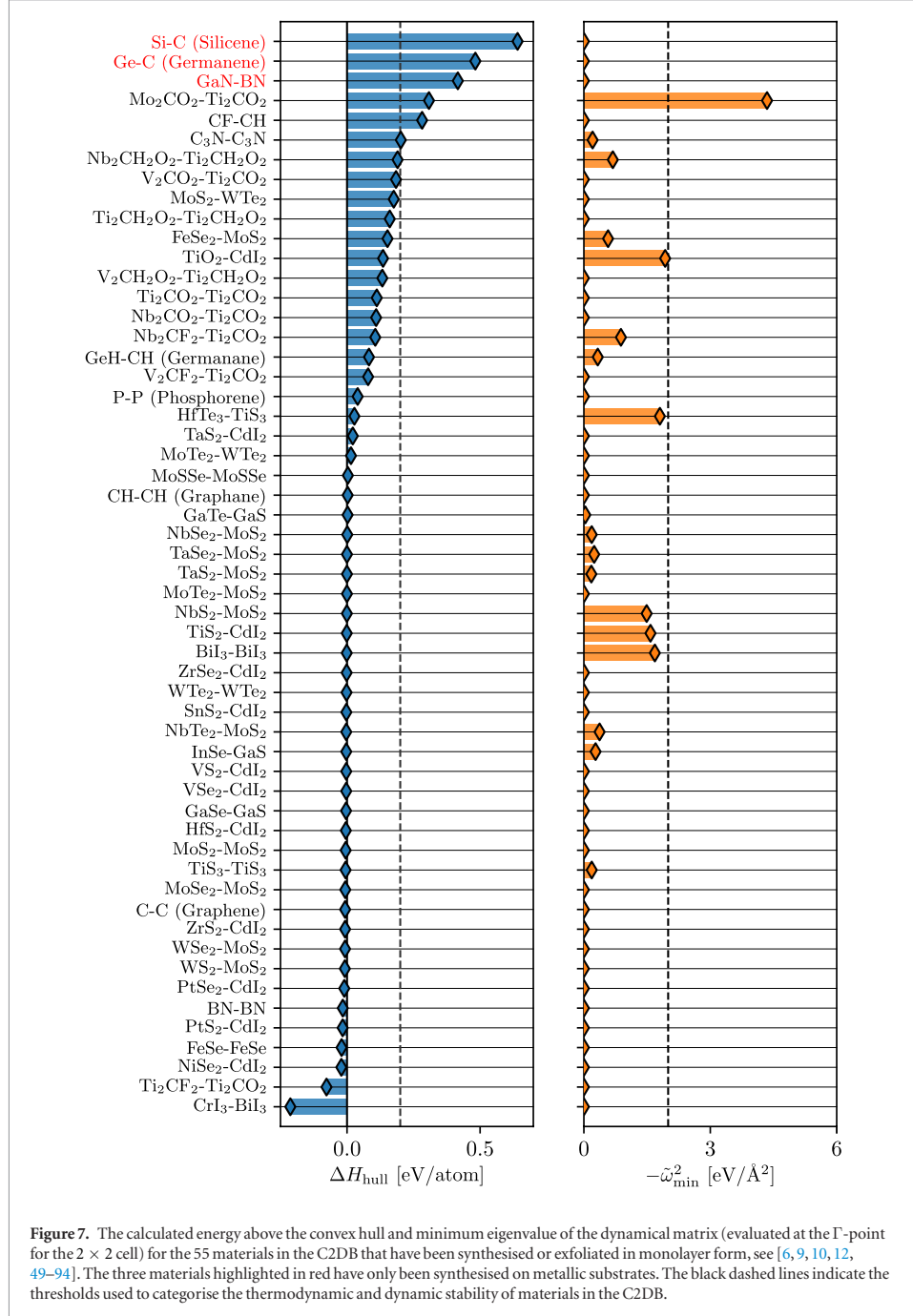
Calculations for the ground state have been performed with plane-wave cutoff and energetic convergence threshold set to 800 eV and 0.5 meV/atom respectively. For all calculations we have used a Γ -centered Monkhorst-Pack k -point with a density of $20/\text{\AA}^{-3}$. The SOC contribution is introduced via a non-self-consistent diagonalisation of the Kohn-Sham Hamiltonian evaluated in the projector-augmented wave formalism [97].

2.7. Projected density of states

The projected density of states (PDOS) is a useful tool for identifying which atomic orbitals comprise a band. It is defined as

$$\rho_i^S(\varepsilon) = \sum_{a \in S} \sum_{\mathbf{kn}} \sum_m |\langle \phi_{l,m}^a | \psi_{\mathbf{kn}} \rangle|^2 \delta(\varepsilon - \varepsilon_{\mathbf{kn}}), \quad (5)$$

where $\psi_{\mathbf{kn}}$ are the Kohn-Sham wave functions with eigenvalues $\varepsilon_{\mathbf{kn}}$ and $\phi_{l,m}^a$ are the spin-paired Kohn-Sham orbitals of atomic species S with angular momentum l (s, p, d, f). We sum over all atoms belonging to species S so every atomic species has one



entry per angular momentum channel. In the PAW formalism this can be approximated as

$$\rho_i^S(\varepsilon) = \sum_{a \in S} \sum_{\mathbf{k}n} \sum_m |\langle \tilde{p}_{l,m}^a | \tilde{\psi}_{\mathbf{k}n} \rangle|^2 \delta(\varepsilon - \varepsilon_{\mathbf{k}n}) \quad (6)$$

where $\tilde{\psi}_{\mathbf{k}n}$ are the pseudo wave functions and $\tilde{p}_{l,m}^a$ are the PAW projectors associated with the atomic orbitals

$\phi_{l,m}^a$. The PDOS is calculated from equation (6) using linear tetrahedron interpolation [98] (LTI) of energy eigenvalues obtained from a ground state calculation with a k -point sampling of $36/\text{\AA}^{-3}$. In contrast to other techniques for calculating the PDOS using smearing, the PDOS yielded by the LTI method returns exactly zero at energies with no states. Examples of PDOS

Table 2. The materials in the C2DB distributed over the nine stability categories defined by the three levels (high, medium and low) of dynamical stability (columns) and thermodynamic stability (rows). The overall stability of the materials is defined as the lower of the two separate stability scales. Materials with low overall stability (bold) are considered unstable.

Thermodynamic stability (eV/atom)	Dynamic stability (eVÅ ⁻²)			Total
	$ \tilde{\omega}_{\min}^2 > 2$ or $C_{ii} < 0$	$10^{-5} < \tilde{\omega}_{\min}^2 < 2$, $C_{ii} > 0$	$ \tilde{\omega}_{\min}^2 < 10^{-5}$, $C_{ii} > 0$	
$\Delta H > 0.2$	6.0%	4.2%	1.7%	12.0%
$\Delta H < 0.2$	14.9%	10.9%	6.4%	32.2%
$\Delta H_{\text{inull}} < 0.2$	11.4%	24.1%	20.3%	55.8%
Total	32.3%	39.2%	28.5%	

Table 3. Planar elastic stiffness coefficients (in N m⁻¹) calculated at the PBE level. The results of this work are compared to previous calculations from the literature and the mean absolute deviation (MAD) is shown.

	C ₁₁ (N m ⁻¹)		C ₂₂ (N m ⁻¹)		C ₁₂ (N m ⁻¹)	
	C2DB	Literature	C2DB	Literature	C2DB	Literature
P (phosphorene)	101.9	105.2 [95]	25.1	26.2 [95]	16.9	18.4 [95]
MoS ₂	131.4	132.6 [19]	131.3	132.6 [19]	32.6	32.7 [19]
WSe ₂	120.6	119.5 [19]	121.3	119.5 [19]	22.8	22.7 [19]
WS ₂	146.3	145.3 [19]	146.7	145.3 [19]	32.2	31.5 [19]
MAD	1.7	—	1.4	—	0.6	—

are shown in figure 9 (right) for respectively the ferromagnetic metal VO₂ and the semiconductor WS₂ in the H phase (MoS₂ prototype).

2.8. Band structures

Electronic band structures are calculated along the high symmetry paths shown in figure 8 for the five different types of 2D Bravais lattices. The band energies are computed within DFT using three different xc-functionals, namely PBE, HSE06, and GLLBSC. These single-particle approaches are complemented by many-body G₀W₀ calculations for materials with a finite gap and up to four atoms in the unit cell (currently around 250 materials). For all methods, SOC is included by non-selfconsistent diagonalisation in the full basis of Kohn–Sham eigenstates. Band energies always refer to the vacuum level defined as the asymptotic limit of the Hartree potential, see figure 12. Below we outline the employed methodology while section 3.2.1 provides an overview and comparison of the band energies obtained with the different methods.

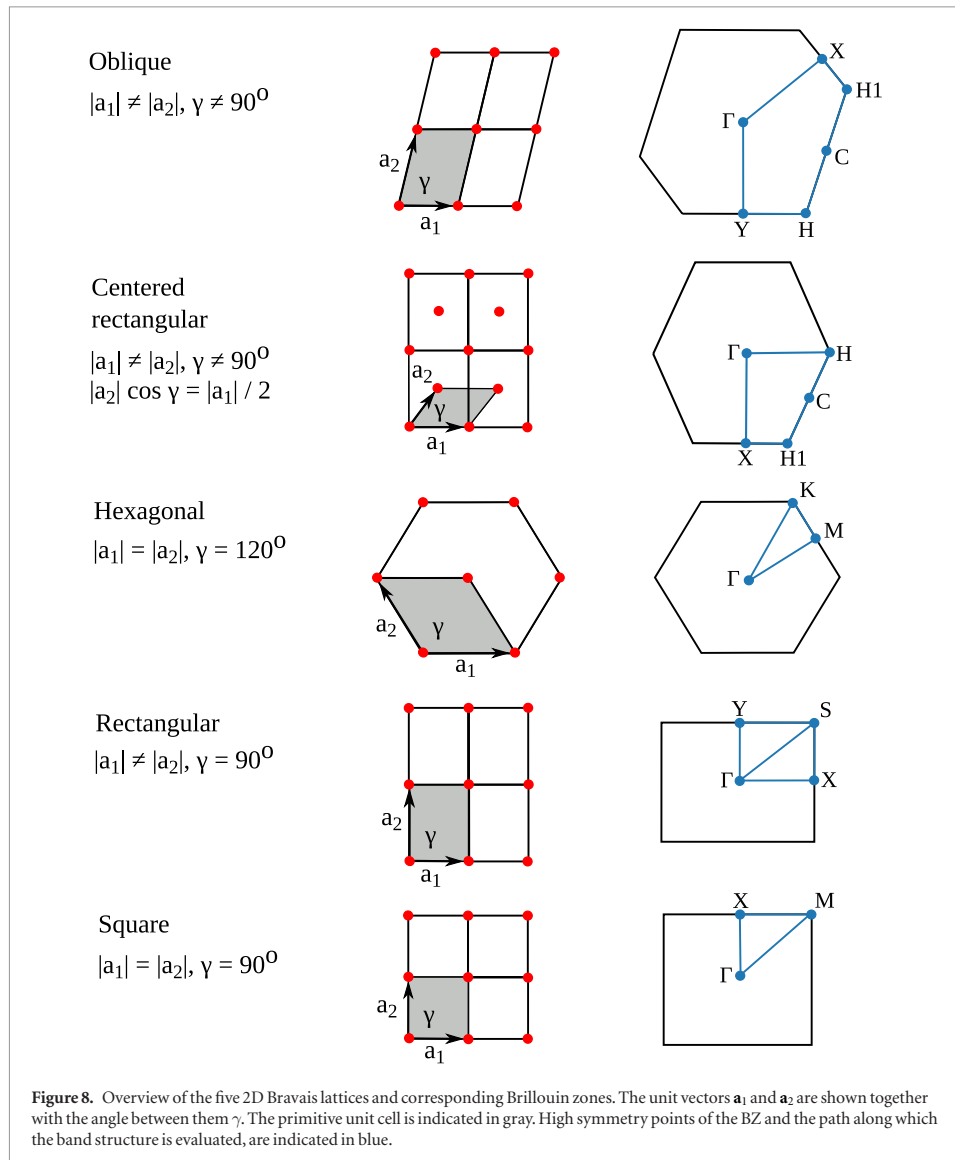
2.8.1. PBE band structure

The electron density is determined self-consistently on a uniform k -point grid of density 12.0/Å⁻³. From this density, the PBE band structure is computed non-selfconsistently at 400 k -points distributed along the band path (see figure 8). Examples of PBE band structures are shown in figure 9 for the ferromagnetic metal VO₂ and the semiconductor WS₂ both in the MoS₂ prototype structure. The expectation value of the out-of-plane spin component, $\langle \chi_{nk\sigma} | \hat{S}_z | \chi_{nk\sigma} \rangle$, is evaluated for each spinorial wave

function, $\chi_{nk\sigma} = (\psi_{nk\uparrow}, \psi_{nk\downarrow})$, and is indicated by the color of the band. For materials with inversion symmetry, the SOC cannot induce band splitting, meaning that $\langle \chi_{nk\sigma} | \hat{S}_z | \chi_{nk\sigma} \rangle$ is ill-defined and no color coding is used. The band structure without SOC is indicated by a dashed grey line. We have compared our PBE + SOC band gaps of 29 different monolayers with those obtained with the VASP code in [41] and find a mean absolute deviation of 0.041 eV.

2.8.2. HSE band structure

The band structure is calculated non-selfconsistently using the range-separated hybrid functional HSE06 [99] on top of a PBE calculation with k -point density 12.0/Å⁻³ and 800 eV plane wave cutoff. We have checked for selected systems that the HSE band structure is well converged with these settings. The energies along the band path are obtained by spline interpolation from the uniform k -point grid. As an example, the HSE band structure of WS₂ is shown in the left panel of figure 10 (black line) together with the PBE band structure (grey dashed). The PBE band gap increases from 1.52 eV to 2.05 eV with the HSE06 functional in good agreement with earlier work reporting band gaps of 1.50 eV (PBE) and 1.90 eV (HSE) [100] and 1.55 eV (PBE) and 1.98 eV (HSE) [101], respectively. A more systematic comparison of our results with the HSE + SOC band gaps obtained with the VASP code in [41] for 29 monolayers yield a mean absolute deviation of 0.14 eV. We suspect this small but non-zero deviation is due to differences in the employed PAW potentials and the non-selfconsistent treatment of the HSE in our calculations.



2.8.3. GLLBSC fundamental gap

For materials with a finite PBE band gap, the fundamental gap (i.e. the difference between the ionisation potential and electron affinity) also sometimes referred to as the quasiparticle gap, is calculated self-consistently using the GLLBSC [102] xc-functional with a Monkhorst–Pack k -point grid of density $12.0/\text{\AA}^{-3}$. The GLLBSC is an orbital-dependent exact exchange-based functional, which evaluates the fundamental gap as the sum of the Kohn–Sham gap and the xc-derivative discontinuity, $E_{\text{gap}} = \epsilon_{\text{gap}}^{\text{KS}} + \Delta_{\text{xc}}$. The method has been shown to yield excellent quasiparticle band gaps at very low

computational cost for both bulk [102, 103] and 2D semiconductors [36].

In the exact Kohn–Sham theory, ϵ_v^{KS} should equal the exact ionisation potential and thus Δ_{xc} should be used to correct only the conduction band energies [104]. Unfortunately, we have found that in practice this procedure leads to up-shifted band energies (compared with the presumably more accurate G_0W_0 results, see figure 20). Consequently, we store only the fundamental gap and Δ_{xc} in the database. However, as will be shown in section 3.2.1 the center of the gap is in fact reasonably well described by PBE suggesting that efficient and fairly accurate predictions of the absolute

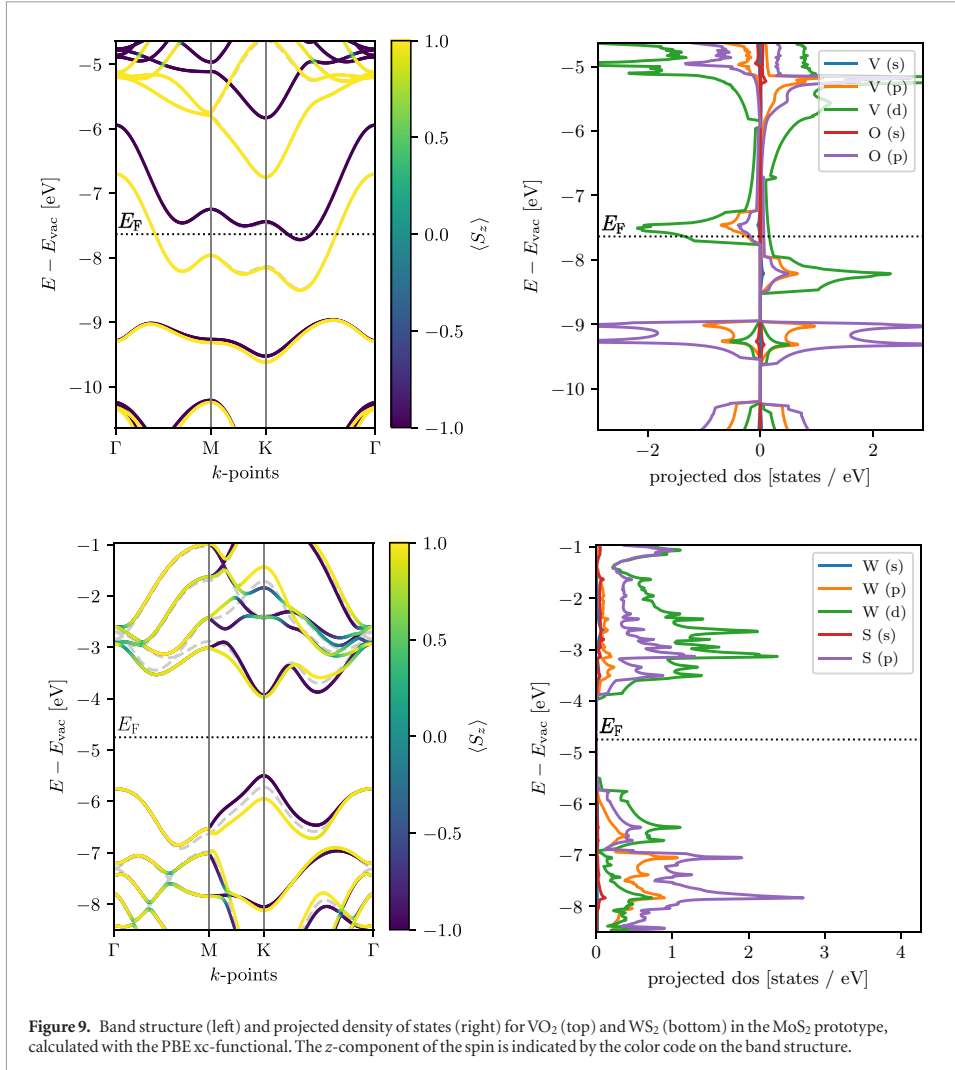


Figure 9. Band structure (left) and projected density of states (right) for VO_2 (top) and WS_2 (bottom) in the MoS_2 prototype, calculated with the PBE xc-functional. The z-component of the spin is indicated by the color code on the band structure.

band edge energies can be obtained by a symmetric GLLBSC correction of the PBE band edges.

2.8.4. G_0W_0 band structure

For materials with finite PBE band gap the quasiparticle (QP) band structure is calculated using the G_0W_0 approximation on top of PBE following our earlier work [105, 106]. Currently, this resource demanding step is performed only for materials with up to four atoms in the unit cell. The number of plane waves and the number of unoccupied bands included in the calculation of the non-interacting density response function and the GW self-energy are always set equal. The individual QP energies are extrapolated to the infinite basis set limit from calculations at plane wave cutoffs of 170, 185 and 200 eV, following the standard $1/N_G$ dependence [107, 108], see figure 11 (right). The screened Coulomb interaction is represented on a non-linear real frequency grid ranging from 0 eV to

230 eV and includes around 250 frequency points. The exchange contribution to the self-energy is calculated using a Wigner–Seitz truncation scheme [109] for a more efficient treatment of the long range part of the exchange potential. For the correlation part of the self-energy, a 2D truncation of the Coulomb interaction is used [110, 111]. We stress that the use of a truncated Coulomb interaction is essential to avoid unphysical screening from periodically repeated layers which otherwise leads to significant band gap reductions.

Importantly, the use of a truncated Coulomb interaction leads to much slower k -point convergence because of the strong q -dependence of the 2D dielectric function around $q = 0$. We alleviate this problem by using an analytical expression for the screened interaction when performing the BZ integral around $q = 0$ [106]. This allows us to obtain well converged results with a relatively low k -point density of $5.0/\text{\AA}^{-1}$ (corresponding to

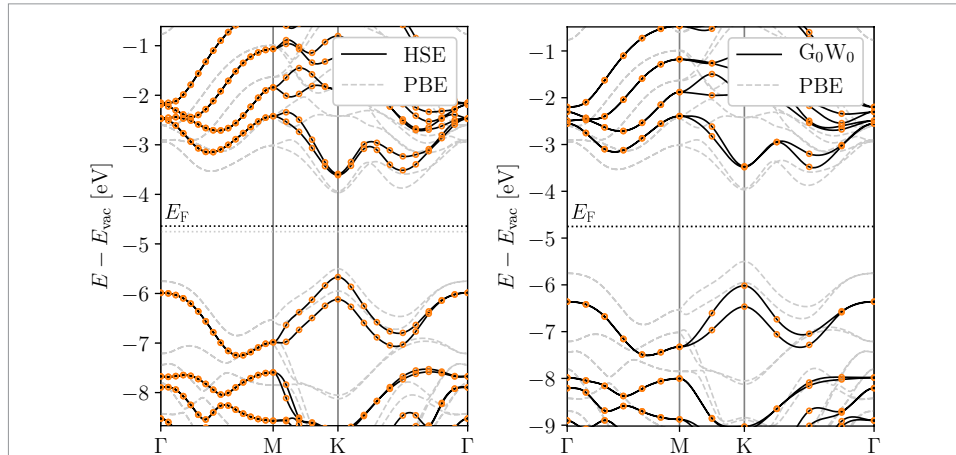


Figure 10. Band structure of WS_2 calculated with the HSE06 functional (left) and G_0W_0 (right). For comparison the PBE result is also shown (grey dashed). Spin-orbit coupling (SOC) is included in all calculations. The band energies refer to the vacuum level. The points show the calculated eigenvalues from which the band structure is interpolated. The relatively coarse k -point grid used for G_0W_0 is justified by the analytical treatment of the screened interaction $W(q)$ around $q = 0$, see figure 11.

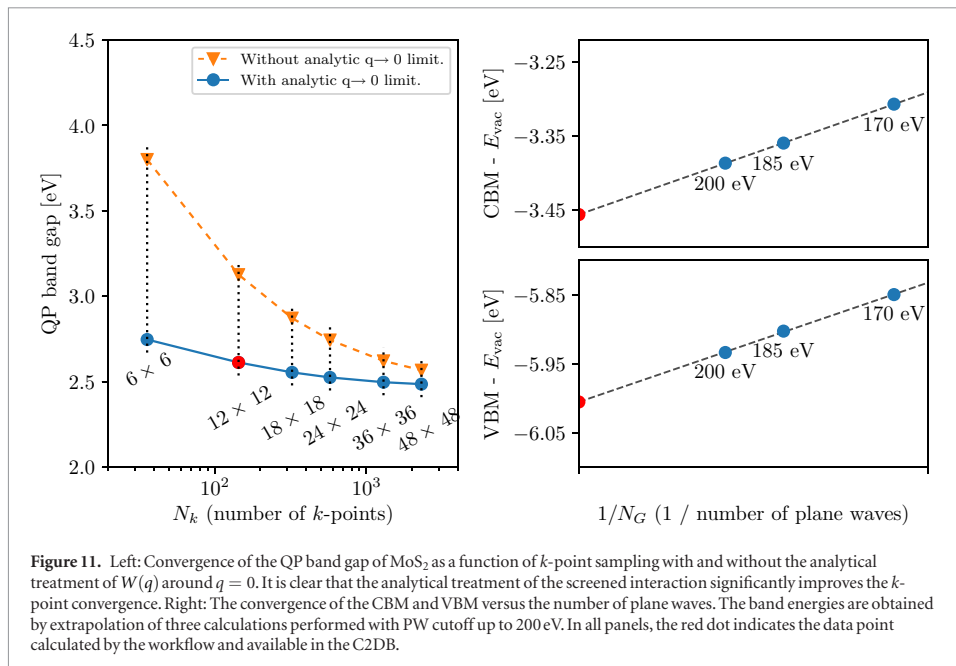


Figure 11. Left: Convergence of the QP band gap of MoS_2 as a function of k -point sampling with and without the analytical treatment of $W(q)$ around $q = 0$. It is clear that the analytical treatment of the screened interaction significantly improves the k -point convergence. Right: The convergence of the CBM and VBM versus the number of plane waves. The band energies are obtained by extrapolation of three calculations performed with PW cutoff up to 200 eV. In all panels, the red dot indicates the data point calculated by the workflow and available in the C2DB.

12×12 k -points for MoS_2). For example, with this setting the G_0W_0 band gap of MoS_2 is converged to within 0.05 eV, see figure 11 (left). In comparison, standard BZ sampling with no special treatment of the $q = 0$ limit, requires around 40×40 k -points to reach the same accuracy.

Figure 10 (right) shows the PBE and G_0W_0 band structures of WS_2 (including SOC). The G_0W_0 self-energy opens the PBE band gap by 1.00 eV and the HSE gap by 0.47 eV, in good agreement with previous stud-

ies [112]. We note in passing that our previously published G_0W_0 band gaps for 51 monolayer TMDCs [36] are in good agreement with the results obtained using the workflow described here. The mean absolute error between the two data sets is around 0.1 eV and can be ascribed to the use of PBE rather than LDA as starting point and the use of the analytical expression for W around $q = 0$.

A detailed comparison of our results with previously published G_0W_0 data is not meaningful because

Table 4. Comparison between calculated and experimental band gaps for four freestanding monolayers. The experimental values have been corrected for substrate screening. MAD refers to the mean absolute deviation between the predicted values and the measured values.

Material	Band gap (eV)				Experiment
	PBE	HSE06	GLLBSC	G_0W_0	
MoS ₂	1.58	2.09	2.21	2.53	2.50 [125]
MoSe ₂	1.32	1.80	1.88	2.12	2.31 [126]
WS ₂	1.53	2.05	2.16	2.53	2.72 [127]
P (phosphorene)	0.90	1.51	1.75	2.03	2.20 [124]
MAD w.r.t. experiment	1.10	0.57	0.43	0.15	—

of the rather large differences in the employed implementations/parameter settings. In particular, most reported calculations do not employ a truncated Coulomb interaction and thus suffer from spurious screening effects, which are then corrected for in different ways. Moreover, they differ in the amount of vacuum included in the supercell, the employed k -point grids and basis sets, the in-plane lattice constants, and the DFT starting points. For example, published values for the QP band gap of monolayer MoS₂ vary from from 2.40 to 2.90 eV [113–120] (see [119] for a detailed overview). The rather large variation in published GW results for 2D materials is a result of the significant numerical complexity of such calculations and underlines the importance of establishing large and consistently produced benchmark data sets like the present.

For bulk materials, self-consistency in the Green's function part of the self-energy, i.e. the G_0W_0 method, has been shown to increase the G_0W_0 band gaps and improve the agreement with experiments [121]. The trend of band gap opening is also observed for 2D materials [106, 120, 120, 122], however, no systematic improvement with respect to experiments has been established [122]. For both bulk and 2D materials, the fully self-consistent GW self-energy systematically overestimates the band gap [121, 122] due to the neglect of vertex corrections [122, 123]. In G_0W_0 the neglect of vertex corrections is partially compensated by the smaller band gap of the non-interacting Kohn–Sham Green's function compared to the true interacting Green's function. In this case, the vertex corrections will affect mainly the absolute position of the bands relative to vacuum while the effect on the band gap is relatively minor [122].

In table 4 we compare calculated band gaps from C2DB with experimental band gaps for three monolayer TMDCs and phosphorene. The experimental data has been corrected for substrate interactions [122, 124], but not for zero-point motion, which is expected to be small (<0.1 eV). The G_0W_0 results are all within 0.2 eV of the experiments. A further (indirect) test of the G_0W_0 band gaps against experimental values is provided by the comparison of our BSE spectra against experimental photoluminescence data in table 7, where we have used a G_0W_0 scissors operator. Finally, we stress that the employed PAW potentials are not norm-conserving, and this can lead to errors for bands with highly localised states (mainly $4f$ and $3d$ orbitals),

as shown in [108]. Inclusion of vertex corrections and use of norm conserving potentials will be the focus of future work on the C2DB.

2.9. Band extrema

For materials with a finite band gap, the positions of the valence band maximum (VBM) and conduction band minimum (CBM) within the BZ are identified together with their energies relative to the vacuum level. The latter is defined as the asymptotic value of the electrostatic potential, see figure 12. The PBE electrostatic potential is used to define the vacuum level in the non-selfconsistent HSE and G_0W_0 calculations. For materials with an out-of-plane dipole moment, a dipole correction is applied during the selfconsistent DFT calculation, and the vacuum level is defined as the average of the asymptotic electrostatic potentials on the two sides of the structure. The PBE vacuum level shift is also stored in the database.

2.10. Fermi surface

The Fermi surface is calculated using the PBE xc-functional including SOC for all metallic compounds in the database. Based on a ground state calculation with a k -point density of at least $20/\text{\AA}^{-3}$, the eigenvalues are interpolated with quadratic splines and plotted within the first BZ. Figure 13 (left) shows an example of the Fermi surface for VO₂-MoS₂ with color code indicating the out-of-plane spin projection (S_z). The band structure refers to the ferromagnetic ground state of VO₂-MoS₂, which has a magnetic moment of $0.70 \mu_B$ per unit cell, characterised by alternating spin-polarised lobes with $\langle S_z \rangle = \pm 1$.

2.11. Effective masses

For materials with a finite PBE gap, the effective electron and hole masses are calculated from the PBE eigenvalues; initially these are calculated on an ultrafine k -point mesh of density $45.0/\text{\AA}^{-3}$ uniformly distributed inside a circle of radius 0.015\AA^{-1} centered at the VBM and CBM, respectively. The radius is chosen to be safely above the noise level of the calculated eigenvalues but still within the harmonic regime; it corresponds to a spread of eigenvalues of about 1 meV within the circle for an effective mass of $1 m_0$. For each band within an energy window of 100 meV above/below the CBM/VBM, the band

curvature is obtained by fitting a third order polynomial. Even though the masses represent the second derivative of the band energies, we have found that the inclusion of 3rd order terms stabilises the fitting procedure and yields masses that are less sensitive to the details of the employed k -point grids. For each band the mass tensor is diagonalised to yield heavy and light masses in case of anisotropic band curvatures. The masses (in two directions) and the energetic splitting of all bands within 100 meV of the band extremum are calculated both with and without SOC and stored in the database. Other approaches exist for calculating effective masses, such as $\mathbf{k} \cdot \mathbf{p}$ perturbation theory (see e.g. [128] and references therein); the present scheme was chosen for its simplicity and ease of application to a wide range of different materials.

In addition to the effective masses at the VBM and CBM, the exciton reduced mass is calculated by applying the above procedure to the direct valence-conduction band transition energies, $\varepsilon_{v-c}(\mathbf{k}) = \varepsilon_c(\mathbf{k}) - \varepsilon_v(\mathbf{k})$. For direct band gap materials the exciton reduced mass is related to the electron and hole masses by $1/\mu_{ex} = 1/m_e^* + 1/m_h^*$, but in the more typical case of indirect band gaps, this relation does not hold.

As an example, figure 14 shows a zoom of the band structure of SnS-GeSe around the VBM and CBM (upper and lower panels). The second order fits to the band energies (extracted from the fitted 3rd order polynomial) are shown by red dashed lines. It can be seen that both the conduction and valence bands are anisotropic leading to a heavy and light mass direction (left and right panels, respectively). The valence band is split by the SOC resulting in two bands separated by ~ 10 meV and with slightly different curvatures. The conduction band exhibits a non-trivial band splitting in one of the two directions. The peculiar band splitting is due to a Rashba effect arising from the combination of spin-orbit coupling and the finite perpendicular electric field created by the permanent dipole of the SnS structure where Sn and S atoms are displaced in the out of plane direction leading to a sizable vacuum level difference of 1.13 eV, see figure 12.

Table 5 shows a comparison between selected effective masses from the C2DB and previously published data also obtained with the PBE xc-correlation functional and including SOC. Overall, the agreement is very satisfactory.

2.12. Work function

For metallic compounds, the work function is obtained as the difference between the Fermi energy and the asymptotic value of the electrostatic potential in the vacuum region, see figure 12. The work function is determined for both PBE and HSE band structures (both including SOC) on a uniform k -point grid of density $12.0/\text{\AA}^{-3}$. Since the SOC is evaluated non-selfconsistently, the Fermi energy is adjusted afterwards based on a charge neutrality condition.

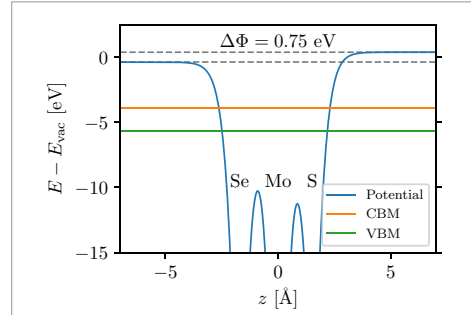


Figure 12. Electrostatic potential profile perpendicular to monolayer MoSe (averaged in plane). The position of the VBM and CBM are indicated together with the splitting of the vacuum levels caused by the out-of-plane dipole moment of the MoSe layer.

2.13. Deformation potentials

For semiconductors, the deformation potentials quantify the shift in band edge energies (VBM or CBM) upon a linear deformation of the lattice. The uniaxial absolute deformation potential along axis i ($i = x, y$) is defined as [129, 130]

$$D_{ii}^{\alpha} = \frac{\Delta E_{\alpha}}{\varepsilon_{ii}}, \quad \alpha = \text{VBM, CBM} \quad (7)$$

where ΔE_{α} is the energy shift upon strain and ε_{ii} are the strains in the i -directions.

The deformation potentials are important physical quantities as they provide an estimate of the strength of the (acoustic) electron-phonon interaction, see section 3.2.2. Moreover, they are obviously of interest in the context of strain-engineering of band gaps and they can be used to infer an error bar on the band gap or band edge positions due to a known or estimated error bar on the lattice constant.

The calculation of D_{ii}^{α} is based on a central difference approximation to the derivative. A strain of $\pm 1\%$ is applied separately in the x and y directions and the ions are allowed to relax while keeping the unit cell fixed. Calculations are performed with the PBE xc-functional, a plane wave cutoff of 800 eV, and a k -point density of $12/\text{\AA}^{-3}$.

The change in band energy, ΔE_{α} , is measured relative to the vacuum level. In cases with nearly degenerate bands, care must be taken to track the correct bands as different bands might cross under strain. In this case, we use the expectation value $\langle \hat{S}_z \rangle$ to follow the correct band under strain. Figure 15 shows how the band structure of MoS₂ changes as a function of strain. Both the VBM and the CBM shift down (relative to the vacuum level) when tensile strain is applied in the x direction, but the conduction band shows a much larger shift, leading to an effective band gap closing under tensile strain.

Table 6 shows a comparison between the deformation potentials in the C2DB, and literature values obtained using similar methods. There is generally

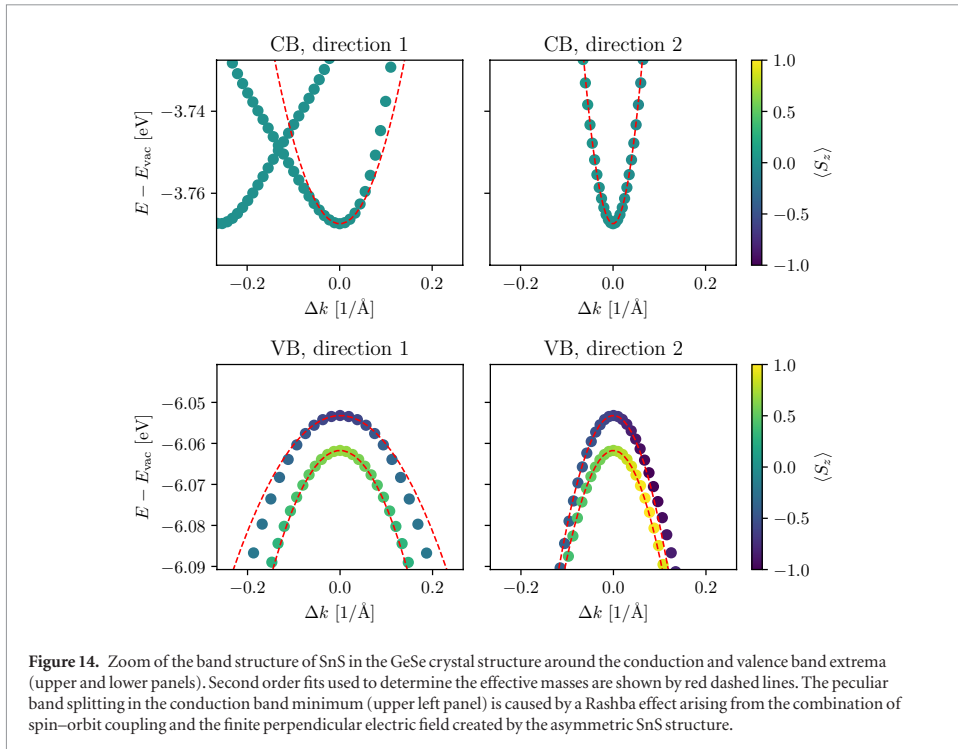
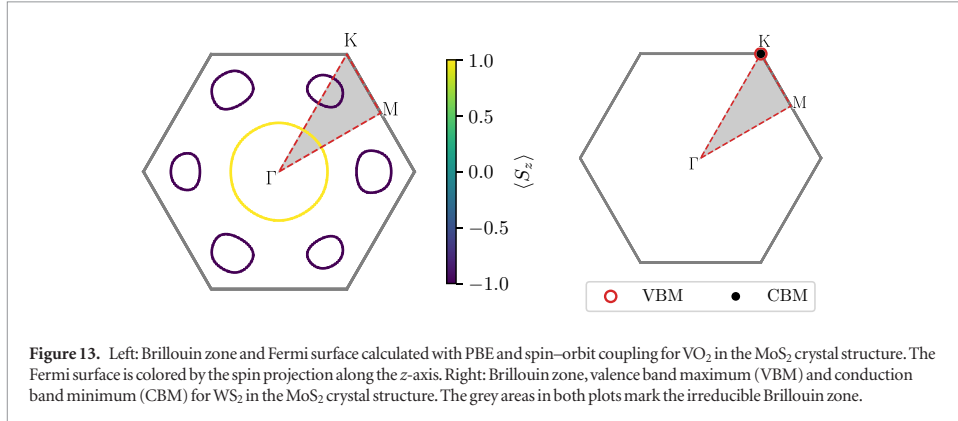
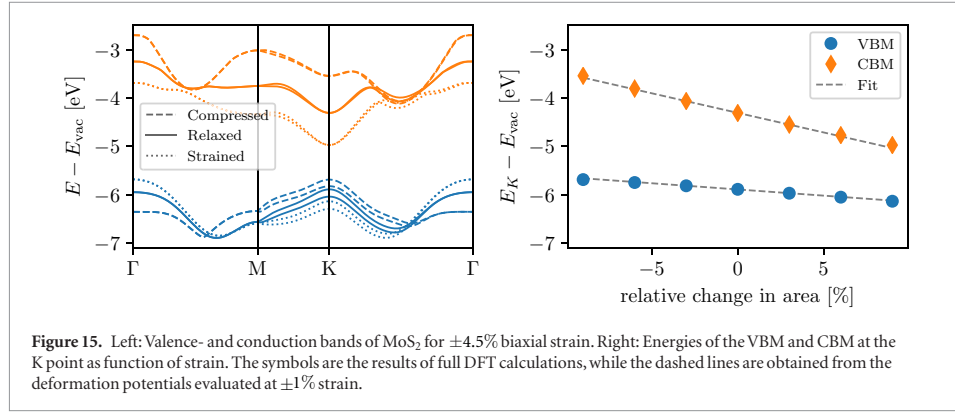


Table 5. Calculated PBE effective masses (in units of m_0), for the highest valence band and lowest conduction band, for different 2D materials. All C2DB values are calculated including spin–orbit coupling.

Material	k -point	Electron mass (m_0)		Hole mass (m_0)	
		C2DB	Literature	C2DB	Literature
MoS_2	K	0.42	0.44 [128]	0.53	0.54 [128]
WSe_2	K	0.46	0.40 [128]	0.35	0.36 [128]
Phosphorene (zig-zag)	Γ	1.24	1.24 [95]	6.56	6.48 [95]
Phosphorene (armchair)	Γ	0.14	0.13 [95]	0.13	0.12 [95]
MAD		0.02	—	0.03	—

Table 6. Absolute deformation potentials (in eV) of the VBM and CBM for different materials. All results are based on the PBE xc-functional.

Material	k -point	Valence band		Conduction band	
		C2DB	Ref. [131]	C2DB	Ref. [131]
MoSe ₂	K	-1.43	-1.86	-5.57	-5.62
WS ₂	K	-1.25	-1.59	-6.66	-6.76
WSe ₂	K	-1.21	-1.43	-6.21	-6.35
<i>h</i> BN	K	-1.57	-1.63	-4.55	-4.62
MAD		0.26	—	0.14	—



good agreement, and part of the discrepancy can be ascribed to the fact that, in contrast to [131], our numbers include spin-orbit coupling.

2.14. Plasma frequencies

The dielectric response of a 2D material is described by its 2D polarisability, α^{2D} (see section 2.15 for a general introduction of this quantity). For metals, it can be separated into contributions from intraband and interband transitions, i.e. $\alpha^{2D} = \alpha^{2D,\text{intra}} + \alpha^{2D,\text{inter}}$. We have found that local field effects (LFEs) are negligible for the intraband component, which consequently can be treated separately and evaluated as an integral over the Fermi surface. Specifically, this leads to the Drude expression for the polarisability in the long wave length limit $\alpha^{2D,\text{intra}}(\omega) = -\omega_{P,2D}^2 / (2\pi\omega^2)$ where $\omega_{P,2D}$ is the 2D plasma frequency, which in atomic units is given by

$$\omega_{P,2D}^2 = \frac{4\pi}{A} \sum_{snk} |\hat{\mathbf{q}} \cdot \mathbf{v}_{snk}|^2 \delta(\epsilon_{snk} - \epsilon_F), \quad (8)$$

where $\mathbf{v}_{snk} = \langle snk | \hat{\mathbf{p}} / m_0 | snk \rangle$ is a velocity matrix element (with m_0 the electron mass), $\hat{\mathbf{q}} = \mathbf{q} / q$ is the polarisation direction, s, n, \mathbf{k} denote spin, band and momentum indices, and A is the supercell area. The 2D plasma frequency is related to the conventional 3D plasma frequency by $\omega_{P,2D}^2(\omega) = \omega_{P,3D}^2(\omega) L / 2$ where L is the supercell height.

The plasma frequency defined above determines the intraband response of the 2D metal to external fields.

In particular, it determines the dispersion relation of plasmon excitations in the metal. The latter are defined by the condition $\epsilon^{2D}(\omega_P) = 1 + 2\pi q \alpha^{2D}(\omega_P) = 0$, where q is the plasmon wave vector. Neglecting interband transitions (the effect of which is considered in section 3.2.4), the 2D plasmon dispersion relation becomes

$$\omega_P(q) = \omega_{P,2D} \sqrt{q}. \quad (9)$$

The plasma frequencies, $\omega_{P,2D}$, for polarisation in the x and y directions, respectively, are calculated for all metals in the C2DB using the linear tetrahedron method [98] to interpolate matrix elements and eigenvalues based on a PBE band structure calculation with a k -point density of $20/\text{\AA}^{-1}$.

2.15. Electronic polarisability

The polarisability tensor α_{ij} is defined by

$$P_i(\mathbf{q}, \omega) = \sum_j \alpha_{ij}(\mathbf{q}, \omega) E_j(\mathbf{q}, \omega), \quad (10)$$

where P_i is the i 'th component of the induced polarisation averaged over a unit cell and E_j is the j 'th component of the macroscopic electric field. Using that $P_i = (D_i - E_i) / (4\pi) = \sum_j (\epsilon_{ij} - \delta_{ij}) E_j / (4\pi)$ one observes that $\alpha_{ij} = (\epsilon_{ij} - \delta_{ij}) / (4\pi)$, where ϵ_{ij} is the dielectric function. In contrast to the dielectric function, whose definition for a 2D material is not straightforward [119], the polarisability allows for a natural generalisation to 2D by considering the induced dipole moment per unit area,

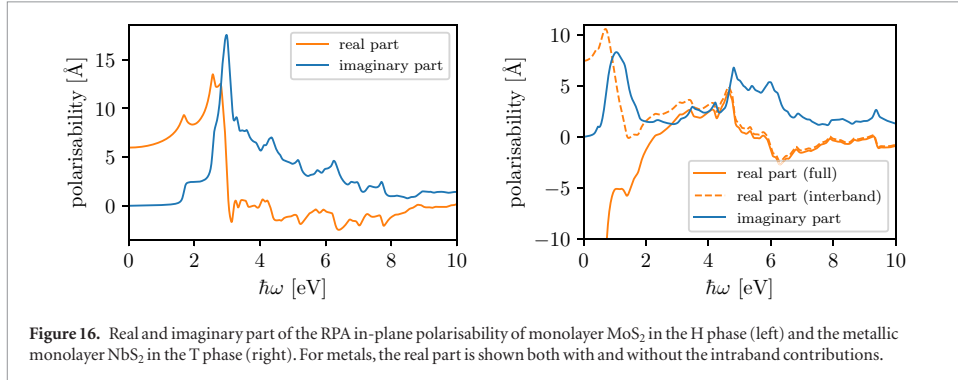


Figure 16. Real and imaginary part of the RPA in-plane polarisability of monolayer MoS₂ in the H phase (left) and the metallic monolayer NbS₂ in the T phase (right). For metals, the real part is shown both with and without the intraband contributions.

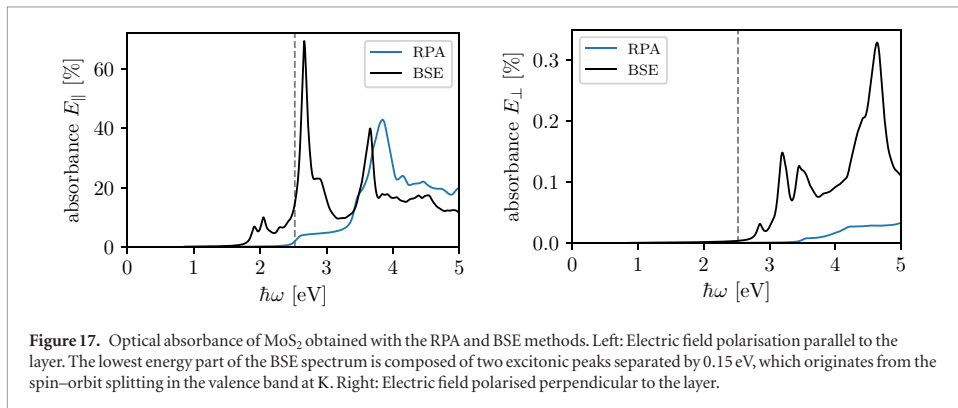


Figure 17. Optical absorbance of MoS₂ obtained with the RPA and BSE methods. Left: Electric field polarisation parallel to the layer. The lowest energy part of the BSE spectrum is composed of two excitonic peaks separated by 0.15 eV, which originates from the spin-orbit splitting in the valence band at K. Right: Electric field polarised perpendicular to the layer.

$$P_i^{2D}(\mathbf{q}, \omega) = \sum_j \alpha_{ij}^{2D}(\mathbf{q}, \omega) E_j(\mathbf{q}, \omega). \quad (11)$$

Since the P_i is a full unit cell average and P_i^{2D} is integrated in the direction orthogonal to the slab, we have $P_i^{2D} = LP_i$ and $\alpha_{ij}^{2D} = L\alpha_{ij}$, where L is the length of the unit cell in the direction orthogonal to the slab.

In the following, we focus on the longitudinal components of the polarisability and dielectric tensors, which are simply denoted by α and ϵ . These are related to the density-density response function, χ , via the relations

$$\alpha^{2D}(\mathbf{q}, \omega) = \frac{L}{4\pi} (\epsilon(\mathbf{q}, \omega) - 1), \quad (12)$$

$$\epsilon^{-1}(\mathbf{q}, \omega) = 1 + \langle v_c(\mathbf{q}) \chi(\omega) \rangle_{\mathbf{q}}, \quad (13)$$

where v_c is the Coulomb interaction and

$$\langle v_c \chi(\omega) \rangle_{\mathbf{q}} = \frac{1}{V} \int_{\text{Cell}} d\mathbf{r} d\mathbf{r}' d\mathbf{r}'' v_c(\mathbf{r}, \mathbf{r}') \chi(\mathbf{r}', \mathbf{r}'', \omega) e^{-i\mathbf{q}(\mathbf{r}-\mathbf{r}'')}, \quad (14)$$

where Cell is the supercell with volume V . The response function, χ , satisfies the Dyson equation [132] $\chi = \chi^{\text{irr}} + \chi^{\text{irr}} v_c \chi$, where χ^{irr} is the irreducible density-density response function. In the random phase approximation (RPA) χ^{irr} is replaced by the non-interacting response function, χ^0 , whose plane wave representation is given by [133, 134]

$$\chi_{\mathbf{G}\mathbf{G}'}^0(\mathbf{q}, \omega) = \frac{1}{\Omega} \sum_{\mathbf{k} \in \text{BZ}} \sum_{mn} (f_{n\mathbf{k}} - f_{m\mathbf{k}+\mathbf{q}}) \times \frac{\langle \psi_{n\mathbf{k}} | e^{-i(\mathbf{q}+\mathbf{G}) \cdot \mathbf{r}} | \psi_{m\mathbf{k}+\mathbf{q}} \rangle \langle \psi_{m\mathbf{k}+\mathbf{q}} | e^{i(\mathbf{q}+\mathbf{G}') \cdot \mathbf{r}} | \psi_{n\mathbf{k}} \rangle}{\hbar\omega + \epsilon_{n\mathbf{k}} - \epsilon_{m\mathbf{k}+\mathbf{q}} + i\eta}, \quad (15)$$

where \mathbf{G}, \mathbf{G}' are reciprocal lattice vectors and Ω is the crystal volume.

For all materials in the database, we calculate the polarisability within the RPA for both in-plane and out-of-plane polarisation in the optical limit $\mathbf{q} \rightarrow 0$. For metals, the interband contribution to the polarisability is obtained from equation (15) while the intraband contribution is treated separately as described in section 2.14. The single-particle eigenvalues and eigenstates used in equation (15) are calculated with PBE, a k -point density of $20/\text{\AA}^{-3}$ (corresponding to a k -point grid of 48×48 for MoS₂ and 60×60 for graphene), and 800 eV plane wave cutoff. The Dyson equation is solved using a truncated Coulomb potential [105, 111] to avoid spurious interactions from neighboring images. We use the tetrahedron method to interpolate the eigenvalues and eigenstates and a peak broadening of $\eta = 50$ meV. Local field effects are accounted for by including \mathbf{G} -vectors up to 50 eV. For the band summation we include 5 times as many unoccupied bands as occupied bands, which roughly corresponds to an

energy cutoff of 50 eV. The calculations are performed without spin–orbit coupling.

In figure 16 we show the real and imaginary part of α^{2D} for the semiconductor MoS₂. The PBE band gap of this material is 1.6 eV and we see the onset of dissipation at that energy. We also see that the initial structure of $\text{Im } \alpha$ is a constant, which is exactly what would be expected from the density of states in a 2D material with parabolic dispersion. Finally, we note that the static polarisability $\text{Re } \alpha|_{\omega=0} \approx 6\text{\AA}$, which can easily be read off the figure. The polarisability is also shown for the metallic 1T-NbS₂ where we display the real part with and without the intraband Drude contribution $\omega_{P,2D}^2/(\hbar\omega + i\eta)^2$.

2.16. Optical absorbance

The power absorbed by a 2D material under illumination of a monochromatic light field with polarisation $\hat{\mathbf{e}}$ is quantified by the dimensionless absorbance:

$$\text{Abs}(\omega) = 4\pi\omega\alpha^{2D}(q\hat{\mathbf{e}} \rightarrow 0, \omega)/c, \quad (16)$$

where c is the speed of light. In section 2.15 we gave a prescription for evaluating α^{2D} in the RPA. However, absorption spectra of 2D semiconductors often display pronounced excitonic effects, which are not captured by the RPA. The Bethe–Salpeter equation (BSE) is a well-known method capable of describing excitonic effects and has been shown to provide good agreement with experimental absorption spectra for a wide range of materials [135].

For materials with finite band gap and up to four atoms per unit cell, we have calculated the RPA and the BSE absorption spectra for electric fields polarised parallel and perpendicular to the layers. The calculations are performed on top of PBE eigenstates and eigenvalues with spin–orbit coupling included and all unoccupied band energies shifted by a constant in order to reproduce the G_0W_0 quasiparticle gap (the scissors operator method). If the G_0W_0 gap is not available we use the GLLBSC gap for non-magnetic materials and the HSE gap for magnetic materials (since GLLBSC is not implemented in GPAW for spin-polarised systems). The screened interaction entering the BSE Hamiltonian is calculated within the RPA using a non-interacting response function evaluated from equation (15) with local field effects (i.e. \mathbf{G} -vectors) included up to 50 eV and 5 times as many unoccupied bands as occupied bands for the sum over states. We apply a peak broadening of $\eta = 50$ meV and use a truncated Coulomb interaction. The BSE Hamiltonian is constructed from the four highest occupied and four lowest unoccupied bands on a k -point grid of density of $20/\text{\AA}^{-2}$, and is diagonalised within the Tamm–Dancoff approximation. We note that the Tamm–Dancoff approximation has been found to be very accurate for bulk semiconductors [136]. For monolayer MoS₂ we have checked that it reproduces

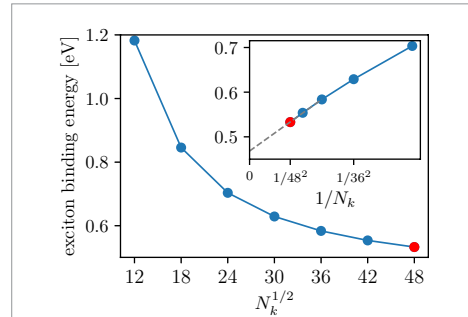


Figure 18. Convergence of the binding energy of the lowest exciton in monolayer MoS₂ obtained from a BSE calculation as a function of k -point mesh. The quasiparticle energies entering the BSE Hamiltonian are obtained from a fully converged PBE calculation with a scissors operator applied to match the G_0W_0 band gap. The red point represents the k -point sampling applied in the database, which is seen to overestimate the extrapolated exciton binding energy by ~ 0.06 eV (inset).

the full solution of the BSE, but its general validity for 2D materials, in particular those with small band gaps, should be more thoroughly tested.

In figure 17 we show the optical absorption spectrum of MoS₂ obtained with the electric field polarised parallel and perpendicular to the layer, respectively. Both RPA and BSE spectra are shown (the in-plane RPA absorbance equals the imaginary part of the RPA polarisability, see figure 16 (left), apart from the factor $4\pi\omega$ and the scissors operator shift). The low energy part of the in-plane BSE spectrum is dominated by a double exciton peak (the so-called A and B excitons) and is in excellent agreement with experiments [55].

In general, calculations of electronic excitations of 2D materials converge rather slowly with respect to k -points due to the non-analytic behavior of the dielectric function in the vicinity of $q = 0$ [119, 137, 138]. In figure 18 we show the k -point dependence of the binding energy of the A exciton in MoS₂ obtained as the difference between the direct band gap and the position of the first peak in figure 17. We observe a strong overestimation of the exciton binding energy at small k -point samplings, which converges slowly to a value of ~ 0.5 eV at large k -point samplings. For 48×48 k -points, corresponding to the k -point sampling used for the BSE calculations in the database, the exciton binding energy is 0.53 eV, whereas a $1/N_k^2$ extrapolation to infinite k -point sampling gives 0.47 eV (see inset in figure 18). In general, the exciton binding energy decreases with increasing k -point sampling, and thus the exciton binding energies reported in the C2DB might be slightly overestimated. However, since G_0W_0 band gaps also decrease when the k -point sampling is increased (see figure 11) the two errors tend to cancel such that the absolute position of the absorption peak from BSE- G_0W_0 converges faster than the band gap or exciton binding energy alone.

Table 7. Comparison between calculated and experimental positions of the first excitonic peak for four different transition metal dichalcogenide monolayers and phosphorene.

Material	Energy of the first bright exciton (eV)	
	BSE@PBE-G ₀ W ₀	Experiment
MoS ₂	2.00	1.83 [140], 1.86 [141], 1.87 [142]
MoSe ₂	1.62	1.57 [140], 1.57 [143], 1.58 [144]
WS ₂	2.07	1.96 [141], 2.02 [144]
WSe ₂	1.71	1.64 [142], 1.66 [143]
P (phosphorene)	1.45	1.45 [145], 1.75 [146]
MAD w.r.t. experiment	0.066	—

The BSE-G₀W₀ method has previously been shown to provide good agreement with experimental photoluminescence and absorption measurements on 2D semiconductors. In table 7 we show that our calculated position of the first excitonic peak agree well with experimental observations for four different TMDCs and phosphorene. Experimentally, the monolayers are typically supported by a substrate, which may alter the screening of excitons. However the resulting decrease in exciton binding energies is largely cancelled by a reduced quasiparticle gap such that the positions of the excitons are only slightly red-shifted as compared with the case of pristine monolayers [139].

3. Database overview

Having described the computational workflow, we now turn to the content of the database itself. We first present a statistical overview of all the materials in the C2DB (i.e. without applying any stability filtering) by displaying their distribution over crystal structure prototypes and their basic properties. We also provide a short list with some of the most stable materials, which to our knowledge have not been previously studied. Next, the predicted stability of the total set of materials is discussed and visualised in terms of the descriptors for thermodynamic and dynamic stability introduced in section 2.4.1. In section 3.2 we analyse selected properties in greater detail focusing on band gaps and band alignment, effective masses and mobility, magnetic properties, plasmons, and excitons. Throughout the sections we explore general trends and correlations in the data and identify several promising materials with interesting physical properties.

3.1. Materials

In table 8 we list the major classes of materials currently included in the database. The materials are grouped according to their prototype, see section 2.2.2. For each prototype we list the corresponding space group, the total number of materials, and the number of materials satisfying a range of different conditions. The atomic structure of some of the different prototypes were shown in figure 4. The vast majority of the 2D materials that have been experimentally synthesised in monolayer

form are contained in the C2DB (the 55 materials in figure 7 in addition to seven metal-organic perovskites). These materials are marked in the database and a literature reference is provided. Additionally, 80 of the monolayers in the C2DB could potentially be exfoliated from experimentally known layered bulk structures [16–19]. These materials are also marked and the ID of the bulk compound in the relevant experimental crystal structure database is provided.

To illustrate how all the materials are distributed in terms of stability, we show the energy above the convex hull plotted against $\tilde{\omega}_{\min}^2$ in figure 19. It can be seen that the structures naturally sort themselves into two clusters according to the dynamic stability. The points have been colored according to the three levels for dynamic stability introduced in section 2.4. The lower panel shows the distribution of the materials in the grey region on a linear scale. While most of the experimentally known materials (red and black dots) have high dynamic stability, a significant part of them fall into the medium stability category. The marginal distributions on the plot show that the more dynamically stable materials are also more thermodynamically stable. The mean energy above the convex hull is 0.12 eV for the materials with high dynamical stability, while it is 0.25 eV for the others.

In table 9 we show the key properties of a selected set of stable materials, distributed across a variety of different crystal structure prototypes. To our knowledge, these materials are not experimentally known, and they are therefore promising candidates further study and experimental synthesis.

3.2. Properties: example applications

In the following sections we present a series of case studies focusing on different properties of 2D materials including band gaps and band alignment, effective masses and mobility, magnetic order, plasmons and excitons. The purpose is not to provide an in-depth nor material specific analysis, but rather to explore trends and correlations in the data and showcase some potential applications of the C2DB. Along the way, we report some of the novel candidate materials revealed by this analysis, which could be interesting to explore closer in the future.

Table 8. Overview of the materials currently in the C2DB. The table shows the number of compounds listed by their crystal structure prototype and selected properties. $E_{\text{gap}} > 0$ and ‘direct gap’ refer to the PBE values, ‘high stability’ refers to the stability scale defined in section 2.4.1, and the last three columns refer to the magnetic state, see section 2.1. In this overview, separate magnetic phases of the same structure are considered different materials.

Prototype	Symmetry	Number of materials						
		Total	$E_{\text{gap}} > 0$	Direct gap	High stability	NM	FM	AFM
C	P6/mmm	4	4	3	1	4	0	0
CH	P $\bar{3}$ m1	8	7	6	1	8	0	0
CH ₂ Si	P3m1	2	2	2	1	2	0	0
BN	P $\bar{3}$ m2	10	9	5	1	10	0	0
GaS	P $\bar{3}$ m2	125	34	95	8	100	18	7
FeSe	P4/nmm	103	13	90	26	74	18	11
GeSe	P3m1	20	19	5	6	20	0	0
PbSe	P4/mmm	44	6	38	1	33	8	3
P	Pmna	9	9	0	1	9	0	0
MoS ₂	P $\bar{3}$ m2	241	85	176	53	156	85	0
CdI ₂	P $\bar{3}$ m1	315	95	231	90	218	80	17
WTe ₂	P2 ₁ /m	75	29	48	34	57	13	5
FeOCl	Pmmm	443	92	385	65	328	63	52
MoSSe	P3m1	9	6	6	5	8	1	0
C ₂ N	P6/mmm	25	1	24	0	25	0	0
YBr ₃	P6/mmm	57	11	51	0	21	24	12
TiCl ₃	P $\bar{3}$ 2m	69	35	51	2	32	23	14
BiI ₃	P $\bar{3}$ m1	123	69	66	15	48	54	21
TiS ₃	Pmmm	34	8	28	5	31	2	1
MnTe ₃	P2 ₁ /m	29	3	27	1	22	4	3
Cr ₃ WS ₈	Pmm2	35	34	18	8	35	0	0
CrWS ₄	Pmm2	18	17	7	8	18	0	0
Ti ₂ CO ₂	P $\bar{3}$ m1	28	8	20	12	19	6	3
Ti ₂ CH ₂ O ₂	P $\bar{3}$ m1	13	3	12	3	10	2	1
Ti ₃ C ₂	P $\bar{3}$ m2	12	0	12	0	7	5	0
Ti ₃ C ₂ O ₂	P $\bar{3}$ m2	26	0	26	0	20	6	0
Ti ₃ C ₂ H ₂ O ₂	P $\bar{3}$ m2	14	0	14	0	10	4	0
PbA ₂ I ₄	P1	27	27	27	0	27	0	0
Sum		1918	626	151	347	1352	416	150

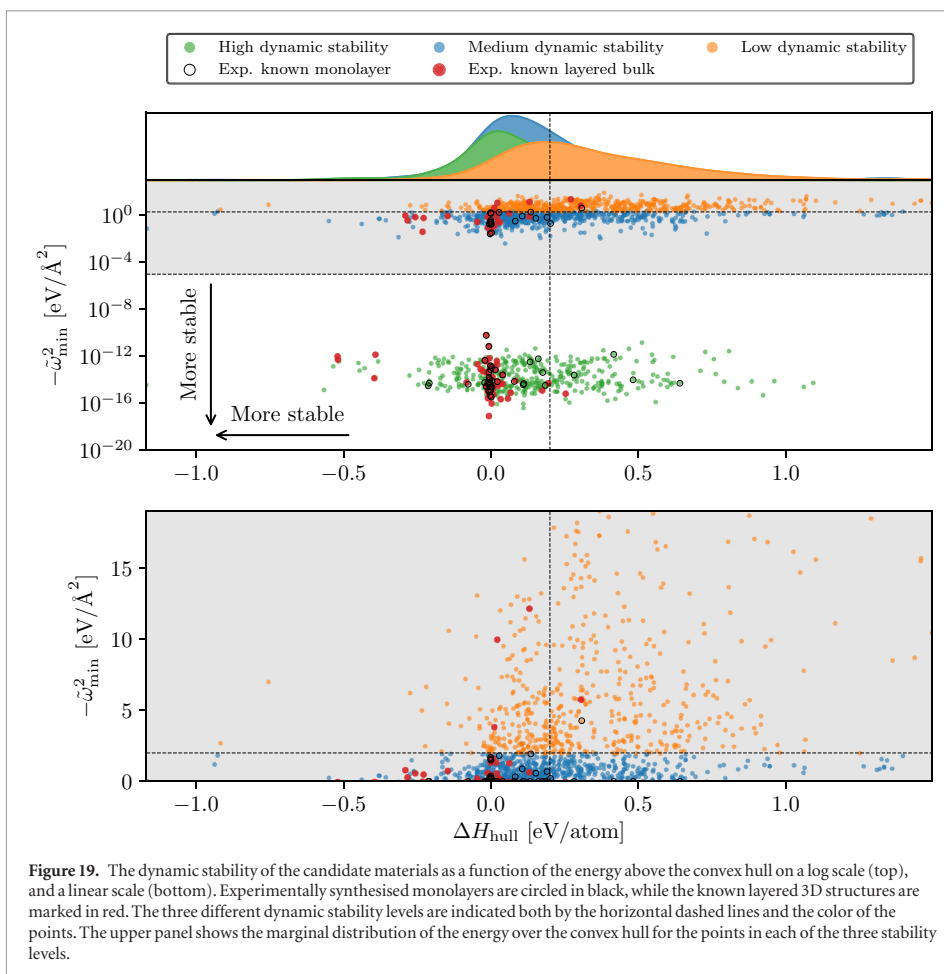
3.2.1. Band gaps and band alignment

The band gaps and band edge positions of all semiconductors and insulators in the C2DB have been calculated with the PBE, HSE06, and GLLBSC xc-functionals while G_0W_0 calculations have been performed for the ~ 250 simplest materials. The relatively large size of these datasets and the high degree of consistency in the way they are generated (all calculations performed with the same code using same PAW potentials and basis set etc) provide a unique opportunity to benchmark the performance of the different xc-functionals against the more accurate G_0W_0 method.

Figure 20 compares the size and center of the band gaps obtained with the density functionals to the G_0W_0 results. Relative to G_0W_0 the PBE functional underestimates the gaps by 45%, i.e. on average the PBE values must be scaled by 1.83 to reproduce the G_0W_0 results. The HSE06 band gaps are closer to G_0W_0 but are nevertheless systematically underesti-

mated by more than 20%. On the other hand, GLLBSC shows very good performance with band gaps only 2% smaller than G_0W_0 on average. Table 10 shows the mean absolute deviations of the DFT methods relative to G_0W_0 . We note that although GLLBSC provides an excellent description of the G_0W_0 band gaps *on average* the spread is sizable with a mean absolute deviation of 0.4 eV.

We note a handful of outliers in figure 20 with large HSE band gaps compared to PBE and G_0W_0 . For one of these, namely the ferromagnetic $\text{CoBr}_2\text{-CdI}_2$, we obtain the band gaps: 0.30 eV (PBE), 3.41 eV (HSE), and 0.91 eV (G_0W_0). For validation, we have performed GPAW and QuantumEspresso calculations with the norm-conserving HGH pseudopotentials and plane wave cutoff up to 1600 eV. The converged band gaps are 0.49 eV (GPAW-HGH-PBE), 0.51 eV (QE-HGH-PBE) and 3.69 eV (GPAW-HGH-HSE), 3.52 eV (QE-HGH-HSE), which are all in reasonable



agreement with the C2DB results. It should be interesting to explore the reason for the anomalous behavior of the HSE band gap in these materials.

Compared to the band gaps, the gap centers predicted by PBE and HSE06 are in overall better agreement with the G_0W_0 results. This implies that, on average, the G_0W_0 correction of the DFT band energies is symmetric on the valence and conduction band. In contrast, the GLLBSC predicts less accurate results for the gap center. This suggests that an accurate and efficient prediction of absolute band energies is obtained by combining the GLLBSC band gap with the PBE band gap center.

Next, we consider the band alignment at the interface between different 2D materials. Assuming that the bands line up with a common vacuum level and neglecting hybridisation/charge transfer at the interface, the band alignment is directly given by the VBM and CBM positions relative to vacuum.

We focus on pairs of 2D semiconductors for which the G_0W_0 band alignment is either Type II ($\Delta E > 0$) or Type III ($\Delta E < 0$), see figure 21 (left). Out of approximately 10 000 bilayers predicted to have Type II band alignment by G_0W_0 , the PBE and HSE06 functionals

predict qualitatively wrong band alignment (i.e. Type III) in 44% and 21% cases, respectively (grey shaded areas). In particular, PBE shows a sizable and systematic underestimation of ΔE as a direct consequence of the underestimation of the band gaps in both monolayers.

3.2.2. Effective masses and mobilities

The carrier mobility relates the drift velocity of electrons or holes to the strength of an applied electric field and is among the most important parameters for a semiconductor material. In general, the mobility is a sample specific property which is highly dependent on the sample purity and geometry, and (for 2D materials) interactions with substrate or embedding layers. Here we consider the phonon-limited mobility, which can be considered as the intrinsic mobility of the material, i.e. the mobility that would be measured in the absence of any sample specific- or external scattering sources.

The effective masses of the charge carriers have been calculated both with and without SOC for ~ 600 semiconductors. Figure 22 shows the electron mass plotted against the hole mass. The data points are scat-

Table 9. Key properties of selected stable materials in the C2DB, which have not been previously synthesised. The calculated properties are the magnetic state, formation energy, energy above the convex hull, work function, PBE gap and the nature of the gap (direct or indirect).

Prototype	Formula	Magnetic state	ΔH (eV)	ΔH_{hull} (eV)	Φ (eV)	PBE gap (eV)	Direct gap
BiI ₃	VI ₃	FM	-0.51	-0.15	5.3		
	CoCl ₃	NM	-0.65	-0.21		1.13	No
	CoBr ₃	NM	-0.41	-0.16		0.96	No
	CoI ₃	NM	-0.14	-0.14		0.53	No
CdI ₂	FeO ₂	FM	-1.14	-0.36	7.31		
	MnSe ₂	FM	-0.47	-0.18	5.09		
	MnS ₂	FM	-0.57	-0.12	5.74		
	PdO ₂	NM	-0.40	-0.08		1.38	No
	CaBr ₂	NM	-2.09	-0.02		4.86	No
FeOCl	RhClO	NM	-0.65	-0.18	5.49		
	NiClO	AFM	-0.64	-0.17	6.32		
	NiBrO	AFM	-0.52	-0.16	5.78		
	ScIS	NM	-1.68	-0.14		1.66	Yes
FeSe	CoSe	FM	-0.27	0.02	4.22		
	RuS	NM	-0.38	0.05	4.72		
	MnSe	AFM	-0.50	-0.20		0.90	No
	MnS	AFM	-0.64	-0.19		0.78	No
GaS	AlSe	NM	-0.72	-0.02		2.00	No
	AlS	NM	-0.89	0.00		2.09	No
GeSe	GeSe	NM	-0.19	0.04		2.22	No
	GeS	NM	-0.22	0.05		2.45	No
	GeTe	NM	-0.01	0.09		1.47	No
	SnSe	NM	-0.33	0.10		2.15	No
MoS ₂	VS ₂	FM	-0.88	-0.02	5.95		
	ScBr ₂	FM	-1.59	-0.40		0.16	No
	YBr ₂	FM	-1.73	-0.23		0.34	No
	FeCl ₂	FM	-0.67	-0.16		0.35	Yes
	TiBr ₂	NM	-1.14	-0.04		0.76	No
	ZrBr ₂	NM	-1.34	-0.04		0.83	No
Ti ₂ CO ₂	Zr ₂ CF ₂	NM	-2.36	-0.08	3.92		
	Hf ₂ CF ₂	NM	-2.26	0.03	3.62		
	Y ₂ CF ₂	NM	-2.50	-0.17		1.12	No
WTe ₂	NbI ₂	NM	-0.37	0.04	3.01		
	HfBr ₂	NM	-1.16	-0.18		0.85	No
	OsSe ₂	NM	-0.17	0.00		0.57	No

tered, with no clear correlation between the electron and hole masses. Overall, the electron masses are generally slightly smaller than the hole masses. The mean electron mass is $0.9 m_0$, while the mean hole mass is $1.1 m_0$, and 80% of the electron masses are below m_0 while the fraction is only 65% for the holes. This is not too surprising, since, on average, the energetically lower valence band states are expected to be more localised and thus less dispersive than the conduction band states.

The right panel of figure 22 shows the effective mass for electrons and holes plotted as a function of the inverse band gap. It can be seen that there is no clear correlation between the two quantities, which is confirmed by calculating the cross-correlation coefficient:

for both electrons and holes it is less than 0.02. This provides empirical evidence against the linear relation between effective masses and inverse band gaps derived from $\mathbf{k} \cdot \mathbf{p}$ perturbation theory. The relation is based on the assumption that the perturbative expansion is dominated by the conduction and valence band and that the momentum matrix element between these states, $\langle u_c | \mathbf{p} | u_v \rangle$, does not vary too much as function of the considered parameter (here the type of material). These assumptions clearly do not hold across a large set of different semiconductors. If we focus on a specific class of materials, e.g. sulfides in the MoS₂ structure indicated by the highlighted symbols, we see a slightly improved trend but still with significant fluctuations.

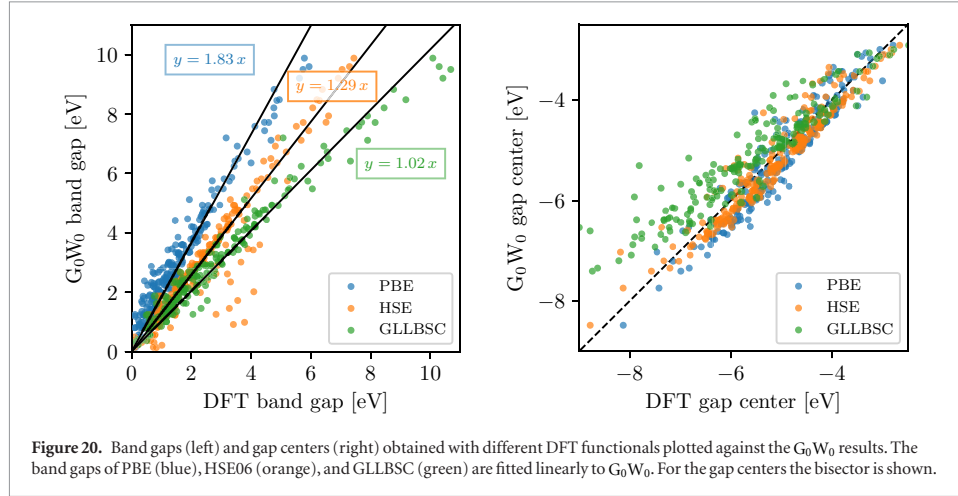


Figure 20. Band gaps (left) and gap centers (right) obtained with different DFT functionals plotted against the G_0W_0 results. The band gaps of PBE (blue), HSE06 (orange), and GLLBSC (green) are fitted linearly to G_0W_0 . For the gap centers the bisector is shown.

Table 10. The mean absolute deviation (in eV) of the band gap and band gap center calculated with three different xc-functionals with respect to G_0W_0 .

	PBE	HSE06	GLLBSC
MAD w.r.t. G_0W_0 (band gap)	1.49	0.82	0.38
MAD w.r.t. G_0W_0 (gap center)	0.37	0.32	0.76

If one assumes energetically isolated and parabolic bands, the intrinsic mobility limited only by scattering on acoustic phonons can be estimated from the Takagi formula [147],

$$\mu_i = \frac{e\hbar^3 \rho v_i^2}{k_B T m_i^* m_d^* D_i^2}. \quad (17)$$

Here i refers to the transport direction, ρ is the mass density, v_i is the speed of sound in the material, m_i^* is the carrier mass, m_d^* is the equivalent isotropic density-of-state mass defined as $m_d^* = \sqrt{m_x^* m_y^*}$, and D_i is the deformation potential. We stress that the simple Takagi formula is only valid for temperatures high enough that the acoustic phonon population can be approximated by the Rayleigh–Jeans law, $n \approx \hbar\omega_{ac}/k_B T$, but low enough that scattering on optical phonons can be neglected.

For the semiconductors in the C2DB we have found that the denominator of equation (17) varies more than the numerator. Consequently, a small product of deformation potential and effective mass is expected to correlate with high mobility. Figure 23 shows the deformation potential plotted against the carrier mass for the valence and conduction bands, respectively. The shaded area corresponds, somewhat arbitrarily, to the region for which $m_i^* D_i < m_0(1 \text{ eV})$. The 2D semiconductors which have been synthesised in monolayer form are indicated with orange symbols while those which have been used in field effect transistors are labeled. Consistent with experimental findings, phosphorene (P) is predicted to be among the

materials with the highest mobility for both electrons and holes.

Interestingly, a number of previously unknown 2D materials lie in this shaded region and could be candidates for high mobility 2D semiconductors. Table 11 lists a few selected materials with high intrinsic mobility according to equation (17), which all have ‘high’ overall stability (see section 2.4.1). In the future, it will be interesting to explore the transport properties of these candidate materials in greater detail.

To put the numbers in table 11 to scale, we consider the well studied example of MoS_2 . For this material we obtain an electron mobility of $240 \text{ cm}^2 \text{ V}^{-1} \text{ s}^{-1}$ while a full *ab initio* calculation found a phonon-limited mobility of $400 \text{ cm}^2 \text{ V}^{-1} \text{ s}^{-1}$ (in good agreement with experiments on hBN encapsulated MoS_2 [148]), with the acoustic phonon contribution corresponding to a mobility of $1000 \text{ cm}^2 \text{ V}^{-1} \text{ s}^{-1}$. Similarly, for the series MX_2 ($M = \text{W}, \text{Mo}, X = \text{S}, \text{Se}$), we calculate room-temperature electron mobilities between $200 \text{ cm}^2 \text{ V}^{-1} \text{ s}^{-1}$ and $400 \text{ cm}^2 \text{ V}^{-1} \text{ s}^{-1}$, which are all within 50% of the *ab initio* results [149]. Presumably, as in the case for MoS_2 , the good quantitative agreement is partly a result of error cancellation between an overestimated acoustic phonon scattering and the neglect of optical phonon scattering. Importantly, however, the relative ordering of the mobilities of the four MX_2 monolayers is correctly predicted by equation (17) for all but one pair (MoS_2 and WSe_2) out of the six pairs. These results illustrate that equation (17) should only be used for ‘order of magnitude’ estimates of the mobility but that relative comparisons of mobilities in different materials are probably reliable.

3.2.3. Magnetic properties

Recently, a single layer of CrI_3 was reported to exhibit ferromagnetic order with a Curie temperature of 45 K [12]. This comprises the first example of a pure 2D material exhibiting magnetic order and there is

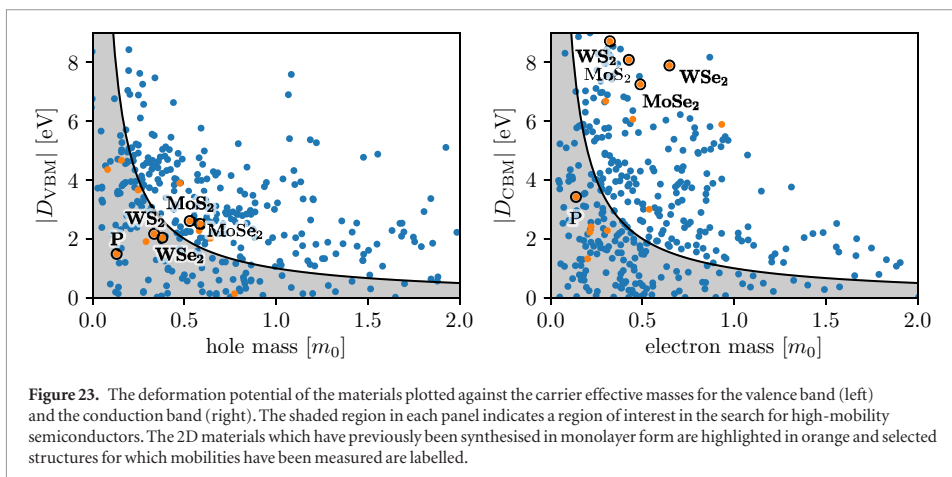
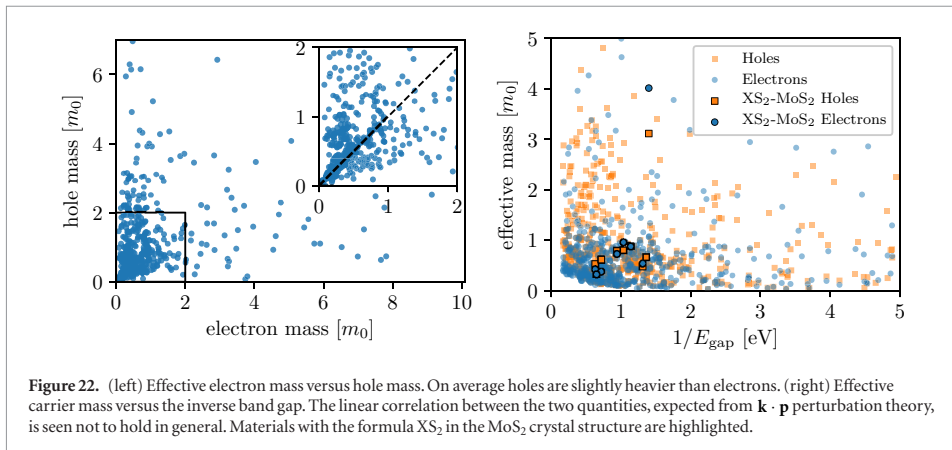
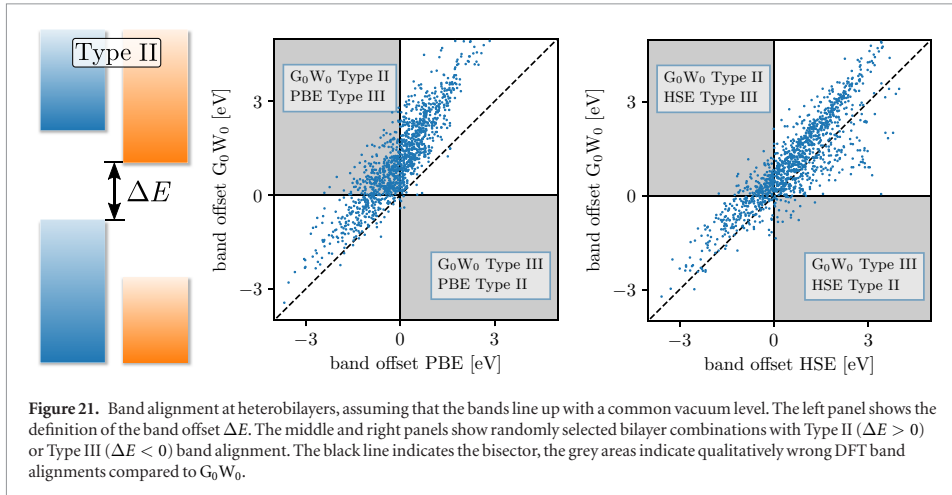


Table 11. Key transport properties of selected materials with high intrinsic room-temperature mobility according to equation (17). All the materials shown have ‘high’ overall stability as defined in section 2.4.1. μ_{high} is the larger value of the mobilities in the x or y directions, m^* is the corresponding effective mass, and $\mu_{\text{high}}/\mu_{\text{low}}$ is the ratio of the mobilities in the two directions.

Carrier	Formula	Prototype	PBE gap (eV)	μ_{high} ($\text{cm}^2 \text{V}^{-1} \text{s}^{-1}$)	m^* (m_0)	$\frac{\mu_{\text{high}}}{\mu_{\text{low}}}$
Holes	PbS ₂	MoS ₂	1.39	30 000	0.62	1.4
	OsO ₂	WTe ₂	0.17	23 000	0.23	3.0
	ZrCl ₂	MoS ₂	0.98	12 000	0.43	1.1
	WSSe	MoSSe	1.40	5500	0.37	1.0
Electrons	PtTe ₂	CdI ₂	0.30	9600	0.17	1.3
	GaO	GaS	1.56	7200	0.32	1.0
	NiS ₂	CdI ₂	0.58	6000	0.29	1.5
	RuTe ₂	WTe ₂	0.64	4600	1.55	8.5

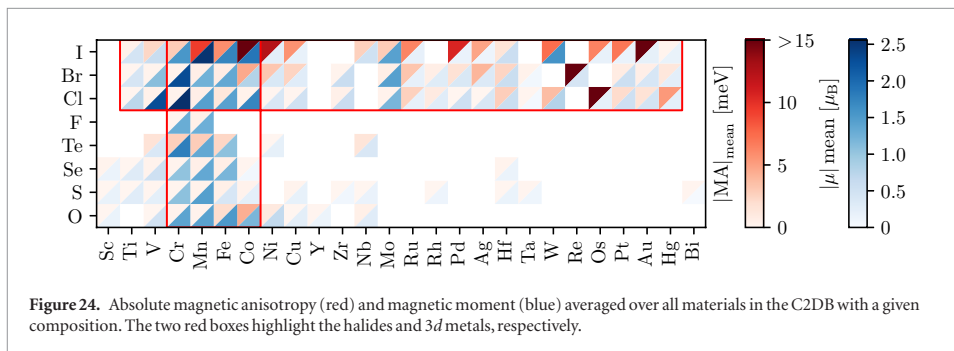


Figure 24. Absolute magnetic anisotropy (red) and magnetic moment (blue) averaged over all materials in the C2DB with a given composition. The two red boxes highlight the halides and 3d metals, respectively.

currently an intense search for new 2D materials with magnetic order persisting above room temperature [150–152].

For 2D materials, magnetic order will only persist at finite temperatures in the presence of magnetic anisotropy (MA). Indeed, by virtue of the Mermin–Wagner theorem, magnetic order is impossible in 2D unless the rotational symmetry of the spins is broken [153]. A finite MA with an out-of-plane easy axis breaks the assumption behind the Mermin–Wagner theorem and makes magnetic order possible at finite temperature. The critical temperature for magnetic order in 2D materials will thus have a strong dependence on the anisotropy.

The MA originates from spin–orbit coupling and is here defined as the energy difference between in-plane and out-of-plane orientation of the magnetic moments, see equation (4). With our definition, a negative MA corresponds to an out-of-plane easy axis. We note that most of the materials in the C2DB are nearly isotropic in-plane. Consequently, if the easy axis lies in the plane, the spins will exhibit an approximate in-plane rotational symmetry, which prohibits magnetic order at finite temperatures. Since spin–orbit coupling becomes large for heavy elements, we generally expect to find larger MA for materials containing heavier elements. In general the magnitude of the MA is small. For example, for a monolayer of CrI₃ with a Curie temperature of 45 K [12] we find a MA of -0.85 meV per Cr atom in agreement with previous

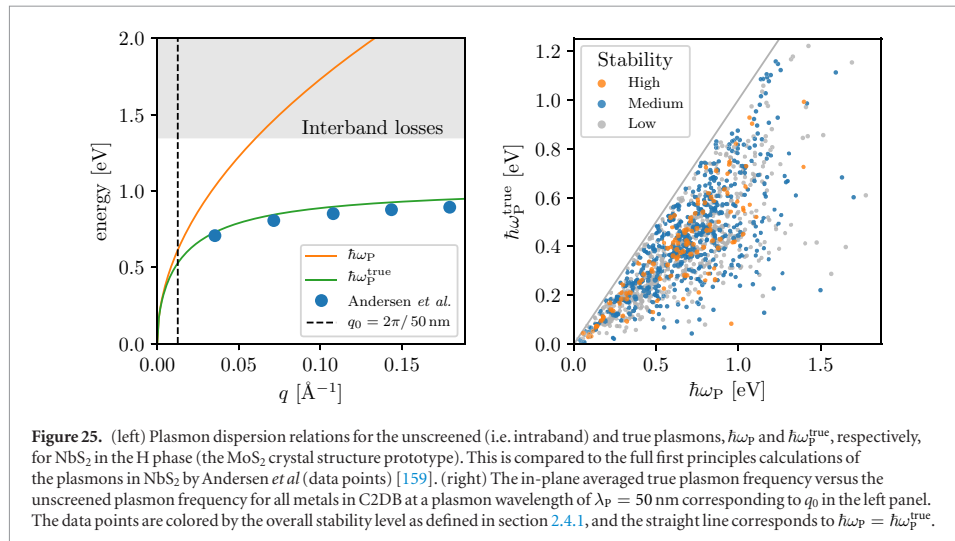
calculations [154]. Although small, the MA is, however, crucial for magnetic order to emerge at finite temperature.

In figure 24 we show the magnitude of the magnetic anisotropy (red triangles) and the magnetic moment per metal atom (blue triangles) averaged over all materials with a given chemical composition. The plot is based on data for around 1200 materials in the medium to high stability categories (see table 2) out of which around 350 are magnetic. It is interesting to note that while the magnetic moment is mainly determined by the metal atom, the MA depends strongly on the non-metal atom. For example, the halides (Cl, Br, I) generally exhibit much larger MAs than the chalcogenides (S, Se, Te). Overall, iodine (I) stands out as the most significant element for a large MA while the 3d metals Cr, Mn, Fe, Co are the most important elements for a large magnetic moment. Since the MA is driven by spin–orbit coupling (SOC) and the spin is mainly located on the metal atom, one would expect a large MA to correlate with a heavy metal atom. However, it is clear from the figure that it is not essential that the spin-carrying metal atom should also host the large SOC. For example, we find large MA for several 3d metal-iodides despite of the relatively weak SOC on the 3d metals. This shows that the MA is governed by a rather complex interplay between the spins, orbital hybridisation and crystal field.

A selection of materials predicted to have high overall stability (see section 2.4.1) and high out-of-plane magnetic anisotropy ($\text{MA} < -0.3$ meV/

Table 12. Selection of magnetic materials with a negative MA per magnetic atom. The prototype, the magnetic moment of the magnetic atom, the energy gap calculated with PBE xc-functional and the magnetic state are also shown. The experimentally synthesised ferromagnetic monolayer CrI₃ is highlighted.

Formula	Prototype	Magnetic moment (μ_B)	PBE gap (eV)	MA (meV/atom)	Magnetic state	ΔH_{hull} (eV/atom)
OsI ₃	BiI ₃	0.9	0.0	-3.17	FM	0.18
CrTe	FeSe	2.6	0.0	-1.85	AFM	0.15
FeCl ₃	BiI ₃	1.0	0.01	-1.84	FM	-0.08
FeTe	FeSe	1.9	0.0	-1.06	FM	0.08
MnTe ₂	CdI ₂	2.7	0.0	-0.94	FM	-0.10
FeBr ₃	BiI ₃	1.0	0.04	-0.88	FM	-0.04
CrI₃	BiI₃	3.0	0.90	-0.85	FM	-0.21
MnTe	FeSe	3.8	0.69	-0.75	AFM	-0.15
NiO	PbSe	1.1	0.0	-0.53	FM	0.05
FeBrO	FeOCl	1.1	0.0	-0.47	FM	-0.05
CrISe	FeOCl	3.0	0.0	-0.45	FM	-0.10
MnSe ₂	CdI ₂	2.8	0.0	-0.40	FM	-0.18
CrIS	FeOCl	3.0	0.35	-0.36	FM	-0.10
MnO ₂	CdI ₂	3.0	1.13	-0.36	FM	0.02
VCl ₃	BiI ₃	2.0	0.0	-0.35	FM	-0.01
MnSe	FeSe	3.7	0.90	-0.31	AFM	-0.20
CrSe	FeSe	2.0	0.0	-0.31	AFM	0.12



magnetic atom) is listed in table 12. We find several semiconductors with anisotropies comparable to CrI₃ and some metals with higher values. If we also look at materials with medium overall stability, we find semiconductors with anisotropies up to 2 meV/atom. It is likely that some of these materials will have Curie temperatures similar to, or even higher than, CrI₃.

In addition to the MA, the critical temperature depends sensitively on the magnetic exchange couplings. We are presently developing a workflow for systematic calculation of exchange coupling constants, which will allow us to estimate the Curie temperature of all the magnetically ordered 2D materials. The database contains several 2D materials with antiferromagnetic order. As a note of caution, we mention

that the magnetic interactions in AFM materials typically arise from the super-exchange mechanism, which is poorly described by PBE and requires a careful verification using a PBE + U scheme [155].

3.2.4. Plasmons

The unique optical properties of 2D materials make them highly interesting as building blocks for nanophotonic applications [156, 157]. Many of these applications involve electron rich components which can capture, focus, and manipulate light via plasmons or plasmon-polaritons. Graphene sheets can host plasmons that are long lived, can be easily tuned via electrostatic or chemical doping, and can be used to confine light to extremely small volumes [158].

Table 13. Selection of 2D metals with high plasmon energies ω_p^{true} for a plasmon wavelength of $\lambda_p = 50$ nm. The interband screening $\alpha^{2\text{D,inter}}$ at $\omega = 0$ and the in-plane averaged 2D plasma frequency $\omega_{p,2\text{D}}$, which are required to reproduce ω_p^{true} , are also reported.

Prototype	Formula	Magnetic state	ω_p^{true} (eV)	$\alpha^{2\text{D,inter}}$ (Å)	$\omega_{p,2\text{D}}$ (eV Å ^{0.5})
TiS ₃	TaSe ₃	NM	0.99	12.54	12.48
FeOCl	PdClS	NM	0.93	4.13	9.52
FeOCl	NiClS	NM	0.90	5.60	9.66
CdI ₂	TaS ₂	NM	0.82	5.59	8.79
FeOCl	ZrIS	NM	0.75	7.68	8.43
CdI ₂	NbS ₂	NM	0.73	8.2	8.42
FeOCl	ZrClS	NM	0.73	13.6	9.35
TiS ₃	TaS ₃	NM	0.73	34.22	12.44
PbSe	NiO	FM	0.72	2.9	7.16

However, due to the limited charge carrier density achievable in graphene, its plasmons are limited to the mid-infrared regime. Here we show that some metallic monolayers support plasmons with significantly higher energies than graphene and could potentially push 2D plasmonics into the optical regime.

Figure 25 (left) shows the plasmon dispersion for monolayer NbS₂ in the MoS₂ crystal structure. The effect of interband transitions on the plasmon is significant as can be seen by comparison to the pure intraband plasmon ($\hbar\omega_p$). The true plasmon energies are obtained from the poles of the (long wave length limit) dielectric function including the interband transitions, $\epsilon = 1 + 2\pi q(\alpha^{2\text{D,intra}} + \alpha^{2\text{D,inter}})$, yielding $\omega_p^{\text{true}} = \omega_{p,2\text{D}} q^{1/2} [1 + 2\pi q \alpha^{2\text{D,inter}}(\omega_p^{\text{true}})]^{-1/2}$. For simplicity we ignore the frequency dependence of the interband polarisability, i.e. we set $\alpha^{2\text{D,inter}}(\omega_p^{\text{true}}) \approx \alpha^{2\text{D,inter}}(\omega = 0)$, which should be valid for small plasmon energies (far from the onset of interband transitions). The validity of this approximation is confirmed by comparing to the full *ab initio* calculations of Andersen *et al* (blue dots) which include the full q - and ω -dependence [159]. The figure shows that interband screening generally reduces the plasmon energy and becomes increasingly important for larger q .

Figure 25 (right) shows the in-plane averaged true plasmon energy of all metals in the C2DB plotted against the intraband plasmon energy at a fixed plasmon wavelength of $\lambda_p = 50$ nm (corresponding to q_0 at the dashed vertical line in the left panel). For comparison, the plasmon energy of freestanding graphene at this wavelength and for the highest achievable doping level ($E_F = \pm 0.5$ eV relative to the Dirac point) is around 0.4 eV. The data points are colored according to the overall stability level as defined in section 2.4.1. Table 13 shows a selection of the 2D metals with ‘high’ overall stability (see section 2.4.1) and large plasmon frequencies. We briefly note the interesting band structures of the metals in the FeOCl prototype (not shown) which exhibits band gaps above or below the partially occupied metallic band(s), which is likely to lead to reduced losses in plasmonic applications [160].

A detailed study of the plasmonic properties of the lead candidate materials will be published elsewhere. However, from figure 25 (right) it is already clear that several of the 2D metals have plasmon energies around 1 eV at $\lambda_p = 50$ nm, which significantly exceeds the plasmon energies in highly doped graphene.

3.2.5. Excitons

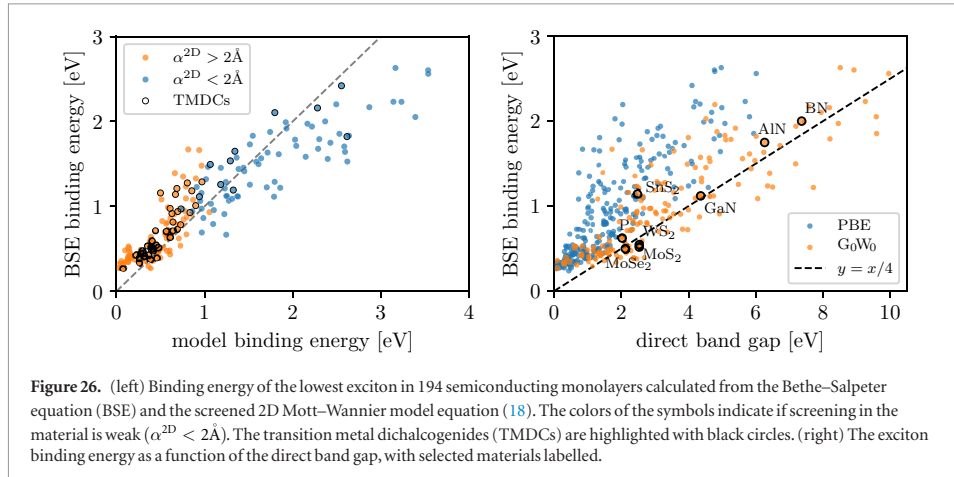
Two-dimensional materials generally exhibit pronounced many-body effects due to weak screening and strong quantum confinement. In particular, exciton binding energies in monolayers are typically an order of magnitude larger than in the corresponding layered bulk phase and it is absolutely crucial to include excitonic effects in order to reproduce experimental absorption spectra.

The electronic screening is characterised by the in-plane 2D polarisability, see equation (12). For a strictly 2D insulator, the screened Coulomb potential can be written as $W^{2\text{D}}(q) = v_c^{2\text{D}}(q)/\epsilon^{2\text{D}}(q)$ with $\epsilon^{2\text{D}}(q) = 1 + 2\pi\alpha^{2\text{D}}q$ and $v_c^{2\text{D}}(q) = 2\pi/q$ is the 2D Fourier transform of the Coulomb interaction. The q -dependence of $\epsilon^{2\text{D}}$ indicates that the screening is non-local, i.e. it cannot be represented by a q -independent dielectric constant, and that Coulomb interactions tend to be weakly screened at large distances (small q vectors) [119, 161, 162]. This is in sharp contrast to the case of 3D semiconductors/insulators where screening is most effective at large distances where its effect can be accounted for by a q -independent dielectric constant. For a two-band model with isotropic parabolic bands, the excitons can be modeled by a 2D Hydrogen-like (Mott–Wannier) Hamiltonian where the Coulomb interaction is replaced by $W = 1/\epsilon r$ and the electron mass is replaced by a reduced excitonic mass μ_{ex} derived from the curvature of conduction and valence bands. It has previously been shown that the excitonic Rydberg series of a 2D semiconductor can be accurately reproduced by this model if the dielectric constant, ϵ , is obtained by averaging $\epsilon^{2\text{D}}(q)$ over the extent of the exciton in reciprocal space [163]. For the lowest exciton ($n = 1$), the binding energy can then be expressed as

$$E_B = \frac{8\mu_{\text{ex}}}{(1 + \sqrt{1 + 32\pi\alpha^{2\text{D}}\mu_{\text{ex}}/3})^2}. \quad (18)$$

It has furthermore been demonstrated that this expression gives excellent agreement with a numerical solution of the Mott–Wannier model employing the full q -dependent dielectric function, $\epsilon^{2\text{D}}(q) = 1 + 2\pi\alpha^{2\text{D}}q$, for 51 transition metal dichalcogenides [163]. We note that the previous calculations were based on LDA and we generally find that the PBE values for $\alpha^{2\text{D}}$ obtained in the present work are 10–20% smaller compared with LDA.

In figure 26, we compare the binding energy of the lowest exciton obtained from BSE-PBE with G_0W_0 scissors operator and the Mott–Wannier model equation (18), respectively. Results are shown for the 194



non-magnetic semiconductors out of the total set of ~ 250 materials for which BSE calculations have been performed. We focus on the optically active zero-momentum excitons and compute the exciton masses by evaluating the curvature of the band energies at the *direct gap*, see section 2.11. For anisotropic materials we average the heavy and light exciton masses as well as the x and y components of the polarisability, α^{2D} , to generate input parameters for the isotropic model equation (18).

Although a clear correlation with the BSE results is observed, it is also evident that the Mott–Wannier model can produce significant errors. The mean absolute deviation between BSE and the model is 0.28 eV for all materials and 0.20 eV for the subset of transition metal dichalcogenides (TMDCs). Furthermore, the Mott–Wannier model seems to overestimate E_B for more strongly bound excitons while the opposite trend is seen for weakly bound excitons. As explained below these trends are a consequence of systematic errors in the Mott–Wannier model which can be traced to two distinct sources.

(i) *Weak screening:* If α^{2D} is small (on the order of 1 \AA), the exciton becomes strongly localised and the orbital character of the states comprising the exciton plays a significant role. In general, the Mott–Wannier model tends to overestimate the exciton binding energy in this case as can be seen from the relatively large deviation of points with model binding energies > 2.0 eV in figure 26. The overestimated binding energy results from the homogeneous electron and hole distributions implicitly assumed in the Mott–Wannier model. In reality, the short range variation of the electron and hole distributions is determined by the shape of the conduction and valence band states. In general these will differ leading to a reduced spatial overlap of the electron and hole and thus a lower Coulomb interaction. For example, SrCl_2 in the CdI_2 prototype ($\alpha^{2D} = 0.68 \text{\AA}$) has a BSE binding

energy of 2.1 eV and a model binding energy of 3.4 eV. From the PDOS of this material (see the C2DB webpage) it is evident that the electron and hole are mainly residing on the Sr and Cl atoms, respectively.

(ii) *Breakdown of the parabolic band approximation:* Materials with small band gaps often exhibit hyperbolic rather than parabolic band structures in the vicinity of the band gap. This typically happens in materials with small band gaps such as BSb in the BN prototype. In figure 26 these materials can be identified as the cluster of points with model binding energies < 0.25 eV and BSE binding energies > 0.25 eV. A similar situation occurs if the conduction and valence bands flatten out away from the band gap region. In both of these cases, the excitons tend to be delocalised over a larger area in the Brillouin zone than predicted by the parabolic band approximation of the Mott–Wannier model. Typically, such delocalisation will result in larger binding energies than predicted by the model. For example, FeI_2 in the CdI_2 prototype exhibits shallow band minima in a ring around the Γ -point and has a BSE binding energy of 1.1 eV and a model binding energy of 0.5 eV because the model assumes that the exciton will be located in the vicinity of the shallow minimum (and thus more delocalised in real space). A detailed inspection reveals that such break down of the parabolic band approximation is responsible for most of the cases where the model underestimates the binding energy.

Other sources of errors come from contributions to the exciton from higher/lower lying bands, i.e. break down of the two-band approximation, and anisotropic exciton masses not explicitly accounted for by equation (18).

Based on this comprehensive and unbiased assessment of the Mott–Wannier model, we conclude that while the model can be useful for understand-

ing trends and qualitative properties of excitons, its quantitative accuracy is rather limited when applied to a broad set of materials without any parameter tuning. For quantitative estimates α^{2D} should not be too small (certainly not less than 2 Å) and the validity of the effective mass approximation should be carefully checked by inspection of the band structure.

It has been argued that there should exist a robust and universal scaling between the exciton binding energy and the quasiparticle band gap of 2D semiconductors, namely $E_B \approx E_{\text{gap}}/4$ [164]. This scaling relation was deduced empirically based on BSE-GW calculations for around 20 monolayers and explained from equation (18) and the relation $\alpha^{2D} \propto 1/E_{\text{gap}}$ from $\mathbf{k} \cdot \mathbf{p}$ perturbation theory. Another work observed a similar trend [165] but explained it from the $1/E_{\text{gap}}$ dependence of the exciton effective mass expected from $\mathbf{k} \cdot \mathbf{p}$ perturbation theory. Based on our results we can completely refute the latter explanation (see figure 22 (right)). In figure 26 (right) we show the exciton binding energy plotted versus the direct PBE and G_0W_0 band gaps, respectively. While there is a correlation, it is by no means as clear as found in [164].

4. Conclusions and outlook

The C2DB is an open database with calculated properties of two-dimensional materials. It currently contains more than 1500 materials distributed over 32 different crystal structures. A variety of structural, elastic, thermodynamic, electronic, magnetic and optical properties are computed following a high-throughput, semi-automated workflow employing state of the art DFT and many-body methods. The C2DB is growing continuously as new structures and properties are being added; thus the present paper provides a snapshot of the present state of the database. The C2DB can be browsed online using simple and advanced queries, and it can be downloaded freely at <https://c2db.fysik.dtu.dk/> under a Creative Commons license.

The materials in the C2DB comprise both experimentally known and not previously synthesised structures. They have been generated in a systematic fashion by combinatorial decoration of different 2D crystal lattices. The full property workflow is performed only for structures that are found to be dynamically stable and have a negative heat of formation. We employ a liberal stability criterion in order not to exclude potentially interesting materials that could be stabilised by external means like substrate interactions or doping even if they are unstable in freestanding form. As an important and rather unique feature, the C2DB employs beyond-DFT methods, such as the many-body GW approximation, the random phase approximation (RPA) and the Bethe–Salpeter equation (BSE). Such methods are essential for obtaining quantitatively accurate descriptions of key properties like band gaps and optical spectra. This is particularly important for 2D materials due to the weak dielectric

screening in reduced dimensions, which tends to enhance many-body effects. For maximal transparency and reproducibility of the data in the C2DB, all relevant parameters have been provided in this paper. Additionally, all scripts used to generate the data are freely available for download under a GPL license.

Beyond its obvious use as a look-up table, the C2DB offers access to numerous well documented, high-quality calculations, making it ideally suited for benchmarking and comparison of different codes and methodologies. The large set of different available properties makes the C2DB interesting as a playground for exploring structure-property relations and for applying and advancing machine learning approaches in materials science. Moreover, the C2DB should be useful as a stepping stone towards the development of theoretical models for more complex 2D structures such as van der Waals heterostructures (see below).

As reported in this work, based on the combinatorial screening approach, we have identified a number of new, potentially synthesisable 2D materials with interesting properties including ferromagnets with large magnetic anisotropy, semiconductors with high intrinsic carrier mobility, and metals with plasmons in the visible frequency range. These predictions are all based on the computed properties of the perfect crystalline materials. While the pristine crystal constitutes an important baseline reference it remains an idealised model of any real material. In the future, it would be interesting to extend the database to monolayers with adsorbed species and/or point defects. Not only would this allow for a more realistic assessment of the magnetic and (opto)electronic properties, it would also facilitate the design and discovery of 2D materials for e.g. battery electrodes and (electro)catalysis [166, 167].

The C2DB should also be useful as a platform for establishing parametrisations of computationally less expensive methods such as tight-binding models [168] and $\mathbf{k} \cdot \mathbf{p}$ perturbation theory [128]. Such methods are required e.g. for device modeling, description of magnetic field effects, and van der Waals heterostructures. The database already provides band structures, spin orbit-induced band splittings, and effective masses, which can be directly used to determine model parameters. It would be straightforward to complement these with momentum matrix elements at band extrema for modeling of optical properties and construction of full $\mathbf{k} \cdot \mathbf{p}$ Hamiltonians. Similarly, the spread functional required as input for the construction of Wannier functions e.g. by the ASE [38] or the Wannier90 [169] packages, could be easily and systematically produced. This would enable direct construction of minimal basis set Hamiltonians and would allow for the calculation of Born charges and piezoelectric coefficients as well as certain topological invariants [170]. A workflow to calculate exchange couplings of magnetic 2D materials is currently being developed with the aim of predicting magnetic phase transitions and critical temperatures.

Of specific interest is the modeling of the electronic and optical properties of vdW heterostructures. Due to lattice mismatch or rotational misalignment between stacked 2D layers, such structures are difficult or even impossible to treat by conventional *ab initio* techniques. Different simplified models have been proposed to describe the electronic bands, including tight-binding Hamiltonians derived from strained lattice configurations [171] and perturbative treatments of the interlayer coupling [172]. In both cases, the data in the C2DB represents a good starting point for constructing such models. The effect of dielectric screening in vdW heterostructures can be incorporated e.g. by the quantum electrostatic heterostructure (QEH) model [173] which computes the dielectric function of the vdW heterostructure from the polarisabilities of the isolated monolayers. The latter are directly available in the C2DB, at least in the long wavelength limit.

Finally, it would be relevant to supplement the current optical absorbance spectra by other types of spectra, such as Raman spectra, infrared absorption or XPS, in order to assist experimentalists in characterising their synthesised samples. The automatic first-principles calculation of such spectra is, however, not straightforward and will require significant computational investments.

Acknowledgments

The Center for Nanostructured Graphene is sponsored by the Danish National Research Foundation, Project DNRFF103. The project also received funding from the European Unions Horizon 2020 research and innovation programme under Grant Agreement No. 676580 with The Novel Materials Discovery (NOMAD) Laboratory, a European Center of Excellence. This work was also supported by a research grant (9455) from VILLUM FONDEN. This project has received funding from the European Research Council (ERC) under the European Union's Horizon 2020 research and innovation programme (grant agreement No 773122, LIMA).

ORCID iDs

Sten Hastrup  <https://orcid.org/0000-0003-3696-0356>

Mohnish Pandey  <https://orcid.org/0000-0002-1715-0617>

Thorsten Deilmann  <https://orcid.org/0000-0003-4165-2446>

Nicki F Hinsche  <https://orcid.org/0000-0002-0176-6038>

Morten N Gjerding  <https://orcid.org/0000-0002-5256-660X>

Kristian S Thygesen  <https://orcid.org/0000-0001-5197-214X>

References

- [1] Ferrari A C *et al* 2015 Science and technology roadmap for graphene, related two-dimensional crystals and hybrid systems *Nanoscale* **7** 4598–810
- [2] Bhimanapati G R *et al* 2015 Recent advances in two-dimensional materials beyond graphene *ACS Nano* **9** 11509–39
- [3] Huang C, Wu S, Sanchez A M, Peters J J, Beanland R, Ross J S, Rivera P, Yao W, Cobden D H and Xu X 2014 Lateral heterojunctions within monolayer mose2–wse2 semiconductors *Nat. Mater.* **13** 1096–101
- [4] Geim A K and Grigorieva I V 2013 Van der waals heterostructures *Nature* **499** 419–25
- [5] Molle A, Goldberger J, Houssa M, Xu Y, Zhang S-C and Akinwande D 2017 Buckled two-dimensional xene sheets *Nat. Mater.* **16** 163–9
- [6] Bianco E, Butler S, Jiang S, Restrepo O D, Windl W and Goldberger J E 2013 Stability and exfoliation of germanane: a germanium graphane analogue *ACS Nano* **7** 4414–21
- [7] Wang Q H, Kalantar-Zadeh K, Kis A, Coleman J N and Strano M S 2012 Electronics and optoelectronics of two-dimensional transition metal dichalcogenides *Nat. Nanotechnol.* **7** 699–712
- [8] Naguib M, Mashtalir O, Carle J, Presser V, Lu J, Hultman L, Gogotsi Y and Barsoum M W 2012 Two-dimensional transition metal carbides *ACS Nano* **6** 1322–31
- [9] Ci L *et al* 2010 Atomic layers of hybridized boron nitride and graphene domains *Nat. Mater.* **9** 430–5
- [10] Al Balushi Z Y *et al* 2016 Two-dimensional gallium nitride realized via graphene encapsulation *Nat. Mater.* **15** 1166
- [11] Lin S-H and Kuo J-L 2014 Towards the ionic limit of two-dimensional materials: monolayer alkaline earth and transition metal halides *Phys. Chem. Chem. Phys.* **16** 20763–71
- [12] Huang B *et al* 2017 Layer-dependent ferromagnetism in a van der Waals crystal down to the monolayer limit *Nature* **546** 270
- [13] Dattatray J *et al* 2012 Gas and gase ultrathin layer transistors *Adv. Mater.* **24** 3549–54
- [14] Hu P, Wen Z, Wang L, Tan P and Xiao K 2012 Synthesis of few-layer gase nanosheets for high performance photodetectors *ACS Nano* **6** 5988–94
- [15] Dou L *et al* 2015 Atomically thin two-dimensional organic-inorganic hybrid perovskites *Science* **349** 1518–21
- [16] Ashton M, Paul J, Sinnott S B and Hennig R G 2017 Topology-scaling identification of layered solids and stable exfoliated 2d materials *Phys. Rev. Lett.* **118** 106101
- [17] Cheon G, Duerloo K-A-N, Sendek A D, Porter C, Chen Y and Reed E J 2017 Data mining for new two- and one-dimensional weakly bonded solids and lattice-commensurate heterostructures *Nano Lett.* **17** 1915–23
- [18] Mounet N, Gibertini M, Schwaller P, Merkys A, Castelli I E, Cepellotti A, Pizzi G and Marzari N 2018 Novel two-dimensional materials from high-throughput computational exfoliation of experimentally known compounds *Nat. Nanotechnol.* **13** 246–52
- [19] Choudhary K, Kalish I, Beams R and Tavazza F 2017 High-throughput identification and characterization of two-dimensional materials using density functional theory *Sci. Rep.* **7** 5179
- [20] Jain A, Persson K A and Ceder G 2016 Research update: the materials genome initiative: data sharing and the impact of collaborative *ab initio* databases *APL Mater.* **4** 053102
- [21] Thygesen K S and Jacobsen K W 2016 Making the most of materials computations *Science* **354** 180–1
- [22] Jain A, Ong S P, Hautier G, Chen W, Richards W D, Dacek S, Cholia S, Gunter D, Skinner D, Ceder G and Persson K A 2013 The materials project: a materials genome approach to accelerating materials innovation *APL Mater.* **1** 011002
- [23] Curtarolo S *et al* 2012 Aflow: an automatic framework for high-throughput materials discovery *Comput. Mater. Sci.* **58** 218–26
- [24] Saal J E, Kirklín S, Aykol M, Meredig B and Wolverton C 2013 Materials design and discovery with high-throughput density

- functional theory: the open quantum materials database (oqmd) *JOM* **65** 1501–9
- [25] Kirklın S, Saal J E, Meredig B, Thompson A, Doak J W, Aykol M, Ruehl S and Wolverton C 2015 The open quantum materials database (oqmd): assessing the accuracy of dft formation energies *NPJ Comput. Mater.* **1** 15010
- [26] <http://nomad-repository.eu>; <https://nomad-coe.eu>
- [27] Lejaeghere K et al 2016 Reproducibility in density functional theory calculations of solids *Science* **351** aad3000
- [28] Hautier G, Fischer C C, Jain A, Mueller T and Ceder G 2010 Finding nature's missing ternary oxide compounds using machine learning and density functional theory *Chem. Mater.* **22** 3762–7
- [29] Ghiringhelli L M, Vybiral J, Levchenko S V, Draxl C and Scheffler M 2015 Big data of materials science: critical role of the descriptor *Phys. Rev. Lett.* **114** 105503
- [30] Ward L and Wolverton C 2017 Atomistic calculations and materials informatics: a review *Curr. Opin. Solid State Mater. Sci.* **21** 167–76
- [31] Şahin H, Cahangirov S, Topsakal M, Bekaroglu E, Akturk E, Senger R T and Ciraci S 2009 Monolayer honeycomb structures of group-IV elements and III–V binary compounds: first-principles calculations *Phys. Rev. B* **80** 155453
- [32] Ciraci S and Cahangirov S 2017 *2D Materials: Properties and Devices* ed P Avouris et al (Cambridge: Cambridge University Press) pp 472–84
- [33] Ataca C, Sahin H and Ciraci S 2012 Stable, single-layer mx₂ transition-metal oxides and dichalcogenides in a honeycomb-like structure *J. Phys. Chem. C* **116** 8983–99
- [34] Lebegue S, Björkman T, Klintonberg M, Nieminen R M and Eriksson O 2013 Two-dimensional materials from data filtering and *ab initio* calculations *Phys. Rev. X* **3** 031002
- [35] Miro P, Audiffred M and Heine T 2014 An atlas of two-dimensional materials *Chem. Soc. Rev.* **43** 6537–54
- [36] Rasmussen F A and Thygesen K S 2015 Computational 2d materials database: electronic structure of transition-metal dichalcogenides and oxides *J. Phys. Chem. C* **119** 13169–83
- [37] Enkovaara J E et al 2010 Electronic structure calculations with gpaw: a real-space implementation of the projector-augmented-wave method *J. Phys.: Condens. Matter* **22** 253202
- [38] Larsen A et al 2017 The atomic simulation environment—a python library for working with atoms *J. Phys.: Condens. Matter* **29** 273002
- [39] Cordero B, Gomez V, Platero-Prats A E, Reves M, Echeverria J, Cremades E, Barragan F and Alvarez S 2008 Covalent radii revisited *Dalton Trans.* **37** 2832–8
- [40] Larsen P M 2017 Structural analysis algorithms for nanomaterials *PhD Thesis* Department of Physics, DTU
- [41] Özcelik V O, Azadani J G, Yang C, Koester S J and Low T 2016 Band alignment of two-dimensional semiconductors for designing heterostructures with momentum space matching *Phys. Rev. B* **94** 035125
- [42] Togo A 2009 Spglib <https://atztogo.github.io/spglib/>
- [43] Pandey M and Jacobsen K W 2015 Heats of formation of solids with error estimation: the mbeef functional with and without fitted reference energies *Phys. Rev. B* **91** 235201
- [44] Stevanović V, Lany S, Zhang X and Zunger A 2012 Correcting density functional theory for accurate predictions of compound enthalpies of formation: fitted elemental-phase reference energies *Phys. Rev. B* **85** 115104
- [45] Anisimov V and Gunnarsson O 1991 Density-functional calculation of effective coulomb interactions in metals *Phys. Rev. B* **43** 7570
- [46] Kuhar K, Crovetto A, Pandey M, Thygesen K S, Seger B, Vesborg P C K, Hansen O, Chorkendorff I and Jacobsen K W 2017 Sulfide perovskites for solar energy conversion applications: computational screening and synthesis of the selected compound layers *Energy Environ. Sci.* **10** 2579–93
- [47] Zhou Y et al 2018 Antiferromagnetic order in epitaxial fese films on srtio 3 *Phys. Rev. Lett.* **120** 097001
- [48] Alfe D 2009 Phon: a program to calculate phonons using the small displacement method *Comput. Phys. Commun.* **180** 2622–33
- [49] Novoselov K S, Geim A K, Morozov S V, Jiang D, Zhang Y, Dubonos S V, Grigorieva I V and Firsov A A 2004 Electric field effect in atomically thin carbon films *Science* **306** 666–9
- [50] Sone J, Yamagami T, Aoki Y, Nakatsuji K and Hirayama H 2014 Epitaxial growth of silicene on ultra-thin ag (111) films *New J. Phys.* **16** 095004
- [51] Dávila M, Xian L, Cahangirov S, Rubio A and Le Lay G 2014 Germanene: a novel two-dimensional germanium allotrope akin to graphene and silicene *New J. Phys.* **16** 095002
- [52] Li L, Yu Y, Ye G J, Ge Q, Ou X, Wu H, Feng D, Chen X H and Zhang Y 2014 Black phosphorus field-effect transistors *Nat. Nanotechnol.* **9** 372
- [53] Yang S et al 2017 C_{3n}—a 2d crystalline, hole-free, tunable-narrow-bandgap semiconductor with ferromagnetic properties *Adv. Mater.* **29** 1605625
- [54] Kappera R, Voiry D, Yalcin S E, Branch B, Gupta G, Mohite A D and Chhowalla M 2014 Phase-engineered low-resistance contacts for ultrathin MoS₂ transistors *Nat. Mater.* **13** 1128
- [55] Mak K F, Lee C, Hone J, Shan J and Heinz T F 2010 Atomically thin MoS₂: a new direct-gap semiconductor *Phys. Rev. Lett.* **105** 136805
- [56] Tonndorf P et al 2013 Photoluminescence emission and raman response of monolayer MoS₂, mose 2 and wse 2 *Opt. Express* **21** 4908–16
- [57] Lu A-Y et al 2017 Janus monolayers of transition metal dichalcogenides *Nat. Nanotechnol.* **12** 744
- [58] Naylor C H et al 2016 Monolayer single-crystal 1T-mote2 grown by chemical vapor deposition exhibits weak antilocalization effect *Nano Lett.* **16** 4297–304
- [59] Wang Y et al 2017 Structural phase transition in monolayer mote 2 driven by electrostatic doping *Nature* **550** 487
- [60] Okada M, Sawazaki T, Watanabe K, Taniguchi T, Hibino H, Shinohara H and Kitaura R 2014 Direct chemical vapor deposition growth of WS₂ atomic layers on hexagonal boron nitride *ACS Nano* **8** 8273–7
- [61] Fei Z, Palomaki T, Wu S, Zhao W, Cai X, Sun B, Nguyen P, Finney J, Xu X and Cobden D H 2017 Edge conduction in monolayer wte 2 *Nat. Phys.* **13** 677
- [62] Xi X, Zhao L, Wang Z, Berger H, Forró L, Shan J and Mak K F 2015 Strongly enhanced charge-density-wave order in monolayer nbse 2 *Nat. Nanotechnol.* **10** 765
- [63] Wang X, Lin J, Zhu Y, Luo C, Suenaga K, Cai C and Xie L 2017 Chemical vapor deposition of trigonal prismatic nbs 2 monolayers and 3r-polytype few-layers *Nanoscale* **9** 16607–11
- [64] Zhang M et al 2015 Controlled synthesis of zrs2 monolayer and few layers on hexagonal boron nitride *J. Am. Chem. Soc.* **137** 7051–4
- [65] Mañas-Valero S, García-López V, Cantarero A and Galbiati M 2016 Raman spectra of zrs2 and zrse2 from bulk to atomically thin layers *Appl. Sci.* **6** 264
- [66] Xu K, Wang Z, Wang F, Huang Y, Wang F, Yin L, Jiang C and He J 2015 Ultrasensitive phototransistors based on few-layered hfs2 *Adv. Mater.* **27** 7881–7
- [67] Fu W et al 2016 Controlled synthesis of atomically thin 1t-tas2 for tunable charge density wave phase transitions *Chem. Mater.* **28** 7613–8
- [68] Ryu H et al 2018 Persistent charge-density-wave order in single-layer tase2 *Nano Lett.* **8** 689–94
- [69] Zhao W, Dong B, Guo Z, Su G, Gao R, Wang W and Cao L 2016 Colloidal synthesis of VSe 2 single-layer nanosheets as novel electrocatalysts for the hydrogen evolution reaction *Chem. Commun.* **52** 9228–31
- [70] Feng J, Sun X, Wu C, Peng L, Lin C, Hu S, Yang J and Xie Y 2011 Metallic few-layered VS₂ ultrathin nanosheets: high two-dimensional conductivity for in-plane supercapacitors *J. Am. Chem. Soc.* **133** 17832–8
- [71] Wang Y et al 2015 Monolayer ptse2, a new semiconducting transition-metal-dichalcogenide, epitaxially grown by direct selenization of pt *Nano Lett.* **15** 4013–8
- [72] Zhao Y, Qiao J, Yu P, Hu Z, Lin Z, Lau S P, Liu Z, Ji W and Chai Y 2016 Extraordinarily strong interlayer interaction in 2d layered pts2 *Adv. Mater.* **28** 2399–407

- [73] Wan C *et al* 2015 Flexible n-type thermoelectric materials by organic intercalation of layered transition metal dichalcogenide *Nat. Mater.* **14** 622
- [74] Shao Y *et al* 2017 Epitaxial fabrication of two-dimensional n₂ on ni (1 1 1) substrate *Appl. Phys. Lett.* **111** 113107
- [75] Tongay S *et al* 2014 Monolayer behaviour in bulk res 2 due to electronic and vibrational decoupling *Nat. Commun.* **5** 3252
- [76] Oyedele A D *et al* 2017 Pdse₂: pentagonal two-dimensional layers with high air stability for electronics *J. Am. Chem. Soc.* **139** 14090–7
- [77] Zhou L *et al* 2018 InSe monolayer: synthesis, structure and ultra-high second-harmonic generation *2D Mater.* **5** 025019
- [78] Del Pozo-Zamudio O *et al* 2015 Photoluminescence of two-dimensional gate and gas films *2D Mater.* **2** 035010
- [79] Zhou Y, Nie Y, Liu Y, Yan K, Hong J, Jin C, Zhou Y, Yin J, Liu Z and Peng H 2014 Epitaxy and photoresponse of two-dimensional gas crystals on flexible transparent mica sheets *ACS Nano* **8** 1485–90
- [80] Island J O, Buscema M, Barawi M, Clamagirand J M, Ares J R, Sánchez C, Ferrer I J, Steele G A, van der Zant H S and Castellanos-Gomez A 2014 Ultrahigh photoresponse of few-layer t_is₃ nanoribbon transistors *Adv. Opt. Mater.* **2** 641–5
- [81] Wang Y-Q *et al* 2016 Tunable electronic structures in wrinkled 2d transition-metal-trichalcogenide (tmt) hft_e3 films *Adv. Electron. Mater.* **2** 1600324
- [82] Song C-L, Wang Y-L, Jiang Y-P, Li Z, Wang L, He K, Chen X, Ma X-C and Xue Q-K 2011 Molecular-beam epitaxy and robust superconductivity of stoichiometric fese crystalline films on bilayer graphene *Phys. Rev. B* **84** 020503
- [83] Liu H-J *et al* 2016 A metal-insulator transition of the buried mno₂ monolayer in complex oxide heterostructure *Adv. Mater.* **28** 9142–51
- [84] Cai L, McClellan C J, Koh A L, Li H, Yalon E, Pop E and Zheng X 2017 Rapid flame synthesis of atomically thin moo₃ down to monolayer thickness for effective hole doping of wse₂ *Nano Lett.* **17** 3854–61
- [85] Xu S *et al* 2015 van der Waals epitaxial growth of atomically thin Bi₂Se₃ and thickness-dependent topological phase transition *Nano Lett.* **15** 2645–51
- [86] Kong D, Dang W, Cha J J, Li H, Meister S, Peng H, Liu Z and Cui Y 2010 Few-layer nanoplates of Bi₂Se₃ and Bi₂Te₃ with highly tunable chemical potential *Nano Lett.* **10** 2245–50
- [87] Mashtalir O, Lukatskaya M R, Zhao M-Q, Barsoum M W and Gogotsi Y 2015 Amine-assisted delamination of Nb₂C mxene for Li-ion energy storage devices *Adv. Mater.* **27** 3501–6
- [88] Liu F, Zhou J, Wang S, Wang B, Shen C, Wang L, Hu Q, Huang Q and Zhou A 2017 Preparation of high-purity V₂C mxene and electrochemical properties as Li-ion batteries *J. Electrochem. Soc.* **164** A709–13
- [89] Lukatskaya M R, Mashtalir O, Ren C E, Dall' Agnese Y, Rozier P, Taberna P L, Naguib M, Simon P, Barsoum M W and Gogotsi Y 2013 Cation intercalation and high volumetric capacitance of two-dimensional titanium carbide *Science* **341** 1502–5
- [90] Melchior S A, Raju K, Ike I S, Erasmus R M, Kabongo G, Sigalas I, Iyuke S E and Ozoemena K I 2018 High-voltage symmetric supercapacitor based on 2d titanium carbide (mxene, ti₂ctx)/carbon nanosphere composites in a neutral aqueous electrolyte *J. Electrochem. Soc.* **165** A501–11
- [91] Liu G, Li Z, Hasan T, Chen X, Zheng W, Feng W, Jia D, Zhou Y and Hu P 2017 Vertically aligned two-dimensional sns₂ nanosheets with a strong photon capturing capability for efficient photoelectrochemical water splitting *J. Mater. Chem. A* **5** 1989–95
- [92] Li J, Guan X, Wang C, Cheng H-C, Ai R, Yao K, Chen P, Zhang Z, Duan X and Duan X 2017 Synthesis of 2d layered bii₃ nanoplates, bii₃/wse₂ van der Waals heterostructures and their electronic, optoelectronic properties *Small* **13** 1701034
- [93] Elias D C *et al* 2009 Control of graphene's properties by reversible hydrogenation: evidence for graphane *Science* **323** 610–3
- [94] Nair R R *et al* 2010 Fluorographene: a two-dimensional counterpart of teflon *Small* **6** 2877–84
- [95] Wang L, Kutana A, Zou X and Yakobson B I 2015 Electro-mechanical anisotropy of phosphorene *Nanoscale* **7** 9746–51
- [96] Wang X, Wang D S, Ruqian W and Freeman A J 1996 Validity of the force theorem for magnetocrystalline anisotropy *J. Magn. Magn. Mater.* **159** 337–41
- [97] Olsen T 2016 Designing in-plane heterostructures of quantum spin hall insulators from first principles: 1T-MoS₂ with adsorbates *Phys. Rev. B* **94** 235106
- [98] MacDonald A H, Vosko S H and Coleridge P T 1979 Extensions of the tetrahedron method for evaluating spectral properties of solids *J. Phys. C: Solid State Phys.* **12** 2991–3002
- [99] Heyd J, Scuseria G E and Ernzerhof M 2003 Hybrid functionals based on a screened coulomb potential *J. Chem. Phys.* **118** 8207–15
- [100] Kośmider K and Fernández-Rossier J 2013 Electronic properties of the MoS₂-WS₂ heterojunction *Phys. Rev. B* **87** 075451
- [101] Kang J, Tongay S, Zhou J, Li J and Wu J 2013 Band offsets and heterostructures of two-dimensional semiconductors *Appl. Phys. Lett.* **102** 012111
- [102] Kuisma M, Ojanen J, Enkovaara J and Rantala T T 2010 Kohn-Sham potential with discontinuity for band gap materials *Phys. Rev. B* **82** 115106
- [103] Castelli I E, Olsen T, Datta S, Landis D D, Dahl S, Thygesen K S and Jacobsen K W 2012 Computational screening of perovskite metal oxides for optimal solar light capture *Energy Environ. Sci.* **5** 5814–9
- [104] Baerends E 2017 From the Kohn-Sham band gap to the fundamental gap in solids, an integer electron approach *Phys. Chem. Chem. Phys.* **19** 15639–56
- [105] Hüser F, Olsen T and Thygesen K S 2013 Quasiparticle GW calculations for solids, molecules and two-dimensional materials *Phys. Rev. B* **87** 235132
- [106] Rasmussen F A, Schmidt P S, Winther K T and Thygesen K S 2016 Efficient many-body calculations for two-dimensional materials using exact limits for the screened potential: band gaps of MoS₂, h-BN, and phosphorene *Phys. Rev. B* **94** 155406
- [107] Tiago M L, Ismail-Beigi S and Louie S G 2004 Effect of semicore orbitals on the electronic band gaps of Si, Ge and GaAs within the GW approximation *Phys. Rev. B* **69** 125212
- [108] Klimeš J, Kaltak M and Kresse G 2014 Predictive GW calculations using plane waves and pseudopotentials *Phys. Rev. B* **90** 075125
- [109] Sundararaman R and Arias T A 2013 Regularization of the coulomb singularity in exact exchange by wigner-seitz truncated interactions: towards chemical accuracy in nontrivial systems *Phys. Rev. B* **87** 165122
- [110] Ismail-Beigi S 2006 Truncation of periodic image interactions for confined systems *Phys. Rev. B* **73** 233103
- [111] Rozzi C A, Varsano D, Marini A, Gross E K U and Rubio A 2006 Exact coulomb cutoff technique for supercell calculations *Phys. Rev. B* **73** 205119
- [112] Lee J, Huang J, Sumpter B G and Yoon M 2017 Strain-engineered optoelectronic properties of 2d transition metal dichalcogenide lateral heterostructures *2D Mater.* **4** 021016
- [113] Ramasubramanian A 2012 Large excitonic effects in monolayers of molybdenum and tungsten dichalcogenides *Phys. Rev. B* **86** 115409
- [114] Cheiwchanhannangij T and Lambrecht W R L 2012 Quasiparticle band structure calculation of monolayer, bilayer and bulk MoS₂ *Phys. Rev. B* **85** 205302
- [115] Komsa H-P and Krashenninnikov A V 2012 Effects of confinement and environment on the electronic structure and exciton binding energy of MoS₂ from first principles *Phys. Rev. B* **86** 241201
- [116] Molina-Sánchez A, Sangalli D, Hummer K, Marini A and Wirtz L 2013 Effect of spin-orbit interaction on the optical spectra of single-layer, double-layer and bulk MoS₂ *Phys. Rev. B* **88** 045412
- [117] Shi H, Pan H, Zhang Y-W and Yakobson B I 2013 Quasiparticle band structures and optical properties of strained monolayer MoS₂ and WS₂ *Phys. Rev. B* **87** 155304
- [118] Conley H J, Wang B, Ziegler J I, Haglund R F, Pantelides S T and Bolotin K I 2013 Bandgap engineering of strained monolayer and bilayer MoS₂ *Nano Lett.* **13** 3626–30

- [119] Hüser F, Olsen T and Thygesen K S 2013 How dielectric screening in two-dimensional crystals affects the convergence of excited-state calculations: monolayer MoS₂ *Phys. Rev. B* **88** 245309
- [120] Qiu D Y, Felipe H and Louie S G 2016 Screening and many-body effects in two-dimensional crystals: monolayer MoS₂ *Phys. Rev. B* **93** 235435
- [121] Shishkin M and Kresse G 2007 Self-consistent GW calculations for semiconductors and insulators *Phys. Rev. B* **75** 235102
- [122] Schmidt P S, Patrick C E and Thygesen K S 2017 Simple vertex correction improves GW band energies of bulk and two-dimensional crystals *Phys. Rev. B* **96** 205206
- [123] Shishkin M, Marsman M and Kresse G 2007 Accurate quasiparticle spectra from self-consistent GW calculations with vertex corrections *Phys. Rev. Lett.* **99** 246403
- [124] Wang X, Jones A M, Seyler K L, Tran V, Jia Y, Zhao H, Wang H, Yang L, Xu X and Xia F 2015 Highly anisotropic and robust excitons in monolayer black phosphorus *Nat. Nanotechnol.* **10** 517
- [125] Klots A et al 2014 Probing excitonic states in suspended two-dimensional semiconductors by photocurrent spectroscopy *Sci. Rep.* **4** 6608
- [126] Ugeda M M et al 2014 Giant bandgap renormalization and excitonic effects in a monolayer transition metal dichalcogenide semiconductor *Nat. Mater.* **13** 1091
- [127] Hill H M, Rigosi A F, Rim K T, Flynn G W and Heinz T F 2016 Band alignment in MoS₂/WS₂ transition metal dichalcogenide heterostructures probed by scanning tunneling microscopy and spectroscopy *Nano Lett.* **16** 4831–7
- [128] Kormanyos A, Burkard G, Gmitra M, Fabian J, Zolyomi V, Drummond N D and Falko V 2015 k.p theory for two-dimensional transition metal dichalcogenide semiconductors *2D Mater.* **2** 022001
- [129] Van De Walle C and Martin R 1989 Absolute deformation potentials—formulation and *ab initio* calculations for semiconductors *Phys. Rev. Lett.* **62** 2028–31
- [130] Resta R, Colombo L and Baroni S 1990 Absolute deformation potentials in semiconductors *Phys. Rev. B* **41** 12358–61
- [131] Wiktor J and Pasquarello A 2016 Absolute deformation potentials of two-dimensional materials *Phys. Rev. B* **94** 245411
- [132] Marques M, Ullrich C, Nogueira F, Rubio A and Gross E 2006 Time-dependent density functional theory (<https://doi.org/10.1007/B11767107>)
- [133] Hybertsen M S and Louie S G 1987 *Ab initio* static dielectric matrices from the density-functional approach. I. Formulation and application to semiconductors and insulators *Phys. Rev. B* **35** 5585–601
- [134] Yan J, Mortensen J J, Jacobsen K W and Thygesen K S 2011 Linear density response function in the projector augmented wave method: applications to solids, surfaces and interfaces *Phys. Rev. B* **83** 245122
- [135] Onida G, Reining L and Rubio A 2002 Electronic excitations: density-functional versus many-body Green's-function approaches *Rev. Mod. Phys.* **74** 601–59
- [136] Sander T, Maggio E and Kresse G 2015 Beyond the tamm-dancoff approximation for extended systems using exact diagonalization *Phys. Rev. B* **92** 045209
- [137] Latini S, Olsen T and Thygesen K S 2015 Excitons in van der Waals heterostructures: the important role of dielectric screening *Phys. Rev. B* **92** 245123
- [138] Da Jornada F H, Qiu D Y and Louie S G 2017 Nonuniform sampling schemes of the Brillouin zone for many-electron perturbation-theory calculations in reduced dimensionality *Phys. Rev. B* **95**
- [139] Drueppel M, Deilmann T, Krueger P and Rohlfing M 2017 Diversity of trion states and substrate effects in the optical properties of an MoS₂ monolayer *Nat. Commun.* **8** 2117
- [140] Mouri S, Zhang W, Kozawa D, Miyauchi Y, Eda G and Matsuda K 2017 Thermal dissociation of inter-layer excitons in MoS₂/MoSe₂ hetero-bilayers *Nanoscale* **9** 6674–9
- [141] Chen H, Wen X, Zhang J, Wu T, Gong Y, Zhang X, Yuan J, Yi C, Lou J, Ajayan P M, Zhuang W, Zhang G and Zheng J 2016 Ultrafast formation of interlayer hot excitons in atomically thin MoS₂/WS₂ heterostructures *Nat. Commun.* **7** 1–8
- [142] Fang H et al 2014 Strong interlayer coupling in van der Waals heterostructures built from single-layer chalcogenides *Proc. Natl Acad. Sci.* **111** 6198–202
- [143] Wilson N R, Nguyen P V, Seyler K, Rivera P, Marsden A J, Laker Z P, Constantinescu G C, Kandyba V, Barinov A, Hine N D, Xu X and Cobden D H 2017 Determination of band offsets, hybridization and exciton binding in 2D semiconductor heterostructures *Sci. Adv.* **3** e1601832
- [144] Ceballos F, Bellus M Z, Chiu H-Y and Zhao H 2015 Probing charge transfer excitons in a MoSe₂-WS₂ van der Waals heterostructure *Nanoscale* **7** 17523–8
- [145] Liu H, Neal A T, Zhu Z, Luo Z, Xu X, Tománek D and Ye P D 2014 Phosphorene: an unexplored 2D semiconductor with a high hole mobility *ACS Nano* **8** 4033–41
- [146] Yang J, Xu R, Pei J, Myint Y W, Wang F, Wang Z, Zhang S, Yu Z and Lu Y 2015 Optical tuning of exciton and trion emissions in monolayer phosphorene *Light Sci. Appl.* **4** 1–7
- [147] Takagi S, Toriumi A and Iwase M 1994 On the universality of inversion layer mobility in Si MOSFET's: part I-effects of substrate impurity concentration *IEEE Trans. Electron Dev.* **41** 2357–62
- [148] Cui X et al 2015 Multi-terminal transport measurements of MoS₂ using a van der Waals heterostructure device platform *Nat. Nanotechnol.* **10** 534–40
- [149] Jin Z, Li X, Mullen J T and Kim K W 2014 Intrinsic transport properties of electrons and holes in monolayer transition-metal dichalcogenides *Phys. Rev. B* **90** 045422
- [150] Gong C et al 2017 Discovery of intrinsic ferromagnetism in two-dimensional van der Waals crystals *Nature* **546** 265–9
- [151] Bonilla M et al 2018 Strong room-temperature ferromagnetism in VSe₂ monolayers on van der Waals substrates *Nat. Nanotechnol.* **13** 289–93
- [152] Huang C, Du Y, Wu H, Xiang H, Deng K and Kan E 2018 Prediction of intrinsic ferromagnetic ferroelectricity in a transition-metal halide monolayer *Phys. Rev. Lett.* **120** 147601
- [153] Mermin N D and Wagner H 1966 Absence of ferromagnetism or antiferromagnetism in one- or two-dimensional isotropic Heisenberg models *Phys. Rev. Lett.* **17** 1133–6
- [154] Lado J L and Fernández-Rossier J 2017 On the origin of magnetic anisotropy in two dimensional CrI₃ *2D Mater.* **4** 035002
- [155] Olsen T 2017 Assessing the performance of the random phase approximation for exchange and superexchange coupling constants in magnetic crystalline solids *Phys. Rev. B* **96** 125143
- [156] Low T, Chaves A, Caldwell J D, Kumar A, Fang N X, Avouris P, Heinz T F, Guinea F, Martin-Moreno L and Koppens F 2017 Polaritons in layered two-dimensional materials *Nat. Mater.* **16** 182
- [157] Gjerding M N, Petersen R, Pedersen T, Mortensen N A and Thygesen K S 2017 Layered van der Waals crystals with hyperbolic light dispersion *Nat. Commun.* **8** 320
- [158] Chen J et al 2012 Optical nano-imaging of gate-tunable graphene plasmons *Nature* **487** 77
- [159] Andersen K and Thygesen K S 2013 Plasmons in metallic monolayer and bilayer transition metal dichalcogenides *Phys. Rev. B* **88** 155128
- [160] Gjerding M N, Pandey M and Thygesen K S 2017 Band structure engineered layered metals for low-loss plasmonics *Nat. Commun.* **8** 15133
- [161] Cudazzo P, Tokatly I V and Rubio A 2011 Dielectric screening in two-dimensional insulators: implications for excitonic and impurity states in graphene *Phys. Rev. B* **84** 085406
- [162] Chernikov A, Berkelbach T C, Hill H M, Rigosi A, Li Y, Aslan O B, Reichman D R, Hybertsen M S and Heinz T F 2014 Exciton binding energy and nonhydrogenic rydberg series in monolayer WS₂ *Phys. Rev. Lett.* **113** 076802

- [163] Olsen T, Latini S, Rasmussen F and Thygesen K S 2016 Simple screened hydrogen model of excitons in two-dimensional materials *Phys. Rev. Lett.* **116** 056401
- [164] Jiang Z, Liu Z, Li Y and Duan W 2017 Scaling universality between band gap and exciton binding energy of two-dimensional Semiconductors *Phys. Rev. Lett.* **118** 266401
- [165] Choi J-H, Cui P, Lan H and Zhang Z 2015 Linear scaling of the exciton binding energy versus the band gap of two-dimensional materials *Phys. Rev. Lett.* **115** 066403
- [166] Seh Z W, Fredrickson K D, Anasori B, Kibsgaard J, Strickler A L, Lukatskaya M R, Gogotsi Y, Jaramillo T F and Vojvodic A 2016 Two-dimensional molybdenum carbide (mxene) as an efficient electrocatalyst for hydrogen evolution *ACS Energy Lett.* **1** 589–94
- [167] Xie J, Zhang H, Li S, Wang R, Sun X, Zhou M, Zhou J, Lou X W D and Xie Y 2013 Defect-rich MoS₂ ultrathin nanosheets with additional active edge sites for enhanced electrocatalytic hydrogen evolution *Adv. Mater.* **25** 5807–13
- [168] Ridolfi E, Le D, Rahman T, Mucciolo E and Lewenkopf C 2015 A tight-binding model for MoS₂ monolayers *J. Phys.: Condens. Matter* **27** 365501
- [169] Mostofi A A, Yates J R, Lee Y-S, Souza I, Vanderbilt D and Marzari N 2008 Wannier90: a tool for obtaining maximally-localised wannier functions *Comput. Phys. Commun.* **178** 685–99
- [170] Taherinejad M, Garrity K F and Vanderbilt D 2014 Wannier center sheets in topological insulators *Phys. Rev. B* **89** 115102
- [171] Bokdam M, Amlaki T, Brocks G and Kelly P J 2014 Band gaps in incommensurable graphene on hexagonal boron nitride *Phys. Rev. B* **89** 201404
- [172] Tritsaris G A, Shirodkar S N, Kaxiras E, Cazeaux P, Luskin M, Plecháč P and Cancès E 2016 Perturbation theory for weakly coupled two-dimensional layers *J. Mater. Res.* **31** 959–66
- [173] Andersen K, Latini S and Thygesen K S 2015 Dielectric genome of van der Waals heterostructures *Nano Lett.* **15** 4616–21

8.7 Paper VII

Efficient Charge Separation in 2D Janus van der Waals Structures with Built-in Electric Fields and Intrinsic p–n Doping

A. C. Riis-Jensen, M. Pandey, and K. S. Thygesen

J. Phys. Chem. C, **122**, 43 (2018)

Reproduced with permission from J. Phys. Chem. C, **122**, 43 (2018) © Copyright 2018 American Chemical Society.

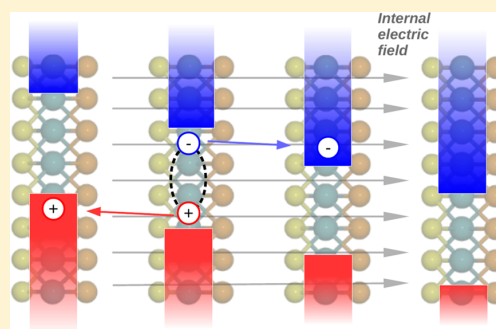
<https://pubs.acs.org/doi/abs/10.1021/acs.jpcc.8b05792>

Efficient Charge Separation in 2D Janus van der Waals Structures with Built-in Electric Fields and Intrinsic p–n Doping

Anders C. Riis-Jensen,^{†,§} Mohnish Pandey,^{†,§} and Kristian S. Thygesen^{*,†,‡,§}

[†]CAMD, Department of Physics and [‡]Center for Nanostructured Graphene (CNG), Department of Physics, Technical University of Denmark, DK-2800 Kongens Lyngby, Denmark

ABSTRACT: Janus MoSSe monolayers have been recently synthesized by replacing S by Se on one side of MoS₂ (or vice versa for MoSe₂). Due to the different electronegativities of S and Se, these structures carry a finite out-of-plane dipole moment. As we show here by means of density functional theory calculations, this intrinsic dipole leads to the formation of built-in electric fields when the monolayers are stacked to form *N*-layer structures. For sufficiently thin structures (*N* < 4), the dipoles add up and shift the vacuum level on the two sides of the film by $\sim N \cdot 0.7$ eV. For thicker films, the vacuum level shift saturates at around 2.2 eV due to compensating surface charges, which in turn leads to the formation of atomically thin n- and p-doped electron gases at the surfaces. The doping concentration can be tuned between 5×10^{12} and 2×10^{13} e/cm² by varying the film thickness. On the basis of band structure calculations and the Mott–Wannier exciton model, we compute the energies of intra- and interlayer excitons as a function of film thickness, suggesting that the Janus multilayer films are ideally suited for achieving ultrafast charge separation over atomic length scales without chemical doping or applied electric fields. Finally, we explore a number of other potentially synthesizable two-dimensional Janus structures with different band gaps and internal dipole moments. Our results open new opportunities for ultrathin optoelectronic components, such as tunnel diodes, photodetectors, or solar cells.



INTRODUCTION

The unique optical properties of atomically thin crystals combined with the possibility to combine them into lateral and vertical heterostructures have placed two-dimensional (2D) materials at the forefront of photonic and optoelectronic materials research.^{4–1} Among the unique optical properties that distinguish the 2D materials from the more conventional bulk semiconductors are their strong light–matter interactions^{8–10} and pronounced excitonic effects.^{11,12} Furthermore, by stacking individual 2D materials into van der Waals (vdW) heterostructures,² their optical properties can be further controlled by engineering of the band structure³ or the dielectric environment.^{13,14}

While the strong excitonic effects in 2D semiconductors are of interest for some applications, they can pose a serious problem for others. This holds in particular for photodetectors and solar cells, which rely on efficient dissociation of photoexcited excitons into free electrons and holes. For in-plane charge separation, the problem has been overcome by forming lateral p–n junctions using split gate techniques,^{15,16} which creates a sufficiently large potential gradient to dissociate the excitons.¹⁷ For out-of-plane device architectures, the exciton dissociation has been achieved using hetero-bilayers, e.g., MoS₂–WSe₂, with natural type-II band alignment^{18,19} or by applying an external bias voltage across an *N*-layer stack, e.g., five layers of WSe₂.²⁰

Here, we propose a novel type of vdW-bonded *N*-layer structure with an intrinsic electric field in the out-of-plane

direction stemming from an out-of-plane asymmetry and finite dipole moment of the individual monolayers. Above a certain critical thickness, the built-in electric field becomes compensated by surface charges accumulating at the surfaces leading to natural n- and p-doping of the two outermost monolayers, thus generating an ultrathin p–n junction. The electric field strength, the electronic band alignment throughout the structure, and the doping concentration at the surface layers can be tuned to some extent by varying the film thickness. We show that the built-in electric field in structures with up to around 20 layers is sufficient to dissociate intralayer excitons into interlayer excitons, which is the critical step for achieving charge separation. Finally, we show that these unique properties are not limited to MoSSe. In fact, our first-principles calculations predict a number of other stable and potentially synthesizable 2D materials with finite dipole moments. By stacking different types of 2D Janus structures, one could potentially engineer not only the band edge positions but also the internal electric field and the doping concentration at the surface layers.

Received: June 18, 2018

Revised: October 5, 2018

Published: October 5, 2018

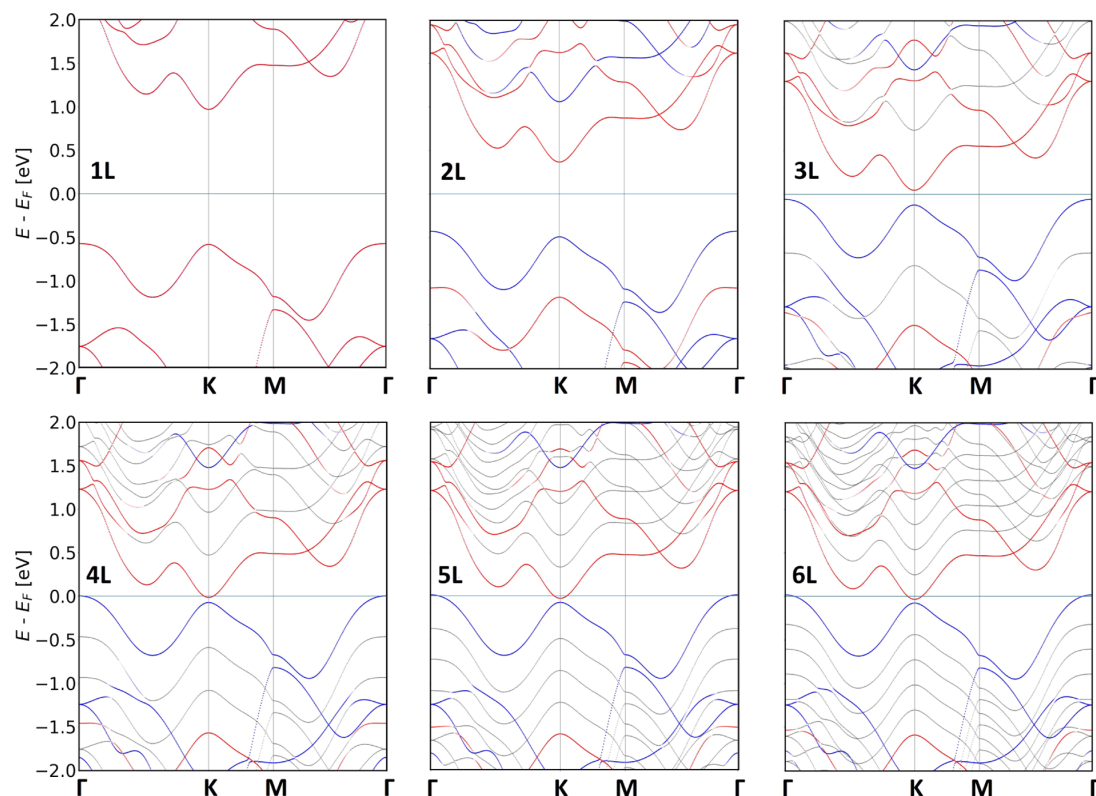


Figure 1. Band structures for the 1–6 layer Janus structure. Red and blue show the bands projected onto the top and bottom layers, respectively, while all layers in between are colored gray. Faded blue or red indicates a high hybridization between neighboring layers. From there, one can see a direct band gap for the monolayer MoSSe at the *K*-point, while all multilayer structures have an indirect band gap from Γ to *K*, with the valence band maximum and conduction band minimum located at the bottom and top layers, respectively.

METHODS

All calculations have been performed with the GPAW²¹ code. The in-plane lattice constant of the monolayer MoSSe is calculated with the Perdew–Burke–Ernzerhof (PBE) functional.²² To get an accurate description of the interlayer distance, we use the Bayesian error estimation functional (BEEF)–vdW functional, which includes a nonlocal van der Waals correction.²³ We find that the calculated interlayer distance does not change as the number of layers in the Janus structure is increased from 2 to 3. Therefore, we take the interlayer distance calculated for the bilayer structure as the optimum distance for all of the multilayer structures. The wave functions are expanded in a plane wave basis with an energy cutoff of 800 eV. For structural relaxations, we employ a $18 \times 18 \times 1$ Monkhorst–Pack grid.²⁴ The PBE band structures are calculated on a very fine $54 \times 54 \times 1$ *k*-point grid with a 800 eV plane wave cutoff and by inclusion of spin–orbit coupling. A vacuum region of 15 Å is inserted in the perpendicular direction to separate the periodically repeated images. A Fermi smearing of 0.01 eV was used for all of the calculations.

To calculate the screened electron–hole (e–h) interaction in the multilayer structures, the dielectric building block of monolayer MoSSe is calculated following ref 13 to be used as input for the quantum electrostatic heterostructure (QEH) model. The calculations are performed in the random phase approximation (RPA) using wave functions and eigenvalues from a PBE ground-state calculation with a $100 \times 100 \times 1$ *k*-

point grid and an 800 eV plane wave cutoff. For the density response function, a plane wave cutoff of 150 eV is used (to account for local field effects). The in-plane exciton effective mass used in the 2D Mott–Wannier model is calculated from the PBE band structure and is found to be $\mu_{\text{ex}} = 0.24m_0$ (for the direct exciton at the *K*-point), where m_0 is the free electron mass. The dielectric constant for bulk MoSSe (in which MoSSe layers are stacked together as in 2H MoS₂ bulk) was calculated in the RPA based on a PBE ground-state calculation. The ground-state calculation of the bulk MoSSe to be used as a starting point for the RPA calculation was done on a $24 \times 24 \times 18$ *k*-point grid using a 800 eV plane wave cutoff. The number of bands was set to six times the number of valence bands, and we converged five times the number of valence bands in the ground-state calculation. All of these bands were used in the RPA calculation, which had a plane wave cutoff of 125 eV.

For more details on the calculation of intra- and interlayer exciton binding energies from the 2D Mott–Wannier model, we refer to the detailed accounts given in refs 25 and 26.

RESULTS AND DISCUSSION

Janus MoSSe monolayers have been recently synthesized using both controlled sulfurization of MoSe₂²⁷ and selenization of MoS₂.²⁸ Following the experimental realizations, a number of computational studies have considered various aspects of MoSSe monolayers, including magnetism^{29,30} as well as electronic, optical, and transport properties.^{31–33} One study

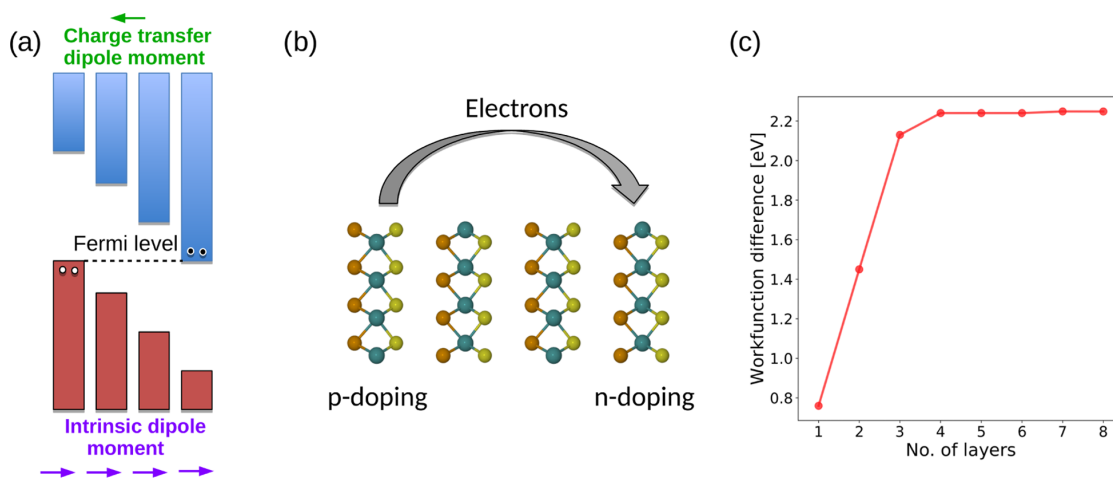


Figure 2. (a) Qualitative sketch of the charge transfer at four layers with the intrinsic dipole moment shown below and the dipole moment due to the charge separation above. (b) Sketch of the p- and n-doping of the outermost layers. (c) Difference between the workfunction on either side of an N -layer Janus structure calculated from the PBE band structure.

also explored multilayers of MoSSe and reported an observed rapid closing of the band gap as a function of the number of layers saturating at a value around 0.1 eV for $N > 3$, but without providing a physical explanation for this effect.³⁴ In contrast to these findings, we show that the Janus multilayers undergo an insulator-to-metal transition at around $N = 4$, which is driven by the internal dipole of the structure.

To obtain the equilibrium structure, we have performed density functional theory (DFT) calculations for AB-stacked MoSSe multilayer structures using the BEEF-vdW exchange-correlation functional²³ as implemented in the GPAW electronic structure code²¹ (see [Methods](#) for more details). We find in-plane lattice constant of 3.251 Å in good agreement with previous work^{27,28,35} and interlayer spacings of 6.896 Å (defined as the Mo–Mo distance), which is found to be practically independent of the number of layers in the multilayer structure. An example of a four-layer structure is shown in [Figure 2b](#).

The difference in electronegativity of sulfur and selenium leads to the formation of a static dipole of 0.038 leÅ per lateral unit cell across each MoSSe monolayer. When several layers are stacked together, these dipoles add up and generate a potential gradient in the direction perpendicular to the film. The evolution of the band structures of MoSSe multilayer structures for $N = 1–6$ are shown in [Figure 1](#). The band structures are obtained with the PBE functional.²² Interestingly, the band structures change dramatically with N despite the fact that wave functions on neighboring layers hybridize only weakly due to the weak vdW bonds. For $N \geq 4$, the band gap vanishes and the Fermi level intersects the valence band maximum (VBM) at the Γ -point and the conduction band minimum (CBM) at the K -point of the lateral 2D Brillouin zone. The bands located on the top and bottom layers are colored red and blue, respectively. Clearly, the charge transfer occurs between the outermost layers of the structure.

The insulator–metal (IM) transition occurs when the built-in potential difference between the top and bottom layers exceeds the band gap, E_G . At this point, the CBM moves below the VBM, resulting in a net positive (negative) charge in the top (bottom) layer. This shift in the charge density creates a dipole in the

direction opposite to the intrinsic dipoles of the MoSSe layers. The effect is clearly visible from the difference in the electrostatic potential on the two sides of the multilayer structure (see [Figure 2c](#)). In the same figure, we show a qualitative sketch of the charge transfer, the intrinsic dipoles of the individual monolayers, and the counter balancing dipole due to the charge transfer (a). The potential difference across an N -layer structure, $\Delta\Phi(N)$, is seen to saturate at a value around 2.2 eV. Adding more layers will increase the potential difference created by the internal dipoles (which simply add up). However, after the onset of the IM transition, any increase in the internal dipole will be counterbalanced by surface charges transferred between the outermost monolayers. The number of layers at which this IM transition occurs is approximately

$$N_{\text{IM}} = E_G / \Delta\Phi_0 + 1 \quad (1)$$

where $\Delta\Phi_0$ is the potential difference across a single layer. For the MoSSe monolayer, we find $\Delta\Phi_0 = 0.76$ eV and $E_G = 1.54$ eV, yielding $N_{\text{IM}} = 3$, in good agreement with the band structure calculations in [Figure 1](#). We note in passing that, due to the well-known underestimation of the band gap by the PBE xc-functional, N_{IM} might also be underestimated. In fact, using the G_0W_0 calculated band gap for monolayer MoSSe of 2.33 eV, we obtain $N_{\text{IM}} = 4$.

For $N > N_{\text{IM}}$, the charge density at either side can be estimated from a simple plate capacitor model

$$\sigma(N) = \frac{\epsilon_{\perp} \Delta\Phi_0}{d} \left(1 - \frac{N_{\text{IM}}}{N} \right) \quad (2)$$

where ϵ_{\perp} is the dielectric constant of bulk MoSSe in the out-of-plane direction, $\Delta\Phi_0$ is the potential difference created by a single layer, and d is the interlayer distance. We have calculated the dielectric constant within the random phase approximation (RPA) for bulk MoSSe and obtained $\epsilon_{\perp} = 3.68\epsilon_0$ (see [Methods](#) for further details). The prefactor in [eq 2](#) corresponding to the charge density in the limit $N \rightarrow \infty$ then becomes $\sigma(\infty) = 2.3 \times 10^{13}$ e/cm².

We next turn to an analysis of the charge separation ability of the Janus structures. Upon light illumination, electron–hole (e–h) pairs will be generated within the structure. Due to the small

spatial overlap of the wave functions in neighboring layers, the generated e–h pairs will predominantly be of the intralayer type. The photoexcited e–h pairs will thermalize rapidly on a sub-picosecond time scale.³⁶ In comparison, e–h recombination in similar transition-metal dichalcogenide (TMD) structures without built-in electric fields occurs on time scales of at least several picoseconds.^{37–39} At room temperature, the e–h recombination is dominated by defect-assisted processes and consequently significantly longer e–h lifetimes are expected for highly pure samples. After thermal relaxation, the resulting nonequilibrium distribution includes hot electrons and holes with energies above the band gap as well as bound excitons. The hot electrons and holes will separate efficiently in the large built-in electric field. Consequently, we focus on the bound excitons, which are more difficult to dissociate.

Excitons in layered TMD structures have binding energies in the range of 0.5 eV (isolated monolayers) to 0.1 eV (bulk), which are significantly larger than $k_B T$ at room temperature. The crucial first step of the exciton dissociation process is the transformation of the intralayer excitons into an interlayer exciton with the electron and hole located on neighboring layers. This process requires that the energy of the interlayer exciton is equal to or lower than the intralayer exciton. In the absence of an electric field, this condition is never satisfied because of the weaker e–h binding energy in the spatially separated interlayer exciton.⁴⁰ However, in structures with a built-in electric field, this energy difference can be overcome by the band offset between neighboring layers.

To determine the conditions for exciton dissociation, we calculate the binding energies of intra- and interlayer excitons in stacked MoSSe as a function of film thickness. We use a 2D Mott–Wannier model, which has been shown to yield accurate binding energies for excitons in mono- and few-layer TMDs^{25,41,42} as well as for interlayer excitons in vdW heterostructures.²⁶ The 2D Mott–Wannier Hamiltonian takes the form

$$\left[-\frac{\nabla_{2D}^2}{2\mu_{\text{ex}}} + W(\mathbf{r}_{\parallel}) \right] F(\mathbf{r}_{\parallel}) = E_B F(\mathbf{r}_{\parallel}) \quad (3)$$

where μ_{ex} is the exciton effective mass and $W(\mathbf{r}_{\parallel})$ is the electron–hole interaction energy. The exciton effective mass is defined as $\mu_{\text{ex}}^{-1} = m_e^{-1} + m_h^{-1}$, where the hole and electron masses must be evaluated at the band extremum of the relevant layer. Assuming direct (i.e., zero-momentum) excitons, both the electron and hole masses should be evaluated at the K-point of the BZ yielding an exciton mass of $\mu_{\text{ex}} = 0.24m_0$. We stress that eq 3 remains valid in the case of interlayer excitons because even though the electron and hole are now spatially separated in the out-of-plane direction, their motion is still confined to their respective layers. On the other hand, this spatial separation affects the screened electron–hole interaction W . We calculate W using the quantum electrostatic heterostructure (QEH) model¹³ to include the additional screening from the surrounding layers. We obtain binding energies for intralayer excitons in the center of the film in the range of 0.38 eV (for $N = 3$) to 0.23 eV (for $N \rightarrow \infty$) and interlayer exciton binding energies from 0.29 eV (for $N = 3$) to 0.15 eV (for $N \rightarrow \infty$).

In Figure 3, we show the difference in binding energy between the intra- and interlayer excitons in the central layers of an N -layer MoSSe structure (green symbols)

$$\Delta E_B(N) = E_B^{\text{intra}}(N) - E_B^{\text{inter}}(N) \quad (4)$$

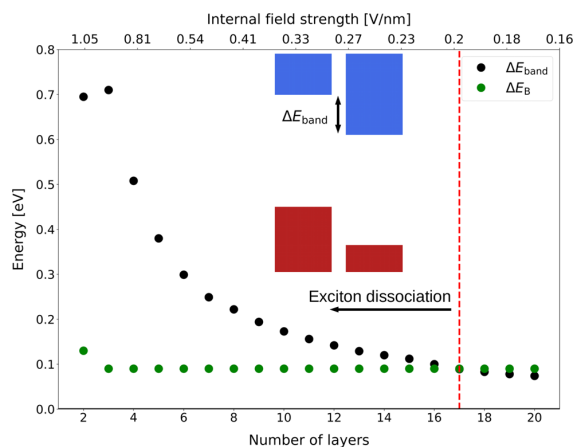


Figure 3. Difference in intralayer exciton binding energy (E_B^{intra}) and interlayer exciton binding energy (E_B^{inter}) in green for the central layer and band offset between neighboring layers in black also for the central layer in an N -layer structure. At the crossover between the two curves at around $N = 17$ layers, the interlayer exciton is no longer energetically favorable and exciton dissociation cannot take place. This critical limit is shown by the red dashed line. The inset shows the definition of the band offset between neighboring layers.

The black curve shows the band offset between two neighboring layers of the structure, as shown in the inset. The two curves cross around $N = 17$, as indicated by the red dashed line. For structures thicker than this critical thickness, the difference in exciton binding energy cannot be overcome by the band offset and the exciton cannot dissociate (more precisely, the driving force for exciton dissociation is strongly reduced).

The above analysis is based on a picture where excitons are composed of electrons and holes bound to specific layers. Alternatively, we can describe the excitons by a homogeneous anisotropic three-dimensional (3D) Mott–Wannier model, where the layered nature of the Janus structure is accounted for by using different dielectric constants and effective masses in the in- and out-of-plane directions. Such a model was developed in ref 43 and applied to bulk TMDs. Using input parameters from first-principles calculations, the model yields binding energies, E_B , of 83 and 52 meV for bulk MoS₂ and MoSe₂, respectively, and exciton radius in the out-of-plane directions (a_0^*) of around 1.1 and 1.4 nm. Assuming similar values for bulk MoSSe, the characteristic field strength at which this exciton dissociates, E_B/a_0^* , becomes roughly 0.1 V/nm. It can be seen that the result for the critical thickness obtained with this homogeneous anisotropic 3D model is in reasonable agreement with the result obtained with the layered 2D exciton model. In fact, by extrapolating the results, we find the internal field strength to reach 0.1 V/nm at around 30 layers. We stress that according to ref 43, the exciton dissociation rate for out-of-plane field strengths of 0.1 V/nm is well above 10^{13} s^{-1} for both direct and indirect excitons in both MoS₂ and MoSe₂. From this, we conclude that exciton dissociation in MoSSe Janus structures up to the critical thickness of about 20 layers occurs much faster than the exciton recombination, which is characterized by rates $< 10^{12} \text{ s}^{-1}$.^{37–39}

In this paper, we have focused on the charge separation ability of MoSSe Janus structures. This property is essential for a number of optoelectronic devices, including photodetectors and solar cells. The latter application might seem impossible

considering the band structures in Figure 1, which shows a decreasing band gap reaching zero for $N > 3$. However, one should keep in mind that this is the situation in equilibrium. Upon excitation, charge carriers excited in the interior of the p–n junction will separate due to the built-in field and electrons (holes) will move to the n (p) side of the structure. This charge imbalance will create a dipole opposite to the built-in field (just like the charge transfer creating the p and n surface doping in equilibrium). The size of the nonequilibrium charge distributions will determine the achievable photovoltage, which is given by the difference in the (quasi-)Fermi levels of electrons and holes, respectively. The size of the nonequilibrium charge distributions, and thus the achievable voltage, will depend on the carrier lifetimes (limited by recombination processes) relative to the rate of charge separation. Assuming a conservative recombination rate of 1 ps, the critical field strength at which perpendicular exciton dissociation in bulk TMDs dominates the recombination is 0.01 V/nm,⁴³ which is easily achieved in the stacked Janus structures (cf. Figure 3). We conclude that it should be possible to realize finite photovoltages in stacked Janus structures, even for films with $N > N_{\text{IM}}$. The situation is illustrated in Figure 4.

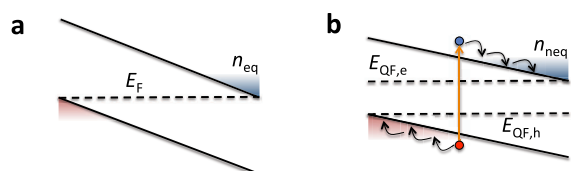


Figure 4. Sketch of the dissociation of excitons. (a) Band alignment at equilibrium; (b) exciton dissociation after photoexcitation and the corresponding quasi-Fermi levels. The spatial separation of the holes and the photoexcited electrons sets up an opposite dipole, which again opens a band gap.

We mention that other applications of (stacked) 2D Janus structures could be envisioned such as the tunnel diodes, e.g., to separate light-absorbing layers in multijunction solar cells, tunnel field-effect transistors,⁴⁴ or for tuning band alignment or Schottky barriers in van der Waals heterostructures.⁴⁵

Finally, we show that finite out-of-plane dipole moments in 2D materials are not limited to the MoSSe monolayer. We have performed DFT calculations for a number of monolayers with similar structures and chemical compositions to MoSSe. The results of these calculations, including the atomic structure, total energies, electronic band structure, and much more, are directly available in the Computational 2D Materials Database (C2DB).⁴⁶ For the monolayers found to be both dynamically and thermodynamically stable (according to the criteria used in the C2DB and described in ref 46), we show in Figure 5 the relation between the G_0W_0 band gap and the workfunction difference. We find a linear relation between the workfunction difference and the internal dipole moment for the five structures sharing the same geometry as MoSSe. We here therefore only show the workfunction difference, which is the interesting parameter for an actual experimental realization. We note in passing that BiTeI is known as layered bulk material and should be easily exfoliable according to ref 47. Indeed, BiTeI has been recently exfoliated and studied in its monolayer form.⁴⁸ Returning to Figure 5, we observe a large variation in the key electronic properties of these Janus structures. This suggests that in addition to controlling the number of layers in the Janus

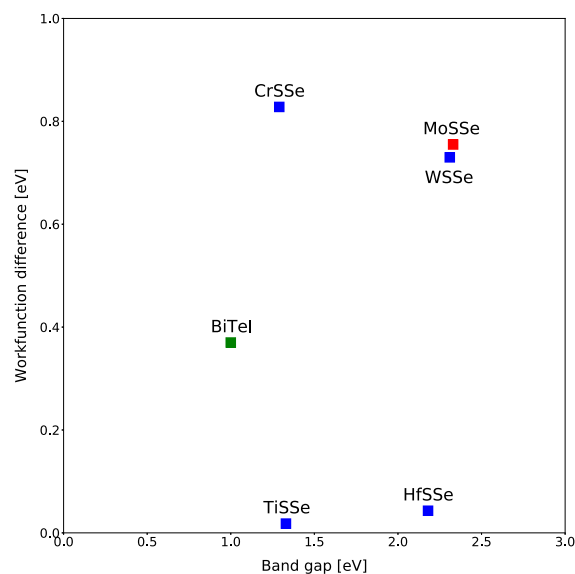


Figure 5. Workfunction difference and G_0W_0 band gap for five different TMD monolayer Janus structures with MoSSe: the structure considered in this study highlighted in red, and in green BiTeI, which has a different structure from MoSSe, and the other four structures in blue, which all share the same structure as MoSSe. This shows that the charge transfer and band alignment shift can also be controlled by the material in addition to adjusting the number of layers.

structure, it is also possible to control the size of the built-in field and therefore the surface layer doping level, by varying the type of material. In particular, by combining different 2D Janus layers into van der Waals heterostructures, it should be possible to design not only the band alignment but also the built-in electric field and, e.g., obtain nonlinear potential profiles.

CONCLUSIONS

In summary, our first-principles calculations show that 2D vdW structures consisting of stacked Janus MoSSe monolayers host a strong built-in electric field of about 0.1 V/Å. The electric field induces a staggered band alignment throughout the structure, and at a critical thickness of three to four layers, the CBM of the top layer meets the VBM of the bottom layer triggering an electron transfer between the outermost monolayers. The charge density on the surface layers of this natural vertical p–n junction can be tuned between about 5×10^{12} and 2×10^{13} e/cm² by varying the film thickness (these values correspond to the cases of 5 and 17 layers, respectively). Using many-body GW calculations in combination with a 2D Mott–Wannier model, we estimated the energy of intra- and interlayer excitons as a function of film thickness. These calculations show that for film thickness below approximately about 20 layers, the shift in band edges at neighboring layers exceeds the difference in binding energy of the intra- and interlayer excitons and thus facilitates the spontaneous dissociation of photogenerated intralayer excitons into spatially separated electron–hole pairs. On the basis of these results, we propose that Janus vdW structures could be used as basis for ultrafast and ultrathin photodetectors or electrical diodes. In the future, it would be interesting to explore the possibility of using 2D Janus structures to introduce highly local potential gradients in intrinsic semiconductors without the need for doping. This could be interesting for charge

separation in solar cells or for tuning band alignment at the interface between two different semiconductors.

AUTHOR INFORMATION

Corresponding Author

*E-mail: thygesen@fysik.dtu.dk.

ORCID

Mohnish Pandey: 0000-0002-1715-0617

Kristian S. Thygesen: 0000-0001-5197-214X

Author Contributions

§A.C.R.-J. and M.P. contributed equally to this work.

Notes

The authors declare no competing financial interest.

ACKNOWLEDGMENTS

This project received funding from the European Research Council (ERC) under the European Union's Horizon 2020 research and innovation programme (grant agreement No. 773122, LIMA). The Center for Nanostructured Graphene is sponsored by the Danish National Research Foundation, Project DNRF103.

REFERENCES

- (1) Cui, X.; Lee, G.-H.; Kim, Y. D.; Arefe, G.; et al. Multi-terminal Transport Measurements of MoS₂ Using a van der Waals Heterostructure Device Platform. *Nat. Nanotechnol.* **2015**, *10*, 534.
- (2) Geim, A. K.; Grigorieva, I. V. Van der Waals Heterostructures. *Nature* **2013**, *499*, 419–425.
- (3) Withers, F.; Del Pozo-Zamudio, O.; Mishchenko, A.; Rooney, A.; Gholinia, A.; Watanabe, K.; Taniguchi, T.; Haigh, S.; Geim, A.; Tartakovsky, A.; et al. Light-Emitting Diodes by Band-Structure Engineering in van der Waals Heterostructures. *Nat. Mater.* **2015**, *14*, 301–306.
- (4) Pandey, M.; Rasmussen, F. A.; Kuhar, K.; Olsen, T.; Jacobsen, K. W.; Thygesen, K. S. Defect-Tolerant Monolayer Transition Metal Dichalcogenides. *Nano Lett.* **2016**, *16*, 2234–2239.
- (5) Gjerding, M. N.; Pandey, M.; Thygesen, K. S. Band Structure Engineered Layered Metals for Low-loss Plasmonics. *Nat. Commun.* **2017**, *8*, No. 15133.
- (6) Pandey, M.; Jacobsen, K. W.; Thygesen, K. S. Band Gap Tuning and Defect Tolerance of Atomically Thin Two-Dimensional Organic-Inorganic Halide Perovskites. *J. Phys. Chem. Lett.* **2016**, *7*, 4346–4352.
- (7) Pandey, M.; Jacobsen, K. W.; Thygesen, K. S. Atomically Thin Ordered Alloys of Transition Metal Dichalcogenides: Stability and Band Structures. *J. Phys. Chem. C* **2016**, *120*, 23024–23029.
- (8) Britnell, L.; Ribeiro, R.; Eckmann, A.; Jalil, R.; Belle, B.; Mishchenko, A.; Kim, Y.-J.; Gorbachev, R.; Georgiou, T.; Morozov, S.; et al. Strong Light-Matter Interactions in Heterostructures of Atomically Thin Films. *Science* **2013**, *340*, 1311–1314.
- (9) Splendiani, A.; Sun, L.; Zhang, Y.; Li, T.; Kim, J.; Chim, C.-Y.; Galli, G.; Wang, F. Emerging Photoluminescence in Monolayer MoS₂. *Nano Lett.* **2010**, *10*, 1271–1275.
- (10) Mak, K. F.; Lee, C.; Hone, J.; Shan, J.; Heinz, T. F. Atomically Thin MoS₂: A New Direct-Gap Semiconductor. *Phys. Rev. Lett.* **2010**, *105*, No. 136805.
- (11) Ye, Z.; Cao, T.; O'Brien, K.; Zhu, H.; Yin, X.; Wang, Y.; Louie, S. G.; Zhang, X. Probing Excitonic Dark States in Single-Layer Tungsten Disulphide. *Nature* **2014**, *513*, 214–218.
- (12) Klots, A. R.; Newaz, A. K. M.; Wang, B.; Prasai, D.; Krzyzanowska, H.; Lin, J.; Caudel, D.; Ghimire, N.; Yan, J.; Ivanov, B.; et al. Probing Excitonic States in Suspended Two-Dimensional Semiconductors by Photocurrent Spectroscopy. *Sci. Rep.* **2014**, *4*, No. 6608.
- (13) Andersen, K.; Latini, S.; Thygesen, K. S. Dielectric Genome of van der Waals Heterostructures. *Nano Lett.* **2015**, *15*, 4616–4621.

(14) Gjerding, M. N.; Petersen, R.; Pedersen, T.; Mortensen, N. A.; Thygesen, K. S. Layered van der Waals Crystals with Hyperbolic Light Dispersion. *Nat. Commun.* **2017**, *8*, No. 320.

(15) Massicotte, M.; Violla, F.; Schmidt, P.; Lundeberg, M. B.; Latini, S.; Hastrup, S.; Danovich, M.; Davydovskaya, D.; Watanabe, K.; Taniguchi, T.; et al. Dissociation of Two-Dimensional Excitons in Monolayer WSe₂. *Nat. Commun.* **2018**, *9*, No. 1633.

(16) Ross, J. S.; Klement, P.; Jones, A. M.; Ghimire, N. J.; Yan, J.; Mandrus, D.; Taniguchi, T.; Watanabe, K.; Kitamura, K.; Yao, W.; et al. Electrically Tunable Excitonic Light-Emitting Diodes Based on Monolayer WSe₂ p-n Junctions. *Nat. Nanotechnol.* **2014**, *9*, 268–272.

(17) Hastrup, S.; Latini, S.; Bolotin, K.; Thygesen, K. S. Stark Shift and Electric-Field-Induced Dissociation of Excitons in Monolayer MoS₂ and hBN/MoS₂ Heterostructures. *Phys. Rev. B* **2016**, *94*, No. 041401.

(18) Peng, B.; Yu, G.; Liu, X.; Liu, B.; Liang, X.; Bi, L.; Deng, L.; Sum, T. C.; Loh, K. P. Ultrafast Charge Transfer in MoS₂/WSe₂ p-n Heterojunction. *2D Mater.* **2016**, *3*, No. 025020.

(19) Chen, H.; Wen, X.; Zhang, J.; Wu, T.; Gong, Y.; Zhang, X.; Yuan, J.; Yi, C.; Lou, J.; Ajayan, P. M.; et al. Ultrafast Formation of Interlayer Hot Excitons in Atomically Thin MoS₂/WS₂ heterostructures. *Nat. Commun.* **2016**, *7*, No. 12512.

(20) Massicotte, M.; Schmidt, P.; Violla, F.; Schädler, K. G.; Reserbat-Plantey, A.; Watanabe, K.; Taniguchi, T.; Tielrooij, K.-J.; Koppens, F. H. Picosecond Photoresponse in van der Waals Heterostructures. *Nat. Nanotechnol.* **2016**, *11*, 42–46.

(21) Enkovaara, J.; Rostgaard, C.; Mortensen, J. J.; Chen, J.; Dulak, M.; Ferrighi, L.; Gavnholt, J.; Glinsvad, C.; Haikola, V.; Hansen, H.; et al. Electronic Structure Calculations with GPAW: A Real-Space Implementation of the Projector Augmented-Wave Method. *J. Phys.: Condens. Matter* **2010**, *22*, No. 253202.

(22) Perdew, J. P.; Burke, K.; Ernzerhof, M. Generalized Gradient Approximation Made Simple. *Phys. Rev. Lett.* **1996**, *77*, 3865–3868.

(23) Wellendorff, J.; Lundgaard, K. T.; Mogelhøj, A.; Petzold, V.; Landis, D. D.; Nørskov, J. K.; Bligaard, T.; Jacobsen, K. W. Density Functionals for Surface Science: Exchange-Correlation Model Development with Bayesian Error Estimation. *Phys. Rev. B* **2012**, *85*, No. 235149.

(24) Monkhorst, H. J.; Pack, J. D. Special Points for Brillouin-Zone Integrations. *Phys. Rev. B* **1976**, *13*, 5188–5192.

(25) Latini, S.; Olsen, T.; Thygesen, K. S. Excitons in van der Waals Heterostructures: The Important Role of Dielectric Screening. *Phys. Rev. B* **2015**, *92*, No. 245123.

(26) Latini, S.; Winther, K. T.; Olsen, T.; Thygesen, K. S. Interlayer Excitons and Band Alignment in MoS₂/hBN/WSe₂ van der Waals Heterostructures. *Nano Lett.* **2017**, *17*, 938–945.

(27) Zhang, J.; Jia, S.; Kholmanov, I.; Dong, L.; Er, D.; Chen, W.; Guo, H.; Jin, Z.; Shenoy, V. B.; Shi, L.; et al. Janus Monolayer Transition-Metal Dichalcogenides. *ACS Nano* **2017**, *11*, 8192–8198.

(28) Lu, A.-Y.; Zhu, H.; Xiao, J.; Chuu, C.-P.; Han, Y.; Chiu, M.-H.; Cheng, C.-C.; Yang, C.-W.; Wei, K.-H.; Yang, Y.; et al. Janus Monolayers of Transition Metal Dichalcogenides. *Nat. Nanotechnol.* **2017**, *12*, 744–749.

(29) Meng, M.; Li, T.; Li, S.; Liu, K. Ferromagnetism Induced by Point Defect in Janus Monolayer MoSSe Regulated by Strain Engineering. *J. Phys. D: Appl. Phys.* **2018**, *51*, No. 105004.

(30) Wang, M.; Pang, Y.; Liu, D. Y.; Zheng, S. H.; Song, Q. L. Tuning Magnetism by Strain and External Electric Field in Zigzag Janus MoSSe Nanoribbons. *Comput. Mater. Sci.* **2018**, *146*, 240–247.

(31) Yin, W.-J.; Wen, B.; Wei, X.-L.; Nie, G.; Liu, L.-M. The Tunable Dipole and Carrier Mobility for Few Layer Janus MoSSe Structure. *J. Mater. Chem. C* **2018**, *6*, 1693–1700.

(32) Li, F.; Wei, W.; Zhao, P.; Huang, B.; Dai, Y. Electronic and Optical Properties of Pristine and Vertical and Lateral Heterostructures of Janus MoSSe and WSSe. *J. Phys. Chem. Lett.* **2017**, *8*, 5959–5965.

(33) Ma, X.; Wu, X.; Wang, H.; Wang, Y. A Janus MoSSe Monolayer: A Potential Wide Solar-Spectrum Water-Splitting Photocatalyst with a Low Carrier Recombination Rate. *J. Mater. Chem. A* **2018**, *6*, 2295–2301.

- (34) Guan, Z.; Ni, S.; Hu, S. Tunable Electronic and Optical Properties of Monolayer and Multilayer Janus MoSSe as a Photocatalyst for Solar Water Splitting: A First-Principles Study. *J. Phys. Chem. C* **2018**, *122*, 6209–6216.
- (35) Ji, Y.; Yang, M.; Lin, H.; Hou, T.; Wang, L.; Li, Y.; Lee, S.-T. Janus Structures of Transition Metal Dichalcogenides as the Heterojunction Photocatalysts for Water Splitting. *J. Phys. Chem. C* **2018**, *122*, 3123–3129.
- (36) Nie, Z.; Long, R.; Sun, L.; Huang, C.-C.; Zhang, J.; Xiong, Q.; Hewak, D. W.; Shen, Z.; Prezhd, O. V.; Loh, Z.-H. Ultrafast Carrier Thermalization and Cooling Dynamics in Few-Layer MoS₂. *ACS Nano* **2014**, *8*, 10931–10940.
- (37) Palumbo, M.; Bernardi, M.; Grossman, J. C. Exciton Radiative Lifetimes in Two-Dimensional Transition Metal Dichalcogenides. *Nano Lett.* **2015**, *15*, 2794–2800.
- (38) Shi, H.; Yan, R.; Bertolazzi, S.; Brivio, J.; Gao, B.; Kis, A.; Jena, D.; Xing, H. G.; Huang, L. Exciton Dynamics in Suspended Monolayer and Few-Layer MoS₂ 2D Crystals. *ACS Nano* **2013**, *7*, 1072–1080.
- (39) Lagarde, D.; Bouet, L.; Marie, X.; Zhu, C.; Liu, B.; Amand, T.; Tan, P.; Urbaszek, B. Carrier and Polarization Dynamics in Monolayer MoS₂. *Phys. Rev. Lett.* **2014**, *112*, No. 047401.
- (40) Deilmann, T.; Thygesen, K. S. Interlayer Excitons with Large Optical Amplitudes in Layered van der Waals Materials. *Nano Lett.* **2018**, *18*, 2984–2989.
- (41) Cudazzo, P.; Tokatly, I. V.; Rubio, A. Dielectric Screening in Two-Dimensional Insulators: Implications for Excitonic and Impurity States in Graphane. *Phys. Rev. B* **2011**, *84*, No. 085406.
- (42) Pulci, O.; Gori, P.; Marsili, M.; Garbuio, V.; Del Sole, R.; Bechstedt, F. Strong Excitons in Novel Two-Dimensional Crystals: Silicene and Germanene. *Europhys. Lett.* **2012**, *98*, No. 37004.
- (43) Pedersen, T. G.; Latini, S.; Thygesen, K. S.; Mera, H.; Nikolić, B. K. Exciton Ionization in Multilayer Transition-Metal Dichalcogenides. *New J. Phys.* **2016**, *18*, No. 073043.
- (44) Sarkar, D.; Xie, X.; Liu, W.; Cao, W.; Kang, J.; Gong, Y.; Kraemer, S.; Ajayan, P. M.; Banerjee, K. A Subthermionic Tunnel Field-Effect Transistor with an Atomically Thin Channel. *Nature* **2015**, *526*, 91–95.
- (45) Lee, M.-H.; Cho, Y.; Byun, K.-E.; Shin, K. W.; Nam, S.-G.; Kim, C.; Kim, H.; Han, S.-A.; Kim, S.-W.; Shin, H.-J.; et al. Two-Dimensional Materials Inserted at the Metal/Semiconductor Interface: Attractive Candidates for Semiconductor Device Contacts. *Nano Lett.* **2018**, *18*, 4878–4884.
- (46) Haastrup, S.; Strange, M.; Pandey, M.; Deilmann, T.; Schmidt, P. S.; Hinsche, N. F.; Gjerding, M. N.; Torelli, D.; Larsen, P. M.; Riis-Jensen, A. C.; et al. The Computational 2D Materials Database: High-throughput Modeling and Discovery of Atomically Thin Crystals. *2D Mater.* **2018**, *5*, No. 042002.
- (47) Mounet, N.; Gibertini, M.; Schwaller, P.; Campi, D.; Merkys, A.; Marrazzo, A.; Sohier, T.; Castelli, I. E.; Cepellotti, A.; Pizzi, G.; et al. Two-Dimensional Materials from High-Throughput Computational Exfoliation of Experimentally Known Compounds. *Nat. Nanotechnol.* **2018**, *13*, 246–252.
- (48) Ma, Y.; Dai, Y.; Wei, W.; Li, X.; Huang, B. Emergence of Electric Polarity in BiTeX (X = Br and I) Monolayers and the Giant Rashba Spin Splitting. *Phys. Chem. Chem. Phys.* **2014**, *16*, 17603–17609.

8.8 Paper VIII

Classifying the Electronic and Optical Properties of Janus Monolayers

A. C. Riis-Jensen, T. Deilmann, T. Olsen, and K. S. Thygesen

ACS Nano, **13**, 11, 13354-13364 (2019)

Reproduced with permission from ACS Nano, **13**, 11, 13354-13364 (2019) © Copyright 2019 American Chemical Society.

<https://pubs.acs.org/doi/abs/10.1021/acsnano.9b06698>

Classifying the Electronic and Optical Properties of Janus Monolayers

Anders C. Riis-Jensen,^{*,†} Thorsten Deilmann,^{*,†,‡} Thomas Olsen,[†] and Kristian S. Thygesen^{†,§}

[†]Computational Atomic-scale Materials Design (CAMD), Department of Physics, Technical University of Denmark, DK-2800 Kongens Lyngby, Denmark

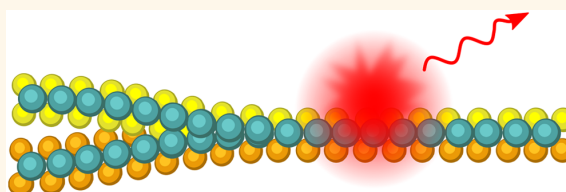
[‡]Institut für Festkörperteorie, Westfälische Wilhelms-Universität Münster, 48149 Münster, Germany

[§]Center for Nanostructured Graphene (CNG), Technical University of Denmark, DK-2800 Kongens Lyngby, Denmark

S Supporting Information

ABSTRACT: Inspired by the recent synthesis of monolayer MoSSe, we conduct a first-principles high-throughput investigation of 216 MXY Janus monolayers consisting of a middle layer of metal atoms (M) sandwiched between different types of chalcogen, halogen, or pnictogen atoms (X,Y). Using density functional theory and many-body perturbation theory, we perform an exhaustive computational characterization of the 70 most stable semiconducting monolayers. These are found to exhibit diverse and fascinating properties including finite out-of-plane dipoles, giant Rashba-splittings, direct and indirect band gaps ranging from 0.7 to 3.0 eV, large exciton binding energies, and very strong light–matter interactions. The data have been generated using the workflow behind the Computational 2D Materials Database and are freely available online. Our work expands the class of known Janus monolayers and points to several potentially synthesizable structures, which could be interesting candidates for valley- or optoelectronic applications or for generating out-of-plane electric fields to control charge transfer, charge separation, or band alignments in van der Waals heterostructures.

KEYWORDS: two-dimensional materials, Janus monolayers, optical properties, electronic properties, excitons, dipole moment



Two-dimensional (2D) semiconductors composed of a single or few layers of covalently bonded atoms exhibit interesting physical properties including layer-dependent band gaps,^{1,2} spin-valley coupling,^{3,4} and strong light–matter interactions^{5,6} dominated by significant excitonic effects.^{7–11} The extreme thinness of these materials makes them highly susceptible to their environment opening up for easy tunability of their properties *via* strain,^{12,13} external fields,^{14–16} or by varying the dielectric environment.^{17,18} The possibility of stacking different 2D layers into van der Waals heterostructures opens further prospects for designing artificial structures with tailored properties.^{19,20}

While the field of 2D materials has long been dominated by graphene, boron-nitride, and the transition-metal dichalcogenides (TMDCs), more recently other types of materials have caught the attention of the community. These include the MXenes (metal-nitrides and -carbides),²¹ metal halides such as the ferromagnetic CrI₃,²² and the monolayers MoSSe and BiTeI with finite out-of-plane dipole moments,^{23–25} which are the subject of the current paper. To date, more than 50 materials have been synthesized in monolayer form,²⁶ but computational studies suggest that many hundreds of known layered bulk crystals can be exfoliated to the single-layer limit.^{27–29} One such database of 2D materials is the

Computational 2D Materials Database (C2DB), which is based on a comprehensive workflow for characterizing the stability and basic properties of hypothetical monolayers.²⁶

Ferroelectric materials are interesting for a number of reasons. For example, the internal electric field in such materials can lead to a staggered band gap profile producing 2D confined electron gases at the surface of a ferroelectric insulator,^{30,31} or it can be used to separate electron–hole pairs in photovoltaic systems.^{32,33} In bulk crystals, the spontaneous polarization is typically driven by the displacement of an ion away from a high-symmetry position. Due to the relatively small energy gain associated with this symmetry breaking, conventional ferroelectrics lose their polarization above a certain phase transition temperature and become paraelectric. In contrast, in the recently synthesized MoSSe and the exfoliated BiTeI monolayers, the finite dipole is not associated with a spontaneous symmetry breaking but is a property of the structure independent of temperature. Theoretical studies have indicated that Janus monolayers could be useful as structural phase transition materials,³⁴ for photocatalytic water split-

Received: August 23, 2019

Accepted: October 15, 2019

Published: October 15, 2019

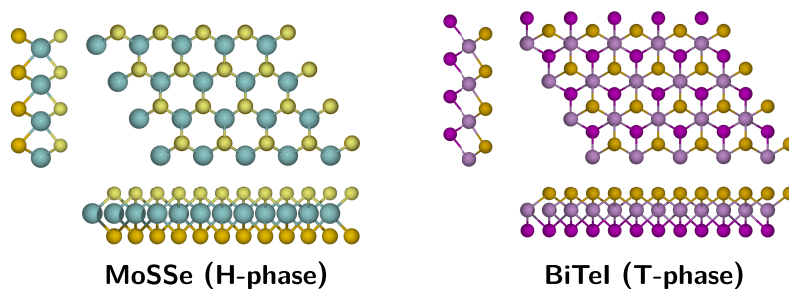


Figure 1. Two types of MXY Janus monolayers considered in this work: MoSSe (left) and BiTeI (right).

ting,³⁵ and for combined in-plane/out-of-plane piezoelectricity.³⁶ In addition, they could facilitate a number of interesting effects when stacked into multilayers or combined with other 2D materials. For example, the large intrinsic dipole could be used to separate intralayer excitons into interlayer excitons,³⁷ move charges between different layers of a heterostructure,^{38,39} or tune band alignment and Schottky barriers at interfaces.

In this paper, we perform a systematic investigation of MXY Janus structures in the crystal structures of MoSSe (H-phase) and BiTeI (T-phase). Following the workflow developed for the C2DB, we first evaluate the thermodynamic and dynamic stability of the materials and next compute the magnetic, elastic, electronic, and optical properties of the 70 most stable materials exhibiting a finite band gap. Due to the known limitations of density functional theory (DFT), we employ the G_0W_0 self-energy method to obtain quasiparticle band structures and the Bethe–Salpeter equation (BSE) for optical excitations. We provide an overview of our results including a discussion of some structure–property relations, a classification of the materials’ electronic properties, and a more in-depth description of a few representative materials. All results are available in the C2DB and can be browsed online or directly downloaded (<https://cmr.fysik.dtu.dk/c2db/c2db.html>).

RESULTS

We consider MXY Janus monolayers in the crystal structures of the experimentally realized MoSSe²³ and BiTeI²⁵ monolayers, respectively. The two structures are shown in Figure 1. Due to the lack of mirror symmetry, such structures possess a macroscopic dipole moment in the out-of-plane direction. The size of the dipole will depend on various factors, but as we will see, it correlates strongly with the difference in electronegativity of the X and Y atoms.

Hypothetical MXY Janus monolayers are produced by decorating the MoSSe and BiTeI prototype crystal structures. For the central M atom, we consider the group IV–V transition-metal atoms (Ti, Zr, Hf, V, Nb, Ta, Cr, Mo, W) as well as the pnictogens (As, Sb, Bi). For the X and Y atoms, we consider the chalcogens (S, Se, Te), halogens (Cl, Br, I), and the pnictogens (As, Sb, Bi). This yields a total of 108 monolayers in each of the two crystal structures. The complete set of considered structures can be deduced from Figures 2 and 3. For these 216 monolayers, various electronic and optical properties are calculated (see Methods section and Figure 13).

STABILITY

We assess the thermodynamic stability of the monolayers from their energy above the convex hull, E_{hull} . The convex hull is a

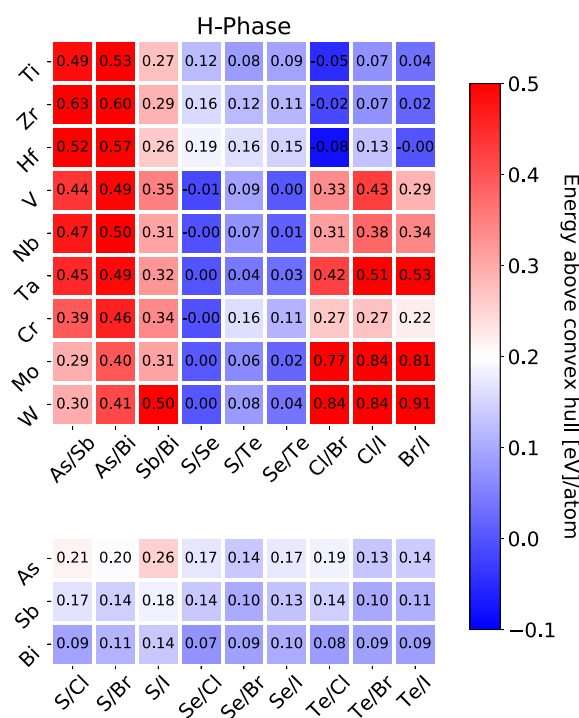


Figure 2. Thermodynamic stability of the H-phase for different MXY Janus monolayers. The colors denote the energy above the convex hull in eV/atom.

phase diagram representing the energy of the most stable (possibly mixed) phase of the material as a function of the stoichiometry. If a hypothesized material lies above the convex hull, that is, if $E_{\text{hull}} > 0$, the material is thermodynamically unstable and will eventually decompose into other phase(s), if it can be synthesized at all. In the current work, the convex hull is constructed from the 2836 most stable binary bulk compounds obtained from the OQMD database.⁴⁰ The total energies of these bulk structures were calculated with the PBE exchange–correlation functional using the GPAW code with the same settings as applied for the Janus monolayers. The calculated energy above convex hull per atom, E_{hull} , for the 216 MXY Janus monolayers is shown in Figures 2 and 3.

In general, the variation in E_{hull} with the type of atoms is much larger than the difference between the two crystal phases, that is, for a given MXY composition, the difference in energy between the two phases is relatively small. The most stable structures are found for: (1) H-phase with M a group V–VI

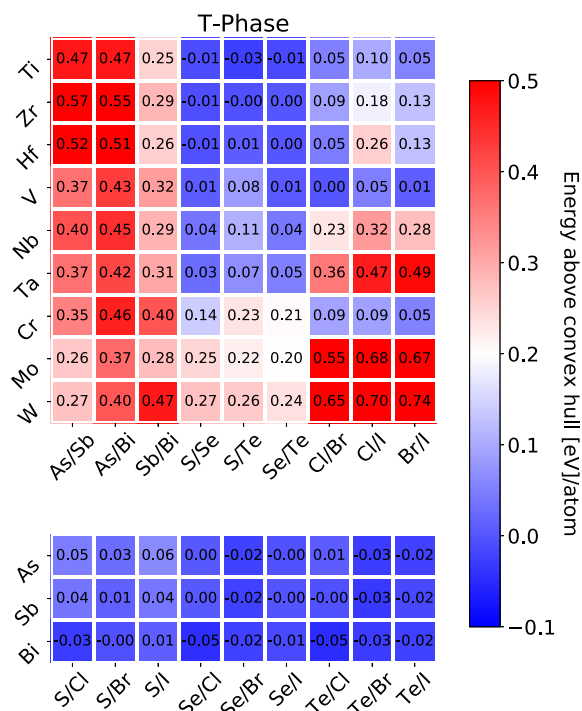


Figure 3. Same as Figure 2, but for the T-phase.

transition metal and both X and Y a chalcogen, (2) H-phase with M a group IV transition metal and both X and Y a halogen, (3) T-phase with M a pnictogen and X/Y a chalcogen/halogen, and (4) T-phase with M a group IV–V transition metal and both X and Y a chalcogen.

To test for dynamical stability, we calculate the elastic coefficients and the phonons at the Γ -point and the corner points of the BZ. Only materials with positive elastic coefficients and no imaginary phonon frequencies are considered stable.

The combined criteria of $E_{\text{hull}} < 0.2$ eV/atom, real phonon frequencies (at high symmetry points) and positive elastic constants, reduces the original set of 216 materials to 93. Out of these, 70 are nonmagnetic and have a finite PBE band gap. These materials are listed in Tables 1 and 2 in appendix A (see Supporting Information), where we list various properties such as PBE, HSE, and GW band gaps, electron and hole effective masses, BSE exciton binding energies, and the vacuum level shift across the monolayers. These 70 monolayers will be discussed further in the following section.

OUT-OF-PLANE DIPOLE

As already mentioned, the lack of mirror symmetry in the Janus structures leads to a finite out-of-plane dipole moment. Because of the difference in electronegativity between the X and Y atoms, charge will be transferred across the metal layer creating an out-of-plane dipole moment. The size of the dipole can be quantified by the shift in the vacuum level on the two sides of the layer, see Figure 4. We note that because of the dipole-induced potential step, the vacuum level on the two sides of the monolayer will in general be different. We choose to reference the band edge energies to the average value of the asymptotic potential on the two sides of the monolayer.

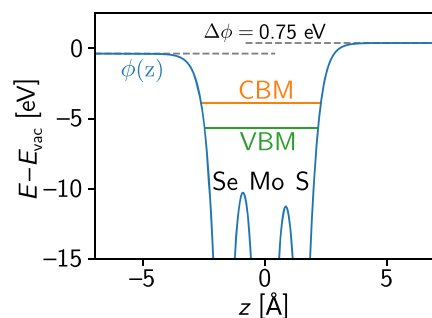


Figure 4. Averaged electrostatic potential, $\phi(z)$, (blue) compared to the vacuum level for H-MoSSe. Between $+z$ and $-z$, a jump in the potential of around 0.75 eV is observed as a consequence of the out-of-plane dipole moment. In green and orange, the VBM and the CBM are indicated.

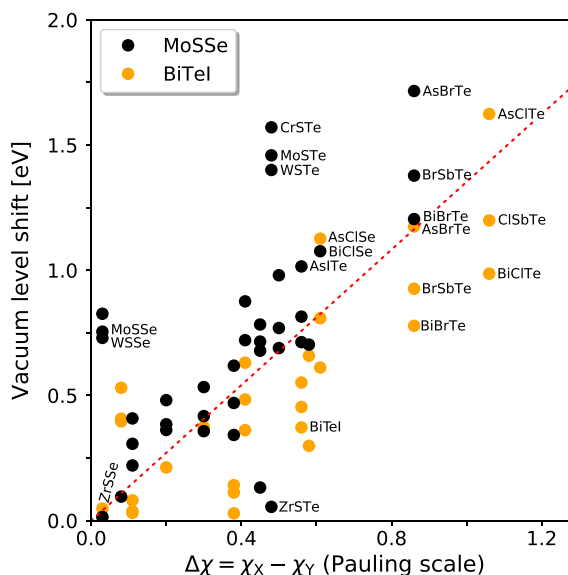


Figure 5. Correlation between the electronegativity difference of X and Y and out-of-plane dipole quantified by the vacuum level shift (see Figure 4). The results for the H-phase (T-phase) are shown in black (orange), and the red line is linear fit with a slope of about 1.35 eV/ $\Delta\chi$ (Pauling scale).

Combined with the size of the potential step (vacuum level shift), this allows to obtain the band energies relative to the vacuum level on either side of the monolayer. Not unexpectedly, the size of the dipole (or equivalently the vacuum level shift) correlates with the difference in electronegativity of the X and Y atoms ($\Delta\chi$), see Figure 5. Pronounced exceptions from this trend occur for, for example, ZrSeTe and ZrSbTe, which have very similar vacuum level shift despite a significant $\Delta\chi$ of 0.5. These deviations suggest that other attributes, such as interatomic distances, the electronegativity of the M atom, and the specific interatomic wave function overlaps, also influence the size of the resulting dipole.

Figure 5 also reveals a wide range of vacuum level shifts possessed by the Janus monolayers, ranging from essentially 0 eV to around 1.8 eV. The wide range of dipoles makes the Janus monolayers ideal for applications in van der Waals

heterostructure-based devices where they could be used to set up internal fields of varying strength to control charge transfer, charge separation, and band alignment.

In the following two sections we provide an overview of the electronic and optical properties of the 70 stable and semiconducting MXY Janus monolayers identified in the previous section. By necessity the discussion will focus on general trends and classifications of the qualitative features. A few band structures and optical spectra will be discussed for specific representative materials, and we refer the interested reader to the C2DB where all data are available.

ELECTRONIC BAND STRUCTURES

Before focusing on the 70 stable semiconductors, we give an overview of the band structure of all the 216 Janus monolayers

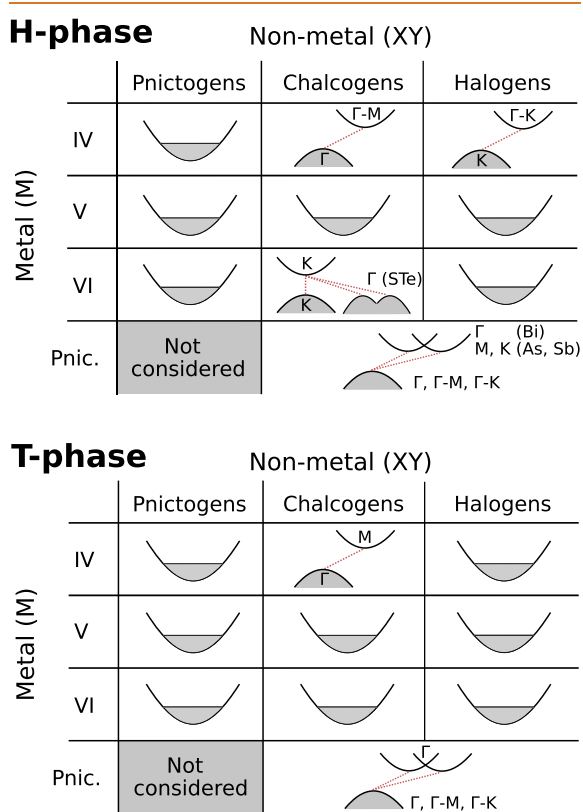


Figure 6. Qualitative classification of the band structure of MXY Janus monolayers in the H-phase (top) and T-phase (bottom). We classify the electronic properties of the MXY monolayers by if they are found to be metallic or semiconducting. For the semiconducting materials, we further state at which high-symmetry point or high-symmetry path the band extrema are located. This is done based on the combination of M (vertical axis) and XY (horizontal) atoms. The classification is based on the PBE band structure omitting the few magnetic materials.

(excluding the few magnetic compounds). By manual inspection, we have found that the qualitative features of the PBE band structures, with very few exceptions, can be classified according to the group of the M and X/Y elements as shown in Figure 6. The plot is divided into the H-phase (top) and the T-phase (bottom). Notice that the bottom rows refer to

structures with mixed chalcogens and halogens for the XY atoms, that is, a chalcogen on one side on the M layer and a halogen on the other side. The matrix plot first of all shows whether the monolayer is metallic or semiconducting for a certain combination of M and XY atoms. For the semiconductors, it is further indicated whether the valence band maximum (VBM) and conduction band minimum (CBM) are located at a high-symmetry point or a high-symmetry path. Materials belonging to the last row are found to exhibit a Rashba split conduction band, while H-phase monolayers with group VI metals in combination with S and Te are found to exhibit a Rashba split VBM (see below for a more detailed discussion). The classification holds for the vast majority of materials, with a few exceptions that we return to below.

The greater part of 216 monolayers are found to be metallic. On the other hand, among the 93 stable materials, only 23 are metals (7 in the H-phase and 16 in the T-phase among which 7 are ferromagnetic), while 70 are semiconducting. The semiconducting structures in the H-phase are found among four combinations of M and XY atoms, while T-phase structures are semiconducting for only two combinations of M and XY atoms. A direct band gap is only found for the H-phase when the M atom is a group VI transition-metal atom (Cr, Mo, W) and XY are chalcogen atoms, except for structures of the form MSeTe. A close to direct band gap is also found in a few cases, namely for structures where M is a pnictogen atom (last row in Figure 6). These structures are, however, subject to a considerable Rashba splitting close to the CBM, and in the H-phase, the position of CBM depends on the nature of the M atom.

There are a few exceptions to the classification found in Figure 6. In both the H- and T-phase with a group IV transition-metal atom and X,Y both chalcogen atoms, some of the structures are found to be semi-metallic with PBE but open a band gap with the HSE functional. These structures are H-HfSTe, H-TiSTe, H-TiSeTe, T-HfSTe, T-HfSeTe, and T-ZrSTe. When the HSE functional is used, the band structures follow the classification in Figure 6. Because the workflow classifies the materials as metals/nonmetals on the basis of the PBE band structure (see Figure 13), these materials are treated as metals, and consequently the G_0W_0 band structure and BSE absorption spectrum have not been calculated. T-TiSTe and T-TiSeTe are predicted to be semi-metallic by both PBE and HSE.

RASHBA SPLITTING

The Rashba effect is a momentum-dependent splitting of the spin band structure in the vicinity of a band extremum. It occurs as a result of spin-orbit coupling in systems lacking an inversion center, most notably in 2D systems with broken mirror symmetry such as surfaces, interfaces, or 2D Janus structures, but has also been observed in bulk crystals such as the layered van der Waals crystal BiTeI.⁴¹ The spin-orbit coupling leads to a splitting of the spin bands by the effective magnetic field, $\mathbf{v} \times \mathbf{E}/c^2$, seen by an electron moving with velocity \mathbf{v} in an electric field, $\mathbf{E}(\mathbf{r})$. In reality, the total electric field has a complex spatial variation on a subatomic length scale. However, the prevailing (over)simplified picture of the Rashba effect, neglects the microscopic details of \mathbf{E} and simply replaces it by a constant out-of-plane polarized field. While this model captures the qualitative features of the Rashba splitting, we show below that it is completely unable to provide a quantitative description.

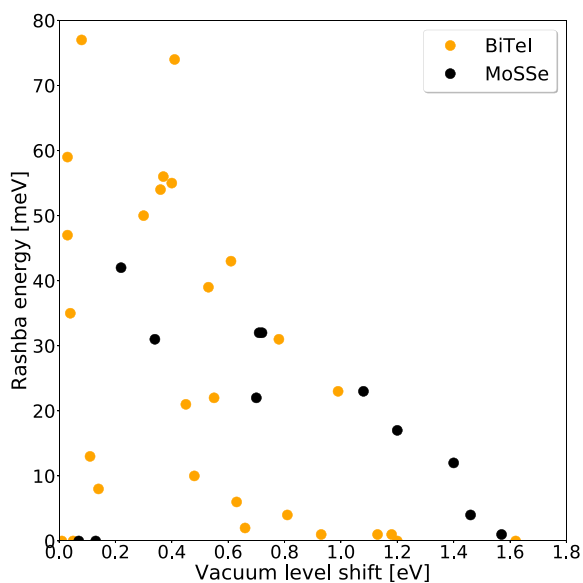


Figure 7. Vacuum level shift (x -axis) against the Rashba energy (y -axis).

Close to an (isotropic) band extremum, the Rashba-split spin bands take the form

$$\varepsilon_{nk} = \frac{\hbar^2}{2m^*} k^2 \pm \alpha k \quad (1)$$

where α is the Rashba coupling parameter which quantifies the strength of the effect. The Rashba coupling parameter is related to the energy and momentum shift of the spin bands via $\alpha = 2E_R/k_R$. In Tables I and II in the Supporting Information, we list E_R and k_R for the Janus monolayers where a notable Rashba splitting is found at either the VBM or CBM.

We find values up to 77 meV for E_R and $82 \text{ m}\text{\AA}^{-1}$ for k_R . For monolayer BiTeI, we find $E_R = 56 \text{ meV}$, which is about half of the measured value of bulk BiTeI.⁴¹ For the VBM, we find Rashba coupling parameters in the range 5–30 meV \AA in good agreement with previous calculated values for H-phase TMDC Janus structures.⁴² For the CBM, we find similar values for most monolayers and much larger values for some monolayers (e.g., T-AsISe, T-BiISe, T-BiTe, T-SbISe, T-SbIS, and T-SbITe) ranging up to some hundreds meV \AA .

In Figure 7 we show that there is absolutely no correlation between the Rashba energy, E_R , and the size of the vacuum level shift. The latter is proportional to the out-of-plane dipole and thus the averaged out-of-plane electric field inside the monolayer. This clearly demonstrates the quantitative limitations of the simple Rashba model. Furthermore, in Figure S1 in the Supporting Information, we show that there is only very weak correlation between E_R and the strength of the spin–orbit coupling (here quantified by the shift of the band edge energy induced by the spin–orbit coupling). These findings underline the complex nature of the Rashba effects.

EXAMPLES OF BAND STRUCTURES

As representatives for H-phase group VI-chalcogen and group IV-halogen MXY monolayers, we show in Figure 8 the band structures of H-WSSe (left panel) and H-TiClI (right panel). We note in passing that all band structures include spin–orbit coupling. The band structure of WSSe is similar to the well-known TMDCs, while TiClI hosts a characteristic flat valence band separated from lower-lying occupied bands. Our PBE results (gray lines) are compared to G_0W_0 (orange symbols), and the band energies are aligned to the vacuum level defined as the average of the vacuum level on the two sides of the layer. As expected, we find a distinct opening of the gaps in G_0W_0 emphasizing the previously found important role of many-body effects in 2D materials.^{5,43} For WSSe, the direct gap at K opens from 1.40 eV (PBE) to 2.33 eV (G_0W_0).

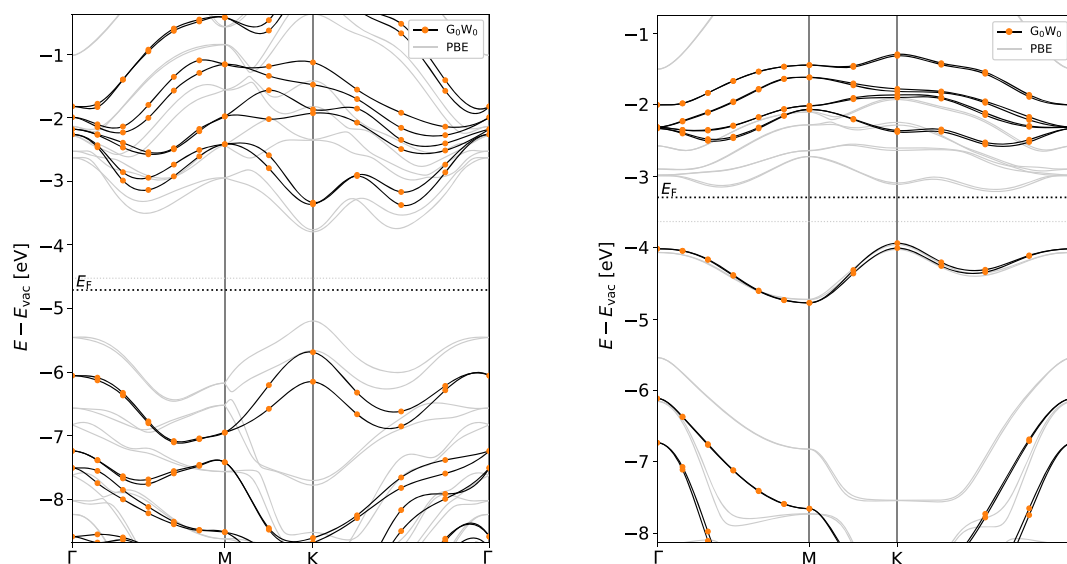


Figure 8. Band structure of H-WSSe (left panel) and H-TiClI (right panel). All energies are referenced to the vacuum level defined as the average of the asymptotic potential on the two sides of the monolayer, see Figure 4. The orange dots and black interpolated lines show the G_0W_0 results, while the gray lines show the PBE result.

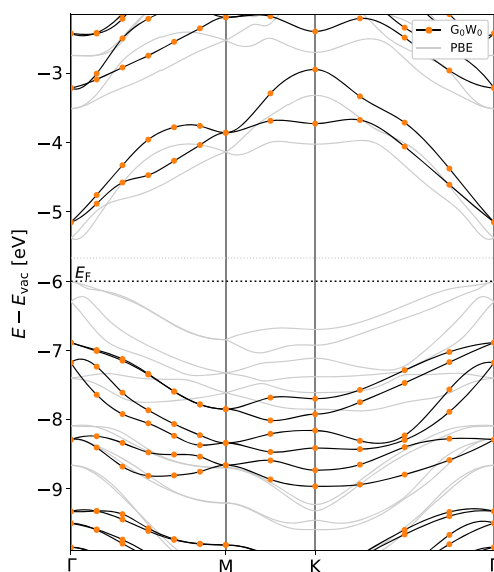


Figure 9. Same as in Figure 8, but for T-BiClTe.

While G_0W_0 produces an almost symmetric shift in opposite directions of the occupied and unoccupied states in WSSE, the situation is very different for TiClI where the intermediate occupied band at around -4 eV is almost unchanged by the G_0W_0 self-energy. We speculate that this is a result of the orbital character of the intermediate band wave function, which contains almost equal amounts of Cl/I p states, which are mostly occupied, and Ti d states, which are mostly unoccupied.

In Figure 9, we show the band structure of BiClTe in the T-phase. Both PBE and G_0W_0 predict a direct gap of 0.64 and 1.74 eV, respectively. However, in contrast to the H-phase group VI-chalcogens discussed above, the direct gap resides at Γ rather than K. Furthermore, we note that the G_0W_0 correction to the PBE bands is rather asymmetric: While the valence bands shift down by about 0.9 eV, the conduction bands shift up by only 0.3 eV. While the valence band at Γ is doubly degenerate with light and heavy hole masses of $0.24m_0$ and $0.31m_0$, respectively, the conduction band has a Mexican hat-like shape due to a Rashba effect driven by the combination of strong spin-orbit coupling and lack of inversion symmetry. This behavior is not reproduced by the

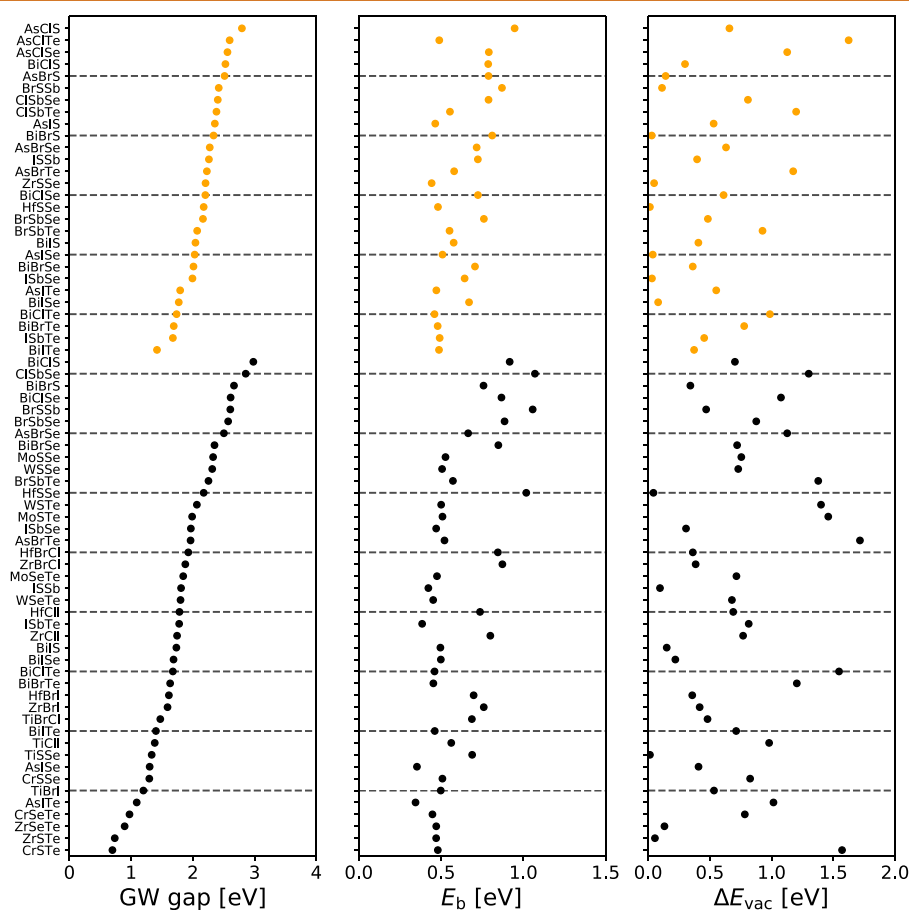


Figure 10. Band gaps (from G_0W_0), exciton binding energies (from BSE), and vacuum level shifts across the monolayer for the 70 MX₂ Janus monolayers found to be stable, nonmagnetic, and nonmetallic. Results for the H-phase and T-phase are shown in black and orange, respectively.

G_0W_0 calculation due to the interpolated nature of the band structure.

Figure 10 shows the distribution of the G_0W_0 band gaps of all 70 MX₂ monolayers. As is the case for the out-of-plane dipole, the band gap size shows rather large variation ranging from 0.7 to 3.0 eV.

OPTICAL ABSORPTION AND EXCITONS

One of the most distinctive characteristics of 2D semiconductors is their strong interaction with light.⁴⁴ This effect

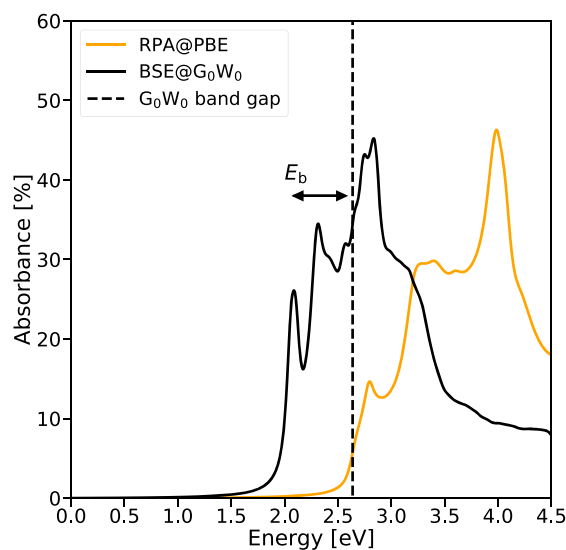


Figure 11. Optical absorbance of AsBrTe in the T-phase. The RPA (orange) is compared to the BSE spectrum that accounts for excitonic effects (black). The vertical line denotes the direct band gap obtained from G_0W_0 .

arises from the localized nature of the electronic states in one direction (quantum confinement) in combination with the weak dielectric screening, which leads to strongly bound electron–hole pairs (excitons) with large oscillator strengths.^{5,6} Specifically for the TMDCs, the optical properties also include spin-valley selective excitation of electron–hole pairs by means of circularly polarized light.^{3,4} However, exploitation of this feature, for example, for valleytronics,⁴⁵ is currently limited by intervalley scattering that reduces the lifetime and mean free path of valley-labeled excitons. Due to the similarity with the TMDCs, both in terms of atomic and electronic structure, some of the MX₂ Janus monolayers might also display spin-valley coupling and thus could become interesting candidates for valleytronics applications.

Here we explore some basic optical and excitonic properties of the 70 stable, semiconducting MX₂ Janus monolayers. Specifically, we calculate the optical absorbance spectrum (essentially the imaginary part of the polarizability) within the random phase approximation (RPA) and the BSE, respectively.⁵ The BSE calculations are performed using the PBE wave functions and energies with a scissors operator correction of the PBE band gap to match the G_0W_0 gap. Spin–orbit coupling is fully included. For more details on the calculations, we refer to ref 26.

In Figure 11 we show, as an example, the optical absorbance spectrum of AsBrTe in the T-phase as calculated with the RPA

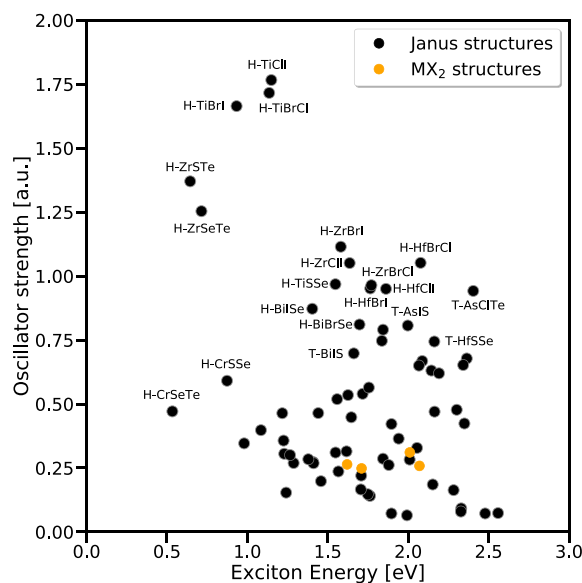


Figure 12. Oscillator strength of the lowest lying exciton peak as a function of the energy of the exciton energy. The oscillator strength has been normalized by the unit cell area. For reference, the orange dots represent the well-known TMDCs MoS₂, MoSe₂, WS₂, and WSe₂.

and BSE methods, respectively. The absorbance, that is, the percentage of incoming light absorbed by the monolayer, can be obtained from the 2D polarizability, α_{2D} , according to $Abs(\omega) = 4\pi\omega\alpha_{2D}(q \rightarrow 0, \omega)/c$, where c is the speed of light. Due to the weak dielectric screening in (freestanding) 2D materials, the RPA spectrum resembles closely the single-particle result which reads

$$\alpha_{2D}(q \rightarrow 0, \omega) = \frac{1}{N_k A \omega^2} \sum_{k \in BZ} \sum_n^{\text{occ}} \sum_{n'}^{\text{unocc}} |\langle \chi_{kn} | \hat{p}_x | \chi_{kn'} \rangle|^2 \delta(\omega - \epsilon_{kn} + \epsilon_{kn'}) \quad (2)$$

where N_k is the number of k -points, A is the area of the in-plane unit cell, and χ denotes spinor wave functions, and we have assumed normal incident light polarization along the x -axis. The BSE spectrum takes a similar form, except that the single-particle matrix elements and energy differences are replaced by their many-body analogues obtained by diagonalizing the two-particle BSE Hamiltonian.

Above the direct quasiparticle (QP) gap of 2.64 eV the RPA spectrum exhibits a number of peaks arising from groups of transitions in the QP band structure with similar energy. Interestingly, the absorbance reaches 10% close to the band gap and exceeds 40% at 4 eV. These high absorption rates are a consequence of the 2D confinement and the similar orbital character of the conduction and valence bands (which both consists of mainly Te and Br p orbitals) giving rise to large oscillator strengths.

Compared to RPA, the BSE spectrum shows a distinct red shift of the excitation energies due to the attractive electron–hole interaction. In particular, strong excitonic peaks appear below the band gap with a binding energy of the lowest exciton of around 0.6 eV. The formation of a correlated excitonic state is associated with a significant increase in oscillator strength resulting in an absorbance exceeding 25%, which dwarfs the absorbance strength of excitons in the TMDCs.

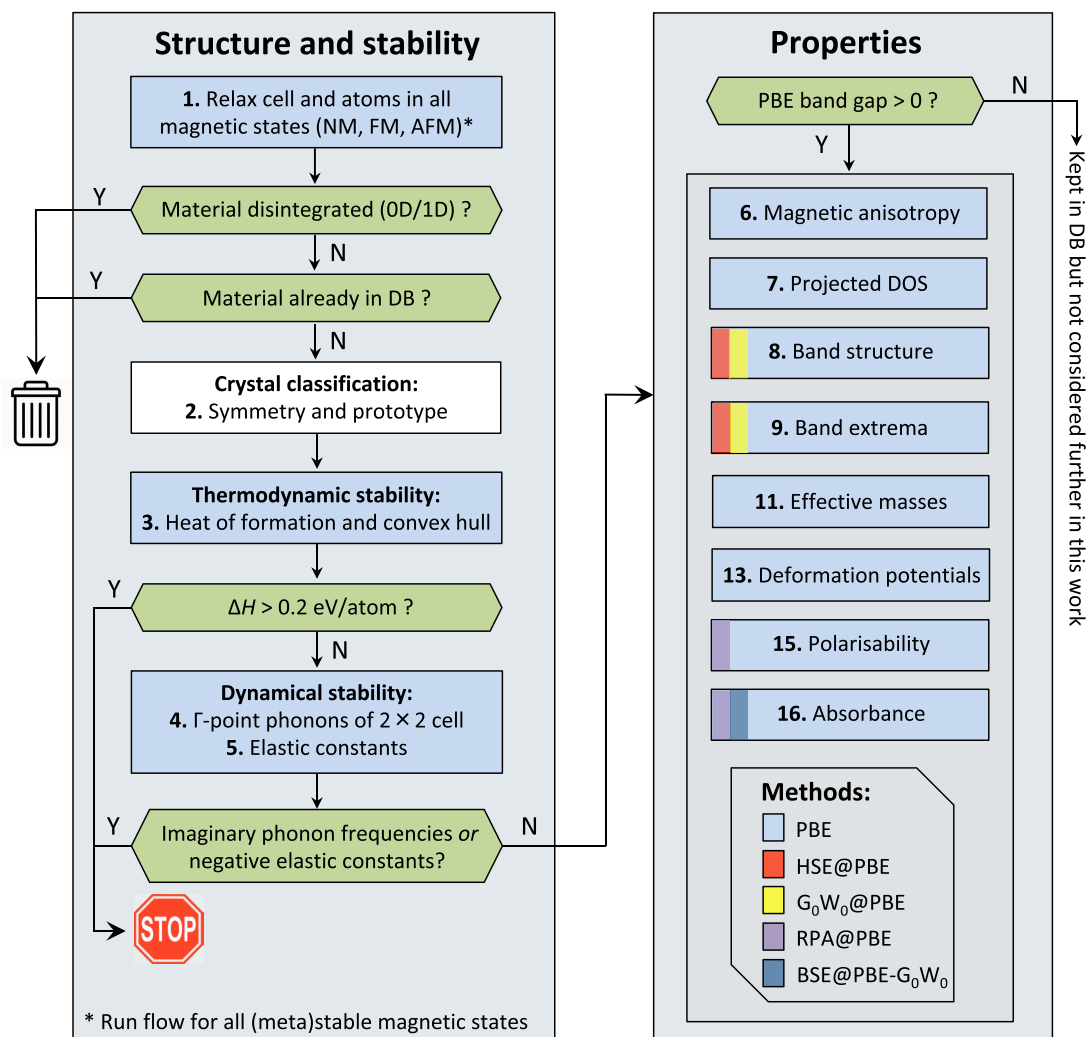


Figure 13. Workflow used to calculate the structure and properties of semiconducting Janus monolayers. Adapted with permission from ref 26. Copyright 2018 IOP Publishing.

An overview of the exciton binding energies, defined as the difference between the direct QP band gap and the lowest eigenvalue of the BSE Hamiltonian, for the 70 semiconducting Janus monolayers can be seen in Figure 10. The values range from 0.3 and 1.0 eV with a tendency of large exciton binding energies to be correlated with large QP band gaps. Such correlations have been observed before and can be explained by an approximate scaling of E_B with the effective dielectric constant of the 2D material, which in turn is inversely proportional to the band gap.^{46,47}

Finally, we consider the oscillator strengths of the lowest excitonic transitions. The oscillator strength is defined as $|\langle 0 | \hat{p}_x | \Psi_{ex} \rangle|^2$, where $|0\rangle$ is the ground state, $|\Psi_{ex}\rangle$ is the lowest bright exciton, and \hat{p}_x is the x components of the momentum operator. In Figure 12 the oscillator strength is plotted against the corresponding exciton energy for the 70 Janus monolayers. For reference, the orange dots represent the well-known TMDCs MoS_2 , $MoSe_2$, WS_2 , and WSe_2 . For several of the Janus structures, the lowest exciton couples significantly stronger to light than is the case for the TMDCs. We find

that strong exciton absorbance is most pronounced for Janus structures containing group IV transition metals (Ti and Zr). For these structures, the valence and conduction bands are both located mainly on the d-orbitals of the transition metal, similar to the well-known TMDCs. We ascribe the strong exciton absorbance in these materials to an unusually high joint density of states (JDOS) around the Γ -point of the BZ. In the group IV compounds, these transitions are located just above the direct band gap and lead to the formation of a highly localized (in real space) and strongly bound exciton. This is in contrast to group V and VI transition-metal MXY and MX_2 structures. For these structures, we also find a high JDOS around the Γ -point but at energies much higher than the direct band gap leading to the formation of the well-known strong C-exciton situated just above the band gap. We note that the extraordinary strong exciton oscillator strength observed for some of the Janus monolayers should not be directly attributed to the lack of mirror symmetry. Indeed, similar absorbance strengths are found for other MX_2 structures containing group IV transition metals, such as PtS_2 (see ref 26).

CONCLUSIONS

In summary, we have performed a systematic computational study of 216 MXY Janus monolayers lacking mirror symmetry. For the 70 most stable materials with a finite band gap, we performed detailed DFT and many-body calculations for the basic electronic and optical properties. The characterizing property of the Janus monolayers is the existence of a finite out-of-plane dipole moment giving rise to a difference in the electrostatic potential on the two sides of the layer. We found that these shifts can be substantial, reaching 1.8 eV for some of the materials. We envision that such layers can be used to set up and control large out-of-plane electric fields inside van der Waals heterostructures. It was found that the band structures of the Janus monolayers can be qualitatively classified according to the groups of the metal (M) and nonmetal (X,Y) atoms. While most combinations yield metallic compounds, the vast majority of the stable materials were found to be semiconducting. The band structures of the 70 most stable and semiconducting monolayers comprise both direct and indirect band gaps ranging from 0.7 to 3.0 eV (from G_0W_0 calculations). A few compounds were found to exhibit Rashba-split valence or conduction bands due to the combination of strong spin-orbit coupling and lack of mirror symmetry. As well-known from other 2D semiconductors, the optical properties of the Janus monolayers are dominated by excitonic effects. The binding energies of the lowest excitons range from 0.3 to 1.0 eV. Interestingly, the lowest excitons in Janus monolayers of group IV metal atoms (Ti and Zr) can exhibit extremely high oscillator strengths (almost 10 times larger than those of the well-known TMDCs), resulting in below-band gap absorbance peaks exceeding 40%. All the data reported in this paper as well as data for other properties not discussed here are available online as part of the Computational 2D Materials Database (C2DB).

METHODS

The workflow used to calculate the properties of the Janus monolayers has been introduced in our previous work.²⁶ It relies on the atomic simulation environment (ASE)⁴⁸ and the electronic structure code GPAW.⁴⁹ The part of the workflow relevant for semiconducting materials, on which we focus in the present work, is shown in Figure 13. In the first part of the workflow (left section), we relax the unit cell and atomic positions, check whether the 2D sheet has disintegrated during relaxation, and whether it is already contained in the database. Next, we classify the material according to crystal symmetries and occupied Wyckoff sites and calculate the heat of formation relative to the standard states of its elements and the energy above the convex hull, E_{hull} . The latter represents the energy relative to other competing bulk phases. In order to account for inaccuracies in the PBE total energy and possible substrate stabilizing effects, we consider materials to be thermodynamically stable if $E_{\text{hull}} < 0.2$ eV/atom. We stress that a criterion of $E_{\text{hull}} < 0.2$ eV/atom is rather conservative and will most likely generate false positives, that is, materials that may not be stable or synthesizable in reality.⁵⁰ On the other hand, with a more stringent stability criterion, we run the risk of missing interesting candidates that might be stable in reality, for example, due to the finite error bars on the DFT energies or possible stabilization *via* substrate interactions. We stress that the interested user can adjust the threshold value for E_{hull} *via* the C2DB Web site. The dynamical stability is assessed by calculating the elastic tensor and phonon frequencies at high-symmetry points of the Brillouin zone (BZ) (the Γ -point and the corners of the BZ). Materials with a negative stiffness coefficient or one or more imaginary phonon frequencies are deemed dynamically unstable and are not given further consideration.

In the second part of the workflow (right section), we calculate the band structure (at the PBE, HSE, and G_0W_0 level), the direct and indirect band gaps, the position of the band edges relative to the vacuum level and the corresponding k -points in the BZ, the out-of-plane dipole moment, the effective masses, the polarizability (at the RPA@PBE level), and the optical absorption spectrum (at the BSE@ G_0W_0 level). We stress that the workflow calculates additional properties (projected density of states, Born charges, elastic tensor, deformation potentials, piezoelectric tensor, lattice contribution to the polarizability, and Raman spectrum). These properties are available in the C2DB but will not be discussed further in the present work. More details about the calculations including parameter settings can be found in ref 26.

ASSOCIATED CONTENT

Supporting Information

The Supporting Information is available free of charge on the ACS Publications website at DOI: 10.1021/acsnano.9b06698.

In tables I and II, some key electronic and optical properties for the 70 nonmagnetic, stable, and semiconducting MXY Janus monolayers investigated in this work are provided. The two tables report the properties for the T-phase and H-phase structures, respectively (PDF)

AUTHOR INFORMATION

Corresponding Authors

*E-mail: achrii@fysik.dtu.dk.

*E-mail: thorsten.deilmann@wwu.de.

ORCID

Anders C. Riis-Jensen: 0000-0002-4914-5820

Kristian S. Thygesen: 0000-0001-5197-214X

Notes

The authors declare no competing financial interest.

ACKNOWLEDGMENTS

K.S.T. acknowledges funding from the European Research Council (ERC) under the European Union's Horizon 2020 research and innovation program (grant agreement no. 773122, LIMA).

REFERENCES

- (1) Mak, K. F.; Lee, C.; Hone, J.; Shan, J.; Heinz, T. F. Atomically Thin MoS₂: a New Direct-Gap Semiconductor. *Phys. Rev. Lett.* **2010**, *105*, 136805.
- (2) Splendiani, A.; Sun, L.; Zhang, Y.; Li, T.; Kim, J.; Chim, C.-Y.; Galli, G.; Wang, F. Emerging Photoluminescence in Monolayer MoS₂. *Nano Lett.* **2010**, *10*, 1271–1275.
- (3) Xiao, D.; Liu, G.-B.; Feng, W.; Xu, X.; Yao, W. Coupled Spin and Valley Physics in Monolayers of MoS₂ and Other Group-VI Dichalcogenides. *Phys. Rev. Lett.* **2012**, *108*, 196802.
- (4) Jones, A. M.; Yu, H.; Ghimire, N. J.; Wu, S.; Aivazian, G.; Ross, J. S.; Zhao, B.; Yan, J.; Mandrus, D. G.; Xiao, D.; Yao, W.; Xu, X. Optical Generation of Excitonic Valley Coherence in Monolayer WSe₂. *Nat. Nanotechnol.* **2013**, *8*, 634.
- (5) Thygesen, K. S. Calculating Excitons, Plasmons, and Quasiparticles in 2D Materials and van der Waals Heterostructures. *2D Mater.* **2017**, *4*, No. 022004.
- (6) Bernardi, M.; Palummo, M.; Grossman, J. C. Extraordinary Sunlight Absorption and One Nanometer Thick Photovoltaics Using Two-Dimensional Monolayer Materials. *Nano Lett.* **2013**, *13*, 3664–3670.
- (7) Mouri, S.; Zhang, W.; Kozawa, D.; Miyachi, Y.; Eda, G.; Matsuda, K. Thermal Dissociation of Inter-Layer Excitons in MoS₂/MoSe₂ Hetero-Bilayers. *Nanoscale* **2017**, *9*, 6674–6679.

- (8) Luong, D. H.; Lee, H. S.; Neupane, G. P.; Roy, S.; Ghimire, G.; Lee, J. H.; Vu, Q. A.; Lee, Y. H. Tunneling Photocurrent Assisted by Interlayer Excitons in Staggered van der Waals Hetero-Bilayers. *Adv. Mater.* **2017**, *29*, 1701512.
- (9) Wang, K.; Huang, B.; Tian, M.; Ceballos, F.; Lin, M.-W.; Mahjouri-Samani, M.; Boulesbaa, A.; Puzetky, A. A.; Rouleau, C. M.; Yoon, M.; Zhao, H.; Xiao, K.; Duscher, G.; Geohegan, D. B. Interlayer Coupling in Twisted WSe₂/WS₂ Bilayer Heterostructures Revealed by Optical Spectroscopy. *ACS Nano* **2016**, *10*, 6612–6622.
- (10) Ceballos, F.; Bellus, M. Z.; Chiu, H.-Y.; Zhao, H. Probing Charge Transfer Excitons in a MoSe₂-WS₂ van der Waals Heterostructure. *Nanoscale* **2015**, *7*, 17523–17528.
- (11) Ceballos, F.; Ju, M.-G.; Lane, S. D.; Zeng, X. C.; Zhao, H. Highly Efficient and Anomalous Charge Transfer in van der Waals Trilayer Semiconductors. *Nano Lett.* **2017**, *17*, 1623–1628.
- (12) Conley, H. J.; Wang, B.; Ziegler, J. I.; Haglund, R. F., Jr; Pantelides, S. T.; Bolotin, K. I. Bandgap Engineering of Strained Monolayer and Bilayer MoS₂. *Nano Lett.* **2013**, *13*, 3626–3630.
- (13) Li, S.; Sun, M.; Chou, J.-P.; Wei, J.; Xing, H.; Hu, A. First-Principles Calculations of the Electronic Properties of SiC-Based Bilayer and Trilayer Heterostructures. *Phys. Chem. Chem. Phys.* **2018**, *20*, 24726–24734.
- (14) Deilmann, T.; Thygesen, K. S. Interlayer Excitons with Large Optical Amplitudes in Layered van der Waals Materials. *Nano Lett.* **2018**, *18*, 2984–2989.
- (15) Fei, Z.; Rodin, A.; Andreev, G. O.; Bao, W.; McLeod, A.; Wagner, M.; Zhang, L.; Zhao, Z.; Thieme, M.; Dominguez, G.; Fogler, M. M.; Castro Neto, A. H.; Lau, C. N.; Keilmann, F.; Basov, D. N. Gate-Tuning of Graphene Plasmons Revealed by Infrared Nano-Imaging. *Nature* **2012**, *487*, 82.
- (16) Qiu, Z.; Trushin, M.; Fang, H.; Verzhbitskiy, I.; Gao, S.; Laksono, E.; Yang, M.; Lyu, P.; Li, J.; Su, J.; Telychko, M.; Watanabe, K.; Taniguchi, T.; Wu, J.; et al. Giant Gate-Tunable Bandgap Renormalization and Excitonic Effects in a 2D Semiconductor. *Sci. Adv.* **2019**, *5*, No. eaaw2347.
- (17) Latini, S.; Olsen, T.; Thygesen, K. S. Excitons in van der Waals Heterostructures: The Important Role of Dielectric Screening. *Phys. Rev. B: Condens. Matter Mater. Phys.* **2015**, *92*, 245123.
- (18) Chernikov, A.; Berkelbach, T. C.; Hill, H. M.; Rigosi, A.; Li, Y.; Aslan, O. B.; Reichman, D. R.; Hybertsen, M. S.; Heinz, T. F. Exciton Binding Energy and Nonhydrogenic Rydberg Series in Monolayer WS₂. *Phys. Rev. Lett.* **2014**, *113*, No. 076802.
- (19) Geim, A. K.; Grigorieva, I. V. Van der Waals Heterostructures. *Nature* **2013**, *499*, 419.
- (20) Cui, X.; Lee, G.-H.; Kim, Y. D.; Arefe, G.; Huang, P. Y.; Lee, C.-H.; Chenet, D. A.; Zhang, X.; Wang, L.; Ye, F.; Pizzocchero, F.; Jessen, B. S.; Watanabe, K.; Taniguchi, T.; Muller, D. A.; Low, T.; Kim, P.; Hone, J. Multi-Terminal Transport Measurements of MoS₂ Using a van der Waals Heterostructure Device Platform. *Nat. Nanotechnol.* **2015**, *10*, 534.
- (21) Naguib, M.; Mochalin, V. N.; Barsoum, M. W.; Gogotsi, Y. 25th Anniversary Article: MXenes: a New Family of Two-Dimensional Materials. *Adv. Mater.* **2014**, *26*, 992–1005.
- (22) Huang, B.; Clark, G.; Navarro-Moratalla, E.; Klein, D. R.; Cheng, R.; Seyler, K. L.; Zhong, D.; Schmidgall, E.; McGuire, M. A.; Cobden, D. H.; Yao, W.; Xiao, D.; Jarillo-Herrero, P.; Xu, X. Layer-Dependent Ferromagnetism in a van der Waals Crystal Down to the Monolayer Limit. *Nature* **2017**, *546*, 270.
- (23) Lu, A.-Y.; Zhu, H.; Xiao, J.; Chuu, C.-P.; Han, Y.; Chiu, M.-H.; Cheng, C.-C.; Yang, C.-W.; Wei, K.-H.; Yang, Y.; Sokaras, D.; Nordlund, D.; Yang, P.; Muller, D. A.; Chou, M.-Y.; Zhang, X.; Li, L.-J. Janus Monolayers of Transition Metal Dichalcogenides. *Nat. Nanotechnol.* **2017**, *12*, 744–749.
- (24) Zhang, J.; Jia, S.; Kholmanov, I.; Dong, L.; Er, D.; Chen, W.; Guo, H.; Jin, Z.; Shenoy, V. B.; Shi, L.; Lou, J. Janus Monolayer Transition-Metal Dichalcogenides. *ACS Nano* **2017**, *11*, 8192–8198.
- (25) Fülöp, B.; Tajkó, Z.; Pető, J.; Kun, P.; Koltai, J.; Oroszlány, L.; Tóvári, E.; Murakawa, H.; Tokura, Y.; Bordács, S.; Tapasztó, L.; Csonka, S. Exfoliation of Single Layer BiTeI Flakes. *2D Mater.* **2018**, *5*, No. 031013.
- (26) Haastrup, S.; Strange, M.; Pandey, M.; Deilmann, T.; Schmidt, P. S.; Hinsche, N. F.; Gjerding, M. N.; Torelli, D.; Larsen, P. M.; Riis-Jensen, A. C.; Gath, J.; Jacobsen, K. W.; Mortensen, J. J.; Olsen, T.; Thygesen, K. S. The Computational 2D Materials Database: High-Throughput Modeling and Discovery of Atomically Thin Crystals. *2D Mater.* **2018**, *5*, No. 042002.
- (27) Lebegue, S.; Björkman, T.; Klintonberg, M.; Nieminen, R. M.; Eriksson, O. Two-Dimensional Materials from Data Filtering and *Ab Initio* Calculations. *Phys. Rev. X* **2013**, *3*, No. 031002.
- (28) Ashton, M.; Paul, J.; Sinnott, S. B.; Hennig, R. G. Topology-Scaling Identification of Layered Solids and Stable Exfoliated 2D Mater. *Phys. Rev. Lett.* **2017**, *118*, 106101.
- (29) Mounet, N.; Gibertini, M.; Schwaller, P.; Campi, D.; Merky, A.; Marrazzo, A.; Sohier, T.; Castelli, I. E.; Cepellotti, A.; Pizzi, G.; Marzari, N. Two-Dimensional Materials from High-Throughput Computational Exfoliation of Experimentally Known Compounds. *Nat. Nanotechnol.* **2018**, *13*, 246.
- (30) Nakagawa, N.; Hwang, H. Y.; Muller, D. A. Why Some Interfaces Cannot Be Sharp. *Nat. Mater.* **2006**, *5*, 204.
- (31) Nazir, S.; Cheng, J.; Yang, K. Creating Two-Dimensional Electron Gas in Nonpolar Oxide Interface *via* Polarization Discontinuity: First-Principles Analysis of CaZrO₃/SrTiO₃ Heterostructure. *ACS Appl. Mater. Interfaces* **2016**, *8*, 390–399.
- (32) Wallace, S. K.; Svane, K. L.; Huhn, W. P.; Zhu, T.; Mitzi, D. B.; Blum, V.; Walsh, A. Candidate Photoferroic Absorber Materials for Thin-Film Solar Cells from Naturally Occurring Minerals: Enargite, Stephanite, and Bournonite. *Sustainable Energy Fuels* **2017**, *1*, 1339–1350.
- (33) Butler, K. T.; Frost, J. M.; Walsh, A. Ferroelectric Materials for Solar Energy Conversion: Photoferroics Revisited. *Energy Environ. Sci.* **2015**, *8*, 838–848.
- (34) Sun, Y.; Shuai, Z.; Wang, D. Janus Monolayer of WSeTe, a New Structural Phase Transition Material Driven by Electrostatic Gating. *Nanoscale* **2018**, *10*, 21629–21633.
- (35) Ma, X.; Wu, X.; Wang, H.; Wang, Y. A Janus MoSSe Monolayer: a Potential Wide Solar-Spectrum Water-Splitting Photocatalyst with a Low Carrier Recombination Rate. *J. Mater. Chem. A* **2018**, *6*, 2295–2301.
- (36) Dong, L.; Lou, J.; Shenoy, V. B. Large In-Plane and Vertical Piezoelectricity in Janus Transition Metal Dichalcogenides. *ACS Nano* **2017**, *11*, 8242–8248.
- (37) Riis-Jensen, A. C.; Pandey, M.; Thygesen, K. S. Efficient Charge Separation in 2D Janus van der Waals Structures with Built-In Electric Fields and Intrinsic *p-n* Doping. *J. Phys. Chem. C* **2018**, *122*, 24520–24526.
- (38) Palsgaard, M.; Gunst, T.; Markussen, T.; Thygesen, K. S.; Brandbyge, M. Stacked Janus Device Concepts: Abrupt *pn*-Junctions and Cross-Plane Channels. *Nano Lett.* **2018**, *18*, 7275–7281.
- (39) Cavalcante, L. S.; Gjerding, M. N.; Chaves, A.; Thygesen, K. S. Enhancing and Controlling Plasmons in Janus MoSSe-Graphene Based Van Der Waals Heterostructures. *J. Phys. Chem. C* **2019**, *123*, 16373.
- (40) Saal, J. E.; Kirklín, S.; Aykol, M.; Meredig, B.; Wolverton, C. Materials Design and Discovery with High-Throughput Density Functional Theory: The Open Quantum Materials Database (OQMD). *JOM* **2013**, *65*, 1501–1509.
- (41) Bahramy, M.; Arita, R.; Nagaosa, N. Origin of Giant Bulk Rashba Splitting: Application to BiTeI. *Phys. Rev. B: Condens. Matter Mater. Phys.* **2011**, *84*, No. 041202.
- (42) Cheng, Y.; Zhu, Z.; Tahir, M.; Schwingschlögl, U. Spin-Orbit-Induced Spin Splittings in Polar Transition Metal Dichalcogenide Monolayers. *Europhys. Lett.* **2013**, *102*, 57001.
- (43) Ugeda, M. M.; Bradley, A. J.; Shi, S.-F.; da Jornada, F. H.; Zhang, Y.; Qiu, D. Y.; Ruan, W.; Mo, S.-K.; Hussain, Z.; Shen, Z.-X.; Wang, F.; Louie, S. G.; Crommie, M. F. Giant Bandgap Renormalization and Excitonic Effects in a Monolayer Transition Metal Dichalcogenide Semiconductor. *Nat. Mater.* **2014**, *13*, 1091.

(44) Britnell, L.; Ribeiro, R.; Eckmann, A.; Jalil, R.; Belle, B.; Mishchenko, A.; Kim, Y.-J.; Gorbachev, R.; Georgiou, T.; Morozov, S.; et al. Strong Light-Matter Interactions in Heterostructures of Atomically Thin Films. *Science* **2013**, *340*, 1311–1314.

(45) Schaibley, J. R.; Yu, H.; Clark, G.; Rivera, P.; Ross, J. S.; Seyler, K. L.; Yao, W.; Xu, X. Valleytronics in 2D materials. *Nat. Rev. Mater.* **2016**, *1*, 16055.

(46) Olsen, T.; Latini, S.; Rasmussen, F.; Thygesen, K. S. Simple Screened Hydrogen Model of Excitons in Two-Dimensional Materials. *Phys. Rev. Lett.* **2016**, *116*, No. 056401.

(47) Jiang, Z.; Liu, Z.; Li, Y.; Duan, W. Scaling Universality Between Band Gap and Exciton Binding Energy of Two-Dimensional Semiconductors. *Phys. Rev. Lett.* **2017**, *118*, 266401.

(48) Larsen, A. H.; Mortensen, J. J.; Blomqvist, J.; Castelli, I. E.; Christensen, R.; Dulak, M.; Friis, J.; Groves, M. N.; Hammer, B.; Hargus, C.; Hermes, E. D.; Jennings, P. C.; Jensen, P. B.; Kermode, J.; Kitchin, J. R.; Kolsbjerg, E. L.; Kubal, J.; Kaasbjerg, K.; Lysgaard, S.; Maronsson, J. B.; et al. The Atomic Simulation Environment—A Python Library for Working with Atoms. *J. Phys.: Condens. Matter* **2017**, *29*, 273002.

(49) Enkovaara, J.; Rostgaard, C.; Mortensen, J. J.; Chen, J.; Dulak, M.; Ferrighi, L.; Gavnholt, J.; Glinsvad, C.; Haikola, V.; Hansen, H. A.; Kristoffersen, H. H.; Kuisma, M.; Larsen, A. H.; Lehtovaara, L.; Ljungberg, M.; Lopez-Acevedo, O.; Moses, P. G.; Ojanen, J.; Olsen, T.; Petzold, V.; et al. Electronic Structure Calculations with GPAW: A Real-Space Implementation of the Projector Augmented-Wave Method. *J. Phys.: Condens. Matter* **2010**, *22*, 253202.

(50) Malý, O. I.; Sopiha, K. V.; Persson, C. Energy, Phonon, and Dynamic Stability Criteria of Two-Dimensional Materials. *ACS Appl. Mater. Interfaces* **2019**, *11*, 24876.

Classifying the Electronic and Optical Properties of Janus Monolayers - Supplementary Information

Anders C. Riis-Jensen,^{*,†} Thorsten Deilmann,^{*,†} Thomas Olsen,[†] and Kristian S.
Thygesen[†]

[†]*CAMD, Department of Physics, Technical University of Denmark, DK-2800 Kongens
Lyngby, Denmark*

[‡]*Institut für Festkörperteorie, Westfälische Wilhelms-Universität Münster, 48149
Münster, Germany*

[¶]*Center for Nanostructured Graphene (CNG), Technical University of Denmark, DK-2800
Kongens Lyngby, Denmark*

E-mail: achrii@fysik.dtu.dk; thorsten.deilmann@wwu.de

Data tables and figures

In tables 1 and 2 we provide some key electronic and optical properties for the 70 non-magnetic, stable, and semiconducting MXY Janus monolayers investigated in this work. The two tables report the properties for the T-phase and H-phase structures, respectively. In figure 1 we show that the Rashba energy only weakly correlates with the amplitude of the spin-orbit coupling for the Rashba split state (see main text for definition).

Table 1: Key electronic and optical properties of MXY Janus monolayers in the T-Phase. The table lists the formula unit, formation energy (E_f) [eV], energy above convex hull (E_{hull}) [eV/atom], PBE band gap ($E_{\text{gap}}^{\text{PBE}}$) [eV], HSE band gap ($E_{\text{gap}}^{\text{HSE}}$) [eV], G_0W_0 band gap ($E_{\text{gap}}^{\text{GW}}$) [eV], nature of the band gap, electron effective mass (m_e), hole effective mass (m_h) [m_{free}], G_0W_0 conduction band minimum ($E_{\text{CBM}}^{\text{GW}}$) [eV], G_0W_0 valence band maximum ($E_{\text{VBM}}^{\text{GW}}$) [eV], exciton binding energy (E_b) [eV], and vacuum level shift across the monolayer (ΔE_{vac}) [eV], Rashba splitting (if present) in the k (k_R) [$\text{m}\text{\AA}^{-1}$] and energy (E_R) [meV] directions. The nature of the Rashba split point is denoted by c (v) for conduction (valence) band and M, K, or G denoting the high symmetry point. Cases where the effective mass could not be determined in a meaningful way because of non-parabolic bands, *e.g.* due to Rashba splitting, are indicated by 'n/a'.

Structure	E_f	E_{hull}	$E_{\text{gap}}^{\text{PBE}}$	$E_{\text{gap}}^{\text{HSE}}$	$E_{\text{gap}}^{\text{GW}}$	Direct gap	m_e	m_h	$E_{\text{CBM}}^{\text{GW}}$	$E_{\text{VBM}}^{\text{GW}}$	E_b	ΔE_{vac}	k_R	E_R
AsBrS	-0.26	0.03	1.39	2.04	2.51	No	n/a	0.62	-4.54	-7.06	0.79	0.14	20(c-G)	8
AsClS	-0.35	0.05	1.54	2.26	2.79	No	n/a	0.78	-4.67	-7.46	0.95	0.66	13(c-G)	2
AsBrSe	-0.29	-0.02	1.23	1.84	2.27	No	n/a	0.5	-4.53	-6.8	0.72	0.63	19(c-G)	6
AsClSe	-0.38	0.0	1.37	2.06	2.56	No	0.87	0.74	-4.63	-7.19	0.79	1.13	7(c-G)	1
AsISe	-0.16	-0.0	1.15	1.68	2.03	No	0.21	n/a	-4.28	-6.31	0.51	0.04	45(c-G)	35
AsIS	-0.11	0.06	1.34	1.95	2.36	No	0.27	0.28	-4.26	-6.61	0.46	0.53	52(c-G)	39
AsBrTe	-0.24	-0.03	1.24	1.84	2.23	No	0.75	0.62	-4.35	-6.58	0.58	1.18	6(c-G)	1
AsClTe	-0.32	0.01	1.48	2.15	2.6	No	0.17	0.94	-4.4	-7.0	0.49	1.62	0	0
AsITe	-0.12	-0.02	0.98	1.5	1.79	No	n/a	0.22	-4.21	-6.01	0.47	0.55	31(c-G)	22
BiBrS	-0.56	-0.0	0.93	1.6	2.34	No	n/a	1.12	-5.34	-7.68	0.81	0.03	73(c-G)	59
BiClS	-0.66	-0.03	1.04	1.74	2.53	No	0.3	1.22	-5.46	-7.99	0.79	0.3	62(c-G)	50
BiBrSe	-0.58	-0.02	0.77	1.36	2.01	No	0.22	0.96	-5.31	-7.32	0.71	0.36	60(c-G)	54
BiClSe	-0.68	-0.05	0.88	1.51	2.2	No	0.2	1.01	-5.38	-7.58	0.72	0.61	48(c-G)	43
BiISe	-0.44	-0.01	0.65	1.22	1.77	No	0.27	0.48	-5.12	-6.89	0.67	0.08	70(c-G)	77
BiIS	-0.41	0.01	0.82	1.47	2.04	No	n/a	0.33	-5.15	-7.19	0.58	0.41	78(c-G)	74
BiBrTe	-0.5	-0.03	0.63	1.16	1.69	No	n/a	0.39	-5.15	-6.84	0.48	0.78	35(c-G)	31
BiClTe	-0.6	-0.05	0.64	1.2	1.74	No	n/a	0.31	-5.15	-6.89	0.46	0.99	29(c-G)	23
BiITe	-0.37	-0.02	0.45	0.93	1.42	No	0.13	0.45	-5.02	-6.44	0.49	0.37	51(c-G)	56
BrSSb	-0.42	0.01	1.22	1.84	2.42	No	n/a	0.71	-4.75	-7.17	0.87	0.11	31(c-G)	13
BrSbSe	-0.44	-0.02	1.07	1.65	2.16	No	n/a	0.7	-4.73	-6.9	0.76	0.48	25(c-G)	10
ClSbSe	-0.54	0.0	1.17	1.8	2.4	No	n/a	0.9	-4.83	-7.24	0.79	0.81	12(c-G)	4
ISbSe	-0.31	-0.0	1.02	1.53	1.99	No	0.27	0.58	-4.44	-6.43	0.64	0.03	54(c-G)	47
ISSb	-0.28	0.04	1.22	1.78	2.26	No	n/a	0.39	-4.41	-6.67	0.72	0.4	67(c-G)	55
BrSbTe	-0.38	-0.03	1.06	1.62	2.07	No	0.58	0.83	-4.53	-6.6	0.55	0.93	6(c-G)	1
ClSbTe	-0.47	-0.0	1.26	1.87	2.38	No	0.16	1.01	-4.55	-6.93	0.55	1.2	0	0
ISbTe	-0.25	-0.02	0.84	1.32	1.68	No	n/a	0.43	-4.4	-6.07	0.49	0.45	29(c-G)	21
ZrSSe	-1.48	-0.01	0.61	1.51	2.21	No	0.41	0.2	-4.64	-6.85	0.44	0.05	0	0
HfSSe	-1.47	-0.01	0.68	1.51	2.18	No	0.31	0.2	-4.69	-6.86	0.48	0.01	0	0

Table 2: Same as table 1 for the H-phase structures.

Structure	E_f	E_{hull}	$E_{\text{gap}}^{\text{PBE}}$	$E_{\text{gap}}^{\text{HSE}}$	$E_{\text{gap}}^{\text{GW}}$	Direct gap	m_e	m_h	$E_{\text{CBM}}^{\text{GW}}$	$E_{\text{VBM}}^{\text{GW}}$	E_b	ΔE_{vac}	k_R	E_R
CrSeTe	-0.27	0.11	0.57	0.99	0.97	Yes	0.99	1.15	-4.28	-5.26	0.45	0.78	0	0
CrSSe	-0.57	-0.0	0.78	1.24	1.29	Yes	0.94	1.01	-4.5	-5.79	0.51	0.83	0	0
CrSTe	-0.32	0.16	0.26	0.82	0.69	No	1.1	5.14	-4.61	-5.31	0.48	1.57	38(v-G)	1
HfBrCl	-1.34	-0.08	0.82	1.36	1.93	No	0.62	0.36	-2.25	-4.18	0.85	0.36	0	0
HfBrI	-0.89	-0.0	0.71	1.16	1.61	No	0.52	0.34	-2.21	-3.82	0.7	0.36	0	0
HfClI	-1.03	0.13	0.81	1.29	1.78	No	0.71	0.41	-2.25	-4.03	0.74	0.69	0	0
HfSSe	-1.28	0.19	0.89	1.64	2.18	No	0.49	0.57	-5.21	-7.38	1.02	0.04	0	0
MoSeTe	-0.48	0.02	1.14	1.59	1.84	Yes	0.56	0.72	-3.18	-5.02	0.48	0.72	0	0
MoSSe	-0.81	0.0	1.45	1.95	2.33	Yes	0.48	0.6	-3.29	-5.62	0.53	0.75	0	0
MoSTe	-0.55	0.06	0.99	1.59	1.99	No	0.66	n/a	-3.41	-5.4	0.51	1.46	67(v-G)	4
TiBrCl	-1.33	-0.05	0.83	1.3	1.47	No	1.27	0.62	-2.62	-4.09	0.69	0.48	0	0
TiBrI	-0.88	0.04	0.68	1.04	1.2	No	1.33	0.59	-2.54	-3.74	0.5	0.53	0	0
TiClI	-1.01	0.07	0.75	1.19	1.38	No	1.49	0.72	-2.55	-3.94	0.56	0.98	0	0
TiSSe	-1.1	0.12	0.51	1.34	1.33	No	1.95	1.12	-5.09	-6.42	0.69	0.01	0	0
WSeTe	-0.32	0.04	1.04	1.49	1.8	Yes	0.56	0.4	-3.28	-5.09	0.45	0.68	0	0
WSSe	-0.72	0.0	1.4	1.91	2.31	Yes	0.43	0.37	-3.37	-5.69	0.51	0.73	0	0
WSTe	-0.42	0.08	1.14	1.68	2.07	No	1.24	n/a	-3.44	-5.5	0.5	1.4	82(v-G)	12
ZrBrCl	-1.51	-0.02	0.91	1.4	1.88	No	0.68	0.43	-2.35	-4.23	0.87	0.38	0	0
ZrBrI	-1.09	0.02	0.77	1.17	1.59	No	0.67	0.42	-2.29	-3.88	0.76	0.42	0	0
ZrClI	-1.23	0.07	0.88	1.32	1.74	No	0.71	0.48	-2.33	-4.07	0.8	0.77	0	0
ZrSeTe	-1.02	0.11	0.26	0.78	0.89	No	n/a	0.74	-4.94	-5.83	0.47	0.13	0	0
ZrSTe	-1.12	0.12	0.21	0.67	0.74	No	n/a	0.65	-4.94	-5.83	0.47	0.06	0	0
BiBrS	-0.44	0.11	1.25	1.98	2.67	No	0.44	0.48	-5.21	-7.87	0.76	0.34	63(c-G)	31
BiClS	-0.54	0.09	1.5	2.27	2.98	No	0.43	0.92	-5.28	-8.26	0.92	0.7	51(c-G)	22
BiClSe	-0.56	0.07	1.29	1.99	2.61	No	0.28	0.51	-5.21	-7.82	0.87	1.08	44(c-G)	23
BiIS	-0.29	0.14	0.45	1.18	1.73	No	0.31	0.26	-5.1	-6.83	0.5	0.15	0	0
BiClTe	-0.47	0.08	0.58	1.15	1.68	Yes	n/a	0.17	-5.1	-6.77	0.46	1.55	0	0
BrSSb	-0.29	0.14	1.43	2.03	2.61	No	n/a	0.43	-4.76	-7.37	1.06	0.47	0	0
ClSbSe	-0.41	0.14	1.67	2.29	2.86	No	0.39	0.49	-4.63	-7.49	1.07	1.3	0	0
BrSbTe	-0.25	0.1	1.32	1.82	2.25	No	0.66	0.31	-4.42	-6.67	0.57	1.38	0	0
ISbSe	-0.18	0.13	1.01	1.59	1.97	No	3.52	0.31	-4.43	-6.4	0.47	0.31	0	0
BiISe	-0.33	0.1	0.48	1.19	1.69	No	0.28	0.28	-5.03	-6.72	0.5	0.22	54(c-G)	42
BiBrTe	-0.39	0.09	0.58	1.16	1.63	No	n/a	0.21	-5.04	-6.67	0.45	1.2	30(c-G)	17
BiITe	-0.26	0.09	0.39	1.0	1.4	No	n/a	0.23	-4.93	-6.34	0.46	0.71	35(c-G)	32
BrSbSe	-0.32	0.1	1.46	2.04	2.57	No	n/a	0.35	-4.51	-7.08	0.89	0.88	0	0
ISSb	-0.13	0.18	0.79	1.46	1.81	No	n/a	0.3	-4.69	-6.5	0.42	0.1	0	0
ISbTe	-0.13	0.11	1.02	1.44	1.78	No	0.53	0.19	-4.27	-6.05	0.39	0.81	0	0
AsBrSe	-0.13	0.14	1.5	2.1	2.5	No	0.63	0.25	-4.41	-6.91	0.66	1.13	0	0
AsISe	0.01	0.17	0.45	1.05	1.3	No	n/a	0.22	-4.41	-5.71	0.35	0.41	0	0
AsBrTe	-0.08	0.13	1.06	1.66	1.96	No	0.58	0.33	-4.56	-6.53	0.52	1.72	0	0
AsITe	0.04	0.14	0.33	0.87	1.09	No	0.51	0.21	-4.39	-5.48	0.34	1.02	0	0

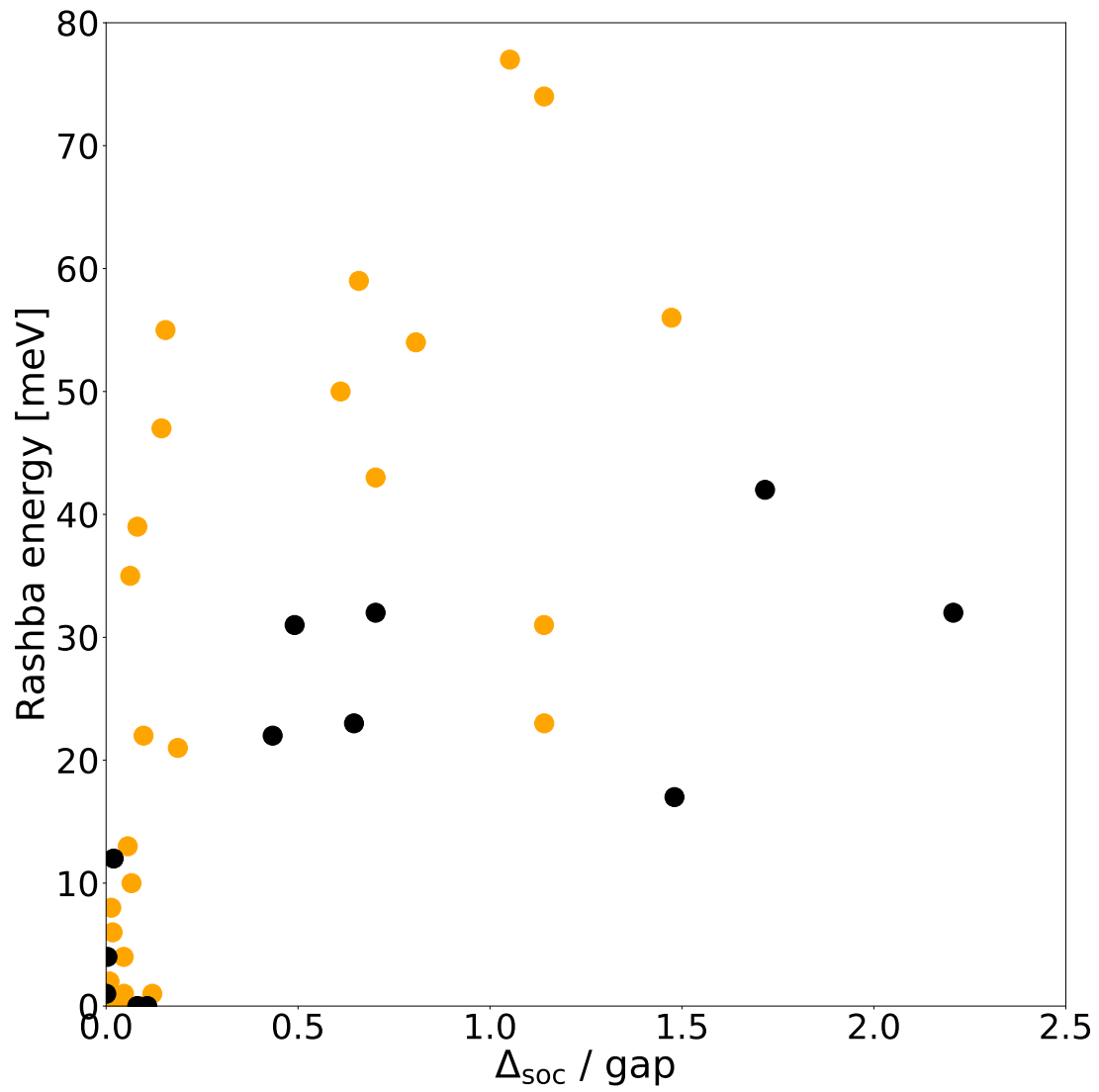


Figure 1: The ratio of the strength of the spin-orbit coupling (see main text) and the band gap against the Rashba energy (y -axis).

8.9 Paper IX

Engineering Atomically Sharp Potential Steps and Band Alignment at Solid Interfaces using 2D Janus Layers

A. C. Riis-Jensen, S. Manti, and K. S. Thygesen

J. Phys. Chem. C, **124**, 17 (2020)

Reproduced with permission from J. Phys. Chem. C, **124**, 17 (2020) © Copyright 2020 American Chemical Society.

<https://pubs.acs.org/doi/abs/10.1021/acs.jpcc.0c01286>

Engineering Atomically Sharp Potential Steps and Band Alignment at Solid Interfaces using 2D Janus Layers

Anders C. Riis-Jensen, Simone Manti, and Kristian S. Thygesen*

Cite This: *J. Phys. Chem. C* 2020, 124, 9572–9580

Read Online

ACCESS |



Metrics & More

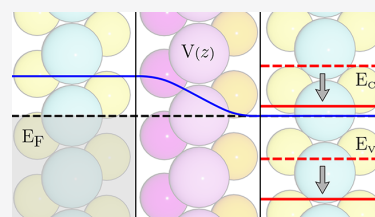


Article Recommendations



Supporting Information

ABSTRACT: The possibility of stacking two-dimensional (2D) materials into van der Waals (vdW) heterostructures has recently created new opportunities for band structure engineering at the atomic level. However, despite the weak vdW interaction, controlling the electrostatic potential governing the band lineup at the 2D interfaces is still posing a significant challenge. Here, we demonstrate that 2D Janus monolayers, possessing an intrinsic out-of-plane dipole moment, can be used to control the band alignment at semiconductor–semiconductor and metal–semiconductor interfaces in a highly predictive manner. Using density functional theory (DFT), we calculate the band structure of a wide range of different vdW interfaces. We find that upon insertion of a Janus structure the band line-ups and Schottky barriers can be controlled to high accuracy. The main result of this work is that the out-of-plane dipole moment of the Janus structure changes little upon insertion in the interface. As a consequence, the effect on the electrostatic potential at the interface can be predicted from the properties of the freestanding Janus structure. In addition to this, we predict 47 stable Janus monolayers, covering a wide range of dipole moments and band edge positions and thus providing a comprehensive library of 2D building blocks for manipulating the band alignment at interfaces.



INTRODUCTION

More than a decade after the discovery of graphene,¹ the class of atomically thin two-dimensional (2D) crystals remains one of the hottest topics in physics. An important reason is that such materials open new possibilities for studying and manipulating electronic quantum states directly at the atomic length scale. By stacking different 2D layers into van der Waals (vdW) heterostructures, it is, at least in principle, possible to design the energy landscape of the electrons, i.e., the band structure, with a precision far beyond what is possible with conventional epitaxial growth.² In this paper, we introduce the idea of using 2D Janus monolayers to control the electrostatic potential and band line up at vdW interfaces.

Many solid-state devices, including semiconductor (SC) lasers,^{3–5} solar cells,^{6,7} and transistors,⁸ rely on heterostructure materials with electronic energy levels carefully aligned across their interfaces. This makes the interfacial band lineup problem one of the most critical challenges for the semiconductor industry. Quite generally, the band alignment at SC heterojunctions can be categorized into three types according to the relative position of valence and conduction bands on the two sides of the interface. In Figure 1, we show examples of type-I and type-II band alignments. It is exceedingly difficult if not impossible by means of conventional techniques employed in the semiconductor industry (doping, strain, alloying) to change the band alignment at an interface without changing the composition or structure of the material(s) in the vicinity of the interface. This clearly implies a risk of degrading other of the material properties, e.g., the carrier mobility, carrier lifetime, etc. A key result of this paper

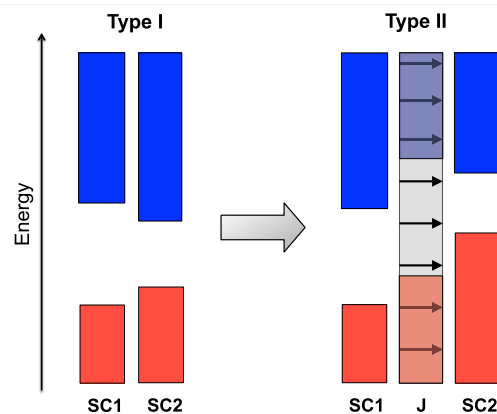
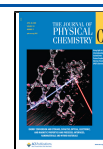


Figure 1. Left: sketch of a type-I band alignment between two different semiconductors. Right: sketch of the achieved type-II band alignment between the two semiconductors by sandwiching a Janus monolayer between them, which shifts the electrostatic potential on either side of the Janus monolayer. In a type III band alignment, the valence band maximum (VBM) of one of the structures is located above the conduction band minimum (CBM) of the other structure.

Received: February 21, 2020

Revised: April 3, 2020

Published: April 3, 2020



is that the band alignment can be controlled elegantly and with high precision in vdW heterojunctions without affecting the material structure or composition.

For metal/SC interfaces, the single most critical parameter used to characterize the band alignment is the height of the Schottky barrier (SB), i.e., the distance between the metal Fermi level and the nearest band edge of the SC (valence band or conduction band). Apart from the position of the bands in the intrinsic materials, i.e., the work function of the metal and the electron affinity and ionization potential of the SC, a number of effects influence the SB including Pauli repulsion and metal-induced gap states (MIGSs).^{9–13} Such effects lead to Fermi-level pinning (FLP)^{10,14–16,18–22} and deviations from the Anderson rule,²³ which makes it difficult to control (in practice minimize) the SB. This is further complicated by the unpredictable effect of the chemical interactions at the interface.¹⁷ One specific and important motivation for developing means to control the SB at metal–2D semiconductor interfaces comes from the huge interest in atomically thin field-effect transistors, e.g., based on transition-metal dichalcogenides (TMDs). For such devices, the SB at the source/drain contacts remains a performance-limiting factor that must be improved for them to become competitive.^{24–33}

Due to the presence of MIGS, it has been proven ineffective to dope SC/metals structures to lower the SB. This has previously been explained by the fact that while originating on the metal the states are still localized deeply into the SC,³⁴ effectively neutralizing the effect of doping. Approaches to overcome this includes inserting a layer of boron nitride between the metal and the SC^{22,35} or different oxide layers;^{36–39} however, the exact effect of all of the above-mentioned mechanisms is extremely difficult to predict.

In this work, we propose an alternative method to control and adjust the band lineup at solid interfaces in a highly predictable manner. By sandwiching a 2D material with a finite out-of-plane dipole moment, i.e., a Janus monolayer, between two materials, it is possible to introduce an atomically sharp potential step across the interface. For SC/SC interfaces, this opens the possibility of controlling the band lineup and even changing the type of band alignment, while for metal/SC interfaces, the SB can essentially be made to vanish. Importantly, we find that the dipole moment of the Janus layer does not change significantly upon insertion in the heterostructure, meaning that the resulting shift in the band offset can be predicted to high accuracy from the properties of the isolated Janus monolayer, at least for systems with small interlayer charge transfer. Beyond pure vdW-bonded structures, we find that the intrinsic dipole moment is unaltered, even when placed on conventional bulk metal surfaces. Using high-throughput density functional theory (DFT) computations, we further predict 47 new Janus monolayers that we find to be stable, have a finite band gap, and a finite out-of-plane dipole moment. The induced shift in electrostatic potential achievable by these novel 2D Janus monolayers range from close to zero to about 2 eV, showing the high degree of band offset tunability offered by the proposed concept.

■ COMPUTATIONAL DETAILS

All calculations were performed with the GPAW code.⁴⁰ Monolayer structures were relaxed using the Perdew–Burke–Ernzerhof (PBE) functional⁴¹ on a Monkhorst–Pack k -point

grid⁴² with a k -point density of 6.0 and a planewave cutoff of 800 eV. The unit cells had 15 Å of vacuum in the perpendicular direction, and a Fermi smearing of 0.05 eV was used. The band structure and the size of the dipole moment were calculated using a k -point density of 12.0. Spin–orbit coupling was not included. For the multilayer structures, the interlayer binding distances were determined using the BEEF-vdW functional.⁴³ All structures were relaxed until the maximum force on any atom was below 0.01 eV/Å and the maximum stress on the unit cell was 0.002 eV/Å³. Since the layers in the heterostructures, in general, will have incommensurable lattices, it is necessary to use larger supercells and strain one or both materials slightly. Table 1

Table 1. Computational Details about the Supercells Used for the Heterostructure Calculations Including the Cell Size, Strain, and Smallest Interlayer Distance d

structure	cell size	strain (%)	d (Å)
graphene/H-MoSSe/hBN	graphene: 4 × 4	1.62	3.82/3.69
	H-MoSSe: 3 × 3	−0.46	
	hBN: 4 × 4	3.31	
T-MoS ₂ /H-MoSSe/H-MoS ₂	T-MoS ₂ : 1 × 1	0	3.51/3.67
	H-MoSSe: 1 × 1	−2.06	
H-MoS ₂ /H-MoSSe/H-MoS ₂	H-MoS ₂ : 1 × 1	0	3.54/3.63
	H-MoSSe: 1 × 1	−2.06	
H-WS ₂ /H-MoSSe/H-WS ₂	H-WS ₂ : 1 × 1	0	3.52/3.66
	H-MoSSe: 1 × 1	−2.06	
H-MoS ₂ /H-CrSSe/H-MoS ₂	H-MoS ₂ : 1 × 1	0	3.61/3.75
	H-CrSSe: 1 × 1	1.76	
H-MoSe ₂ /H-MoSTe/H-MoSe ₂	H-MoSe ₂ : 1 × 1	0	3.61/3.74
	H-MoSTe: 1 × 1	<0.01	
H-MoSe ₂ /H-TaSSe/H-MoSe ₂	H-MoSe ₂ : 1 × 1	0	3.58/3.81
	H-TaSSe: 1 × 1	−2.59	
H-MoSe ₂ /H-TiSSe/H-MoSe ₂	H-MoSe ₂ : 1 × 1	0	3.63/3.86
	H-TiSSe: 1 × 1	−2.93	
H-MoSe ₂ /H-WSeTe/H-MoSe ₂	H-MoSe ₂ : 1 × 1	0	3.66/3.58
	H-WSeTe: 1 × 1	−3.29	
H-MoS ₂ /H-WSSe/H-MoS ₂	H-MoS ₂ : 1 × 1	0	3.54/3.65
	H-WSSe: 1 × 1	−2.10	
H-MoSe ₂ /H-WSTe/H-MoSe ₂	H-MoSe ₂ : 1 × 1	0	3.64/3.68
	H-WSTe: 1 × 1	−1.25	
H-MoSe ₂ /H-ZrBrCl/H-MoSe ₂	H-MoSe ₂ : 1 × 1	0	3.69/3.57
	H-ZrBrCl: 1 × 1	−4.82	
H-MoSe ₂ /H-TiBrCl/H-MoSe ₂	H-MoSe ₂ : 1 × 1	0	3.78/3.64
	H-TiBrCl: 1 × 1	−1.75	

presents a summary of the supercell size and strain applied to each layer in each heterostructure. For H-phase/H-phase interfaces, AB stacking was used, while for H-phase/T-phase interfaces, AA stacking was used, i.e., the metal atoms were stacked on top of each other. These stacking configurations were found to be energetically most stable. To judge the stability (dynamic and thermodynamic) of the new Janus monolayers resulting from the high-throughput study, we followed the criteria of the Computational 2D Materials Database.⁴⁴

■ RESULTS

Recently, both MoSSe^{45,46} and BiTeI⁴⁷ have been realized in the monolayer form experimentally. These structures possess

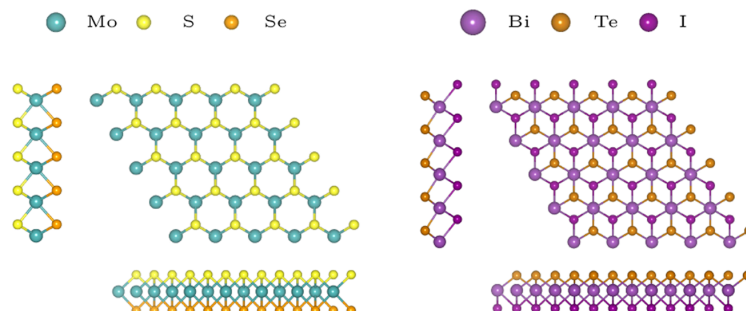


Figure 2. Top and side views of the atomic structures of the MoSse prototype (left) and the BiTeI prototype (right).

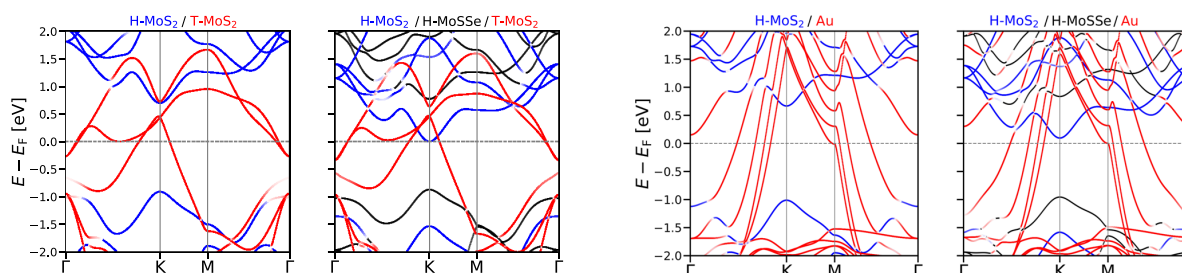


Figure 3. Left: band structure of a bilayer consisting of MoS₂ in the H- and T-phases, respectively. Right: band structure of the same structure with the Janus monolayer MoSse sandwiched in between the two layers. For both plots, red/blue is the projection of the bands onto the T- and H-phase of MoS₂, respectively, while black is the projection onto MoSse. Notice how the insertion of MoSse shifts the band edges of H-MoS₂ with respect to the Fermi level of the structure, effectively lowering the SB.

an out-of-plane dipole moment created by the difference in electronegativity of the S and Se (I and Te) atoms,⁴⁸ which are located on different sides of the central metal layer, see Figure 2. Such structures with broken mirror symmetry and a finite out-of-plane dipole moment are known as Janus monolayers.

In Figure 1, we illustrate the concept of band lineup control at vdW heterojunction interfaces. On the left is shown an example of a bilayer consisting of two (possibly) different

Figure 5. Left: band structure of H-MoS₂ at the bulk Au metal surface. Right: band structure of the same structure with the Janus monolayer MoSse sandwiched in between. For both plots, red/blue is the projection of the bands onto the Au and H-MoS₂, respectively, while black is the projection onto MoSse.

semiconducting 2D monolayers having a type-I band alignment. On the right is shown the same two monolayers, with a Janus monolayer sandwiched in-between. By choosing a Janus monolayer with an appropriate size of the out-of-plane dipole moment, it is possible to shift, for instance, a type-I band alignment into a type-II band alignment as shown. Another obvious application is to use Janus monolayers to lower the SB at metal/SC interfaces. For a general metal/SC interface, where the Fermi level of the metal is located between the valence band maximum (VBM) and conduction band minimum (CBM) of the SC, the bands originating from the

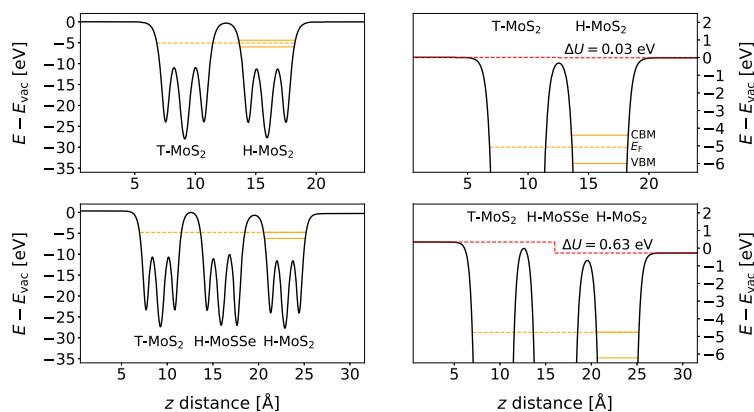


Figure 4. Electrostatic potential, with respect to the vacuum energy, for the bilayer and trilayer structures from Figure 3 in the direction perpendicular to the layers. The right column is a close-up of the top of the figures in the left column, showing the vacuum-level shift ΔU on either side of the heterostructures. In orange is shown the VBM, CBM, and E_F .

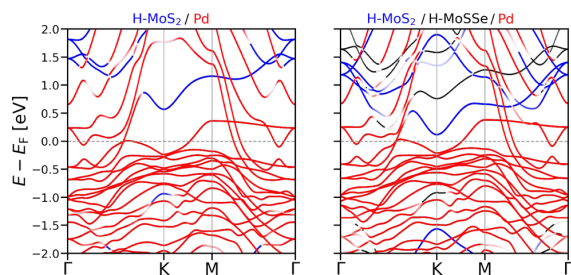


Figure 6. Same as Figure 5 with a Pd(111) surface instead of a Au(111) surface.

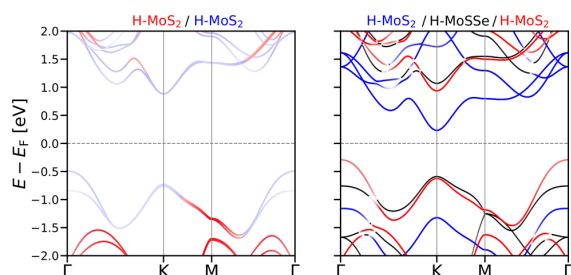


Figure 7. Left: band structure of a bilayer H-MoS₂. Right: band structure of the same structure with the Janus monolayer MoSSe sandwiched in between the two layers. For both plots, red/blue is the projection of the bands onto the two MoS₂ layers, while black is the projection onto MoSSe. Notice how the insertion of MoSSe splits the bands of the two MoS₂ layers at the K-point.

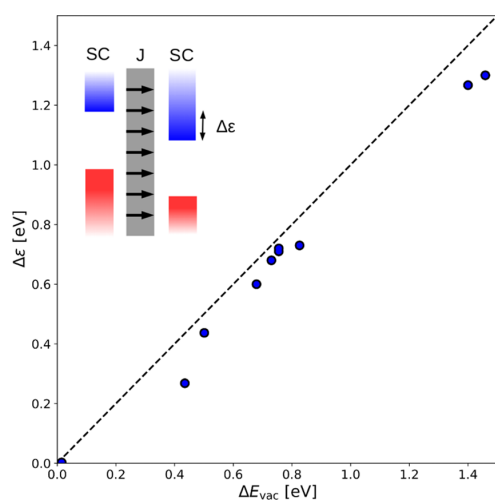


Figure 8. Splitting of the conduction bands $\Delta\epsilon$ for a SC bilayer, upon insertion of a Janus monolayer, as a function of the shift in potential across the freestanding Janus monolayer ΔE_{vac} . Each data point represents a different Janus monolayer sandwiched between two identical SCs. From left to right, the Janus monolayers are TiSSe, ZrBrCl, TiBrCl, WSeTe, WSSe, MoSSe, MoSSe, CrSSe, WSte, and MoTe. The exact trilayer composition can then be deduced from Table 1. We stress that there is little-to-no difference between trilayers H-MoS₂/H-MoSSe/H-MoS₂ and H-WS₂/H-MoSSe/H-WS₂. The fact that the shift in band energies is very close to the shift of the freestanding Janus monolayer shows the highly predictive nature of the proposed strategy for band alignment engineering.

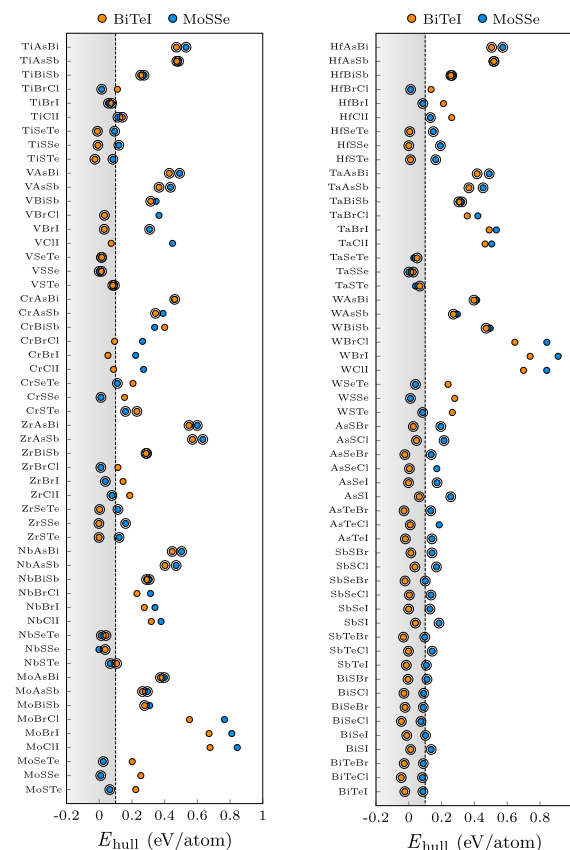


Figure 9. Energy above the convex hull for all Janus monolayers calculated in this study colored according to their phase. Structures with an energy above the convex hull lower than 0.1 eV/atom are considered thermodynamically stable. Dynamical stability is shown by a black circle.

SC will bend at the interface, creating a Schottky barrier. Below we show that by inserting a Janus monolayer between the metal and the SC, one can control the SB.

Schottky Barriers at Metal/SC Interfaces. To illustrate the concept in practice, we have calculated the band structure of both SC/SC and metal/SC vdW heterostructures with and without a Janus monolayer sandwiched in-between. First, consider the two band structures shown in Figure 3. On the left is shown the band structure of bilayer T-MoS₂/H-MoS₂. We note that MoS₂ is well known to be metallic in the T-phase and semiconducting in the H-phase. We note that the T-phase is in fact dynamically unstable and undergoes a transition to the T'-phase; however, this is unimportant for the present discussion. On the right is shown the band structure of the same structure with H-MoSSe sandwiched in-between. For the two cases, we consider an AB and ABA stacking, respectively. The red color represents the bands projected onto the T-MoS₂ layer, blue is projected onto the H-MoS₂ layer, and black is projected onto the Janus H-MoSSe layer. For the bilayer, we see that the bands from T-MoS₂ are crossing the Fermi level, which overall renders the bilayer metallic, while the H-MoS₂ more or less preserves the size of its direct band gap at the K-point. The distance from the CBM of H-MoS₂ to the Fermi level is approximately 0.6 eV,

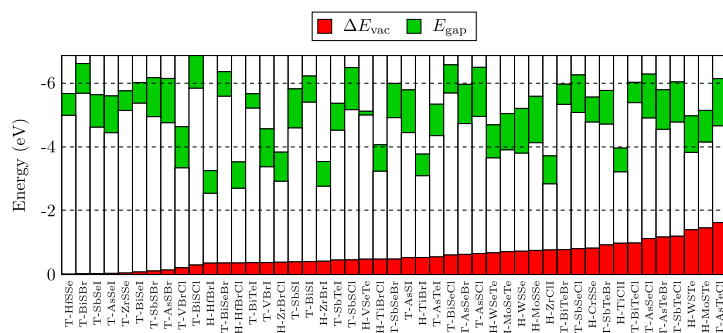


Figure 10. Overview of all stable Janus monolayers in the MoS₂Se (H-phase) and BiTeI (T-phase) prototypes, sorted according to the vacuum-level shift (red). The band gap is shown in green on the absolute scale relative to vacuum, such that the valence band maximum and conduction band minimum can be found from the white/green boundaries. All energies refer to PBE calculations.

which equals the SB of the interface. On the right, after insertion of the MoS₂Se layer, we see how the SB has essentially vanished. Now, the CBM of the H-MoS₂ layer just touches the Fermi level, thus reducing the SB to almost zero. We note that the SB of T-MoS₂/H-MoS₂ has previously been studied, where it was shown that the SB can be shifted by 0.3 eV by varying the stacking pattern.⁴⁹ While this is an interesting result, the method proposed in our study gives the possibility to vary the SB, in a highly controlled manner, anywhere between the electronic band gap and essentially 0 eV, by varying the Janus monolayer material, which will be demonstrated later.

A more detailed picture of the electrostatic discontinuity induced by the Janus monolayer is shown in Figure 4. The top panel shows the electrostatic potential perpendicular to the T-MoS₂/H-MoS₂ bilayer (averaged over the in-plane directions). The lower panel shows the same for the trilayer structure including H-MoS₂Se. Here, the right-hand side plot is a close-up of the upper part of the left plot. For the bilayer, we see a minor change in the electrostatic potential across the bilayer of 0.03 eV. Since both T-MoS₂ and H-MoS₂ have a zero dipole moment in the out-of-plane direction in their freestanding monolayer form, this shift originates from a small interfacial dipole created at the interface. This phenomenon is well known for metal–SC interfaces and has also been seen at graphene/SC interfaces.⁵⁰ After insertion of H-MoS₂Se, we now find a shift of 0.63 eV. This large shift arises because of the internal dipole in the H-MoS₂Se layer and gives the shift in the band structure we observed in Figure 3. We here stress that we in this study consider the manipulation of SB defined by the SC band edges relative to the Fermi level and do not consider the tunneling barrier evident from Figure 4, which for some systems can impose an additional barrier. Modeling of such additional tunneling barriers are system-specific and will be the scope of future studies.

It can be interesting to study how the intrinsic dipole moment of the Janus monolayers are affected by strain effects. To do this, we calculate the vacuum-level shift and band gap of strained monolayer H-MoS₂Se. The applied strain ranges from -3% to +3% (see Figure S1 in the Supporting Information), which we believe are experimentally realizable values. We find that the vacuum-level shift across monolayer MoS₂Se can be varied between 0.74 and 0.77 eV. While this gives rise to only little variation in the intrinsic dipole moment of the Janus monolayers, it shows that the proposed setup is very robust to strain effects. On the other hand, the band gap

changes over a range from 1.1 to 1.6 eV, showing a great possible tunability of the electronic properties of Janus monolayers.

To further illustrate the concept, we consider the band structure of a bulk metal/SC interface and calculate the band structure of H-MoS₂ at the bulk Au(111) surface and at the bulk Pd(111) surface. The bulk metal surface is modeled by a slab of four atomic layers. The calculation has been performed in a 1 × 1 cell, with H-MoS₂ unstrained and Au and Pd strained significantly to match the lattice constant of H-MoS₂. Despite the very large strain, we find that the typical characteristics of both the Au and Pd band structures can be recognized, i.e., the wide 6sp bands crossing the Fermi surface and the flat 5d bands at around -1.5 eV for Au and the 5d bands crossing the Fermi level for Pd. This can be seen in Figures 5 and 6. Notice that the same color coding has been used as that for the previous band structure plot. Comparing the SB with and without H-MoS₂Se, we find a reduction of the SB of about 0.6 eV for the Au surface, which is close to the reduction found for T-MoS₂/H-MoS₂. For the Pd surface, the reduction is closer to 0.5 eV, showing a larger cancellation of the internal dipole of MoS₂Se in this case. We note here that no chemical interactions are taking place at the MoS₂/Au interface, while a considerable chemical bond strength is present at the MoS₂/Pd interface.⁵¹ Thus, this stronger interaction explains the larger cancellation of the internal dipole. This is further stressed by the interlayer distance between H-MoS₂ and Au/Pd. For H-MoS₂/Au, the smallest out-of-plane interlayer distance is 3.4 Å, while it is only 2.0 Å for H-MoS₂/Pd. This shows that the reduction of the out-of-plane dipole moment is rather modest, even at metal surfaces that couple strongly to the Janus monolayer.

Band Alignment at SC/SC Interfaces. Next, we consider how the band alignment can be tuned for SC/SC interfaces. Specifically, we consider bilayer H-MoS₂ with and without a H-MoS₂Se layer sandwiched in between. The band structure of both cases is depicted in Figure 7 using the same coloring as in Figure 3. We first notice the direct to indirect band gap transition in going from the monolayer to bilayer H-MoS₂, where the VBM is located at the K-point for monolayer H-MoS₂ and at the Γ -point for bilayer H-MoS₂. The two layers hybridize strongly around the Γ point, leading to significant band splitting. In contrast, the interlayer hybridization is negligible around the K-point and the two bands are essentially degenerate. Therefore, the relative band positions at the K-point can be used to deduce the effect of electrostatic

Table 2. Material Properties of All Semiconducting Stable Material Candidates^a

material	phase	<i>a</i> (Å)	$E_{\text{gap}}^{(\text{PBE})}$	$E_{\text{gap}}^{(\text{HSE})}$	ΔE_{vac}	$E_{\text{center}}^{(\text{PBE})}$	ΔH_f	ΔH_{full}
HfSSe	T	3.71	0.68	1.51	0.01	5.32	-1.47	-0.01
BiSBr	T	4.11	0.93	1.60	0.03	6.13	-0.56	-0.00
SbSeI	T	4.17	1.02	1.53	0.03	5.12	-0.31	-0.00
AsSeI	T	3.93	1.15	1.68	0.04	5.01	-0.16	-0.00
ZrSSe	T	3.74	0.61	1.51	0.05	5.44	-1.48	-0.01
BiSeI	T	4.27	0.65	1.22	0.08	5.68	-0.44	-0.01
SbSBr	T	3.99	1.22	1.84	0.11	5.55	-0.42	0.01
AsSBr	T	3.72	1.39	2.04	0.14	5.44	-0.26	0.03
VBrCl	T	3.75	1.29	3.77	0.21	3.98	-1.01	0.00
BiSCL	T	4.07	1.04	1.74	0.30	6.35	-0.66	-0.03
HfBrI	H	3.64	0.71	1.16	0.36	2.90	-0.89	-0.00
BiSeBr	T	4.19	0.77	1.36	0.36	5.96	-0.58	-0.02
HfBrCl	H	3.43	0.82	1.36	0.36	3.11	-1.34	-0.08
BiTeI	T	4.42	0.45	0.93	0.37	5.43	-0.37	-0.02
VBrI	T	3.99	1.19	3.49	0.37	3.96	-0.66	0.01
ZrBrCl	H	3.49	0.91	1.40	0.38	3.37	-1.51	-0.02
SbSI	T	4.08	1.22	1.78	0.40	5.20	-0.28	0.04
BiSI	T	4.19	0.82	1.47	0.41	5.80	-0.41	0.01
ZrBrI	H	3.70	0.77	1.17	0.42	3.15	-1.09	0.02
SbTeI	T	4.32	0.84	1.32	0.45	4.93	-0.25	-0.02
SbSCL	T	3.94	1.32	1.99	0.46	5.82	-0.51	0.04
VSeTe	H	3.47	0.12	0.75	0.48	5.05	-0.50	0.00
TiBrCl	H	3.38	0.83	1.30	0.48	3.65	-1.33	-0.05
SbSeBr	T	4.08	1.07	1.65	0.48	5.44	-0.44	-0.02
AsSI	T	3.84	1.34	1.95	0.53	5.11	-0.11	0.06
TiBrI	H	3.63	0.68	1.04	0.53	3.43	-0.88	0.04
AsTeI	T	4.09	0.98	1.50	0.55	4.84	-0.12	-0.02
BiSeCl	T	4.15	0.88	1.51	0.61	6.12	-0.68	-0.05
AsSeBr	T	3.82	1.23	1.84	0.63	5.34	-0.29	-0.02
AsSCL	T	3.65	1.54	2.26	0.66	5.71	-0.35	0.05
WSeTe	H	3.43	1.04	1.49	0.68	4.17	-0.32	0.04
MoSeTe	H	3.43	1.14	1.59	0.72	4.47	-0.48	0.02
WSSe	H	3.25	1.40	1.91	0.73	4.50	-0.72	0.00
MoSSe	H	3.25	1.45	1.95	0.75	4.85	-0.81	0.00
ZrClI	H	3.64	0.88	1.32	0.77	3.27	-1.23	0.07
BiTeBr	T	4.34	0.63	1.16	0.78	5.64	-0.50	-0.03
SbSeCl	T	4.03	1.17	1.80	0.81	5.66	-0.54	0.00
CrSSe	H	3.13	0.78	1.24	0.83	5.16	-0.57	-0.00
SbTeBr	T	4.24	1.06	1.62	0.93	5.23	-0.38	-0.03
TiClI	H	3.55	0.75	1.19	0.98	3.58	-1.01	0.07
BiTeCl	T	4.30	0.64	1.20	0.99	5.69	-0.60	-0.05
AsSeCl	T	3.76	1.37	2.06	1.13	5.58	-0.38	0.00
AsTeBr	T	3.98	1.24	1.84	1.18	5.16	-0.24	-0.03
SbTeCl	T	4.19	1.26	1.87	1.20	5.40	-0.47	-0.00
WSTe	H	3.36	1.14	1.68	1.40	4.39	-0.42	0.08
MoSTe	H	3.36	0.99	1.59	1.46	4.64	-0.55	0.06
AsTeCl	T	3.93	1.48	2.15	1.62	5.39	-0.32	0.01

^aThe table contains information about elements, structural phase, in-plane lattice constant [Å], PBE and HSE electronic band gaps [eV], shift in the electrostatic potential across the Janus monolayer [eV], the PBE band gap center relative to vacuum [eV], the heat of formation [eV/atom], and the energy above the convex hull [eV].

shift induced by the Janus monolayer. After insertion of the H-MoSSe layer, we see the splitting of both the conduction and valence bands at the *K*-point, effectively turning the perfect band alignment into a type-II band alignment. For the H-MoS₂/H-MoSSe/H-MoS₂ heterostructure, we find a splitting of 0.72 eV, which equals that of the T-MoS₂/H-MoSSe/H-MoS₂ heterostructure to within about 0.1 eV. Upon further stacking of Janus monolayers in a multilayer structure, recent studies^{48,52} have shown that the effect is to

close the band gap, effectively creating a naturally doped p–n junction. This also shows that more than one Janus monolayer can be inserted if a larger shift in the potential is desired.

It is also interesting to see how the interface can be controlled for a SC at a graphene monolayer because of the semimetallic nature of graphene, and we therefore now consider the two graphene/hBN and graphene/H-MoSSe/hBN systems, where hBN is hexagonal boron nitride. In the same manner as for T-MoS₂/H-MoSSe/H-MoS₂, we find for

graphene/H-MoSSe/hBN that the bands of hBN shift down by 0.69 relative to the Fermi level after the inclusion of H-MoSSe. This is larger than the shift observed for T-MoS₂/H-MoSSe/H-MoS₂; however, the comparison to this system is not completely justified because in the latter case the conduction band gets pinned at the Fermi level. It is more interesting to observe that the shift is slightly smaller than that for H-MoS₂/H-MoSSe/H-MoS₂. This observation can be explained by the larger cancellation of the internal dipole of H-MoSSe by graphene as compared to that of H-MoS₂. The larger cancellation of the internal dipole in H-MoSSe on graphene compared to that in H-MoS₂ can be understood from the simple point that the S and Se atoms in H-MoSSe are spatially longer separated from the valence states of H-MoS₂ (located on the Mo atoms) compared to the states in graphene.

To investigate whether the induced band offset for a SC/Janus/SC vdWH can be predicted from the dipole moment of the freestanding Janus monolayer, we have calculated the band structure for ten different SC/Janus/SC vdWHs. For a given trilayer, the same SC is used on both sides (in analogy to the H-MoS₂/H-MoSSe/H-MoS₂ structure studied above). For the SC, we use either H-MoS₂ or H-MoSe₂ (depending on what fits the lattice constant of the Janus monolayer better) and then investigate the effect of changing the Janus monolayer. The Janus monolayers have been chosen such that they span a wide range of dipole moments and their lattice constants are close to those of MoS₂ or MoSe₂ to minimize the applied strain (see the next section for a discussion on the other Janus monolayers). We also include the structure H-WS₂/H-MoSSe/H-WS₂ to study the effect of having the same Janus monolayer sandwiched between two different pairs of SCs. We use an in-plane 1 × 1 unit cell for the calculations, and only apply strains to the Janus monolayer to keep the band structure of the SC unchanged. We calculate the shift of the electrostatic potential on either side of the freestanding strained Janus monolayer and the induced band shift of the SC in the SC/Janus/SC configuration. These values are plotted against each other in Figure 8. It is evident that the induced band shift of the bands between the two SCs in the SC/J/SC trilayer can be predicted from the out-of-plane dipole moment of the freestanding Janus monolayer. We note in passing that there is a linear relationship between the shift in electrostatic potential and the internal out-of-plane dipole moment of the Janus monolayer. One more point is worth noticing from Figure 8. First, we see to within 0.01 eV the same band shift for the H-MoS₂/MoSSe/H-MoS₂ and H-WS₂/H-MoSSe/H-WS₂, showing that the band shift induced by a Janus monolayer is only little affected by the choice of SC. This effect can be ascribed to the fact that the bands get pinned at the Fermi level, limiting the possible band shift (as seen above for T-MoS₂/H-MoSSe/H-MoS₂), and second, for metallic heterostructures, the free carriers can more effectively screen the internal dipole of the Janus monolayer. This is also the reason why the shift in potential is smaller in the SC/Janus/SC system compared to the potential shift for the freestanding Janus monolayer for all systems since there will always be a small finite cancellation of the internal dipole moment. If the concentration of S and Se atoms on either side is altered, this will affect the intrinsic out-of-plane dipole moment. To achieve the interface manipulations discussed in this chapter experimentally, we stress that the proposed

method is highly dependent on the quality of the transfer of the Janus monolayer into (or onto) the desired structures.

Janus Monolayer Library. To further expand the prospects of the ideas put forward in this study, we consider the set of Janus monolayers from our previous study by Riis-Jensen et al.⁵³ In this study, an initial set of 216 Janus monolayers with the chemical formula MXY in the H- and T-phases commonly known from the transition-metal dichalcogenides (TMDs) were investigated.

In the following, we adopt the notation used in the Computational 2D Materials Database (C2DB)⁵⁴ and in Riis-Jensen et al. and refer to the H and T crystal structures as the MoSSe and BiTeI prototypes. All structures and properties shown in this work are available in the C2DB. The 216 candidate materials were constructed by combinatorial lattice decoration of the MoSSe and BiTeI prototype structures using elements with similar chemical properties. Specifically, for both MoSSe and BiTeI prototypes, all possible combinations using one of the transition metals from groups V, VI, and VII (for the central metal atom in the prototypes) in combination with two elements from either the pnictogens (As, Sb, Bi), or chalcogens (S, Se, Te), or halogens (Cl, Br, I) were considered. In addition, the study considered all combinations using one of the pnictogens as the metal atom, one element from the chalcogens, and one element from the halogens. This makes a total of 108 candidate structures for each prototype. To assess the thermodynamic stability, we calculate the heat of formation and the energy above the convex hull, with the latter defined as the most stable elementaries and binaries, see C2DB⁴⁴ for more details. For the dynamic stability, we calculate the Γ -point phonons of the 2 × 2 cell as well as the elastic tensor. An imaginary phonon frequency or negative elastic constant implies a dynamically unstable material. In Figure 9, we show the calculated energy above the convex hull for all 216 structures. The MoSSe prototype is shown in blue, and the BiTeI prototype is shown in orange. Taking uncertainties in the calculated heat of formation into account, we consider a material to be thermodynamically stable if its energy above the convex hull is less than 0.1 eV/atom, as marked by the gray area. Points that have a black circle indicate materials that are dynamically stable and have a finite band gap.

We predict 47 materials that are both semiconducting, thermodynamically stable, and dynamically stable. Out of these, 27 are in the BiTeI phase with a pnictogen atom as the central metal atom, and among these is the experimentally realized BiTeI. For the 47 materials that we find to be semiconducting and predicted to be stable, we plot the shift in the electrostatic potential across the material (red), together with the band edges (white/green boundaries) in Figure 10. All stable semiconducting materials, their in-plane lattice constant, electronic band gap, band gap center, the shift in the potential, heat of formation, and the energy above the convex hull are summarized in Table 2. The large variation in the band edge position and dipole strength underlines the flexibility of the proposed concept.

CONCLUSIONS

We have proposed, and critically assessed, a new method for tuning the band lineup at solid-state interfaces by the insertion of a Janus monolayer in the interface. Due to its out-of-plane dipole moment, the Janus monolayer creates a step in the electrostatic potential, which gives rise to a relative shift of the

band energies on the two sides of the interface. Our DFT calculations show that the dipole of the Janus monolayer is almost unperturbed by the interface. Consequently, the shift in band alignment is determined by the intrinsic dipole of the Janus monolayer and therefore can be predicted to high accuracy. This important finding is a result of the inertness of the Janus monolayer and stands in contrast to existing methods that involve the formation of chemical bonds and complex charge transfer processes whose effects on the band energies are difficult to predict. Finally, we conducted a computational screening for new Janus monolayers and identified 47 (meta)stable candidates with a large range of out-of-plane dipole moments, providing great flexibility for tuning of band alignment.

■ ASSOCIATED CONTENT

Supporting Information

The Supporting Information is available free of charge at <https://pubs.acs.org/doi/10.1021/acs.jpcc.0c01286>.

Vacuum-level shift and band gap; band structure of bilayer graphene/hBN; band structure of bilayer graphene/H-MoSSe/hBN (PDF)

■ AUTHOR INFORMATION

Corresponding Author

Kristian S. Thygesen – CAMD, Department of Physics and Center for Nanostructured Graphene (CNG), Department of Physics, Technical University of Denmark, DK-2800 Kongens Lyngby, Denmark; orcid.org/0000-0001-5197-214X; Email: thygesen@fysik.dtu.dk

Authors

Anders C. Riis-Jensen – CAMD, Department of Physics, Technical University of Denmark, DK-2800 Kongens Lyngby, Denmark; orcid.org/0000-0002-4914-5820

Simone Manti – CAMD, Department of Physics, Technical University of Denmark, DK-2800 Kongens Lyngby, Denmark

Complete contact information is available at:

<https://pubs.acs.org/doi/10.1021/acs.jpcc.0c01286>

Notes

The authors declare no competing financial interest.

■ ACKNOWLEDGMENTS

This project has received funding from the European Research Council (ERC) under the European Union's Horizon 2020 Research and Innovation Programme (grant agreement no. 773122, LIMA). The Center for Nanostructured Graphene is sponsored by the Danish National Research Foundation (Project DNRF103).

■ REFERENCES

- (1) Novoselov, K. S.; Geim, A. K.; Morozov, S. V.; Jiang, D.; Zhang, Y.; Dubonos, S. V.; Grigorieva, I. V.; Firsov, A. A. Electric Field Effect in Atomically Thin Carbon Films. *Science* **2004**, *306*, 666–669.
- (2) Geim, A. K.; Grigorieva, I. V. Van der Waals Heterostructures. *Nature* **2013**, *499*, 419.
- (3) Wu, S.; Buckley, S.; Schaibley, J. R.; Feng, L.; Yan, J.; Mandrus, D. G.; Hatami, F.; Yao, W.; Vučković, J.; Majumdar, A.; et al. Monolayer Semiconductor Nanocavity Lasers with Ultralow Thresholds. *Nature* **2015**, *520*, 69.
- (4) Ye, Y.; Wong, Z. J.; Lu, X.; Ni, X.; Zhu, H.; Chen, X.; Wang, Y.; Zhang, X. Monolayer Excitonic Laser. *Nat. Photonics* **2015**, *9*, 733.
- (5) Salehzadeh, O.; Djavid, M.; Tran, N. H.; Shih, I.; Mi, Z. Optically Pumped Two-Dimensional MoS₂ Lasers Operating at Room-Temperature. *Nano Lett.* **2015**, *15*, 5302–5306.
- (6) Linghu, J.; Yang, T.; Luo, Y.; Yang, M.; Zhou, J.; Shen, L.; Feng, Y. P. High-Throughput Computational Screening of Vertical 2D van der Waals Heterostructures for High-Efficiency Excitonic Solar Cells. *ACS Appl. Mater. Interfaces* **2018**, *10*, 32142–32150.
- (7) Bernardi, M.; Palummo, M.; Grossman, J. C. Semiconducting Monolayer Materials as a Tunable Platform for Excitonic Solar Cells. *ACS Nano* **2012**, *6*, 10082–10089.
- (8) Chhowalla, M.; Jena, D.; Zhang, H. Two-Dimensional Semiconductors for Transistors. *Nat. Rev. Mater.* **2016**, *1*, No. 16052.
- (9) Tersoff, J. Schottky Barriers and Semiconductor Band Structures. *Phys. Rev. B: Condens. Matter Mater. Phys.* **1985**, *32*, 6968.
- (10) Gong, C.; Colombo, L.; Wallace, R. M.; Cho, K. The Unusual Mechanism of Partial Fermi Level Pinning at Metal-MoS₂ Interfaces. *Nano Lett.* **2014**, *14*, 1714–1720.
- (11) Henck, H.; Ben Aziza, Z.; Zill, O.; Pierucci, D.; Naylor, C. H.; Silly, M. G.; Gogneau, N.; Oehler, F.; Collin, S.; Brault, J.; et al. Interface Dipole and Band Bending in the Hybrid p-n Heterojunction MoS₂/GaN(0001). *Phys. Rev. B* **2017**, *96*, No. 115312.
- (12) Sahoo, A.; Nafday, D.; Paul, T.; Ruiter, R.; Roy, A.; Mostovoy, M.; Banerjee, T.; Saha-Dasgupta, T.; Ghosh, A. Out-of-Plane Interface Dipoles and Anti-Hysteresis in Graphene-Strontium Titanate Hybrid Transistor. *npj 2D Mater. Appl.* **2018**, *2*, No. 9.
- (13) Si, C.; Lin, Z.; Zhou, J.; Sun, Z. Controllable Schottky Barrier in GaSe/Graphene Heterostructure: the Role of Interface Dipole. *2D Mater.* **2017**, *4*, No. 015027.
- (14) Kim, C.; Moon, I.; Lee, D.; Choi, M. S.; Ahmed, F.; Nam, S.; Cho, Y.; Shin, H.-J.; Park, S.; Yoo, W. J. Fermi Level Pinning at Electrical Metal Contacts of Monolayer Molybdenum Dichalcogenides. *ACS Nano* **2017**, *11*, 1588–1596.
- (15) Allain, A.; Kang, J.; Banerjee, K.; Kis, A. Electrical Contacts to Two-Dimensional Semiconductors. *Nat. Mater.* **2015**, *14*, 1195.
- (16) Das, S.; Chen, H.-Y.; Penumatcha, A. V.; Appenzeller, J. High Performance Multilayer MoS₂ Transistors with Scandium Contacts. *Nano Lett.* **2013**, *13*, 100–105.
- (17) Kang, J.; Liu, W.; Banerjee, K. High-Performance MoS₂ Transistors with Low-Resistance Molybdenum Contacts. *Appl. Phys. Lett.* **2014**, *104*, No. 093106.
- (18) Kang, J.; Liu, W.; Sarkar, D.; Jena, D.; Banerjee, K. Computational Study of Metal Contacts to Monolayer Transition-Metal Dichalcogenide Semiconductors. *Phys. Rev. X* **2014**, *4*, No. 031005.
- (19) Guo, Y.; Liu, D.; Robertson, J. 3D Behavior of Schottky Barriers of 2D Transition-Metal Dichalcogenides. *ACS Appl. Mater. Interfaces* **2015**, *7*, 25709–25715.
- (20) Guo, Y.; Liu, D.; Robertson, J. Chalcogen Vacancies in Monolayer Transition Metal Dichalcogenides and Fermi Level Pinning at Contacts. *Appl. Phys. Lett.* **2015**, *106*, No. 173106.
- (21) Mönch, W. Role of Virtual Gap States and Defects in Metal-Semiconductor Contacts. *Phys. Rev. Lett.* **1987**, *58*, 1260–1263.
- (22) Bokdam, M.; Brocks, G.; Katsnelson, M. I.; Kelly, P. J. Schottky Barriers at Hexagonal Boron Nitride/Metal Interfaces: A First-Principles Study. *Phys. Rev. B: Condens. Matter Mater. Phys.* **2014**, *90*, No. 085415.
- (23) Anderson, R. Germanium-Gallium Arsenide Heterojunctions [letter to the editor]. *J. Res. Dev.* **1960**, *4*, 283–287.
- (24) Amani, M.; Chin, M.; Glen Birdwell, A.; P. O'Regan, T.; Najmaei, S.; Liu, Z.; M. Ajayan, P.; Lou, J.; Dubey, M. Electrical Performance of Monolayer MoS₂ Field-Effect Transistors Prepared by Chemical Vapor Deposition. *Appl. Phys. Lett.* **2013**, *102*, No. 193107.
- (25) Wang, Q. H.; Kalantar-Zadeh, K.; Kis, A.; Coleman, J. N.; Strano, M. S. Electronics and Ptoelectronics of Two-Dimensional Transition Metal Dichalcogenides. *Nat. Nanotechnol.* **2012**, *7*, 699.
- (26) Allain, A.; Kang, J.; Banerjee, K.; Kis, A. Electrical Contacts to Two-Dimensional Semiconductors. *Nat. Mater.* **2015**, *14*, 1195.

- (27) Duan, X.; Wang, C.; Pan, A.; Yu, R.; Duan, X. Two-Dimensional Transition Metal Dichalcogenides as Atomically Thin Semiconductors: Opportunities and Challenges. *Chem. Soc. Rev.* **2015**, *44*, 8859–8876.
- (28) Lembke, D.; Bertolazzi, S.; Kis, A. Single-Layer MoS₂ Electronics. *Acc. Chem. Res.* **2015**, *48*, 100–110.
- (29) Chhowalla, M.; Jena, D.; Zhang, H. Two-dimensional Semiconductors for Transistors. *Nat. Rev. Mater.* **2016**, *1*, No. 16052.
- (30) Manzeli, S.; Ovchinnikov, D.; Pasquier, D.; V. Zayzev, O.; Kis, A. 2D Transition Metal Dichalcogenides. *Nat. Rev. Mater.* **2017**, *2*, No. 17033.
- (31) Ma, Y.; Kou, L.; Li, X.; Dai, Y.; Heine, T. Two-Dimensional Transition Metal Dichalcogenides with a Hexagonal Lattice: Room-Temperature Quantum Spin Hall Insulators. *Phys. Rev. B* **2016**, *93*, No. 035442.
- (32) Kou, L.; Frauenheim, T.; Chen, C. Nanoscale Multilayer Transition-Metal Dichalcogenide Heterostructures: Band Gap Modulation by Interfacial Strain and Spontaneous Polarization. *J. Phys. Chem. Lett.* **2013**, *4*, 1730–1736.
- (33) Radisavljevic, B.; Radenovic, A.; Brivio, J.; Giacometti, V.; Kis, A. Single-Layer MoS₂ Transistors. *Nat. Nanotechnol.* **2011**, *6*, 147.
- (34) Min, K.-A.; Park, J.; Wallace, R. M.; Cho, K.; Hong, S. Reduction of Fermi Level Pinning at Au-MoS₂ Interfaces by Atomic Passivation on Au Surface. *2D Mater.* **2017**, *4*, No. 015019.
- (35) Farmanbar, M.; Brocks, G. Controlling the Schottky Barrier at MoS₂/Metal Contacts by Inserting a BN Monolayer. *Phys. Rev. B* **2015**, *91*, No. 161304.
- (36) Chuang, S.; Battaglia, C.; Azcatl, A.; McDonnell, S.; Kang, J. S.; Yin, X.; Tosun, M.; Kapadia, R.; Fang, H.; Wallace, R. M.; et al. MoS₂ P-type Transistors and Diodes Enabled by High Work Function MoO_x Contacts. *Nano Lett.* **2014**, *14*, 1337–1342.
- (37) McDonnell, S.; Azcatl, A.; Addou, R.; Gong, C.; Battaglia, C.; Chuang, S.; Cho, K.; Javey, A.; Wallace, R. M. Hole Contacts on Transition Metal Dichalcogenides: Interface Chemistry and Band Alignments. *ACS Nano* **2014**, *8*, 6265–6272.
- (38) Chen, J.-R.; Odenthal, P. M.; Swartz, A. G.; Floyd, G. C.; Wen, H.; Luo, K. Y.; Kawakami, R. K. Control of Schottky Barriers in Single Layer MoS₂ Transistors with Ferromagnetic Contacts. *Nano Lett.* **2013**, *13*, 3106–3110.
- (39) Nam, S.-G.; Cho, Y.; Lee, M.-H.; Shin, K. W.; Kim, C.; Yang, K.; Jeong, M.; Shin, H.-J.; Park, S. Barrier Height Control in Metal/Silicon Contacts with Atomically Thin MoS₂ and WS₂ Interfacial Layers. *2D Mater.* **2018**, *5*, No. 041004.
- (40) Enkovaara, J.; Rostgaard, C.; Mortensen, J. J.; Chen, J.; Dulak, M.; Ferrighi, L.; Gavnholt, J.; Glinsvad, C.; Haikola, V.; Hansen, H. A.; et al. Electronic Structure Calculations with GPAW: a Real-Space Implementation of the Projector Augmented-Wave Method. *J. Phys.: Condens. Matter* **2010**, *22*, No. 253202.
- (41) Perdew, J. P.; Burke, K.; Ernzerhof, M. Generalized Gradient Approximation Made Simple. *Phys. Rev. Lett.* **1996**, *77*, 3865–3868.
- (42) Monkhorst, H. J.; Pack, J. D. Special Points for Brillouin-Zone Integrations. *Phys. Rev. B* **1976**, *13*, 5188–5192.
- (43) Wellendorff, J.; Lundgaard, K. T.; Møgelhøj, A.; Petzold, V.; Landis, D. D.; Nørskov, J. K.; Bligaard, T.; Jacobsen, K. W. Density Functionals for Surface Science: Exchange-Correlation Model Development with Bayesian Error Estimation. *Phys. Rev. B* **2012**, *85*, No. 235149.
- (44) Haastrup, S.; Strange, M.; Pandey, M.; Deilmann, T.; Schmidt, P. S.; Hinsche, N. F.; Gjerding, M. N.; Torelli, D.; Larsen, P. M.; Riis-Jensen, A. C.; et al. The Computational 2D Materials Database: high-throughput modeling and discovery of atomically thin crystals. *2D Mater.* **2018**, *5*, No. 042002.
- (45) Zhang, J.; Jia, S.; Kholmanov, I.; Dong, L.; Er, D.; Chen, W.; Guo, H.; Jin, Z.; Shenoy, V. B.; Shi, L.; et al. Janus Monolayer Transition-Metal Dichalcogenides. *ACS Nano* **2017**, *11*, 8192–8198.
- (46) Lu, A.-Y.; Zhu, A.; Xiao, J.; Chu, C.-P.; Han, Y.; Chu, M.-H.; Cheng, C.-C.; Yang, C.-W.; Wei, R.-H.; Yang, Y.; et al. Janus Monolayers of Transition Metal Dichalcogenides. *Nat. Nanotechnol.* **2017**, *12*, 744–749.
- (47) Fülöp, B.; Tajkov, Z.; Petó, J.; Kun, P.; Koltai, J.; Oroszlány, L.; Tóvári, E.; Murakawa, H.; Tokura, Y.; Bordács, S.; et al. Exfoliation of Single Layer BiTeI Flakes. *2D Mater.* **2017**, No. 031013.
- (48) Riis-Jensen, A. C.; Pandey, M.; Thygesen, K. S. Efficient Charge Separation in 2D Janus van der Waals Structures with Built-in Electric Fields and Intrinsic p-n Doping. *J. Phys. Chem. C* **2018**, *122*, 24520–24526.
- (49) Hu, X.; Wang, Y.; Shen, X.; Krashennnikov, A. V.; Sun, L.; Chen, Z. 1T phase as an Efficient Hole Injection Layer to TMDs Transistors: A Universal Approach to Achieve p-Type Contacts. *2D Mater.* **2018**, No. 031012.
- (50) Jin, C.; Rasmussen, F. A.; Thygesen, K. S. Tuning the Schottky Barrier at the Graphene/MoS₂ Interface by Electron Doping: Density Functional Theory and Many-Body Calculations. *J. Phys. Chem. C* **2015**, *119*, 19928–19933.
- (51) Fontana, Marcio.; Deppe, Tristan.; Boyd, Anthony K.; Rinzan, Mohamed.; Liu, Amy Y.; Paranjape, Makarand.; Barbara, Paola. Electron-Hole Transport and Photovoltaic Effect in Gated MoS₂ Schottky Junctions. *Sci. Rep.* **2013**, *3*, No. 1634.
- (52) Guan, Z.; Ni, S.; Hu, S. Tunable Electronic and Optical Properties of Monolayer and Multilayer Janus MoSSe as a Photocatalyst for Solar Water Splitting: A First-Principles Study. *J. Phys. Chem. C* **2018**, *122*, 6209–6216.
- (53) Riis-Jensen, A. C.; Deilmann, T.; Olsen, T.; Thygesen, K. S. Classifying the Electronic and Optical Properties of Janus Monolayers. *ACS Nano* **2019**, *13*, 13354–13364.
- (54) C2DB Webpage. 2019. <https://cmr.fysik.dtu.dk/c2db/c2db.html> (accessed Jan 27, 2019).

8.10 Paper X

Engineering Covalently Bonded 2D Layered Materials by Self-Intercalation

X. Zhao, P. Song, C. Wang, A. C. Riis-Jensen, W. Fu, Y. Deng, D. Wan, L. Kang, S. Ning, J. Dan, T. Venkatesan, Z. Liu, W. Zhou, K. S. Thygesen, X. Luo, S. J. Pennycook, and K. P. Loh

Nature, **581**, 171–177 (2020)

© 2020 Nature All Rights Reserved

<https://www.nature.com/articles/s41586-020-2241-9>.

Article


Engineering covalently bonded 2D layered materials by self-intercalation

<https://doi.org/10.1038/s41586-020-2241-9>

Received: 2 November 2019

Accepted: 4 March 2020

Published online: 13 May 2020

 Check for updates

Xiaoxu Zhao^{1,2,9}, Peng Song^{2,9}, Chengcai Wang³, Anders C. Riis-Jensen⁴, Wei Fu², Ya Deng⁵, Dongyang Wan⁶, Lixing Kang⁵, Shoucong Ning¹, Jiadong Dan¹, T. Venkatesan^{1,6}, Zheng Liu⁵, Wu Zhou⁷, Kristian S. Thygesen⁸, Xin Luo^{8,9}, Stephen J. Pennycook^{1,8} & Kian Ping Loh^{2,9}

Two-dimensional (2D) materials^{1–5} offer a unique platform from which to explore the physics of topology and many-body phenomena. New properties can be generated by filling the van der Waals gap of 2D materials with intercalants^{6,7}; however, post-growth intercalation has usually been limited to alkali metals^{8–10}. Here we show that the self-intercalation of native atoms^{11,12} into bilayer transition metal dichalcogenides during growth generates a class of ultrathin, covalently bonded materials, which we name ic-2D. The stoichiometry of these materials is defined by periodic occupancy patterns of the octahedral vacancy sites in the van der Waals gap, and their properties can be tuned by varying the coverage and the spatial arrangement of the filled sites^{7,13}. By performing growth under high metal chemical potential^{14,15} we can access a range of tantalum-intercalated TaS(Se)_y, including 25% Ta-intercalated Ta₉S₁₆, 33.3% Ta-intercalated Ta₇S₁₂, 50% Ta-intercalated Ta₁₀S₁₆, 66.7% Ta-intercalated Ta₈Se₁₂ (which forms a Kagome lattice) and 100% Ta-intercalated Ta₈Se₁₂. Ferromagnetic order was detected in some of these intercalated phases. We also demonstrate that self-intercalated V₁₁S₁₆, In₁₁Se₁₆ and Fe_xTe_y can be grown under metal-rich conditions. Our work establishes self-intercalation as an approach through which to grow a new class of 2D materials with stoichiometry- or composition-dependent properties.

Increased research into 2D materials has heralded a new branch of condensed-matter physics concerned with the description of electrons in atomically thin structures. So far, research efforts have primarily focused on 2D monolayers² and their hetero-stacked structures³, in which new properties can be engineered by generating superlattices of different moiré wavelengths. However, these hetero-stacked structures are currently produced by bottom-up methods that are low yielding and show poor reproducibility¹⁶. An alternative method of compositional tuning involves the intercalation of foreign atoms into the van der Waals (vdW) gap that is sandwiched by the chalcogen atoms; this has been shown to induce pseudo-2D characteristics in bulk crystals and modify their electronic properties^{4,6,7}. Depending on the interlayer stacking registries, the vdW gaps in transition metal dichalcogenides (TMDs) contain either octahedral and tetrahedral vacancies or trigonal-prismatic vacancies¹³, which provide docking sites for a diverse range of intercalants. Examples of successful intercalants include alkali metals^{8–10} such as Li, Na and K; transition metals^{17–21} such as Cu, Co, Ni, Fe and Nb; noble metals^{22–24} such as Ag, Au and Pt; as well as Sn and various organic molecules^{25–27}. Charge transfer from the intercalants⁷—or increased spin–orbit coupling due to the presence of heavy atoms^{7,24,28}—can enhance superconductivity¹⁰,

thermoelectricity²⁵ or spin polarization⁷. Intercalation is typically achieved using post-growth, diffusion-limited processes, either electrochemical or in the solid state. A well-defined intercalated phase with long-range crystalline order is difficult to obtain by such methods and usually requires harsh treatment conditions^{21,22,29}. Moreover, an intercalation phase diagram that correlates the density and spatial distribution of the intercalated atoms with the mesoscopic properties of the intercalation compound is currently lacking. Compared with the intercalation of foreign atoms into a TMD, the intercalation of native atoms—those that are present in the TMD itself—has so far received little attention^{11,29,30}. Such self-intercalated TMD compounds may exist as local energy minima in the region of the intercalation phase diagram in which a metal-rich stoichiometry is promoted by growth conditions involving metal atoms at high chemical potential. However, growth windows of TMDs using high metal chemical potentials have so far remained relatively unexplored^{31,32}.

In this work, the growth of 2D TMDs using both molecular beam epitaxy (MBE) and chemical vapour deposition (CVD) methods was investigated under high metal chemical potentials. We discovered that—independent of the growth method used—a metal-rich chemical potential promotes the self-intercalation of a metal (M) into MX, MX₂

¹Department of Materials Science and Engineering, National University of Singapore, Singapore, Singapore. ²Department of Chemistry and Centre for Advanced 2D Materials, National University of Singapore, Singapore, Singapore. ³Department of Electrical and Electronic Engineering, Southern University of Science and Technology, Shenzhen, China. ⁴CAMD and Center for Nanostructured Graphene (CNG), Department of Physics, Technical University of Denmark, Kongens Lyngby, Denmark. ⁵School of Materials Science and Engineering, Nanyang Technological University, Singapore, Singapore. ⁶NUSNNI-NanoCore, National University of Singapore, Singapore, Singapore. ⁷School of Physical Sciences and CAS Centre for Excellence in Topological Quantum Computation, University of Chinese Academy of Sciences, Beijing, China. ⁸State Key Laboratory of Optoelectronic Materials and Technologies, Centre for Physical Mechanics and Biophysics, Sun Yat-sen University, Guangzhou, China. ⁹These authors contributed equally: Xiaoxu Zhao, Peng Song. [✉]e-mail: luox77@mail.sysu.edu.cn; steve.pennycook@nus.edu.sg; chmlhkp@nus.edu.sg

Article

or M_2X_3 layered 2D compounds (M, metal; X, chalcogen), producing covalently bonded M_xX_y compounds. We term this class of materials ic-2D. Taking TaS_2 as an example, the intercalated Ta atoms occupy the octahedral vacancies in the vdW gap to form distinct topographical patterns, as verified by atomic resolution scanning transmission electron microscopy–annular dark field (STEM–ADF) imaging. By varying the ratio of intercalating atoms to octahedral vacancies in the vdW gap, we grew Ta_xS_y or Ta_xSe_y films and quantified the extent of Ta-intercalation using σ , the percentage of initial total vacancy sites that are occupied by intercalated atoms. Our results indicate that self-intercalation is common to a broad class of vdW crystals, and it offers a powerful approach through which to transform layered 2D materials into ultrathin, covalently bonded ic-2D crystals with ferromagnetic properties.

We first describe the self-intercalation of native atoms—that is, Ta—into a TaS_2 bilayer during MBE deposition on a silicon wafer, as a means to demonstrate the formation of an ic-2D film via octahedral vacancy filling of a 2D bilayer material. Wafer-scale Ta-intercalated TaS_2 bilayer films were grown on 2-inch, 285-nm SiO_2/Si wafers in a dedicated MBE system¹⁴. Ultra-pure Ta and S molecular beams were evaporated from an e-beam evaporator and a sulfur cracker cell equipped with a valve, respectively (Fig. 1a, b). We could routinely grow 2H-phase TaS_2 bilayer films using a high S chemical potential—that is, a Ta-to-S flux ratio of around 1:10 (Fig. 1a, Supplementary Fig. 1)—for 3 h and a substrate temperature of 600 °C. When the Ta:S flux ratio was increased to 1:6 (Fig. 1b, c), the film became non-stoichiometric with respect to TaS_2 owing to the excess of Ta atoms. A fingerprint of the Ta-rich environment is the presence of Ta adatoms (Fig. 1d) occupying the centre of the honeycombs (Fig. 1e) or situated on top of the Ta sites (Fig. 1f) in the monolayer TaS_2 film, as observed by STEM when the growth was interrupted partway through (Supplementary Fig. 2). When Ta and S are continually supplied in the appropriate ratio, the Ta adatoms become embedded in the TaS_2 structure, occupying the octahedral vacancies between two S layers (Fig. 1g). The ic-2D crystals therefore have a sequential, TaS_2 -Ta- TaS_2 -Ta layer-by-layer growth mechanism; as such, multilayer or bulk-phase ic-2D crystals can be readily accessed simply by increasing the growth time. The thermodynamic stability of such intercalated phases was assessed using energy-composition phase diagrams generated through density functional theory (DFT) calculations (Fig. 1h). It was found that stoichiometric H-phase TaS_2 is formed only under S-rich conditions (when the chemical potential of sulfur, μ_S , exceeds -5.3 eV), whereas at higher Ta:S flux ratios (low μ_S), various Ta-intercalated Ta_xS_y configurations—ranging from Ta_9S_{16} (25% Ta intercalation) to Ta_8S_{12} (66.7% Ta intercalation)—entered a thermodynamically stable state.

Notably, a Ta:S flux ratio of approximately 1:6 produced a $\sqrt{3}a \times \sqrt{3}a$ superlattice of Ta atoms (Fig. 2a) sandwiched between two TaS_2 monolayers. The extent of intercalation (σ) was 33.3%, and the overall stoichiometry of the crystal became Ta_7S_{12} , as corroborated by both the real-space STEM image (Fig. 2b) and the corresponding fast Fourier transform (FFT) pattern (Fig. 2c). Image simulation and sequential STEM images capturing the diffusion of intercalated atoms showed that the periodically arranged bright spots in the STEM image were induced by the intercalation of Ta (Fig. 2d, Supplementary Information section 1, Supplementary Videos 1, 2). We also collected STEM cross-section images (Fig. 2e, f) to verify the existence of an intercalated Ta atomic layer in the vdW gap of ic-2D films grown by CVD.

The homogeneous Ta_7S_{12} phase was grown directly on a 2-inch silicon wafer (Supplementary Fig. 3). The Ta_7S_{12} film was formed by the coalescence of nano-domain crystals (around 50 nm) separated by mirror twin boundaries or tilted grain boundaries (Supplementary Information section 2). The amorphous islands and gaps seen in the STEM images were attributed to the poor stability of Ta_xS_y , and to sample damage incurred during transfer. Energy dispersive X-ray spectroscopy (EDS) and electron energy loss spectroscopy (Supplementary Fig. 4) verified that the film was composed solely of Ta and S, with no foreign

elements, and X-ray photoelectron spectroscopy (Supplementary Fig. 5) confirmed that the chemical stoichiometry agreed very well with Ta_7S_{12} . The Raman spectra of the film exhibited two prominent E_g^3 and A_{1g}^3 peaks at 300 cm^{-1} and 400 cm^{-1} , respectively, matching those of H-phase TaS_2 films. The fingerprint of the intercalation was a series of minor peaks in the 100 cm^{-1} to 170 cm^{-1} range (Supplementary Fig. 6), which were absent in pure H-phase TaS_2 ³³ and are attributed to the covalent bonds between the intercalated Ta atoms and their octahedrally coordinated S atoms (Supplementary Fig. 7).

25% Ta-intercalated TaS_2 has a stoichiometry of Ta_9S_{16} and was produced at a slightly lower Ta chemical potential than Ta_7S_{12} , corresponding to a Ta:S ratio of around 1:8. The intercalated Ta atoms occupy the octahedral vacancies in every $2a \times \sqrt{3}a$ unit length, and this phase was distinguished by the square symmetry of the intercalated atomic lattice (Fig. 2g, k, Supplementary Fig. 8). When the Ta:S flux ratio was further increased to 1:5, a $Ta_{10}S_{16}$ phase ($\sigma = 50\%$) was successfully grown (Fig. 2h). The intercalation concentration—the percentage of total vacancy sites that were occupied—was determined to be exactly 50% via atom counting (Supplementary Fig. 9). Notably, this phase is characterized by atomic chains that are interconnected over a short range, forming an overall glassy phase. Clear diffusive rings were observed in the proximity of the first-order FFT spots (Fig. 2l, Supplementary Fig. 10), confirming this short-range ordered structure³⁴. When the Ta:S flux ratio was further increased, the glassy phase was retained, but the short atomic chains became denser before fully evolving into a complete atomic plane when σ reached approximately 100% (Supplementary Fig. 11). The use of growth conditions intermediate between those that give rise to high-symmetry phases resulted in phase separations, and atomically sharp domain boundaries separating two high-symmetry phases were apparent (Supplementary Information section 3).

To verify that ic-2D films could be produced by methods other than MBE, we used CVD to grow self-intercalated Ta_xSe_y crystals using excess Ta precursors. The crystal domains of these films were in the micrometre range—considerably larger than the nanosized domains grown by MBE (Supplementary Fig. 12). A typical Ta_8Se_{12} crystal ($\sigma = 66.7\%$) is depicted in Fig. 2i. Notably, it possesses a Kagome lattice belonging to the P_6 wallpaper symmetry group. A well-defined $\sqrt{3}a \times \sqrt{3}a$ periodic lattice can be unambiguously identified in the atomic-resolution STEM image (Fig. 2m; for the simulated image, see Supplementary Fig. 13). At even higher Ta chemical potential we successfully synthesized Ta_9Se_{12} crystals ($\sigma = 100\%$), in which the trigonal prismatic vacant sites in AA-stacked Ta_9Se_{12} were fully occupied (Fig. 2j)—as seen from the top view (Fig. 2n) and side view (Fig. 2e, Supplementary Fig. 14) STEM images. By precisely controlling the metal:chalcogen ratio during growth, we can prepare a full range of Ta-intercalated Ta_xSe_y or Ta_xS_y compounds with intercalation levels ranging from $\sigma = 25\%$ to over 100%, as verified by EDS (Supplementary Fig. 15, Supplementary Table 1).

In ic-2D films, the intercalated Ta atoms are octahedrally coordinated to the S_6 cage, as opposed to the trigonal-prismatic coordination that is adopted in pristine TaS_2 . Charge transfer from the intercalated Ta atoms to the TaS_2 host layers creates new electron ordering and modifies the Ta d -band splitting. Because the amount of charge transfer is dependent on the concentration of the intercalant, the system can be tuned. To investigate whether ferromagnetic order is present in the intercalated samples, magneto-transport measurements were carried out on MBE-grown Ta_7S_{12} ($\sigma = 33.3\%$) with a predominantly 2H_a stacking registry (Fig. 3a, Supplementary Fig. 16) and bilayer thickness (Supplementary Fig. 17). Figure 3c shows the temperature-dependent resistivity, in which a non-saturating upturn is observed below 30 K owing to the disorder-induced metal–insulator transition in the polycrystalline sample³⁵. Linear magnetoresistance up to 9 T is observed at low temperatures in Ta_7S_{12} (Fig. 3d), owing to density and mobility fluctuations³⁶. The anomalous Hall effect (AHE) arises from the interplay of spin–orbit interactions and ferromagnetic order, and is

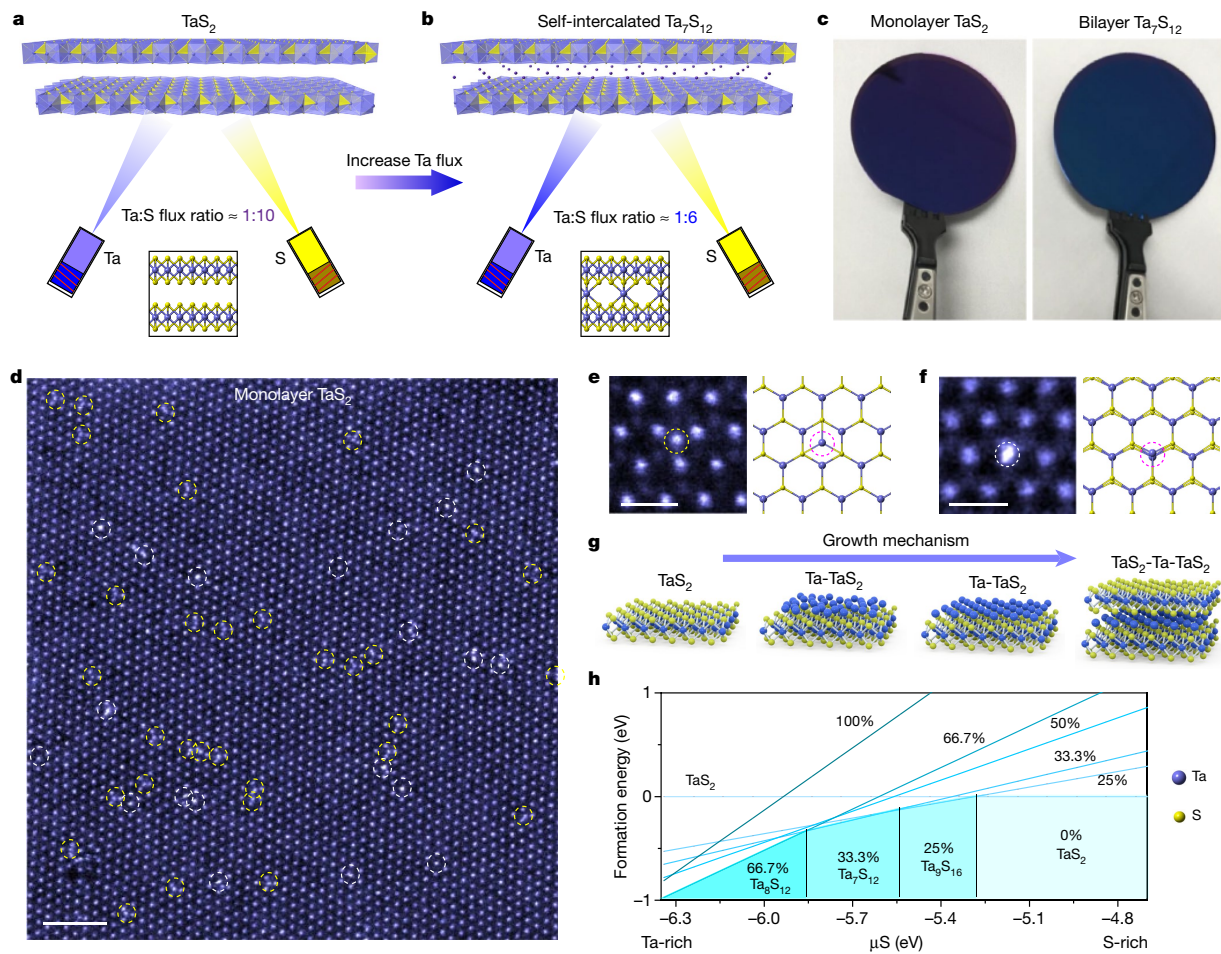


Fig. 1 | Self-intercalation in TaS₂ crystals. **a, b**, Schematic showing the growth of pristine TaS₂ (**a**) and self-intercalated Ta₇S₁₂ (**b**) by MBE under a low and a high Ta-flux environment, respectively. The lower Ta flux produces stoichiometric TaS₂, whereas a higher Ta flux generates a self-intercalated phase. **c**, Photographs of monolayer TaS₂ and bilayer Ta₇S₁₂, grown by MBE on a 2-inch SiO₂/Si wafer. **d–f**, Atomic-resolution STEM-ADF image of monolayer TaS₂ under Ta-rich conditions (**d**), showing an abundance of interstitial Ta atoms at

the centre of honeycomb (**e**) or on top of the Ta site (**f**). In **e, f**, the corresponding atomic models are depicted on the right. **g**, Schematic depicting the layer-by-layer growth of 2D crystals. **h**, Calculated formation energies of various self-intercalated Ta_xS_y phases with intercalation concentrations of 25%, 33.3%, 50%, 66.7% and 100%, as a function of the chemical potential of sulfur. Scale bars: **d**, 2 nm; **e, f**, 0.5 nm.

a potentially useful probe of spin polarization. We observed AHE in Ta₇S₁₂ in addition to the linear ordinary Hall effect (OHE). Figure 3e shows a nonlinear Hall effect in the proximity of zero magnetic field and a linear OHE at high field. Although both multiband conduction and the AHE contribute to the nonlinear Hall effect, the observed linear OHE suggests single-carrier (hole) conduction in Ta₇S₁₂ and thus excludes multiband transport as the origin of the nonlinear Hall effect^{37,38}. The nonlinear Hall effect is therefore ascribed to AHE, which arises from ferromagnetism in conductors³⁹. After subtracting the linear OHE, anomalous Hall resistance of up to 0.75 Ω is observed at 1.5 K; this decreases with increasing temperature and disappears at 10 K, which is in line with Monte Carlo simulations based on the Ising model (Supplementary Fig. 18).

The effects of self-intercalation on the electrical properties of TMDs were further assessed in Ta₈Se₁₂ ($\sigma = 66.7\%$), which forms a Kagome lattice. It was found that the intercalation of Ta atoms and the formation of Kagome lattices stabilize the charge-density wave states. The temperature-dependent Hall signal reveals an AHE below 15 K and confirms ferromagnetic order in Ta₈Se₁₂ (Supplementary Fig. 19, 20).

We performed DFT calculations in order to understand the origin of the magnetization in self-intercalated Ta₇S₁₂. Perfect bilayer 2H₁-stacked TaS₂ (Supplementary Fig. 21) possesses a non-magnetic ground state, in which ferromagnetism can be induced by the double exchange mechanism⁴⁰, triggered by the charge transfer from intercalated Ta to pristine TaS₂ (Fig. 3f). When the intercalated Ta adopts a $\sqrt{3}a \times \sqrt{3}a$ superstructure, six S atoms bond with one intercalated Ta atom to form an octahedral unit in the vdW gap. By contrast, each S atom is shared by three Ta atoms in the pristine TaS₂ layer. This difference in local bonding arrangement induces charge transfer from the octahedral-coordinated intercalated Ta atom to the prismatic-coordinated Ta atom in the TaS₂ layer (Fig. 3f). In pristine H-phase TaS₂, the Ta *d* orbitals and the S *p* orbitals are well separated in terms of energy, with the states at the Fermi level having mainly Ta *d*_{xy} and Ta *d*_{x²-y² characteristics (Supplementary Fig. 21). In Ta₇S₁₂ ($\sigma = 33.3\%$), the intercalated Ta atoms introduce additional spin-split bands across the Fermi level, and a magnetic ground state develops (Fig. 3g, h). The magnetic moments are localized on the *d* orbitals of the intercalated Ta atom, as evidenced by the calculated intercalated Ta orbital-resolved spin-up and spin-down band structures in Fig. 3g}

Article

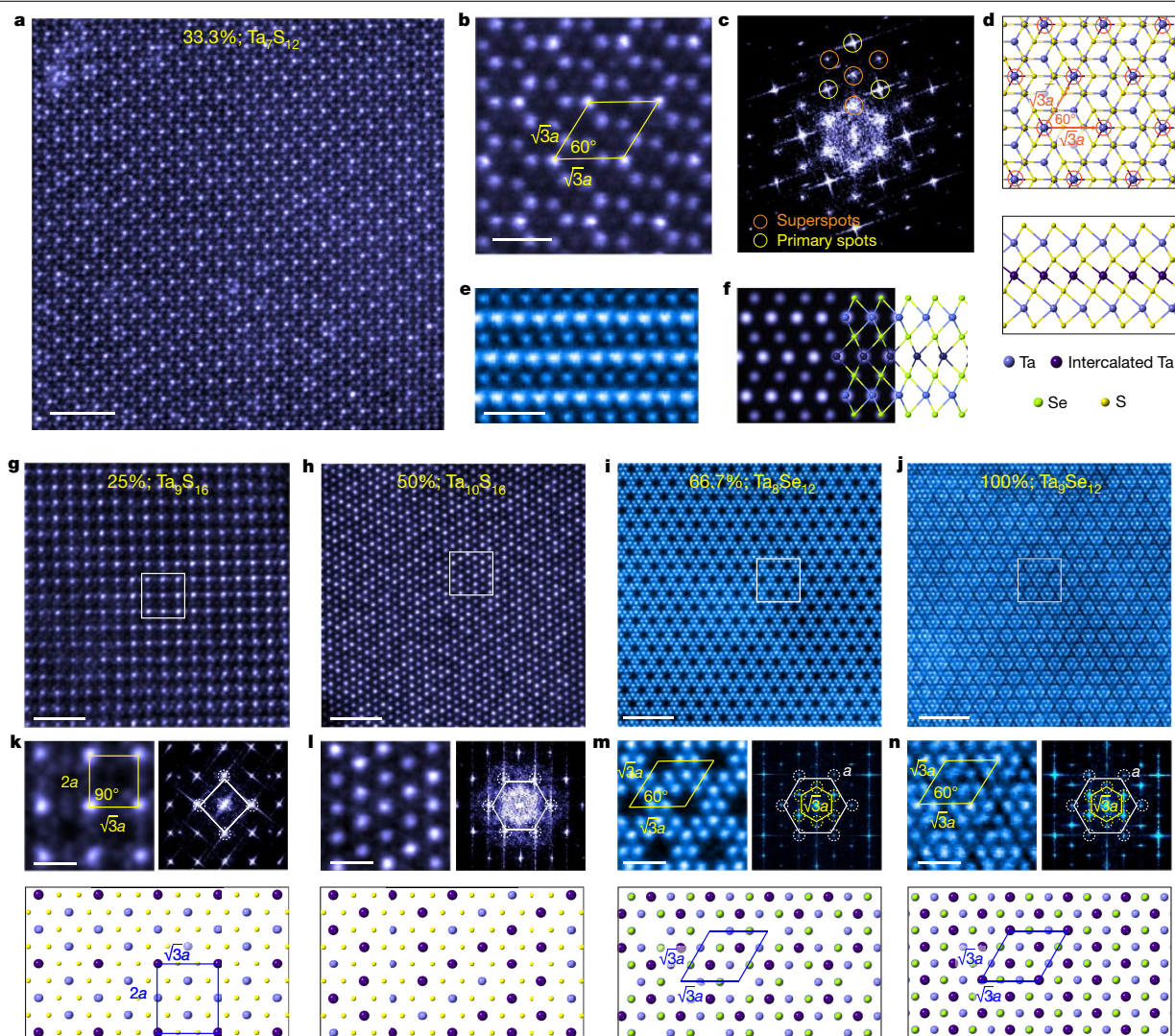


Fig. 2 | Compositional engineering of Ta_xS_y and Ta_xSe_y with different concentrations of intercalated Ta. **a, b**, Atomic-resolution STEM-ADF images of self-intercalated Ta_7S_{12} , grown by MBE, showing the well-defined $\sqrt{3}a \times \sqrt{3}a$ superstructure (**a**), and an enlarged image (**b**). **c**, The corresponding FFT pattern of **a**, with $\sqrt{3}a$ superspots highlighted by orange circles. **d**, Atomic model of self-intercalated Ta_7S_{12} . **e, f**, STEM cross-section view of 100% Ta-intercalated Ta_9Se_{12} (**e**) and its corresponding simulated image derived from

the DFT-optimized atomic model (**f**). **g–j**, Atomic-resolution STEM images of 25% Ta-intercalated Ta_9S_{16} (**g**), 50% Ta-intercalated $Ta_{10}S_{16}$ (**h**), 66.7% Ta-intercalated Ta_9Se_{12} (**i**) and 100% Ta-intercalated Ta_9Se_{12} (**j**) ic-2D crystals. **k–n**, Left, enlarged STEM images corresponding to the regions highlighted with white boxes in **g–j**, respectively; right, the corresponding FFT patterns; bottom, the corresponding atomic models. Scale bars: **a, g–j**, 2 nm; **b, e, k–n**, 0.5 nm.

and Fig. 3h, respectively. The states at the Fermi level comprise the prismatic-centred Ta d_{z^2} orbitals hybridized with the spin-up band of the $d_{x^2-y^2}$ orbital of the intercalated Ta. However, only the intercalated Ta atoms exhibit a net spin density, as illustrated in Fig. 3i, in which the top view spin density isosurface matches the shape of the $d_{x^2-y^2}$ orbital. In addition, the non-magnetic $3a \times 3a$ charge-density wave state of Ta_7S_{12} can be ruled out owing to its relative instability compared with the ferromagnetic state⁴¹.

The existence of a magnetic moment correlates with a large degree of charge transfer between the intercalated Ta and the TaS_2 layers. Strong charge transfer occurs when the proportion of intercalated Ta atoms is low, whereas charge transfer becomes relatively weak in a heavily intercalated (Fig. 3j) compound, in accordance with the calculated

charge difference and the variation of Bader charge on the Ta atoms (Supplementary Fig. 22, Supplementary Table 2).

To investigate whether the self-intercalation phenomenon occurred for other TMDs, we performed a high-throughput DFT study of 48 different intercalated TMD bilayers, using a semi-automated workflow for maximal consistency and veracity⁴². Specifically, we considered TMDs of the transition metals Mo, W, Nb, Ta, Ti, Zr, Hf, V, Cr, Mn, Fe, Co, Ni, Pd and Pt, as well as Sn, and the chalcogens S, Se and Te (Fig. 4a) at σ values of 33.3% or 66.7%. Out of this set of TMDs, we observed that 14 bilayer configurations— Ti_8S_{12} , Ti_8Se_{12} , Ti_8Te_{12} , Co_7S_{12} , Co_7Se_{12} , Co_7Te_{12} , Nb_7S_{12} , Nb_7Se_{12} , Nb_7Te_{12} , Mo_7S_{12} , Mo_7Se_{12} , Ta_7S_{12} , Ta_7Se_{12} and Ta_7Te_{12} (highlighted by specific σ values and chalcogens in Fig. 4a and Supplementary Table 3 for magnetic moment)—develop ferromagnetic

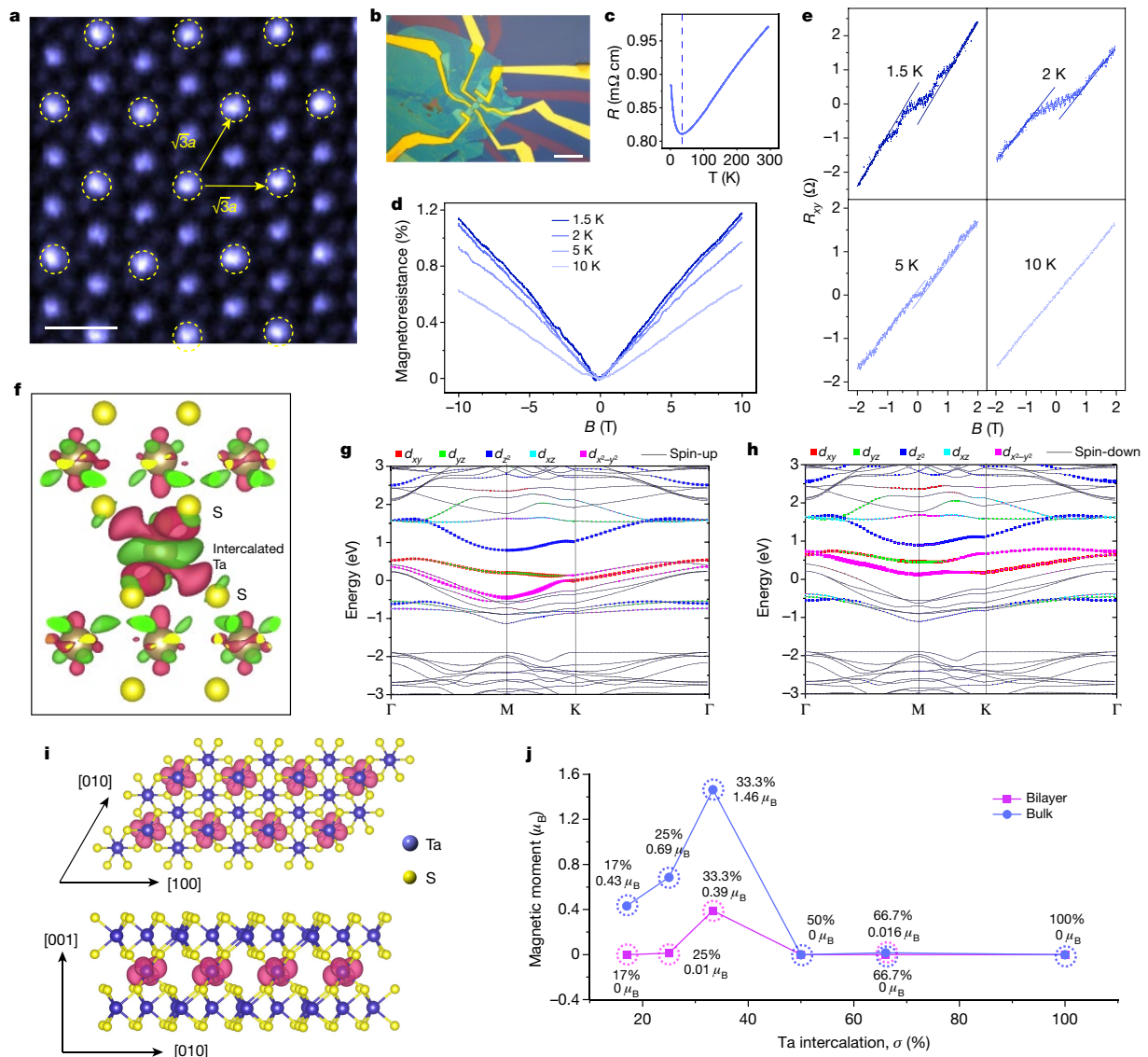


Fig. 3 | Ferromagnetism in Ta-intercalated Ta_7S_{12} ic-2D crystals.

a, Atomic-resolution STEM-ADF image of a typical self-intercalated Ta_7S_{12} film. This image was collected using a half-angle range from about 30 mrad to 110 mrad to enhance the contrast of S. **b**, Optical microscopy image of a Ta_7S_{12} Hall bar device encapsulated with hexagonal boron nitride. **c**, Resistivity of the Ta_7S_{12} ic-2D crystal as a function of temperature. **d**, **e**, Temperature-dependent magnetoresistance (**d**) and Hall resistance (R_{xy}) (**e**) of Ta_7S_{12} under an

out-of-plane magnetic field. **f**, Contour plot of charge density difference in Ta-intercalated Ta_7S_{12} . **g**, **h**, Orbital-resolved spin-up (**g**) and spin-down (**h**) band structures of the intercalated Ta in Ta_7S_{12} . **i**, Top view (top) and side view (bottom) spin density isosurface of Ta-intercalated Ta_7S_{12} . **j**, Calculated magnetic moments as a function of the Ta-intercalation concentration (σ) in 2H_x -stacked nonstoichiometric Ta_xS_y . μ_B , Bohr magneton. Scale bars: **a**, 0.5 nm; **b**, 20 μm .

order upon self-intercalation, whereas their parental MX_2 bilayers are nonferromagnetic. Notably, group V and group VI TMDs exhibit strong ferromagnetism after self-intercalation (Fig. 4b). MX_2 bilayers that are intrinsically ferromagnetic—that is, VX_2 , CrX_2 , MnX_2 and FeX_2 —retain ferromagnetism upon self-intercalation (highlighted by orange triangles in Fig. 4a). Among the 14 self-intercalated 2D ferromagnets that we generated, the formation energies of 12 of these—the two exceptions being MoS_2 and MoSe_2 —were lower than or similar to those of the non-intercalated materials (Supplementary Figs. 23, 24), indicating that self-intercalation is energetically feasible.

To validate our theoretical predictions, we attempted to grow a wide variety of ic-2D materials (Fig. 4a). In this figure, blue triangles

indicate that the self-intercalation can be experimentally realized^{11,12}, whereas grey triangles indicate that intercalation was not successful under our experimental conditions. We succeeded in growing several ic-2D crystals—namely $\text{V}_{11}\text{S}_{16}$ (Fig. 4c, Supplementary Fig. 25), $\text{In}_{11}\text{Se}_{16}$ (Fig. 4d, Supplementary Fig. 26) and Fe_xTe_y (Fig. 4e, Supplementary Fig. 27)—by either CVD or MBE. The topological features and corresponding FFT patterns of these crystals are depicted in Fig. 4f–h. The intercalated $\text{V}_{11}\text{S}_{16}$ has a $2a \times 2a$ superstructure, and the intercalation concentration was estimated at 75% (Fig. 4f). $\text{In}_{11}\text{Se}_{16}$ also showed a $2a \times 2a$ superstructure; however, in this case, the intercalated In atoms reveal a signature honeycomb structure (Fig. 4g). The crystal structure of self-intercalated Fe_xTe_y was complicated—additional Fe atoms were

Article

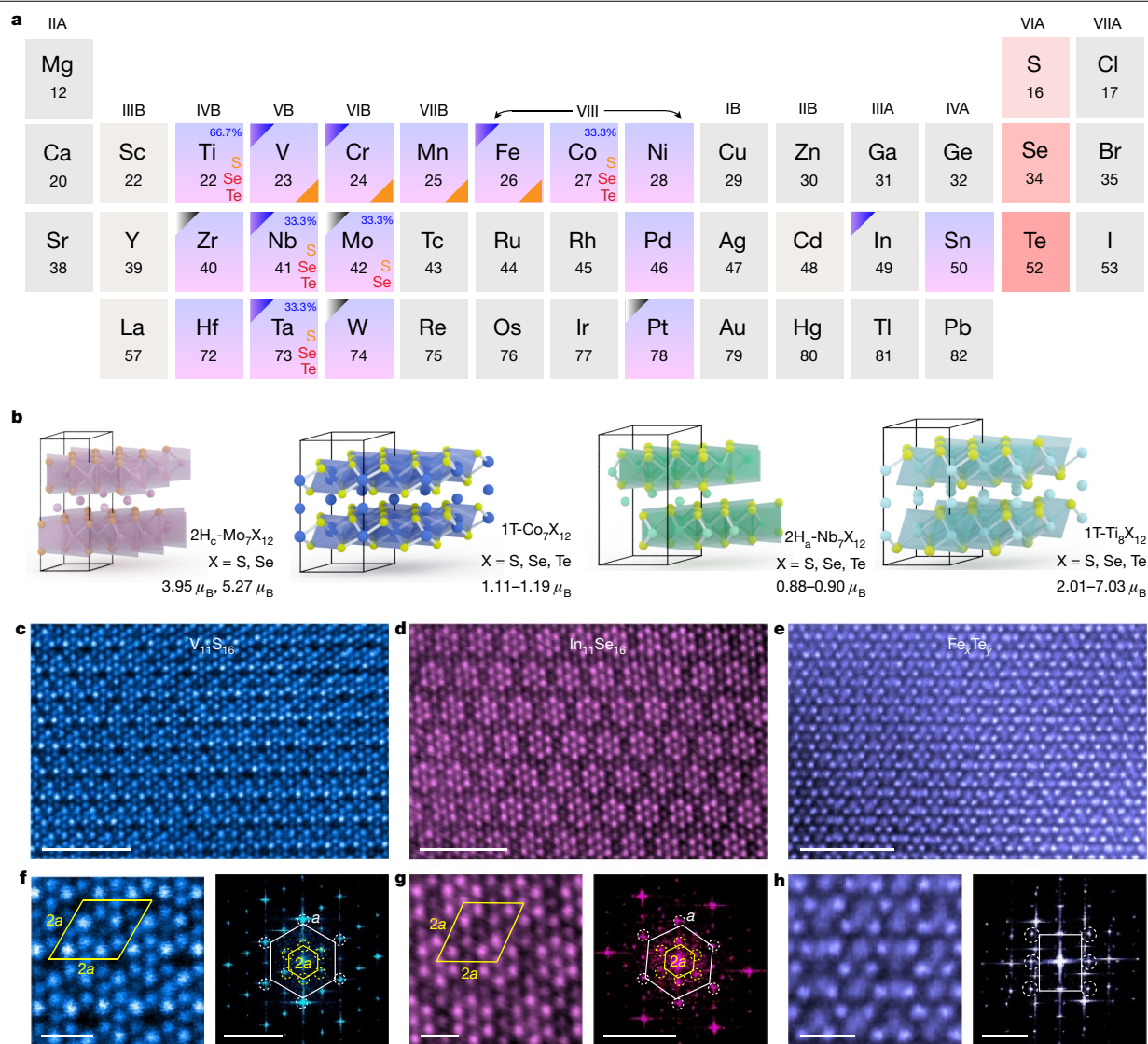


Fig. 4 | A library of ic-2D crystals. **a**, Periodic table showing metal (blue) and chalcogen (red) combinations that form ic-2D crystals according to our DFT calculations; the list is not exhaustive. Blue triangles indicate that self-intercalation can be experimentally realized, whereas grey triangles indicate that intercalation was not successful under our experimental conditions. MX_2 structures with intrinsic ferromagnetism are highlighted with

orange triangles. **b**, Atomic models, obtained from DFT calculations, of ic-2D crystals that exhibit ferromagnetism. **c–e**, STEM-ADF images of V-intercalated $V_{11}S_{16}$ (**c**), In-intercalated $In_{11}Se_{16}$ (**d**) and Fe-intercalated Fe_xTe_y (**e**). **f–h**, Left, enlarged STEM images of **c–e**, respectively; right, the corresponding FFT patterns. Scale bars: **c–e**, 2 nm; **f–h**, 0.5 nm; FFT patterns in **f–h**, 5 nm^{-1} .

found to be intercalated into the atomic network of the pristine FeTe matrix as interstitials, because telluride-based TMDs offer the largest spacing between the host atoms⁴³. Upon intercalation, the Fe_xTe_y phase reveals new symmetries, as confirmed by the emergence of superspots in the FFT pattern (Fig. 4h). A similar complex intercalation network was also observed in V_xTe_y (Supplementary Fig. 28).

We have developed a robust method to engineer the composition of a broad class of TMDs, by means of self-intercalation with native metal atoms during growth. Because the main principle is the application of high chemical potential of metal atoms to provide the driving force for intercalation during growth, this technique should be compatible with most growth methods. The metal intercalants occupy octahedral vacant sites in the vdW gap, and distinct

stoichiometric phases are produced depending on the levels of intercalation. High-throughput DFT simulations—supported by growth experiments—show that the self-intercalation method is applicable to a large class of 2D layered materials, thus enabling a library of materials with potentially new properties to be created from existing layered materials. Owing to the versatility with which the composition can be controlled, it is possible to tune—in one class of materials—properties such as ferromagnetism and the formation of spin-frustrated Kagome lattices. The implication of this work is that bilayer (or thicker) TMDs can be transformed into ultrathin, covalently bonded 3D materials, with stoichiometry that can be tuned over a broad range by varying the concentration of the intercalants.

Online content

Any methods, additional references, Nature Research reporting summaries, source data, extended data, supplementary information, acknowledgements, peer review information; details of author contributions and competing interests; and statements of data and code availability are available at <https://doi.org/10.1038/s41586-020-2241-9>.

- Chhowalla, M. et al. The chemistry of two-dimensional layered transition metal dichalcogenide nanosheets. *Nat. Chem.* **5**, 263–275 (2013).
- Zhou, J. et al. A library of atomically thin metal chalcogenides. *Nature* **556**, 355–359 (2018).
- Jin, C. et al. Ultrafast dynamics in van der Waals heterostructures. *Nat. Nanotechnol.* **13**, 994–1003 (2018).
- Wang, C. et al. Monolayer atomic crystal molecular superlattices. *Nature* **555**, 231–236 (2018).
- Novoselov, K. S. et al. Two-dimensional atomic crystals. *Proc. Natl Acad. Sci. USA* **102**, 10451–10453 (2005).
- Wan, J. et al. Tuning two-dimensional nanomaterials by intercalation: materials, properties and applications. *Chem. Soc. Rev.* **45**, 6742–6765 (2016).
- Friend, R. H. & Yoffe, A. D. Electronic properties of intercalation complexes of the transition metal dichalcogenides. *Adv. Phys.* **36**, 1–94 (1987).
- Wang, X., Shen, X., Wang, Z., Yu, R. & Chen, L. Atomic-scale clarification of structural transition of MoS₂ upon sodium intercalation. *ACS Nano* **8**, 11394–11400 (2014).
- Tan, S. J. R. et al. Chemical stabilization of 1T' phase transition metal dichalcogenides with giant optical Kerr nonlinearity. *J. Am. Chem. Soc.* **139**, 2504–2511 (2017).
- Kanetani, K. et al. Ca intercalated bilayer graphene as a thinnest limit of superconducting C₆Ca. *Proc. Natl Acad. Sci. USA* **109**, 19610–19613 (2012).
- Yang, J. et al. Ultrahigh-current-density niobium disulfide catalysts for hydrogen evolution. *Nat. Mater.* **18**, 1309–1314 (2019).
- Cui, F. et al. Controlled growth and thickness-dependent conduction-type transition of 2D ferrimagnetic Cr₂S₃ semiconductors. *Adv. Mater.* **32**, 1905896 (2020).
- Mortazavi, M., Wang, C., Deng, J., Shenoy, V. B. & Medhekar, N. V. Ab initio characterization of layered MoS₂ as anode for sodium-ion batteries. *J. Power Sources* **268**, 279–286 (2014).
- Fu, D. et al. Molecular beam epitaxy of highly crystalline monolayer molybdenum disulfide on hexagonal boron nitride. *J. Am. Chem. Soc.* **139**, 9392–9400 (2017).
- Chen, J. et al. Homoepitaxial growth of large-scale highly organized transition metal dichalcogenide patterns. *Adv. Mater.* **30**, 1704674 (2018).
- Liao, M. et al. Twist angle-dependent conductivities across MoS₂/graphene heterojunctions. *Nat. Commun.* **9**, 4068 (2018).
- Koski, K. J. et al. Chemical intercalation of zerovalent metals into 2D layered Bi₂Se₃ nanoribbons. *J. Am. Chem. Soc.* **134**, 13773–13779 (2012).
- Guilmeau, E., Barbier, T., Maignan, A. & Chateigner, D. Thermoelectric anisotropy and texture of intercalated TiS₂. *Appl. Phys. Lett.* **111**, 133903 (2017).
- Wang, M. et al. Chemical intercalation of heavy metal, semimetal, and semiconductor atoms into 2D layered chalcogenides. *2D Mater.* **5**, 045005 (2018).
- Dungey, K. E., Curtis, M. D. & Penner-Hahn, J. E. Structural characterization and thermal stability of MoS₂ intercalation compounds. *Chem. Mater.* **10**, 2152–2161 (1998).
- Gong, Y. et al. Spatially controlled doping of two-dimensional SnS₂ through intercalation for electronics. *Nat. Nanotechnol.* **13**, 294–299 (2018).
- Chen, Z. et al. Interface confined hydrogen evolution reaction in zero valent metal nanoparticles-intercalated molybdenum disulfide. *Nat. Commun.* **8**, 14548 (2017).
- Liu, C. et al. Dynamic Ag⁺-intercalation with AgSnSe₂ nano-precipitates in Cl-doped polycrystalline SnSe₂ toward ultra-high thermoelectric performance. *J. Mater. Chem. A* **7**, 9761–9772 (2019).
- Bouwmeester, H. J. M., van der Lee, A., van Smaalen, S. & Wiegers, G. A. Order–disorder transition in silver-intercalated niobium disulfide compounds. II. Magnetic and electrical properties. *Phys. Rev. B* **43**, 9431–9435 (1991).
- Wan, C. et al. Flexible n-type thermoelectric materials by organic intercalation of layered transition metal dichalcogenide TiS₂. *Nat. Mater.* **14**, 622–627 (2015).
- Jeong, S. et al. Tandem intercalation strategy for single-layer nanosheets as an effective alternative to conventional exfoliation processes. *Nat. Commun.* **6**, 5763 (2015).
- O'Brien, E. S. et al. Single-crystal-to-single-crystal intercalation of a low-bandgap superatomic crystal. *Nat. Chem.* **9**, 1170–1174 (2017).
- Kumar, P., Skomski, R. & Pushpa, R. Magnetically ordered transition-metal-intercalated WSe₂. *ACS Omega* **2**, 7985–7990 (2017).
- Kim, S. et al. Interstitial Mo-assisted photovoltaic effect in multilayer MoSe₂ phototransistors. *Adv. Mater.* **30**, 1705542 (2018).
- Zhang, M. et al. Electron density optimization and the anisotropic thermoelectric properties of Ti self-intercalated Ti_{1-x}S₂ compounds. *ACS Appl. Mater. Interfaces* **10**, 32344–32354 (2018).
- Wang, S. et al. Shape evolution of monolayer MoS₂ crystals grown by chemical vapor deposition. *Chem. Mater.* **26**, 6371–6379 (2014).
- Zhao, X. et al. Mo-terminated edge reconstructions in nanoporous molybdenum disulfide film. *Nano Lett.* **18**, 482–490 (2018).
- Mounet, N. et al. Two-dimensional materials from high-throughput computational exfoliation of experimentally known compounds. *Nat. Nanotechnol.* **13**, 246–252 (2018).
- Azizi, A. et al. Spontaneous formation of atomically thin stripes in transition metal dichalcogenide monolayers. *Nano Lett.* **16**, 6982–6987 (2016).
- Motome, Y., Furukawa, N. & Nagaosa, N. Competing orders and disorder-induced insulator to metal transition in manganites. *Phys. Rev. Lett.* **91**, 167204 (2003).
- Parish, M. M. & Littlewood, P. B. Non-saturating magnetoresistance in heavily disordered semiconductors. *Nature* **426**, 162–165 (2003).
- Jiang, Z. et al. Structural and proximity-induced ferromagnetic properties of topological insulator-magnetic insulator heterostructures. *AIP Adv.* **6**, 055809 (2016).
- Jiang, Z. et al. Independent tuning of electronic properties and induced ferromagnetism in topological insulators with heterostructure approach. *Nano Lett.* **15**, 5835–5840 (2015).
- Nagaosa, N., Sinova, J., Onoda, S., MacDonald, A. H. & Ong, N. P. Anomalous Hall effect. *Rev. Mod. Phys.* **82**, 1539–1592 (2010).
- Zener, C. Interaction between the *d* shells in the transition metals. *Phys. Rev.* **81**, 440–444 (1951).
- Coelho, P. M. et al. Charge density wave state suppresses ferromagnetic ordering in VSe₂ monolayers. *J. Phys. Chem. C* **123**, 14089–14096 (2019).
- Hastrup, S. et al. The computational 2D materials database: high-throughput modeling and discovery of atomically thin crystals. *2D Mater.* **5**, 042002 (2018).
- Karthikeyan, J., Komsa, H.-P., Batzill, M. & Krasheninnikov, A. V. Which transition metal atoms can be embedded into two-dimensional molybdenum dichalcogenides and add magnetism? *Nano Lett.* **19**, 4581–4587 (2019).

Publisher's note Springer Nature remains neutral with regard to jurisdictional claims in published maps and institutional affiliations.

© The Author(s), under exclusive licence to Springer Nature Limited 2020

Article

Methods

Growth of self-intercalated TMD films by MBE

Ta-intercalated Ta_xS_y films were grown in a dedicated MBE chamber (base pressure $<6 \times 10^{-10}$ torr). Before growth, the 2-inch SiO_2 substrates were degassed in the same chamber at 500 °C for 2 h. Ultrapure Ta (99.995%, Goodfellow) and S powders (99.5% Alfa Aesar) were evaporated from a mini electron-beam evaporator and a standard sulfur valved cracker, respectively. The flux density of Ta was precisely controlled by adjusting the flux current. The temperature of the S cracker cell was maintained at 110 °C, and the flux density was controlled by the shutter of the cracker valve. The substrate temperature was maintained at 600–650 °C and the growth time was about 3 h for all thin films. Controlled growth of 25% Ta-intercalated Ta_9S_{16} , 33.3% Ta-intercalated Ta_7S_{12} and 50% Ta-intercalated $Ta_{10}S_{16}$ films was achieved when the Ta/S ratio was set at around 1:8, around 1:6 and around 1:5, respectively. A slightly higher growth temperature facilitates the self-intercalation process. After growth, both Ta and S sources were turned off and the sample was further annealed for another 30 min before cooling to room temperature. In-intercalated In_xSe_y samples were grown in a customized MBE chamber (base pressure $<6 \times 10^{-10}$ torr). Before growth, the 1 cm \times 1 cm SiO_2 substrate was degassed in the chamber at 600 °C for 1 h. Ultrapure In_2Se_3 powder (99.99%) and Se pellets (99.999%) were evaporated from a mini electron-beam evaporator and an effusion cell, respectively. The temperature of the Se effusion cell was set at 150 °C with a hot-lip at 220 °C. The substrate temperature was maintained at 400 °C and the growth time was about 2 h. Controlled growth of $In_{11}Se_{16}$ films was achieved when the In_2Se_3/Se ratio was set at around 1:3.

Growth of self-intercalated TMD films by CVD

Ta-intercalated Ta_xSe_y crystals were grown by CVD. Before growth, the SiO_2 substrate was sequentially cleaned using water and acetone, followed by 5 min of O_2 plasma. The furnace was purged by 300 standard cubic centimetres (sccm) of Ar gas for 5 min. Se powders and mixed Ta/TaCl₅ powders were applied as precursors that were located upstream in a one-inch quartz tube. 40 sccm Ar and 10 sccm H_2 was used as a carrier gas. The samples were grown at 800 °C for 30 min. After growth, the sample was cooled down quickly in a continuous stream of Ar. Controlled growth of 66.7% Ta-intercalated Ta_8Se_{12} and 100% Ta-intercalated Ta_9Se_{12} was achieved when the content of Se powders and mixed Ta/TaCl₅ powders were 1 g/15 mg/1.5 mg and 1 g/30 mg/3 mg, respectively. V-intercalated V_xS_y crystals were grown by CVD. Before growth, the SiO_2 substrates were treated by the same method as indicated for the growth of Ta_xSe_y . Two quartz boats containing 0.5 g S and 0.3 g VCl₃ were loaded upstream of the one-inch quartz tube to dispense the precursors. The carrier gas was 40 sccm Ar together with 10 sccm H_2 . The sample was grown at 680 °C for 30 min. After growth, the sample was cooled quickly under the protection of 100 sccm Ar. Fe-intercalated Fe_xTe_y crystals were grown by CVD. Before growth, the SiO_2 substrates were treated by the same method as indicated for the growth of Ta_xSe_y . Two quartz boats containing Te (>99.997%) and FeCl₂ (>99.9%) were placed upstream of the one-inch quartz tube to dispense the precursors. The sample was grown at 600 °C for 30 min. After growth, the sample was cooled quickly under the protection of 100 sccm Ar.

Sample characterization

X-ray photoelectron spectroscopy was performed using a SPECS XR 50 X-ray Al K α (1,486.6 eV) source with a pass energy of 30 eV. The chamber base pressure was lower than 8×10^{-10} mbar. Raman spectra were collected at room temperature using the confocal WiTec Alpha 300R Raman Microscope (laser excitation, 532 nm).

STEM sample preparation, image characterization and image simulation

The as-grown TMD films were transferred via a poly (methyl methacrylate) (PMMA) method under the protection of graphene. A

continuous graphene film was coated on fresh Ta_7S_{12} film to protect the surface oxidation via a conventional PMMA method. Subsequently, graphene/ Ta_7S_{12} composites were immersed in 1 M KOH solution to detach the PMMA/ Ta_7S_{12} composite from the SiO_2 substrate, followed by rinsing in deionized water. The PMMA/graphene/ Ta_7S_{12} film was then placed onto a Cu quantifoil TEM grid that was precoated with continuous graphene film⁴⁴. The TEM grid was then immersed in acetone to remove the PMMA films. Atomic-resolution STEM-ADF imaging was performed on an aberration-corrected JEOL ARM200F, equipped with a cold field-emission gun and an ASCOR corrector operating at 60 kV. The convergence semiangle of the probe was around 30 mrad. Image simulations were performed with the QSTEM package assuming an aberration-free probe with a probe size of approximately 1 Å. The convergence semiangle of the probe was set at around 30 mrad, and the accelerating voltage was 60 kV in line with the experiments. The collection angle for high-angle annular dark-field imaging was between 81 and 280 mrad and for medium angle annular dark-field imaging was from 30 to 110 mrad. The phonon configurations were set at 30 with defocus value of 0. The STEM-EDS were collected and processed in an Oxford Aztec EDS system.

Device fabrication and measurements

MBE-grown Ta_7S_{12} and CVD-grown Ta_8Se_{12} were selected to fabricate Hall-bar devices using e-beam lithography and e-beam evaporation of Ti/Au (2/60 nm). The MBE-grown Ta_7S_{12} film was then etched into Hall-bar geometry using deep reactive-ion etching. The final devices were encapsulated with hexagonal boron nitride flakes using a dry-transfer method in the glovebox (both O_2 and H_2O less than 1 ppm), to avoid the degradation of Ta_7S_{12} and Ta_8Se_{12} under ambient conditions. Low-temperature transport measurements were carried out in an Oxford Teslatron system. All resistances were derived from four-terminal measurements using an SR830 lock-in amplifier, with a constant excitation current of 1 μ A.

DFT calculations

First-principles calculations based on DFT were implemented in the plane wave code VASP⁴⁵ using the projector-augmented wave potential approach. For the exchange and correlation functional, both the local density approximation and the Perdew–Burke–Ernzerhof (PBE)⁴⁶ flavour of the generalized gradient approximation were used, and no discernible difference were found in the results. A kinetic energy cut off of 500 eV was used for the TaS_2 . A Monkhorst Pack⁴⁷ k -grid sampling with a k -point density of 6.0 \AA^{-3} was used for geometry optimization. For thin-film calculations, a vacuum thickness of 20 Å was added in the slab to minimize the interaction between adjacent image cells. Geometry optimization was performed with the maximum force convergence criterion of $0.005 \text{ eV \AA}^{-1}$. To treat the strong on-site Coulomb interaction of localized Ta d orbitals, we used Dudarev's approach⁴⁸ with an effective U parameter of $U_{\text{eff}} = 3.0 \text{ eV}$. The zone centre phonon modes were calculated using density functional perturbation theory with the local density approximation functionals.

High-throughput DFT calculations

These were carried out with the electronic structure code GPAW⁴⁹ following a semi-automated workflow for maximal consistency and accuracy⁴². The relaxations of the self-intercalated bilayers were done on a Monkhorst-Pack⁴⁷ grid with a k -point density of 6.0 \AA^{-3} using the PBE⁴⁶ and BEEF-vdW functionals⁵⁰ for describing exchange-correlation effects. A vacuum of 15 Å was used in the out-of-plane direction to avoid non-physical periodic interactions. The plane-wave expansion was cut off at 800 eV. All systems were relaxed until the maximum force on any atom was 0.01 eV \AA^{-1} and the maximum stress on the unit cell was $0.002 \text{ eV \AA}^{-3}$. All systems were calculated in the intercalated structure with both a spin-paired calculation and a spin-polarized calculation. If the total energy of the spin-polarized structure was found to be more than

0.01 eV per atom lower than the spin-paired structure, the structure was concluded to be magnetically more stable than its non-magnetic counterpart. The atomic structures of calculated self-intercalated TMDs (33.3% and 66.7% intercalation concentration) are presented in Supplementary Fig. 29, in which the polymorphism of single-layer MoX_2 , WX_2 , NbX_2 and TaX_2 ($X = \text{S}, \text{Se}$ and Te) reveals an H-phase, whereas the rest of the TMDs are T-phase, adopting an AA stacking polytype. MoX_2 and WX_2 adopt the AA' stacking order whereas NbX_2 and TaX_2 adopt AB' stacking. All intercalants occupy the octahedral vacancies in the vdW gap.

Data availability

The main data supporting the findings of this study are available within the paper and its Supplementary Information. Additional data are available from the corresponding authors upon reasonable request.

Code availability

The Python code is available in the Supplementary Information.

44. Wang, H. et al. High-quality monolayer superconductor NbSe_2 grown by chemical vapour deposition. *Nat. Commun.* **8**, 394 (2017).
45. Kresse, G. & Furthmüller, J. Efficient iterative schemes for ab Initio total-energy calculations using a plane-wave basis set. *Phys. Rev. B* **54**, 11169–11186 (1996).
46. Perdew, J. P., Burke, K. & Ernzerhof, M. Generalized gradient approximation made simple. *Phys. Rev. Lett.* **77**, 3865–3868 (1996).
47. Monkhorst, H. J. & Pack, J. D. Special points for Brillouin-zone integrations. *Phys. Rev. B* **13**, 5188–5192 (1976).
48. Dudarev, S. L. Electron-energy-loss spectra and the structural stability of nickel oxide: An LSDA+U study. *Phys. Rev. B* **57**, 1505 (1998).
49. Enkovaara, J. et al. Electronic structure calculations with GPAW: a real-space implementation of the projector augmented-wave method. *J. Phys. Condens. Matter* **22**, 253202 (2010).
50. Wellendorff, J. et al. Density functionals for surface science: exchange-correlation model development with Bayesian error estimation. *Phys. Rev. B* **85**, 235149 (2012).

Acknowledgements K.P.L. thanks A*STAR Project 'Scalable Growth of Ultrathin Ferroelectric Materials for Memory Technologies' (grant number A1983c0035) and support from the Centre for Advanced 2D Materials, National University of Singapore. W.Z. acknowledges support from the National Key R&D Program of China (2018YFA0305800) and the Natural Science Foundation of China (51622211). S.J.P. is grateful to the National University of Singapore for funding and the Ministry of Education (MOE) for a Tier 2 grant 'Atomic scale understanding and optimization of defects in 2D materials' (MOE2017-T2-2-139). Z.L. thanks the MOE for a Tier 2 grant (2017-T2-2-136) and a Tier 3 grant (2018-T3-1-002), and the A*STAR QTE programme. X.L. acknowledges support from the National Natural Science Foundation of China (grant number 11804286) and the Fundamental Research Funds for the Central Universities (grant number 19lgpy263). DFT calculations were performed using resources of the National Supercomputer Center in Guangzhou supported by the Special Program for Applied Research on Super Computation of the NSFC Guangdong Joint Fund (second phase). K.S.T. acknowledges funding from the European Research Council under the European Union's Horizon 2020 research and innovation programme (grant number 773122, LIMA). The Center for Nanostructured Graphene is sponsored by the Danish National Research Foundation, project DNR103. We thank J. P. Shi, F. F. Cui and Y. F. Zhang for providing high-quality CVD samples.

Author contributions X.Z., S.J.P. and K.P.L. conceived the idea. S.J.P. and K.P.L. supervised the execution of the whole work. X.Z. and W.Z. performed the electron microscopy experiments and data analysis. X.L., A.C.R.-J. and C.W. performed the DFT calculations and data analysis. A.C.R.-J. and K.S.T. performed the high-throughput DFT calculations. W.F., Y.D., L.K. and Z.L. grew the samples. D.W. and T.V. measured the magnetism. P.S. performed device fabrication and measurement. J.D. and S.N. developed the Python scripts for data analysis. All authors discussed the results and participated in writing the manuscript.

Competing interests The authors declare no competing interests.

Additional information

Supplementary information is available for this paper at <https://doi.org/10.1038/s41586-020-2241-9>.

Correspondence and requests for materials should be addressed to X.L., S.J.P. or K.P.L.

Peer review information *Nature* thanks Thomas Heine and the other, anonymous, reviewer(s) for their contribution to the peer review of this work.

Reprints and permissions information is available at <http://www.nature.com/reprints>.

APPENDIX A

Abbreviations

ND	N Dimensional
BSE	Bethe-Salpeter Equation
C2DB	Computational 2D Materials Database
DFT	Density Functional Theory
CVD	Chemical Vapor Deposition
CBM	Conduction Band Minimum
FD	Finite Difference
GGA	Generalized Gradient Approximation
GPAW	Grid-based Projector-Augmented Wave method
HOMO	Highest Occupied Molecular Orbital
IQE	Internal Quantum Efficiency
LCAO	Linear Combination of Atomic Orbitals
LCAOS	Linear Combination of Atomic Orbitals Scissors-operator
LDA	Local Density Approximation
MBE	Molecular Beam Epitaxy
MW	Mott-Wannier
NC	Norm Conserving
PCE	Power Conversion Efficiency
PBE	Perdew-Burke-Ernzerhof
PW	Plane-Wave
QEH	Quantum Electrostatic Heterostructure
RPA	Random Phase Approximation

SBH	Schottky Barrier Height
TMD	Transition Metal Dichalcogenide
VBM	Valence Band Maximum
vdWH	van der Waals Heterostructure

APPENDIX B

Calculation of the Electronic Density in GPAW

We will start our discussion by taking our starting point around eq. 2.19 where we defined the expectation value of the atomic energy levels in terms of the smooth wave functions and the transformed Hamiltonian. When calculating the expectation value of the electronic density, we do this from the single-particle wave function:

$$n = \sum_n f_n |\psi_n|^2. \quad (\text{B.1})$$

Note that as in the main text we omit the notation of the real-space coordinate \mathbf{r} . In basis of the real space projectors $|\mathbf{s}\rangle$ this can be written as:

$$n = \sum_n f_n \langle \psi_n | |\mathbf{s}\rangle \langle \mathbf{s} | | \psi_n \rangle. \quad (\text{B.2})$$

As mentioned in the main text, to ease the computational difficulties the frozen core approximation is typically applied. This means that the expectation value must be split into a term calculating the (system independent) expectation value for the frozen core orbitals and the free valence wave functions:

$$n = \sum_n^{\text{core}} \langle \psi_n^c | |\mathbf{s}\rangle \langle \mathbf{s} | | \psi_n^c \rangle + \sum_n^{\text{val}} f_n \langle \psi_n | |\mathbf{s}\rangle \langle \mathbf{s} | | \psi_n \rangle \quad (\text{B.3})$$

where we have specifically denoted the core orbitals as ψ_n^c and the summations now run over core and valence states separately. The first term is part of the atomic basis setup. The last term is numerically easier to evaluate with the smooth wave functions and we therefore apply the transformation to the expectation value as we did in eq. 2.19:

$$n = \sum_n^{\text{core}} \langle \psi_n^c | |\mathbf{s}\rangle \langle \mathbf{s} | | \psi_n^c \rangle + \sum_n^{\text{val}} f_n \langle \tilde{\psi}_n | \hat{T}^\dagger | |\mathbf{s}\rangle \langle \mathbf{s} | \hat{T} | \tilde{\psi}_n \rangle. \quad (\text{B.4})$$

We now split the transformation operator \hat{T} as in the main text: $\hat{T} = (1 + \hat{T}^a)$, however before we insert this in expression above we realise that, since the smooth wave function can be expanded as a linear combinations of partial waves with coefficients \tilde{p}_i^a , $\tilde{\phi}_i^a$ and \tilde{p}_i^a must constitute a complete set, so can the transformation operator confined to the augmentation sphere:

$$\hat{T}^a = \sum_i \hat{T}^a | \tilde{\phi}_i^a \rangle \langle \tilde{p}_i^a |. \quad (\text{B.5})$$

Now, since $|\mathbf{s}\rangle$ simply maps any state $\langle\psi||\mathbf{s}\rangle \rightarrow \psi$ by inserting this and the above form of the transformation operator we immediately find that we get two terms, as we would expect. These are simply the core- and (smooth) valence densities respectively: $\sum_n^{\text{core}} |\psi_n^c|^2 + \sum_n^{\text{val}} f_n |\tilde{\psi}_n|^2$ plus a correction term that in fact includes the projector function overlaps: $P_{i,n}^a = \langle\tilde{p}_i^a||\psi_n\rangle$. By carefully carrying out the analysis of the remaining terms one finds that the final expression for the expectation value of the electronic density take the following form:

$$n = \sum_n^{\text{core}} |\psi_n^c|^2 + \sum_n^{\text{val}} f_n |\tilde{\psi}_n|^2 + \sum_{a,i_1,i_2} f_n \langle\tilde{\psi}_n||\tilde{p}_{i_1}^a\rangle \langle\tilde{p}_{i_2}^a||\tilde{\psi}_n\rangle \left(\phi_{i_1}^a \phi_{i_2}^a - \tilde{\phi}_{i_1}^a \tilde{\phi}_{i_2}^a \right), \quad (\text{B.6})$$

where we have used the expansion of the smooth wave functions into partial waves in eq. 2.21 and we notice that $D_{i_1,i_2}^a = f_n \langle\tilde{\psi}_n||\tilde{p}_{i_1}^a\rangle \langle\tilde{p}_{i_2}^a||\tilde{\psi}_n\rangle$. This gives the form of the electronic density within the PW mode in GPAW from the smooth wave functions.

APPENDIX C

Derivation of a State-Dependent Scissors-Operator within the Plane-Wave Description

In the following is presented the generalized state-dependent (k -point, band) within the PW formalism of GPAW, for example, but not limited to, improve the description of interlayer orbital hybridisation of van der Waals heterostructures. This is done by finding an analytical expression for the correction to the DFT Hamiltonian to obtain the desired eigenvalue correction for each state, which here is taken to be the difference between the GGA and G0W0 eigenvalues for each freestanding monolayer. To do this we consider the evaluation of the eigenvalues from the GPAW Hamiltonian, eq. 2.26:

$$\epsilon_{nk} = \langle \tilde{\psi}_{nk} | \hat{H} | \tilde{\psi}_{nk} \rangle, \quad (\text{C.1})$$

with $\tilde{\psi}_{nk}$ being the pseudo wave function with band index (n) and k -point index (k). It follows that, adding a correction $M_{i_1 i_2}^a$ to eq. 2.27, will give a correction to the eigenvalues corresponding to:

$$\Delta\epsilon_{nk} = \sum_{i_1, i_2}^a \langle \tilde{\psi}_{nk} | \tilde{P}_{i_1}^a \rangle M_{i_1 i_2}^a \langle \tilde{P}_{i_2}^a | \tilde{\psi}_{nk} \rangle, \quad (\text{C.2})$$

or defining the expansion coefficients: $P_{nkj}^a = \langle \tilde{\psi}_{nk} | \tilde{P}_j^a \rangle$ we get:

$$\Delta\epsilon_{nk} = \sum_{i_1, i_2}^a P_{nki_1}^a M_{i_1 i_2}^a (P_{nki_2}^a)^*. \quad (\text{C.3})$$

We now seek a generalized form of $M_{i_1 i_2}^a$. For each of the 2D layers in the van der Waals heterostructure we want to apply a correction to each state (band and k -point), corresponding to the difference between the PBE eigenvalue and the G0W0 quasi-particle energy for the freestanding monolayer. For each layer we will denote this by: $\Delta E_{nk}^d = E_{nk}^{\text{GW}} - E_{nk}^{\text{GGA}}$, where d is the layer index, and the corrections for each state in the van der Waals heterostructure is then the collection of the corrections to all layers:

$E_{nk} = \sum_d R_{nk}^d E_{nk}^d$, where R_{nk}^d is the mapping between the states in each monolayer and the states in the van der Waals heterostructure. To find $M_{i_1 i_2}^a$ we start out by minimising the (squared) error (to be denoted Ω) between the actual corrections contributed by $M_{i_1 i_2}^a$ in the Hamiltonian, eq. C.3, and the desired corrections, ΔE_{nk} :

$$\Omega = \sum_{nk} \sum_{i_1, i_2}^a \left[P_{nki_1}^a M_{i_1 i_2}^a \left(P_{nki_2}^a \right)^* - \Delta E_{nk} \right]^2. \quad (\text{C.4})$$

Differentiating Ω with respect to $M_{i_1 i_2}^a$ and equalling zero, simplifying, and rearranging this can be put on the form:

$$\sum_{nk} \left(P_{nki_1}^a \right)^* P_{nki_2}^a \Delta E_{nk} + c.c. = \sum_{nk} \sum_{i_1, i_2}^a M_{i_1 i_2}^a P_{nki_1}^a \left(P_{nki_2}^a \right)^* \left(P_{nki_1}^{a'} \right)^* P_{nki_2}^{a'} + c.c., \quad (\text{C.5})$$

where *c.c.* denotes the complex conjugate. This equation only involves the difference in PBE eigenvalues and G0W0 quasi-particle energies for each monolayer and the expansion coefficients from which $M_{i_1 i_2}^a$ can be determined, by inverting the equation for each set (i_1, i_2, a) to determine $M_{i_1 i_2}^a$.

APPENDIX D

Effect of the Tamm-Dancoff Approximation on the BSE Absorption Spectra of 2D TMD Monolayers

In fig. D.1 is shown the BSE absorption spectrum for freestanding monolayer MoS₂ within the Tamm-Dancoff approximation (black) and without invoking the Tamm-Dancoff approximation (grey). The calculations is carried out without including spin-orbit effects and only excitations from the two highest valence bands to the two lowest conduction bands are considered. The absorption spectrum is calculated with respect to the G0W0 quasi-particle band gap. In agreement with previous observations [108], we find a negligible difference for the absorbance with/without the Tamm-Dancoff approximations with an overall slightly higher oscillator strength within the Tamm-Dancoff approximation. Overall, the result in fig. D.1 shows the small effect of the off-diagonal coupling terms in the full BSE Hamiltonian between the positive energy and negative energy excitations, and thus validates the use of this approximation, at least for 2D TMD monolayers. To underline the computational advantage of employing the Tamm-Dancoff approximation, we list some computation details. We stress that both the full BSE calculation and the BSE calculation within the Tamm-Dancoff approximation has been run on the same number of cores for the k-point and pair-orbital decomposition. For the full BSE calculation the BSE Hamiltonian consists of 59904 pair orbitals and took 27 hours to complete. Within the Tamm-Dancoff approximation the number of pair orbitals is reduced to 14976 and the computational time is reduced by over a factor of 10: to about 2½ hours. Note the reduction of the number of pair orbitals exactly equals a factor of 4 as expected since we only consider the $\{vc\}$ entry of the two-particle BSE Hamiltonian within the Tamm-Dancoff approximation. These computational details excellently shows the reduced size of the BSE Hamiltonian within the Tamm-Dancoff approximation (as explained in the main text in chapter 3), and the non-linear relation between the computational time required to diagonalise a matrix and the size of the matrix.

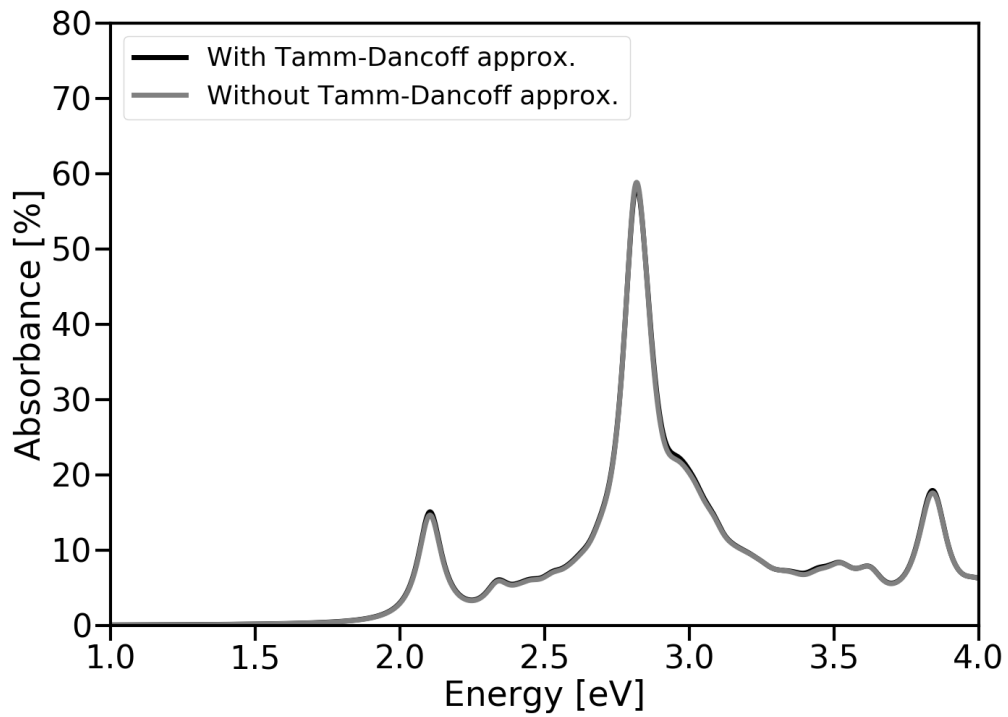


Figure D.1: Absorption spectrum of monolayer MoS₂ calculated within the BSE approximation. The BSE eigenvalues are evaluated for the excitations from the two highest valence bands to the two lowest conduction bands without the effect of spin-orbit coupling. This is done within the Tamm-Dancoff approximation (black) and without invoking the Tamm-Dancoff approximation (grey). The spectrum is calculated with respect to the G0W0 quasi-particle band gap.

APPENDIX E

Quasi-Particle Ionisation Potentials and Electron Affinities from GLLB-SC and PBE

In this appendix we briefly explore the idea that accurate G0W0 quasi-particle ionisation potentials and electron affinity energies can be computationally feasibly obtained by combining the PBE band gap center with the GLLBSC electronic band gap size. As shown in chapter 5, while the PBE functional significantly underestimates the electronic band gap, compared to the quasi-particle band gap calculated with the G0W0 approximation, it accurately predicts the center of the electronic band gap with respect to the vacuum energy. On the other hand the GLLBSC (which includes the derivative discontinuity in its estimate of the electronic band gap), provides a on average good description of the size of the electronic band gap, but fails to predict the exact position of the ionisation potential and electron affinity level accurately. Thus the knowledge of the PBE band gap center and the GLLBSC band gap size could potentially give a good description of the G0W0 quasi-particle band edges. In fig. E.1 (left) we plot the difference between the G0W0 ionisation potential and the PBE VBM in blue and similarly the difference between the G0W0 electron affinity and the PBE CBM. This is done for all materials in the C2DB where a G0W0 calculation have been performed. On the right plot of fig. E.1 we plot the same difference, where the PBE band edges have been symmetrically shifted according the difference between the PBE and the GLLBSC electronic band gaps. Comparing the PBE band edge energies with G0W0 quasi-particle electron ionisation and electron affinity energy, we find that this overestimates (underestimates) the ionisation energy (electron affinity) by on average around 1 eV (0.7 eV) with a significant standard deviation of the ionisation potential up to more than 1 eV. Including the shift of the PBE band edges defined by the GLLBSC electronic band gaps is found to significantly improve the description of the ionisation potential and electron affinity energies. Including this shift the ionisation potential (electron affinity) is centered around -0.3 eV (-0.1 eV) with standard deviations less than 0.6 eV. While this method is not suitable to provide accurate predictions of single systems, it can with advantage be used in larger screening studies where accurate many-body calculations cannot be afforded to be carried out.

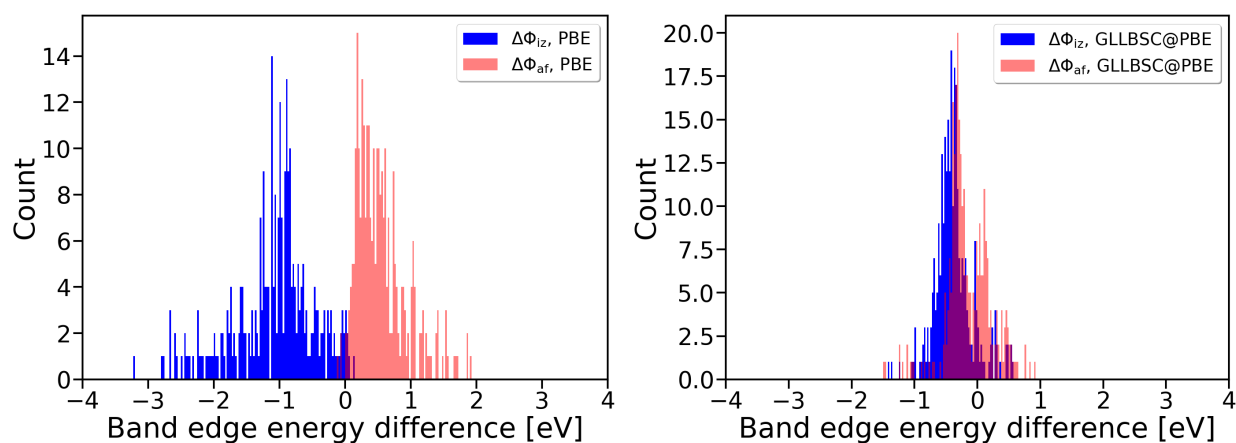


Figure E.1: Left: Difference between the G0W0 ionisation potential and the PBE VBM in blue ($\Delta\Phi_{iz}$) and similarly the difference between the G0W0 electron affinity and the PBE CBM in red ($\Delta\Phi_{af}$). Right: same as left, where the PBE band edges have been symmetrically shifted according the difference between the PBE and the GLLBSC electronic band gaps.

Bibliography

- [1] URL: <http://nomad-repository.eu/>.
- [2] URL: <https://data.nist.gov/od/id/mds2-2147>.
- [3] Evgeny M Alexeev et al. “Resonantly hybridized excitons in moiré superlattices in van der Waals heterostructures”. In: *Nature* 567.7746 (2019), pp. 81–86.
- [4] Kirsten Andersen, Simone Latini, and Kristian S Thygesen. “Dielectric genome of van der Waals heterostructures”. In: *Nano letters* 15.7 (2015), pp. 4616–4621.
- [5] RL Anderson. “Germanium-gallium arsenide heterojunctions [letter to the editor]”. In: *IBM Journal of Research and Development* 4.3 (1960), pp. 283–287.
- [6] Ferdi Aryasetiawan and Olle Gunnarsson. “The GW method”. In: *Reports on Progress in Physics* 61.3 (1998), p. 237.
- [7] Marco Bernardi, Maurizia Palummo, and Jeffrey C Grossman. “Extraordinary sunlight absorption and one nanometer thick photovoltaics using two-dimensional monolayer materials”. In: *Nano letters* 13.8 (2013), pp. 3664–3670.
- [8] David Bohm and David Pines. “A collective description of electron interactions: III. Coulomb interactions in a degenerate electron gas”. In: *Physical Review* 92.3 (1953), p. 609.
- [9] David Bohm and David Pines. “A collective description of electron interactions. I. Magnetic interactions”. In: *Physical Review* 82.5 (1951), p. 625.
- [10] Sven Borghardt et al. “Engineering of optical and electronic band gaps in transition metal dichalcogenide monolayers through external dielectric screening”. In: *Physical Review Materials* 1.5 (2017), p. 054001.
- [11] Max Born and Robert Oppenheimer. “Zur quantentheorie der molekeln”. In: *Annalen der physik* 389.20 (1927), pp. 457–484.
- [12] Yuan Cao et al. “Unconventional superconductivity in magic-angle graphene superlattices”. In: *Nature* 556.7699 (2018), pp. 43–50.
- [13] Fabio Caruso et al. “Benchmark of GW approaches for the GW 100 test set”. In: *Journal of chemical theory and computation* 12.10 (2016), pp. 5076–5087.
- [14] Andres Castellanos-Gomez et al. “Local strain engineering in atomically thin MoS₂”. In: *Nano letters* 13.11 (2013), pp. 5361–5366.

- [15] Andres Castellanos-Gomez et al. “Spatially resolved optical absorption spectroscopy of single-and few-layer MoS₂ by hyperspectral imaging”. In: *Nanotechnology* 27.11 (2016), p. 115705.
- [16] Ivano E Castelli et al. “New light-harvesting materials using accurate and efficient bandgap calculations”. In: *Advanced Energy Materials* 5.2 (2015), p. 1400915.
- [17] F. Ceballos et al. “Highly Efficient and Anomalous Charge Transfer in van der Waals Trilayer Semiconductors”. In: *Nano. Lett.* 17 (2017), pp. 1623–1628.
- [18] Frank Ceballos et al. “Probing Charge Transfer Excitons in a MoSe₂-WS₂ van der Waals Heterostructure”. In: *Nanoscale* 7.41 (2015), pp. 17523–17528.
- [19] Xiaolong Chen et al. “Widely tunable black phosphorus mid-infrared photodetector”. In: *Nature communications* 8.1 (2017), pp. 1–7.
- [20] YC Cheng et al. “Spin-Orbit-Induced Spin Splittings in Polar Transition Metal Dichalcogenide Monolayers”. In: *Europhys. Lett.* 102.5 (2013), p. 57001.
- [21] Alexey Chernikov et al. “Exciton binding energy and nonhydrogenic Rydberg series in monolayer WS₂”. In: *Physical review letters* 113.7 (2014), p. 076802.
- [22] Ming-Hui Chiu et al. “Spectroscopic signatures for interlayer coupling in MoS₂-WSe₂ van der Waals stacking”. In: *ACS nano* 8.9 (2014), pp. 9649–9656.
- [23] Hiram J Conley et al. “Bandgap engineering of strained monolayer and bilayer MoS₂”. In: *Nano letters* 13.8 (2013), pp. 3626–3630.
- [24] Pierluigi Cudazzo, Ilya V Tokatly, and Angel Rubio. “Dielectric screening in two-dimensional insulators: Implications for excitonic and impurity states in graphene”. In: *Physical Review B* 84.8 (2011), p. 085406.
- [25] Stefano Curtarolo et al. “AFLOW: an automatic framework for high-throughput materials discovery”. In: *Computational Materials Science* 58 (2012), pp. 218–226.
- [26] Adolfo De Sanctis et al. “Strain-engineered inverse charge-funnelling in layered semiconductors”. In: *Nature communications* 9.1 (2018), pp. 1–7.
- [27] Cory R Dean et al. “Boron nitride substrates for high-quality graphene electronics”. In: *Nature nanotechnology* 5.10 (2010), pp. 722–726.
- [28] Thorsten Deilmann and Kristian Sommer Thygesen. “Interlayer trions in the MoS₂/WS₂ van der Waals heterostructure”. In: *Nano letters* 18.2 (2018), pp. 1460–1465.
- [29] R Del Sole, Lucia Reining, and RW Godby. “GWF approximation for electron self-energies in semiconductors and insulators”. In: *Physical Review B* 49.12 (1994), p. 8024.
- [30] Claudia Draxl and Matthias Scheffler. “The NOMAD laboratory: from data sharing to artificial intelligence”. In: *Journal of Physics: Materials* 2.3 (2019), p. 036001.

- [31] JE Enkovaara et al. “Electronic structure calculations with GPAW: a real-space implementation of the projector augmented-wave method”. In: *Journal of physics: Condensed matter* 22.25 (2010), p. 253202.
- [32] HY Fan. “Temperature dependence of the energy gap in semiconductors”. In: *Physical Review* 82.6 (1951), p. 900.
- [33] Hui Fang et al. “Strong interlayer coupling in van der Waals heterostructures built from single-layer chalcogenides”. In: *Proceedings of the National Academy of Sciences* 111.17 (2014), pp. 6198–6202.
- [34] Vladimir Fock. “Näherungsmethode zur Lösung des quantenmechanischen Mehrkörperproblems”. In: *Zeitschrift für Physik* 61.1-2 (1930), pp. 126–148.
- [35] Fontana Marcio et al. “Electron-hole transport and photovoltaic effect in gated MoS₂ Schottky junctions”. In: *Scientific Reports* 3 (Apr. 2013), p. 1634. DOI: 10.1038/srep01634;10.1038/srep01634.
- [36] Tobias Förster, Peter Krüger, and Michael Rohlfing. “Two-dimensional topological phases and electronic spectrum of Bi₂Se₃ thin films from G W calculations”. In: *Physical Review B* 92.20 (2015), p. 201404.
- [37] RH Friend and AD Yoffe. “Electronic properties of intercalation complexes of the transition metal dichalcogenides”. In: *Advances in Physics* 36.1 (1987), pp. 1–94.
- [38] Bálint Fülöp et al. “Exfoliation of Single Layer BiTeI Flakes”. In: *2D Mater.* 5.3 (2018), p. 031013.
- [39] M Gajdoš et al. “Linear optical properties in the projector-augmented wave methodology”. In: *Physical Review B* 73.4 (2006), p. 045112.
- [40] Luca M Ghiringhelli et al. “Big data of materials science: critical role of the descriptor”. In: *Physical review letters* 114.10 (2015), p. 105503.
- [41] Feliciano Giustino. “Electron-phonon interactions from first principles”. In: *Reviews of Modern Physics* 89.1 (2017), p. 015003.
- [42] Pranjal Kumar Gogoi et al. “Layer Rotation-Angle-Dependent Excitonic Absorption in van der Waals Heterostructures Revealed by Electron Energy Loss Spectroscopy”. In: *ACS nano* 13.8 (2019), pp. 9541–9550.
- [43] Dorothea Golze, Marc Dvorak, and Patrick Rinke. “The GW compendium: A practical guide to theoretical photoemission spectroscopy”. In: *Frontiers in chemistry* 7 (2019).
- [44] David J Griffiths. “Introduction to quantum mechanics”. In: (2005).
- [45] Stefan Grimme et al. “A consistent and accurate ab initio parametrization of density functional dispersion correction (DFT-D) for the 94 elements H-Pu”. In: *The Journal of chemical physics* 132.15 (2010), p. 154104.
- [46] Andreas Grüneis et al. “Ionization potentials of solids: the importance of vertex corrections”. In: *Physical review letters* 112.9 (2014), p. 096401.

- [47] I Guilhon et al. “Out-of-plane excitons in two-dimensional crystals”. In: *Physical Review B* 99.16 (2019), p. 161201.
- [48] Qiushi Guo et al. “Black phosphorus mid-infrared photodetectors with high gain”. In: *Nano letters* 16.7 (2016), pp. 4648–4655.
- [49] Sten Hastrup et al. “The Computational 2D Materials Database: high-throughput modeling and discovery of atomically thin crystals”. In: *2D Materials* 5.4 (2018), p. 042002.
- [50] SJ Haigh et al. “Cross-sectional imaging of individual layers and buried interfaces of graphene-based heterostructures and superlattices”. In: *Nature materials* 11.9 (2012), pp. 764–767.
- [51] Lars Hedin. “New method for calculating the one-particle Green’s function with application to the electron-gas problem”. In: *Physical Review* 139.3A (1965), A796.
- [52] Lauri Himanen et al. “DScribe: Library of descriptors for machine learning in materials science”. In: *Computer Physics Communications* 247 (2020), p. 106949.
- [53] Pierre Hohenberg and Walter Kohn. “Inhomogeneous electron gas”. In: *Physical review* 136.3B (1964), B864.
- [54] Mark S Hybertsen and Steven G Louie. “Electron correlation in semiconductors and insulators: Band gaps and quasiparticle energies”. In: *Physical Review B* 34.8 (1986), p. 5390.
- [55] Mark S Hybertsen and Steven G Louie. “First-principles theory of quasiparticles: calculation of band gaps in semiconductors and insulators”. In: *Physical review letters* 55.13 (1985), p. 1418.
- [56] John David Jackson. *Classical electrodynamics*. 1999.
- [57] Luis A Jauregui et al. “Electrical control of interlayer exciton dynamics in atomically thin heterostructures”. In: *Science* 366.6467 (2019), pp. 870–875.
- [58] Line Jelver et al. “Determination of Schottky barriers in 2D heterophase devices”. In: *arXiv preprint arXiv:1911.09521* (2019).
- [59] Frank Jensen. *Introduction to computational chemistry*. John wiley & sons, 2017.
- [60] Chenhao Jin et al. “Observation of moiré excitons in WSe₂/WS₂ heterostructure superlattices”. In: *Nature* 567.7746 (2019), pp. 76–80.
- [61] John Edward Jones. “On the determination of molecular fields.—II. From the equation of state of a gas”. In: *Proceedings of the Royal Society of London. Series A, Containing Papers of a Mathematical and Physical Character* 106.738 (1924), pp. 463–477.
- [62] Kohei Kanetani et al. “Ca intercalated bilayer graphene as a thinnest limit of superconducting C₆Ca”. In: *Proceedings of the National Academy of Sciences* 109.48 (2012), pp. 19610–19613.

- [63] Ouri Karni et al. “Infrared Interlayer Exciton Emission in MoS₂/WSe₂ Heterostructures”. In: *Physical Review Letters* 123.24 (2019), p. 247402.
- [64] Emmanouil Kioupakis et al. “First-principles calculations of indirect Auger recombination in nitride semiconductors”. In: *Physical Review B* 92.3 (2015), p. 035207.
- [65] Walter Kohn and Lu Jeu Sham. “Self-consistent equations including exchange and correlation effects”. In: *Physical review* 140.4A (1965), A1133.
- [66] Tjalling Koopmans. “Über die Zuordnung von Wellenfunktionen und Eigenwerten zu den einzelnen Elektronen eines Atoms”. In: *Physica* 1.1-6 (1934), pp. 104–113.
- [67] Sabine Körbel, Miguel AL Marques, and Silvana Botti. “Stable hybrid organic–inorganic halide perovskites for photovoltaics from ab initio high-throughput calculations”. In: *Journal of Materials Chemistry A* 6.15 (2018), pp. 6463–6475.
- [68] Sabine Körbel et al. “Benchmark many-body GW and Bethe–Salpeter calculations for small transition metal molecules”. In: *Journal of chemical theory and computation* 10.9 (2014), pp. 3934–3943.
- [69] Ryogo Kubo. “Statistical-mechanical theory of irreversible processes. I. General theory and simple applications to magnetic and conduction problems”. In: *Journal of the Physical Society of Japan* 12.6 (1957), pp. 570–586.
- [70] Korina Kuhar et al. “High-throughput computational assessment of previously synthesized semiconductors for photovoltaic and photoelectrochemical devices”. In: *ACS Energy Letters* 3.2 (2018), pp. 436–446.
- [71] M Kuisma et al. “Kohn-Sham potential with discontinuity for band gap materials”. In: *Physical Review B* 82.11 (2010), p. 115106.
- [72] Jens Kunstmann et al. “Momentum-space indirect interlayer excitons in transition-metal dichalcogenide van der Waals heterostructures”. In: *Nature Physics* 14.8 (2018), pp. 801–805.
- [73] Ask Hjorth Larsen et al. “Localized atomic basis set in the projector augmented wave method”. In: *Physical Review B* 80.19 (2009), p. 195112.
- [74] Simone Latini, Thomas Olsen, and Kristian Sommer Thygesen. “Excitons in van der Waals heterostructures: The important role of dielectric screening”. In: *Physical Review B* 92.24 (2015), p. 245123.
- [75] Simone Latini et al. “Interlayer excitons and band alignment in MoS₂/hBN/WSe₂ van der Waals heterostructures”. In: *Nano letters* 17.2 (2017), pp. 938–945.
- [76] Yilei Li et al. “Measurement of the optical dielectric function of monolayer transition-metal dichalcogenides: MoS₂, MoSe₂, WS₂, and WSe₂”. In: *Physical Review B* 90.20 (2014), p. 205422.
- [77] Jiajun Linghu et al. “High-throughput computational screening of vertical 2D van der Waals heterostructures for high-efficiency excitonic solar cells”. In: *ACS applied materials & interfaces* 10.38 (2018), pp. 32142–32150.

- [78] Xiao-Chen Liu et al. “Spontaneous self-intercalation of copper atoms into transition metal dichalcogenides”. In: *Science advances* 6.7 (2020), eaay4092.
- [79] Ang-Yu Lu et al. “Janus Monolayers of Transition Metal Dichalcogenides”. In: *Nat. Nanotechnol.* 12.8 (Aug. 2017), pp. 744–749. ISSN: 1748-3387. DOI: 10.1038/nnano.2017.100. URL: <https://www.nature.com/nnano/journal/v12/n8/full/nnano.2017.100.html>.
- [80] Keld T Lundgaard et al. “mBEEF-vdW: Robust fitting of error estimation density functionals”. In: *Physical Review B* 93.23 (2016), p. 235162.
- [81] Dinh Hoa Luong et al. “Tunneling Photocurrent Assisted by Interlayer Excitons in Staggered van der Waals Hetero-Bilayers”. In: *Adv. Mater.* 29.33 (2017), p. 1701512.
- [82] Kin Fai Mak et al. “Atomically thin MoS₂: a new direct-gap semiconductor”. In: *Physical review letters* 105.13 (2010), p. 136805.
- [83] Philipp Merkl et al. “Ultrafast Transition from Intra-to Interlayer Exciton Phases in a Van Der Waals Heterostructure”. In: *CLEO: Science and Innovations*. Optical Society of America. 2019, JTh5C–6.
- [84] Alejandro Molina-Sánchez et al. “Temperature-dependent excitonic effects in the optical properties of single-layer MoS₂”. In: *Physical Review B* 93.15 (2016), p. 155435.
- [85] Jens Jørgen Mortensen, Lars Bruno Hansen, and Karsten Wedel Jacobsen. “Real-space grid implementation of the projector augmented wave method”. In: *Physical Review B* 71.3 (2005), p. 035109.
- [86] Nicolas Mounet et al. “Two-dimensional materials from high-throughput computational exfoliation of experimentally known compounds”. In: *Nature nanotechnology* 13.3 (2018), pp. 246–252.
- [87] Shinichiro Mouri et al. “Thermal Dissociation of Inter-Layer Excitons in MoS₂/MoSe₂ Hetero-Bilayers”. In: *Nanoscale* 9.20 (2017), pp. 6674–6679.
- [88] Dmitrii Nabok, Andris Gulans, and Claudia Draxl. “Accurate all-electron G₀W₀ quasiparticle energies employing the full-potential augmented plane-wave method”. In: *Physical Review B* 94.3 (2016), p. 035118.
- [89] Kostya S Novoselov et al. “Electric field effect in atomically thin carbon films”. In: *science* 306.5696 (2004), pp. 666–669.
- [90] Thomas Olsen et al. “Simple screened hydrogen model of excitons in two-dimensional materials”. In: *Physical review letters* 116.5 (2016), p. 056401.
- [91] Runhai Ouyang et al. “SISSO: A compressed-sensing method for identifying the best low-dimensional descriptor in an immensity of offered candidates”. In: *Physical Review Materials* 2.8 (2018), p. 083802.
- [92] Wolfgang Pauli. “Über den Zusammenhang des Abschlusses der Elektronengruppen im Atom mit der Komplexstruktur der Spektren”. In: *Zeitschrift für Physik* 31.1 (1925), pp. 765–783.

- [93] Thomas Garm Pedersen et al. “Exciton Ionization in Multilayer Transition-Metal Dichalcogenides”. In: *New J. Phys.* 18.7 (2016), p. 073043.
- [94] N Peimyoo et al. “Laser-writable high-k dielectric for van der Waals nanoelectronics”. In: *Science advances* 5.1 (2019), eaau0906.
- [95] John P Perdew, Kieron Burke, and Matthias Ernzerhof. “Generalized gradient approximation made simple”. In: *Physical review letters* 77.18 (1996), p. 3865.
- [96] David Pines and David Bohm. “A collective description of electron interactions: II. Collective vs individual particle aspects of the interactions”. In: *Physical Review* 85.2 (1952), p. 338.
- [97] J Pollmann et al. “Ab initio calculations of structural and electronic properties of prototype surfaces of group IV, III–V and II–VI semiconductors”. In: *Applied surface science* 104 (1996), pp. 1–16.
- [98] LA Ponomarenko et al. “Tunable metal–insulator transition in double-layer graphene heterostructures”. In: *Nature Physics* 7.12 (2011), pp. 958–961.
- [99] Diana Y Qiu, H Felipe, and Steven G Louie. “Optical spectrum of MoS₂: many-body effects and diversity of exciton states”. In: *Physical review letters* 111.21 (2013), p. 216805.
- [100] Zhizhan Qiu et al. “Giant gate-tunable bandgap renormalization and excitonic effects in a 2D semiconductor”. In: *Science advances* 5.7 (2019), eaaw2347.
- [101] Ashwin Ramasubramaniam. “Large excitonic effects in monolayers of molybdenum and tungsten dichalcogenides”. In: *Physical Review B* 86.11 (2012), p. 115409.
- [102] Filip A Rasmussen et al. “Efficient many-body calculations for two-dimensional materials using exact limits for the screened potential: Band gaps of mos₂, h-bn, and phosphorene”. In: *Physical Review B* 94.15 (2016), p. 155406.
- [103] Antoni Rogalski, Krzysztof Adamiec, and Jaroslaw Rutkowski. *Narrow-gap semiconductor photodiodes*. Vol. 77. SPIE Press, 2000.
- [104] Michael Rohlfing, Peter Krüger, and Johannes Pollmann. “Quasiparticle band-structure calculations for C, Si, Ge, GaAs, and SiC using Gaussian-orbital basis sets”. In: *Physical Review B* 48.24 (1993), p. 17791.
- [105] David A Ruiz-Tijerina and Vladimir I Fal’ko. “Interlayer hybridization and moiré superlattice minibands for electrons and excitons in heterobilayers of transition-metal dichalcogenides”. In: *Physical Review B* 99.12 (2019), p. 125424.
- [106] James E Saal et al. “Materials design and discovery with high-throughput density functional theory: the open quantum materials database (OQMD)”. In: *Jom* 65.11 (2013), pp. 1501–1509.
- [107] Edwin E Salpeter and Hans Albrecht Bethe. “A relativistic equation for bound-state problems”. In: *Physical Review* 84.6 (1951), p. 1232.
- [108] Tobias Sander, Emanuele Maggio, and Georg Kresse. “Beyond the Tamm-Dancoff approximation for extended systems using exact diagonalization”. In: *Physical Review B* 92.4 (2015), p. 045209.

- [109] Jonathan Schmidt et al. “Recent advances and applications of machine learning in solid-state materials science”. In: *npj Computational Materials* 5.1 (2019), pp. 1–36.
- [110] Michiel J van Setten et al. “GW 100: Benchmarking G 0 W 0 for molecular systems”. In: *Journal of chemical theory and computation* 11.12 (2015), pp. 5665–5687.
- [111] M Shishkin and G Kresse. “Self-consistent G W calculations for semiconductors and insulators”. In: *Physical Review B* 75.23 (2007), p. 235102.
- [112] William Shockley and Hans J Queisser. “Detailed balance limit of efficiency of p-n junction solar cells”. In: *Journal of applied physics* 32.3 (1961), pp. 510–519.
- [113] John Clarke Slater. “The self consistent field and the structure of atoms”. In: *Physical Review* 32.3 (1928), p. 339.
- [114] Andrea Splendiani et al. “Emerging photoluminescence in monolayer MoS2”. In: *Nano letters* 10.4 (2010), pp. 1271–1275.
- [115] A Steinhoff, TO Wehling, and M Rösner. “Frequency-dependent substrate screening of excitons in atomically thin transition metal dichalcogenide semiconductors”. In: *Physical Review B* 98.4 (2018), p. 045304.
- [116] Engin Torun et al. “Interlayer and intralayer excitons in MoS2/WS2 and MoSe2/WSe2 heterobilayers”. In: *Physical Review B* 97.24 (2018), p. 245427.
- [117] Mads L Trolle, Thomas G Pedersen, and Valerie Vénard. “Model dielectric function for 2D semiconductors including substrate screening”. In: *Scientific reports* 7 (2017), p. 39844.
- [118] Jiayu Wan et al. “Tuning two-dimensional nanomaterials by intercalation: materials, properties and applications”. In: *Chemical Society Reviews* 45.24 (2016), pp. 6742–6765.
- [119] Chen Wang et al. “Monolayer atomic crystal molecular superlattices”. In: *Nature* 555.7695 (2018), pp. 231–236.
- [120] Kai Wang et al. “Interlayer Coupling in Twisted WSe2/WS2 Bilayer Heterostructures Revealed by Optical Spectroscopy”. In: *ACS Nano* 10.7 (2016), pp. 6612–6622.
- [121] Xuefeng Wang et al. “Atomic-scale clarification of structural transition of MoS2 upon sodium intercalation”. In: *ACS nano* 8.11 (2014), pp. 11394–11400.
- [122] Kirsten T Winther and Kristian S Thygesen. “Band structure engineering in van der Waals heterostructures via dielectric screening: the G Δ W method”. In: *2D Materials* 4.2 (2017), p. 025059.
- [123] Jun Yan, Karsten W Jacobsen, and Kristian S Thygesen. “Optical properties of bulk semiconductors and graphene/boron nitride: The Bethe-Salpeter equation with derivative discontinuity-corrected density functional energies”. In: *Physical Review B* 86.4 (2012), p. 045208.

-
- [124] XL Yang et al. “Analytic solution of a two-dimensional hydrogen atom. I. Non-relativistic theory”. In: *Physical Review A* 43.3 (1991), p. 1186.
- [125] Xuechao Yu et al. “Atomically thin noble metal dichalcogenide: a broadband mid-infrared semiconductor”. In: *Nature communications* 9.1 (2018), pp. 1–9.
- [126] Shaofan Yuan et al. “Air-stable room-temperature mid-infrared photodetectors based on hBN/black arsenic phosphorus/hBN heterostructures”. In: *Nano letters* 18.5 (2018), pp. 3172–3179.
- [127] Changjian Zhang et al. “Absorption of light by excitons and trions in monolayers of metal dichalcogenide Mo S 2: Experiments and theory”. In: *Physical Review B* 89.20 (2014), p. 205436.
- [128] Jing Zhang et al. “Janus Monolayer Transition-Metal Dichalcogenides”. In: *ACS Nano* 11.8 (Aug. 2017), pp. 8192–8198. ISSN: 1936-086X. DOI: 10.1021/acsnano.7b03186.

